DEVELOPMENT OF A MICROREACTOR SYSTEM FOR UNSTEADY-STATE FISCHER-TROPSCH SYNTHESIS

by

Gary Ken Whiting

Dissertation submitted to the Faculty of the

Virginia Polytechnic Institute and State University

in partial fulfillment of the requirements for the degree of

DOCTOR OF PHILOSOPHY

in

Chemical Engineering

APPROVED:

Arthur M. Squires, Co-Chairman

Y. A. Liu, Co-Chairman

Gerhard H. Beyer

Mark E. Davis

Kenneth Konrad

March, 1985

Blacksburg, Virginia

DEVELOPMENT OF A MICROREACTOR SYSTEM FOR UNSTEADY-STATE FISCHER-TROPSCH SYNTHESIS

by

Gary Ken Whiting

Committee Chairmen: Arthur M. Squires
Y.A. Liu
Chemical Engineering

(ABSTRACT)

Vibrofluidized microreactor systems have been developed for studies of unsteady-state Fischer-Tropsch synthesis. This development is aimed at preventing carbon deposition on a fused-iron catalyst in a novel reactor called the "heat-tray." This reactor involves a supernatant gas flowing over a shallow fluidized bed of catalyst particles. Three systems were built: (1) a vibrofluidized-bed microreactor system for obtaining baseline carbon deposition information under industrially important reaction conditions; (2) a sliding-plug vibrofluidized-bed microreactor system for rapid switching of feed gases in the F-T synthesis; and (3) a cold-flow microreactor model for studying the gas mixing characteristics of the sliding-plug vibrofluidized-bed microreactor.

The results show that catalyst defluidization occurred under steady-state synthesis conditions below 395°C using a feed gas of H_2/CO ratio of 2:1 or less. Above 395°C, the probability of hydrocarbon chain growth (α) on the fused-iron catalyst was low enough ($\alpha < 0.50$) to prevent accumulation of high-molecular-weight species that cause defluidization. Carbon deposition was rapid above 395°C when a feed gas of H_2/CO ratio of 2:1 or less was used.

Spent catalyst fractions in the form of free-flowing catalyst and "bugdust" were quantitatively analyzed for carbon and iron. Mössbauer spectroscopic analysis of free-flowing catalyst showed mainly Hägg carbide (χ-Fe_5C_2) and magnetite (Fe_3O_4) with a smaller fraction present as α-Fe. Scanning electron microscopic analysis of the bugdust revealed a mass of highly porous, fine particles with a high carbon content (18-30 wt%).

Cold-flow microreactor model studies show that rapid (on the order of seconds), quantitative switching of feed gases over a vibrofluidized-bed of catalyst could be achieved. Vibrofluidization of the catalyst bed induced little backmixing of feed gas over the investigated flow-rate range of 417 to 1650 actual mm^3/s. Further, cold-flow microreactor model studies showed intense solid mixing when a -150+300 μ bed of fused-iron catalyst was vibrofluidized at 24 cycles per second with a peak-to-peak amplitude of 4 mm.

The development of this microreactor system has provided an easy way of accurately determining integral fluid-bed kinetics in a laboratory reactor. Further, the unique ability of the microreactor system to rapidly switch feed gases over an intensely-mixed solid has important applications in chemical kinetics and reaction engineering.

ACKNOWLEDGMENTS

The research presented in this work was funded by the U.S. Department of Energy, Pittsburgh Energy Technology Center (PETC), under Grant No. DE-FG-82P50791. Dr. of PETC served as the project manager. I wish to acknowledge the Virginia Mining and Minerals Resources and Research Institute for awarding me a fellowship.

I would like to thank the members of my graduate committee for their help and friendship throughout the course of my studies at Virginia Tech. Each member has contributed significantly to my knowledge both in the classroom and in the laboratory. Particularly, I would like to express my thanks to my chairmen Dr. A. M. Squires and Dr. Y. A. Liu. I am deeply indebted to Dr. Squires for the countless hours of discussion required to bring these ideas to fruition. His unceasing optimization and inventive mind kept me going. Similarly, I am extremely grateful to Dr. Liu for his endless help and dedication. The long nights he spent in the laboratory running the rig and his patience in editing this dissertation are testimonials to his concern for his students.

Messrs. , , and deserve thanks for their assistance in completion of my experimental program. The other members of the Novel Fluid-Particle Research Laboratories and the Catalysis group merit thanks for their support and friendship. Thanks are due to Messrs. , and whose consumate skill in machining and fabrication made

this development possible. Thanks to for his help in designing the computer interface and for his help with the cold-flow microreactor system circuits.

Most of all I want to thank my wife, , and our families for their continuous support and encouragement.

Finally, I would like to thank , who I gave ulcers, and , who I gave pneumonia, for their patient and competent typing of the text and figure titles, respectively.

TABLE OF CONTENTS

TABLE OF CONTENTS (Continued)

TABLE OF CONTENTS (Continued)

TABLE OF CONTENTS (Continued)

TABLE OF CONTENTS (Continued)

LIST OF TABLES

LIST OF TABLES (Continued)

LIST OF TABLES (Continued)

LIST OF TABLES (Continued)

LIST OF FIGURES

LIST OF FIGURES (Continued)

LIST OF FIGURES (Continued)

LIST OF FIGURES (Continued)

LIST OF FIGURES (Continued)

LIST OF FIGURES (Continued)

LIST OF FIGURES (Continued)

LIST OF FIGURES (Continued)

LIST OF FIGURES (Continued)

LIST OF FIGURES (Continued)

LIST OF FIGURES (Continued)

LIST OF FIGURES (Continued)

CHAPTER 1

INTRODUCTION

1.1 Technical Background

Fischer-Tropsch (F-T) synthesis involves the reaction of hydrogen and carbon monoxide, typically produced from a coal gasifier, over a transition metal catalyst to produce a wide range of products such as hydrocarbons and oxygenates. A summary of the basic reactions in F-T synthesis and competing reactions is presented in Table 1.1.

The F-T synthesis reactions can be reduced to two general equations involving (1) the F-T conversion, and (2) the water-gas shift reaction:

$$(1)\quad CO + 2H_2 \rightarrow (-CH_2-) + H_2O \qquad \Delta H_R(227°C) = -165.0\ kJ$$

$$(2)\quad CO + H_2O \rightarrow H_2 + CO_2 \qquad \Delta H_R(227°C) = -39.8\ kJ$$

On iron catalysts, the water-gas shift reaction is rapid and the net synthesis reaction becomes:

$$(3)\quad 2CO + H_2 \rightarrow (-CH_2-) + CO_2 \qquad \Delta H_R(227°C) = -204.7\ kJ$$

Competing reactions include direct methane formation, carbon formation, carbide formation and to a lesser degree, coke deposition (see Table 1.1). Carbide formation is initiated as soon as a reduced iron catalyst is exposed to the synthesis gas and it continues until the bulk structure of the iron catalyst is completely carburized. Carbon formation and coke deposition are extremely detrimental to the

TABLE 1.1

Basic Reactions for Fischer-Tropsch Synthesis and Competing Reactions

Basic Reactions	
Paraffin Formation:	$(2n+1)H_2 + nCO \rightarrow C_nH_{2n+2} + nH_2O$
	$(n+1)H_2 + 2nCO \rightarrow C_nH_{2n+2} + nCO_2$
Olefin Formation:	$2nH_2 + nCO \rightarrow C_nH_{2n} + nH_2O$
	$nH_2 + 2nCO \rightarrow C_nH_{2n} + nCO_2$
Oxygenate Formation:	$2nH_2 + nCO \rightarrow C_nH_{2n+1}OH + (n-1)H_2O$
	$(n+1)H_2 + (2n-1)\ CO \rightarrow C_nH_{2n+1}OH + (n-1)CO_2$
Water-Gas Shift:	$CO + H_2O \rightarrow CO_2 + H_2$
Competing Reactions	
Methane Formation:	$CO + 3H_2 \rightarrow CH_4 + H_2O$
Carbon Formation:	$2CO \rightarrow C + CO_2$
Coke Deposition:	$H_2 + CO \rightarrow C + H_2O$
Carbide Formation:[a]	$xM + C \rightarrow M_xC$

[a]Note: "M" is used to denote a catalytic surface site.

operation of F-T synthesis reactors, particularly when operated with iron catalysts. Carbon, in some cases, blocks active catalytic sites, resulting in decreased catalytic activity. In other cases, it creates internal stresses in a catalyst particle, fragmenting the particle. The fragmented particles, in turn, have a higher surface area, leading to greater catalytic activity.

Work on the Fischer-Tropsch synthesis has gone on for more than sixty years. Two excellent reviews of historical developments of the F-T synthesis have been given by Pichler (1952) and Anderson (1984), and only a brief summary of these developments is presented below.

In 1923, Franz Fischer and Hans Tropsch reported their results of high-pressure experiments reacting hydrogen with carbon monoxide over an alkalized iron catalyst to produce a liquid mixture of hydrocarbons and oxygen-containing compounds. Their discovery led to the investigation in 1935-36 of the medium-pressure synthesis by Fischer and Pichler using iron and cobalt catalysts (Fischer and Pichler, 1936). The first four F-T production plants were constructed in 1936 by Ruhrchemie. By 1944, the potential capacity of F-T plants in Germany had reached 700,000 tons per year using fixed-bed reactors and cobalt catalysts.

The pioneering work of Fischer and Tropsch had also led to the initiation of F-T synthesis research by a number of groups outside of Germany. For example, the British Fuel Research Station started work on F-T synthesis in 1935. The United States Government conducted some F-T synthesis research before World War II and activity in this area

was increased in 1944 by the Synthetic Liquid Fuels Act. The U.S. Bureau of Mines was in charge of this early effort. In 1948, a F-T production plant was built in Brownsville, Texas by Hydrocarbon Research, Inc. using fixed-fluidized-bed reactors. The plant's design capacity was 360,000 tons per year but this level of production was never reached because of technical problems. After its first owner went through bankruptcy in 1953, its second owner shut the plant down in 1958 because production costs were too high. An excellent review of the developmental efforts and operational problems in the Brownsville plant can be found in Squires (1982).

South Africa became involved in large-scale F-T synthesis in 1955, when SASOL One came on stream at Sasolburg producing 270,000 tons per year of F-T products. Both Arbeitsgemeinschaft (ARGE) fixed-bed and Kellogg "Synthol" entrained-bed reactors were used at SASOL One. (SASOL is now the South African Coal, Oil and Gas Co., Ltd.) After the Arab oil embargo and the resulting oil crisis of 1973, SASOL made plans for expansion. In 1980 and 1982, the SASOL Two and SASOL Three plants, respectively, came on stream at Secunda. Each of these plants was about 10 times bigger than SASOL One. An improved version of the entrained-bed reactor was used for these nearly identical plants.

Over the course of development of F-T synthesis processes, four major types of reactors have been used for large scale synthesis. These reactors include: fixed bed, circulating-fluidized bed, fixed-fluidized bed, and liquid-phase or slurry reactors. Typical operating conditions and parameters for these reactors systems are shown in Table 1.2.

TABLE 1.2

Operating Conditions and Parameters for Major Types of Reactors Used for Fischer-Tropsch Synthesis

Reactor Type	Operating Temperature (°C)	Operating Pressure (kPa)	Fresh Feed H_2/CO Ratio	H_2/CO Ratio with Recycle	Recycle to Fresh Feed Ratio	Fresh Feed Space Velocity (hr^{-1})	Total Conversion (%)	Catalyst Type	Catalyst Size	References
Sasol Fixed Bed	220-250	2700	1.3-2.0	-	2.5	500	65-70	Precipitated Iron	2-5 mm	Dry (1982) Frohning et al. (1982)
Sasol Circulating Fluidized Bed	320-360	2000-2500	~2.4	~6.1	2-2.5	500-1000	77-85	Fused Iron	30-150 μm	Dry (1982) Frohning et al. (1982)
Brownsville Fixed-Fluidized Bed	300-350	2500-3000	>2.0	3	1.5	2000-3000	96	Fused Iron	30-150 μm	Frohning et al. (1982)
Rheinpreussen-Koppers Liquid Phase	268	1200	0.67	-	0.6	270	90	Precipitated Iron	1-10 μm	Frohning et al. (1982)
Huff and Satterfield Slurry Phase	232-269	275-1480	0.34-1.81	no recycle		1100-8500	up to 95	Fused Iron	<990 μm	Huff (1982)

A comparison of the advantages and disadvantages attributed to each system is presented in Table 1.3. An ideal F-T reaction process should have the following attributes:

1. it utilizes an inexpensive catalyst such as iron;
2. it has high selectivity to olefinic products;
3. it produces high yields of desired products;
4. it has excellent thermal efficiency;
5. it is simple to operate; and
6. it is compatible with second-generation coal gasifiers producing a synthesis gas of a low H_2/CO ratio ($< 1:1$).

A reactor system with these qualities would greatly improve the economics of the F-T synthesis process at SASOL, for example. The greatest savings would be achieved by replacing the present coal gasifiers with second-generation coal gasifiers. Coal gasification costs are 65% of SASOL's total cost (Chemical and Engineering News, Jan. 7, 1985). Presently, SASOL uses Lurgi gasifiers to supply their fixed- and entrained-bed processes. This is because Lurgi gasifiers are reliable and produce a synthesis gas of a H_2/CO ratio of approximately 2.4:1. These Lurgi gasifiers are thermally inefficient and lose 19% of the carbon in the coal as methane (Gray et al., 1981 and LeBlanc et al., 1981). The most thermally-efficient coal gasifiers operate at low steam to oxygen ratios and produce a synthesis gas of a low H_2/CO ratio. An example of a thermally-efficient second-generation coal gasifier is the Lurgi slagging gasifier developed by the British Gas Corporation which produces a synthesis gas with a H_2/CO ratio of 0.5:1 (Shinnar and Kuo, 1978).

TABLE 1.3

A Comparison of Advantages and Disadvantages Attributed to Four Major Reactor Systems

Reactors	Advantages	Disadvantages
Fixed Bed	- can utilize feed gases of low H_2/CO ratios - ease of operation	- large recycle - operates at low temperatures - low space-time yield - produces paraffinic product and waxes - poor thermal efficiency
Entrained Bed	- good removal of heat of reaction - produces product of high olefin content	- must use a feed gas of high H_2/CO ratio - high recycle rate - difficult operation
Fixed-Fluidized Bed	- high space-time yield - good heat transfer - produces product of high olefin content - simple operation - reduced plant costs	- must use a high H_2/CO ratio - carbon deposition possible - agglomeration possible - particle attrition possible - produces low-molecular-weight products
Liquid-Phase or Slurry Reactor	- can use CO-rich feed gases (low H_2/CO ratio) - good heat transfer - produces product of high olefin content - low mechanical strength catalyst can be used	- catalyst activity decreases more rapidly

Of the reactor types summarized in Tables 1.2 and 1.3, the slurry reactors seem to possess the most desirable attributes. Slurry reactors have high thermal efficiency and can produce high yields of olefinic products. Perhaps a more important attribute is the fact that slurry reactors can operate with the synthesis gas of low H_2/CO ratios produced by second-generation coal gasifiers. The reason for this seems to lie in the degree of liquid backmixing and the water-gas shift activity of the iron catalysts typically used. In particular, Satterfield and Huff (1982a) state that as long as the H_2/CO usage ratio in the reactor is less than that in the feed gas, the H_2/CO ratio in the reactor will increase with the extent of conversion. Under these conditions, water is shifted to form hydrogen via the water-gas shift reaction. Because the slurry reactors possess a high degree of backmixing, and because the catalyst moves intimately with the liquid, the effective H_2/CO ratio in the reactor is relatively uniform. Consequently, the H_2/CO ratio of the liquid surrounding the catalyst, even at the feed-gas inlet, is much higher than the H_2/CO ratio in the feed gas under these conditions.

1.2 Scope of the Study

A dry fluidized-bed alternative to the slurry reactor for processing synthesis gas of low H_2/CO ratios has been proposed by Squires and described, for example, in Liu et al. (1982). Figure 1.1 shows a conceptual diagram of the shallow fluidized-bed "heat-tray" reactor for F-T synthesis from a synthesis gas of low H_2/CO ratio.

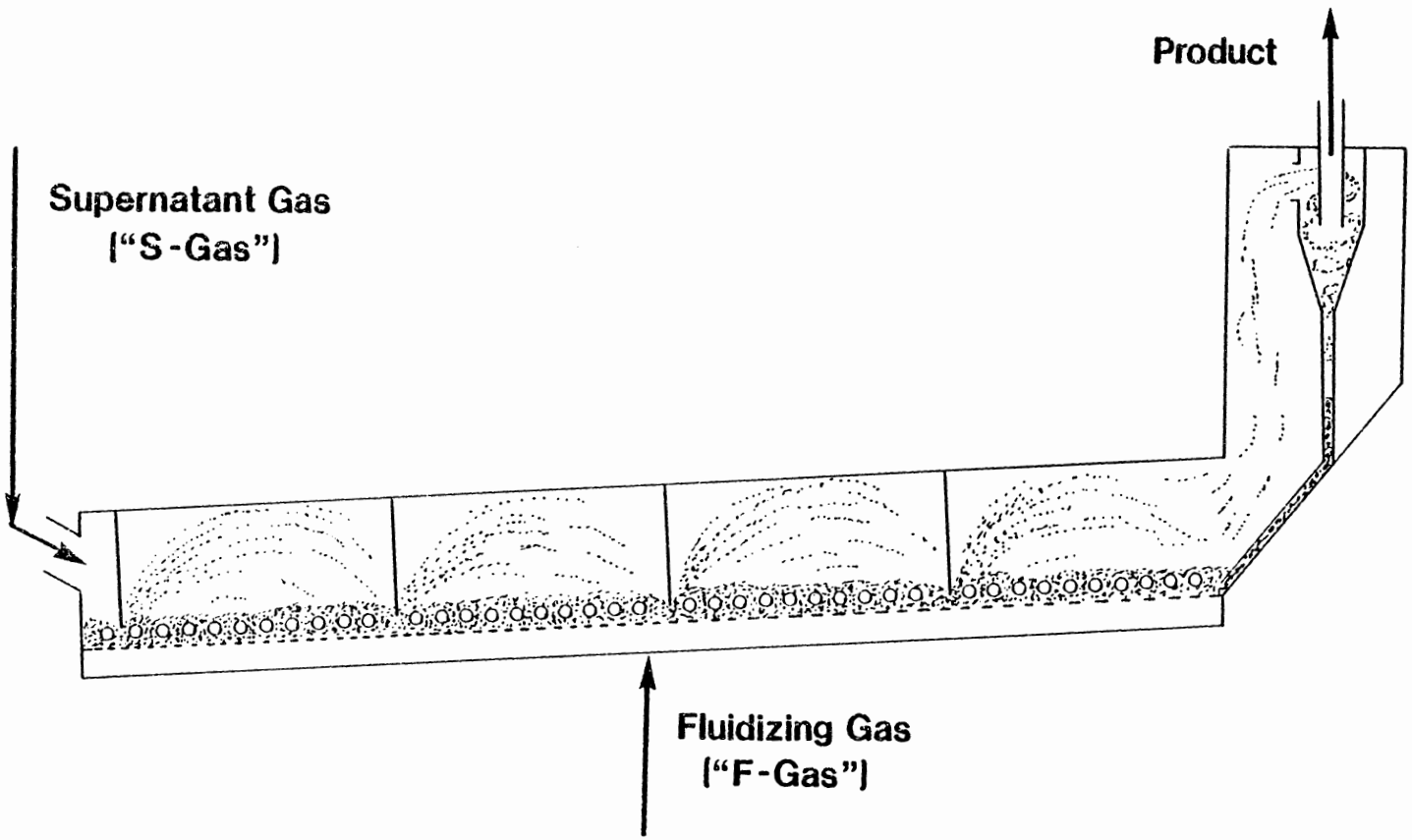

Figure 1.1. An Illustration of the Concept of a "Heat-Tray" Reactor for Fischer-Tropsch Synthesis from a Low H_2:CO Gas in a Dry Fluidized Bed.

As shown in the figure, a shallow bed of iron catalyst less than 100 mm deep is fluidized by a relatively low flow rate of a hydrogen-rich fluidizing gas, or F-gas. The heat of reaction is removed by raising steam in heat-exchange tubes passing through this shallow-fluidized bed. A much higher flow rate of a synthesis gas of low H_2/CO ratio passes over the freeboard region of the shallow bed in the supernatant space. This second gas stream is called the supernatant gas, or S-gas. The S-gas flow is directed downward into the shallow-bed through the use of baffles at different sections of the bed, throwing iron catalyst upward into the supernatant space. In this way, a typical catalyst particle will spend a long period of time in the shallow bed (H_2-rich F-gas region), and will be exposed only momentarily to the CO-rich S-gas in the supernatant space. It is hoped that by alternately subjecting the iron catalyst to a high flow rate of CO-rich S-gas for a short period and a low flow rate of H_2-rich F-gas for a long period, carbon formation on the catalyst can be reduced.

Other probable advantages of the heat-tray reactor include:

1. better bed-to-surface heat transfer characteristic of shallow fluidized beds, resulting in the use of far less heat-transfer surface;
2. low extent of catalyst attrition in shallow fluidized beds;
3. low pressure-drop characteristic of shallow fluidized beds;
4. high yields of olefinic products;

5. decrease in agglomeration due to alternate exposure to H_2-rich fluidizing gas; and

6. treatment of synthesis gas containing high levels of steam without rapid loss of catalyst activity.

The main objective of this study is to develop a microreactor system to simulate the conditions that the iron catalyst will experience in the heat-tray reactor. In this way, the extreme expense of constructing and operating a full-scale dry fluidized-bed system will be avoided. The microreactor system will serve as a tool for studies of cabon deposition on iron catalysts.

In order to properly simulate the catalyst's experience in the heat-tray reactor, the microreactor must be able to do two things. First, it must allow rapid switching (on the order of seconds) between H_2-rich and CO-rich synthesis gas under industrially significant reaction conditions. Secondly, it must maintain the iron catalyst in a fluidized state. Bock (1984) has recently emphasized the previously known, but rarely understood, fact that the type of reactor, and therefore the catalyst history, has a significant effect on the reaction kinetics. It is desirable, therefore, to use a vibrofluidized-bed integral reactor rather than a fixed-bed differential reactor.

This study has been broken down into three major parts:

1. Utilization of a vibrofluidized-bed microreactor system to obtain steady-state carbon deposition information on a fused-iron catalyst;

2. Gas mixing and catalyst vibrofluidization studies in a cold-flow vibrofluidized-bed microreactor model; and

3. Design and construction of a vibrofluidized-bed microreactor system for unsteady-state Fischer-Tropsch synthesis.

The contents of the rest of this dissertation are as follows. A detailed review of the relevant literature on Fischer-Tropsch synthesis, unsteady-state methods for kinetics studies and vibrofluidized beds is presented in Chapter 2. In Chapter 3, an introduction to experimental approaches to both steady-state and unsteady-state F-T synthesis is described. Chapter 4 presents the experimental apparatus, procedure and results of steady-state F-T synthesis in the vibrofluidized-bed microreactor. Chapter 5 reports the results from gas mixing and catalyst vibrofluidization studies in a cold-flow vibrofluidized-bed microreactor model. Chapter 6 descibes the design and construction of the vibrofluidized-bed microreactor system for unsteady-state F-T synthesis from a low H_2:CO gas. Finally, Chapter 7 summarizes the general conclusions and significant results of this study and recommends some direction for further research.

CHAPTER 2

LITERATURE REVIEW

This chapter presents a detailed review of relevant literature on the Fischer-Tropsch synthesis, unsteady-state methods, and vibrofluidized beds. The specific topics covered include the following:

1. thermodynamics of the reactions involved in F-T synthesis;
2. fused-iron catalysts used for F-T synthesis;
3. proposed reaction mechanisms of F-T synthesis;
4. kinetics of the F-T synthesis over iron;
5. product selectivity shown by F-T synthesis over iron catalysts;
6. carburization of iron catalysts after exposure to mixtures of hydrogen and carbon monoxide;
7. carbon deposition on iron catalysts during F-T synthesis;
8. unsteady-state methods used both for kinetics studies and conversion and selectivity improvement; and
9. description and use of vibrofluidized beds.

2.1 Fischer-Tropsch Synthesis Reactions

2.1.1 Thermodynamics

Thermodynamic considerations with respect to Fischer-Tropsch synthesis are thoroughly described in the literature (Storch et al., 1951; Anderson, 1956; Dry, 1981; Anderson, 1984). Thermodynamics, of course, sets only the possible equilibrium concentrations of reactants

and products as expressed in terms of the equilibrium constant. Anderson (1984) has reviewed thermodynamic knowledge in this area developed over the past thirty years. Most F-T synthesis reactions are exothermic and result in a reduction in the number of moles in the system. Because of this exothermicity, the equilibrium constant for the reaction decreases as the temperature is raised. Increasing operating pressure results in greater equilibrium conversions due to the molar contraction of the reactions.

Standard Gibbs free energies and standard heats of reaction as functions of temperature of formation of products from hydrogen and carbon monoxide have been calculated by Anderson (1956). It was concluded from the calculations that formation of a large assortment of molecules was thermodynamically feasible up to 400°C, and to a lesser extent at temperatures between 400 and 500°C. Likely products include branched and unbranched olefins and paraffins, alcohols, ketones and organic acids. Anderson et al. (1976) also determined the equilibrium products of multicomponent systems of reactants and typical F-T synthesis products. The main conclusion derived from these calculations was that methane would likely be the principle product of reaction unless a selective catalyst was used.

Based on thermodynamic feasibility studies, Anderson (1956) points out that primary products of F-T synthesis may undergo further reactions. A summary of potential reactions follows:

1. isomerization
2. hydrogenation of olefins

3. incorporation of olefins
4. hydrogenolysis of paraffins
5. limited incoropration of paraffins
6. dehydration of alcohols
7. incorporation of alcohols
8. limited incorporation of elemental and carbidic carbon.

While thermodynamics dictate the maximum possible conversion at equilibrium, the intrinsic kinetics determine how close the reaction actually comes to equilibrium. Dry (1981) illustrates this fact by comparing experimental selectivity data obtained using an iron catalyst to results thermodynamically predicted by Christoffel et al. (1978). Table 2.1 shows the comparison at 327°C and 16 atm. with a feed gas H_2/CO ratio of 2 to 1. Thermodynamics predict a large production of methane and negligible higher hydrocarbons. Actual experimental results show that significant amounts of hydrocarbons are produced.

2.1.2 Fused-Iron Catalysts

Fused-iron catalysts have long been used in F-T synthesis because of their low cost, relatively high catalytic activity and their physical strength. They are used at SASOL in the high-temperature entrained-bed Synthol reactors. In addition they have been used in many laboratory studies and therefore have been well characterized.

Table 2.1

A Comparison Between Experimental Selectivity Data (Dry, 1981) and Thermodynamically Predicted Results (Christoffel, et al., 1978) for Fischer-Tropsch Synthesis from a Feed Gas of H_2/CO Ratio of 2:1 at 327°C and 16 atm.

Compound	Experimental Selectivity Data (Wt%)	Thermodynamically Predicted Data (g/m^3_n, H_2+CO)[a]
CH_4	10	170
C_2H_4	4	1.7×10^{-7}
C_2H_6	4	9.6×10^{-3}
C_3H_6	12	1.1×10^{-9}
C_3H_8	2	2.0×10^{-6}
C_5H_{12}	2	1.4×10^{-13}
C_2H_5OH	2	3.0×10^{-9}

[a] m^3_n is a cubic meter of gas measured at standard conditions.

Fused-iron catalysts are typically made by electrically fusing millscale from a steel works in the presence of promoters. Structural promoters, such as oxides of Ca, Mn, Mg, Ti and Al, form a solid solution with Fe_3O_4. These promoters serve to increase and stabilize the surface area of the iron catalyst. In addition, the aforementioned structural promoters allow for good distribution of alkali promoters such as K_2O. Another structural promoter, silica, doesn't dissolve in Fe_3O_4 and restricts alkali promoters from dissolving in the solid solutions (Dry and Ferreria, 1967).

Group I metals are used as chemical promoters in iron catalysts, because they sharply change the selectivity and also modify the catalyst's activity somewhat. Alkali affects the basicity of the catalyst through interaction with structural promoters. As the catalyst becomes more basic, more acids are produced in the synthesis, the selectivity shifts toward longer chain molecules, and the product slate becomes more olefinic.

Alkali promotion increases the iron catalyst's activity at low concentrations. After a certain concentration is reached, no increase in activity is experienced; instead a decrease in activity is found (Dry, 1981). The shift in selectivity has been explained by Dry et al. (1969) through studies of heats of adsorption. At low surface coverage, the alkali (for example, K_2O) decreases the initial heat of adsorption of hydrogen while increasing the heat of adsorption of carbon monoxide. This, in turn, decreases the surface coverage by

hydrogen and strengthens the iron-carbon bond. In general, hydrogenation of olefins and chain-termination probability are thought to decrease because of the decrease in surface hydrogen. The detailed explanation of this phenomenon varies depending on the mechanism assumed (Dry et al., 1969).

Alkali promoters may also increase carbon deposition due to the increased rate of CO dissociation (Dry et al., 1970). Carbon deposition will be discussed further in Section 2.1.7.

In the past, alkali promoters were thought to also decrease the poisoning of iron sites by sulfur (Anderson et al., 1965). Recently, Dry (1981) has stated that in SASOL's experience, alkali promoters had a diminutive effect on the sulfur poisoning of iron catalysts.

Nitriding of fused-iron catalysts by ammonia after reduction has been shown to increase catalyst activity, while making them more resistant to oxidation and carbon deposition (Anderson et al., 1950). Extensive investigations into nitriding have been carried out at the U.S. Bureau of Mines and are reviewed by Anderson (1980).

Before synthesis is initiated over a fused-iron catalyst, the catalyst must be reduced in order to develop the desirable large surface area. Pure hydrogen has been found to be most effective in reducing the catalyst as opposed to carbon monoxide or a mixture of hydrogen and carbon monoxide (Dry, 1981). The typical temperature range used for reduction is 350 to 450°C. Structural promoters such as MgO and Al_2O_3, slow the rate of reduction but provide for increased surface area. Dry (1981) shows that increasing the hydrogen space velocity increases the

initial rate of reduction of fused-iron catalyst, as illustrated in Figure 2.1.

There are a number of other factors which affect the reduction of fused-iron catalysts. For example, if water is not removed rapidly, it will limit the forward reaction in the reduction equation:

$$4H_2 + Fe_3O_4 \rightarrow 3Fe + 4H_2O.$$

Hall et al. (1950) found that the surface area of a fused Fe_3O_4-MgO-K_2O catalyst increased linearly with the extent of reaction, while the average pore volume remained constant. They also concluded that increasing the reduction temperature significantly increased the pore diameter.

Changes in the surface and composition of fused-iron catalyst during reaction will be discussed in connection with carburization of iron catalysts in Section 2.1.6.

2.1.3 Reaction Mechanisms

In recent years, several detailed reviews of the Fischer-Tropsch reaction mechanism have been published (Anderson, 1984; Frohning et al., 1982; Vannice, 1976, 1982; Rofer-DePoorter, 1981; Dry, 1981; Bell, 1981; Mutterties and Stein, 1979; Ponec, 1978; Schulz and Zein el Deen, 1977; Biloen, 1976). Table 2.2 summarizes the key features of these published reviews, and only a broad overview of the subject will be presented below.

Generally speaking, three mechanisms have provided the basis for mechanistic theories for F-T synthesis. All three mechanisms assume

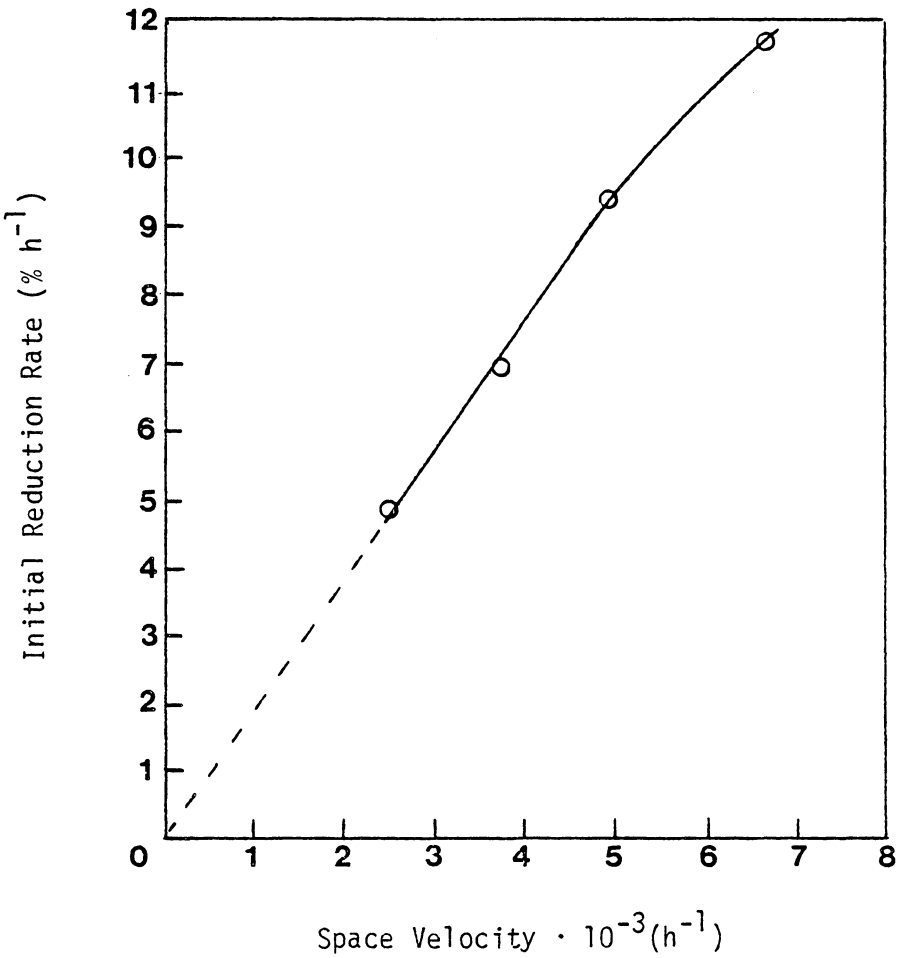

Figure 2.1. The Effect of Increasing Hydrogen Space-Velocity on Initial Rate of Reduction of a Fused-Iron Catalyst (Dry, 1981).

TABLE 2.2

A Summary of Key Features of Recent Reviews of Fischer-Tropsch Reaction Mechanisms

Reviewers	Mechanistic Theory Proposedπ	CO Adsorption After Initial Adsorption on Catalysts Surface	Hydrocarbon Chain Growth Mechanism
Anderson (1984)	No	Associate or Dissociative	A summary of possible mechanisms is given
Frohning et al. (1982)	No	Associative	A summary of possible mechanisms is given
Vannice (1976, 1982)	No	Metal Dependent	A summary of possible mechanisms is given
Rofer-DePoorter (1981)	Yes, Unifying	Two types of Associative and Dissociative Possible	A network of reaction paths
Dry (1981)	Yes, Unifying	Associative with Dissociative Possible	CH_2 Interaction or CO Insertion
Bell (1981)	Yes	Dissociative	CH_2 Insertion
Muetterties α Stein (1979)	Yes	Dissociative	CH_x Insertion
Ponec (1978)	Yes	Dissociative	CO Insertion and Partial Hydrogenolysis
Schulz α Zein el Deen (1977)	Yes	Associative	Ligand Insertion
Biloen (1976)	Yes	Associative	Chain jumps from one site to a $-CH_2$ occupied site

adding carbon species to a growing chain one at a time in their chain growth steps. These mechanisms are illustrated in Figure 2.2

2.1.3.1 Carbide Mechanism

The carbide mechanism was introduced by Fischer (1926, 1932) and supported by Rideal (1939). Metal carbides are formed from carbon produced via adsorbed CO. These carbides are subsequently reduced to methylene groups. Chain propogation occurs by insertion of a methylene group into a metal-alkyl bond. Shortcomings of this description include its lack of prediction of oxygenate formation and the recent finding that only methane is produced when bulk metal carbides are hydrogenated (Raupp and Delgass, 1979c).

2.1.3.2 Enolic or Bureau of Mines Mechanism

Associatively-chemisorbed CO is hydrogenated to hydroxylated species. Chain propogation occurs by the elimination of water. This mechanism was proposed at the U.S. Bureau of Mines in the early 1950's (Anderson, 1956). Since that time, little substantive proof for this mechanism has been forwarded in the literature.

2.1.3.3 Direct Insertion or Complex Chemistry Mechanism

A version of the direct insertion mechanism was first proposed by Pichler and Schulz (1970). Henrici-Olivé and Olivé (1976) more recently have supported this type of mechanism.

Carbon monoxide, which is associatively chemisorbed on the catalyst surface, inserts into a metal hydride forming chain stable surface carbonyl compounds; and propogation continues with further insertion

Carbide Mechanism

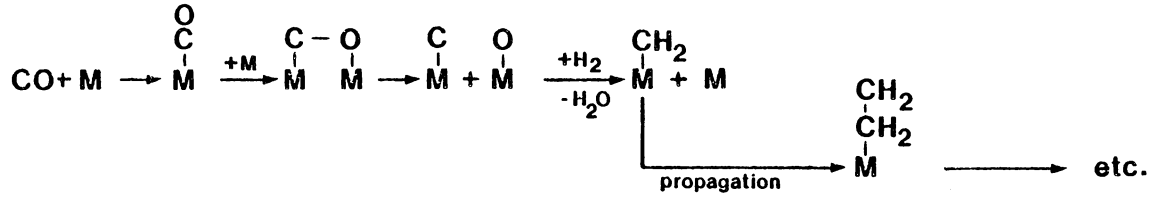

Enolic Mechanism

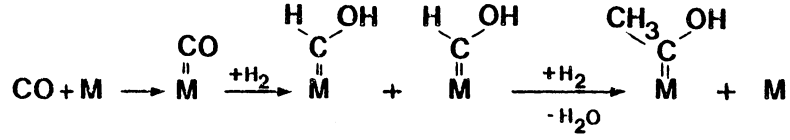

Direct Insertion Mechanism

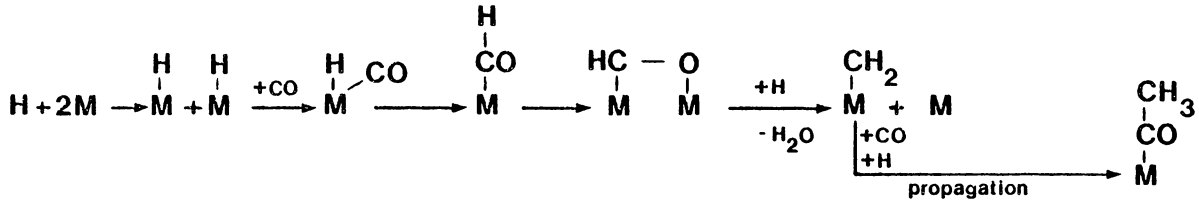

Figure 2.2. Three Basic Mechanisms that have been Proposed for F-T Synthesis: In the Figure, "M" Represents a Catalytic Surface Site.

of CO. This mechanism has been likened to CO insertion into metal-carbon bonds during homogeneous catalytic carbonylation and hydroformylation. Anderson (1984) points out, however, that homogeneous reactions such as these "never initiate a growing chain and usually only add one carbon to a reactive molecule." Therefore, the similarity in mechanistic steps is in doubt.

2.1.3.4 Hybrid and Unifying Mechanisms

In the past ten years, several hybrid or unifying theories for the mechaism of F-T synthesis have been suggested. These unifying mechanisms most often place strong emphasis of the dissociative chemisorption of CO, as in the carbide theory. These mechanisms also emphasize the insertion of undissociated CO to form oxygenated species, as in the direct insertion mechanism. Dry (1981) has proposed just such a scheme.

Rofer-DePoorter (1981) made a systematic analysis of mechanistic steps in a recent review. The resulting unifying mechanistic theory consists of a collection of elementary reactions that have been sufficiently supported in the literature. This approach resulted in a "network" of reaction paths, many of a parallel nature. Because of the complex nature of the unifying mechanism, further details should be obtained by referring to Rofer-DePoorter (1981).

Bell (1981) has proposed a mechanism as illustrated in Figure 2.3. In the mechanism, methylene insertion is treated as the major pathway for the formation of nonoxygenated species. Oxygenates are produced via CO insertion into metal-alkyl bonds. Secondary reactions, such as reincorporation of ethylene, take place if the gas-phase concentration of hydrocarbons is significantly high.

In a review published in 1978, Ponec has proposed a combined mechanism for F-T synthesis. This mechanism involves dissociation of CO followed by the formation of CH_x species. Chain growth occurs by CO insertion and partial hydrogenolysis. Ponec's theory allows for the elimination of oxygen in the growing chain and suggests that chain termination occurs by hydrogenation.

In view of the studies supporting the different aspects of the above mechanisms, it would seem likely that the true mechanism for F-T synthesis involves a number of contributing intermediates. Furthermore, some substances are likely to be produced via several reaction pathways. The degree to which various pathways contribute is a function of reaction conditions as well as catalyst makeup, including metal, support and promoters.

2.1.4 Kinetics over Iron Catalysts

Several short reviews of recent advances in F-T kinetics can be found in the literature (Frohning et al., 1982; Dry, 1981; Vannice, 1976) as well as more detailed reviews of earlier work (Storch et al., 1951; Anderson, 1956; Anderson et al., 1964). In a recent paper, Huff and Satterfield (1984b) present a summary of kinetic studies for F-T

1. $CO + S \rightleftharpoons CO_S$

2. $CO_S + S \rightleftharpoons C_S + O_S$

3. $H_2 + 2S \rightleftharpoons 2H_S$

4a. $O_S + H_2 \text{ (or } 2H_2) \rightarrow H_2O + 2S$

4b. $O_S + CO \text{ (or } CO_S) \rightarrow CO_2 + 2S$

5. $C_S + H_S \rightleftharpoons CH_S + S$

6. $CH_S + H_S \rightleftharpoons CH_{2_S} + S$

7. $CH_{2_S} + H_S \rightleftharpoons CH_{3_S} + S$

8. $CH_{3_S} + H_S \rightleftharpoons CH_4 + S$

9. $CH_{3_S} + CH_{2_S} \rightarrow CH_3CH_{2_S} + S$

10. $CH_3CH_{2_S} + CH_{2_S} \rightarrow CH_3CH_2CH_{2_S} + S$

11. $CH_3CH_{2_S} + S \rightarrow CH_2CH_2 + H_S$

12. $CH_3CH_{2_S} + H_s \rightarrow CH_3CH_3 + 2S$

FIGURE 2.3: A Mechanism Proposed By Bell (1981) For Hydrocarbon Synthesis From CO and H_2 Over Group VIII Metals. Active Surface Sites Are Given As "S" And "S'".

A. METHANOL

$$S{=}C{=}O + S' \leftrightarrow S{=}C{=}O\cdots S'$$

$$S{=}C{=}O\cdots S' + H_S \leftrightarrow \underset{H}{S{-}C{=}O}\cdots S'$$

$$\underset{H}{S{-}C{=}O}\cdots S' + H_S \leftrightarrow S{-}CH_2{-}O{-}S'$$

$$S{-}CH_2{-}O{-}S' + H_S \rightarrow CH_3{-}O{-}S' + 2S$$

$$CH_3{-}O{-}S' + H_S \rightarrow CH_3OH + S' + S$$

B. ALDEHYDES

$$S{-}R + CO_S \rightarrow \underset{R}{S{-}C{=}O}$$

$$\underset{R}{S{-}C{=}O} + H_S \rightarrow RCHO + 2S$$

C. HIGHER ALCOHOLS

$$\underset{R}{S{-}C{=}O} + S' \leftrightarrow \underset{R}{S{-}C{=}O}\cdots S'$$

$$\underset{R}{S{-}C{=}O}\cdots S' + H_S \leftrightarrow S{-}CRH{-}O{-}S'$$

$$S{-}CRH{-}O{-}S' + H_S \rightarrow RCH_2{-}O{-}S' + 2S$$

$$RCH_2{-}O{-}S' + H_S \rightarrow RCH_2OH + S' + S$$

Figure 2.3 (Continued)

synthesis over iron catalysts. This is reproduced here as Table 2.3 with the results of Huff and Satterfield's studies in a slurry reactor included.

When examining the tabulated information, it is important to keep in mind several considerations as to why a uniform picture is not presented. The intrinsic rate expressions and reported activation energies may differ from one study to the other for many reasons. Some discrepencies may be caused by differences in catalyst makeup, interference by transport limitations, or merely because of reactor types. Catalyst effects, such as supports, promoters and pretreatment, undoubtedly could contribute to the inconsistency in the reported results. Vannice (1975) has determined the intrinsic activities of Group VIII metals in an attempt to clarify the relative activities of these metals.

An omnipresent problem in kinetic studies of F-T synthesis is the formation of wax which remains on the surface and in the pores of the catalyst. Diffusional resistances caused by the liquid wax will be reflected in the apparent activation energy. The activation energy is, of course, deduced from the effect of temperature on reaction rate. An example of diffusional resistance is given by the apparent activation energy of 37 kJ/mol reported by Thomson et al. (1980) for a flame-sprayed iron catalyst in a Berty-reactor. Huff (1982) points out that this activation energy is approximately one-half of the typical value reported, possibly indicating pore diffusional resistances.

TABLE 2.3

A Summary of Kinetic Studies for Fischer-Tropsch Synthesis Over Iron Catalysts. Reproduced from Huff and Satterfield (1984b).

Catalyst	Reactor	Range of Condition: temp °C	pressure MPa	$(H_2/CO)_{feed}$
iron	vapor-phased, fixed bed	π	π	π
reduced fused-iron promoted with K_2O and MgO	vapor,phase, fixed- and fluidized beds and liquid-phase, surry bed	250-320	2.2-4.2	2.0
reduced and nitrided iron	vapor-phase, fixed bed	π	π	π
reduced, nitrided fused-iron	vapor-phase, fixed-bed	225-240	2.2	0.25-2.0
fused-iron (NH_3 syn. cat.) and precipitated iron promoted with MgO, Cu, and K_2CO_3	vapor-phase, fixed-bed	200-280	10	CO to H_2O feed of 3:1
reduced and nitrided fused-iron promoted with Cr_2O_3, SiO_2 MgO, and K_2O	vapor-phase, fixed-bed	225-255	2.2	0.25-2.0
reduced fused-iron promoted with K_2O, Al_2O_3 and SiO_2	vapor-phase, fixed-bed operated in a differential mode	225-265	1.0-1.8	1.2-7.2
15% Fe/Al_2O_3	vapor-phase fixed-bed operated in a differential mode	220-255	0.1	3.0
iron	vapor phase, fixed bed	π	π	π
reduced, nitrided fused-iron promoted with K_2O, Al_2O_3, SiO_2	gradientless, fixed-bed	250-315	2.0	2.0
plasma-sprayed iron onto flat plates	vapor-phased, recirculating reactor	250-300	0.77-3.1	1.5-3.9
reduced precipitated iron with Cu and K_2O	vapor-phase, fixed-bed	220-270	1.0-2.0	1.0-6.0
reduced fused-iron promoted with Al_2O_3, K_2O, CaO and SiO_2	continuous flow slurry reactor	232-263	0.45-1.48	0.55-1.81

TABLE 2.3 (Continued)

Catalyst	intrinsic kinetics: rate expression	act. energy, kJ/mol	reference
iron	$R_{hydrocarbon} = aP_{H_2}^{2}P_{CO}$	88	Brötz (1949) as reported in Frohning et al. (1952)
reduced fused-iron promoted with K_2O and MgO	$-R_{H_2+CO} = aP_{total}$	79 (est)	Hall et al. (1952)
reduced and nitrided iron	$-R_{H_2+CO} = aP_{H_2}$ for conversions to 60% then $-R_{H_2+CO} = aP_{H_2}/(1+bP_{H_2O}/P_{CO})$	84 for a	Anderson (1956)
reduced, nitrided fused-iron	$-R_{H_2+CO} = aP_{H_2}^{0.6}P_{CO}^{0.4} - bP_{H_2}^{0.5}P_{H_2+CO}$	84 for a and 79 for b	Anderson and Karn (1960)
fused-iron (NH_3 syn. cat.) and precipitated iron promoted with MgO, Cu, and K_2CO_3	$-R_{CO} = aP_{H_2}^{1.5}P_{CO}^{0.2} + bP_{H_2O}^{0.2}P_{CO}^{0.5}$	105 for a and a >> b over range studied	Kölbel et al. (1960)
reduced and nitrided fused-iron promoted with Cr_2O_3, SiO_2 MgO, and K_2O	$-R_{H_2+CO} = aP_{H_2}^{0.66}P_{CO}^{0.34}$	71 to 100	Anderson et al. (1964)
reduced fused-iron promoted with K_2O, Al_2O_3 and SiO_2	$-R_{H_2+CO} = aP_{H_2}$	71	Dry et al. (1972)
15% Fe/Al_2O_3	$R_{hydrocarbon} = aP_{H_2}^{1.1\pm0.1}P_{CO}^{0.1\pm0.1}$	88 ± 4	Vannice (1976): conditions were such that methanation was only significant reaction.
iron	$-R_{H_2+CO} = aP_{H_2}/(1 + bP_{H_2O}/P_{CO})$	63 for a	Dry (1976)
reduced, nitrided fused-iron promoted with K_2O, Al_2O_3, SiO_2	$-R_{H_2+CO} = aP_{H_2}/(1 + bP_{H_2O}/P_{CO})$	84 for a and -8 for b	Atwood and Bennett (1979)
plasma-sprayed iron onto flat plates	$-R_{H_2+CO} = aP_{H_2}/(1 + bP_{H_2O}/P_{CO})$	37 for a and -6 for b	Thomson et al. (1980)
reduced precipitated iron with Cu and K_2)	$-R_{H_2+CO} = aP_{H_2}/P_{CO}^{0.25}$	70 for C_2-C_4 hydrocarbons 92 for CH_4	Feimer et al. (1981)
reduced fused-iron promoted with Al_2O_3, K_2O, CaO and SiO_2	$-R_{H_2+CO} = \frac{ab'P_{CO}P_{H_2}^{2}}{(P_{H_2O}+b'P_{CO}P_{H_2})}$	83	Huff and Satterfield (1984)

Dry (1981) speculates that outside-film diffusional resistances may be the cause of experimental results showing catalytic activity increasing linearly with external surface area. These results were reported for an iron catalyst in a fixed-bed reactor at 220°C under differential conditions.

Huff (1982) points out that the first six studies shown in Table 2.3 were all performed using fixed-bed, vapor-phase, integral reactors. The partial pressures of the gases vary along the axis of the reactor as does the rate of reaction and thus the bed temperature. Imprecise temperature control was not uncommon in the early studies. The above factors contribute to the discrepencies in rate expressions proposed in these six investigations.

Before the recent publication by Huff and Satterfield (1984b), one kinetic rate expression stood out from the rest (Anderson, 1956),

$$-R_{H_2+CO} = \frac{aP_{H_2}}{(1 + bP_{H_2O}/P_{CO})} \qquad (1)$$

This intrinsic kinetic expression for the rate of hydrogen plus carbon monoxide conversion over an iron catalyst was first proposed by Anderson (1956). It had been verified throught the experimental rate data obtained by Dry (1976), Thomson et al. (1980) and Atwood and Bennett (1979), with the latter using a gradientless reactor. However, Huff and Satterfield (1984b, 1984c) have recently published results that deviate from rate expression (1) given above. These researchers studied in detail F-T synthesis in a well-mixed slurry reactor at 232 to

263°C, 0.455 to 1.48 MPa and H_2/CO ratios ranging from 0.55 to 1.81. A wide range of conversion was studied, specifically H_2 conversions from 17 to 68% and CO conversions from 16 to 98%. The catalyst used in this study was a fused-magnetite ammonia-synthesis catalyst promoted with Al_2O_3, K_2O, CaO, and SiO_2. (Note: The same catalyst was used in the present study.) Huff and Satterfield's data did not correlate well with Anderson's expression, Equation (1), at high conversions. Under conditions of high conversion, the partial pressure of water becomes significant in the reacting system. In view of this result, Huff and Satterfield put forth a new intrinsic rate expression, Equation (2), which was derived in part from mechanistic considerations:

$$-R_{H_2+CO} = \frac{ab'P_{CO}P_{H_2}^2}{P_{H_2O} + b'P_{CO}P_{H_2}} \qquad (2)$$

where:

$a = 2.39 \times 10^8 e^{(-19700/RT)}$ $\quad \frac{\mu mol \cdot H_2 + CO \text{ converted}}{g \text{ unreduced catalyst} \cdot min \cdot kPa}$

$b' = 9.50 \times 10^6 (-24000/RT)$ $\quad kPa^{-1}$

T = temperature $\quad K$

R = 1.987 $\quad cal/g\text{-}mole \cdot K$

The only difference between Equation (1) and Equation (2) is that the partial pressure of hydrogen is associated with b in the second equation. If b in Equation (1) is replaced by $1/b'P_{H_2}$, then Equation (2)

is obtained. This additional dependence on hydrogen parital pressure had not been identified before in the literature, since the hydrogen partial pressure was held practically constant in most previous studies. In particular, iron catalysts are very active for the water-gas shift reaction. When the ratio of hydrogen to carbon monoxide used (H_2/CO usage ratio) in the reaction surpasses the ratio of H_2 to CO fed to the reactor, the partial pressure of hydrogen in the reactor may stay constant. Huff and Satterfield attribute this to the contraction of gas in the reactor compensating for the hydrogen consumption, even over the spectrum of conversions. These investigators cite data of Atwood and Bennett (1979). Under conditions of constant total pressure and inlet H_2/CO ratios, the partial pressure of hydrogen was found to be nearly constant for all of the experiments reported by Atwood and Bennett. Satterfield and Huff further suggest that one can vary the hydrogen partial pressure either by varying the total pressure of the system when high H_2/CO ratios are used, or by using low H_2/CO ratios for reactor feed.

Under conditions of low partial pressure of water, Equation (1) and Equation (2) both reduce to the following expression:

$$-R_{H_2+CO} = aP_{H_2} \qquad (3)$$

This was first demonstrated by Anderson (1956) and later confirmed by Dry et al. (1972) in a differential reactor. In another recent publication, Huff and Satterfield (1984c) set bounds on the use of this "first-order" expression, Equation (3). These bounds are expressed primarily in terms

of the degree of conversion; other factors, such as H_2/CO feed ratios which affect the useful range of Equation (3), have not been considered in defining those bounds.

High partial pressures of water normally would exist only under conditions of high conversion on iron catalysts, because of the high activity of the water-gas shift reaction. When water is present, it depresses the rate of reaction through oxidation of the iron and strong adsorption on the catalyst surface. Reymond et al. (1980) have found through the use of transient studies that water competes with carbon monoxide for surface sites. Further, it causes the formation of CO_2 by inducing the reaction of adsorbed oxygen atoms with surface carbon thus reducing the carbon surface coverage. CO_2 plays no direct role in the kinetic rate expression. It does, however, play an important role indirectly via the water-gas shift reaction.

The fact that the rate expression depends only on the partial pressure of hydrogen at low conversions brings to light the influence that the type of laboratory reactor has on the development of the kinetic rate expression. The use of differential reactors simplifies the interpretation of results by reducing conversion per pass and eliminating heat and mass transfer effects. However, unless product recycle is used, differential reactors ignore the possible effect of product-gas partial pressure on the kinetics of the reaction.

It should be noted that Equation (2) is primarily applicable to integral-reactor experiments, while Equation (3) is mainly useful for differential reactor data. This difference is thought to be due in part to the preferential adsorption of CO. The heat of adsorption of CO is

greater than that of hydrogen. Under conditions of low conversion, such as in differential reactors, the partial pressure of hydrogen and carbon monoxide are of the same order of magnitude. Carbon monoxide preferentially adsorbs on the active sites and the rate-controlling step is either hydrogen adsorption or reaction of adsorbed hydrogen with an adsorbed carbon species. Consequently, the partial pressure of hydrogen is the only term found in the rate expression under differential conditions such as Equation (3). Under integral conditions of higher conversions, water is produced and some CO is consumed via the water-gas shift reaction. The partial pressure of carbon monoxide may drop to a level where it becomes rate-controlling and enters the kinetic expression. Finally, the water produced depresses the activity of the catalyst and its partial pressure also enters into the rate expression.

In summary, the following conclusions concerning the kinetics over promoted iron catalysts can be drawn from the literature:

1. The integral activity increases as the partial pressure of hydrogen or carbon monoxide is increased.

2. The partial pressure of CO_2 has a negligible effect on activity.

3. Increasing the partial pressure of H_2O at higher conversions decreases the catalytic activity.

4. The overall rate of reaction increases nearly linearly with the total pressure, assuming that all other factors are held constant.

5. The effect of temperature on the catalytic activity of F-T reactions is reflected in the overall activation energy which lies between 71 and 105 kJ/mol.

2.1.5 Product Selectivity

2.1.5.1 Polymerization Distribution Law (PDL)

As explained earlier in the discussion of the mechanism of F-T synthesis, there is no consensus on the detailed mechanistic steps of F-T synthesis. It is generally acknowledged, however, that chain growth occurs via stepwise addition of units containing one carbon atom to a growing chain on the catalyst surface (Dry, 1981). Chain termination is thought to occur by simple chain desorption. Thus, the product distribution is generally described by a chain-growth polymerization mechanism. The latter may be expressed by the equation (Flory, 1936; Schulz, 1935):

$$W_n = n\alpha^{n-1}(1-\alpha)^2 \qquad (4)$$

where:

W_n = weight fraction of carbon number n

n = carbon number of the products

α = chain-growth factor or probability of chain propogation.

This formalism is ascribed the title "Schulz-Flory," "Schulz-Flory-Anderson" or "Flory" equation.

In this work, Equation (4) will be called the Polymerization Distribution Law (PDL) according to Jacobs and Van Wouwe (1982), as it aptly describes the origin of the equation. A review of the historical developments behind the use and modification of the PDL will follow in Section 2.1.5.2.

The carbon-number product distribution is determined through the scheme adopted from Dry (1981), as shown in Figure 2.4 The distribution is calculated by first choosing a maximum carbon-number product. The selectivities of individual products are then calculated by dividing (1) the number of carbon atoms desorbed from individual products, by (2) the total number of carbon atoms desorbed. By repeating this procedure at different values of α (the probability of chain growth), a plot of the product selectivity as a function of the probability of chain growth can be made. This has been done by Satterfield et al. (1982) and is reproduced in Figure 2.5. The plot illustrates that if the Polymerization Distribution Law holds true and the composition of one fraction is fixed, the remaining fraction's compositions will be fixed. For example, if the weight fraction of products in the gasoline fraction is maximized, the composition of the diesel, light petroleum gas (LPG), and wax fractions are consequently fixed.

Another direct way of representing selectivity limitations given by the PDL was presented in the same publication (Satterfield et al., 1982) and is reproduced in Figure 2.6. As the probability of chain growth increases, the product distribution shifts towards higher and higher carbon numbers.

In practice, the probability of chain growth can be altered in three ways:

1. by selecting different types of catalysts, such as cobalt, iron or ruthenium;
2. by adjusting the content of promoters such as K_2O; and
3. by altering the synthesis conditions.

		Carbon Atoms Desorbed as C_n	/ Total Carbon Atoms Desorbed
100 $*C_1$			
| $\alpha = 0.4$	$\underline{1-\alpha = 0.6}\rightarrow$ 60 CH_4		60/60
↓			
40 $*C_1$			
+			
40 new $*C_1$			
↓			
40 $*C_2$	$\underline{0.6}\rightarrow$ 24 C_2H_6		48/108
| 0.4			
↓			
16 $*C_2$			
+			
16 new $*C_1$			
↓			
16 $*C_3$	$\underline{0.6}\rightarrow$ 9.6 C_3H_8		28.8/136.8
| 0.4			
↓			
6.4 $*C_3$			
+			
6.4 new $*C_1$			
↓			
6.4 $*C_4$	$\underline{0.6}\rightarrow$ 3.84 C_4H_{10}		15.36/152.16
|			
↓ 0.4			
etc.			

FIGURE 2.4: A Scheme For Calculating The Carbon-Number Product Distribution. This Example Assumes Only Olefins Are Formed. An Adsorped Species is Designated *C. Adapted From Dry (1981).

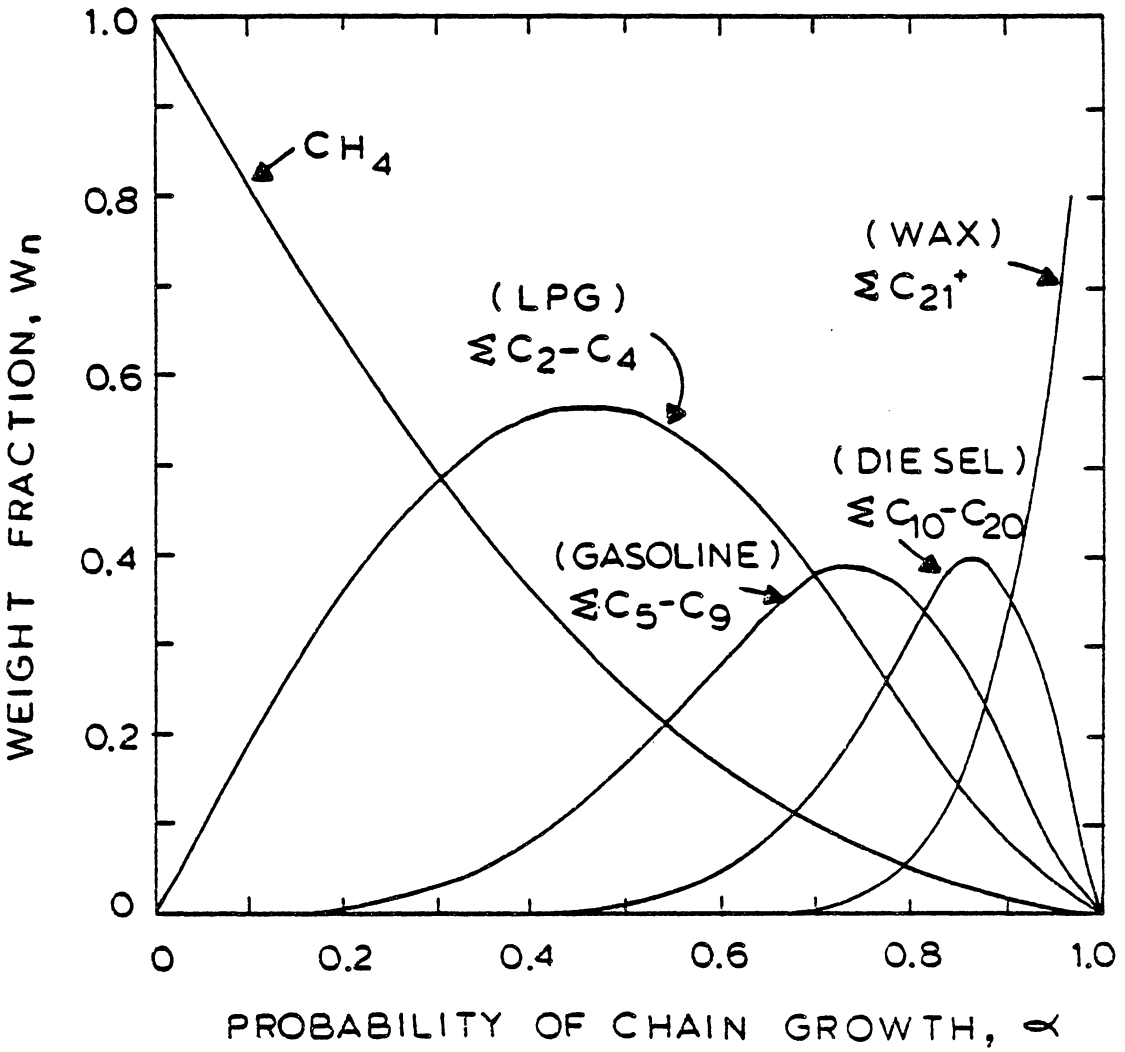

Figure 2.5. The Selectivity of Various Hydrocarbon Cuts in F-T Synthesis (Satterfield et. al., 1981).

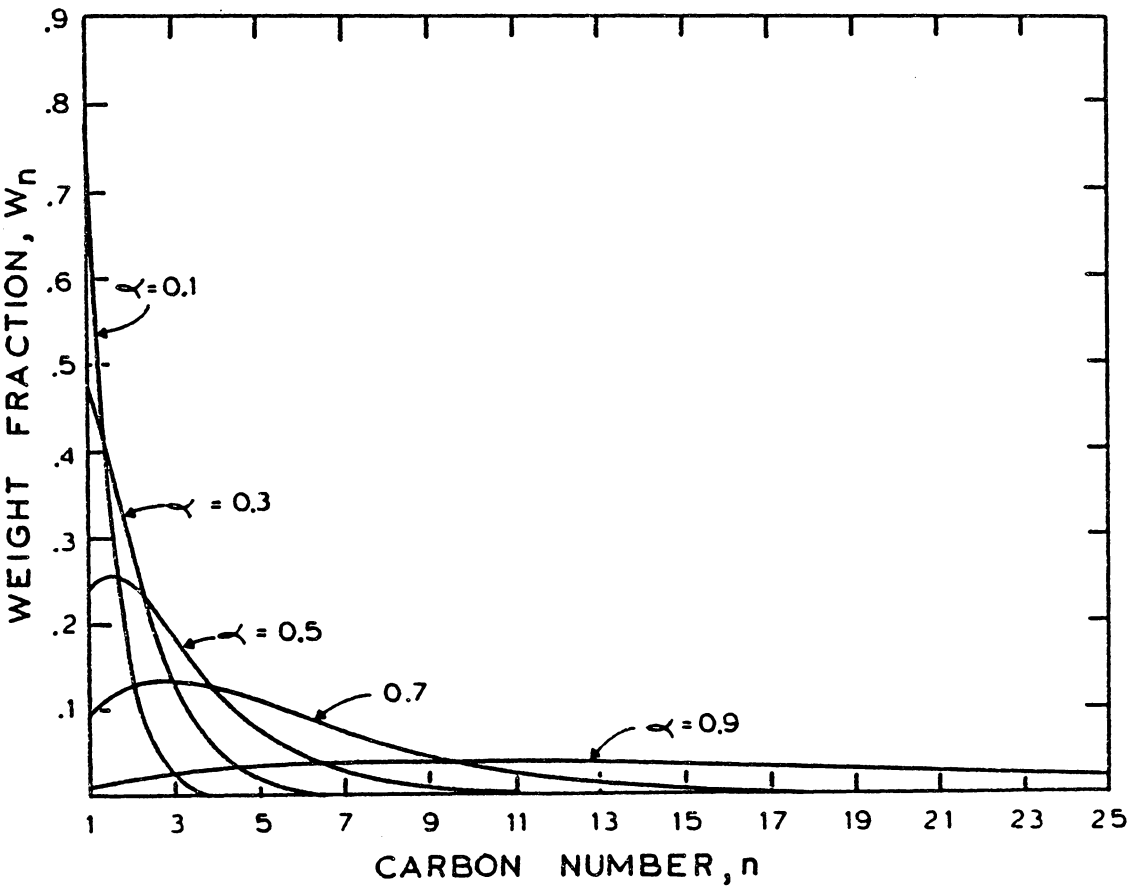

Figure 2.6. Selectivity Limitations in F-T Synthesis as Predicted by the PDL or Flory Distribution (Satterfield et al., 1981).

Dry (1981) and others also found that as these parameters are altered, the apportionment of compounds within a given carbon number is changed. Bounds currently found for the probability of chain growth, α, are: 0.50-0.70 for iron catalysts; 0.70-0.80 for cobalt catalysts; and 0.85-0.95 for ruthenium catalysts (Jacobs and Van Wouwe, 1982).

Table 2.4 shows the distribution of products within a product cut from SASOL's fixed-bed and Synthol reactors (Dry, 1981). It is thought that α-olefins and primary alcohols may be initial products of the synthesis (Anderson, 1984). On iron in fluidized bed-reactors olefins account for more than 50 percent of the species in a given carbon number. Water is also a primary product but undergoes rapid conversion to produce CO_2 via the water-gas shift reaaction.

Moderate amounts of aromatics and napthenes are also formed in fluidized beds of iron catalysts as shown in Table 2.4. Production of methanol is limited and production of higher alcohols decrease from a maximum at C_2.

The effect of synthesis conditions on product selectivity has been reviewed by Dry (1981). Generally, it is found that as the reaction temperature is increased, the product slate shifts to lower molecular-weight species. This trend is indicated by all F-T catalysts. At SASOL, fluidized fused-iron catalysts show this trend as temperature increases. In addition, these catalysts lead to an increase in olefinity, but a decrease in acid and alcohol selectivities.

The effect of pressure on product distribution is not as clear cut as the effect of temperature. Anderson et al. (1964) have found no change in the degree of unsaturation with pressure on fused-iron catalysts. Most of the studies of pressure effects show that as pressure increases, hydrocarbon

TABLE 2.4

Selected Properties of Liquid and Solid Products from SASOL Reactors Using Iron Catalysts (Dry, 1981).

Product Cut	Property	Fixed Bed[a] (wt%)	Synthol[a] (wt%)
Gasoline C_5-C_{11}	Olefins	32	65
	Paraffins	60	14
	Aromatics	0	7
	Alcohols	7	6
	Ketones	0.6	6
	Acids	0.4	2
	%n-Paraffins	95[b]	55[b]
Diesel C_{12}-C_{18}	Olefins	25	73
	Paraffins	65	10
	Aromatics	0	10
	Alcohols	6	4
	Ketones	<1	2
	Acids	0.05	1
	%n-Paraffins	93[b]	60[b]
Medium Wax C_{24}-C_{35}	Olefins	10%	-

[a] wt% of Product Cut.

[b] % of paraffins which are straight chained.

selectivity shifts toward more oxygenated and heavier products while not altering olefinity much. Dry (1981) speculates that this is due to the influence of the partial pressures of individual components rather than total pressure per se. Increasing the H_2/CO ratio in the reactor tends to shift the product distribution towards lighter and less olefinic products.

In sum, changes in factors which affect the probability of chain growth in the polymerization distribution law seem to be rather complex. Changes such as going from a fixed- to fluidized-bed reactor probably affect the product selectivity through actual partial pressures of CO, H_2, CO_2 and H_2O in the reactor.

2.1.5.2 Development of and Modifications to the PDL

A relationship between chain growth and termination was first proposed for F-T synthesis in 1946. Herington (1946) defined β_n as the ratio of rates of chain termination (r_t) to chain propogation (r_p):

$$\beta_n = \frac{r_t}{r_p} \qquad (5)$$

Herington discussed this relationship in terms of experimental results over a $Co\text{-}ThO_2$-kieselguhr catalyst.

Friedel and Anderson (1950) extended Herington's result by defining the following:

$$\beta_n = \phi_n / \sum_{n+1}^{\infty} \phi_i \quad \text{and} \quad \beta_n = \frac{1-\alpha_n}{\alpha_n}$$

where:

ϕ_i = the number of moles of hydrocarbons of chain length i in the product

α_n = the probability of growth of a chain of length n.

They showed that if β_n and α_n were constant over a range of n greater than x, then:

$$\phi_n = \phi_x \alpha^{n-x} \qquad (7)$$

A plot of ln ϕ_n against n should be linear. This result was later used by Anderson (1956) in analyzing data collected from F-T synthesis over iron and Co-ThO_2-kieselguhr catalysts.

Anderson et al. (1951) later generalized the preceding development in order to provide for prediction of the hydrocarbon isomer distribution. In this scheme, addition at end or adjacent-to-end carbon atoms of the largest chain is envisioned. The general form of the resulting equation is as follows (Madon, 1979):

$$\phi_n = 2\phi_2 g_n(f)\alpha^{n-2} \qquad (8)$$

where:

ϕ_n = the number of moles of hydrocarbon of chain length n

f = the ratio of the rate of appearance of C_n upon addition to an adjacent-to-end carbon of C_{n-1} to the rate of appearance of C_n upon addition to the end carbon of C_{n-1}

$g_n(f)$ = a function of f.

Le Roux and Dry (1972) developed a statistical method for predicting the distribution of normal, mono-, di-, and tri-methyl paraffins in F-T synthesis products. The general form of this equation follows:

$$W_p = \frac{1}{p!} q(q-1) \ldots (q-p+1)s^p(1-s)^{q-p} \qquad (9)$$

where:

q = the number of internal carbon atoms

s = the probability of an internal carbon atom having a branch attached to it

p = the degree of branching, 0, 1, 2, or 3

W_p = the probabiity of p-fold branching, e.g., W_1 = monomethyl.

It is assumed that 3-fold branching is the maximum degree of branching. By knowing q and that $\sum W_p = 1$, the above equation can be solved interatively yielding s and W_p. Equation (9) was found to be "quite adequate" for lighter products and was also applied to products in the wax range (Le Roux and Dry, 1972).

Henrici-Olivé and Olivé (1976), apparently unaware of the previous work in this area, noted that F-T synthesis is actually a polymerization process. They advanced the use of the Schulz-Flory distribution of molecular weights for prediction of weight fractions obtained by synthesis (Schulz, 1935; Flory, 1936):

$$W_n = n\alpha^{n-1}(1-\alpha)^2 \qquad (4)$$

where

W_n = weight fraction of carbon number n

α = probability of chain growth

Note that Equation (4) was mentioned previously in Section 2.1.5.1. As later noted by Anderson (1978) and proven by Madon (1981), Equation (4) as used by Henrici-Olivé and Olivé (1978) is exactly that developed by Friedel and Anderson (1950) at the U.S. Bureau of Mines.

In recent years, attempts have been made to predict in more detail the distribution of products actually obtained experimentally from F-T synthesis. Schulz and Zein el Deen (1977) have determined quantitative relationships for homologous series of straight-chain and branched alcohols, acids and ketones from medium-pressure fixed- and entrained-bed processes with iron catalysts. Their relationships are based on analogies to the formulas of Herington (1946) and Anderson (1950), namely the Polymerization Distribution Law:

$$C_n = A \cdot W^n \qquad (10)$$

where:

C_n = moles of compound with carbon number n

A = termination function

W = growth function

Values of A and W were obtained from experimental data and relationships between homologous series were postulated in terms of a reaction scheme.

Kibby and Kobylinski (1978) have modified the PDL in order to allow for cracking of synthesis products, reincorporation of ethylene, chain branching, and changing chain growth probability with chain length. This type of model is used to rationalize deviations from the PDL particularly at low carbon numbers. These deviations will be discussed in Section 2.1.5.3.

Anderson and Chan (1978) have proposed a computer simulation for more complicated chain-growth schemes. An example of such schemes includes three constants and can be used to predict isomer distributions. Note that

the PDL, Equation (4), is a 2-constant scheme, not involving isomer prediction.

Nijs and Jacobs (1980) have presented a new model that attempts to "account for all possible F-T product distributions." Their model, called the "Extended Schulz-Flory model," is based on the theory that metal particle-size effects are the key to F-T synthesis selectivity. It is postulated that only a molecule of a certain carbon number can be made on a metal particle of a particular size. In addition, polymerization on each metal particle follows the Schulz-Flory (PDL) kinetics given by Equation (4). Besides metal particle size, other key parameters in their model include the polymerization growth rate and the width of the size distribution. By numerically solving a series of equations describing the above parameters, Nijs and Jacobs have been able to fit Madon's (1979) nonclassical distribution obtained using an alumina-supported ruthenium catalyst. In addition, product distributions obtained from using RuLaY and RuNaY zeolites as well as alumina-supported cobalt catalysts are fitted.

In a series of papers, Novak et al. (1981, 1984) have investigated modifications to the Polymerization Distribution Law or Flory model. The purpose of these investigations was to create quantitative models as guides for interpreting results and stimulating future experimental work. In their first paper, the authors outlined four modifications which supplement the chain growth and termination mechanisms of the Flory model. These modifications were described by Novak and coworkers as:

1. growth via a two-carbon intermediate;

2. second-order termination by combination of two chains on the catalytic surface with subsequent desorption;

3. same as (2) but with a fraction of the combined chains allowed to participate in growth on the surface; and

4. catalytic hydrocracking.

Mechanisms 2 and 4 are described as holding the most promise in terms of selectivity increases over that predicted by the Polymerization Distribution Law. In their second paper, Novak and Madon (1984) have looked further into the model for hydrocarbon-chain growth and cracking. By adding cracking functionalities to a catalyst, this study shows how potential increases in liquid hydrocarbon selectivity could be gained. Their calculations reveal that through the use of bifunctional catalysts, a possible three-fold increase in peak height can be observed on a plot of weight percent versus carbon number.

In a novel approach to manipulation of the Polymerization Distribution Law, Peacock-Lopez and Lindenberg (1984) have proposed the "Transient Flory Model." This model involves the use of the following expression:

$$\theta_n(t) = k_p\theta_{n-1} - k_p\theta_n - k_t\theta_n \qquad n \geq 2 \qquad (11)$$

and

$$\theta_1 = \text{constant } (C_1^* \text{ at steady state})$$

where:

k_p = pseudo-first-order rate constant for chain propogation

k_t = pseudo-first-order rate constant for chain termination

θ_n = fraction of active catalytic sites occupied by C_n^*, the number of adsorbed chains.

Equation (11) can be simplified by considering $\theta_n(t)$ at steady-state conditions, leading to the Flory distribution, Equation (4), as discussed previously.

$$P_n^{ss} = n(1-\alpha)^2\alpha^{n-1} \qquad (4)$$

where

P_n^{ss} = weight fraction of carbon number n

α = probability of chain growth = $\dfrac{k_p}{k_p + k_t}$

At steady state, however, it is impossible to separately determine k_p and k_t. Analysis of the simplest transient regime requires keeping θ_1 in Equation (11) constant. In the transient case, $\theta_n(t)$ is not equal to zero and therefore Equation (11) is most easily dealt with by using Laplace transforms. Peacock-Lopez and Lindenberg arrive at the expression for the weight percent distribution of desorbed hydrocarbon chains, or the "Transient Flory Model:"

$$P_n\ (t) = \frac{nC_n(t)}{\sum_{n-1}^{\infty} nC_n(t)} = \frac{nC_n(t)}{W(t)} \qquad (12)$$

where

C_n = concentration of desorbed species, $C_n = f(\theta_n^{ss}, k_t, t, \alpha, s)$

$W(t)$ = weight of desorbed chains as a function of time.

Examination of the predicted transient product distribution as a function of time, carbon number and probability of chain growth brought the researchers to the following conclusions:

1. Transient behavior can be used to preferentially produce shorter rather than longer chains.

2. The larger the value of α ($\alpha \geq 0.9$), the more effective transient operation will be.

3. By judicious choice of pulse length, short chains theoretically should be produced more abundantly.

2.1.5.3 Deviations from the PDL

Increased yields of methane and decreased yields of C_2 products over those predicted by the PDL have been observed over F-T synthesis catalysts since the PDL was proposed (Herington, 1946; Friedel and Anderson, 1950). Early studies showed this phenomenon for both cobalt and iron catalysts, while recent work give similar results for Ru on Al_2O_3 catalysts (Everson et al., 1978; Madon et al., 1977). Deviations have also been observed for products with higher molecular weights, particularly in the wax region.

Recent papers by Satterfield et al. (1982b) and Dictor and Bell (1983) and a review by Jacobs and Van Wouwe (1982) focus on the reasons for deviations from the PDL. A brief listing of reported reasons is as follows:

1. Experimental artifacts:
    a. Reactor design and operation problems;
    b. Transient reaction conditions;
    c. Wax deposition in the catalysts bed and downstream equipment; and
    d. Sampling artifacts.

2. Secondary reactions:
    a. Incorporation of ethylene; and
    b. Secondary hydrogenation.

3. Mechanistic effects.

Experimental artifacts may be a major reason for reported deviations from the PDL. Temperature gradients, hot spots and mass-transfer limitations may exist in fixed-bed reactors. If sufficient time is not permitted for the reaction to reach steady-state conditions, misleading product distributions may be obtained. Wax may condense in the catalyst bed and downstream equipment because of the existing vapor-liquid equilibrium conditions (Dictor and Bell, 1983; Satterfield et al., 1982b). Satterfield et al. (1982b) have shown that for a fused-iron catalyst, inclusion of oxygenated products in the product distribution is critical to providing accurate results. It was found that oxygenates made up approximately 70 percent of C_2 and C_3 fractions over iron catalysts. When all collected samples are combined in a proper fashion (minimizing vapor phase loss), the products strictly follow the Flory distribution. There is, however, a change in the probability of chain growth, α, near C_{10}. This change has been noted by Huff and Satterfield (1984a) and by Schulz and Zein el Deen (1977) for medium-pressure synthesis conditions. The new α value has been shown to hold true, even at very high carbon numbers (Stenger et al., 1984).

Perhaps the most common explanation for deviations of C_2 products from the PDL is that ethylene can initiate new hydrocarbon chains, or can be incorporated into growing chains.

For example, through the use of ^{14}C labelling over iron and cobalt catalysts, Schulz et al. (1970) have shown that α-olefins, particularly ethylene and to a lesser extent propylene, initiate chains, incorporate into growing chains and also crack to form methane. The splitting of the added α-olefin to methane was found to be greater over cobalt than iron

catalysts. Incorporation reactions were observed to take place more over iron than cobalt catalysts. Dwyer and Somorjai (1979) in studies using well-characterized single iron-crystal surfaces produced results that were, for the most part, in agreement with those reported by Schulz et al. (1970). Dwyer and Somorjai (1979) have concluded that "readsorption and secondary reaction is an important pathway leading to the formation of large molecular weight hydrocarbons during F-T synthesis." In a theoretical exploration of possible secondary reactions of α-olefins, Novak et al. (1982) have found that the readsorption and growth of α-olefins in principle can change the shape of the product distribution. However, an analysis of theoretical distributions from a continuously-stirred tank reactor (CSTR) and a plug-flow reactor indicate that the Flory distribution should be obtained.

Mechanistic arguments for increased methane yields have been forwarded by Ponec (1978) and Feimer et al. (1982, 1984) as well as by others. Dual mechanistic arguments suggest that methane is produced via the chain-growth mechanism, and also by another mechanism such as hydrogenation of a surface carbidic species.

2.1.5.4 Attempts to Circumvent Selectivity Limitations

Much interest has been focused in recent years on improving the selectivity of F-T synthesis. In particular, products in the C_5 to C_{10} range are desired as liquid transportation fuels.. A review by King et al. (1981) addresses this effort. The problem has been approached in a variety of ways. Madon and Shaw (1977) have reviewed the use of selective poisoning to alter product selectivity. This approach has the inherent problem of decreased catalyst activity and is not considered promising.

Physical limitations imposed by alumina supports of different pore sizes and zeolites have been used to bypass selectivity limitations of F-T synthesis catalysts (Fraenkel and Gates, 1980; Nijs et al., 1979; Vanhove et al., 1979). Mobil Research and Development Corporation has recently used bifunctional catalysts to produce light hydrocarbons (Caesar et al., 1979; Chang et al., 1978; 1979). In Mobil's scheme, an alcohol or hydrocarbon intermediate is produced using one catalytic functionality, such as supported iron; while a second catalytic functionality, namely, a synthetic zeolite called H-ZSM-5, converts the intemediate to a light hydrocarbon.

The most recent trend in circumventing selectivity limitations has been the use of unsteady-state feed-gas pulsing to promote chain termination and desorption. Dautzenberg et al. (1977) first attempted this using a pulsing scheme in conjunction with a $Ru/\alpha\text{-}Al_2O_3$ catalyst. As will be discussed in Section 2.2.2, there is some controversy over whether high molecular-weight products were inhibited by the pulsing, by the catalyst, or by both. Using a precipitated copper-potassium-promoted iron catalyst, Feimer et al. (1982, 1984) did not observe any change in product distribution over that obtained at steady state other than an increased time averaged rate of methane production. This former result is not suprising when considered in light of Peacock-Lopez and Lindenberg's (1984) transient Flory model, Equations (11) and (12) as described in Section 2.1.5.2. According to the transient Flory model, selectivity improvements are not likely for unsteady-state F-T synthesis over iron catalysts. This is because of the lower probability of chain growth, α, associated with iron catalysts.

A more detailed examination of unsteady-state methods will be undertaken in Section 2.2.

2.1.6 Carburization of Iron Catalysts

2.1.6.1 Phases Present During Synthesis

Changes in the bulk and surface compositions of iron catalysts upon exposure to hydrogen and carbon monoxide during F-T synthesis have long been known to occur. Storch et al. (1951) reviewed early work in the area. Pichler and Merkel (1949) performed the first major study of carbide formation, generally called "carburization," on iron catalysts. These investigators exposed a potassium-promoted precipitated iron catalyst to carbon monoxide at 0.1 atm and 325°C and identified Hägg carbide (Fe_2C, or Fe_5C_2 in the newer literature) and magnetite (Fe_3O_4) on the used catalyst. It was also determined that the rate of carbide formation varied inversely with pressure and that free-carbon formation increased with temperature, particularly becoming significant above 325°C.

Table 2.5 summarizes representative investigations of phase changes occurring on different iron catalysts for F-T synthesis. Catalyst makeup and manner of preparation have been found to strongly affect the type of bulk carbides that are formed and also the structure of the active catalyst. Reaction conditions are no less important to, and are intimately involved in the combinations of carbides that are formed. Extensive work has been carried out at the Bureau of Mines both on promoted precipitated iron catalysts and, to a greater extent, on promoted fused-iron ammonia-synthesis catalysts. This work was recently reviewed by Anderson (1984). Using the above precipitated iron catalyst, Hofer et al. (1949) showed that hexagonal

TABLE 2.5

Phases Present in Representative Iron Catalysts for Fischer-Tropsch Synthesis

Catalyst Type	Reactor	Conditions			Phases Present in Variable Range	Reference
		H_2/CO	Pressure kPa	Temp °C		
1. Reduced fused-iron ammonia synthesis catalyst containing oxides of Mg, K, Si, and Cr	Vapor-phase-fixed-bed, integral conversions	1:1	788	240-280	Fe_2C(Hägg) Fe_3O_4, α-Fe	Anderson et al. (1950)
2. Reduced calcined-iron catalyst contining Mg, K and Si two formulations	Vapor-phase-fixed-bed, differential	0 to 3:1	101-1010	200	Fe_2C(Hägg), α-Fe, Fe_2C (hcp)*, Fe_3C (Phase depends on temp, pressure and H_2/CO)	Sancier et al. (1979)
3. Reduced unpromoted, precipitated (unsupported) metallic iron catalyst	Vapor-phase-fixed-bed, differential	1:1	101	160-450	Fe_xC (unidentified), χ-Fe_5C_2(Hägg) ε'-$Fe_{2.2}C$, θ-Fe_3C (cementite) α-Fe or Fe_3O_4 (phase depends on temp)	Neimantsverdriet et al. (1980)
4. Reduced, supported Fe/SiO_2 and Fe/MgO Catalyst	Vapor-phase-fixed bed, differential	3.3:1	101	250	χ-Fe_5C_2(Hägg) or ε'-$Fe_{2.2}$(hcp), ε-Fe_2C (transition from hcp to Hägg) (phase depends on particle size and support)	Raupp and Delgass (1979b,c)

*Note: "hcp" = hexagonal close-packed.

(Fe_2C) carbide was converted to Hägg carbide at 380°C. Hägg carbide, in turn, decomposed to cementite (Fe_3C) and free carbon at 580°C. Stein et al. (1957) found that upon exposure to synthesis gas, the ferric oxide gel of precipitated catalysts was reduced to magnetite and carbide was formed from part of the iron. This resulted in an active catalyst of low mechanical strength, in which the surface area had been greatly reduced.

In carburization experiments using a fused-iron ammonia-synthesis catalyst, Hägg carbide was found to be formed directly. It decomposed slowly to cementite at 400°C, but more rapidly at 500°C. At 600°C, it decomposed further producing iron and carbon. Bureau of Mines work has shown both cementite and Hägg carbide to be active for F-T synthesis (Anderson, 1984). Anderson et al. (1950) performed long-duration experiments over fused-iron catalysts under the conditions outlined in Table 2.5. Magnetite was found to form at a slow rate, while α-Fe was consumed to form both carbide and oxide. A maximum of 29% Hägg carbide was formed from α-Fe after 200 hours. Hall et al. (1952) determined the physical changes produced by carburization of the fused-iron ctalyst. As interstitial carbide formed, the metal lattace expanded resulting in an increase in pore volume and total catalyst volume. Despite this volume increase, the net surface area of the catalyst did not change significanly. Anderson (1984) terms this phenomenon an "expanding matrix effect."

The second study cited in Table 2.5 is a more recent investigation into carburization on a promoted iron catalyst by Sancier et al. (1979). Two formulations of calcined iron catalysts were studied using mass gain and magnetic susceptibility measurements. These catalysts, designated B-2 and B-6, were promoted with different amounts of SiO_2, MgO and K_2O. The main difference in the two was that catalyst B-2 had a higher SiO_2 content. Temperature-programmed experiments between 177 and 327°C using catalyst B-6 indicated that Hägg carbide increased while α-Fe decreased and cementite only appeared transiently. A series of isothermal experiments over the temperature range of 200-325°C showed that as temperature increased, the fraction of Hägg carbide increased while Fe_2C (hcp, or hexagonal close-packed) and α-Fe decreased. Hägg carbide was the dominant phase above 325°C, while cementite contributed significantly above this temperature. Fe_2C (hcp) was formed only in the high-SiO_2 catalyst (B-2) and was not found after the catalyst had registered a weight gain of 4.5%.

In contrast to catalyst composition and reaction temperature, pressure was found to have little effect on the relative amounts of ferromagnetic phases (Sancier et al., 1979). The effect of H_2/CO ratio was investigated at several temperatures for promoted iron catalyst B-6. Although the bulk-phase composition changed with H_2/CO ratio, no distinct pattern in phase changes could be identified. An interesting result was that exposure of the catalyst to pure CO at 400°C produced only cementite. If the feed contained hydrogen, however, the majority of the catalyst was transformed to Hägg carbide.

Table 2.6 summarizes the principal carburization reactions and associated phase changes over iron catalysts for F-T synthesis (Sancier et al., 1979).

Neimantsverdriet et al. (1980) studied the phases present in an unpromoted, unsupported iron catalyst after exposure to a synthesis gas H_2/CO ratio of 1:1 at 1 atm, and between 160 and 450°C. The phases identified include the following:

Fe_xC	160°C, 190°C, and early in 240°C
ε'-$Fe_{2.2}C$(hcp)	190°C to 350°C
χ-Fe_5C_2	190°C to 350°C
θ-Fe_3C	350°C, 450°C
α-Fe and/or Fe_3O_4	in small amounts

The investigators identified Fe_xC as "a poorly-defined structure between α-Fe and a crystallographic carbide." Except for the presence of this phase, these results are in agreement with the information given in Table 2.6.

Supported iron catalysts yield results somewhat different from unsupported (fused, precipitated or calcined) catalysts. Raupp and Delgass (1979b) studied iron supported on SiO_2 and MgO and observed phase dependence on both support type and metal particle size. At 250°C, larger iron particles were found to form Hägg carbide (χ-Fe_5C_2), while smaller particles yielded less stable ε'-$Fe_{2.2}C$(hcp) and ε-Fe_2C (identified as transition from hcp to Hägg).

TABLE 2.6

Principle Carburization Reactions and Phase Changes of Iron (Sancier et al., 1979)

Carburization Reactions

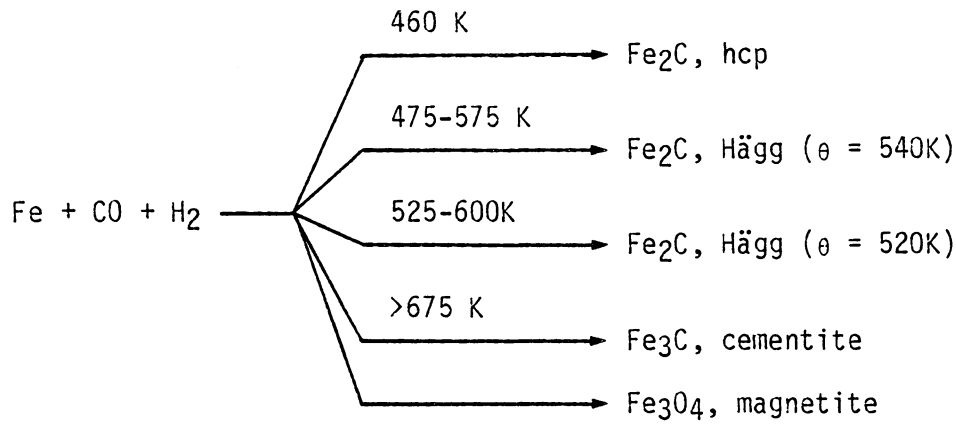

Phase Changes

$$Fe_2C, \text{ hcp} \xrightarrow{616K} Fe_2C, \text{ Hägg}$$

$$Fe_2C, \text{ Hägg } (\theta = 540K) \xrightarrow{630K} Fe_2C, \text{ Hägg } (\theta = 520K)$$

$$Fe_2C + Fe \xrightarrow{<770K} Fe_3C$$

$$3Fe_2C \xrightarrow{770K} 2Fe_3C + C$$

$$Fe_3C \xrightarrow{873K} 3Fe + C$$

In early studies, X-ray diffraction and carbon content determinations were the main means of determining carbide phases present during F-T synthesis. Later, magnetic susceptibility studies were added. More recently, Mössbauer spectroscopy has become the main technique for iron carbide determination. Several carbides of iron have reportedly been observed during F-T synthesis using Mössbauer spectroscopy. These iron carbides are shown in Table 2.7. A detailed discussion of conclusions drawn from Mössbauer spectroscopic studies of F-T synthesis has been presented by Le Caër et al. (1981). As seen in Table 2.7, depending on the way carbon atoms occupy sites in carbides, there are two general types of carbide configurations namely: (1) trigonal prismatic (TP), and (2) octahedral (O). Hägg carbide, cementite and Eckstrom Adcock carbide all possess structures with carbon atoms in TP interstices. These three structures have been experimentally verified by several methods in the literature (Le Caër et al., 1981). This is not the case for ε-Fe_2C, ε'-$Fe_{2.2}C$ and Fe_XC, which are classified by Le Caër and coworkers as octohedral (O) carbides.

As was discussed earlier, Niemantsverdriet et al. (1980) identified ε'-$Fe_{2.2}C$ and Fe_XC, while Raupp and Delgass (1979b) found ε'-$Fe_{2.2}C$ and ε-Fe_2C, with both research groups using Mössbauer spectroscopy. Le Caër and his colleagues point out that while iron atoms are generally thought to form a hexagonal close-packed (hcp) array, the ordering of carbon atoms in the octahedral interstices of the iron array has not been established. Therefore, there is no justification for the use of the specific designation "ε" in the description of these species. The

TABLE 2.7

Iron Carbides Reported in Fischer-Tropsch Synthesis Literature (Compiled with information from Raupp and Delgass, 1979b; Le Caër, 1982; Anderson, 1984; and Neimantsverdriet et al., 1980)

Carbide	Common Name	Arrangement of Iron Atoms	Sites Occupied by Carbom Atoms	Curie Point (K)
ε-Fe_2C	-	hexagonal close -packed (hcp)	Octahedral (O)	653-673
ε'-$Fe_{2.2}C$	-	transition from hcp to monoclinic	Octahedral	723
Fe_xC	-	π	Octahedral	-
χ-Fe_5C_2 (χ-Fe_2C)	Hägg	Monoclinic	Trigonal Prismatic (TP)	525
θ-Fe_3C	Cementite	Orthorhombic	Trigonal Prismatic	480
Fe_7C_3	Eckstrom Adcock	-	Trigonal Prismatic	-

carbon concentration of these octahedral carbides range from $Fe_{2.4\pm0.1}C$ to Fe_2C, with the limit close to the composition of Hägg carbide. In terms of stability of the coordinated carbon, a trigonal prismatic (TP) polyhedron is more stable than an octahedral (O) polyhedron. Thus, octahedral carbides will tend toward conversion to trigonal prismatic carbides such as Hägg carbide and cementite. The driving force for the transformation to TP carbides appears to be twofold. First, there is a propensity to obtain stronger chemical bonds; and, secondly, "chemical stresses" are relieved by this action. A mechanism has been suggested by Le Caër et al. (1982) from their investigation of Fe/Al_2O_3 carburization using Mössbauer spectroscopy and from the Mössbauer investigations of others. The mechanism is outlined below:

1. Carbon atoms migrate along the defects of an initial particle and smaller carbide particles are formed.

2. The specific surface area increases due to the carbon deposition and development of microcracks in small carbide particles.

3. In the beginning phase of carburization, a range of carbon concentrations exists, encompassing octahedral carbides. It is extremely difficult at present to identify any single discrete carbon composition of carbide (i.e., ε-Fe_2C).

4. Support interactions, structural defects, and surface effects may stabilize the octahedral carbides.

5. There exists a competition between diffusion of carbon into the bulk phase and the utilization of carbon atoms in surface chemical reactions.

6. As carburization advances, either carbon-rich carbides form or χ (or "χ faulted") carbides form. This is dependent on the type and degree of stabilizing interactions. Higher temperatures can cause direct formation of trigonal prismatic carbides but octahedral carbides may be formed first, depending on the surface reactions taking place.

2.1.6.2 Catalyst Activity with Respect to Carburization

Even though the function of carbides in F-T synthesis is still in question, there is no uncertainty in the fact that the rate of reaction is closely related to carbide formation.

Shultz et al. (1955) at the Bureau of Mines showed that reduced fused-iron catalysts had lower activities than those converted to Hägg carbide. After the carbide composition of the catalyst stabilized, the catalytic activity was found to be constant or to increase slightly with time. Although Raupp and Delgass (1979) were using a supported iron catalyst, they found a similar dependence of catalytic activity on bulk carbide formation. It was concluded that the number of active sites were controlled by incorporation of carbon atoms into the iron particles until the catalyst had completely carbided.

Using a transient method over a commercial fused-iron catalyst at 250°C and 1 atm, Matsumoto and Bennett (1978) and later Reymond et al. (1980) studied the catalytic activity and surface species. It was observed that the bulk iron in the catalyst reacted with carbon from CO disproportionation. This was followed by a gradual increase in surface carbon needed for hydrocarbon synthesis, as the bulk iron carburized

to Hägg carbide. A slow decline in catalytic activity was then observed, as active surface carbon is converted to graphite. This is similar to the mechanism proposed by Sancier et al. (1979). However, Bennett and coworkers went on to postulate a common intermediate for the formation of Hägg carbide and methane.

Niemantsverdriet et al (1980) studied the conversion of unpromoted, unsupported iron catalysts using Mössbauer spectroscopy, X-ray diffraction, carbon-content determination, and reaction-kinetics measurements. The conversion of α-Fe into carbides was observed to start at a "high rate and decrease rapidly." This result was similar to findings of Pichler and Merkel (1949) and Sancier et al. (1979), who had found bulk carburization to be complete within several hours. Conversion of CO to hydrocarbons, however, proceeded at an initially low rate, went through a maximum and gradually leveled off. This observation is illustrated in Figure 2.7

In order to explain the results illustrated in Figure 2.7 and the observations of others concerning catalyst activity, Niemantsverdriet and Van der Kraan (1981) proposed three models describing catalyst activity:

1. Carbide Model: The catalyst has an iron-carbide bulk structure with active sites on its surface. The model suggests that iron is not active for F-T synthesis.

2. Competition Model: Active sites are surface iron atoms. Three reactions compete for adsorbed carbidic carbon, C*:

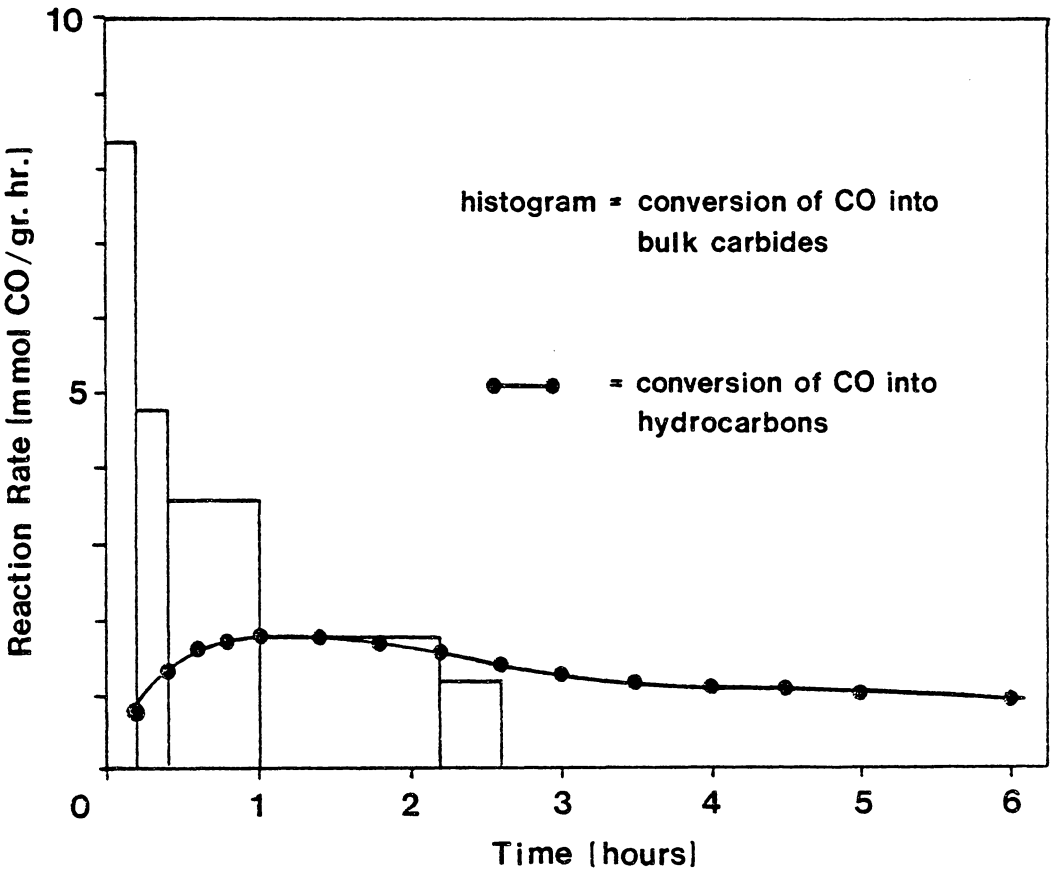

Figure 2.7. The Conversion Rate of CO into Hydrocarbons and Bulk Carbides on an Iron Catalyst at 240°C (Niemantsverdriet et al., 1980).

$$C^* + \text{iron} \rightarrow \text{carbides} \quad (13a)$$

$$C^* + xH^* \rightarrow \overset{*}{CH_x} \quad (13b)$$

$$C^* + yC^* \rightarrow \text{inactive carbon} \quad (13c)$$

3. Slow Activation Model: The model is characterized by fast adsorption and dissociation of CO. Enough carbon atoms are present to provide for both carbide formation and hydrocarbon formation.

Niemantsverdriet and Van der Kraan (1981) attribute the carbide model to Raupp and Delgass (1979b) and Amelse et al. (1978). This model, as well as the Slow Activation model, were rejected by Niemantsverdriet and Van der Kraan based on evidence obtained from four experiments from the literature. It is desirable to take a close look at the competition model. Specifically, as the reaction begins, surface carbidic carbon, C^*, is drawn into the bulk of the catalyst forming carbide, Equation (13a). This, in turn, causes a surface carbon deficiency in the initial stage. As bulk carburization advances, more and more carbidic carbon atoms, C^*, are available at the surface to initiate or propagate chains via Equation (13b) or cause deactivation via Equation (13c). Thus, three forms of carbon exist, namely: (1) bulk-carbidic carbon, (2) inactive (free) carbon, and (3) surface carbidic carbon.

Ino et al. (1981), apparently unaware of the work by Niemansverdriet et al. (1980), studied catalytic activity and effect of carbon on a precipitated iron catalyst for F-T synthesis. These workers

ascribe a drop in percent CO conversion during the first few hours of reaction to "carburization of iron active sites." They show the weight percent of C_2-C_4 hydrocarbons dropping only slightly, while methane production increases. Undoubtedly, much of the CO converted was actually involved in carburizing the bulk structure of the iron catalyst. Therefore, equating CO conversion to catalytic activity is a risky proposition, especially in the initial stages of reaction where CO uptake by the iron catalyst is greatest. Their results are relatively well-established and, when compared to those of Neimantsverdriet et al. (1980), can be attributed to building of the bulk carbide structure of the catalyst.

2.1.6.3 Formation of Iron Oxides

In the previous section, several studies were cited in which little or no magnetite was found upon analysis of the catalyst after synthesis (Sancier et al., 1979; Niemantsverdriet et al., 1980; Raupp and Delgass, 1979b). These studies were performed in the vapor phase under differential conditions which typically creates a more reducing atmosphere. Under normal F-T synthesis conditions where conversions are high and particle sizes are larger, magnetite (Fe_3O_4) is typically found. This is the case both in the Bureau of Mines work (Anderson, 1956) and under commercial conditions at SASOL (Dry, 1981). Figure 2.8 shows the phase changes of an iron catalyst in a fluidized-bed reactor at SASOL over the course of several days at 327°C. As can be seen, the magnetite composition increases initially at the expense of α-Fe and later at the expense of Hägg carbide.

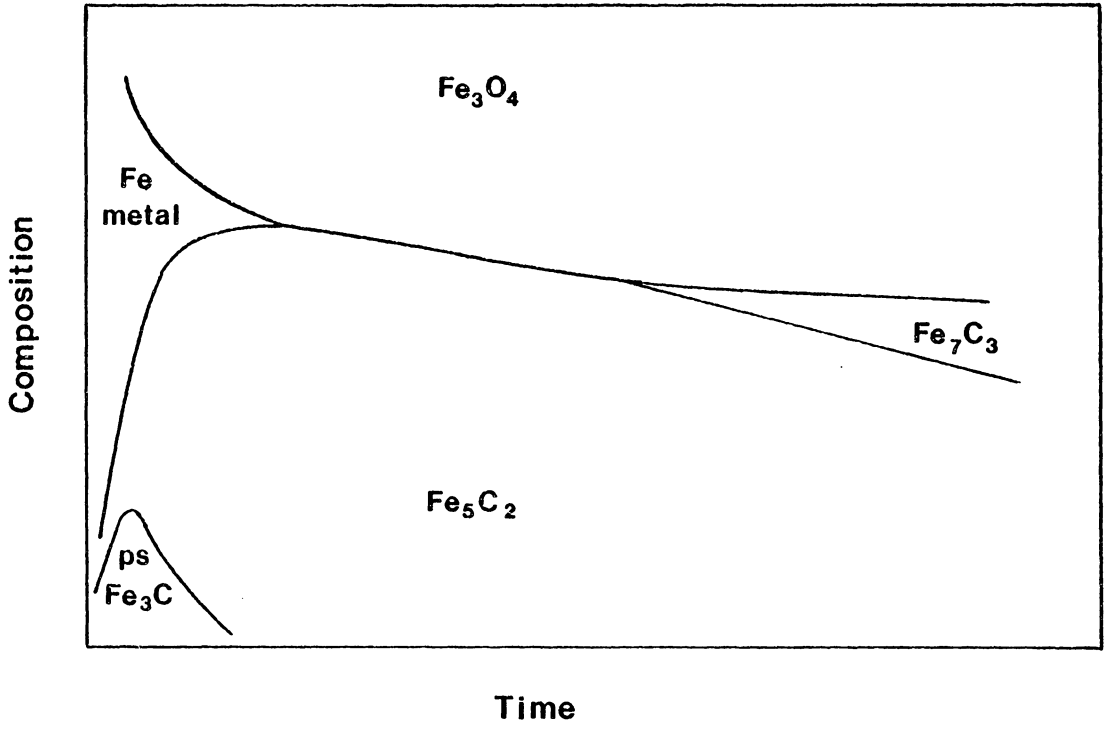

Figure 2.8. Phase Changes of a Fluidized Iron Catalyst for F-T Synthesis at SASOL over the Course of Several Days at 327°C (Dry, 1981).

Citing data obtained at the Bureau of Mines, Anderson (1984) set bounds on the oxidation of iron and iron carbide. A series of tests were performed at 250°C, 788 and 2161 kPa over a fused-magnetite catalyst that had been converted to Hägg carbide. The partial pressures of H_2, CO, H_2O, CO_2 and CH_4 in the reactor-exit gases were determined and H_2O:H_2 and CO_2:CO ratios were calculated. These ratios were then compared the H_2O:H_2 and CO_2:CO ratios required thermodynamically to form oxide. It was found that oxidation of iron or iron carbide was possible at all conversions larger than approximately 5%, due to the prevailing H_2O:H_2 ratio. However, the ratio of CO_2:CO only became sufficient to cause oxidation at conversions of approximately 80%.

Studies at SASOL in fluidized beds indicate that as particle size decreases, the ratio of carbides to oxides increases. With large-size particles, water and CO_2 are formed in the catalysts pores from reacting hydrogen and carbon monoxide. Hence, the catalyst particle becomes oxidized in the center. This is reflected in the observation that reduction of fused-iron catalysts beyond a certain level does not increase the catalytic activity (Dry, 1981).

2.1.7 Carbon Deposition on Iron Catalysts

F-T synthesis has long been plagued by the problem of carbon deposition, and this phenomenon is especially problematic when iron catalysts are used. Carbon is a product of CO disproportionation, as opposed to coke which is formed by condensation or decomposition of hydrocarbons on metals (Bartholomew, 1982). Carbon can deactivate the catalyst by fouling the active metal surface and by blocking the catalyst

pores. Physical degradation of the catalyst structure is also caused by carbon formation. Carbon buildup induces severe stresses, causing particle swelling and disintegration. The resulting low density particles are high in carbon content. Researchers at Hydrocarbon Research, Inc. called these fine particles "bugdust" because of their behavior in their fluidized beds for F-T synthesis (Arnold and Keith, 1951). Bugdust elutriates from fluidized beds, fouling downstream equipment; and it also causes a net loss of catalyst from the bed. In addition, bugdust can end up in the heavy-oil fraction from the process. In fixed-bed reactors, these fine carbon particles produce high pressure drops and lead to eventual plugging of the bed (Dry, 1981).

Carbon deposition is influenced by three main factors: temperature, gas composition and catalyst formulation. In the past, carbon deposition has been avoided through the use of low reaction temperature and high hydrogen partial pressure. At SASOL in South Africa, synthesis gas of H_2/CO ratio of 6:1 is used in the entrained bed process feed to surpress carbon deposition (Frohning et al., 1982). The use of hydrogen partial pressure to control carbon deposition, in the past, has not been an economical proposition. Shinnar and Kuo (1978) have shown that the most thermally-efficient coal gasifiers produce a synthesis gas with a H_2/CO ratio of 0.5:1. It is, therefore, desirable to search for other means of preventing carbon deposition such as using different catalyst formulations or "engineering" the reaction.

The latter approach has been attempted in this study, and will be discussed in the experimental sections of this thesis.

2.1.7.1 Thermodynamics and Kinetics

Carbon deposits can be envisioned as occurring through the following reactions:

$$2CO \rightarrow C + CO_2 \quad (14a)$$

$$CO + H_2 \rightarrow C + H_2O \quad (14b)$$

$$CH_4 \rightarrow C + 2H_2 \quad (14c)$$

$$2H_2 + CO_2 \rightarrow C + 2H_2O \quad (14d)$$

Equation (14a) is termed the Boudouard reaction if carbon monoxide is the only species present. The thermodynamics of carbon-deposition reactions have been explored by several investigators (Storch et al., 1951; Greyson, 1956; White et al., 1975). White et al. (1975) express equilibrium reactions in terms of ternary composition diagrams of C, O_2 and H_2. These diagrams show regimes where carbon theoretically should and should not form at various temperatures and pressures. Similarly, work performed at the U.S. Bureau of Mines (Greyson, 1956) produced thermodynamic equilibrium curves of carbon deposition (formation in F-T synthesis for feed gases of various H_2/CO ratios. Above these curves, carbon formation is not thermodynamically favored.

Available experimental information described in the preceding references has shown that the formation of carbon in carbon-deposition reactions, Equations (14a) to (14d), is kinetically controlled. This is similar to the case in the production of products in F-T synthesis

reactions. In other words, the rate of carbon deposition does not actually depend on equilibrium, but rather kinetic considerations. This is reflected in the fact that severe carbon deposition occurs under conditions where thermodynamic calculations show that it should not occur (Dry, 1980).

The rate of carbon deposition on iron catalysts is extremely temperature-dependent. At temperatures above 250°C, the formation of elemental carbon begins to be noticed. The rate of carbon deposition by the Boudouard reaction, Equation (14a), becomes measurable in the range 325-350°C (Pichler and Merkel, 1949; Bartholomew, 1982). Dry et al. (1970) found the activation energy of the Boudouard reaction, in the absence of hydrogen, to be 113 kJ/mol. This is somewhat higher than that (approximately 83 kJ/mol) of the overall F-T synthesis reaction on iron catalysts. Results obtained in fluidized-bed studies at SASOL indicate that the rate of carbon deposition typically "increases by fifty percent for a 10 K rise in average bed temperature."

Dry (1980) also studied the influence of gas composition on the rate of carbon deposition on iron catalysts under typical F-T synthesis conditions. The rate was found to be directly proportional to the partial pressure of carbon monoxide and inversely proportional to the square of the hydrogen partial pressure, i.e.,

$$r_{\text{carbon deposition}} = \frac{k\, P_{CO}}{P_{H_2}^2} \qquad (15)$$

Changes in the partial pressure of carbon dioxide were found to have little effect on this ratio.

It should be noted that the above dependence was determined in a fluidized bed. Available research suggests that for fixed beds, Equation (15) should be applied over the total bed length in order to obtain an integrated carbon-deposition rate (Dry, 1980). The dependence of carbon-deposition rate on partial pressures is different from the earlier observation that this rate was controlled merely by the H_2/CO ratio (Storch et al., 1951). The fact that increasing the reaction pressure decreases the rate of carbon formation is readily apparent from the above rate equation. Consequently, lower H_2/CO ratios of feed gases can be utilized when higher reaction pressures are used.

Dry et al. (1970) studied the Boudouard reation, Equation (14a) over a fused-iron catalyst that had been converted to Hägg carbide. The goal of these studies was to obtain information about the role of promoters, and the influence of gas phase species on the rate of carbon deposition. As stated before, structural promoters (such as Al_2O_3, CaO and SiO_2) were found to merely increase the surface area of the catalyst. Chemical promoters that are strong bases, such as K_2O, were found to actually increase the intrinsic rate of the Boudouard reaction. Bonzel and Krebs (1981) reached a similar conclusion after studying carbon deposition under hydrogen and carbon monoxide on iron foils promoted with potassium.

In other research, Dry et al. (1970) perceived an increase in the rate of the Boudouard reaction on iron carbide in the presence of water

vapor, small amounts of hydrogen, aliphatic acids, alcohols, or ketones. The molecular hydrogen from these species was thought to enhance the rate of the Boudouard reaction. However, the increase in the rate of the Boudouard reaction was also found to be independent of the amount of the added gases.

2.1.7.2 Mechanism and Nature of Carbon Formation

Carbon uptake and deposition on iron catalysts are characterized by two distinct rate regions. The first region is believed to be the diffusion-controlled formation of iron carbide; and the second is a slower rate of surface deposition of inactive carbon. Free carbon is typically observed after iron has been converted to carbide. This phenomenon has been observed in many studies. Typical ones are those by Pichler and Merkel (1949), Sancier, et al. (1979), Niemantsverdriet et al. (1980), Ott et al. (1980) and Krebs et al. (1981). Figure 2.9 illustrates the results of Sancier et al. (1979) over two calcined, promoted iron catalysts for F-T synthesis. The two distinct regions of weight gain can be seen in the figure.

The activity of the catalyst is affected by the carbon content of the catalyst. The activity generally increases as Hägg carbide is formed. It then goes through a maximum as carburization of the catalyst becomes complete and inactive carbon begins to form.

In Section 2.1.6.1, the competition model for carbon utilization was discussed with reference to Equations (13a) and (13c). In the model, surface reactions for the formation of bulk carbides, F-T chain intermediates, and inactive carbon are all in competition for surface

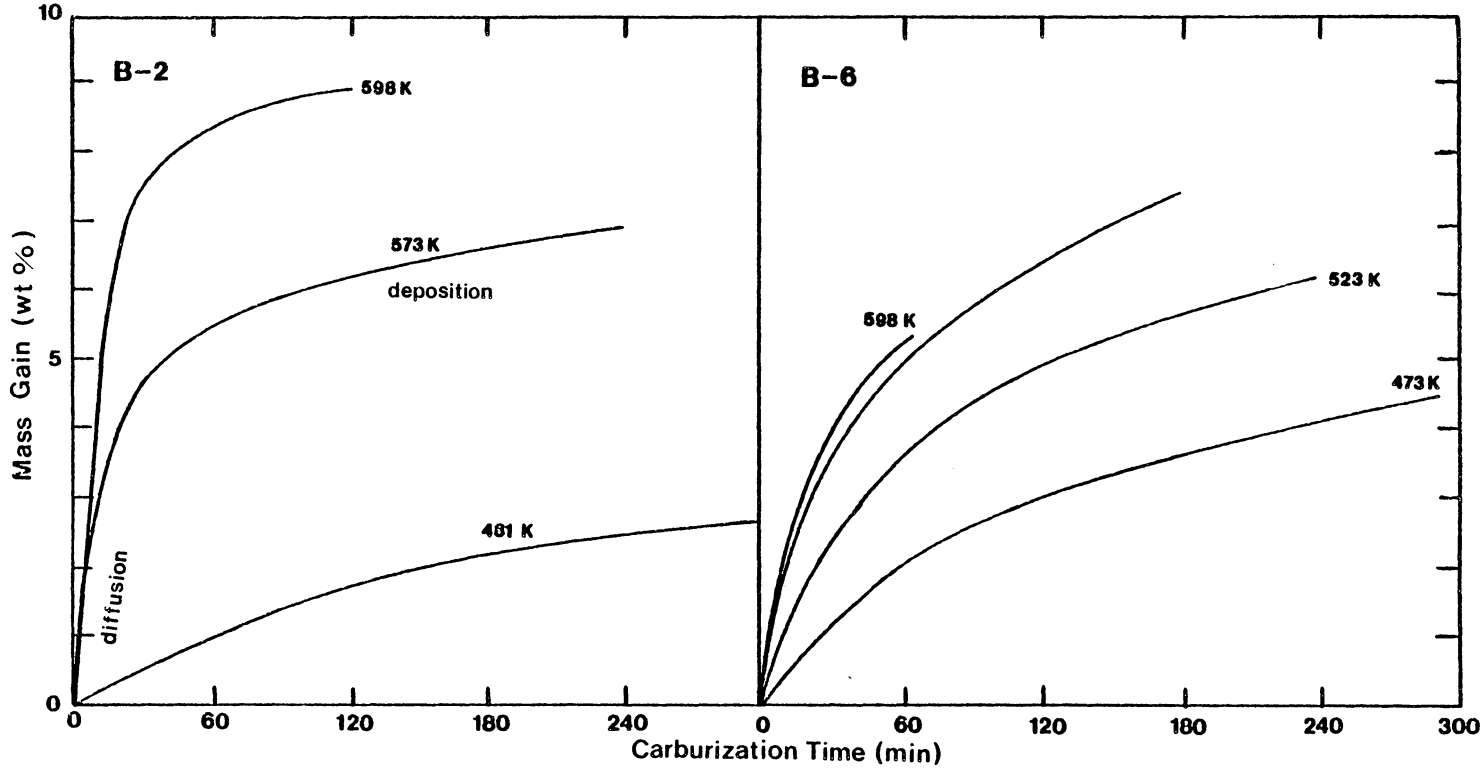

Figure 2.9. Two Distinct Regions of Mass Gain During Isothermal Carburization of Promoted Iron Catalysts B-2 and B-6 in H_2/CO (3:1) at 101 kPa. (Sancier et al., 1979): "Diffusion" Indicating Diffusion-Controlled Formation of Iron Carbide and "Deposition" Indicating Surface Deposition of Inactive Carbon.

carbide species. Additional credence is lent to this model by Dry's (1981) finding that elemental carbon formation did not increase as the production of F-T synthesis products were increased. Therefore, inactive carbon is believed not to be produced as part of the product slate, but rather via another reaction scheme such as the competition model, Equations (13a) to (13c).

The exact mechanism for inactive carbon formation on iron catalysts is not known. It is thought to be similar to the mechanism on nickel catalysts. However, iron carbide most certainly plays a more important role in carbon formation on iron compared to that nickel carbides play in the nickel system (Trimm, 1982). A large body of studies has been reported on carbon formation in methanation (200-450°C) and steam reforming (600-900°C) over nickel catalysts. This information has been reviewed by Trimm (1977) and Bartholomew (1982). Carbon deposition on iron catalysts has not been pursued with the same zeal, most likely due to the complex mechanisms involved. The studies that have been performed generally focus on inactive carbon formation above 500°C (Kehrer and Leidheiser, 1954; Ruston et al., 1969; Renshaw et al., 1970; Boehm, 1973; Baker et al., 1982; Sacco et al., 1984).

The forms of carbon produced on iron catalysts have generally been deduced through analogy to carbon formation on nickel catalysts. Table 2.8 summarizes the possible forms of carbon species on metals, but primarily on nickel (Bartholomew, 1982). Adsorbed atomic carbon species, C_α, are analogous to the surface carbidic species, C^*, suggested by Niemantsverdriet et al. (1981). In the case of iron

TABLE 2.8

Forms and Reactivities of Carbon Species Formed by Decomposition of CO on Nickel (Bartholomew, 1982)

Structural type	Designation	Temperature (°C) formed	Peak temperature (°C) for reaction with H_2
1. Adsorbed, atomic (dispersed, surface carbide)	C_α	200-400	200
2. Polymeric, amorphous films or filaments	C_β	250-500	400
3. Vermicular (polymeric, amorphous)	C_v	300-1000	400-600
a. filaments			
b. fibers			
c. whiskers		150-250	275
4. Nickel carbide (bulk)	C_γ	500	550-850
5. Graphitic (crystalline)	C_c	550	
a. platelets			
b. films			

catalysts, it is believed that C_α can convert to a less active, amorphous, form of carbon (C_β) on the surface. This form of carbon has a low degree of organization and is associated with lower formation temperatures. C_β is thought to be a precursor to graphite formation. Amorphous carbon formation causes a decrease in catalytic synthesis activity through fouling via the encapsulation of metal crystallites. This occurs more readily on iron than on nickel catalysts (Cooper and Trimm, 1980). Amorphous carbon may also block pores decreasing the effective area for catalytic synthesis. Graphitic carbon typically forms as filaments of carbon and does not diminish catalytic activity. In fact, it may actually increase the activity of the catalyst by dispersing the iron in finely divided carbon.

It is believed that amorphous or poorly crystalline carbon is catalytically recrystalized by Hägg carbon or cementite. This carbon diffuses through the carbide phase, explaining why the rate of carbon deposition is diffusion-rate limited (Cooper and Trimm, 1980). Graphitic carbon then grows on a crystal face of the iron carbide by utilizing the carbon dissolved in the carbon lattice. This is shown in Figure 2.10 (Boehm, 1973). A particle or a crystal of iron may be contained in the head of this filament, as it grows. Finally, stress in the catalyst particle, caused by growing filaments and expanding regions of carbon, leads to particle disintegration. In an active environment such as a fluidized bed, filaments readily break off and catalyst particles crumble.

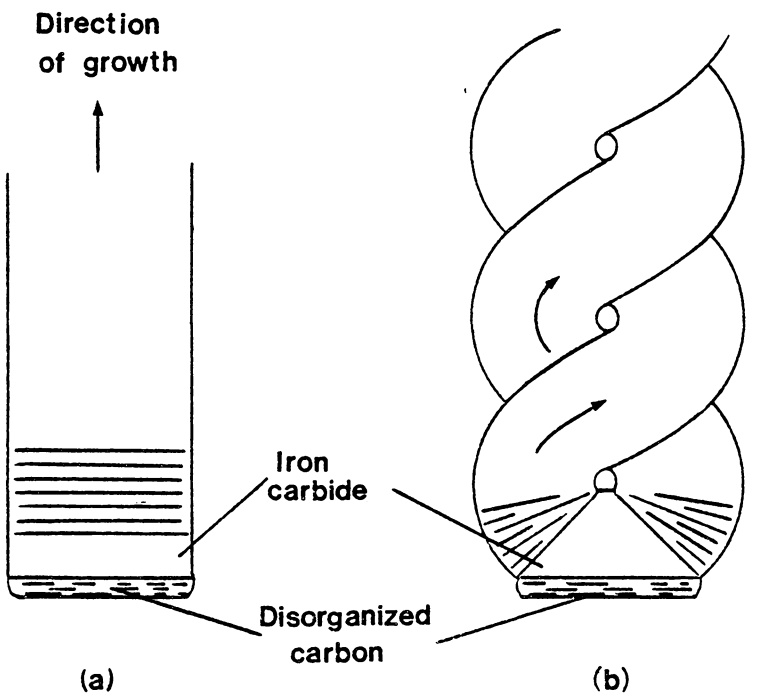

Figure 2.10. A Schematic Representation of the Growth Mechanism of Filamentary Carbon on Iron Carbide: (a) on a Rectangular Carbide Particle; and (b) on a Carbide Particle with Faces at Oblique Angles (Boehm, 1973).

Evidence of graphitic carbon formation on iron catalysts during F-T synthesis has been presented by several researchers. Reymond et al. (1980) using X-ray photoelectron spectroscopy (ESCA) showed graphite formed on a fused-iron catalyst at 250°C. Similarly, Agrawal et al. (1980) detected its formation of Fe/Al_2O_3 at 287°C using Auger electron spectroscopy (AES). Krebs et al. (1981) found graphite to be formed at 297°C on both iron foil and reduced magnetite using X-ray photoelectron spectroscopy (XPS). Thus, graphitic deposits on iron surfaces have been shown to occur at relatively low temperatures under F-T synthesis conditions.

2.2 Unsteady-State Methods

Unsteady-state methods have generally been directed toward two objectives in the past. The first school of thought uses transient methods to discern the kinetics of a particular reaction, focusing on the elementary reaction mechanism. The second utilizes forced cycling of a reaction parameter (such as feed flow rate or reaction temperature) in order to attain improved selectivity and/or increased conversion from a given reaction. These two approaches invariably intertwine since both the reaction mechanism and operating parameters cannot be considered separately.

Reviews by Kobayashi and Kobayashi (1975) and Bennett (1976, 1982) generally focus on the use of the transient method as a tool to obtain fundamental kinetic information. Other reviews by Bailey (1973) and Boreskov and Matros (1983), approach the subject of unsteady-state

operation in a more applied sense, emphasizing the selectivity shifts and increased conversion.

2.2.1 Transient Method for Kinetic Studies

Transient methods for kinetic studies typically involve sending an input signal, such as a pulsed amount of reactant gases, into a reactor and then observing the time-dependent changes of certain reaction variables, such as reaction temperatures and species concentration. In order for the transient response to truly reflect the kinetics of the reaction being investigated, the reactor must be operated under conditions that are free of heat- and mass-transfer limitations. Transient experiments generally provide more information than steady-state experiments. Once the kinetic information has been obtained under transient conditions, it must be described by successive elementary steps (an elementary-step model). Similarly, the buildup of adsorbed intermediates on the catalyst during transients must be described by mass balances. If this model adequately describes the system under study, it can be used for reactor design calculations or control algorithms.

Forcing functions used in the transient method are generally generated using four-way chromatographic valves. Analytical methods for following the response typically involve the use of mass spectroscopy, and to a lesser extent, gas chromatography. Recently, in-situ surface techniques have been developed. The reactor itself is usually a differential reactor operating at atmospheric conditions and measurable conversions, resulting in simplified analysis. Use of

isotopic tracers allows transient kinetics to be studied without altering feed-gas concentrations. Complex surface interactions can be discerned by following the decay of labelled species on the catalyst surface after switching to an unlabelled feed.

A recent monograph edited by Bell and Hedegus (1982) includes many articles on catalysis under transient conditions; and two review papers by Bennett (1976, 1982) describe in some detail the basic theory and applications of transient methods in heterogeneous catalysis. Biloen (1983) also gives a brief summary of ideas to be considered when using transient kinetic methods.

Transient methods have been used in attempts to identify the reaction intermediates and rate-limiting steps in Fischer-Tropsch synthesis. For example, Matsumoto and Bennett (1978) and Reymond et al. (1980) applied the transient method to study the kinetics of the reaction of carbon monoxide with hydrogen to form methane. A promoted fused-iron catalyst was used in a tubular reactor at 250°C and atmospheric pressure. When a gas stream of the reaction mixture (H_2/CO = 9:1) flowing over the catalyst was suddenly changed to pure hydrogen, large amounts of methane were formed. The surface of the catalyst was found to be covered mostly by a carbon intermediate, while the bulk of the catalyst was identified as Hägg carbide. The rate-determining step was found to be the hydrogenation of surface carbon. Similar studies on nickel methanation catalysts have identified two basic types of surface carbon on nickel catalysts (Wentrcek et al., 1976; McCarty and Wise, 1979).

Ino et al. (1981) found two kinds of carbon species using the transient method on a precipitated iron catalyst. A carbidic surface carbon was found to be highly reactive when exposed to hydrogen while amorphous free carbon was less reactive. Kieffer and Van Der Baan (1982) suggested that the rate of propogation of hydrocarbon chains could not be the rate-determining step of F-T synthesis. This conclusion was reached from transient experiments in a microreactor packed with precipitated iron-zinc catalysts at 277°C and 2.5 atm. More recently, Bennett and coworkers (Bianchi et al., 1983) used the transient method in conjunction with in-situ Mössbauer effect spectroscopy to study surface and bulk changes in an Fe/Al_2O_3 catalyst. These surface species were discovered: (1) CH_x, a reactive species; (2) CH_y a less reactive species; and (3) an inert "graphite-like" species. Bennett and coworkers (Underwood and Bennett, 1984; Suib et al., 1984) have also examined the reaction of hydrogen and carbon monoxide over nickel-alumina catalysts, as well as F-T synthesis over iron-containing zeolites using the transient method.

The transient method has been used to study methanation and F-T synthesis reactions over alumina-supported ruthenium catalysts as well. Dautzenberg et al. (1977) used 3% Ru on γ-Al_2O_3 in a fixed-bed reactor at 210°C and 10 bar. A H_2/CO mixture of 1:1 ratio was passed over the catalyst for several minutes followed by pure hydrogen. In addition, the bed temperature was cycled to 350°C and then rapidly cooled to 210°C. The purpose of this transient study was to determine the rate constants of the propogation reaction for the production of

hydrocarbon chains. Cant and Bell (1982) used transient response tracing in conjunction with in-situ infrared spectroscopy to determine the elementary steps of CO hydrogenation over ruthenium catalysts.

2.2.2 Improved Conversion and Selectivity

Based on theoretical and computational studies, Bailey and Horn (1967, 1971) and Douglas and Rippon (1966, 1967) have suggested that selectivity improvements can be made by cycling the reactor feed-concentration. Silverston, Hudgins and coworkers (Unni, et al., 1973; Abdul-Kareem et al., 1980; Jain et al., 1982a, 1982b, 1982c, 1983a, 1983b) have experimentally shown that the forced cycling of feed composition can significantly increase the catalyst activity.

In a review paper, Bailey (1973) describes periodic operation in terms of two characteristic terms: (1) the period or cycle time, τ; and (2) the characteristic response time of the system, τ_c. A quasi-steady-state system (QSS) results from the imposition of periodic behavior on a system, where the cycle time is much greater than the response time of the system ($\tau >> \tau_c$). More product can be obtained through QSS operation using an equivalent amount of reactants as in steady-state operation, but by cyclic feeding. The most important concept for QSS systems is that their output can be obtained by "mixing the outputs of several parallel processes operated at different steady states." In the latter operational mode, it seems to be more economical to run several parallel reactors and mix the outputs than to operate one system cyclically.

A second type of operation is termed relaxed steady-state. Here, the response time of the system is much slower than the cycle time of the forcing function ($\tau << \tau_c$). The system is unable to follow the rapid cycling and produces a time-invariant state, which may be called a relaxed steady-state.

Intermediate periodic operation is the final condition mentioned by Bailey (1973). In this case, the cycle time and the system response time are generally of the same order of magnitude.

Whether or not forced unsteady-state operation has an effect on a heterogeneous system depends on how the changing reaction medium affects the catalyst and on the dynamics of the reactor system itself (Boreskov and Matros, 1983). By manipulating reactor inlet parameters such as composition, temperature, pressure and space velocity in a periodic fashion, unsteady-state conditions can be maintained. The constantly changing reaction medium can influence the catalyst in two ways. The concentration of surface intermediates can change from what they were in steady-state. Alternately, the state of the catalyst surface itself can differ from when it was under the steady-state fluid composition. As discussed in previous sections, F-T synthesis catalysts in particular are dynamic parts of the reaction system. The bulk and surface compositions of F-T synthesis catalysts depend both on temperature and feed composition.

Hudgins, Silverston and coworkers (Jain et al., 1983) have introduced certain nomenclature that facilitates understanding in the study of periodic operation. Figure 2.11 is a plot of an optimization

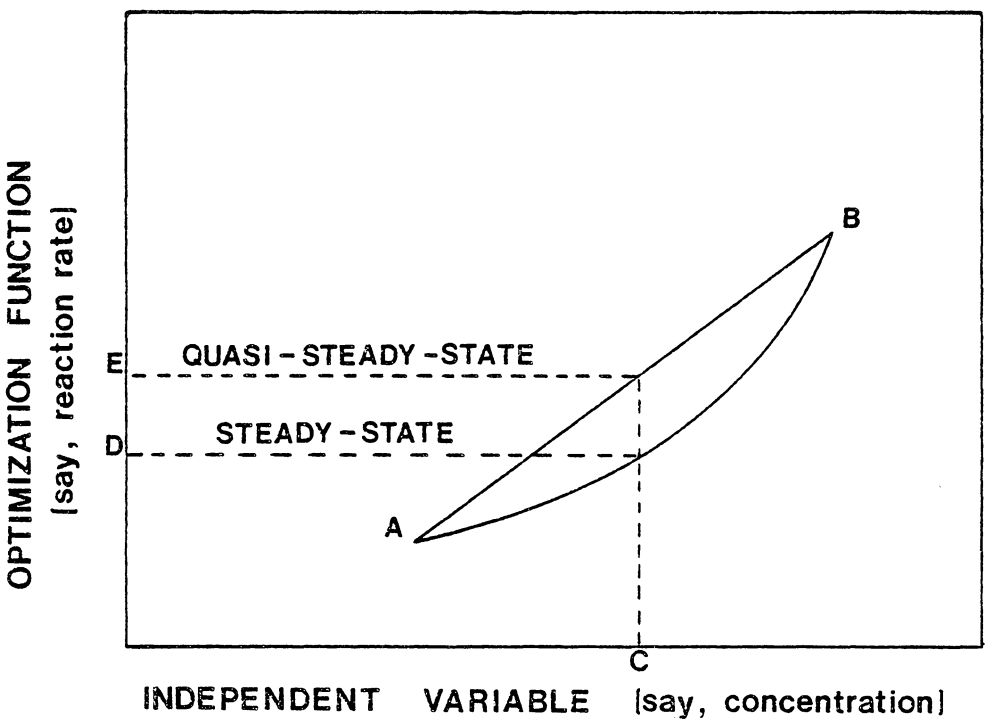

Figure 2.11. The Relationship Between the Steady-State and Quasi-Steady-State Kinetic Systems (Jain et al., 1983b).

function (such as reaction rate) versus an independent operating variable (such as feed concentration). Curve AB is the experimental reaction rate determined at various reactant concentrations for steady-state operation. For a given reactant concentration labelled by C in the figure, a reaction rate, labelled by D, will be observed at the steady state. Point E in the figure represents the reaction rate at the quasi-steady state. Recalling the description of QSS above, point E would be obtained by appropriately weighting the reactant feeds and mixing their outputs. Periodic operation would be obtained if the feed composition to a reactor is cycled between two concentrations, labelled A and B in the figure. This would result in a mean concentration, C.

If the above periodic operation is achieved by using a square-wave input signal, several more terms are defined. Figure 2.12 illustrates the terms used in cycling operations. The period, τ, is the time necessary for one full cycle. The cycle split, s, is the ratio of the time for the first partial cycle to the period (τ). The line segment AB in Figure 2.11 thus represents a series of quasi-steady-state reaction rates. These are the maximum reaction rates that can be obtained by mixing the outputs of parallel steady-state reactors. Therefore, any improvement in the time-average reaction rate would correspond to a point above the quasi-steady-state line segment AB. This point would accordingly be beyond the range of steady-state rates under the same time-averaged values of pressure, temperature and composition. If the steady-state curve were concave downward instead, the quasi-steady-state line would lie below the curve.

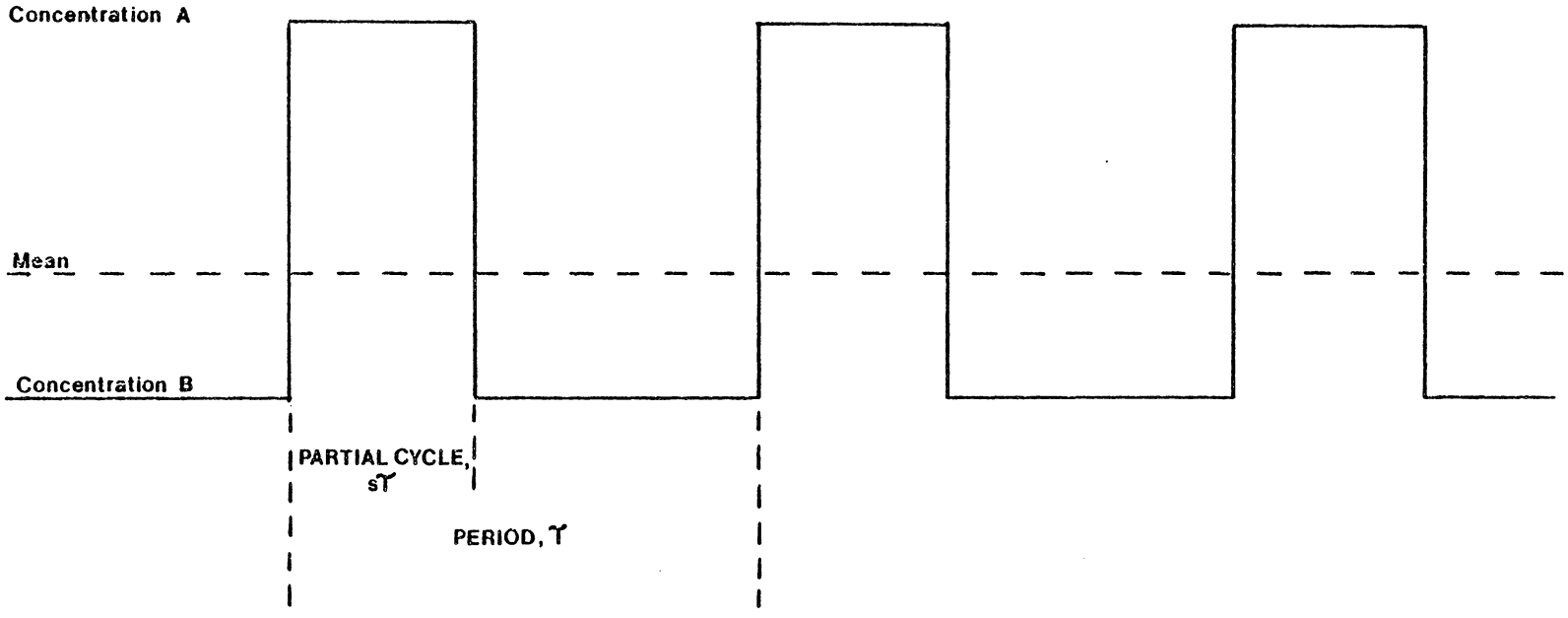

Figure 2.12. An Illustration of Terms Used in Cycling Operations (Jain et al., 1983b).

Using the above unsteady-state operational concepts and definitions, a systematic study of carbon-deposition rate as a function of ratio of hydrogen to carbon monoxide in the feed in a cycled-feed system could be undertaken. This was an objective of the present study.

Table 2.9, as adopted from Boreskov and Matros (1983) with several additions, lists processes where improvements in product selectivity and reactant conversion have been attained through unsteady-state operations. One representative example of these processes is ammonia synthesis on fused-iron catalysts as studied by Jain et al. (1982a, 1982c, 1983b). Cycling between a nitrogen-rich (hydrogen-poor) and a nitrogen-poor (hydrogen-rich) gas using periods of one to sixty minutes, it was found that the time-averaged reaction rate could be improved between 30 to 50 percent. Conditions of the synthesis were 23.8 atm and 360-400°C. These researchers speculate that nitrogen is dissolved in the bulk phase of the iron catalyst during the nitrogen-rich concentration portion of the cycle. The nitrogen diffusses back to the catalyst surface when the gas-phase concentration of nitrogen is low.

Only two experimental studies and one theoretical paper have examined possible selectivity improvements in Fischer-Tropsch synthesis. These studies were carried out in part to attempt to shift the standard "polymerization distribution law" or "Flory" distribution towards liquid products and away from high-molecular-weight species. Dautzenberg et al. (1977), cited previously, claimed selectivity improvements over a Ru/Al_2O_3 catalyst. A synthesis gas of a H_2/CO ratio of 1:1 was passed over the catalyst for 4 to 12 minutes, followed by pure hydrogen at an elevated temperature. It was shown that as the

TABLE 2.9

Examples of Processes Performed Under Forced Unsteady-State Conditions
(Adapted from Boreskov and Matros, 1983)

	Process	Forcing Variable	Effect	Reference
1.	Synthesis of ammonia on iron	Initial mixture composition	Increase in rate of conversion	Jain et al. (1982c, 1983b)
2.	Oxidation of CO over V_2O_5	Initial mixture composition	Increase in rate of conversion	Abdul-Kareem et al. (1980)
3.	Oxidation of CO over platinum	Initial mixture composition	Increase in rate of conversion	Cutlip (1979)
4.	Oxidation of sulfur anhydride on vanadium catalyst	Initial mixture composition	Increase in rate of conversion	Unni et al. (1973) Briggs et al. (1977)
5.	Polymerization of olefins on Ziegler-Natta catalysts	Hydrogen concentration	Change in the distribution of molecular weights	Claybaugh et al. (1969)
6.	Polymerization of styrene	Concentration of styrene and initiator	Increase in yield	Crone and Renken (1979)
7.	Production of ethyl acetate in a stationary catalyst bed	Concentration of acetic acid	Decrease of catalyst deactivation	Leupold and Renken (1977)
8.	Ethylene hydrogenation on platinum-aluminum catalyst	Space velocity of the initial mixture	Increase of productivity	Renken et al. (1975) Baiker and Richarz (1976) Helrick et al. (1974)
9.	Ethylene oxidation on supported silver catalyst	Initial mixture composition	Increase of selectivity	Renken et al. (1976)
10.	Chlorination of n-decane in a two-phase adiabatic reactor	Concentration of n-decane	Change in selectivity	Ding et al. (1974)

TABLE 2.9 (Continued)

	Process	Forcing Variable	Effect	Reference
11.	Ethanol dehydrogenation in a catalyst bed	Temperature of the cooling agent	Increase rate of conversion	Denis and Kabel (1970a,b)
12.	liquid-phase hydrogenation of α-methyl styrene on paladium catalyst	Space velocity of the initial mixture	Increase of productivity	Biskis and Smith (1963)
13.	Oxidation of butane, cyclohexane on platinum nets	Initial mixture composition	Change in selectivity	Wandrey and Renken (1977)
14.	Oxidation of SO_2 on vanadium catalyst	Switching of the direction of the reaction mixture flow in the catalyst bed	Reduction of capital investments; possibly to process gases with variable and low initial concentration; increase of conversion	Boreskov and Matros (1983)
15.	Catalytic detoxication of noxious industrial gases from CO and organic substances	Switching of the direction of the reaction mixture flow in the catalyst bed	Reduction of capital investments, possibly to process gases with variable and low initial concentration; increase of conversion	Boreskov et al. (1981a, 1982a)
16.	Synthesis of ammonia on iron catalyst	Switching of the direction of the reaction mixture flow in the catalyst bed	Reduction of capital investments, possibly to process gases with variable and low initial concentration; increase of conversion	Boreskov et al. (1981b)
17.	Oxidation of sulfur anhydride on vanadium catalyst	Temperature of inlet mixture		Boreskov et al. (1982a,b)

chain length increased, deviations from the polymerization distribution law became greater. This claim was made by simply comparing unsteady-state experimental results to the theoretical product distribution predicted by the polymerization distribution law. No steady-state experimental results were presented. Madon (1979) later pointed out that the polymerizaion distribution law did not apply to data obtained over alumina-supported ruthenium catalysts. Madon et al. (1977) have shown steady-state product distributions that are similar to those of Dautzenberg et al. (1977) obtained under cyclical conditions on Ru/Al_2O_3.

Feimer et al. (1981, 1982b, 1984) studied the effect of forced cycling of hydrogen and carbon monoxide concentration in the feed gas over a precipitated, copper-potassium-promoted iron catalyst in a fixed-bed reactor at 246°C and 3.8 atm. Differential conversons were measured using pulsed amounts of hydrogen-rich and hydrogen-poor mixtures of H_2 and CO for different time periods varying from one to thirty minutes. Steady-state and step-change measurements were also undertaken to supplement the cycling studies. The step-change experiments suggest that altering the H_2/CO ratio in the feed gas changes the relative amounts of hydrogen and carbon monoxide adsorbed on the surface of the iron catalyst. Under rapid cycling with one pulse containing pure hydrogen, methane was produced at a rate 80% higher than the corresponding reaction under steady-state conditions. This was taken as evidence that methane was produced via hydrogenation of a surface carbide as well as through the standard chain-building route.

The results also indicated that a decrease in the time period between hydrogen-rich and hydrogen-poor pulses increased the time-averaged production rates of higher hydrocarbons. However, these production rates were smaller than those observed under steady-state conditions. These investigators thus suggested that under their experimental conditions, no significant improvement in rate or selectivity to liquid hydrocarbons could be achieved. It follows that their results obey the polymerization distribution law with the exception of methane.

As discussed earlier, Peacock-Lopéz and Lindenberg (1984) showed that the use of transient operating conditions may, theoretically, significantly alter the F-T product distribution. This model predicts, in one instance, that a majority of products being produced would be C_5 to C_{20}, or liquid products. For a steady-state reaction with the same probability of chain growth (α), the polymerization distribtion law suggests that the majority of products will contain 20 or more carbon units. One important conclusion of this study was that deviations from the polymerization distribution law were more pronounced as the probability of chain growth approached unity (i.e., $\alpha \geq 0.9$).

Note that the probability of chain growth can be altered in three ways: (1) by selecting different types of catalysts; (2) by adjusting catalyst promoter content; and (3) by altering the synthesis conditions. Catalyst selection has the most pronounced effect on the probability of chain growth. Jacobs and Van Wouwe (1982) describe typical bounds on this parameter for F-T synthesis catalysts:

Fe $\alpha \simeq 0.50\text{-}0.70$

Co $\alpha \simeq 0.70\text{-}0.80$

Ru $\alpha \simeq 0.85\text{-}0.95$

If the results by Feimer et al. (1981, 1982b, 1984) are examined in light of Peacock-Lopéz and Lindenberg's (1984) prediction, it is understandable why no deviation from the polymerization distribution law model was observed. Feimer and coworkers obtained a probability of chain growth of approximately 0.67 on their precipitated and promoted iron catalyst. This observed probability was well below the values necessary to show deviations.

2.3 Vibrofluidized Beds

A vibrofluidized bed is typically created by imparting vertical sinusoidal vibrations to a vessel containing a granular solid. In a conventional fluidized bed, particles are bouyed up from beneath throught the action of gas impinging on the particle. A vibrofluidized bed, however, typically does not have a fluidizing gas flowing through it from below.

Recently, a distinction has been made between systems with and without a forced fluidizing gas flow from beneath. Systems without a forced gas flow from beneath, yet possessing vibrational accelerations $A\omega^2/g > 1$, are termed "vibrated beds" (A = vibrational amplitude in length; ω = angular frequency in radians per second; g = acceleration due to gravity). All beds with $A\omega^2/g > 1$ and gas velocities less than the minimum fluidization velocity (U_{mf}) for gas-fluidization are termed "vibrofluidized beds." Finally, all beds with gas velocities greater

than U_{mf} for gas fluidization that are also being vibrated at any frequency are called "vibrated fluid beds." These terms were defined in a recent review of the theory and applications of vibrated beds and vibrated fluid beds (Pakowski et al., 1984). A detailed review of vibrofluidized beds and their applications has been presented by Hirt (1984).

Vibrofluidized beds possess characteristics which make them uniquely different from conventional gas-fluidized beds. Vibrofluidized beds can operate at very low gas flow rates, consequently extending the range of fluidization. A uniform gas distribution can be readily achieved in a vibrofluidized bed, eliminating channelling or gas-bubble formation as observed in gas-fluidized beds. The solid, nevertheless, is intensely mixed by the vibration. This vigorous mixing promotes both heat and mass transfer between the particles and the gas, as well as, heat transfer to the walls. Excellent heat transfer results in a virtually isothermal bed. These characteristics lead to an uninterrupted phase of gas and solid of uniform bed height with little backmixing of gas under most conditions (Chlenov and Mikhailov, 1964, 1965; Baird, 1966; Bratu and Jimescu, 1971).

Bachman (1940) was probably the first to describe and attempt to model the dynamic behavior of particles inside a vibrated, vertical cylinder. Kroll (1955) also examined solid circulation in a vibrated vessel. Enhanced heat transfer coefficients in vibrated beds were found by Bretsnajder et al. (1963). About the same time, Chlenov and Mikhailov (1964, 1965) coined the term "vibro-fluidization." These two

researchers were also the first to suggest practical uses for vibrofluidized beds. They advocated its use for drying of the free-flowing material, roasting of granules and reduction of metals. They noted that because of their unique characteristics, vibrofluidized beds would be particularly well suited for exothermic reactions.

In the first laboratory application of vibrofluidized beds to catalytic reactions, Shchel'tsyn et al. (1968) used a vibrofluidized bed to screen catalysts and determine the kinetics of the gas-phase vinylation of α-pyrrolidone. In this study, 35 to 50 ml of 0.25-1 mm diameter catalyst particles were charged to the reaction vessel. The vibrofluidized bed used did not have a permeable base plate, but rather α-pyrrolidone vapor was introduced to the base of the bed via a trumpet-shaped dip tube. The reaction was run at 260-320°C, 1 atm with a α-pyrrolidone vapor space-velocity of 250 hr^{-1}. The vibration frequency of the reaction vessel was set at 100 cycles per second, which resulted in ideal solid mixing with no diffusional reaction limitation.

No other references to the use of vibrofluidized beds as catalytic reactors could be found in the literature. Several references to vibrated fluid-beds for gas-solid and gas-phase catalytic reactors have been found. Wronski et al. (1976) procured a patent in Poland for desublimation of phtalic anhydride vapors in a vibrated fluidized bed. The vapors were condensed in a bed of particles vibrating at 15 Hertz (or cycles per second) with an amplitude of 15 mm. The effect of grid-plate vibration rate on the mass transfer coefficient was the subject of experiments by Reusov et al. (1980). Mass transfer between the fluid and solid was found to increase significantly with increasing vibration rate

and fluid flow rate, and with decreasing bed porosity. Also in 1980, Alekseeva et al. examined the catalytic oxidation of HCl to Cl_2 over $CuCl_2$ and KCl. A 25-ml vibrated fluidized-bed reactor was used for studies at temperatures ranging from 387-427°C. More recently, the kinetics of the catalytic pyrolysis of ethane were investigated in a vibrated fluidized bed. Indium-oxide (In_2O_2) catalyst was vibrated at a frequency of 20-25 Hz and an amplitude of 2-3 mm in the presence of ethane diluted with oxygen. The reaction conditions were 650-800°C and presumably 1-atm total pressure.

Several observations can be made from the above examination of reaction studies in vibrofluidized and vibrated fluid beds. First, a vast majority of work on this subject originates from the Soviet Union and Eastern Europe and, therefore, has been written in languages other than English. This results in a very slow transfer of concepts to English-speaking researchers. Secondly, most if not all of these studies have been perfomed at low pressures. Vibrofluidized beds can, of course, operate under high pressures as well as high temperatures. In this work, a vibrofluidized-bed microreactor has been developed for F-T synthesis studies at approximately 2,200 kPa (about 22 atm) and nearly 400°C.

CHAPTER 3

EXPERIMENTAL APPROACH

3.1 An Overview

As discussed in Section 2.2, unsteady-state operation of chemical reactors has been shown to improve the conversion and/or selectivity of several reactions. The ultimate goal of the research undertaken at Virginia Tech is to determine if a reduction in carbon deposition on a promoted fused-iron catalyst can be achieved through rapid forced concentration-cycling of microreactor feed gases. It is hoped that through cycling of a feed gas of a low H_2/CO ratio (< 1:1) followed by a hydrogen-rich feed gas, active surface carbon will be utilized before it can degrade into an inactive form. It is also hoped that that cycling of feed gases in this manner would simulate the catalyst residence time in the heat-tray reactor described previously in Chapter 1.

The experimental studies presented in this dissertation have been broken down into three phases:

1. Steady-State Fischer-Tropsch Synthesis in a Vibrofluidized-Bed Microreactor System.
2. Gas Mixing and Catalyst Vibrofluidization Studies in a Cold-Flow Vibrofluidized-Bed Microreactor Model.
3. Design and Construction of a Vibrofluidized-Bed Microreactor System for Unsteady-State Fischer-Tropsch Synthesis.

The first phase involved obtaining information on carbon deposition under steady-state synthesis conditions as well as determining operating conditions. The second phase required characterization of a newly developed unsteady-state microreactor system by using a cold-flow model.

The final phase utilized the results obtained from the cold-flow microreactor model to design a high-pressure, high-temperature system for unsteady-state Fischer-Tropsch synthesis. Using the unsteady-state vibrofluidized-bed microreactor system developed here, investigations of the effect of feed cycling on carbon-deposition rate during F-T synthesis will be performed in the near future.

3.2 Steady-State and Unsteady-State Carbon Deposition Studies

Researchers at the University of Waterloo have developed a nomenclature for the study of forced concentration feed cycling (Jain et al., 1983b). This system has been explained in Section 2.3.2. Implementation of their concepts results in a plot of the optimization function versus an independent variable as shown in Figure 2.11. By plotting unsteady-state experimental results on such a plot, any improvement over steady-state operation can be seen.

In the present study, the optimization function is the carbon-deposition rate, while the mole fraction of hydrogen in the feed can be taken as an independent variable. As an example, Dry's equation for carbon deposition rate, Equation (15) in Section 2.1.7.1, can be used to construct a steady-state carbon-deposition rate curve. For this example, the relative partial pressures of H_2 and CO are assumed to be constant throughout the reactor. If a feed gas of a H_2/CO ratio of 0.11:1 (point A in Figure 3.1) were fed for 3/4 of a cycle and pure hydrogen (point B in Figure 3.1) were fed for the remainder of the cycle at the same flow rate, the mean composition of the feed gas would have a H_2/CO ratio of 0.44:1 (point C in Figure 3.1). The quasi-steady-state carbon-deposition

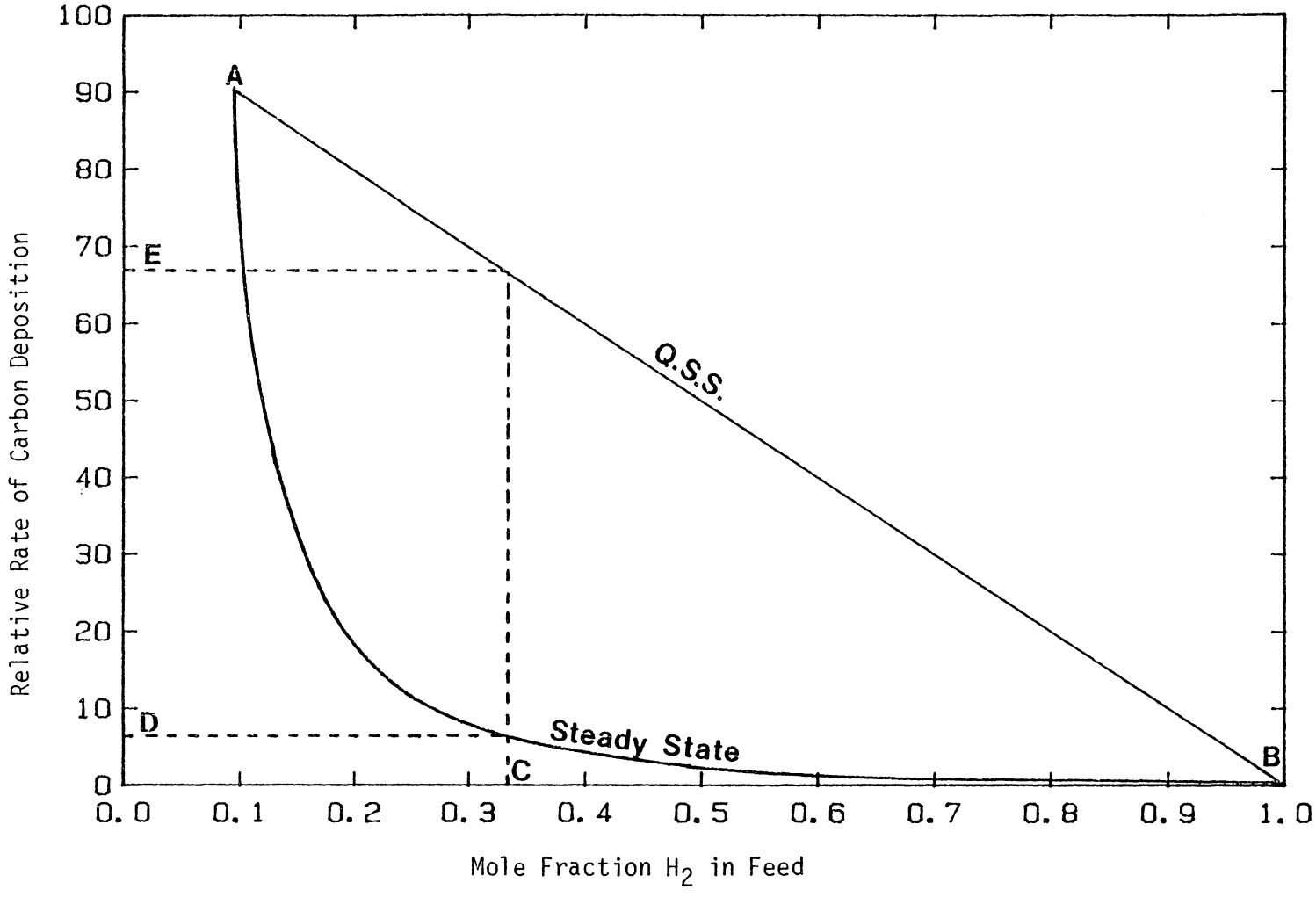

Figure 3.1. Hypothetical Quasi-Steady-State (Q.S.S.) and Steady-State Carbon-Deposition Rate Curves for Carbon Deposition as a Function of H_2 Mole Fraction in Feed.

rate would correspond to that given by point E in Figure 3.1. Point D in the figure is the rate that would be obtained through the steady-state reaction of the mean-composition gas. Any improvement, therefore, would be expressed by a reduction of carbon-deposition rate below the steady-state rate given by point D.

In reality, carbon-deposition rate is a function of the partial pressures of hydrogen and carbon monoxide in the reactor. These partial pressures, in turn, depend on the feed-gas compostion and the reaction conditions. The partial pressures of H_2 and CO vary through the catalyst bed and are affected by the extent of reaction and by the water-gas shift reaction. A proper study of the effect of forced feed-concentration cycling on the carbon-deposition rate during F-T synthesis would involve:

1. The determination of steady-state rates of carbon deposition as a function of feed partial-pressures of hydrogen and carbon monoxide.

2. The determination of unsteady-state rates of carbon deposition as a function of cycle split. Cycle split is defined as the duration of the cycle during which one concentration feed gas is being feed relative to the total cycle period. A feed with the same partial pressures of hydrogen and carbon monoxide as was chosen for the steady-state studies should be used.

3. The comparison of results from both steady-state and unsteady-state experiments.

CHAPTER 4

STEADY-STATE FISCHER-TROPSCH SYNTHESIS IN A VIBROFLUIDIZED-BED REACTOR SYSTEM

4.1 Experimental Apparatus and Procedures

4.1.1. Experimental Apparatus

4.1.1.1 Microreactor System

Fischer-Tropsch experiments were performed in a specially-designed vibrofluidized-bed microreactor system operated isothermally in the range of 360 to 400°C. All experiments were undertaken at a total system pressure of 2,220 kPa (320 psia or 22 atm).

All steady-state experiments were performed in a reactor system that also functioned as a preliminary design for the unsteady-state experimental apparatus.

Figure 4.1 is a schematic of this steady-state vibrofluidized-bed reactor system. Premixed feed gases, either a H_2:CO:Ar mixture or pure hydrogen, enter the system through stainless-steel high-pressure regulators (Airco model 49). The feed gas then passes through an activated-carbon filter used to remove impurities followed by a 15-micron filter which protects downstream solenoid and needle valves. The gas is stored upstream of solenoid valves 1-4 at 4,811 kPa in 1000-ml 304-stainless-steel sample cylinders. Two-way, normally-closed, high-pressure solenoid valves are used to select gas flow to the reactor. These solenoid valves (1-4), and also downstream solenoid valve 5, are stainless-steel valves (Circle Control model SV10) with Nylatron seats. Low-flow stainless-steel needle valves (Nupro series SG and SGD) are

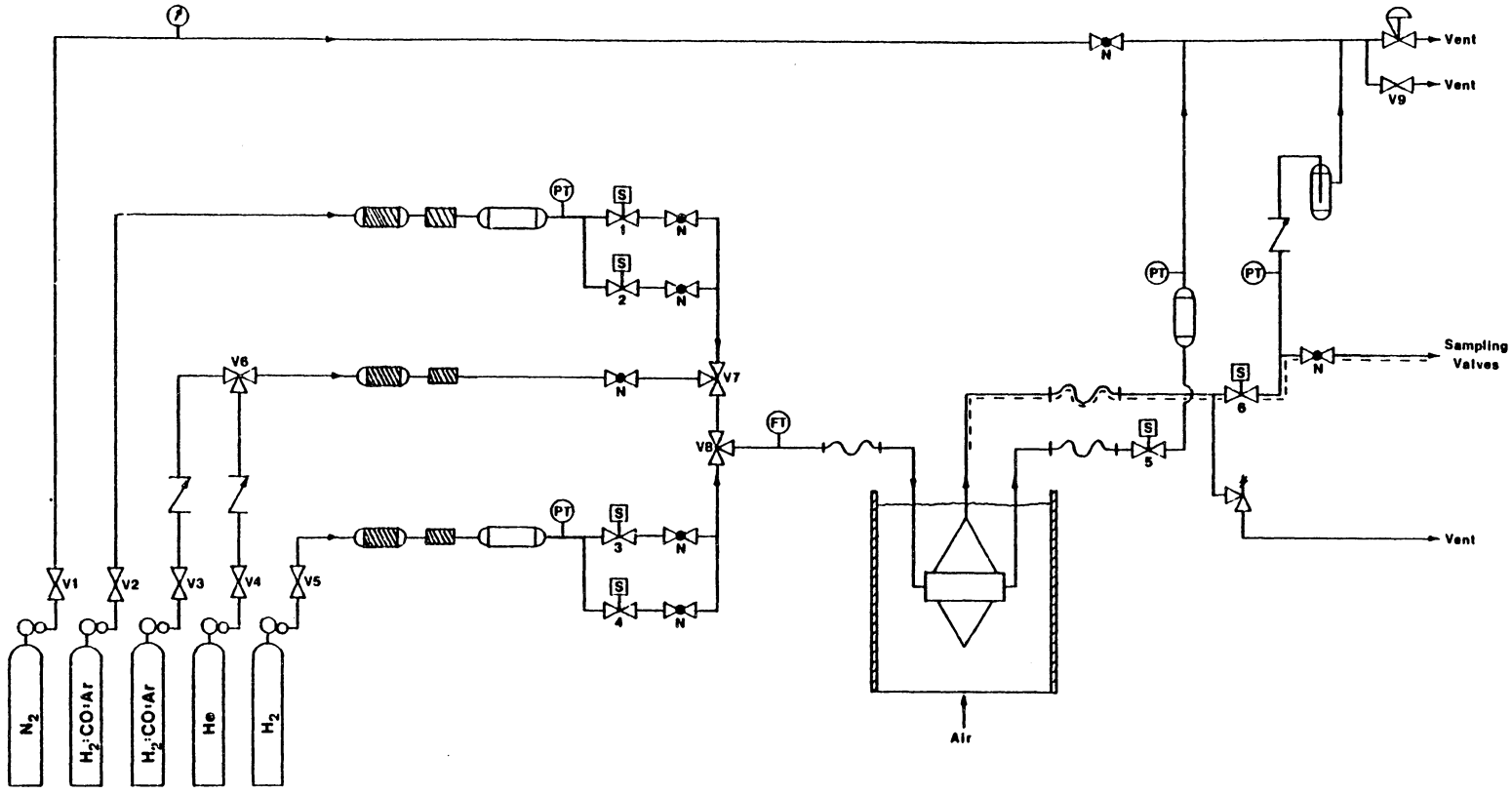

Figure 4.1a. A Schematic Diagram of the Steady-State Vibro-fluidized-Bed Microreactor System.

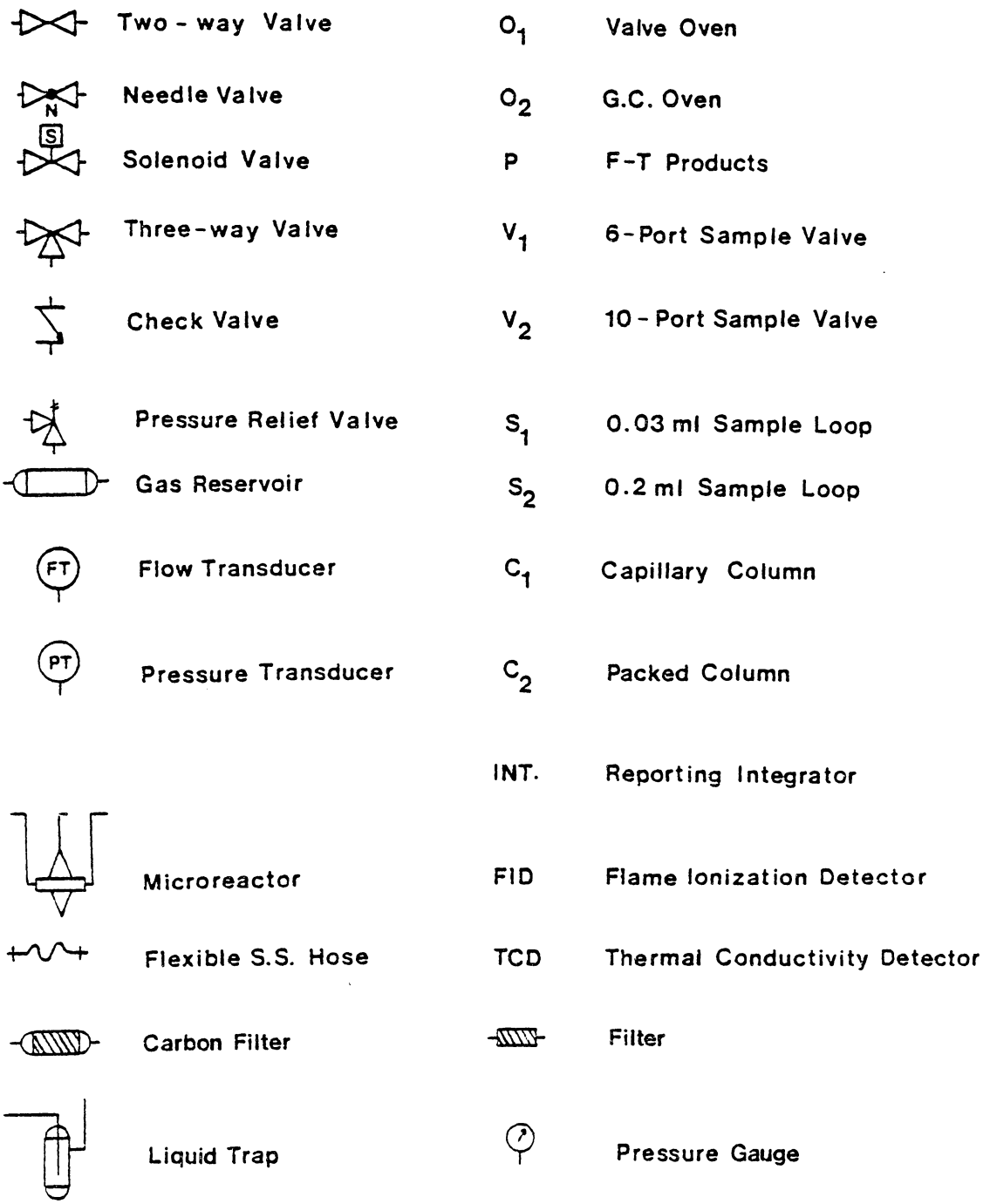

Figure 4.1b. Equipment Symbols Used in Figures of Experimental Systems.

used in conjunction with a Thermal Mass Flowmeter (Brooks model 5810) to manually set feed-gas flow rates.

A critical pressure drop is maintained across the needle valves, making the flow rate through these valves independent of downstream pressure. Creating a critical pressure drop involves setting the upstream pressure at a sufficiently high pressure, thereby causing gas flows through the needle valves to be at the sonic velocity. A three-way valve in the synthesis gas line after solenoid valve 2 allows for switching to helium feed for system purging or to a synthesis gas of a higher H_2/CO ratio for precarburization of the catalyst.

The reactor itself is suspended down into a constant-temperature fluidized bath (Techne SBL-2D) where its temperature is controlled to $\pm 1°C$ by a controller (Techne model TC4). Flexible stainless-steel hoses connect the fixed feed- and exit-gas lines to the vibrating microreactor. The exit line from the right-hand side of the microreactor is used only for purging gases from the reactor-feed line. This purge line was originally designed for use during unsteady-state F-T synthesis experiments. Therefore, solenoid valve 5 is kept closed during steady-state operations.

The vertical line exiting the top of the microreactor is the product exit line. Synthesis gas or reducing hydrogen enters the reactor from the left-hand feed-gas line, passes up through the vibrofluidized catalyst bed where it is converted and exits through the heated product exit line. This line is traced with heating tape and is held at 200°C.

Solenoid valve 6 is a high-temperture, high-pressure, normally-closed valve. It is a series-1000 stainless-steel unit with a Teflon seat manufactured by Atkomatic Solenoid Valves. This valve is held open during catalyst reduction and synthesis. A double-needle valve (Nupro Model SGD) allows for a small amount of product gas to be drawn off continuously through 1/16-inch O.D. stainless-steel tubing for sample analysis by gas chromatography.

System pressure is maintained at 2,220 kPa through the use of a back-pressure regulator (BPR) manufactured by Circle Seal Controls (model number BPR-8A). The back-pressure regulator maintains the system pressure within ±35 kPa, when a nitrogen ballast gas flow is used. The flow rate of product gases through the back-pressure regulator is normally too small to keep the BPR from "searching." Therefore, a larger, constant flow of nitrogen is used to supplement the product-gas flow through the BPR.

A check valve and a liquid trap lie between the product exit line and the nitrogen ballast line. The system pressure is monitored by two strain-gage absolute-pressure transducers (Schaevitz type P720). By using these transducers in connection with 3-way valves, pressure can be read in more than one position if care is exercised. A manual valve is mounted in parallel to the back-pressure regulator to allow for pressure letdown at the end of an experiment. As a safety precaution, an over-pressure relief valve has been mounted between the reactor exit and solenoid valve 6. This valve will release gas to vent if the reactor pressure rises above 4,220 kPa.

All equipment and tubing in contact with hydrogen or synthesis gas are constructed of either 304- or 316- stainless steel. Regulators and tubing coming in contact with only helium or nitrogen are made of brass. In general, all tubing is 316- stainless steel 1/4-inch O.D. with 0.035-inch wall thickness. The maximum safe working pressure of this system at 21°C is approximately 7,000 kPa.

4.1.1.2 Vibrofluidized-Bed Microeactor

Figure 4.2 and 4.3 are cross-sectional schematic diagrams of the vibrofluidized-bed microreactor used for steady-state Fischer-Tropsch experiments. This microreactor consists of three sections: (1) the base section; (2) the reaction section; and (3) the product-exit section.

As shown in Figures 4.2 and 4.3, the base section consists of a 6.35-mm hole drilled through a solid, cone-shaped piece of 316-stainless steel. A 1/4-inch O.D. tube with 0.035-inch wall thickness was slid through this hole and welded in place. Starting in the center of the flat, top surface of the base section, a 3.175-mm wide slot was milled down through the 1/4-inch tube. This slot extends 12.7 mm in each direction from the centerline and in line with the 1/4-inch tube. A wider, 6.35-mm slot was milled in the same fashion, but only 1.588-mm deep. This second slot allows a sintered stainless-steel distributor plate to be recessed into the base section of the microreactor, The gas space below the distributor plate is termed "the plenum zone."

Other features of the microreactor base section include an O-ring groove and threaded holes to receive connecting bolts. Two guide rods

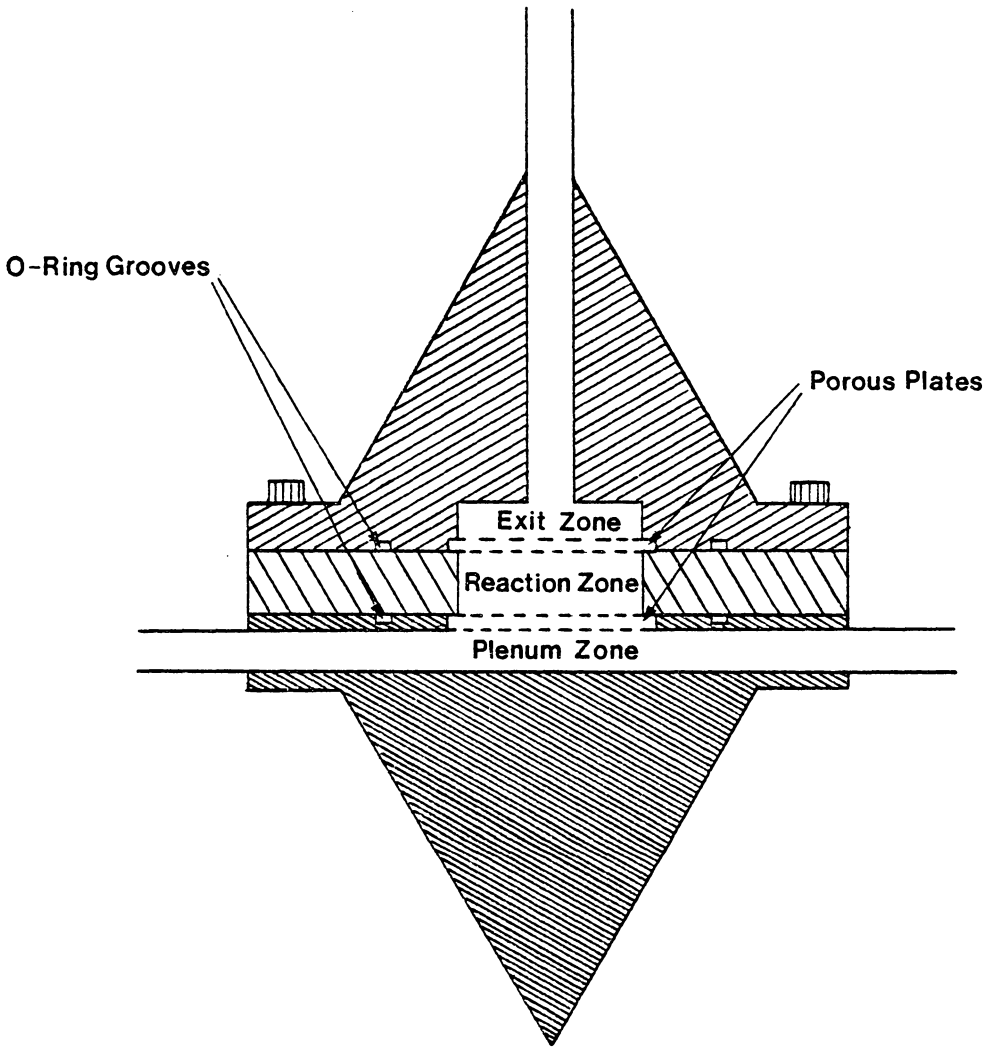

Figure 4.2. A Cross-Sectional Schematic Diagram of the Vibrofluidized-Bed Microreactor (front view).

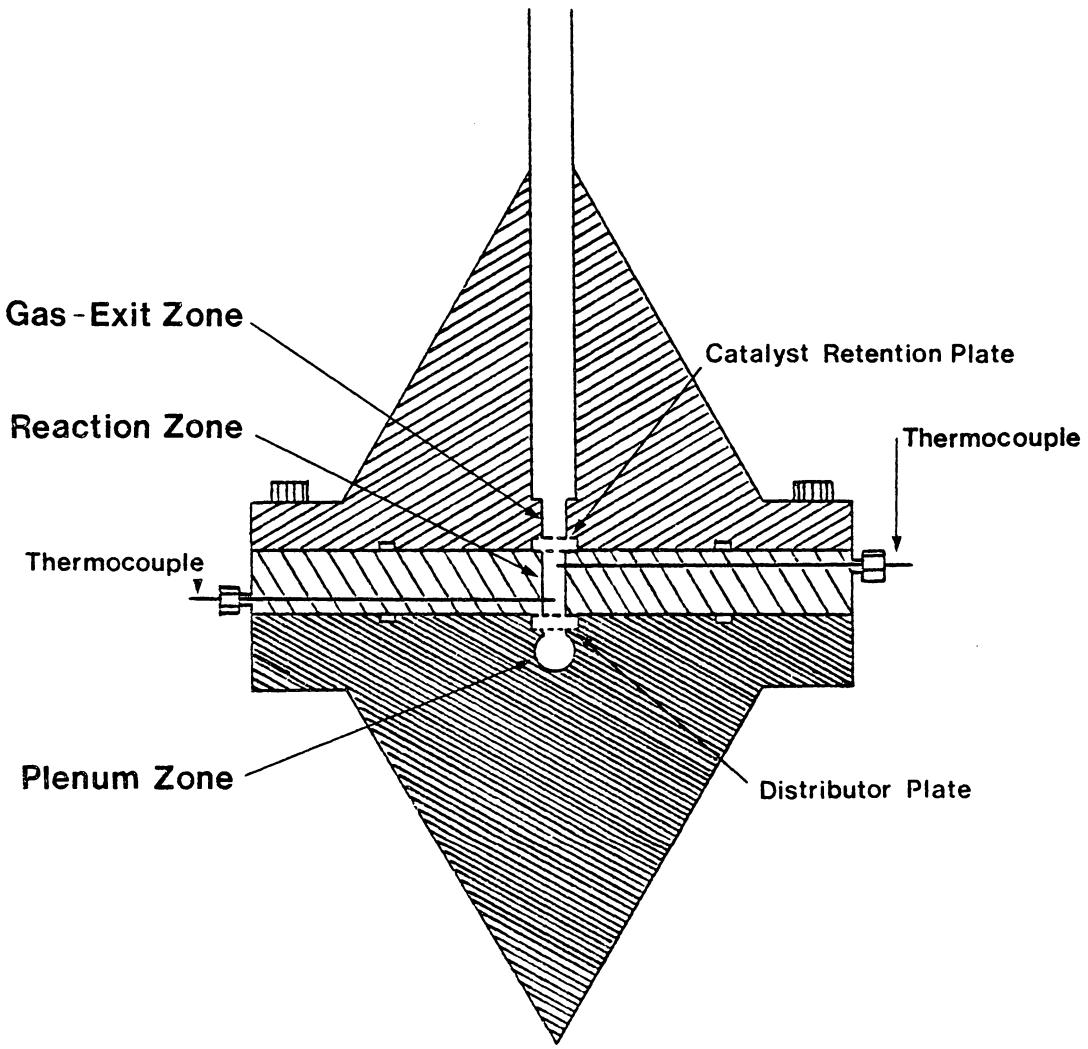

Figure 4.3. A Cross-Sectional Schematic Diagram of the Vibrofluidized-Bed Micro-reactor (side view).

press fitted into the base section facilitate alignment of the reaction section and the product-exit section.

The reaction section consists of a 14.29-mm thick, 316- stainless-steel disk, 63.5 mm in diameter. A 3.175-mm by 25.4-mm slot or "reaction zone" has been milled through the center of the disk. Two 1.50-mm stainless-steel sheathed type J thermocouples extended into the center of the reaction zone. The first is mounted 3 mm above the distributor plate while the second is 3 mm below the top of the reaction zone.

The final section of the microreactor, the product exit section, is a solid piece of 316- stainless steel in the form of an inverted cone. A slot, 25.4-mm long by 3.175-mm wide by 6.35-mm deep, has been milled in the flat surface to match the slot cut in the reaction section. A recess identical to the one milled into the base section holds a sintered stainless-steel catalyst retention plate. This plate keeps the catalyst from blowing out of the reaction zone during periods of high gas flow rate, for example, during purging. A vertical 1/4-inch O.D. stainless-steel tube with a 0.035-inch wall thickness passes down through the centerline of the product-exit section and connects with the milled slot.

During F-T synthesis experiments, gas first passes into the plenum zone, where it flows up through the distributor plate into the bed of vibrofluidized catalyst particles. Product gases and unreacted feed gases then flow through the catalyst retention plate and out of the reactor via the product-exit section. The reaction zone was designed as a slot, rather than a cylinder, in order to provide a maximum heat-transfer area. In addition, a reaction zone in the form of a slot provides for no dead volume in the reaction zone. The latter provision becomes extremely

important when rapid gas cycling is desired. This will be discussed further below in connection with unsteady-state F-T synthesis experiments.

This microreactor must remain leak-tight at temperatures up to 450°C and pressures to 2,229 kPa. Conventional gasket materials can not withstand these severe conditions and therefore metal O-rings must be used. A silver-plated stainless-steel O-ring (American Seal and Engineering Company) was used (1) between the reaction section and base section and (2) between the reactor section and product-exit section of the microreactor. Grooves in the base and product-exit sections of the microreactor accept these O-rings.

The three microreactor sections are bolted together using eight 1/4-20 hardened bolts. The O-rings are smashed into their grooves and gas pressure acts to force the ring against the metal, sealing the reactor. New O-rings are used for each experiment and provide enough sealing power to prevent even hydrogen from leaking. A "Grafoil" gasket, manufactured by Union Carbide, is used around the edges of the distribution plate to prevent the possibility of feed gas bypassing the distributor by going around its edges. The exterior shape of the microreactor is conical in order to promote the breaking of gas bubbles in the fluidized constant-temperature bath. This, in turn, provides for better bath-to-reactor heat transfer and promotes more vertical vibration of the microreactor.

4.1.1.3 Vibrating System

Figure 4.4 is a schematic diagram of the vibrating and suspension system of the microreactor. The microreactor is suspended down into the constant-temperature bath by four threaded rods. These rods are bolted to a 101.6-mm square plate, 6.35-mm thick. This square is attached to a support structure by four 177.8-mm long leaf springs, 25.4 mm wide. Each spring consists of two 1.59-mm thick tempered spring-steel leaves. A single threaded bolt connects the square reactor support in the center of the leaf springs to the vibrator. The vibrator is securely anchored to the wall through the use of an I-beam. It was found that support systems with a smaller mass than the I-Beam tended to resonate. The vibrator itself is manufactured by Ling Dynamic Systems (model V203). The maximum peak-to-peak amplitude for this unit is physically limited to 6 mm. The vibrator is driven by a function generator (Wavetak model 182A) with an inhouse-constructed amplifier. The microreactor is typically operated at the resonance frequency of the leaf-spring support structure. This is generally between 18 and 24 Hz.

4.1.1.4 Product Sampling System and Gas Chromatographic Analysis

In the steady-state vibrofluidized-bed microreactor system, F-T synthesis products and unreacted feed gases are continuously drawn through gas sampling valves for gas chromatographic analysis. Figure 4.5 is a schematic diagram of the product sampling and analysis systems. The major components of this system include: (1) two Valco sampling valves, a six-port and a ten-port valve; and (2) a gas chromatograph (Hewlett Packard 5730A). Product gases (P) are drawn from the

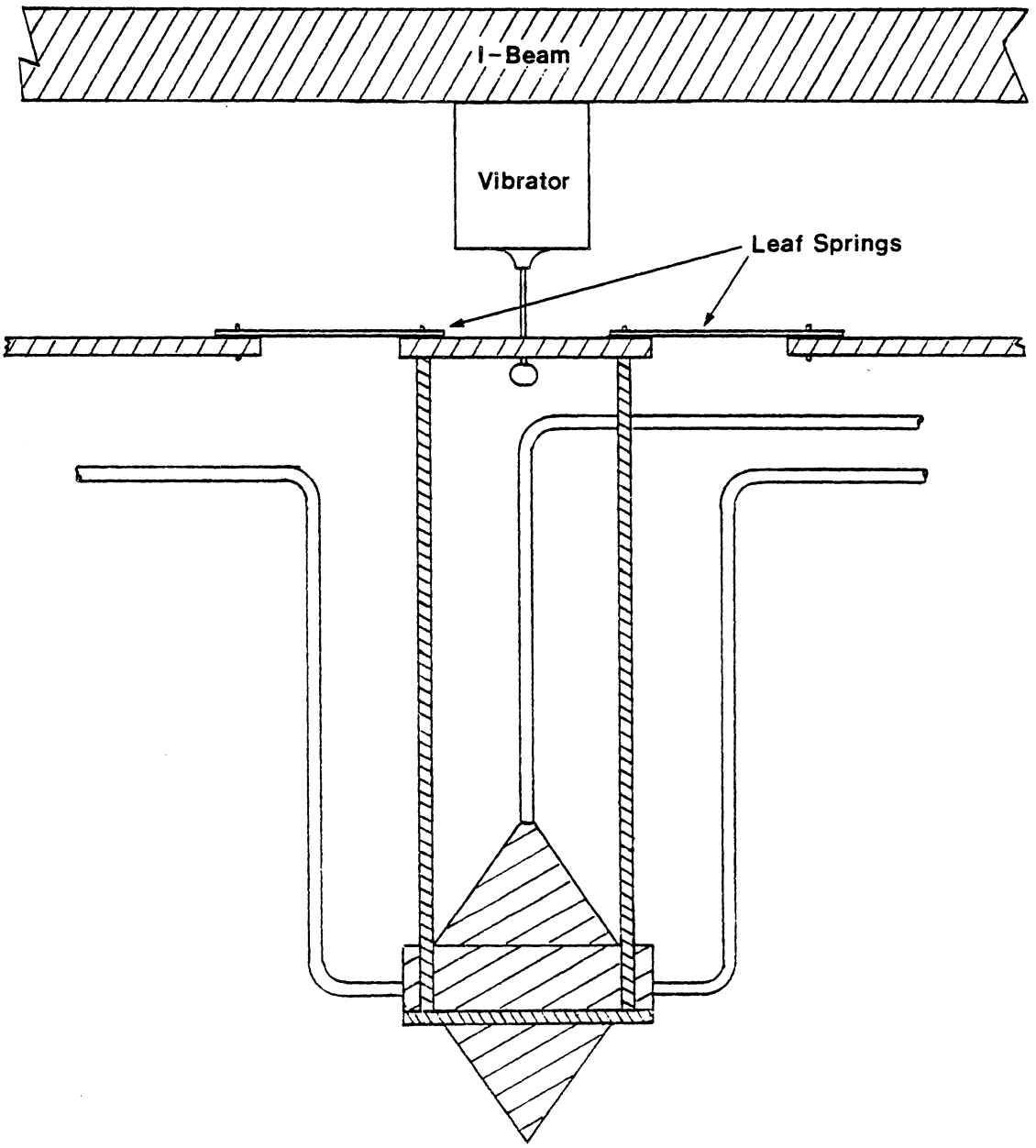

Figure 4.4. A Schematic Diagram of the Micro-reactor Vibrating and Suspension System.

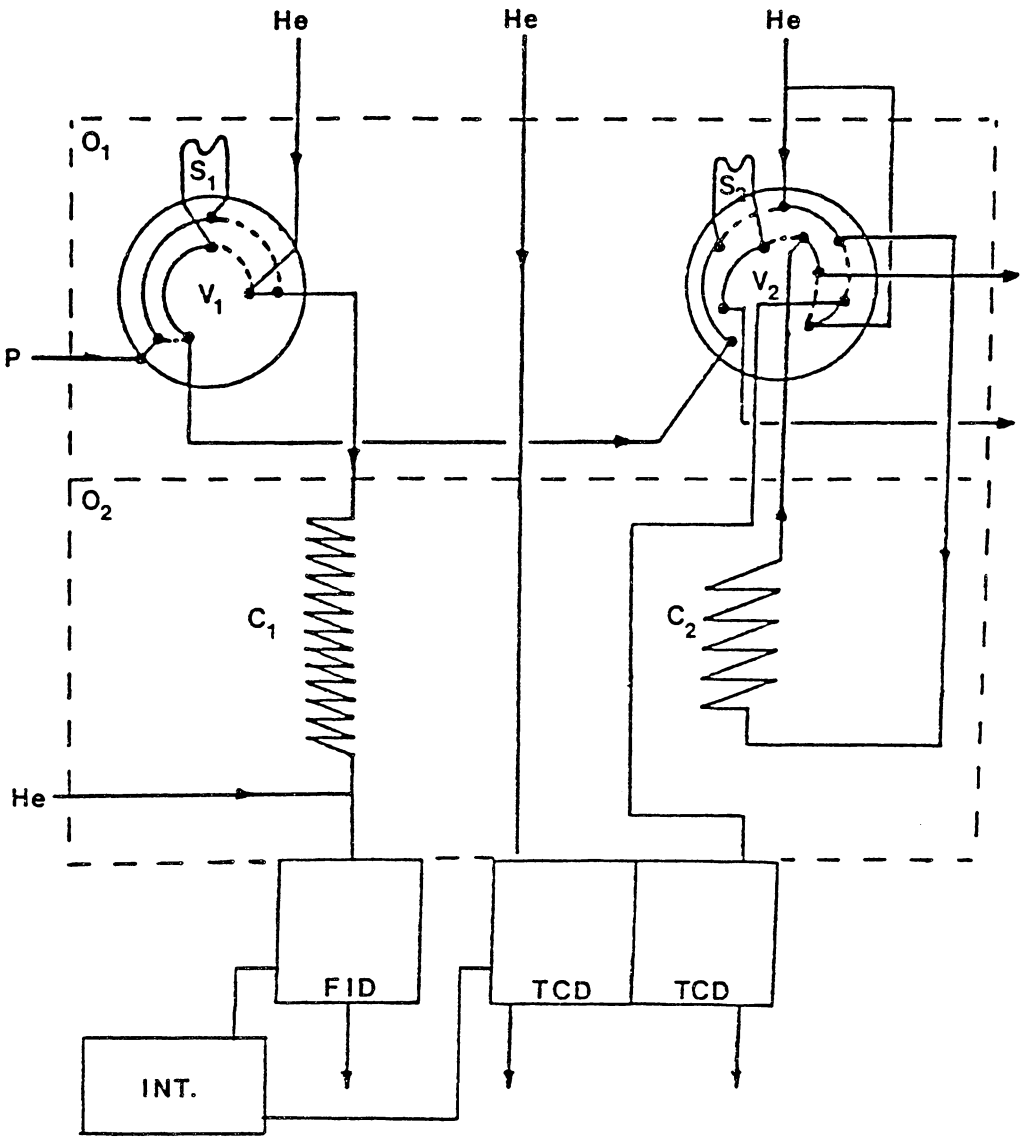

Figure 4.5. A Schematic Diagram of the Product Sampling and Analysis Systems in the Backflush Mode. Refer to Figure 4.1b for an Explanation of Equipment Symbols.

high-pressure reactor system at 50 standard mm^3 per second through a double-needle valve through which the pressure is reduced to nearly atmospheric pressure. The gases pass through a 1/16-inch O.D. tube to the two high-temperature Valco sampling valves.

Both the tubing and the sampling valves are maintained at 200°C (O_1) through the use of direct metal-contact heating cords with an insulating tape. The heating cords are regulated by three variacs. The first sampling valve (V_1) is a 6-port valve for injecting 0.03-ml samples into a 60-m fused-silica capillary column (C_1) with a (J&W Scientific Durabond DB-1) 0.25-micron film thickness. This column is connected to a flame ionization detector (FID) for analysis of C_1 to C_{10} hydrocarbons as well as some oxygenated compounds. The other sampling valve (V_2) is a 10-port valve for injecting 0.2 ml samples into a 6-ft Analabs Spherocarb 80/100-mesh packed column (C_2). This column is connected to the thermal conductivity detector (TCD) of the gas chromatograph for detection of light gases, including CO, CO_2, methane and argon (which serves as an internal standard).

Figure 4.5 shows the normal position of the sampling valves and the usual gas flow path. Helium flows continuously through the capillary column (C_1) in the forward direction, while the packed column (C_2) is backflushed. Backflushing the packed column removes higher-molecular-weight species that have adsorbed on the front of the column during the previous 10-port valve sampling.

Figure 4.6 shows both sample valves (S_1 and S_2) flushing samples into their respective columns. Samples are taken automatically using a Heathkit H-89 microcomputer, which is interfaced to the air-actuated

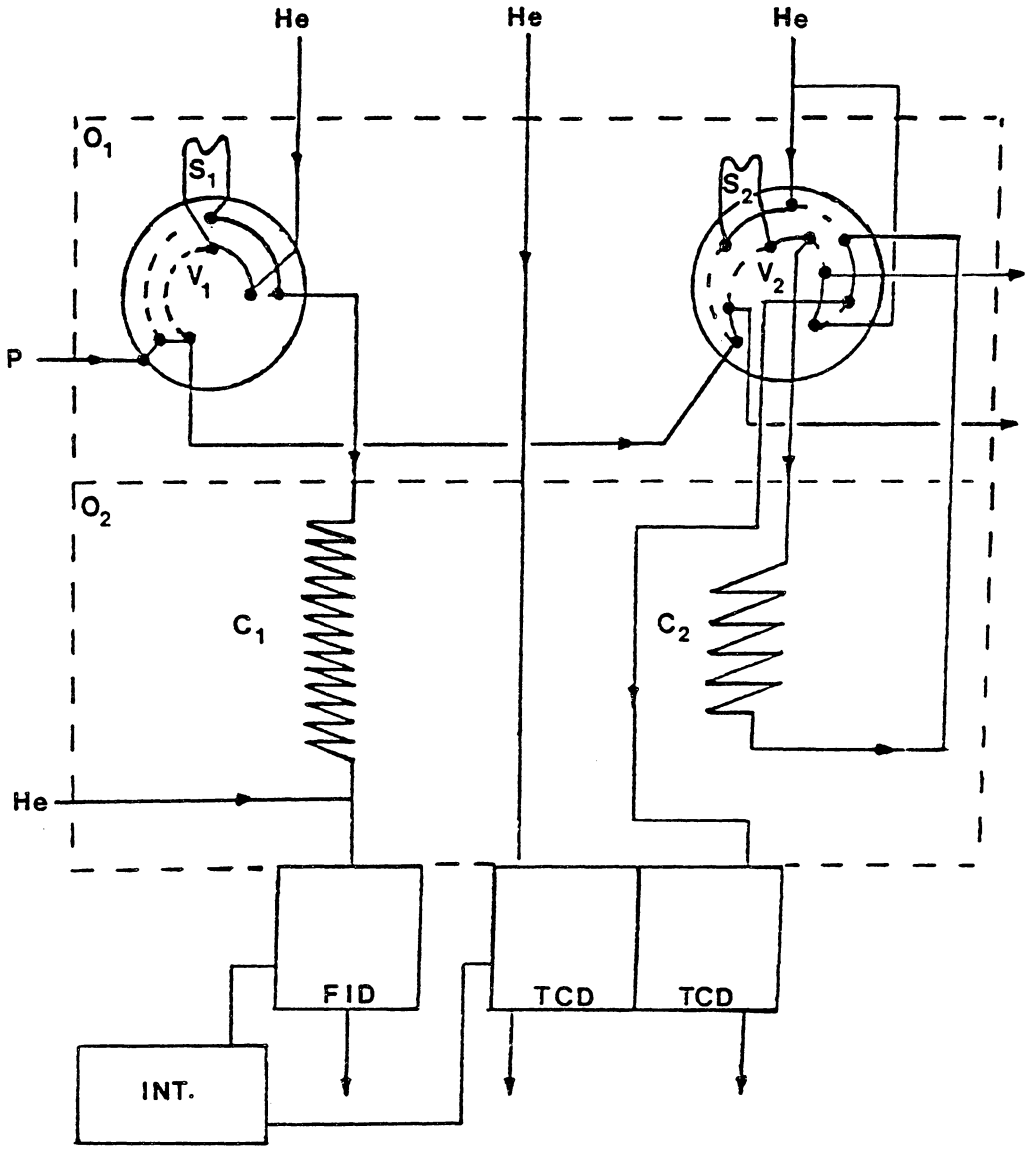

Figure 4.6. A Schematic Diagram of the Product Sampling and Analysis Systems in the Sampling Mode. Refer to Figure 4.1b for an Explanation of Equipment Symbols.

Valco sampling valves. Sample valve V_1 is switched to the position shown in Figure 4.6 only momentarily allowing sufficient time for the sample to be flushed from the sample loop into the capillary column. Conversely, sample valve V_2 remains in the pictured position until the last peak of interest (CO_2) elutes.

Gas sampling valves, V_1 and V_2, can be actuated simultaneously, flushing identical samples into the columns which, in turn, yields quantitative information on all major species of interest except hydrogen and water. Accurate amounts of carbon-containing species can be determined by relating the weighted argon peak-area on the packed-column chromatogram to the percent argon in the premixed synthesis gas and to the synthesis-gas flow rate. A methane peak appears on both chromatograms and serves as a basis for equating the analysis of species in both chromatograms. In this way, it is possible to determine quantitatively the carbon monoxide conversion and the carbon number distribution of the products.

In practice, simultaneous packed and capillary column samples are rarely taken. The short duration (on the order of hours) of F-T carbon-deposition experiments does not allow for complete analyses. This is because it takes over an hour for a temperature-programmed capillary sample to ellute from the column. In the present work, isothermal (70°C) light gas samples are normally taken once every 37 minutes and only one capillary analysis is done at the conclusion of the experiment. These 37-minute cycles of light-gas sampling are made up of a 17-minute period for peak elution followed by a 20-minute backflush period.

Figure 4.7 is a typical light-gas chromatogram produced under isothermal (70°C) conditions and recorded using a recording integrator (Hewlett Packard model 3390A). The first peak to elute is hydrogen which can not be quantitatively detected using a pure helium carrier-gas because of their similar thermal conductivities. The remaining peaks are argon, carbon monoxide, methane and finally carbon dioxide. In order to quantify these peaks, thermal-conductivity weighting factors must be used.

Figure 4.8 is a typical product-gas chromatogram as separated by the fused-silica capillary column and detected by the flame ionization detectors. The chromatograph oven was held at -20°C for two minutes (using a liquid-nitrogen subambient unit) followed by temperature-programmed heating to 150°C at 4°C/min.

Major products have been identified through retention-time analysis and comparison to chromatograms obtained by Huff (1982), who employed a 50-m fused capillary column similar to the one used here. The first peak is actually two peaks, which overlap somewhat. The first of these overlapping peaks is methane while the second is a fused ethane-ethylene peak. C_3 olefins and paraffins also appear as a single fused peak. It should be noted that a pattern occurs for hydrocarbon elution. Normal-alpha-olefins of a given carbon number, C_n, elute first in the greatest quantity followed by a lesser amount of normal paraffins of carbon number C_n. Finally, beta-olefins elute in much smaller quantities.

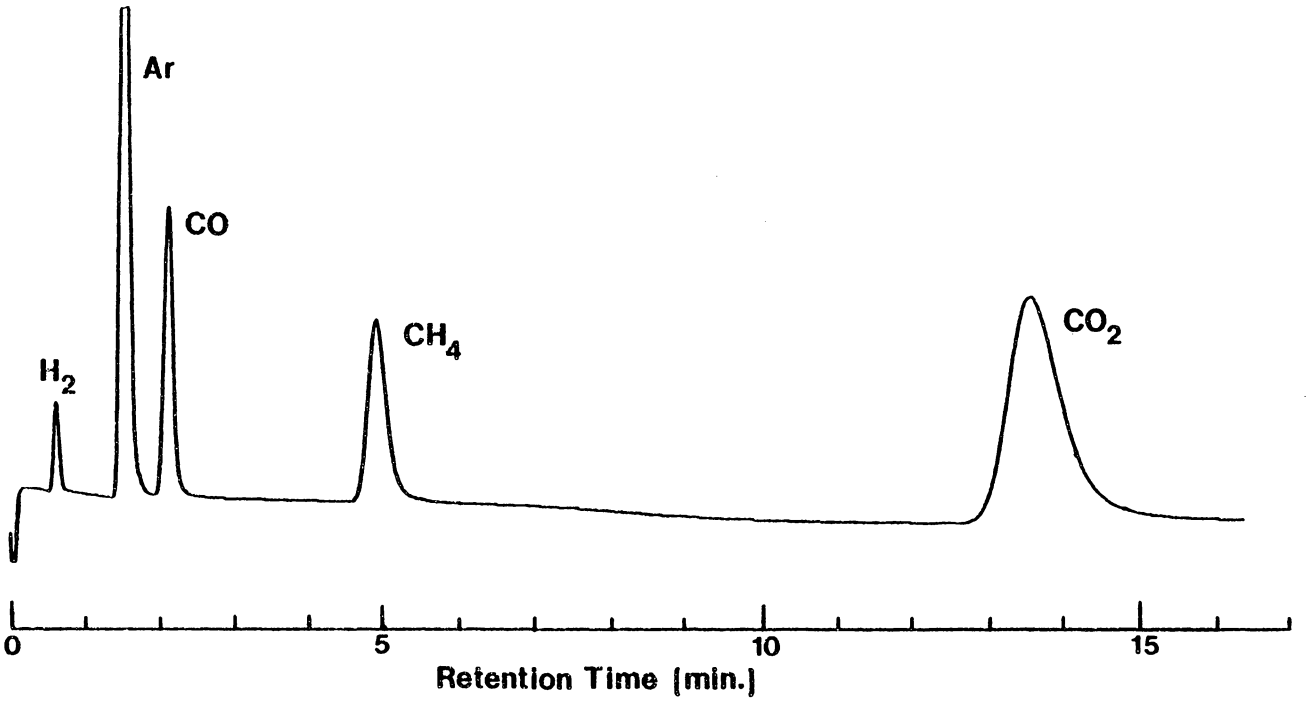

Figure 4.7. A Typical Light-Gas Product Chromatogram.

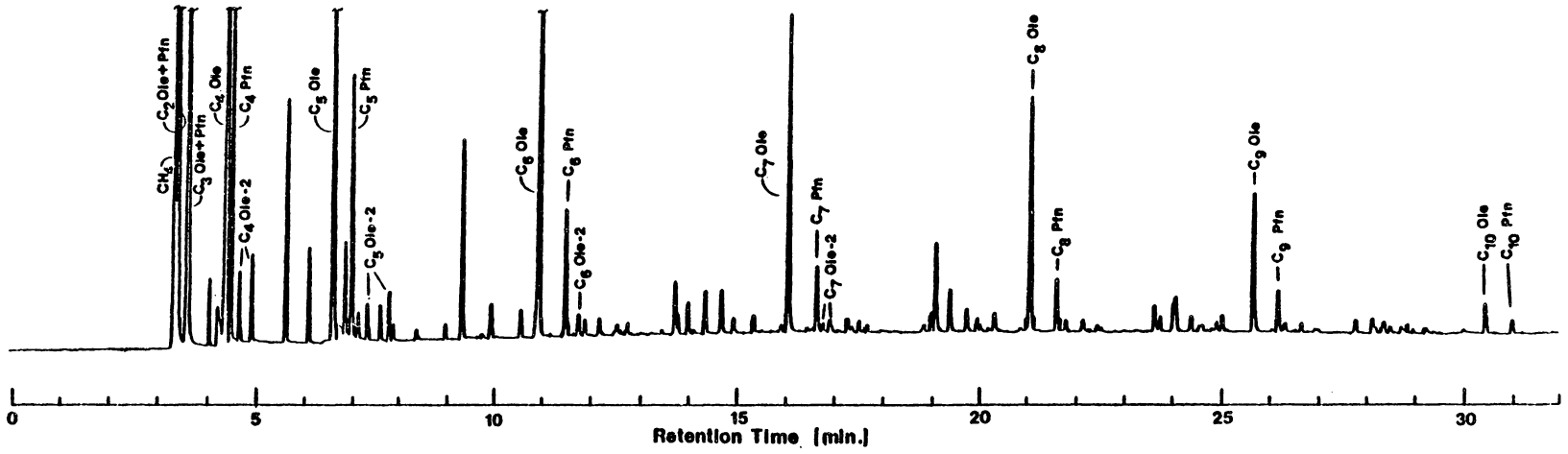

Figure 4.8. A Typical Product-Gas Chromatogram Separated on a Fused-Silica Capillary Column (Threshold is -2, Peak Width is 0.04, n-paraffins= Pfn, n-alpha-olefins=Ole, beta-olefins=Ole-2).

4.1.2 Materials

4.1.2.1 Catalyst

The catalyst used throughout the F-T studies is a commerical fused-iron ammonia-synthesis catalyst manufactured by United Catalysts, Incorporated. This catalyst is designated C-73-1-01 and has the composition shown in Table 4.1. The catalyst was originally supplied as granules, but has been crushed and sieved to a -150+300 micron fraction for these experiments. This size fraction provides for ease of vibrofludization.

4.1.2.2 Gases

Gases for system purging, catalyst reduction, and F-T synthesis were suplied by Airco-Industrial Gases, Research Triangle Park, NC. All carbon monoxide was supplied as C.P. grade; while hydrogen, argon, helium and nitrogen were prepurified grade. The trace impurities found in these gases are summarized in Table 4.2 as given by the manufacturer.

4.1.2.3 Distributor and Catalyst Retention Plates

The distributor and catalyst retention plates used in this study were made by sintering 316- stainless-steel powder. The manufacturer, Mott Metallurgical Corportion, differentiates the filtering capabilities of the plates through the use of "micron-filter grades." The filtration grade in units of microns corresponds to the nominal spherical particle retention of the plate if it did not have a tortuous path. The actual particle size retention is much smaller than the filtration grade because of the porous matrix of the sintered plates. In subsequent discussions, the plates will be referred to by their filtration grade.

TABLE 4.1

Chemical Analysis and Physical Characteristics of Fused-Iron Catalyst C73-1-01

Item	Amount
1. Composition	
FeO	30-37%
Fe_2O_3	65-58%
Free Fe	< 0.5%
Total Fe	67-69%
Al_2O_3	2.0-3.0%
K_2O	0.5-0.8%
CaO	0.7-1.2%
SiO_2	< 0.4%
P	< 0.015%
S	< 0.001%
Cl	< 0.002%
Fe^{++}/Fe^{+++}	0.45-0.65%
2. Bulk Density	2723 ± 160 kg/m^3

TABLE 4.2

Purity of Feed and Purge Gases

	CO	H_2	Ar	He	N_2
Minimum Purity %	99.3	99.995	99.998	99.995	99.995
Total Maximum Impurities (ppm)	-	50	20	50	50
Maximum Individual Impurities (ppm)					
Ar	-	-	-	-	35
H_2	-	-	2	2	2
N_2	1500	20	10	20	-
O_2	600	5	2	6	1
$CO + CO_2$	50	2	2	2	0.5
THC	-	5	2	0.5	0.5
H_2O	-	8	-	10.0	10
Ne	-	-	5	-	10

4.1.3 Experimental Procedure

4.1.3.1 Microreactor Cleaning and Catalyst Charging

Before each experiment, the mating surfaces of the three sections (see Figures 4.2 and 4.3) of the microreactor were polished with Δ600 emory cloth on a surfacing table. The reactor was then flushed thoroughly with acetone and wiped with Kimwipes. Particular attention was focused on the reaction zone. After cleaning, the base section of the microreactor was clamped in a vise using a wooden support apparatus. A new 20-micron distributor plate was then weighed and inserted into the recessed slot in the base. A small oval-shaped Grafoil gasket was then placed around the mating edges of the distributor plate and the base. A new silver-plated stainless-steel O-ring was placed in the O-ring groove of the base section.

The reaction section of the microreactor was then slipped down over the guide rods of the base section. One gram of the -150+300 micron fused-iron catalyst was then weighed and poured into the reaction zone. A 40-micron catalyst retention plate was placed into the recess in the product-exit section. In addition, a new O-ring was placed in the O-ring groove in this top section. The product-exit section was slid down over the guide rods coming to rest on top of the reaction zone.

The sections were then bolted together using eight hex-head bolts. These bolts were tightened in an alternating pattern one-half turn at a time and then torqued to 27 N-m with a torque wrench. The 1/4-inch O.D. tubes of the microreactor were then temporarily capped off to prevent the reactor from being contaminated.

4.1.3.2 Mounting of the Microreactor

Following catalyst loading, the microreactor had to be attached to the vibrational support system. A yoke was bolted to the base section of the microreactor. Four 1/4-inch threaded rods were then screwed into the yoke. This support and the microreactor were slipped down into the fluidized constant-temperature bath. The threaded rods were then bolted to the leaf-spring supports. The three 1/4-inch O.D tubes leading to the microreactor were attached to the flexible stainless-steel hoses using compression fittings. This effectively connected the microreactor to the remainder of the system.

Finally, the vibrator itself was mounted to the underside of the I-beam support and connected to the microreactor support system (see Figure 4.4). The vibrational frequency of the frequency generator was then adjusted to the point where the microreactor was vibrating at the maximum amplitude. This corresponded to a reasonance frequency of 18-24 Hz with a microreactor peak-to-peak amplitude of 4 mm.

4.1.3.3 System Startup and Catalyst Reduction

The reader is suggested to refer to Figure 4.1a for the following discussion. Before system startup, the portion of the system located downstream of solenoid valves 1-4 was flushed thoroughly with helium. This was done by opening valves V4 and V9, and solenoid valves 5 and 6, and then directing three-way valves V6, V7, and V8 so that helium flows through the system. The portion of the system located upstream of solenoid valves 1-4 was normally kept under pressure. This upstream portion therefore need only be purged after changing out a gas cylinder.

After the system has been purged with helium, solenoid valves 5 and 6 were closed and the microreactor was checked for leaks at 3,435-kPa helium atmosphere. Valve V9 was closed so that all exiting gas must go through the back-pressure regulator or the sampling valves. The pressure upstream of solenoid valves 1-4 was set to 4,807 kPa using the two pressure transducers. These transducers were then switched to read gas pressures downstream of the microreactor by turning the appropriate three-way valves.

The nitrogen ballast gas was introduced to the back-pressure regulator by opening valve V1. The system pressure downstream of the microreactor was then set to 2,210 kPa by adjusting the nitrogen ballast gas pressure and flow along with the back-pressure regulator setting.

Once the system pressure had been set, the flow rates of reducing gas, precarburization and main reaction synthesis gases could be set. First, the flow rate of synthesis gas was set using the needle valve associated with solenoid valve 2. This was performed by first purging the system with synthesis gas through opening solenoid valves 1, 2, 5 and 6 and letting gas flow through the reactor at 6.7×10^4 standard mm^3 per second for one minute. Solenoid valves 1 and 5 were shut and synthesis gas passed solely up through the microreactor reaction zone. The flow rate of synthesis gas was finally set by adjusting the needle valve associated with solenoid valve 2, while monitoring the flow rate using the flow transducer.

Precarburization synthesis gas originated in the center cylinder shown in Figure 4.1a. The flow rate of this gas was set in a similar

fashion to that described above for the reaction synthesis gas. Solenoid valves 5 and 6 were opened and the reactor was purged with precarburization synthesis gas. After one minute of purging at a flow rate of 6.7×10^4 standard mm^3 per second, valve 5 was closed and the flow rate through the reactor was set by adjusting the needle valve before three-way valve V7. Finally, the gas flow rate of reducing hydrogen was set using the needle valve associated with solenoid valve 4, after sufficient purging of the reactor had been completed.

The hydrogen flow path consisted of gas flowing through valves V5 and V8 in conjunction with solenoid valves 4 and 6. At this point, the reduction period was nearly ready to be started. Air was started to the fluidized constant-temperature bath, and the bath temperature-controller along with the variacs controlling the heating cords were switched on. The microreactor was started vibrating and the gas chromatograph was set up.

The reduction period consisted of a 2.5-hour bath heat-up period followed by a 6-hour isothermal duration at 450°. The hydrogen flow rate during reduction was 3,670 standard mm^3 per second.

4.1.3.4 Precarburization and Steady-State Synthesis

Precarburization was used in order to convert the fused-iron catalyst to Hägg carbide without excessive carbon deposition. A higher ratio of hydrogen to carbon monoxide is used for precarburization (about 4:1) than that for reaction during steady-state synthesis. After the reduction period had been completed, the catalyst was first exposed, in some cases, to the precarburization synthesis gas for two hours. This

precarburization step was followed by exposure of the carburized catalyst to the reaction synthesis gas of a lower H_2/CO ratio. The exposure to the synthesis gas of a lower H_2/CO ratio initiated carbon deposition.

Precarburization was initiated by closing solenoid valve 4 (shutting of the H_2-flow) and switching three-way valves V6, V7, and V8 so that precarburization gas flowed through the microreactor. The flow rate of this gas had been previously set, so no needle-valve adjustment was necessary.

Immediately after the start of precarburization synthesis-gas flow, a timing computer-program was started using the Heathkit H-89 microcomputer. After the first twenty minutes of precarburization synthesis, a product gas sample was flushed into the packed column of the gas chromatograph automatically by the computer-actuated sampling valves. Seventeen minutes after the product gas sample was taken, all compounds of interest had eluted and the computer backflushed the heavy products from the packed column. This process was repeated every 37 minutes throughout the precarburization and synthesis portions of the experiments. The course of the reaction can be monitored through the use of the two thermocouples in the reaction zone. The exothermicity of the F-T synthesis reaction showed up typically several minutes after the precarburization synthesis gas starts flowing. It takes this long for the new gas to replace hydrogen in the reactor feed-lines.

After two hours of precarburization with H_2/CO gas of a 4:1 ratio, the catalyst was sufficiently carburized and the steady-state synthesis

period began with a synthesis gas of a low H_2/CO ratio. The precarburization synthesis gas was shut off and reaction synthesis gas was started by switching three-way valve V7 and opening solenoid valve 2. Automatic product gas sampling was continued and the experiment proceeded for the specified amount of time.

Several minutes before the end of an experiment, the gas chromatorgaph oven was cooled down to -20°C with liquid nitrogen and a sample was manually flushed into the capillary column. A sample could not be in the packed column while the oven was cooling because the baseline changed with temperature. After the sample had been flushed into the capillary column, the temperature program and the integrator were started. The system could be shut down without any effect on the gas chromatograph.

4.1.3.5 System Shut-Down

After the synthesis period was completed, it was desirable to shut down the system as rapidly as possible, while blanketing the catalyst in an inert gas. This was done by flushing the catalyst and the microreactor system lines with helium and rapidly reducing the system to atmospheric pressure. Synthesis was stopped and flushing was started by shutting solenoid valve 2 and immediately directing three-way valves V6 and V7 towards the helium cylinder. The nitrogen ballast flow was shut off using valve V1, and vent valve V9 was opened slowly over the course of several minutes. It is important that vent valve V9 not be opened too rapidly. Otherwise, gas will pass through the reaction zone

at a velocity high enough to plaster the catalyst against its retention plate. The flow rate of gas through the reaction zone should be maintained below 2,200 standard mm^3 per second in order to prevent this. Yet the flow rate should be high enough to prevent condensation of residual F-T products.

Once the system had been purged with helium and had reached atmospheric pressure, the temperature controller to the constant-temperature bath was shut off. The vibrator and the heating tapes were left on until the system had cooled. The cool-down period typically lasted five hours after which the vibrator and heating tapes were shut off.

4.1.3.6 Catalyst Collection and Analysis

After the microreactor had been cooled to ambient temperature, it was removed from the constant-temperature bath. The microreactor was detached from the flexible stainless-steel hoses and the helium flow was stopped. The tubes leading to the microreactor were capped and it was dismounted from the suspension apparatus.

Following removal from the bath, the reactor was clamped into a vise, where the exterior was cleaned and the connecting bolts were removed. The top or product-exit section was then removed and carefully placed aside, taking care not to lose any carbon fines that may have been sticking to the catalyst retention plate. If all had gone well during the reaction, the catalyst in the reaction zone was free flowing (not sticky) and maybe darkened somewhat by carbon deposition. The catalyst was then extracted from the reaction zone using a suction-filter

apparatus. The latter consisted of a pasture pipet, a piece of filter paper, some tygon tubing, a filter flask and an asparator. The catalyst was drawn up into the pipet by suction, and any fine carbon powder or "bugdust" was collected on the filter paper. The heavier catalyst was then dumped into a vial by releasing suction. The bugdust was placed in a second vial by tapping the pipet gently.

An additional accumulation of bugdust was sometimes found pressed against the catalyst retention plate. This accumulation was removed by the suction-filter apparatus and added to the bugdust vial. By weighing the vials and the filter apparatus before and after, an accurate determination of the disposition of the spent catalyst was made. Furthermore, any weight gain experienced by the catalyst retention plate was considered bugdust.

The spent catalyst and bugdust vials were purged with nitrogen and portions were mailed to Gailbiarth Laboratories, Knoxville, TN where carbon and iron analyses were performed. Other select samples were sent to the Physics Department at West Virginia University where Mössbauer spectroscopic studies of the iron phases were undertaken.

4.2 Experimental Results and Discussion

The results of steady-state synthesis runs are presented in this section. The aim of these studies was twofold. First, conditions had to be found where production and condensation of liquid products and/or waxes on the catalyst surface did not affect catalyst vibrofluidization. Secondly, carbon deposition data had to be obtained for feed gases of

several different H_2/CO ratios under conditions where the catalyst would not defluidized.

Table 4.3 gives a summary of experimental conditions and results for pertinent steady-state runs applicable to the catalyst defluidization studies. Similarly, Table 4.4 lists the experimental conditions and results for the steady-state carbon-deposition runs. The letter assigned to a particular run number designates a particular reaction temperature, while the associated number indicates the chronological order of the experiments. Several of the steady-state catalyst defluidization experiments in Table 4.3 are also applicable to the carbon deposition studies listed in Table 4.4.

In addition, many other steady-state runs were performed before these experiments. These earlier experiments led to the present vibrofluidized-bed microreactors design. The history of this development is documented in Appendix E. Appendix B provides a compilation of primary and secondary results from steady-state experimental runs. For each run, the CO conversion as well as the CO_2 and CH_4 produced are presented as a function of time. In addition, a derived mass balance allows an approximate mass balance to be performed. The results of the balance are also listed.

4.2.1 Catalyst Defluidization

Vibrofluidized fused-iron catalysts for F-T synthesis have been found to be subject to defluidization. The reason for the loss of fluidity has been proven in earlier studies undertaken in this

TABLE 4.3

A Summary of Steady-State Results and Run Conditions for Vibrofluidized-Bed Microreactor Defluidization Studies

Run Number	Duration of Synthesis hours; min.	H_2/CO Feed Gas Ratio	Temperature °C	Total Pressure kPa	Catalyst Charged, g	Distributor Plate Opening, μ
B-1	10; 0	2.08	360	2220	1.0077	20
B-2	2; 3	2.08	360	2220	1.0077	20
B-3	10; 0	4.0	360	2220	1.0168	20
B-4	1; 2	1.03	360	2220	1.0176	40
B-5	2; 13	1.03	360	2220	1.0060	40
B-6	2; 57	2.08	360	2220	1.0020	40
B-7	2; 45	2.08	360	2220	1.0030	20
C-1	2; 4	2.08	400	2220	1.0089	20
C-2	1; 0	1.03	400	2220	1.0175	20
D-1	1; 15	1.03	380	2220	1.0135	20
D-2	2; 48	2.08	380	2220	1.0053	20
E-1	2; 50	2.08	390	2220	1.0479	20

TABLE 4.3 (Continued

Run Number	Distribution of Spent Catalyst After Run, g: Free Flowing	Defluidized	Bugdusted (Carbon Powder)	Net Weight Change of Reaction-Zone Material, mg	Comments
B-1	-	1.3007	-	+369.3	Black, Sticky
B-2	0.7417	---→ 0.1980 ←---		-62.8	Unclear
B-3	0.8407	0.6320	-	-63.7	Somewhat sticky, no bugdust
B-4	0.9260	---→ 0.0111 ←---		-71.0	Unclear
B-5	0.1315	0.8945	-	+56.5	Sticky
B-6	0.1484	0.7852	-	-52.6	Sticky
B-7	-	0.9569	-	+45.9	Sticky
C-1	0.9629	-	0.0510	+10.4	Bugdust
C-2	-	-	1.1492	+146.4	Totally bugdust
D-1	0.9027	-	0.1258	+18.1	Bugdust
D-2	0.5762	---→ 0.4615 ←---		+51.1	Unclear
E-1	0.8685	-	0.2628	+83.4	Bugdust

NOTE: The space velocity was 34,320 hr^{-1} for all runs listed in this table.

TABLE 4.4

A Summary of Steady-State Results and Run Conditions for Vibrofluidized-Bed Microreactor Carbon-Deposition Studies

Run Number	Duration of Synthesis hours; min.	H_2/CO Feed Gas Ratio	Catalyst Charged, g	Distribution of Spent Catalyst After Run, g			Net Weight Change of Reaction-Zone Material, mg	Comments
				Free Flowing	Defluidized	Bugdusted (Carbon Powder)		
F-1	3; 30	4.0	1.0039	0.9312	-	-	-72.7	No Bugdust
F-2	2; 0	4.0	1.0042	0.8981	-	-	-106.1	No Bugdust
F-3	2, 0 (precarburization)	4.0	1.0000	0.9046	-	0.0337	-61.7	Bugdust
	1; 0 (synthesis)	2.08						
F-4	2; 0 (precarburization	4.0	1.0018	0.9524	-	0.0273	-22.1	Bugdust
	2; 0 (synthesis)	2.08						
F-5	2; 0 (precarburization	4.0	1.0042	0.8971	-	0.0688	-38.3	Bugdust
	0; 22 (synthesis)	1.03						

Note: The following conditions were identical for all runs listed in the table: temperature = 395°C; pressure = 2,200 kPa; space velocity = 34,320 hr^{-1}; and distributor plate type = 20μ.

investigation. It is caused by the buildup of condensed liquid products and/or waxes in the catalyst pores, on the catalyst surface and, to a lesser extent, in the reaction zone.

In order to avoid defluidization in the virbofluidized bed of -150+300 μ catalyst particles, the product distribution must be shifted toward lower molecular-weight species. As explained in Section 2.2.5, the average molecular weight of products, respresented by the probability of chain growth (α), can be altered by changing the synthesis conditions.

Runs B-1 through E-1 were a series of systematic experiments designed to identify a temperature at which future steady-state experiments could be performed in the vibrofluidized-bed microreactor without fear of catalyst defluidization. Preliminary experiments at lower temperatures produced a sticky catalyst mass and pointed to a reaction temperature of at least 360°C (see, for example, Runs B-1 to B-7, listed in Table 4.3). A complication to using high reaction temperatures is that carbon deposition becomes much more rapid as temperature increases. Dry (1981) states that for every 10K rise in bed temperature, a 50% increase in carbon deposition rate can be expected.

All defluidization experiments (Runs B-1 through E-1) consisted of catalyst reduction by hydrogen at 450°C and a space velocity of 34,320 hr^{-1} followed by reaction at the conditions listed in Table 4.3 Note that the space velocity is the volume of feed gas (standard mm^3) fed per hour per volume of unreduced fused-iron catalyst. No precarburization step was used during these runs because of their exploratory nature.

Figure 4.9 shows the weight percent of catalyst that had defluidized as a function of reaction time for feed gases of three different H_2/CO ratios at 360°C. This temperature corresponds to the "B" series of experiments, B-1 through B-6.

For feed gases of H_2/CO ratios of 2:1 (Runs B-1, B-2, B-6, B-7) and 1:1 (Runs B-4 and B-5), defluidization of the vibrofluidized catalyst bed occurs after 2 to 3 hours of synthesis under the specified conditions. For a feed gas of a H_2/CO ratio of 4:1 (Run B-3), only approximately 42 percent of the catalyst has defluidized after 10 hours of steady-state synthesis.

During previous exploratory experiments, it was observed that a relationship existed between the degree of fluidity of the vibrofluidized catalyst bed and the temperature fluctuation at the lower thermocouple in the reaction zone. For each of the steady-state experiments, this fluctuation was observed and recorded periodically throughout the run. A typical observation involved watching the temperature output for 30 seconds and recording the difference between the high and low value. It was thought that the temperature fluctuation was induced by the vibration. The vibration caused periodic contact between the thermocouple and the catalyst particles where the highly exothermic reaction was taking place.

Figure 4.10 is a plot of the lower-thermocouple temperature fluctuation as a function of time for Run B-1 using a feed gas of 2:1 H_2/CO ratio at 360°C. During the first two hours of the experiment, the temperature fluctuation ranged from 0.6 to 1.0°C. After three hours had

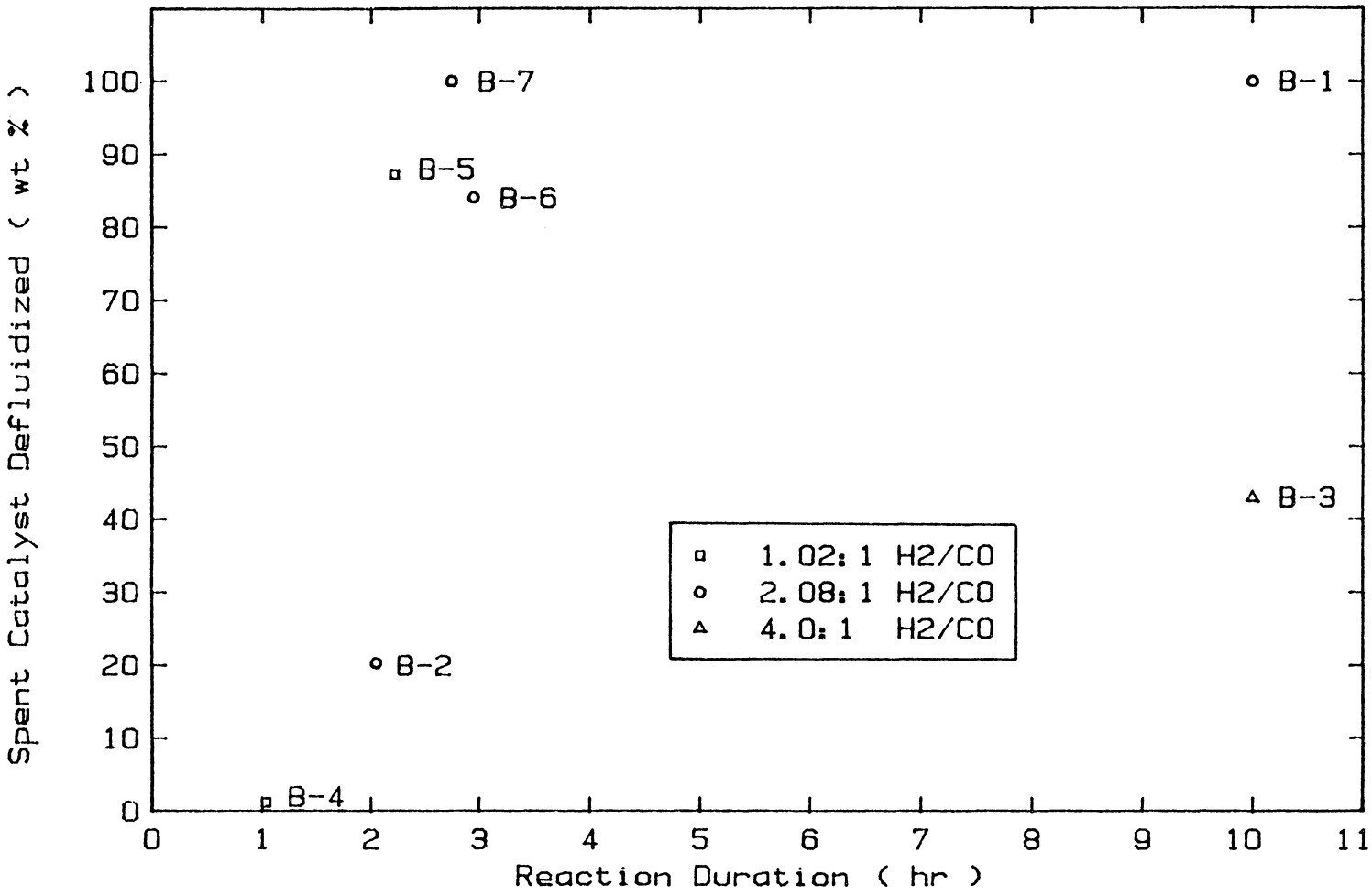

Figure 4.9. Defluidization Characteristics of Feed Gases of Three H_2/CO Ratios at 360°C and 2220 kPa.

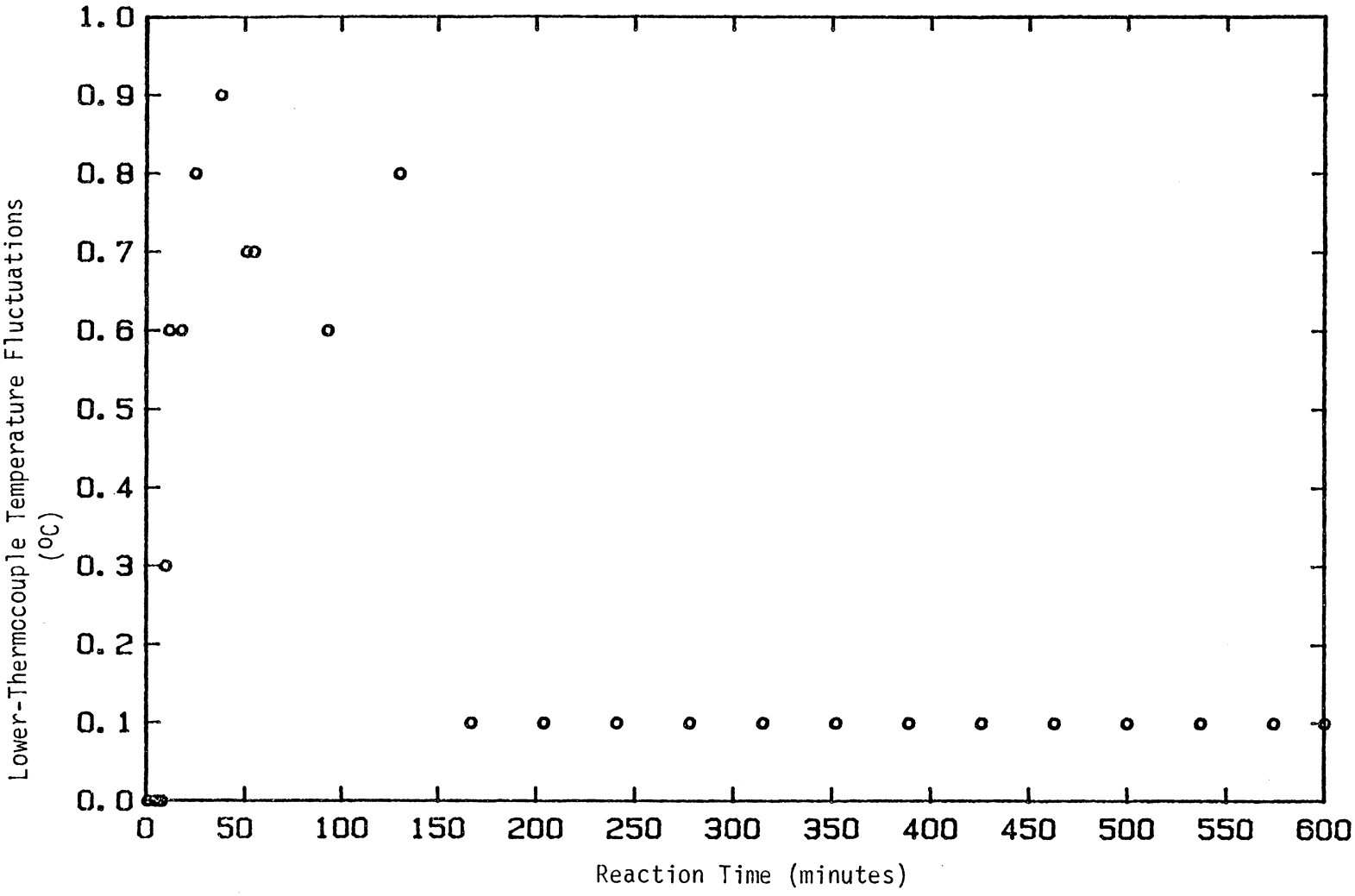

Figure 4.10. Lower-Thermocouple Temperature Fluctuation as a Function of Time for Run B-1 Using a Feed Gas of 2:1 H_2/CO Ratio at 360°C and 2220 kPa.

elapsed, the fluctuation had dropped to 0.1°C and remained essentially constant. At this point, the catalyst bed was defluidized.

Figure 4.11, for Run B-7, gives a more detailed picture of the defluidization phenomenon in the vibrating microreactor. For 1.0 g of fused-iron catalyst at 360°C and 2,220 kPa and with a feed gas of 2:1 H_2/CO ratio, the catalyst defluidized gradually over a period of about one hour. Similar plots of temperature fluctuation varying with time are given for Runs B-2 through B-5 in Appendix B.

Runs C-1 and C-2 were steady-state synthesis experiments performed, respectively, with feed gases of 2:1 and 1:1 H_2/CO ratios at 400°C. The feed gas of 2:1 H_2/CO ratio at this temeprature did not cause the catalyst to defluidize during the two-hour run as refelcted in Figure 4.12. Similarly, Run C-2 using a feed gas of 1:1 H_2/CO ratio produced no defluidization after one hour, but carbon deposition was excessive. This will be further examined in Section 4.2.3.

Runs D-1 and D-2 were undertaken at 380°C using feed gases of 1:1 and 2:1 H_2/CO ratios, respectively. The plots of temperature fluctuations as a function of time indicate catalyst defluidization after two hours and fifty minutes of operation.

Run E-1 involved raising the temperature to 390°C and repeating the defluidization study using a 2:1 H_2/CO feed-gas ratio. Upon opening the mciroreactor after this run, the catalyst was found to be free flowing and very slightly sticky. When vacuumed up with the suction-filter apparatus, some of the catalyst stuck to the walls of the pipet. From Runs C-1 and C-2, it was known that the vibrofluidized catalyst would not defluidize before excessive carbon formation began at 400°C. Run E-1

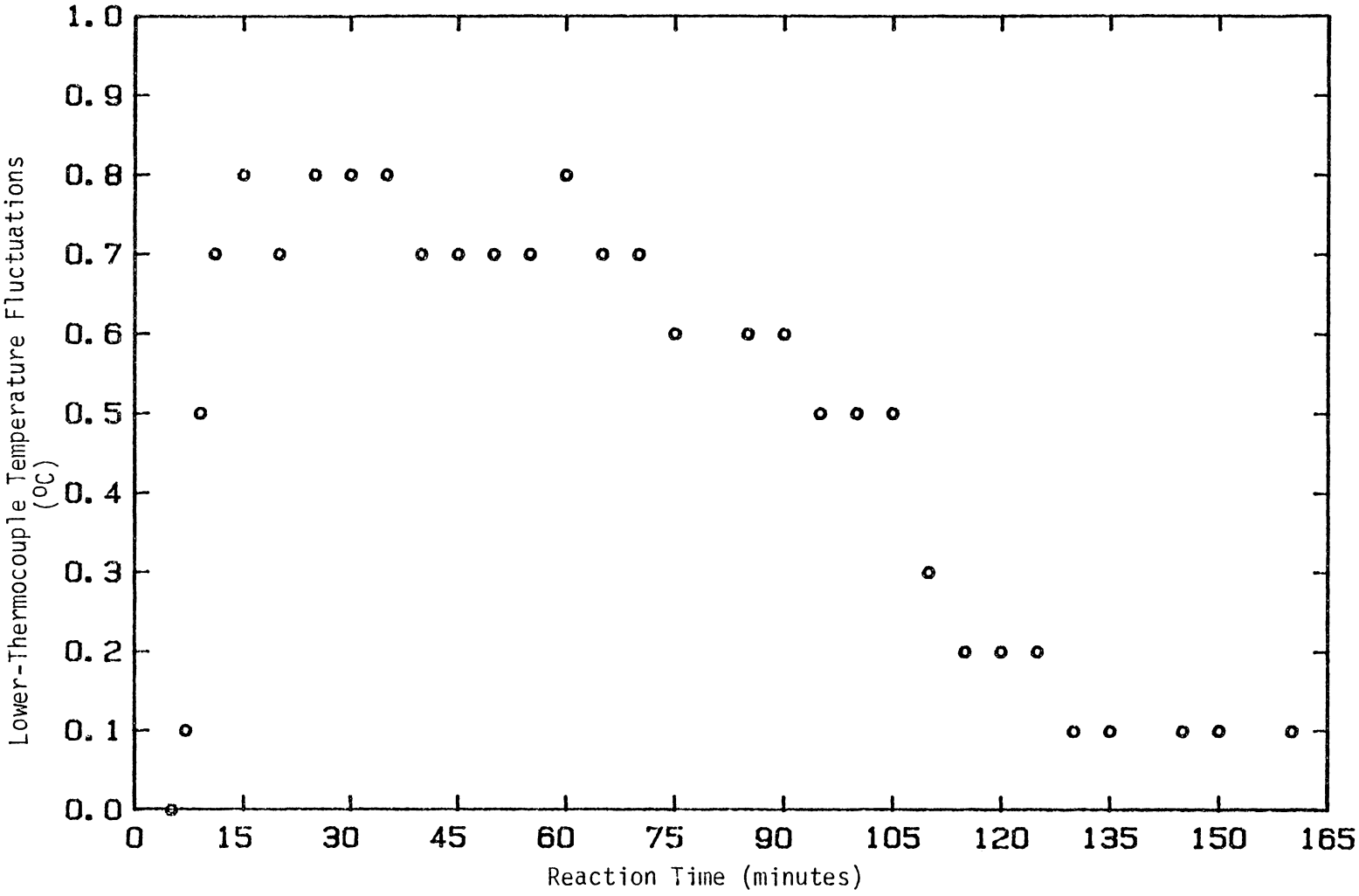

Figure 4.11. Lower-Thermocouple Temperature Fluctuation as a Function of Time for Run B-7 Using a Feed Gas of 2:1 H_2/CO Ratio at 360°C and 2220 kPa.

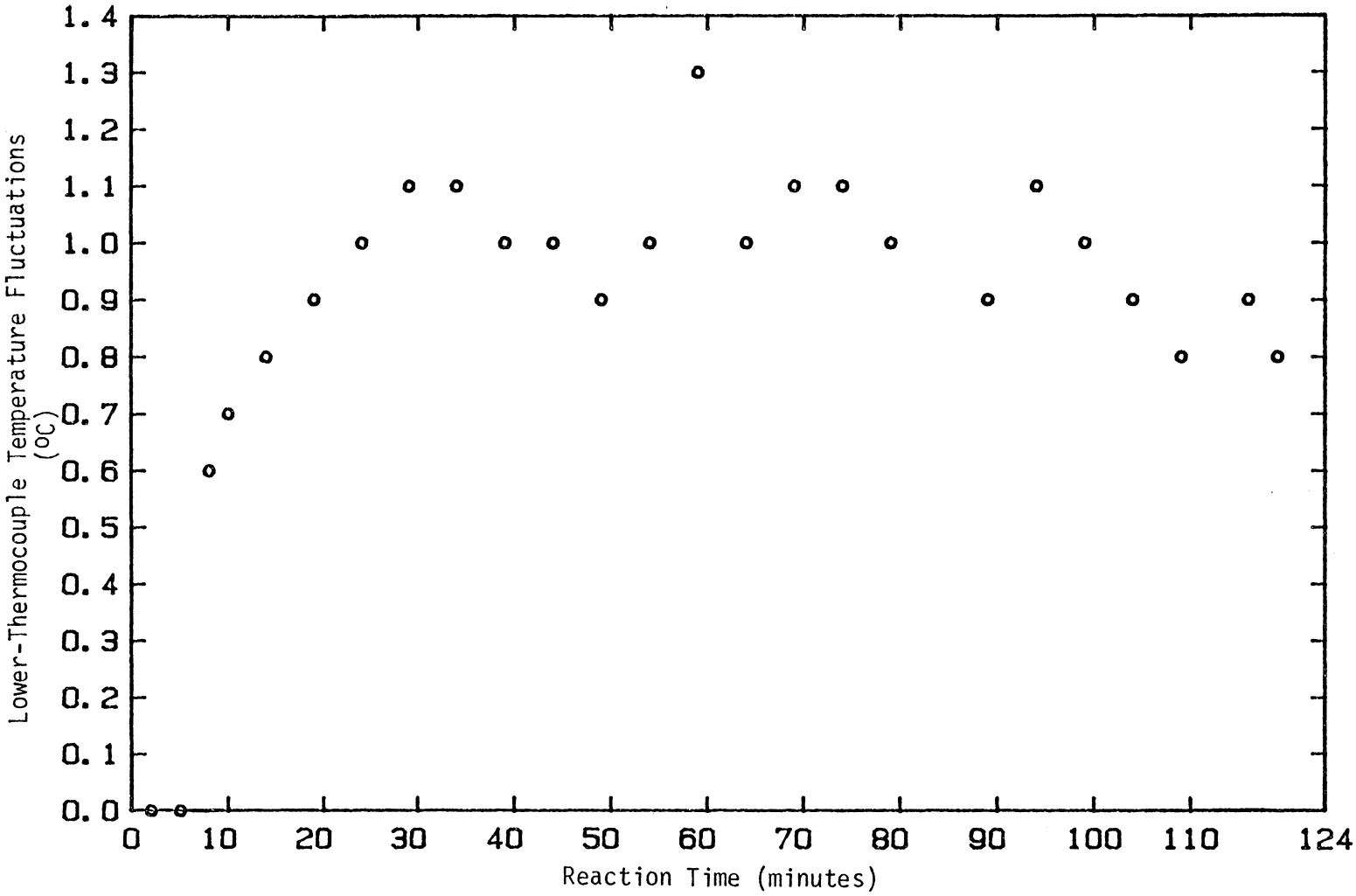

Figure 4.12. Lower-Thermocouple Temperature Fluctuation as a Function of Time for Run C-1 Using a Feed Gas of 2:1 H_2/CO Ratio at 400°C and 2220 kPa.

indicated that the spent catalyst was only very slightly sticky after synthesis with a feed gas of 2:1 H_2/CO ratio at 390°C. Consequently, it was concluded that an appropriate temperature for the steady-state carbon-deposition studies in the vibrofluidized-bed microreactors would be 395°C.

4.2.2 Hydrocarbon Product Distribution

It has been explained in Section 2.1.5.3 that excluding oxygenated products in an analysis of the product distribution from a F-T synthesis run can cause inaccuracies. For instance, in a plot of the Flory distribution or Polymerization Distribution Law, Equation (4), Section 2.1.5, where the logarithm of the mole fraction of each product carbon number is plotted against the carbon number, significant deviations are observed for C_2 products. This is because approximately 20-30 percent of C_2 products for this iron catalyst are oxygenates (Huff, 1982). In order to provide an accurate Flory plot, it is necessary to carefully trap and separate product fractions, as well as to identify these fractions. The goal of the present study, however, was not to obtain these detailed data, but to observe general trends in product distribution as reaction parameters were changed.

Therefore, the on-line product analysis system described in Section 4.4.4.1 was utilized to obtain the distribution of C_1 to C_{10} hydrocarbon products. Chromatographic analyses of hydrocarbon products were performed for selected steady-state experiments. The normal paraffin, normal alpha-olefin and beta-olefins for each carbon number up to C_{10}

were considered when the peak could be identified. These results are listed in Appendix B.

During the compilation of the data, the weight fraction, mole fraction, and rate of production of each identified hydrocarbon species was determined. Figure 4.13 through Figure 4.16 show Flory plots for hydrocarbon products from Runs B-1, B-2, B-3, and C-1. As can be seen, a significant dip occurs at C_2 in all four plots. The reason for this is that a greater percentage of C_2 fraction products (20-30%) are oxygenates than for other carbon numbers.

The main points of interest in these plots are the slopes of the plots which represent the values of probability of chain growth, α. Comparing Figure 4.13 (Run B-1) to Figure 4.15 (Run B-3), the probability of chain growth drops from 0.56 to 0.49. This result reflects the influence of the H_2/CO ratio in the feed gas on α. Run B-1 consisted of 10 hours of steady-state synthesis at 360°C and 2,220 kPa using a 2.08:1 H_2/CO ratio. Run B-3 was an identical run except that a 4:1 H_2/CO ratio was used. The difference between the results from Run B-1 (Figure 4.13) and Run B-3 (Figure 4.15) is consistent with existing Fischer-Tropsch data indicting that the product distribution shifts to lower molecular-weight products (smaller α), as the H_2/CO ratio in the feed gas increases. On going to a higher reaction temperature, the probability of chain growth dropped. Run B-2 (Figure 4.14) consisted of approximately two hours of steady-state synthesis at 360°C and 2,220 kPa using a feed gas of 2:08:1 H_2/CO ratio. Run C-1 (Figure 4.16) was identical to Run B-2, but was undertaken at 400°C. On going from 360°C to 400°C,the probability of

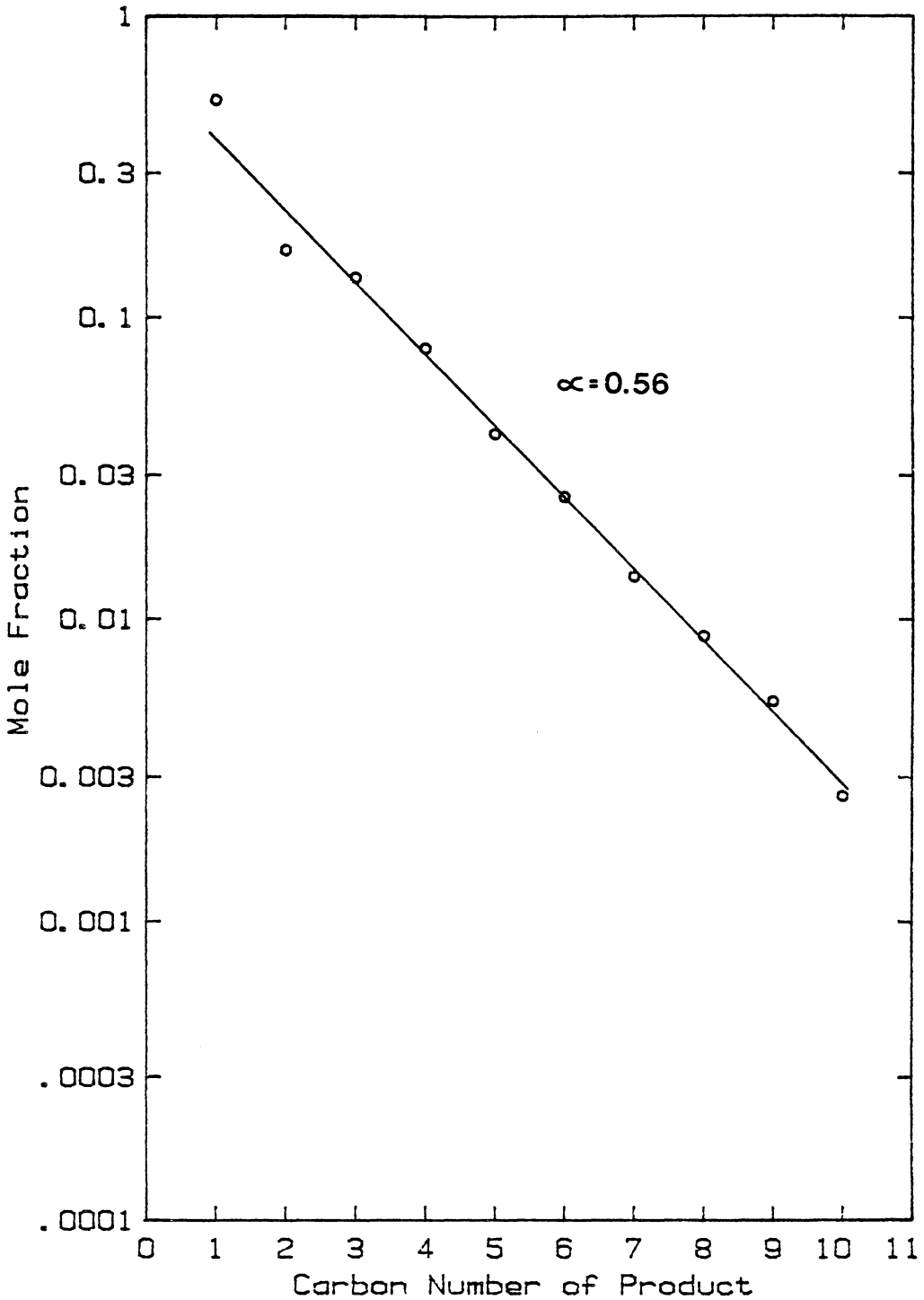

Figure 4.13. A Flory Plot of the Hydrocarbon Product Distribution from Steady-State Fischer-Tropsch Synthesis, Run B-1 (see Table 4.3 for Experimental Conditions).

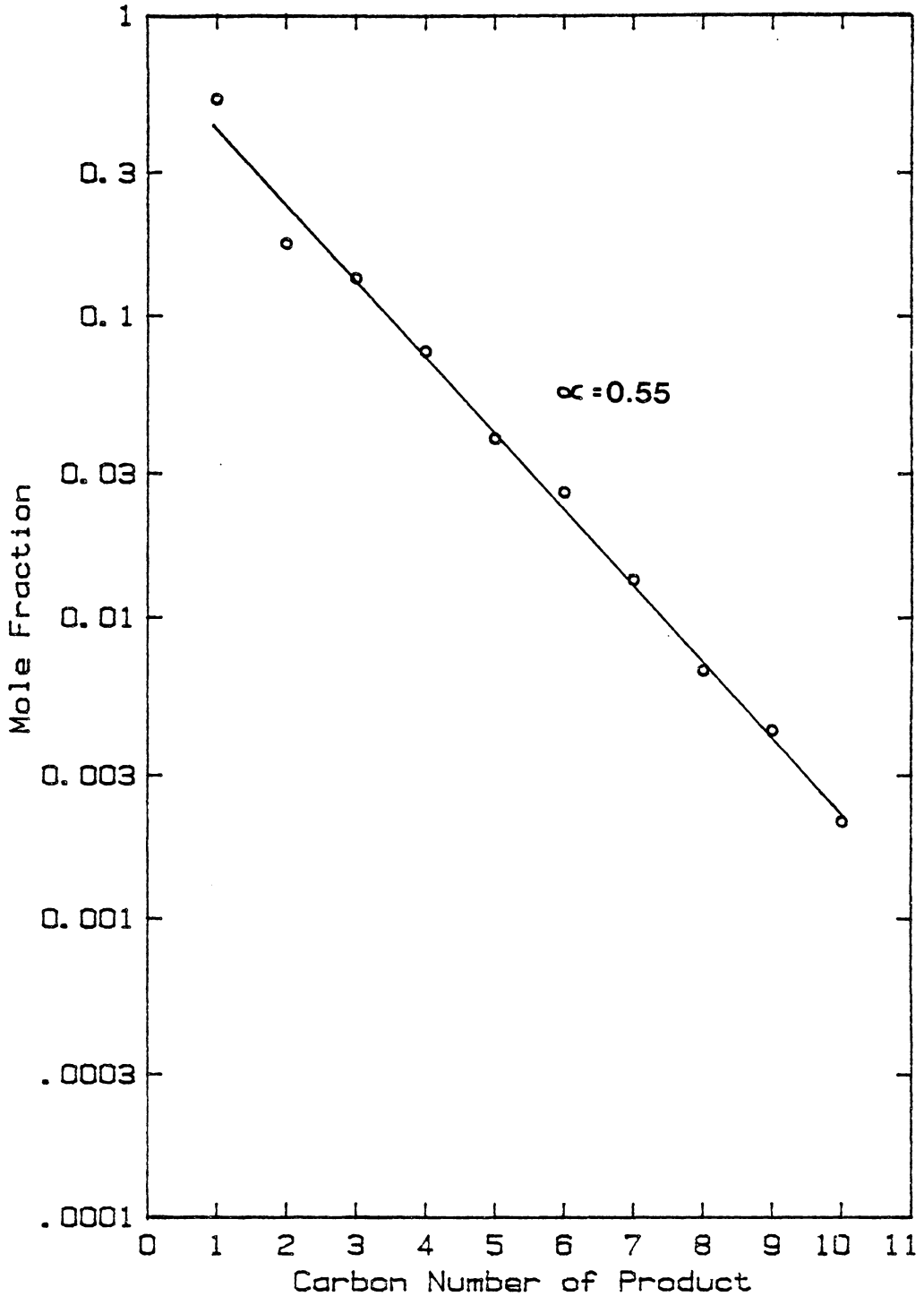

Figure 4.14. A Flory Plot of the Hydrocarbon Product Distribution from Steady-State Fischer-Tropsch Synthesis, Run B-2 (see Table 4.3 for Experimental Conditions).

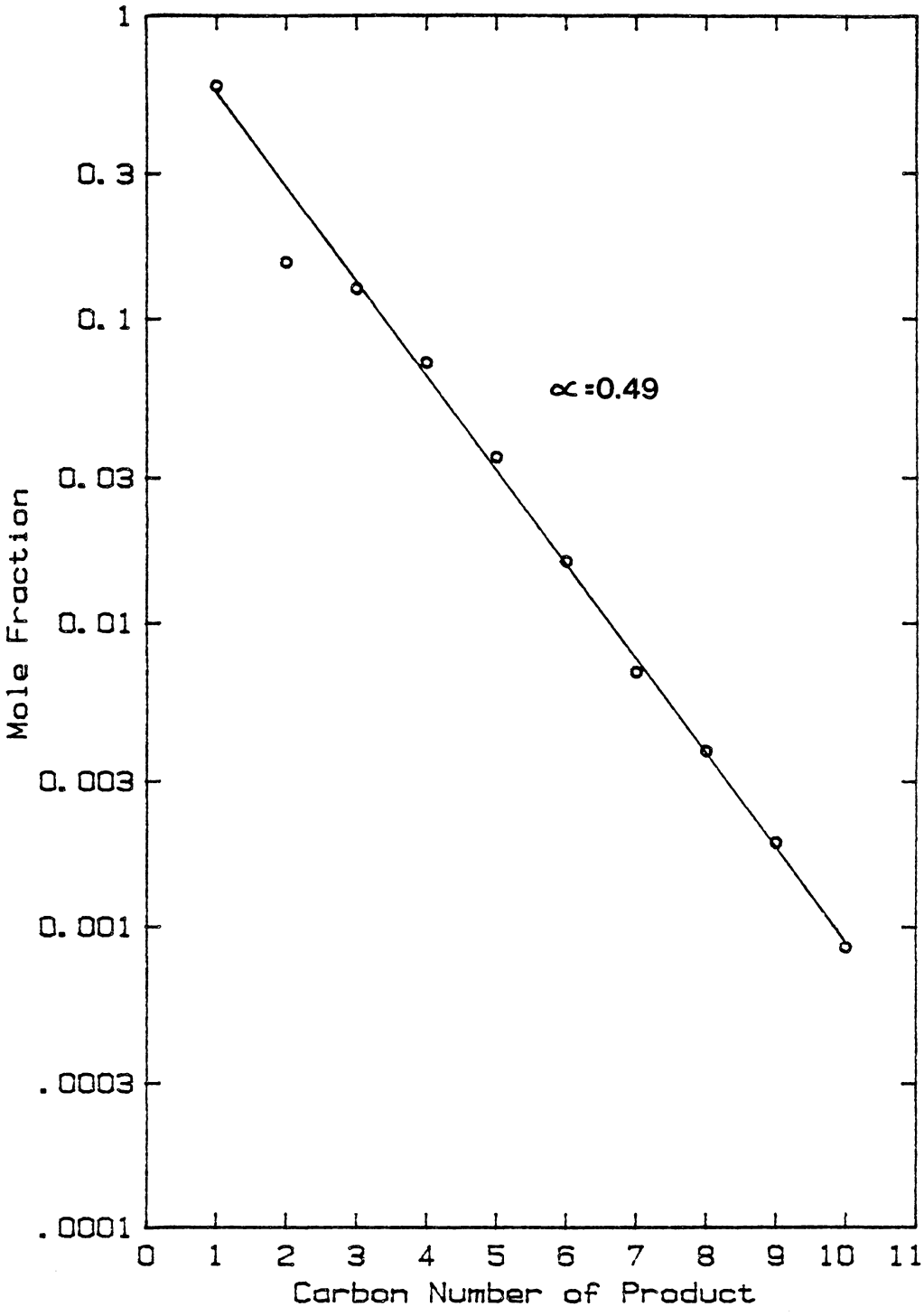

Figure 4.15. A Flory Plot of the Hydrocarbon Product Distribution from Steady-State Fischer-Tropsch Synthesis, Run B-3 (see Table 4.3 for Experimental Conditions).

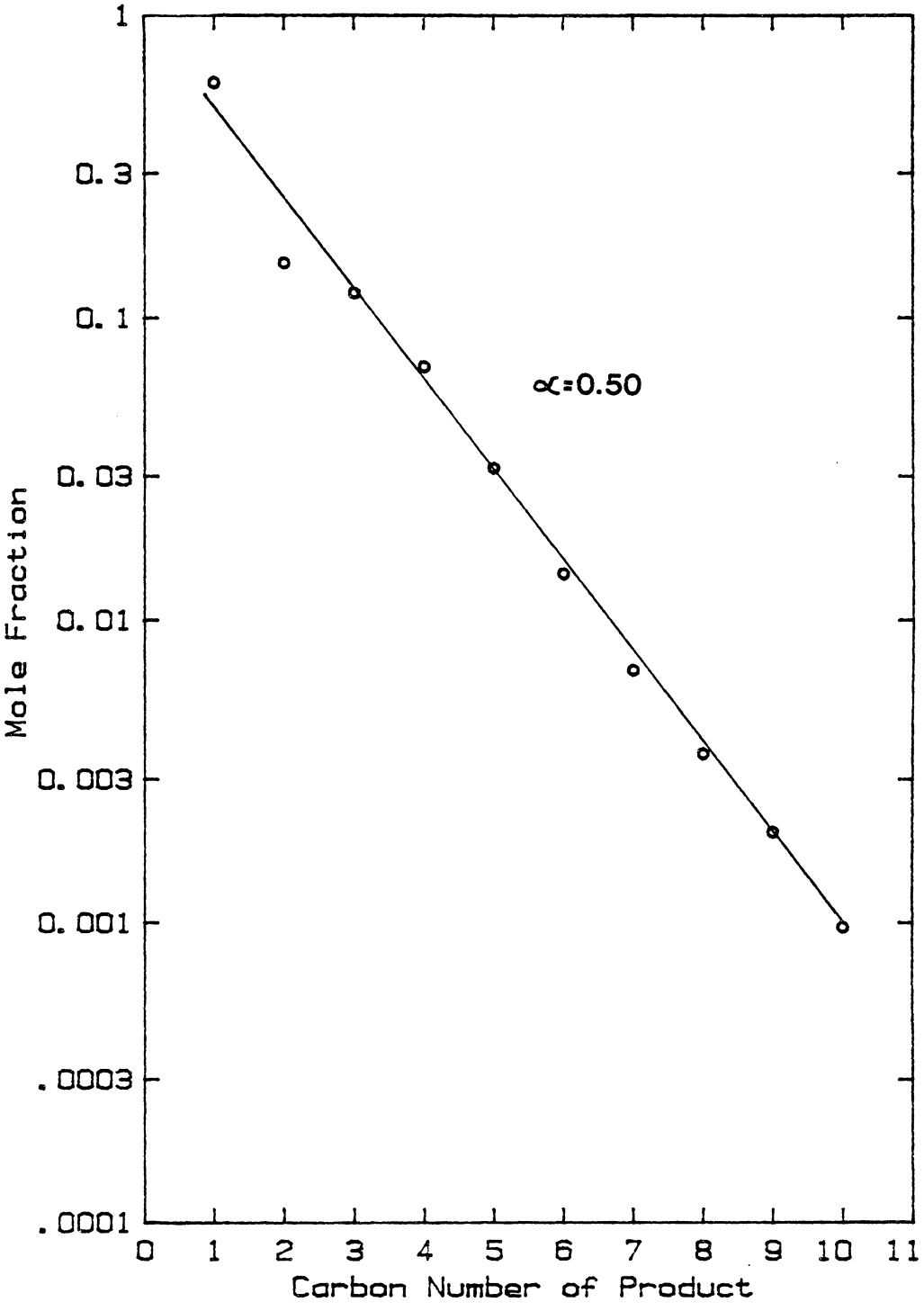

Figure 4.16. A Flory Plot of the Hydrocarbon Product Distribution from Steady-State Fischer-Tropsch Synthesis, Run C-1 (see Table 4.3 for Experimental Conditions).

chain growth (as observed from Figures 4.14 and 4.15) dropped from 0.55 to 0.50. These shifts in hydrocarbon product distribution are the reason why the catalyst was 42% defluidized after 10 hours of synthesis in Run B-3, and why it was not defluidized at all after 2 hours of synthesis in Run C-1.

4.2.3 Steady-State Carbon Deposition Studies

During the defluidization experiments, it was difficult to collect and identify a discrete bugdust fraction. This was caused by condensed liquid products and waxes in the reaction zone, which turned the spent catalyst and bugdust into an agglomerated mass. However, in four of the defluidization experiments, a discrete, free-flowing catalyst fraction and a discrete bugdust fraction could be separated. The bugdust consisted of small particles of low density, which tended to accumulate on the catalyst retention plate, forming a thin black layer. The bugdust layer and the free-flowing catalyst are illustrated schematically in Figure 4.17. The physical separation of these two fractions made it easier to collect the spent catalyst.

4.2.3.1 Trends in Carbon Deposition

Referring to Table 4.3 given in previously Section 4.2, several trends in carbon-deposition rate can be observed. These trends are in agreement with results presented in the literature. Experiments D-1 and C-2 were both performed using a feed gas of 1:1 H_2/CO ratio. Upon increasing the reaction temperature from 380°C in Run D-1 to 400°C in Run C-2, the weight fraction of bugdust present at the end of the run increased drastically. After 1 hour and 15 minutes of reaction at 380°C,

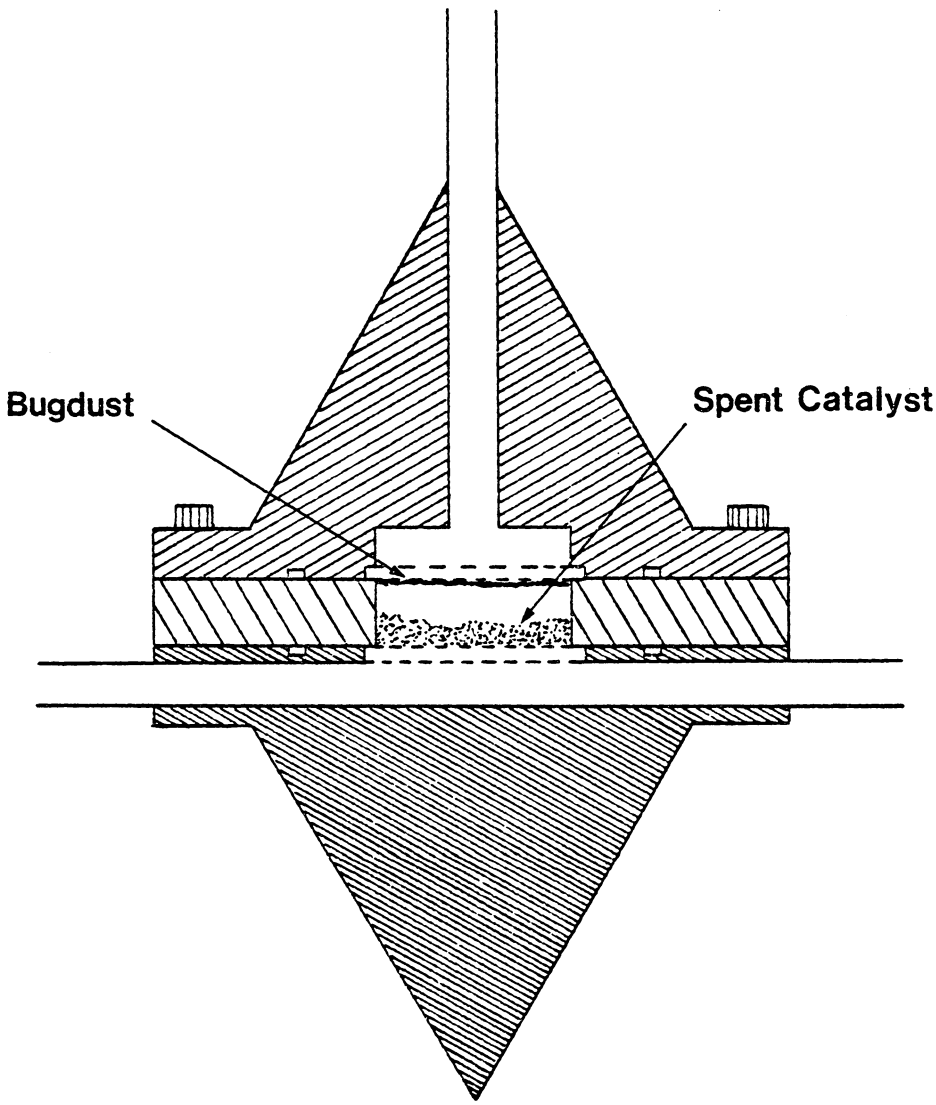

Figure 4.17. An Illustration of the Bugdust Layer and the Free-Flowing Spent Catalyst in the Microreactor After a Steady-State Run.

the reaction zone contained approximately 12 percent bugdust by weight. In contrast, after only 1 hour of reaction at 400°C, the reaction zone contained 100 percent bugdust. Carbon had completely destroyed the physical structure of the fused-iron catalyst. The net weight gain of material in the reaction zone for Run D-1 was 18.1 mg. Run C-2, however, showed a net weight gain of 146.4 mg for the contents of the reaction zone. The gain in weight of the contents of the reaction zone are largely due to accumulation of carbon in the reaction zone.

4.2.3.2 Carbon Deposition at 395°C

As discussed in Section 4.2.1, a synthesis temperature of 395°C, has been identified as sufficient to avoid defluidization of the vibrofluidized fused-iron catalyst. A final group of experiments, Runs F-1 through F-5 as summarized in Table 4.4, involved characterizing the precarburization synthesis period (Runs F-1 and F-2) and then performing baseline, steady-state carbon deposition experiments (Runs F-3, F-4, and F-5). The absolute amounts of free-flowing catalyst and bugdust collected at the end of Runs F-1 to F-5 have been presented previously in Table 4.4

Table 4.5 lists the elemental and molecular-phase compositions of bugdust and free-flowing spent catalyst fractions for Runs F-1 through F-5. Elemental carbon was determined by coulometric determination of CO_2 after complete oxidation of the sample. Total iron was determined by Atomic Absorption spectroscopy. Both elemental determinations were performed by Galbraith Laboratories, Knoxville, Tenn.

The molecular-phase determinations were performed by Professor P.A. Montano at West Virginia University. Mössbauer spectroscopy was used

TABLE 4.5

Elemental and Molecular Composition of Free-Flowing Spent Catalyst and Bugdust Fractions for Baseline Steady-State Fischer-Tropsch Synthesis Experiments

Run Number	Spent Fraction	Relative Amount of Each Spent Fraction (wt%)	Elemental Composition (wt%)[a]		Approximate Molecular Composition by Mössbauer Spectroscopy (wt%)[b]		
			Carbon	Iron	α-Fe	χ-Fe_5C_2	Fe_3O_4
F-1	Free-flowing Catalyst	100	7.61	70.47	5	55	40
F-2	Free-flowing Catalyst	100	5.14	72.71	7	56	37
F-3	Free-flowing Catalyst	96.4	7.36	70.64	8	49	43
	Bugdust	3.6	18.82	63.95	-[c]	-	-
F-4	Free-flowing Catalyst	97.2	9.83	69.15	4	54	42
	Bugdust	2.8	29.56	50.60	-	-	-
F-5	Free-flowing Catalyst	92.9	9.13	70.12	8	47	45
	Bugdust	7.1	26.97	56.63	-	-	-

Note: See Table 4.4 for experimental conditions and for absolute amounts of free-flowing catalyst and bugdust fractions collected at the end of each run.

[a]The difference is assumed to be oxygen bound as Fe_3O_4 and promoters.

[b]Assumes that the (1) particle sizes and (2) Debeye-Waller factors are equivalent for all three species.

[c]The small bugdust sample sizes precluded the use of Mössbauer spectroscopy for identification of iron-contining phases.

to identify the iron containing phases in the free-flowing spent catalysts. The approximate quantitative composition of the catalyst was determined by the latter method also.

Figure 4.18 is the Mössbauer spectrum of the spent catalyst from Run F-1. The sites for magnetite (Fe_3O_4), alpha-iron (α-Fe) and Hägg carbide (χ-Fe_5C_2) have been identified in the figure. Figures 4.19 and 4.20 show the Mössbauer spectra of the free-flowing spent catalyst from Runs F-1 through F-3, and F-4 and F-5, respectively. These samples were said to contain similar quantities of the three aforementioned iron-containing phases. If the Mössbauer results were quantitatively accurate, the amount of elemental free carbon in the free-flowing spent catalyst could be determined. Free carbon is not detected by Mössbauer spectroscopy so it must be obtained by difference. This would be done in the following manner.

1. Four phases are attributed to the sample: (1) α-Fe; (2) Fe_3O_4; (3) χ-Fe_5C_2; and (4) free C.
2. The weight percent iron obtained by Mössbauer spectroscopy (molecular determination) is equated to that obtained in the elemental analysis by Atomic Absorption spectroscopy.
3. The weight percent of carbon present as χ-Fe_5C_2 is subtracted from the weight percent of carbon obtained in the elemental analysis.
4. The difference in carbon content can be attributed to elemental free carbon.

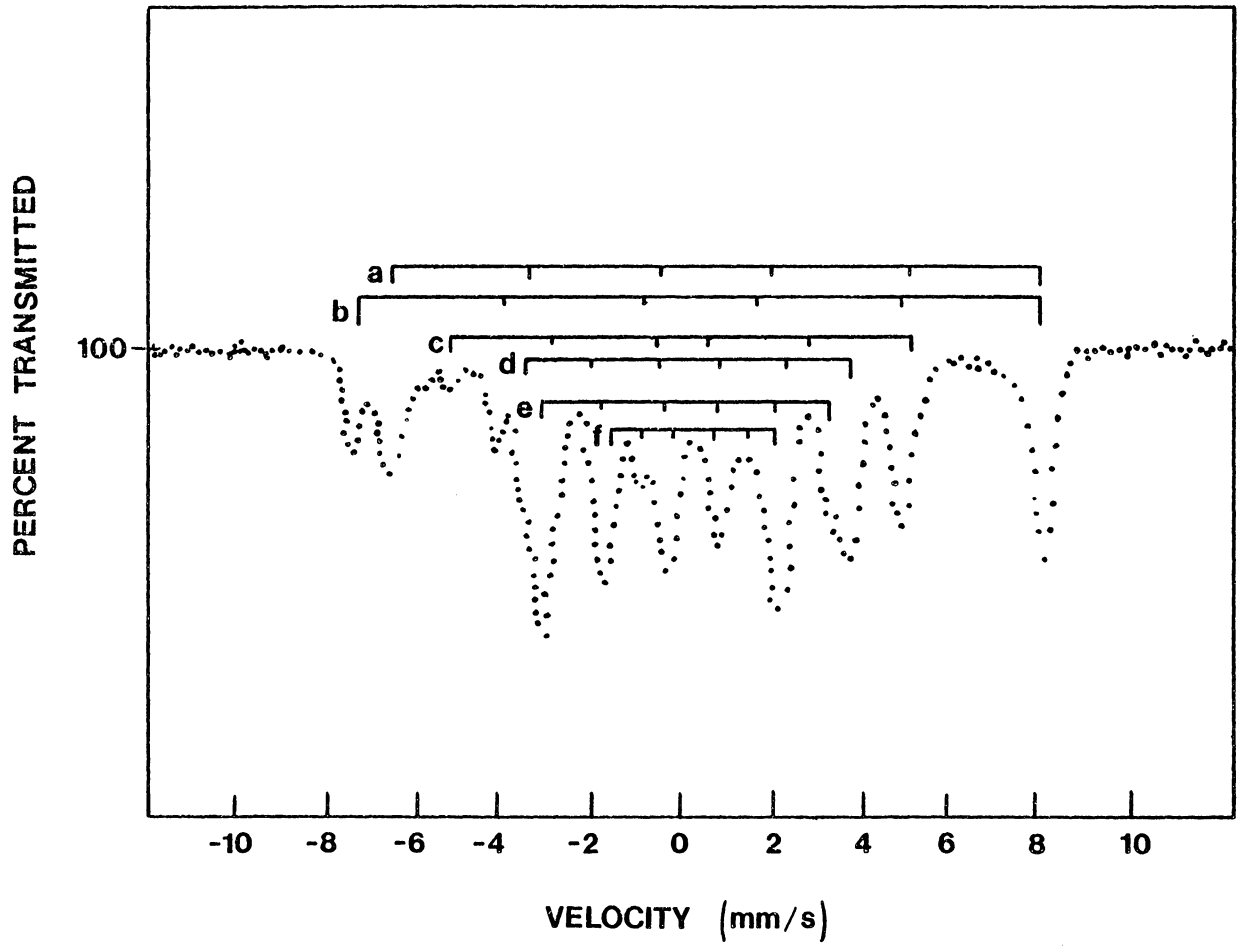

Figure 4.18 A Mössbauer Spectrum of the Free-Flowing Spent Catalyst From Run F-1. Sites include: 1) a and b for α-Fe; 2) c for Fe_3O_4; and 3) d, e and f for χ-Fe_5C_2.

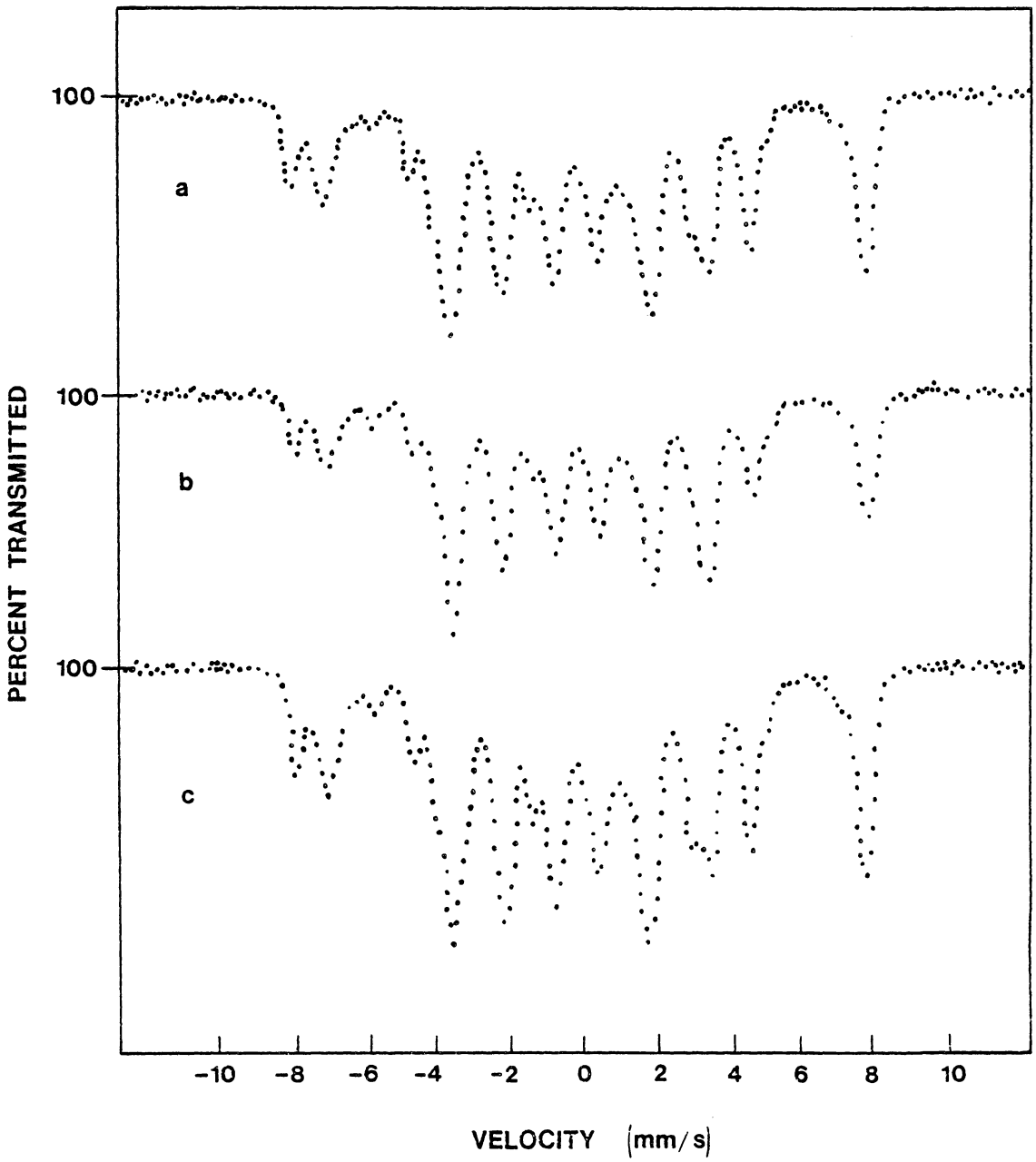

Figure 4.19. The Mössbauer Spectra of Free-Flowing Spent Catalyst From: a) Run F-1; b) Run F-2; and c) Run F-3.

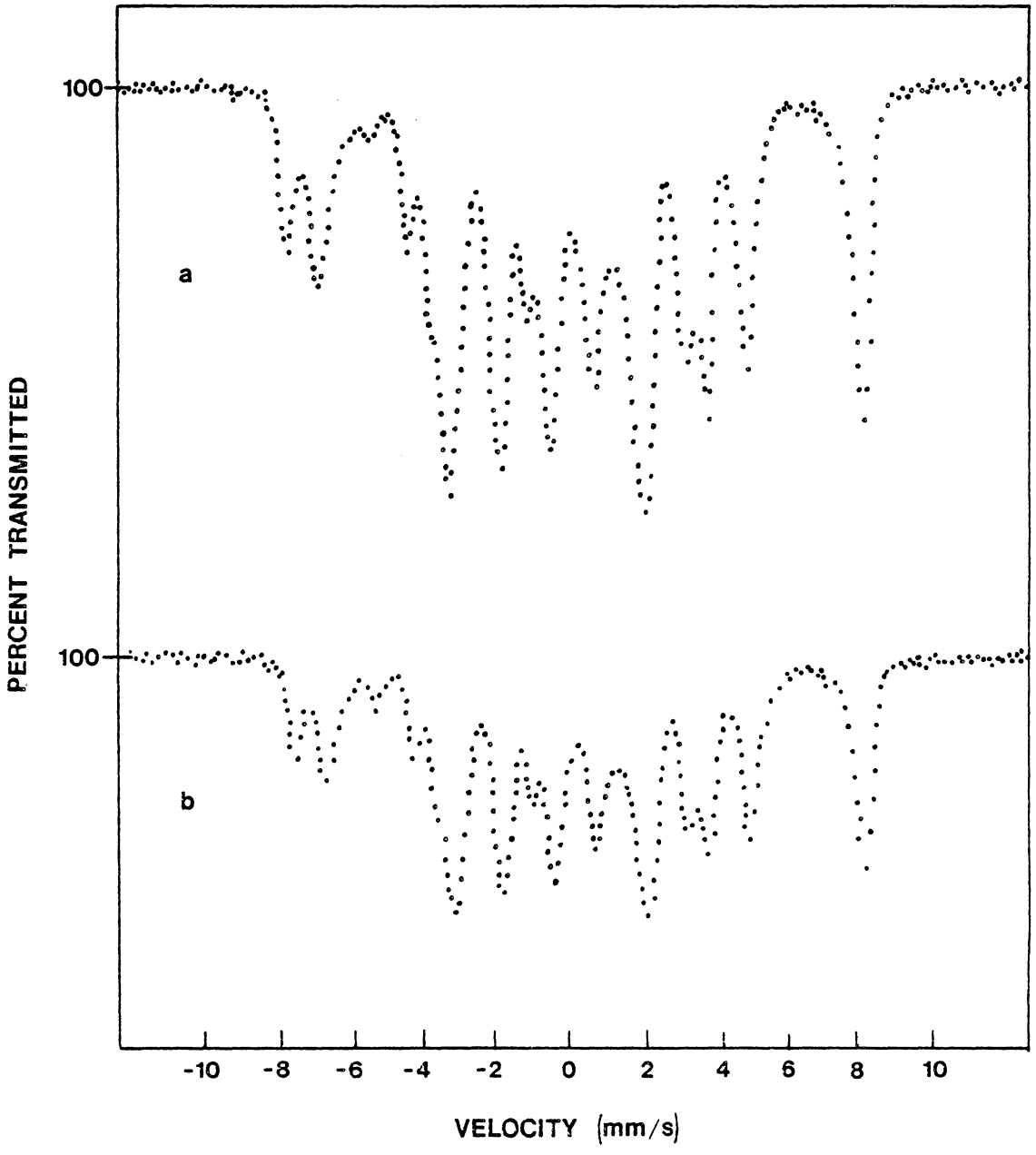

Figure 4.20. The Mössbauer Spectra of Free-Flowing Spent Catalyst From: a) Run F-4; and b) Run F-5.

Attempts to obtain elemental free carbon by difference proved futile, presumably because of the approximate nature of the quantitative Mössbauer determinations. One reason for the lack of accuracy may be because the Debeye-Waller factors were assumed to be equivalent for all three phases. Cohen (1976) states that the size and parametric dependence of the recoil-free fraction (Debeye-Waller factor) is a prime goal of Mössbauer experiments when quantitative analysis is desired. Therefore, the molecular compositions presented in Table 4.5 should be taken as semi-quantitative results.

Table 4.6 is a summary of the total amount of carbon formed, both as carbides and elemental carbon in Runs F-1 through F-5. The time-averaged rate of carbon uptake in the reaction zone has also been calculated for each run. Several useful trends in carbon deposition can be obtained from the results in this table. The time-averaged rate of carbon uptake increases after switching from a gas of H_2/CO of 4:1 to a gas of H_2/CO ratio of 2:1 or 1:1. When using a synthesis gas of H_2/CO ratio of 4:1, the rate of carbon deposition was low and the spent catalyst was gray in color (Runs F-1 and F-2). When a synthesis gas of H_2/CO ratio of 2:1 or 1:1 was used, carbon deposition was rapid as reflected in the formation of bugdust and the blackening of the catalyst.

The time-averaged rate of carbon deposition increased nearly six-fold (from 0.385 to 2.478 mg/min) upon switching to a gas of H_2/CO ratio of 1:1 (Run F-5). In addition, the rate was over five times greater when a synthesis gas of H_2/CO ratio of 1:1 was used than when one of 2:1 was used. The total weight gain attributed to carbon during

TABLE 4.6

A Summary of the Total Amount of Carbon Formed (As Carbides and Elemental Carbon) and the Rate of Carbon Uptake in the Reaction Zone for Runs F-1 through F-5

Run Number	Precarburization Period with a H_2/CO Gas of 4:1 ratio (min)	Duration of Synthesis (min)	H_2/CO Ratio of Gas Used in Synthesis Period	Total Amount of Carbon in the Reaction Zone After the run (mg)	Carbon as Percent of Total Sample (wt%)	Time Averaged Carbon Uptake During the Precarburization Period (mg/min)	Time Average Carbon Uptake During the Synthesis Period (mg/min)
F-1	210	-	-	70.9	7.61	0.337	-
F-2	120	-	-	46.2	5.14	0.385	-
F-3	120	60	2.08:1	72.9	7.77	0.385[a]	0.445
F-4	120	120	2.08:1	101.7	10.38	0.385[a]	0.463
F-5	120	22	1.03:1	100.5	10.40	0.385[a]	2.468

[a]Assumed carbon uptake rate based on Run F-2.

two hours of synthesis with a gas of H_2/CO ratio of 2:1 (Run F-4) was the same as that obtained after 22 minutes of synthesis with a gas of H_2/CO ratio of 1:1 (Run F-5). However, a greater percentage of the carbon was present in the bugdust fracton after Run F-5 than after Run F-4.

4.2.3.3 The Nature of Bugdust

Bugdust is fine, low-density particles consisting of elemental carbon, iron carbides and Fe_3O_4. It is produced when severe carbon deposition takes place on the surface of the iron catalyst, resulting in eventual breakup of the physical structure of the catalyst.

Figures 4.21, 4.22 and 4.23 are micrographs of a typical bugdust sample taken at magnifications of 100X, 1000X and 10,000X, respectively. Figure 4.21 shows that bugdust consists of irregular-shaped particles, ranging in size from less than 1μ to more than 70μ.

Figure 4.22 presents a closer view of individual bugdust particles. The particle inside the bordered area is approximately 10μ in length. Its surface appears to have a porous structure.

Figure 4.23 is a further enlargement of the particle outlined in Figure 4.22. The surface is a highly porous, coral-like structure. This structure is presumably built up by carbon being deposited on an iron and iron-carbide-bulk structure.

The elemental composition obtained in this study indicates that the bugdust fraction contains 18 to 30 weight percent carbon, 50 to 64 weight percent iron with the remainder present as oxygen and small amounts of promoters.

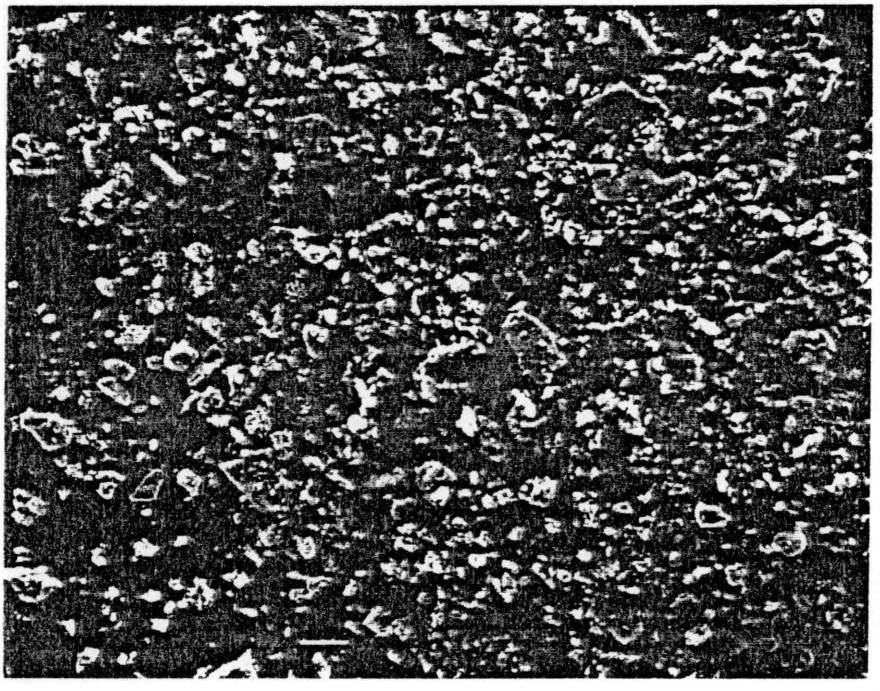

Figure 4.21. An Electron Micrograph of a Typical Bugdust Sample at a Magnification of 100X (1 mm = 10μ).

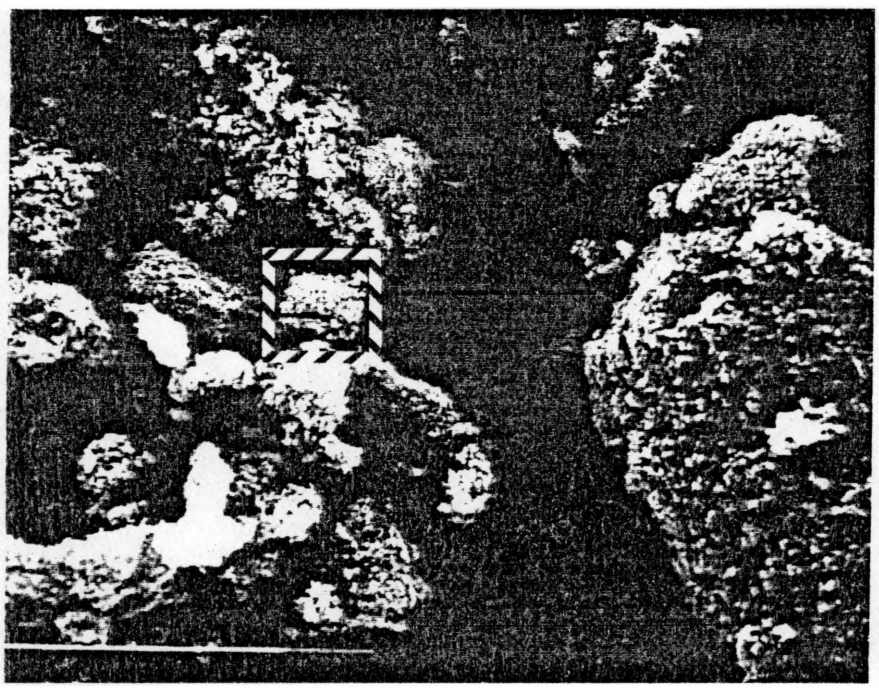

Figure 4.22. An Electron Micrograph of a Typical Bugdust Sample at a Magnification of 1000X (1 mm = 1μ).

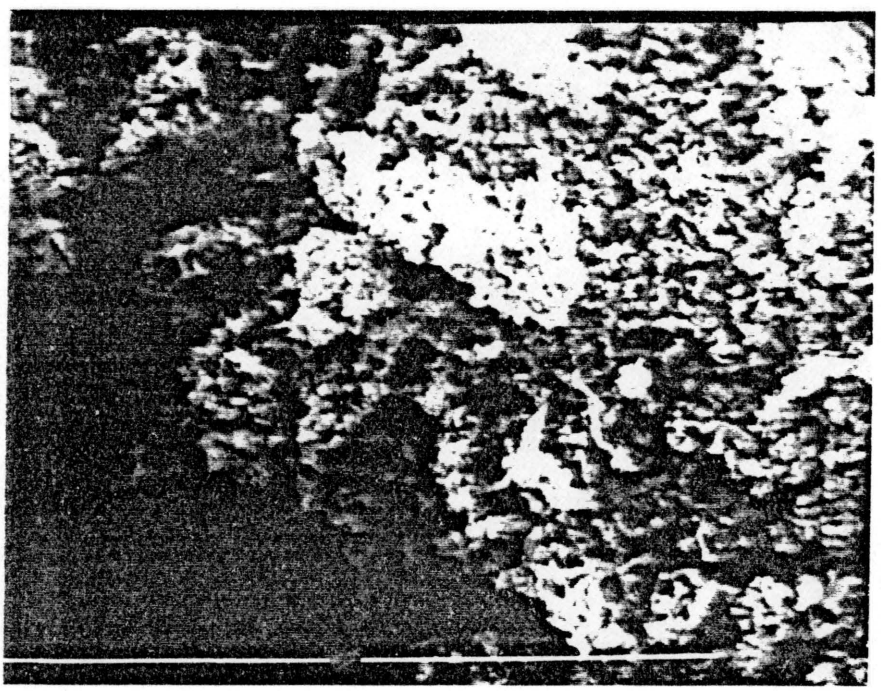

Figure 4.23. An Electron Micrograph of the Surface of the Bugdust Particle Outlined in Figure 4.19 at a Magnification of 10,000X (1 mm = 0.1μ).

CHAPTER 5

GAS MIXING AND CATALYST VIBROFLUIDIZATION STUDIES IN A COLD-FLOW VIBROFLUIDIZED-BED MICROREACTOR MODEL

5.1 Apparatus and Procedures

5.1.1 Experimental Apparatus

5.1.1.1 Microreactor Model System

Gas-mixing and differential-pressure measurements were made in a cold-flow model of the unsteady-state vibrofluidized-bed microreactor system. The primary goal of these measurements was to determine the characteristics of the newly-designed, rapidly switching system.

Figure 5.1 is a schematic diagram of the sliding-plug vibrofluidized-bed microreactor system for cold-flow studies. Figure 5.2 is a photograph of the system. Referring to Figure 5.1, argon or helium enters the system through a low-pressure two-stage gas regulator and is stored in a gas reservoir (1.0×10^6 mm^3 in volume) made of PVC pipe. Two-way solenoid valves (Precision Dynamics model 2012), controlled through an interface to a Heath H-89 microcomputer, direct which gas is flowing to the microreactor. Flow rates are manually set using double-needle valves (Nupro model 2SGA) located downstream of the solenoid valves. All tubing is 1/4-inch O.D. brass with a 0.035-inch wall thickness. Flexible braided-metal hoses connect the feed and exit lines to the sliding-plug microreactor itself. These hoses allow the microreactor to vibrate, while maintaining a gas-tight seal in the system.

A 0.36-mm diameter wire runs through the 1/4-inch O.D. tubing from each solenoid plunger to the sliding plug in the plenum region of the

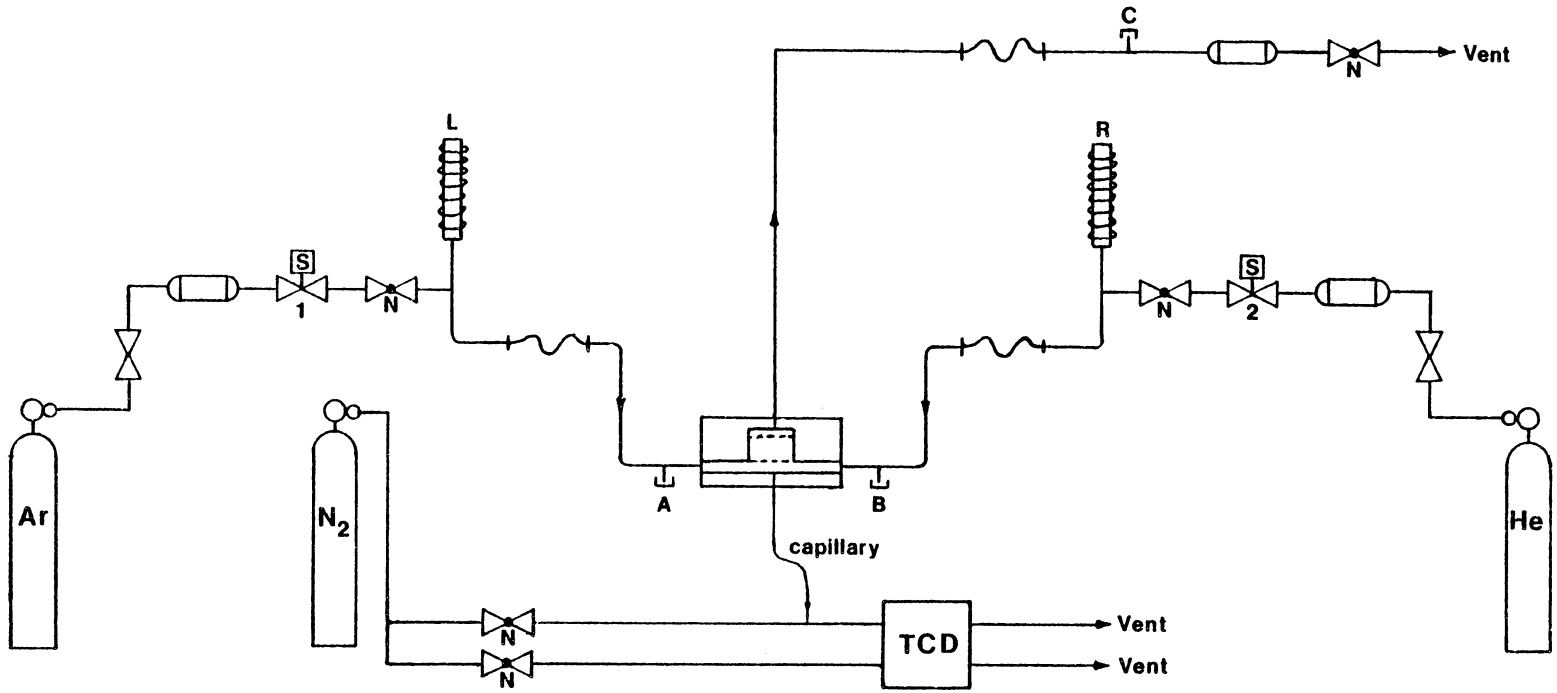

Figure 5.1. A Schematic Diagram of the Sliding-Plug Vibrofluidized-Bed Microreactor System for Cold-Flow Studies (see Figure 4.1b for Equipment Symbols Included in the Figure).

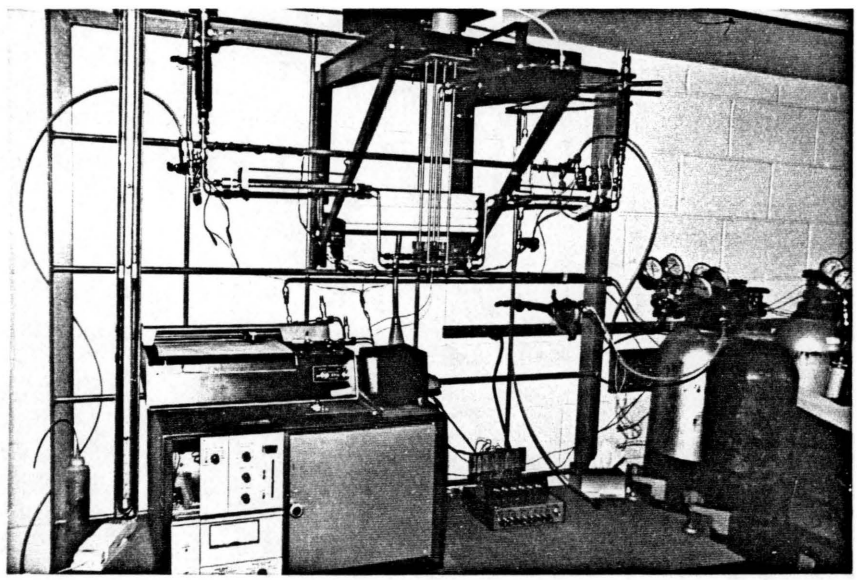

Figure 5.2. A Photograph of the Sliding-Plug Vibro-fluidized-Bed Microreactor System for Cold-Flow Studies.

microreactor. The wire is connected to the plungers and the plug by eyelets. It is threaded through these eyelets and then twisted around itself.

The solenoid design will be examined in Section 5.1.1.3. Downstream of the microreactor, exit gas is held in a gas reservoir (5.0×10^5 mm^3) and bled off through a Nupro 4SG needle valve. A pressure tap exists in both feed lines to the microreactor as well as in the exit line. A rapid-response differential-pressure transducer (MKS Instruments model 223AH, 0-100 torr) is used in conjunction with these pressure taps to obtain pressure drop and pressure swing information. The response of the transducer is recorded on a storage oscilloscope (Tektronic T912 10 MHz).

Stainless-steel capillary tubing 1/15-inch O.D. with a 0.028-inch wall thickness allows a small amount of gas to be continuously drawn off from the sliding-plug microreactor. The capillary can be connected to the microreactor in one of three places: (1) the plenum zone; (2) the catalyst zone; or (3) the gas-exit zone. The taps in the microreactor can also be used for differential-pressure measurements. Gas flowing through the capillary from the microreactor bleeds into a stream of pre-purified nitrogen flowing through a 1/8-inch O.D. copper tubing directly to a thermal conducting detector (TCD).

Signal balance is maintained in the TCD through the use of another parallel nitrogen stream set at an equivalent flow rate. The signal from the TCD is recorded using a strip chart recorder (Cole-Parmer model 8386).

The microreactor is vibrated in an identical fashion and by identical equipment as that described in Section 4.1.1.2.

5.1.1.2 Cold-Flow Sliding-Plug Vibrofluidized-Bed Microreactor

Cold-flow model experiments for gas mixing and differential pressure measurements involved the use of the sliding-plug vibrofluidized-bed microreator pictured in Figure 5.3. Cross-sectional schematic diagrams of this microreactor are shown in Figures 5.4 and 5.5 The design and construction features of this microreactor are similar to the steady-state microreactor which was illustrated previously in Figure 4.1 and described in Section 4.1.1.2.

The lexan microreactor consists of three main sections: (1) the base section; (2) the catalyst section; and (3) the gas-exit section. The base section contains a plenum zone in which a sliding brass-plug resides. The plenum consists of a 6.35-mm diameter hole, 76.2 mm in length. At either end of the plenum, a Swagelok straight threaded-fitting connects the feed lines to the plenum.

A groove was machined into the end face of the Swagelok fittings in order to accept a 6.35-mm O.D. rubber O-ring. The O-ring, which has been epoxied to the fitting, serves as a seat for the sliding brass plug. The brass plug is 6.248 mm in diameter and 25.4-mm long. Eyelets entend aproximately 3 mm from each end of the plug, so that the conencting wire can be affixed to the plug.

The distributor plate is recessed into a 1.59-mm deep slot in the base section, which is 6.35-mm wide and 25.4 mm in total length. The ends of this slot are rounded.

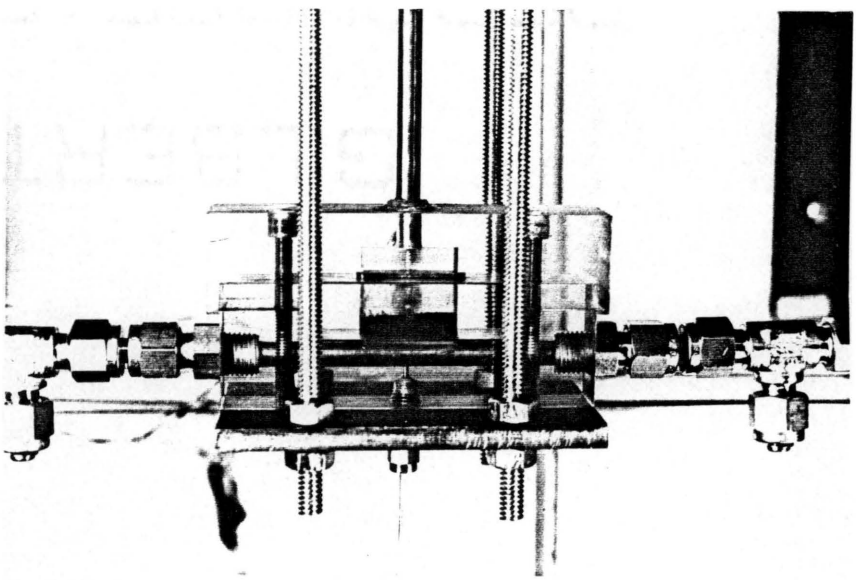

Figure 5.3. A Photograph of the Sliding-Plug Vibro-fluidized-Bed Microreactor Model for Cold-Flow Experiments.

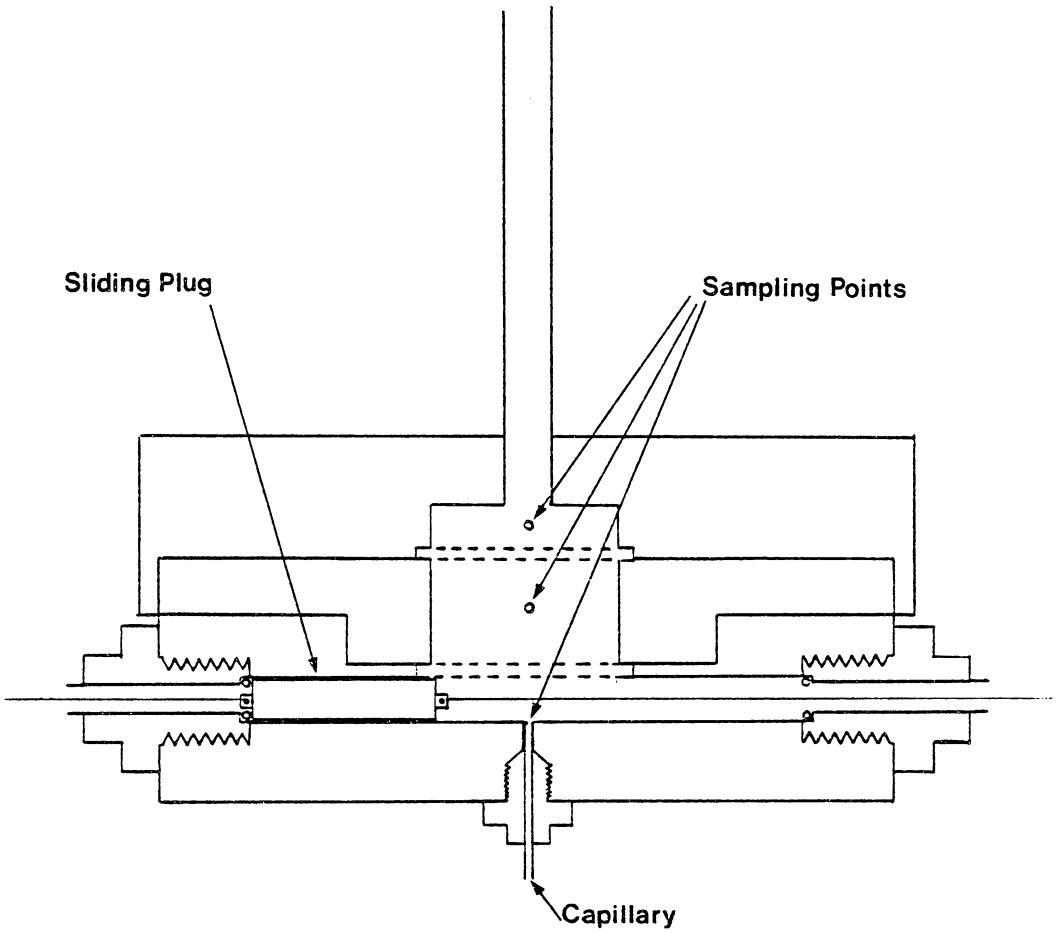

Figure 5.4. A Schematic Cross-Sectional Diagram of the Sliding-Plug Vibrofluidized-Bed Microreactor Model (front view).

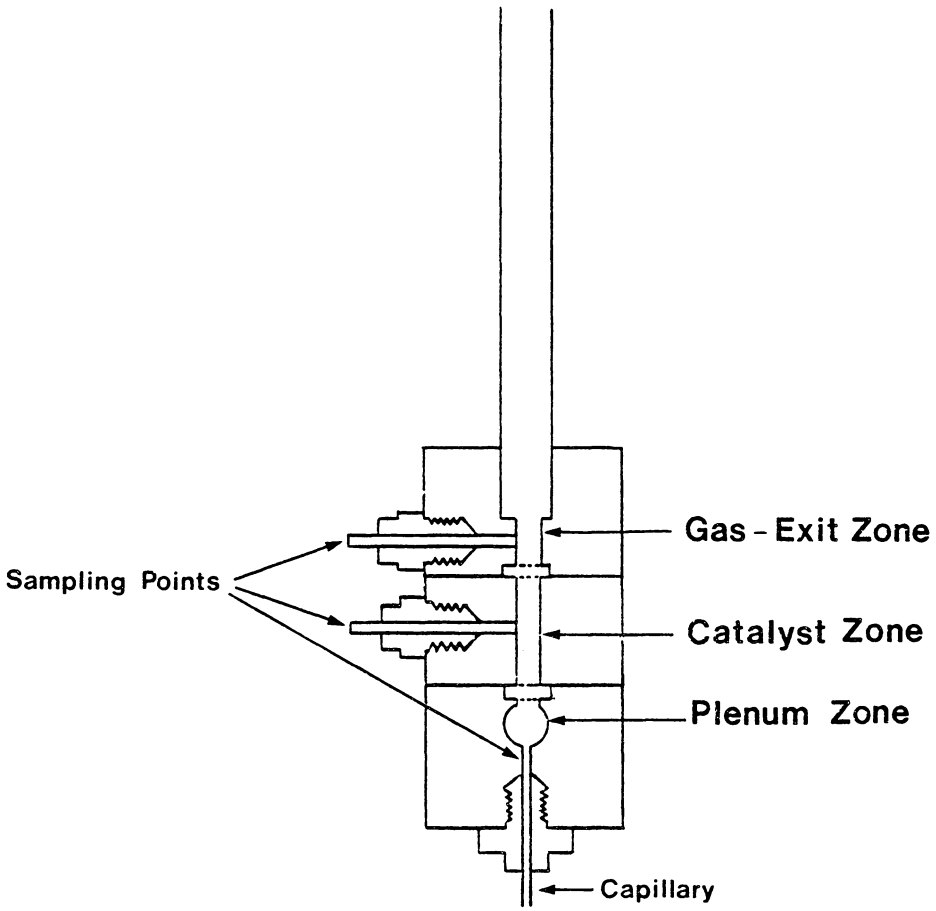

Figure 5.5. A Schematic Cross-Sectional Diagram of the Sliding-Plug Vibrofluidized-Bed Microreactor Model (end view).

The positioning of the distributor plate relative to the plenum space is illustrated in Figure 5.4. The bottom of the distributor plate is at the appex of the plenum. This creates a very small dead volume between the plenum and the distributor plate.

The catalyst section and gas-exit section are identical in internal dimensions to the reaction zone and product gas-exit zone of the microreactor used for steady-state F-T synthesis studies (Section 4.1.1.2). The catalyst zone consists of a 3.175-mm wide slot, milled 25.4 mm long in the 14.29-mm deep catalyst section. The ends of the slot are milled round, so that no corners exist to trap the catalyst. The gas-exist zone consists of a slot (3.175 mm × 6.35 mm × 25.4 mm) milled from the bottom surface to match the slot cut in the catalyst section. A recess identical to the one milled in the base section holds the sintered stainless-steel catalyst retention plate. A 1/4-inch O.D. tube extends down into the gas-exit section from above breaking through to the slot.

The external dimensions of this microreactor are approximately 101.6-mm long, 50.8-mm tall and 25.4-mm wide.

The three sections (zones, i.e., the plenum zone, the reaction zone and the gas-exit zone) are held together by four 10-32 Allen head-cap screws. A gas-tight seal is maintined between the sections by using silicone rubber during assembly. A 1.59-mm clearance hole extends into each section, allowing the sampling capillary to be inserted into any one of the three zones. When not in use, these holes are filled with 1.59-mm rods which are swaged in place for a leak-proof seal.

5.1.1.3 Solenoids

Two solenoids control the sliding movement of the brass plug in the plenum zone. Each solenoid consists of a 216-mm long piece of 1.2-inch O.D. 316- stainless-steel (non-magnetizable) tubing with a 0.049-inch wall thickness. The winding begins 44.5 mm up from the base of the tube and is 108 mm in total length. The winding contains 2,880 turns of number 23 AWG copper solenoid-winding wire, producing a minimum force of 1.33 N at the start of the plunger stroke.

An adjustable carbon-steel (magnetizable) stop extends down into the tube and the winding area. The stop causes the flux lines of the magnetic field to be re-directed so that the force on the plunger increases greatly as it approaches the stop.

The plunger itself is a 10.0-mm diameter piece of carbon-steel, 76.2 mm in length. Two 3.175-mm wide grooves, 1.27-mm deep, have been milled the length of the plungers in order to keep gas from being compressed in front of the plungers when the solenoids are activated. A small nipple, 3.23 mm in length, has been machined into the lower end of the plungers. A small hole has been drilled in these nipples in order to attach a 0.356-mm wire that controls the sliding-plug movement.

The solenoid windings are electrically connected to a relay which controls the power input to each solenoid. In particular, one solenoid is on while the other is off. Inside the soleniod that is on (solenoid "L" in Figure 5.1), the plunger has been drawn upward nearly coming in contact with the plunger stop. The force on the plunger at

this point is very high. This creates tension on the wire connecting the plunger in the actuated solenoid to the sliding plug. The sliding plug, in turn, is drawn up tightly against the seat created by the O-ring. The other, de-energized solenoid (solenoid "R" in Figure 5.1) is, at the same time, resting at the base of the solenoid tube.

The wire connecting this plunger to the other side of the sliding plug has several millimeters of slack in it so as not to keep the plug from seating. When the relay is switched, solenoid R is energized and solenoid L is de-energized. The plug is drawn from left to right and seats against the right-hand O-ring. Both solenoids are kept cool using small fans in order to maintain a maximum force on the plungers.

5.1.1.4 Valve and Solenoid Switching Circuit

The solenoid valves and solenoids control whether argon or helium is being fed to the catalyst zone of the sliding-plug vibrofluidized-bed microreactor. Solenoids L and R shown in Figures 5.1 are alternately actuated through the use of a 24 volt relay. The power inputs to the solenoid valves, solenoids, and this relay are all provided by a 24-volt power supply.

Switching of the solenoid valves 1 and 2 as well as the relay is accomplished through the use of a Heath H-89 microcomputer and a parallel-port computer interface. Figure 5.6 is a diagram of one circuit of the interface. One such circuit is provided for each valve or relay. A transistor-transistor-logic (TTL) signal (0 or 5 volts) is produced at the parallel output port by the microcomputer. The interface then uses this signal to determine whether 0 volt or +24

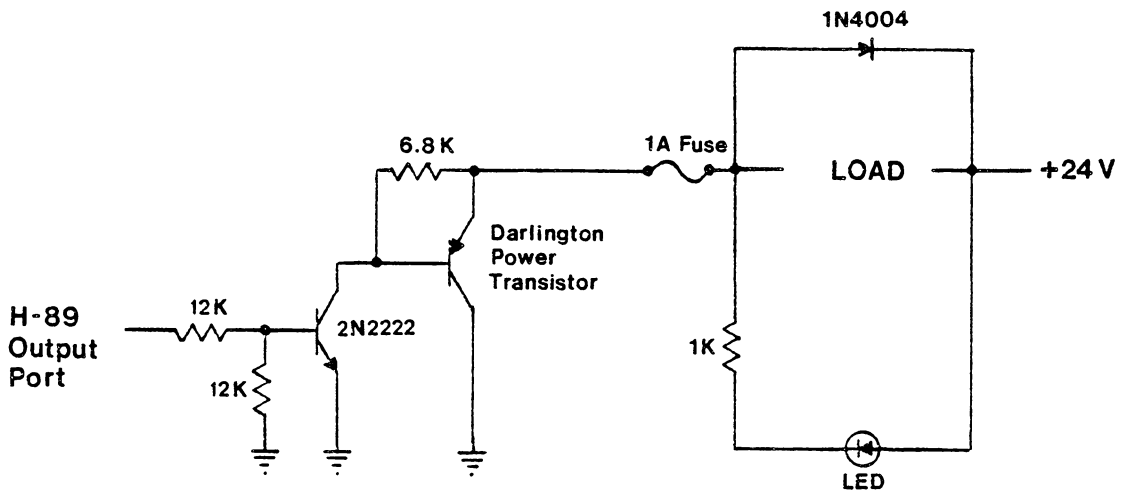

Figure 5.6. A Diagram of One Circuit in the Interface Between the Experiment and the H-89 Microcomputer Parallel Port.

volts should be supplied to the solenoid valve or relay. The 2N2222 transistor amplifies the signal from the computer so that it can activate the Darlington power transistor. When activated, the power-transistor output drops from 24 volts to 0 volt. This, in turn, causes a 24-volt drop across the coil of the solenoid valve or relay (LOAD), inducing the valve to open or the relay to switch.

5.1.2 Materials

The material used as the fluidization media in the cold-flow model studies was -150-300 μ fused-iron catalyst. This catalyst was described previously in Section 4.1.2.1. The gases used were prepurified grade argon, helium and nitrogen supplied by Airco.

5.1.3 Experimental Procedures

5.1.3.1 Cold-Flow Microreactor Model Loading

The base section of the sliding-plug vibrofluidized-bed microreactor was first attached to the suspension apparatus. A distributor plate made of sintered stainless-steel was then fitted into the recess in the base section. Several distribution plates of different porosities were used over the course of these experiments. Silicone rubber was used as a gasket material between the sections of the cold-flow model. A bead of silicone was placed around the edge of the distributor plate in contact with the lexan. The silicone was allowed to set for several minutes and the catalyst section of the model was then put in place making certain that no silicone flowed into the catalyst zone. At this point, the silicone was allowed to dry for

at least two hours. One gram of the fused-iron catalyst was weighed out and poured into the reaction zone.

The gas-exit zone, containing a 20μ catalyst retention plate was affixed to the catalyst section in a similar fashion. The silicone rubber gasket material was allowed to cure for twenty-four hours. The four bolts that held the three sections of the cold-flow model together were then inserted and tightened. Care must be taken not to overtighten these bolts. Only a thin piece of lexan lies between the distributor plate and the plenum zone. If the bolts are overtightened, the distributor plate deforms the lexan below it and restricts the brass-plug movement.

5.1.3.2 Mounting the Sliding Plug

Approximately 1 meter of 0.356-mm diameter wire was attached to each end of the sliding brass-plug. The plug was slid into the plenum zone of the cold-flow model. The wire on each end of the plug was then fed through a Swagelok fitting containing the O-ring, one for each end of the base section. These fittings were then screwed into the base section and sealed using silicone rubber.

The wire was threaded up through the brass tubing and the flexible metal hose using a large-diameter guide wire. The plug wire finally exits the 1/4-inch brass tubing at a vertical 1/4-inch to 1/2-inch reducing union. This union serves as the lower resting stop of the plunger when it is de-energized . At this point, the sliding plug could be drawn back and forth freely by hand in the plenum zone.

The plug was next pulled tight against the left end of the plenum zone and the wire was fed through the eyelet of the left plunger. Approximately 57.2 mm of wire must be between the lower resting stop and the bottom of the left-hand plunger. The actual full length movement of the plug is 50.8 mm. The additional length of wire insures that the de-energized solenoid will not prevent the sliding plug from seating. The wire on this side was twisted around itself securing the left-hand plunger.

The left-hand solenoid, a 12.7-mm O.D. tube with a coil wound on it, was then lowered over the left-hand plunger and secured to the reducing union. The sliding plug was drawn to the right end of the plenum by hand and the operation was repeated.

Following the orientation of both the left- and right-hand solenoids, plunger stops were inserted down into the magnetic-field region of each solenoid. These plunger stops were held in place using a 1/2-inch bored through Swagelok union and nylon ferrules. Initially, these stops were only roughly adjusted.

The system was pressure-tested by closing the outlet needle valve and pressurizing the system to a pressure of 170 kPa absolute (about 25 psia). The system was then returned to atmospheric pressure and sealing of the "plug seat," where the sliding plug comes in contact with the O-ring, was checked. If gas was leaking across the plug seat when the respective feed line was pressurized to 170 kPa absolute, the plunger stop was raised somewhat. This, in turn, caused more tension in the wire connecting the plunger and the plug, and more force against the plug seat.

At the conclusion of the above procedure, the cold-flow model was ready for gas-mixing or differential-pressure experiments.

5.1.3.3 Feed Gas Flow Rates

Feed-gas flow rates were set using the needle valves located just downstream of solenoid valves 1 and 2 in Figure 5.1. Again a critical pressure drop was maintained across these needle valves, making the flow rate independent of the downstream system pressure. Typically, the pressure upstream of solenoid valves 1 and 2 was maintained at 274.8 kPa (gauge) and the downstream pressure at 34.0 kPa (gauge).

The argon flow rate was set by first activating solenoid valve L, causing the sliding plug to seal against the left-hand plug seat. Pressure tap A (see Figure 5.1) was then opened and a bubble meter was connected to it using tygon tubing. Solenoid valve 1 (shown in Figure 5.1) was opened and the associated needle valve was adjusted to allow the desired flow rate of argon. This procedure was repeated in the helium feed-line.

The flow rate of feed gas used in the steady-state F-T synthesis experiments in the hot vibrofluidized-bed microreactor system was 3,670 standard mm^3 per second. This flow rate corresponds to a flow rate at conditions (395°C, 2,220 kPa absolute) of approximately 409 actual mm^3 per second. Feed-gas flow rates of argon and helium used in the cold flow model expriments were maintained at approximating 417 actual mm^3 per second in order to duplicate the velocity in the hot rig.

5.1.3.4 Gas-Mixing Studies

Experiments were performed in the cold-flow model of the sliding-plug virbofluidized-bed microreactor in order to determine the extent of gas mixing in the three zones of the microreactor after switching from one feed gas to the other. For example, the gas-mixing properties of the plenum zone can be determined by first inserting the capillary sample tube into the base section of the model. The top of the capillary was inserted so that it was flush with the plenum zone wall and did not interfere with the movement of the sliding-plug. The nitrogen flow to the thermal conductivity detector was started at 1,170 standard mm^3 per second and the detector temperature and sensitivity were set to 100°C and 2, respectively. Helium and argon were allowed to flow into the gas reservoirs located upstream of solenoid valves 1 and 2 in Figure 5.1. These reservoirs were allowed to pressurize to 274.8 kPa (gauge). The remainder of the cold-flow model was then brought up to between 27 and 34 kPa (gauge) in the following fashion (refer to Figure 5.1). The exit-line needle valve was closed and the left solenoid (L) in the argon feed-line was actuated. This causes the sliding plug to move to the left end of the plenum zone. Solenoid valve 2 in the helium feed line was then opened, allowing helium to flow through the system. After two minutes of helium flow, solenoid valve 1 was opened and solenoid valve 2 was closed. At the same moment, the relay to the solenoids was switched causing solenoid L to de-energize, while solenoid R was energized. This drew the plug to the right-hand

end of the plenum. Argon was allowed to flow though the system for 2 minutes before flow of helium was resumed.

The switching procedure described above was continuously repeated using a microcomputer program, until the system reached the operating pressure. The exit-line needle valve was then opened slightly to allow the pressure to stabilize at the desired value. The microcomputer control continued switching the solenoid valves and the relay, while a thermal conductivity trace was obtained on the chart recorder.

The above procedure was repeated with the capillary sampling tube inserted into the catalyst zone and the gas-exit zone of the cold-flow model. In addition, several feed-gas flow rates were used. The effect of catalyst vibrofluidization on gas mixing was investigated by vibrating the cold-flow model at a frequency of 18 to 24 Hertz (Hz) and a peak-to-peak amplitude of 4 mm.

Finally, a method of feed-gas flow staggering was devised. Staggering involves opening the opposite solenoid valve several seconds before the plug slides, thus allowing feed-gas valve openings to overlap somewhat. This causes the gas pressure to build up behind the plug seat. When the plug is moved to the opposite seat, the gas pressure rapidly sweeps the plenum zone.

5.1.3.5 Differential-Pressure Studies

Experiments were conducted in the cold-flow model in order to identify pressure buildup and pressure drop characteristics of the sliding-plug microreactor system. The procedure for these studies typically involved connecting a fast-response pressure transducer

(0 to 100 torr) between two pressure taps and then starting the feed-gas cycling. For example, a pressure-drop experiment involved connecting the high-pressure inlet of the transducer to pressure tap A (shown in Figure 5.1) and the low-pressure inlet to the tap in the center of the catalyst section of the cold-flow model. This effectively placed the differential-pressure transducer across the distributor plate. The output of this fast-response transducer was connected to the storage oscilloscope and a digital multimeter. The system was pressurized in the manner described in Section 5.1.3.4 and the microcomputer initiated the feed-gas cycling. Using this rapid-response differential-pressure transducer setup, both steady-state and transient pressures could be recorded. Thus, pressure changes during plug movement could be monitored.

5.2 Experimental Results and Discussion

The objective of the cold-flow experiments in the sliding-plug vibrofluidized-bed microreactor model was to determine the gas-mixing properties of the microreactor upon rapid switching between two feed gases. In addition, it was desired to optimize the microreactor design so as to obtain rapid replacement of gas in the plenum zone and subsequently in the catalyst zone.

Experiments were performed using two distributor plates of different porosities, the second being chosen using information obtained with the first plate in the microreactor. Rapid-response differential-pressure measurements were used as the primary tool for the selection of distributor plates.

After choosing an appropriate distributor plate, the effects of vibrofluidization, feed-gas flow rate, and feed-gas staggering on gas mixing in the three zones (i.e., the plenum zone, the catalyst zone and the gas-exit zone) of the cold-flow microreactor model were explored.

Table 5.1 summarizes the experimental conditions and results for the cold-flow model studies. Each experiment is designated by a series number followed by an experiment number. Series 1 involved the use of a 20-micron distributor plate with the gas-sampling point located in the plenum zone of the model. Series 2, 3, and 4 all involved using a 2-micron distributor plate with the sampling point in the plenum zone, catalyst zone and gas-exit zone, respectively. Strip-chart recorder traces of the thermal conductivity detector output for all of these experiments are located in Appendix F.

5.2.1 Baseline Gas-Mixing Information

In order to determine the minimum observable transition time when switching from argon to helium and from helium to argon, a series of baseline experiments were performed. These experiments involved replacing the cold-flow microreactor model with a manual 3-way ball valve. The remainder of the system was not altered. The capillary sampling tube was placed so that its tip extended directly into the center of the ball valve, as shown schematically in Figure 5.7. The system pressure was maintained at 37.2 kPa and the flow rates were set at 417, 833 and 1650 actual mm^3/sec for the three experiments. Thermal conductivity detector settings were those specified in Section 5.1.3.

TABLE 5.1

Experimental Conditions and Results for the Cold-Flow Model Studies

Experiment Number	Plate Grade (μ)		Feed-Gas Flow Rate (actual mm^3/s)		System Pressure (kPa)	Capillary Sampling Position	Catalyst Vibrofluidized
	Distributor	Catalyst Retention	Helium	Argon			
1-1	20	40	435	435	38.5	Plenum	No
1-2	20	40	435	435	31.3	Plenum	No
1-3	20	40	435	435	31.3	Plenum	No
1-4	20	40	435	435	36.5	Plenum	No
1-5	20	40	435	435	36.5	Plenum	No
1-6	20	40	435	435	36.5	Plenum	No
1-7	20	40	435	435	36.5	Plenum	No
1-8	20	40	435	435	31.6	Plenum	No
1-9	20	40	417	417	38.2	Plenum	No
1-10	20	20	417	417	33.8	Plenum	No

TABLE 5.1 (Continued)

Experiment Number	Feed-Gas Staggering (s)	Fast Response ΔP Measurement	ΔP Transducer Connections	Chart Speed (cm/min)	Recent Full-Scale Transition After 2.4 seconds (%)	
					He-to-Ar Transition	Ar-to-He Transition
1-1	No	No	-	2	93.7	71.3
1-2	No	Yes	Tap A to Catalyst Zone	2	-	-
1-3	Yes, 5	Yes	Tap A to Catalyst Zone	2	95.1	87.9
1-4	No	Yes	Tap A to Tap B	2	91.8	69.6
1-5	Yes, 5	Yes	Tap A to Tap B	2	96.2	86.6
1-6	Yes, 5	Yes	Tap B to Catalyst Zone	2	96.1	87.2
1-7	No	Yes	Tap B to Catalyst Zone	2	91.6	72.3
1-8	No	Yes	Tap A to Catalyst Zone	2	92.4	69.0
1-9	No	Yes	Tap A to Tap B	2	86.2	-
1-10	No	No	-	2, 10	89.4	75.6

TABLE 5.1 (Continued)

Experiment Number	Plate Grade (μ)		Feed-Gas Flow Rate (actual mm^3/s)		System Pressure (kPa)	Capillary Sampling Position	Catalyst Vibrofluidized
	Distributor	Catalyst Retention	Helium	Argon			
2-1	2	20	417	417	27.1	Plenum	No
2-2	2	20	417	417	33.5	Plenum	No
2-3	2	20	800	800	31.8	Plenum	No
2-4	2	20	417	417	31.8	Plenum	Yes
2-5	2	20	417	417	31.8	Plenum	Yes
2-6	2	20	417	417	31.8	Plenum	No
2-7	2	20	417	417	31.8	Plenum	No
2-8	2	20	417	417	33.8	Plenum	No
2-9	2	20	417	417	33.8	Plenum	No
2-10	2	20	833	833	34.5	Plenum	No
2-11	2	20	833	833	34.5	Plenum	No
2-12	2	20	1650	1650	38.2	Plenum	No
2-13	2	20	1650	1650	36.5	Plenum	No

TABLE 5.1 (Continued)

Experiment Number	Feed-Gas Staggering (s)	Fast Response ΔP Measurement	ΔP Transducer Connections	Chart Speed (cm/min)	Percent Full-Scale Transition After 2.4 seconds (%)	
					He-to-Ar Transition	Ar-to-He Transition
2-1	No	No	-	2	95.6	88.7
2-2	No	No	-	2, 10	97.1	90.2
2-3	No	No	-	2, 10	96.9	93.2
2-4	Yes, 2	No	-	2	-	-
2-5	Yes, 5	No	-	2	-	-
2-6	Yes, 2	No	-	2, 10	96.8	93.6
2-7	Yes, 5	No	-	2, 10	97.1	95.7
2-8	No	Yes	Tap A to Catalyst Zone	2	95.9	91.1
2-9	No	Yes	Tap B to Catalyst Zone	2	97.0	89.8
2-10	No	No	-	10	97.0	93.9
2-11	Yes, 5	No	-	10	97.8	97.8
2-12	No	No	-	10	99.4	96.2
2-13	Yes, 5	No	-	10	99.5	99.1

TABLE 5.1 (Continued)

Experiment Number	Plate Grade (μ)		Feed-Gas Flow Rate (actual mm^3/s)		System Pressure (kPa)	Capillary Sampling Position	Catalyst Vibrofluidized
	Distributor	Catalyst Retention	Helium	Argon			
3-1	2	20	417	417	31.8	Catalyst Zone	No
3-2	2	20	417	417	31.8	Catalyst Zone	Yes
3-3	2	20	417	417	31.8	Catalyst ZOne	No
3-4	2	20	417	417	36.9	Catalyst Zone	Yes
3-5	2	20	850	850	32.8	Catalyst Zone	No
3-6	2	20	850	850	35.5	Catalyst Zone	Yes
3-7	2	20	850	850	35.5	Catalyst Zone	No
3-8	2	20	850	850	35.5	Catalyst Zone	Yes
3-9	2	20	1650	1650	29.8	Catalyst Zone	No
3-10	2	20	1650	1650	30.8	Catalyst Zone	Yes
3-11	2	20	1650	1650	30.8	Catalyst Zone	No
3-12	2	20	1650	1650	30.8	Catalyst Zone	Yes

TABLE 5.1 (Continued)

Experiment Number	Feed-Gas Staggering (s)	Fast Response ΔP Measurement	ΔP Transducer Connections	Chart Speed (cm/min)	Percent Full-Scale Transition After 2.4 seconds (%)	
					He-to-Ar Transition	Ar-to-He Transition
3-1	No	No	-	2, 10	89.6	63.0
3-2	No	No	-	2, 10	83.3	60.2
3-3	Yes, 5	No	-	2, 10	95.6	89.4
3-4	Yes, 5	No	-	2, 10	93.6	77.3
3-5	No	No	-	2, 10	92.6	81.1
3-6	No	No	-	2, 10	84.1	73.0
3-7	Yes, 5	No	-	2, 10	97.3	93.8
3-8	Yes, 5	No	-	2, 10	96.7	93.4
3-9	No	No	-	2, 10	97.0	91.0
3-10	No	No	-	2, 10	90.6	88.0
3-11	Yes, 5	No	-	2, 10	97.3	97.3
3-12	Yes, 5	No	-	10	97.3	97.3

TABLE 5.1 (Continued)

Experiment Number	Plate Grade (μ)		Feed-Gas Flow Rate (actual mm^3/s)		System Pressure (kPa)	Capillary Sampling Position	Catalyst Vibrofluidized
	Distributor	Catalyst Retention	Helium	Argon			
4-1	2	20	417	417	38.9	Exit Zone	No
4-2	2	20	417	417	37.9	Exit Zone	Yes
4-3	2	20	417	417	37.9	Exit Zone	No
4-4	2	20	417	417	37.9	Exit Zone	Yes
4-5	2	20	833	833	37.6	Exit Zone	No
4-6	2	20	833	833	37.6	Exit Zone	Yes
4-7	2	20	833	833	39.3	Exit Zone	No
4-8	2	20	833	833	39.3	Exit Zone	Yes
4-9	2	20	1650	1650	32.1	Exit Zone	No
4-10	2	20	1650	1650	32.1	Exit Zone	Yes
4-11	2	20	1650	1650	34.9	Exit Zone	No
4-12	2	20	1650	1650	34.9	Exit Zone	Yes

TABLE 5.1 (Continued)

Experiment Number	Feed-Gas Staggering (s)	Fast Response ΔP Measurement	ΔP Transducer Connections	Chart Speed (cm/min)	Percent Full-Scale Transition After 2.4 seconds (%)	
					He-to-Ar Transition	Ar-to-He Transition
4-1	No	No	-	2, 10	78.7	42.5
4-2	No	No	-	2, 10	79.7	42.4
4-3	Yes, 5	No	-	2, 10	93.0	74.1
4-4	Yes, 5	No	-	2, 10	90.8	67.2
4-5	No	No	-	2, 10	83.5	61.0
4-6	No	No	-	2, 10	83.3	54.7
4-7	Yes, 5	No	-	2, 10	97.5	88.2
4-8	Yes, 5	No	-	2, 10	96.6	86.8
4-9	No	No	-	2, 10	96.2	75.9
4-10	No	No	-	2, 10	91.7	73.0
4-11	Yes, 5	No	-	2, 10	98.6	92.8
4-12	Yes, 5	No	-	2, 10	98.1	95.1

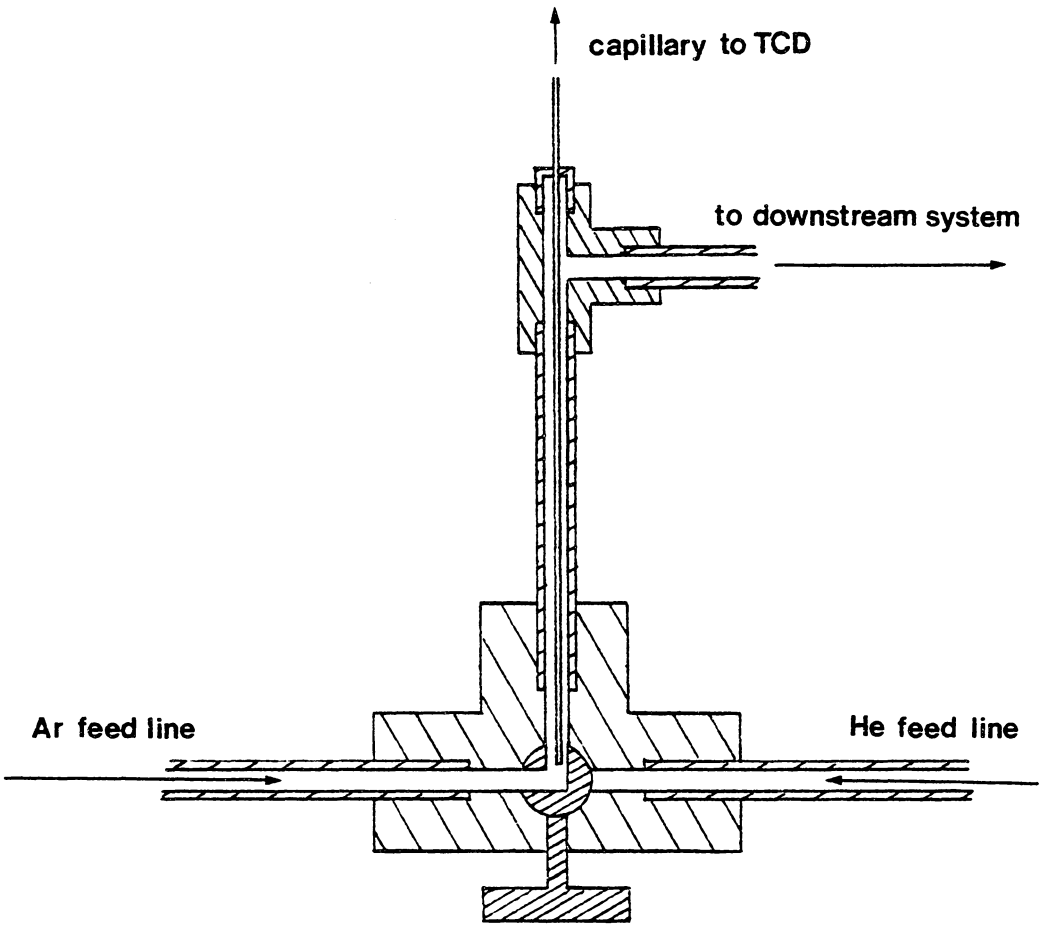

Figure 5.7. A Schematic Diagram of the Manual 3-way Valve Setup for Baseline Gas-Mixing Information.

In sum, the system equipment and variables were the same as those used throughout the cold-flow model experiments with the exception of the replacement of the sliding-plug microreactor by a 3-way manual valve.

The procedure for this experiment involved rapidly turning the 3-way valve in synchronization with the computer switching of the solenoid valve. Figure 5.8 is the TCD (thermal conductivity detector) response for switching between helium and argon feeds at 417 actual mm^3 per second.

As shown in Figure 5.8, the upper plateau is the argon baseline, while the lower plateau is the helium baseline. At 77°C, the thermal conductivities of helium, argon and nitrogen are 0.166, 0.0200 and 0.0293 W/m-K, Therefore, the pure nitrogen baseline lies between the baseline of the argon-nitrogen mixture (upper baseline) and the helium-nitrogen mixture (lower baseline). These gas mixtures are produced when the gas being sampled via the capillary bleeds into the nitrogen carrier gas stream going to the TCD.

Figures 5.9 and 5.10 are similar TCD outputs for flow rates of 833 and 1650 actual mm^3 per second. The time for a 100% transition from the argon baseline to the helium baseline as well as from the helium baseline to the argon baseline is approximately 2.4 seconds.

Comparing Figures 5.8, 5.9, and 5.10, it can be seen that this transition time is unaffected by feed-gas flow rates. This indicates that the gas sampling and detection system introduces a very small amount of gas mixing. This mixing could possibly be introduced at the

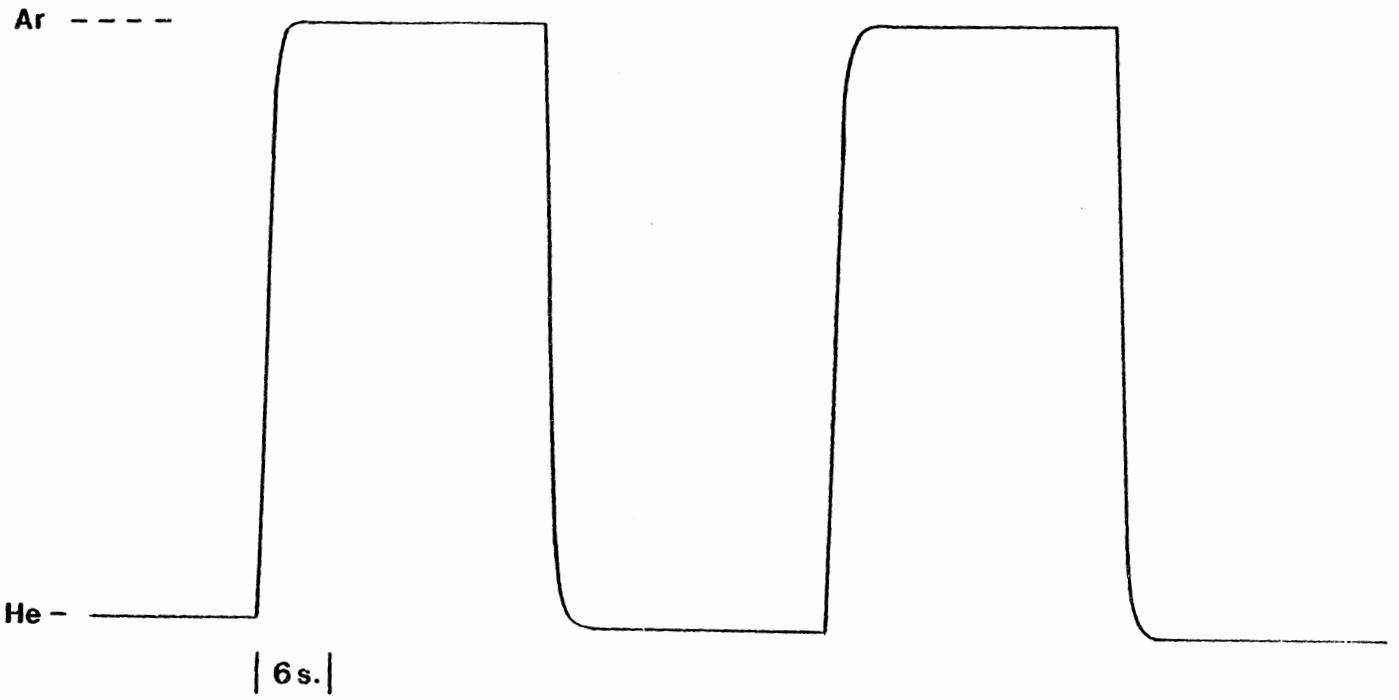

Figure 5.8. The TCD Response for Switching Between Helium and Argon Feeds at 417 Actual mm^3/s Substituting a Manual 3-Way Valve for the Microreactor. (Ar=Argon baseline, He= Helium baseline).

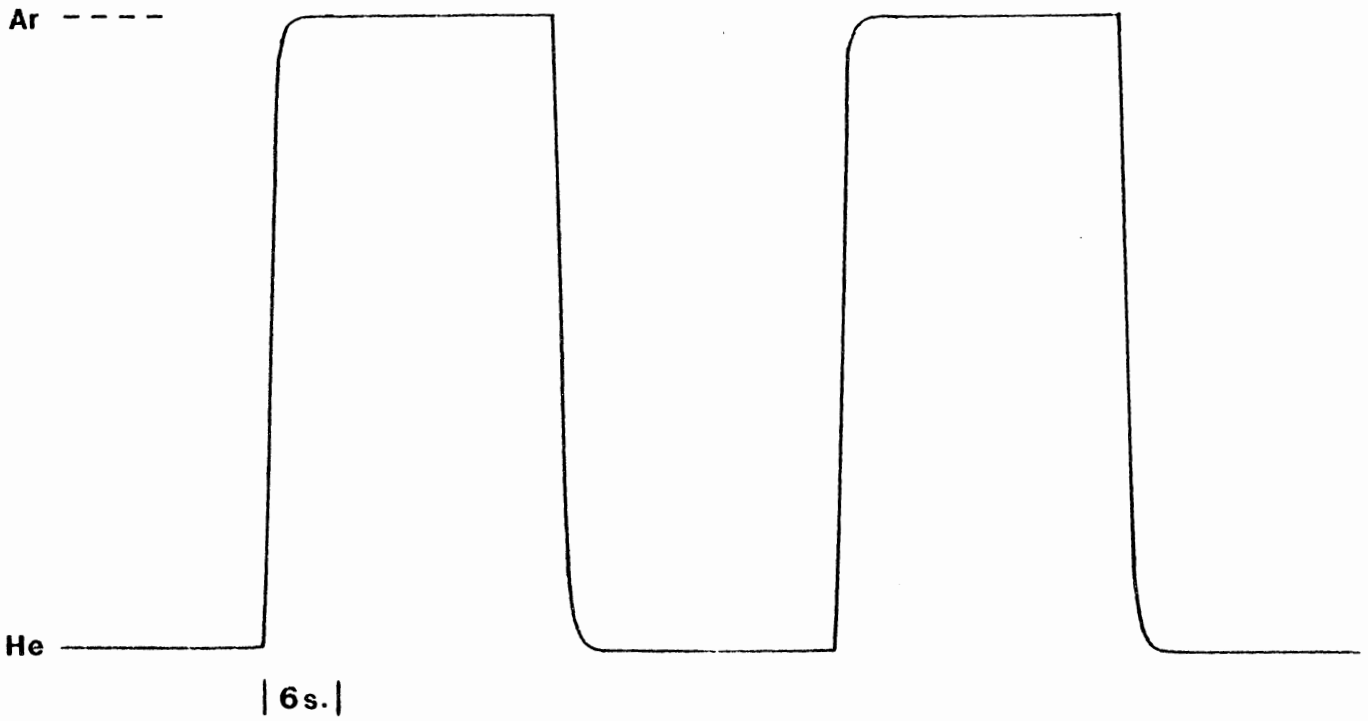

Figure 5.9. The TCD Response for Switching Between Helium and Argon Feeds at 833 Actual mm^3/d Substituting a Manual 3-Way Valve for the Micro-reactor (Ar=Argon baseline, He=Helium baseline).

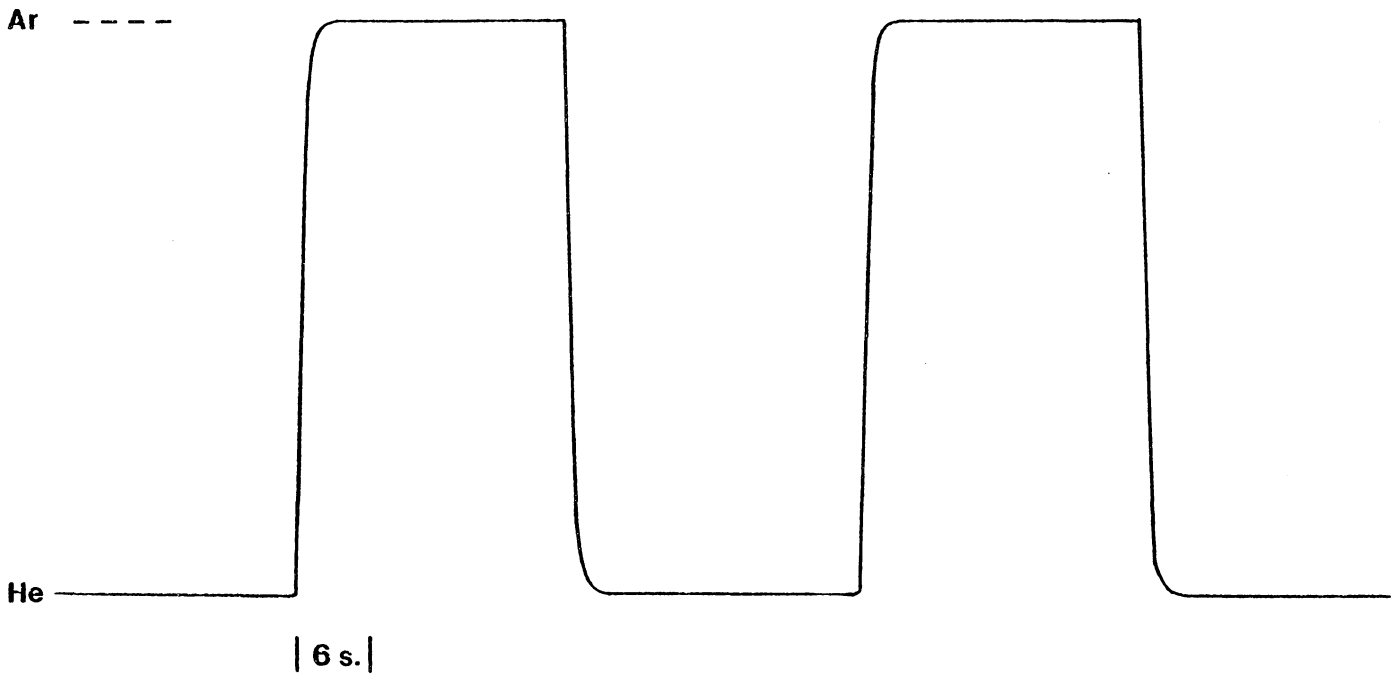

Figure 5.10. The TCD Response for Switching Between Helium and Argon Feeds at 1650 Actual mm^3/s Substituting a Manual 3-Way Valve for the Micro-reactor (Ar=Argon baseline, He=Helium baseline).

point where the capillary tubing bleeds argon or helium into the nitrogen carrier gas stream (refer to Figure 5.1). In addition, mixing could be induced by the flow path through the thermal conductivity cell in the detector. At any rate, the shortest possible transition time for 100% change in the feed gas is 2.4 seconds for the gas sampling and detection system. Therefore, a transition time of 2.4 seconds has been used as a reference for gas-mixing transitions throughout this study.

5.2.2 Cold-Flow Model Gas-Mixing Experiments Using a 20-Micron Distributor Plate

Preliminary experiments (Experiments 1-1 through 1-10) were undertaken in the cold-flow sliding-plug vibrofluidized-bed microreactor model with a 20-micron distributor plate at feed-gas flow rates in the range of 435 actual mm^3 per second.

Figure 5.11 (Experiment 1-10) shows the TCD output for gas mixing in the plenum zone of the cold-flow model. The helium-to-argon transition shows that 89.4% of the helium in the plenum has been replaced by argon after 2.4 seconds. However, the trace indicates a slight hysteresis effect, followed by a slow transition to the argon baseline.

The argon-to-helium transition shows a similar but more pronounced effect as that described above. Initially, only 75.6% of the argon in the plenum is replaced by helium after 2.4 seconds. Following the rather rapid, initial 2.4-second transition, it takes approximately one minute for the new feed gas to completely purge the old gas in the plenum. This hysteresis or rebound effect and the slow transition are

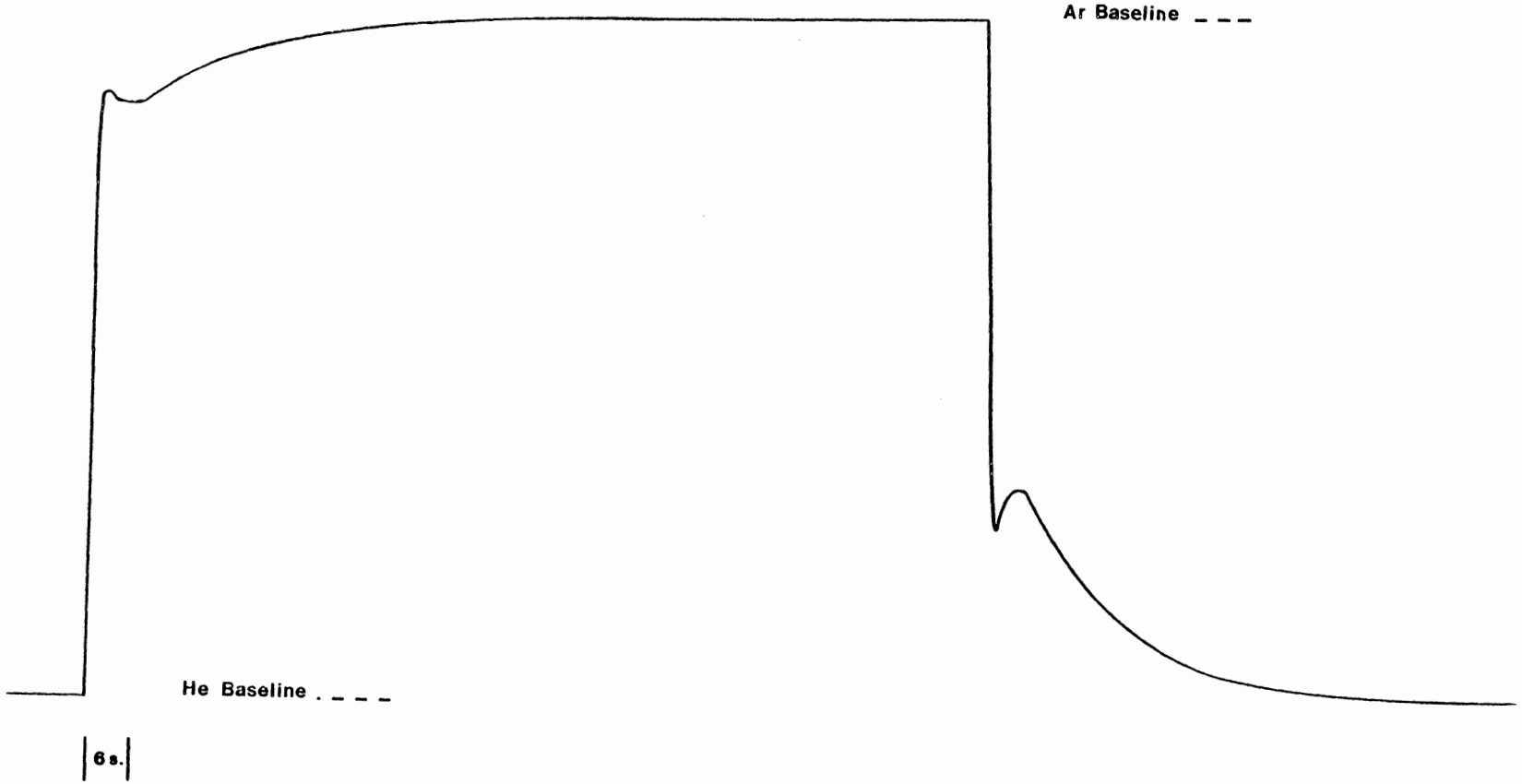

Figure 5.11. The TCD Response for Switching Between Helium and Argon Feeds at 417 Actual mm^3/s in the Cold-Flow Microreactor Model with a 20-Micron Distributor Plate (see Experiment 1-10 in Table 5.1 for Experimental Conditions).

signs of incomplete gas removal in the plenum zone. In order to explain the rebound and slow transition, two theories were developed and tested: (1) the backflow theory; and (2) the annular-flow theory.

5.2.2.1 Backflow Theory

In principle, there should be no mixing of feed gases in the plenum zone upon sliding of the plug. The plug should effectively "pump out" and compress the previous feed gas, while simultaneously drawing in the new feed gas. This should cause a discrete transition in feed gases in the plenum. However, this is not the case (as shown in Figure 5.11).

The theory of backflow speculates that a region of high pressure is created in the catalyst zone by the sliding plug, while a region of low pressure develops behind the plug as it moves. If the distributor plate is too porous, gas in front of the plug is compressed into the catalyst zone as well as the feed-gas line, as the plug slides. Behind the plug, the increased volume of the space causes the pressure to drop. As the plug approaches the end of its stroke, high-pressure gas from the catalyst zone (gas A) backflows through the porous plate into the lower-pressure plenum zone containing the new feed gas (gas B). This backflow results in gas mixing in the plenum zone.

In order to test this theory, plug-velocity and rapid-response differential-pressure measurements were made. The velocity of the plug was measured using a circuit shown in Figure 5.12. When the plug is in contact with either end stop, the output from the circuit is +28 VDC. As soon as the plug begins to move, it breaks contact with the stop and the circuit output falls to ground potential. When the plug contacts

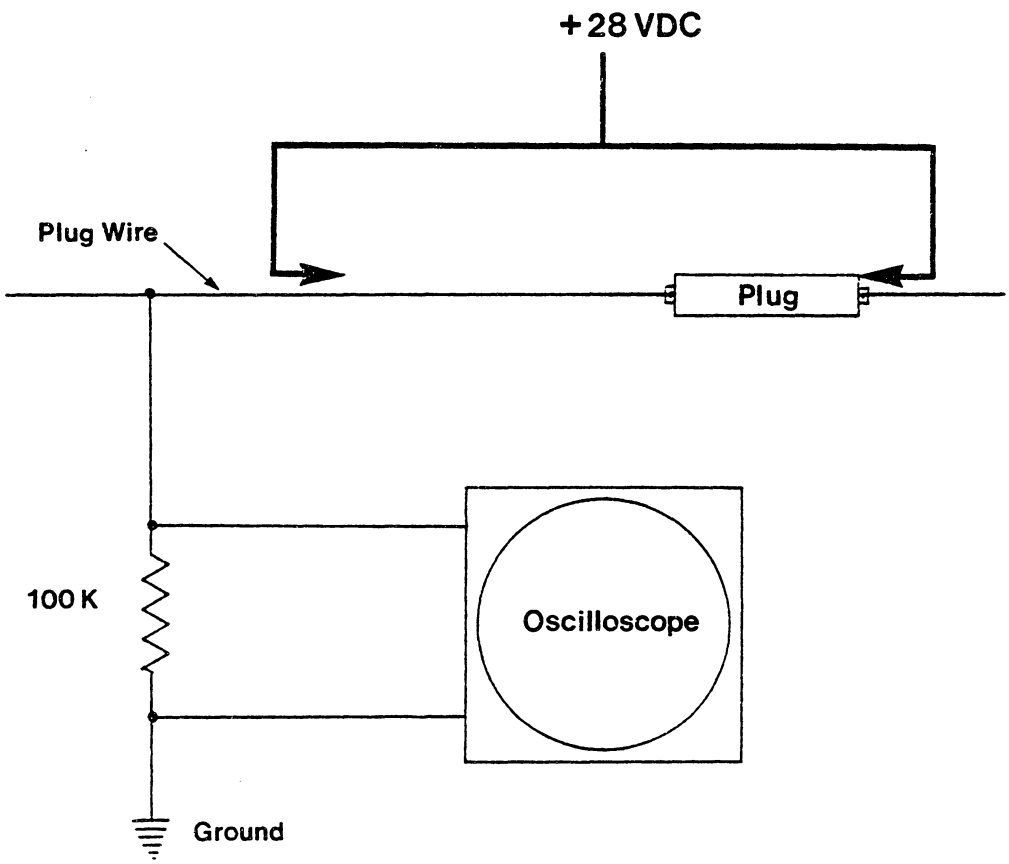

Figure 5.12. A Schematic of the Plug-Velocity Measurement Circuit.

the other plug stop, the potential again rises to +28 VDC. The output is recorded as a square-wave valley on the oscilloscope. The plug was found to move 50.8 mm in 65 msec, resulting in a velocity of 0.78 m/sec. At this velocity, no significant velocity head is developed. This result indicates that the drop in pressure behind the plug is mainly caused by the effective increased volume of the feed line.

Rapid-response differential-pressure measurements consisted of experiments with the transducer in three different positions.

1. Experiments 1-2, 1-3, and 1-8 involved connecting the transducer between tap A (see Figure 5.1) in the argon feed-line and the catalyst zone.

2. Experiments 1-6 and 1-7 involved connecting the transducer between tap B (see Figure 5.1) in the helium feed-line and the catalyst zone.

3. Finally, experiments 1-4, 1-5, and 1-9 involved connecting the differential-pressure transducer between tap A in the argon feed-line and tap B in the helium feed-line.

Experiments 1-2 through 1-7 were performed using a 10-torr rapid-response differential-pressure transducer. This transducer has been calibrated to a range of ±4.98 kPa, at which point it saturates producing a constant output. Experiments 1-8 and 1-9, however, were performed using a 100-torr rapid-response differential-pressure transducer. Therefore, these latter experiments had a linear range between ±13.1 kPa. Figure 5.13 is an oscilloscope trace for the helium-to-argon and argon-to-helium transitions during Experiment 1-2.

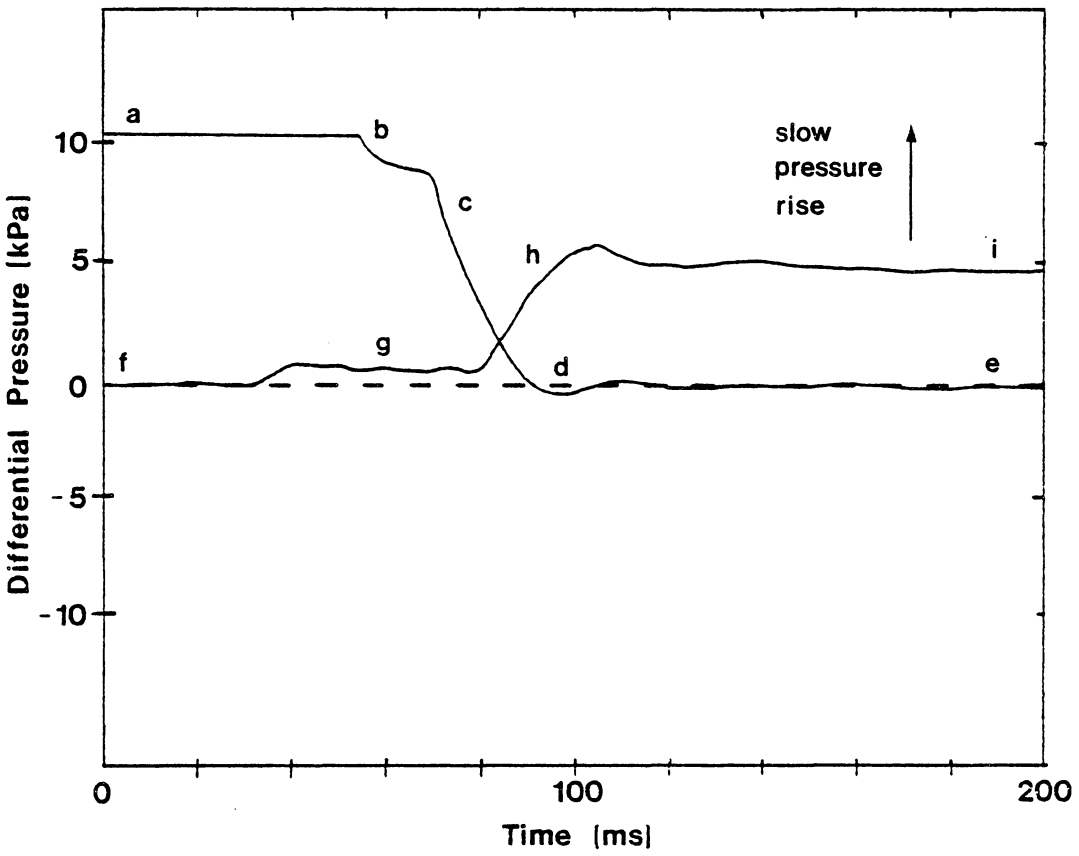

Figure 5.13. An Oscilloscope Trace from a Differential-Pressure Transducer Placed Between the Argon Feed-Line (Tap A in Figure 5.1) and the Catalyst Zone. The Oscilloscope Triggered at the Beginning of Plug Movement. See Text for Explanations of Points a to i. (Experiment 1-2 in Table 5.1).

Referring to the system diagram shown in Figure 5.1, the following sequence of events indicating the pressure behavior during plug movement has been pieced together.

1. Point "a": The plug is against the left-hand stop. Helium is being fed through the microreactor and argon is stagnant in its feed-line. The pressure in the argon feed-line is greater than that in the catalyst zone, because argon has been compressed into its feed-line by the previous plug transition. The transducer is saturated at this point.

2. Point "b": The plug has begun to move away from the left-hand stop and toward the right-hand stop. As soon as the plug begins moving, solenoid valve 1 is opened, while 2 is closed.

3. Point "c": The plug is approximately in the middle of its stroke. The pressure difference between the argon feed-line and the catalyst zone drops. Gas is compressed into the heliuim feed-line and the catalyst zone.

4. Point "d": The plug is at the end of its stroke, at the righ-hand stop. The pressure in the catalyst zone is greater than that in the argon feed-line.

5. Point "e": Argon is now being fed to the microreactor and the pressures in the argon feed-line and the catalyst zone have equalized.

6. Point "f": Similar to point "e". Argon is being fed and helium is stagnant behind the plug.

7. Point "g": The plug has started moving from right to left. The pressure in the argon feed-line builds up slightly and levels off for 40

ms. This is due to simultaneous buildup of pressure in the catalyst zone as well. Therefore, the differential pressure stabilizes for approximately 40 ms.

8. Point "h": The plug-end has past the left end of the distributor plate. In this region, gas is being compressed into the argon feed-line only. Therefore, the differential pressure between the argon feed-line and the catalyst zone builds up rapidly.

9. Point "i": The pressure difference between the stagnant argon feed-line and the catalyst zone containing flowing helium has stabilized somewhat. The differential pressure continues to increase, because of pressure buildup in the argon feed-line due to a phenomenon called "bleed-down." Briefly, "bleed-down" is the transfer of high-pressure gas trapped between the feed-line solenoid valve and needle valve after the solenoid valve closes. The pressure increases until the transducer saturates producing a pressure level identical to that of point "a".

Figure 5.14 is a similar oscilloscope trace taken in Experiment 1-7. During this experiment, the rapid-response differential-pressure transducer was placed between tap B in the helium feed-line and the catalyst zone. This trace is a near identical mirror-image of Figure 5.13, indicating similar pressure behavior in the helium feed-line and the argon feed-line.

The most interesting point shown in Figures 5.13 and 5.14 is the time period when the pressure in the catalyst zone becomes greater than that in the feed line. For this short period of time, gas actually

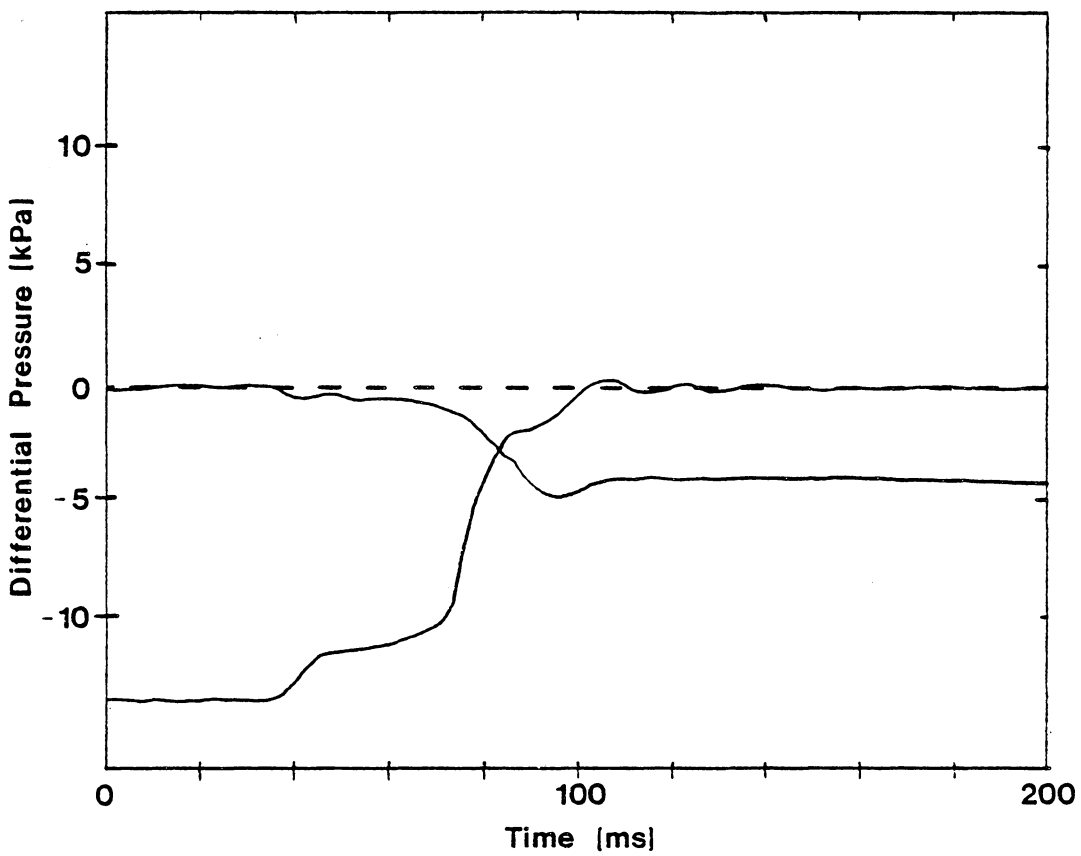

Figure 5.14. An Oscilloscope Trace from a Differential-Pressure Transducer Placed Between the Helium Feed-Line (Tap B in Figure 5.1) and the Catalyst Zone. The Oscilloscope Triggered at the Beginning of Plug Movement. (Experiment 1-7 in Table 5.1).

backflows from the catalyst zone through the distributor plate into the plenum zone. Experiment 1-7 was performed in order to determine the magnitude and duration of this pressure inversion. Figures 5.15 and 5.16 illustrate the results of this experiment. The pressure inversion lasts 13 msec, and its magnitude is approximately 0.346 kPa. The total system pressure during the experiment was 36.5 kPa. Therefore, the pressure inversion was 0.95% of the total.

The volume of gas which can backflow across the 20μ distributor plate in 13 msec with a pressure inversion of 0.346 kPa can be calculated using the standard equation for pressure drop as a function of gas flow as provided by the sintered stainless-steel plate manufacturer. This calculation is presented in Appendix A. It was determined that the possible volume of gas backflowing during the pressure inversion period is approximately 126.4 mm^3 of argon during the argon-to-helium transition and 1447.5 mm^3 of helium during the helium-to-argon transition. This corresponds to 8% and 90% of the plenum volume, respectively.

Calculations were performed for 5-, 2- and 0.5-micron distributor plates assuming the same magnitude and duration of pressure inversion. It was found that the theoretical backflow volume was reduced greatly on going to less porous distributors. Indeed, it seemed possible that backflow could be eliminated all together during the sliding-plug movement if the distributor-plate pressure drop was high enough to force gas compression in the feed line rather than the catalyst zone.

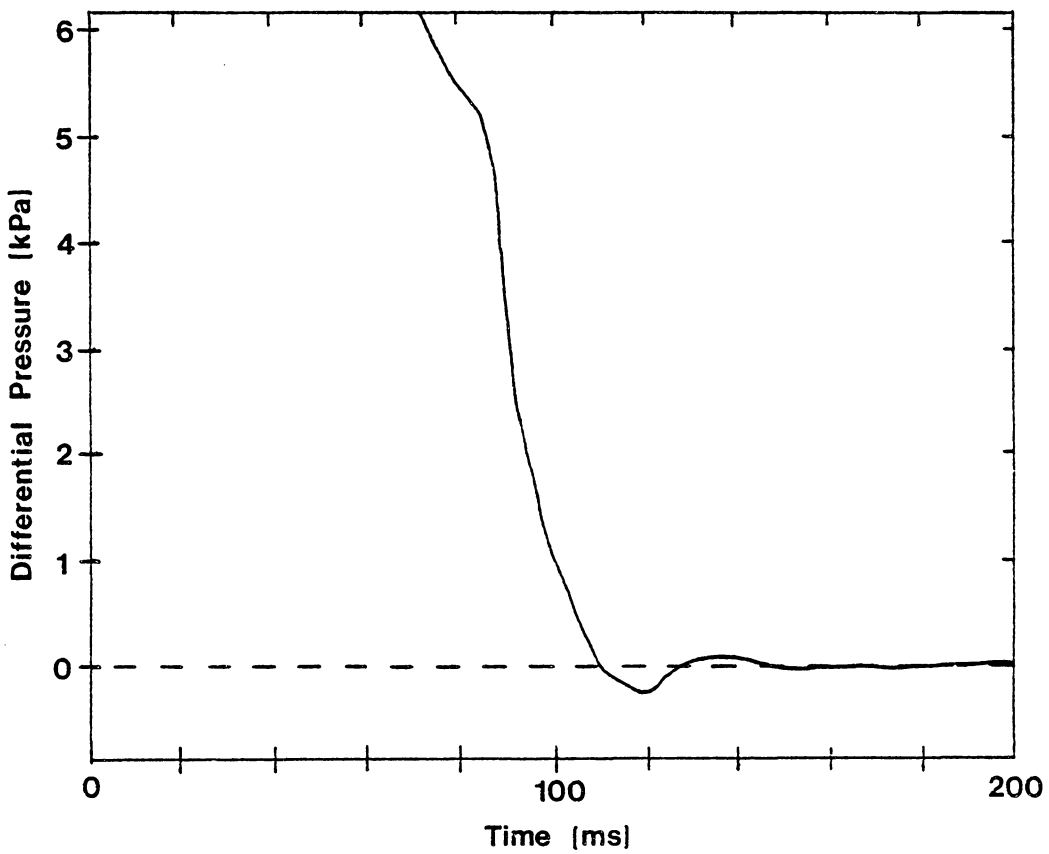

Figure 5.15. The Oscilloscope Trace from a Differential-Pressure Transducer Placed Between the Argon Feed-Line (Tap A in Figure 5.1) and the Catalyst Zone. The Y Axis Has Been Expanded and the Helium-to-Argon Transition Is Shown. (Experiment 1-8 in Table 5.1).

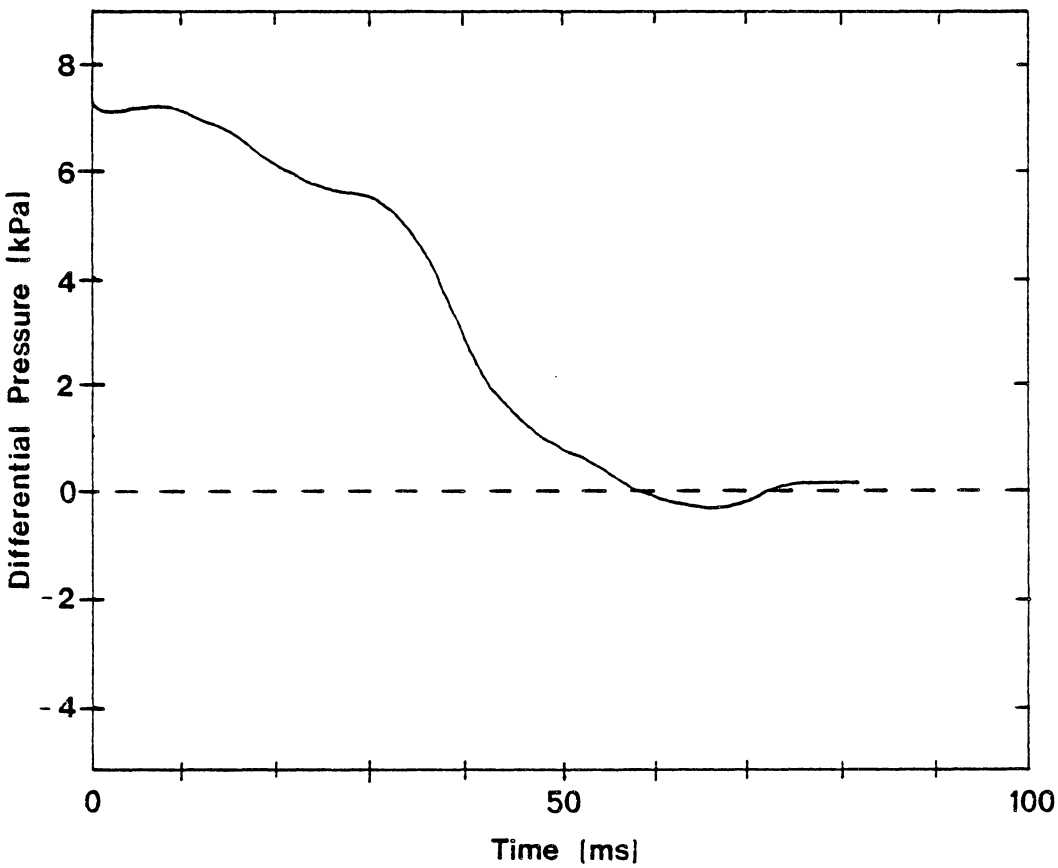

Figure 5.16. The Oscilloscope Trace from a Differential-Pressure Transducer Placed Between the Argon Feed-Line (Tap A in Figure 5.1) and the Catalyst Zone. The Time Axis Has Been Expanded and the Helium-to-Argon Transition Is Shown. (Experiment 1-7 in Table 5.1).

Experiment 1-4 was performed in order to determine the differential pressure between the argon and helium feed-lines during plug movement. The 10 torr rapid-response differential-pressure transducer was connected between tap A in the argon feed-line and tap B in the helium feed-line. Figure 5.17 shows the transducer output for the transition from helium to argon feed (trace A) and from argon to helium feed (trace B). The differential pressures immediately following these transitions are shown in the time period of 120 to 200 ms. Using these initial differential pressures, the approximate amount of gas compressed from the plenum zone into the feed line could be determined. Using the system volumes specified earlier and the system pressure given in Table 5.1 for experiment 1-4, it was calculated that only 37% of argon feed gas was compressed back into the feed line.

Similarly, it was determined that during the helium-to-argon feed transition, only 33% of the helium feed gas was compressed into the helium feed-line. It follows that the remaining 63% and 67% of these gases are compressed into the catalyst zone, or are lost to annular flow around the sliding plug. Once the plug has reached the end of the plenum zone and sealed against the seat, the pressure in the sealed feed line slowly begins to build up due to the bleed-down phenomenon previously mentioned.

When a feed-gas solenoid valve is closed, a small amount of gas is trapped between the solenoid valve and the needle valve. The trapped gas, initially at the cylinder-regulator delivery pressure of 274.8 kPa, slowly bleeds across the needle valve into the stagnant feed-line,

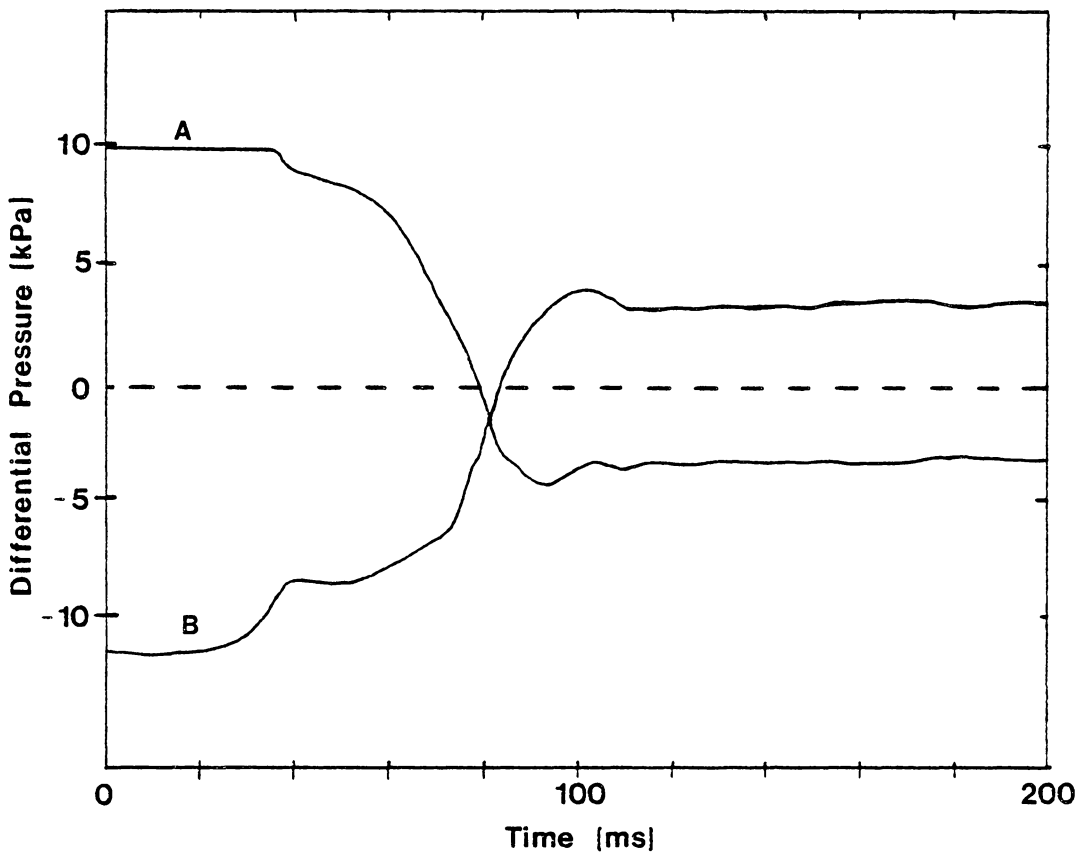

Figure 5.17. The Oscilloscope Trace from a Differential-Pressure Transducer Placed Between the Argon Feed Line (Tap A in Figure 5.1) and the Helium Feed-Line (Tap B in Figure 5.1). Curve A Is the Helium-to-Argon Transition and Curve B Is the Argon-to-Helium Transition. (Experiment 1-4 in Table 5.1).

causing the pressure in that line to build up. An example of the magnitude of this pressure buildup is illustrated by considering the stagnant argon feed-line. Immediately after the plug is switched and the argon flow is shut off, the pressure in the argon feed-line is 3.18 kPa. After 90 seconds of bleed-down, the pressure has more than doubled to 8.47 kPa as shown in Figure 5.18 (Experiment 1-8). The volume of argon added by bleed-down after 90 seconds is approximately 1,681 mm^3, coincidentally just slightly more than the volume displaced when the plug moves across the plenum zone (1,609 mm^3). During an actual synthesis experiment using a sliding-plug microreactor, the plug-switching period would be on the order of seconds rather than minutes and bleed-down would not play a significant role in pressure buildup.

A way of artifically eliminating backflow when using the 20-micron distribtor plate was also developed. Consider, for example, helium being fed to the microreactor and argon sitting stagnant behind the plug. Five seconds before the movement of the plug, solenoid valve 1 would be opened in the argon feed-line allowing pressure to build up behind the plug. During the subsequent plug movement, the pressure in the argon feed-line would not fall below that of the catalyst zone and backflow would not occur. The same procedure of premature Solenoid-valve opening would be repeated in the helium feed-line before the next plug transition. This method of pressure buildup behind the sliding plug is termed "Staggering." Five-second staggering implies that the feed-gas solenoid is opened 5 seconds before the plug is moved.

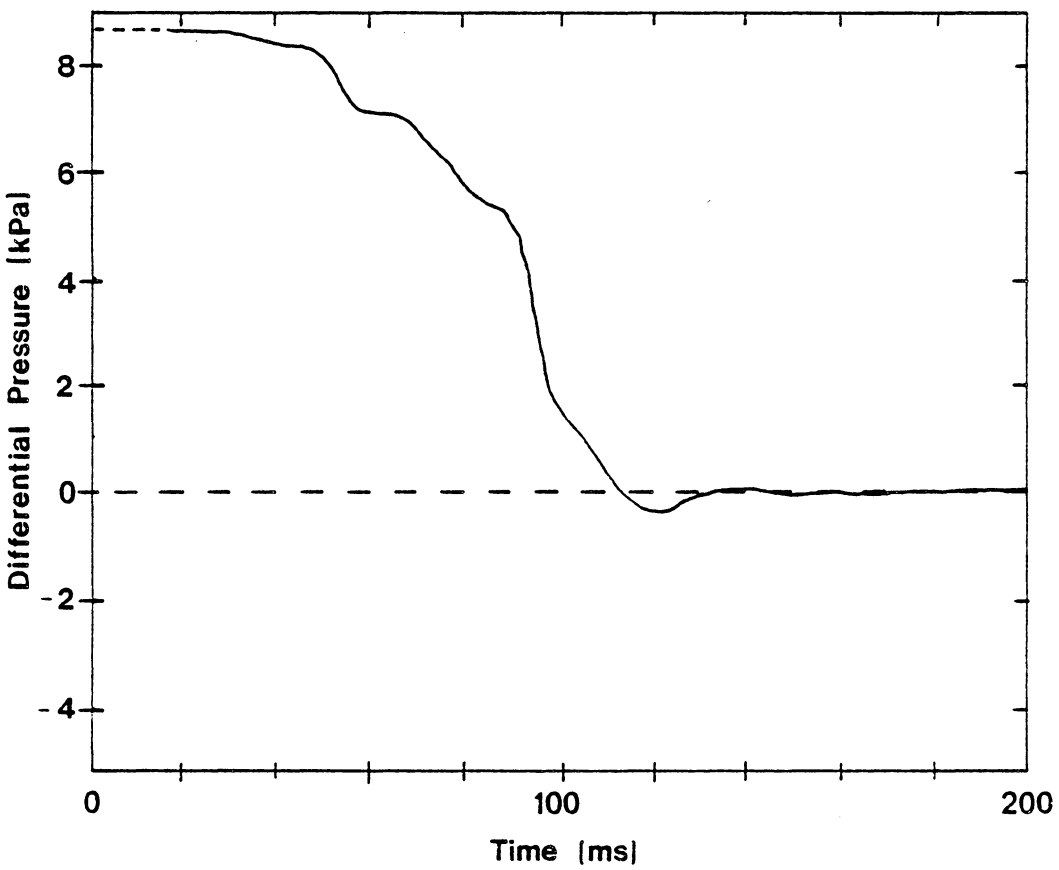

Figure 5.18. The Oscilloscope Trace from a Differential-Pressure Transducer Placed Between the Argon Feed-Line (Tap A in Figure 5.1) and the Catalyst Zone. The Y Axis Has Been Expanded and the Helium-to-Argon Transition Is Shown (Experiment 1-8 in Table 5.1).

Figures 5.19 and 5.20 show the results of 5-second staggering obtained in Experiments 1-5 and 1-6. The pressure inversion experienced in Figures 5.13 and 5.14 has been totally eliminated. Figure 5.21 is the TCD trace of gas mixing produced in the plenum during Experiment 1-3, in which 5-second staggering was used. Comparing these results to those of Experiment 1-10 with no staggering (Figure 5.11), a number of differences can be seen. Using staggering, the hysteresis effect has been greatly reduced. Where a spike appeared before, a plateau in now found. The percent change in gas in the plenum zone after 2.4 seconds has been increased from 89.4% to 95% for the helium-to-argon transition and from 75.6% to nearly 88% for the argon-to-helium transition.

5.2.2.2 Annular-Flow Theory

A second theory was developed to explain the cause of gas mixing in the plenum zone of the cold-flow sliding-plug vibrofluidized-bed microreactor model. It was speculated that when the plug was in transit, gas could be passing through the annular region between the plug and the plenum wall.

Experiment 1-9 was designed to test the validity of the annular flow theory. A diaphragm and the fast-response differential-pressure transducer were placed between taps A and B in the feed lines of the cold-flow model system. The diaphragm consisted of a Bellofram gauge protector, which is claimed to be able to respond to as little change as 0.249 kPa. The diaphragm inside the gauge protector is more flexible in one direction than the other due to the way it was manufactured. The more flexible side was connected to the argon feed-stream (tap A),

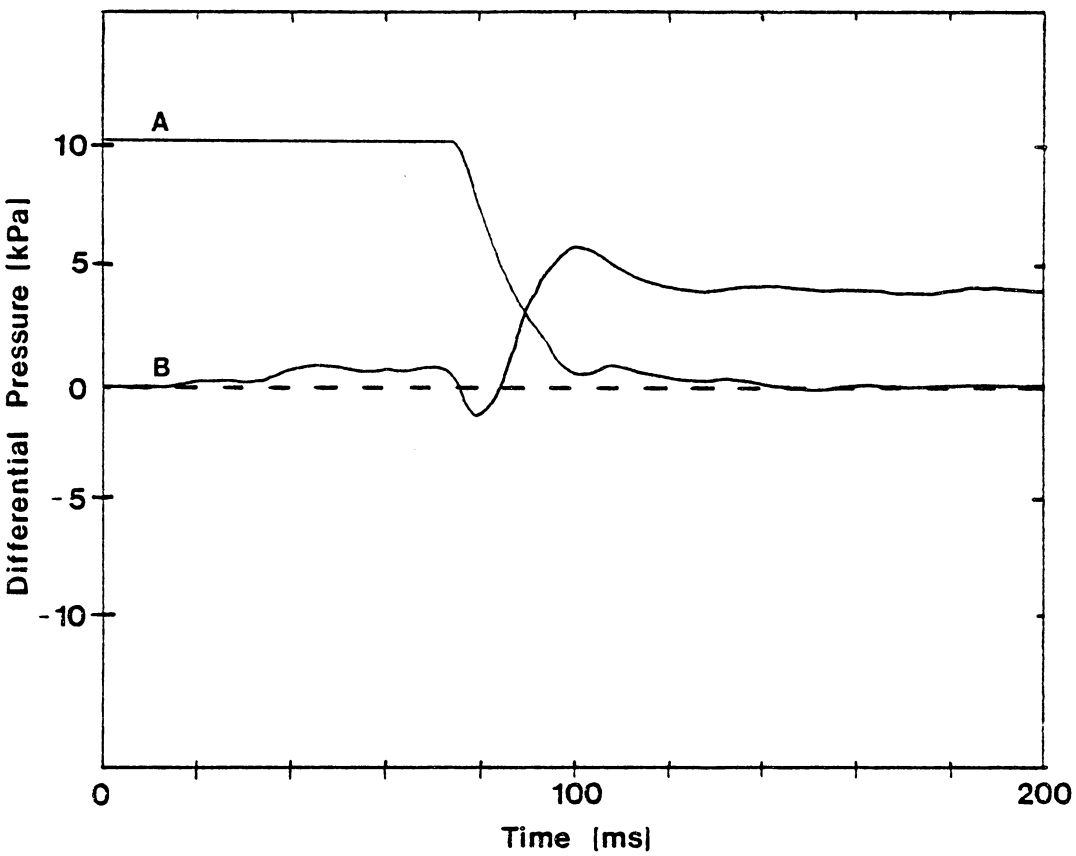

Figure 5.19. The Oscilloscope Trace from a Differential-Pressure Transducer Placed Between the Argon Feed-Line (Tap A in Figure 5.1) and the Catalyst Zone with 5-Second Staggering. (Experiment 1-5 in Table 5.1). Curve A Is the Helium-to-Argon Transition and Curve B Is the Argon-to-Helium Transition.

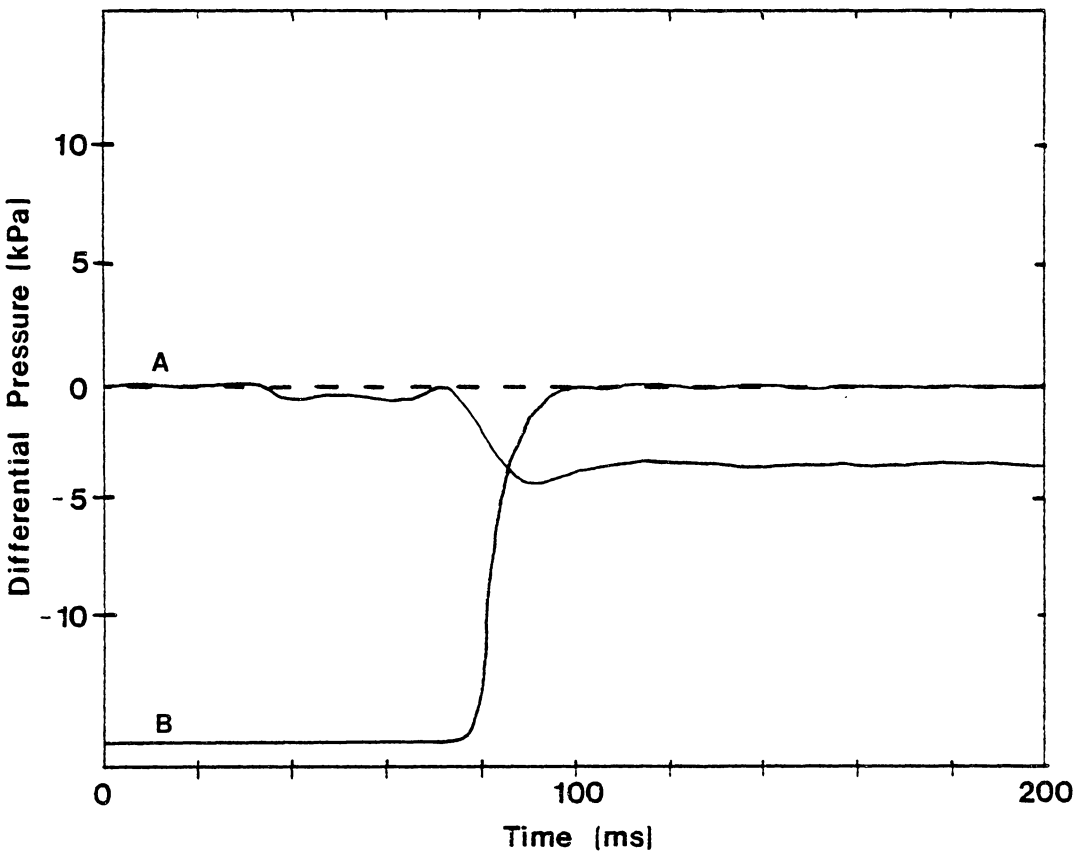

Figure 5.20. The Oscilloscope Trace from a Differential-Pressure Transducer Placed Between the Helium Feed-Line (Tap B in Figure 5.1) and the Catalyst Zone with 5-Second Staggering. (Experiment 1-6 in Table 5.1). Curve A Is the Helium-to-Argon Transition and Curve B Is the Argon-to- Helium Transition.

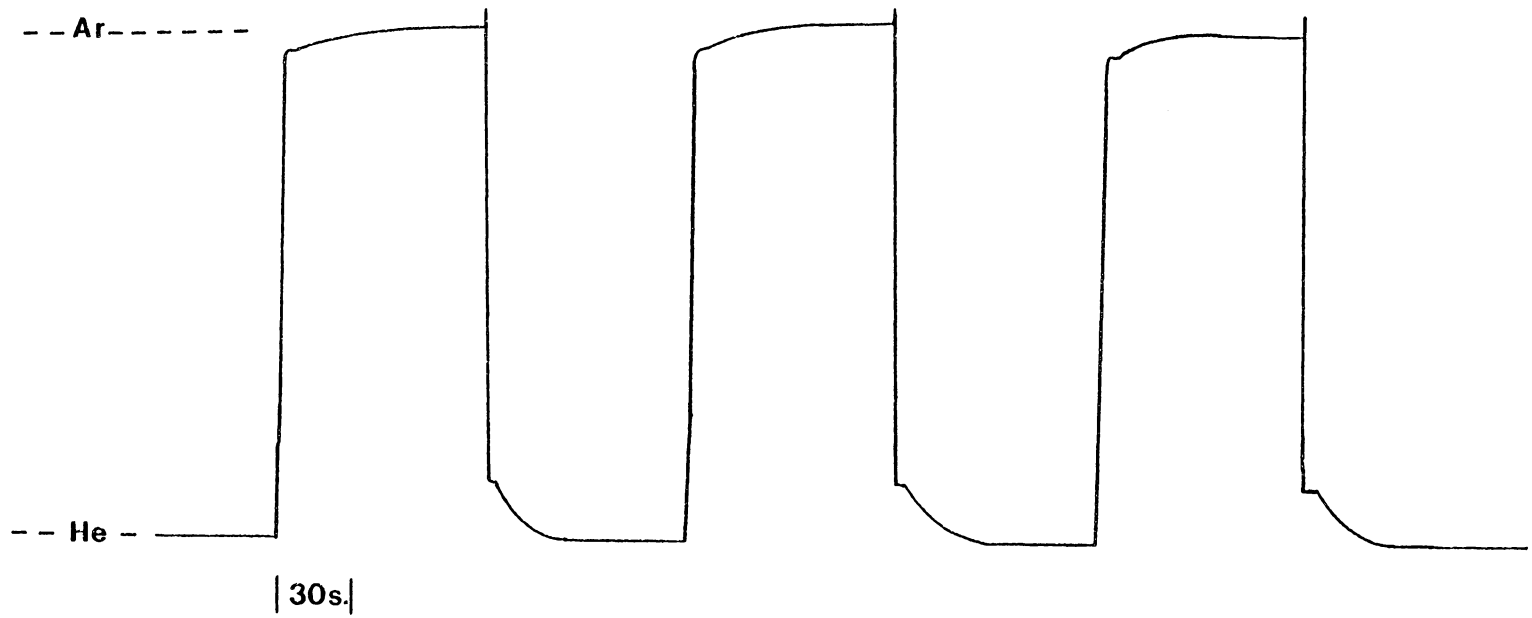

Figure 5.21. The TCD Response for Switching Between Helium and Argon Feeds at 435 Actual mm^3/s with 5-Second Feed-Gas Staggering in the Cold-Flow Microreactor Model Using a 20-Micron Distributor Plate. (Experiment 1-3 in Table 5.1).

while the less flexible side was connected to the helium feed-stream (tap B). The high-pressure side of the transducer was connected to tap A and to the low-pressure side to tap B.

Typical fast-response differential-pressure traces upon switching from argon to helium feeding, and from helium to argon feeding are shown in Figures 5.22 and 5.23, respectively. These traces were taken after the fourth full cycle. The offset, i.e., positive differential pressures, indicates that the argon feed-line pressure is slowly building up over the helium feed-line pressure. This is due to the greater flexibility of the side of the diaphragm in contact with argon. These traces also show that the differential pressure between the argon and helium feed-lines is continuously being adjusted while the plug is moving. Figure 5.24 is the TCD trace of gas mixing during Experiment 1-9. The striking change produced by the diaphragm installation is the elimination of the hysteresis effect that was seen in Experiment 1-10 (Figure 5.11) when using the 20-micron distributor in the cold-flow model.

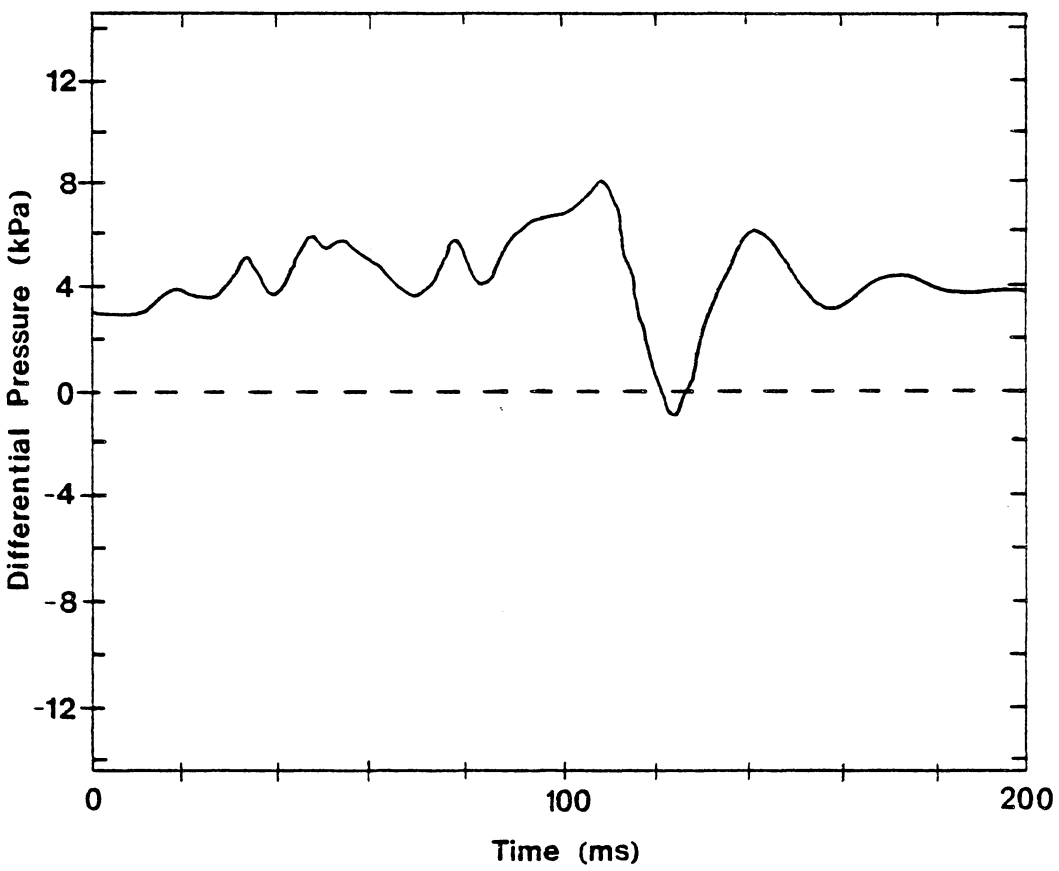

Figure 5.22. The Oscilloscope Trace from a Differential Pressure Transducer Placed Between the Helium Feed-Line and the Argon Feed-Line in Parallel with a Diaphragm. The Argon-to-Helium Feeding Transition Is Shown (Experiment 1-9 in Table 5.1).

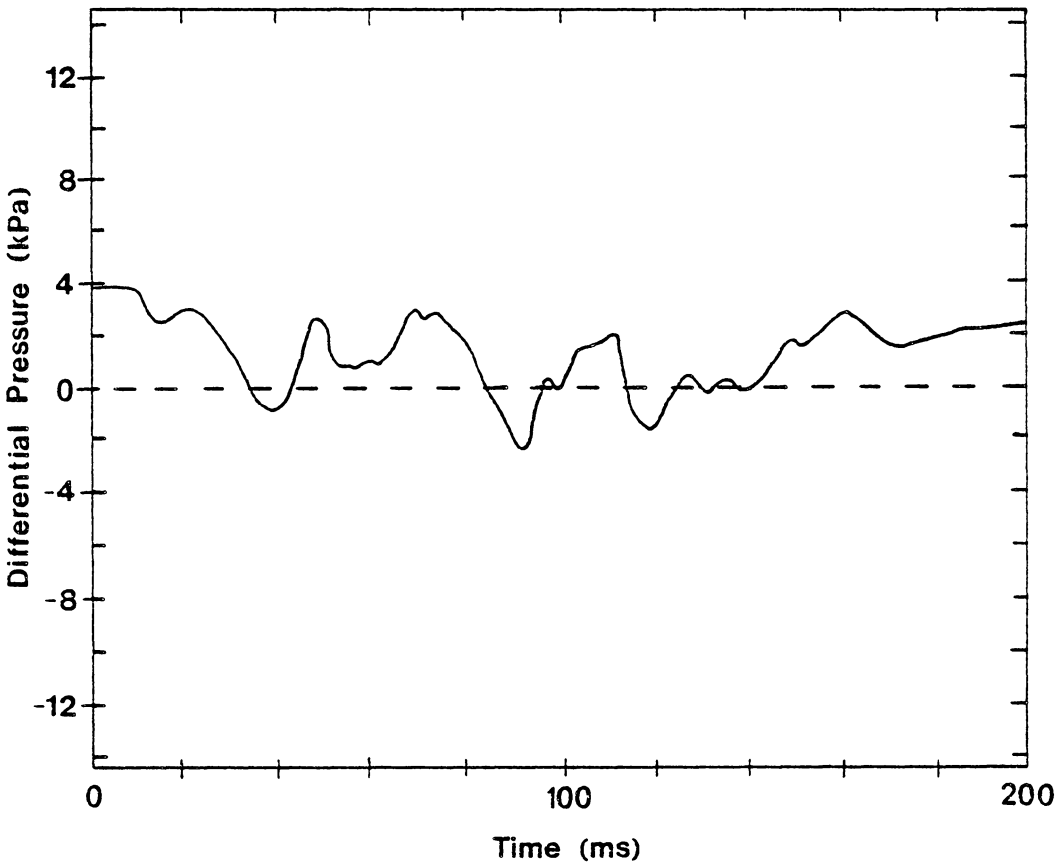

Figure 5.23. The Oscilloscope Trace from a Differential-Pressure Transducer Placed Between the Helium Feed-Line and the Argon Feed-Line in Parallel with a Diaphragm. The Helium-to-Argon Feeding Transition Is Shown. (Experiment 1-9 in Table 5.1).

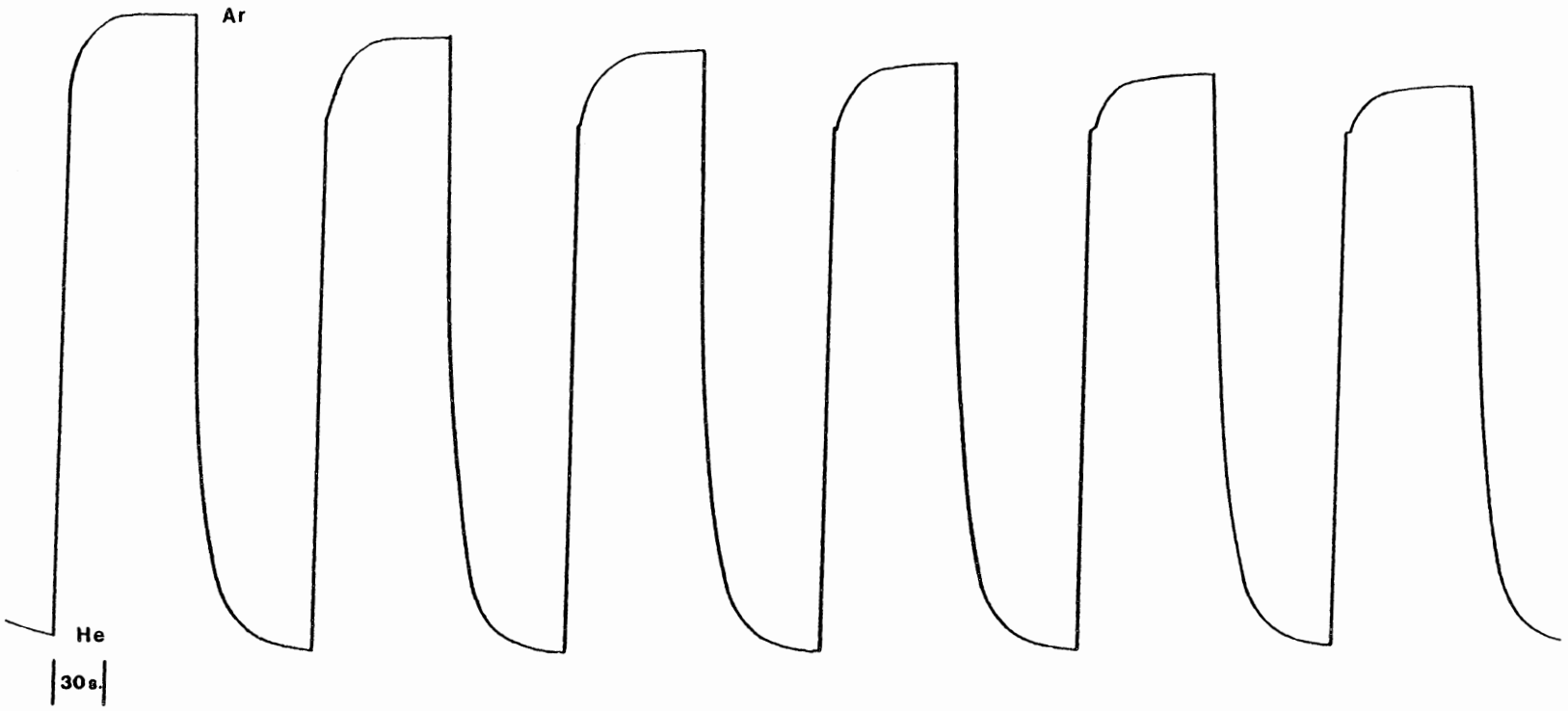

Figure 5.24. The TCD Response for Switching Between Helium and Argon Feeds at 417 Actual mm^3/s with a Diaphragm Between the Feed Lines. (Experiment 1-9 in Table 5.1).

5.2.3 Cold-Flow Model Experiments Using a 2-Micron Distributor Plate

Experiments in the cold-flow sliding-plug microreactor model using a 20-micron distributor plate pointed to the use of a less porous distributor plate in order to eliminate the gas backflow into the plenum zone. Figure 5.25 is the TCD trace for Experiment 2-2. This experiment is identical to Experiment 1-10 (Figure 5.11) except that a 2-micron distributor plate was used. The flow rate of feed gas was set at 417 actual mm^3/s and the sampling capillary was placed in the plenum zone.

Figure 5.25 shows that a significant improvement has been achieved in both the helium-to-argon and argon-to-helium transitions over those shown in Figure 5.11. The helium-to-argon transition is 97.1% complete in 2.4 seconds after the sliding plug has traversed the plenum, whereas the argon-to-helium transition is 90.2% complete. The hysteresis effect has been eliminated from the helium-to-argon transition and greatly reduced during the argon-to-helium transition. In addition, the final return to the baseline from both transitions has been cut in half to approximately 30 seconds. Fast-response differential-pressure transducer experiments were performed under these conditions with the 2-micron distributor plate in order to check for pressure inversions.

Experiments 2-8 and 2-9 were carried out with the transducer placed between tap A and the catalyst zone, and between tap B and the catalyst zone, respectively. Figures 5.26 and 5.27 show the oscilloscope traces recorded during plug movement for these two experiments. The time-scale differs from that shown in Figures 5.13 and 5.14 in that it has been expanded from 200 ms to 500 ms. The pressure

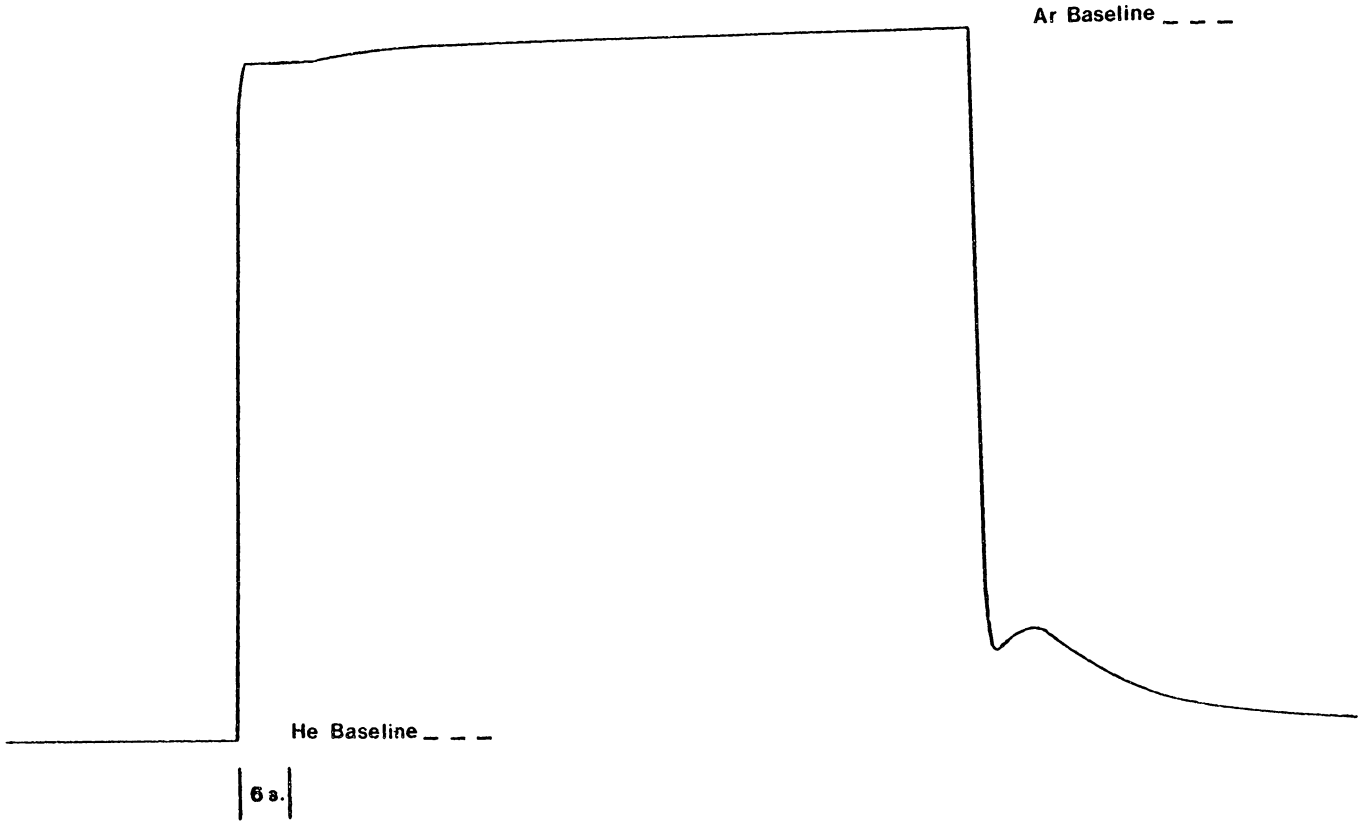

Figure 5.25. The TCD Response for Switching Between Helium and Argon Feeds at 417 Actual mm^3/s in the Cold-Flow Microreactor Model with a 2-Micron Distributor Plate. (Experiment 2-2 in Table 5.1).

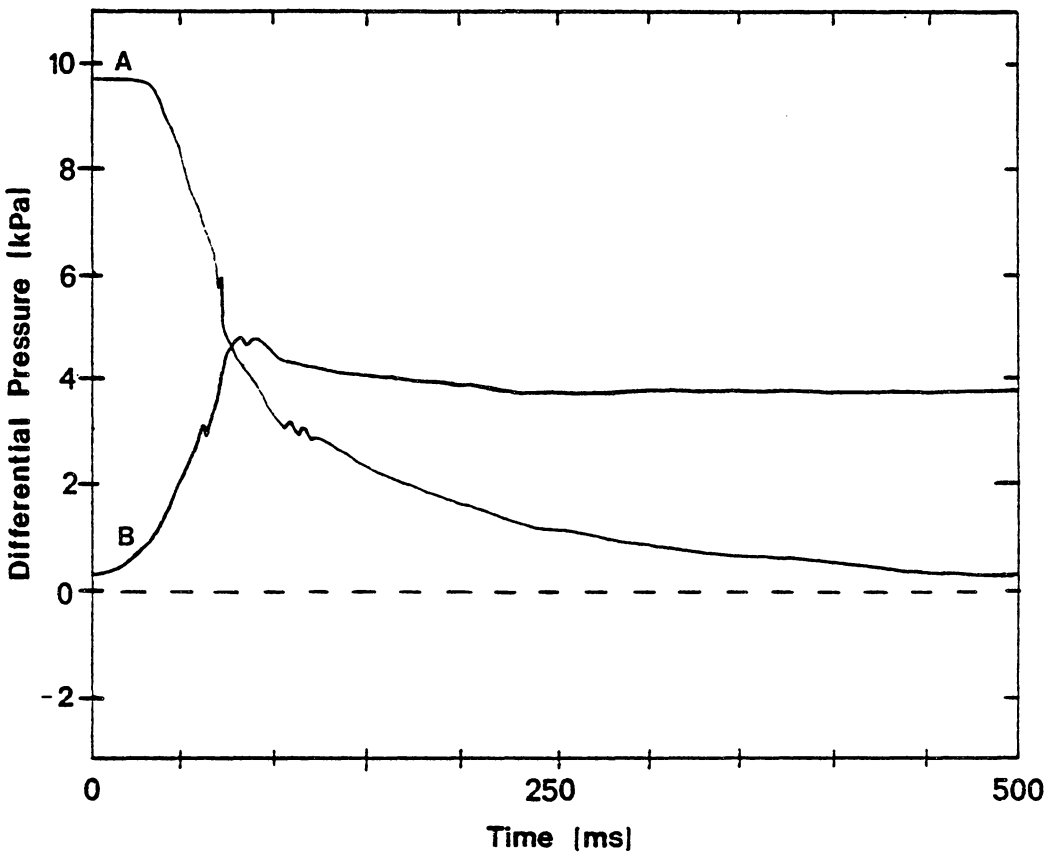

Figure 5.26. An Oscilloscope Trace from a Differential-Pressure Transducer Placed Between the Argon Feed-Line (Tap A in Figure 5.1) and the Catalyst Zone. A 2-Micron Distributor Plate Is in Use. (Experiment 2-8 in Table 5.1). Curve A Is the Helium-to-Argon Transition and Curve B Is the Argon-to-Helium Transition.

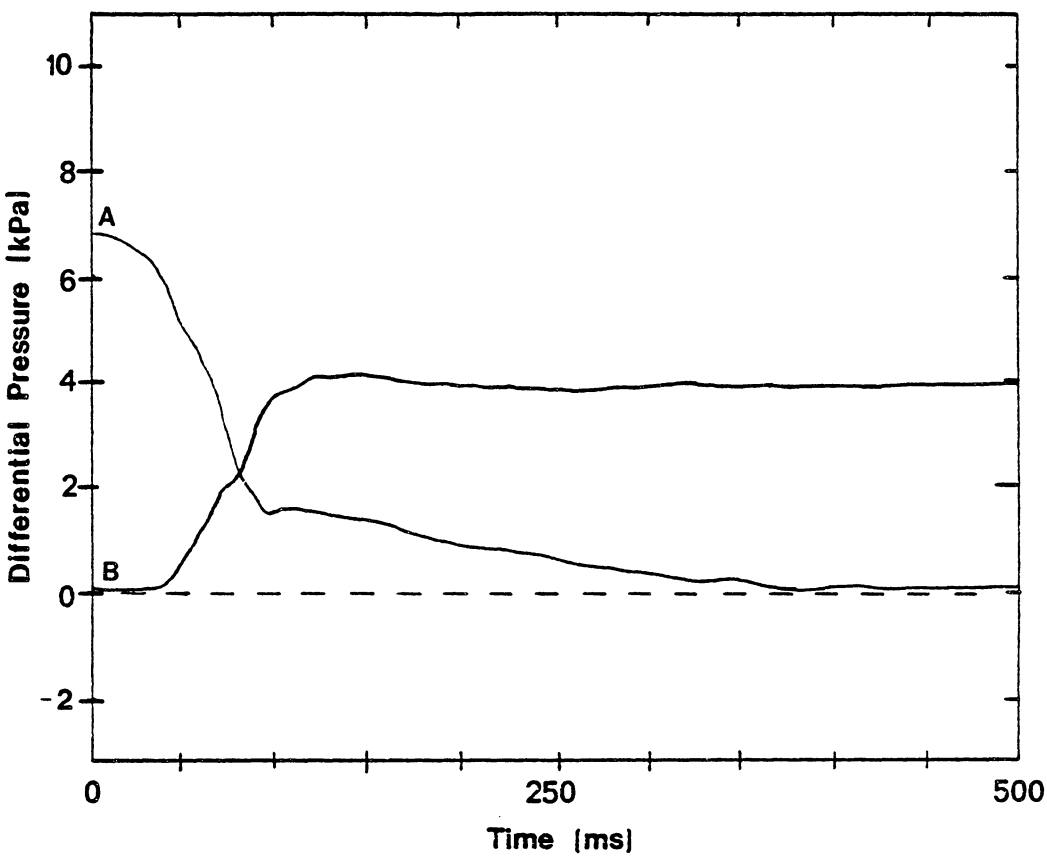

Figure 5.27. An Oscilloscope Trace from a Differential Pressure Transducer Placed Between the Helium Feed-Line (Tap B in Figure 5.1) and the Catalyst Zone. A 2-Micron Distributor Plate Is in Use. (Experiment 2-9 in Table 5.1). Curve A Is the Argon-to-Helium Transition and Curve B Is the Helium-to-Argon Transition.

inversion has been totally eliminated and the pressure transition after the plug movement follows a smooth return to the distributor-plate pressure drop.

After the improvements in reduction of gas mixing utilizing a 2-micron distributor plate were demonstrated, a series of experiments were performed in the cold-flow model. This series of experiments had several goals.

1. To study gas mixing in the plenum zone, catalyst zone, and gas-exit zone without catalyst vibrofluidization. This was done in order to determine the influence of the microreactor geometry on gas mixing.

2. To study gas mixing in the catalyst zone and gas-exit zone in order to determine the extent of gas mixing induced by vibrofluidizing the catalyst.

3. To study the effect of 5-second staggering on gas mixing in the plenum zone, catalyst zone, and gas-exit zones both with and without the catalyst bed being vibrofluidized.

4. To study the effect of feed-gas flow rate on gas mixing during the experiments involved in items 1 to 3 above. The flow rates used in these experiments were 417, 833, and 1,650 actual mm^3/sec. Helium and argon flows were always equal during these experiments. The lowest flow rate corresponds to the actual flow rate of gas through the microreactor during the steady-state Fischer-Tropsch studies in the vibrofluidized-bed microreactor.

The above experiments have been classified as Series 2, 3, and 4 experiments listed in Table 5.1. The results are generally presented

in the form of graphs of the percent transition in 2.4 seconds after the initial detector response versus feed-gas flow rate. Separate curves are presented on each plot for the response in the plenum zone, catalyst zone, and gas-exit zone. A separate graph is offered for the helium-to-argon and argon-to-heliuim transitions. A series of bar graphs interrelate the effects of microreactor geometry, catalyst vibrofluidization, and feed-gas staggering at a given flow rate. Again, separate figures are presented for the helium-to-argon and argon-to-helium transitions. All data presented in graphical form are contained in Appendix F in the form of thermal conductivity detector (TCD) output traces.

5.2.3.1 Gas Mixing Induced by Reactor Geometry

Figures 5.28 and 5.29 illustrate the effect of microreactor geometry on gas mixing when switching from helium to argon, and from argon to helium at three separate flow rates. The degree of gas mixing observed in the center of the catalyst zone at 417 actual mm^3/s is significantly more pronounced than that observed in the plenum. In addition, upon travelling from the catalyst zone to the gas-exit zone, considerably more mixing is induced. This trend is more pronounced for the argon-to-helium transition than for the helium-to-argon transition. For example, the transition observed in the gas-exit zone at a feed-gas flow rate of 417 actual mm^3/s is only 42.5% complete after 2.4 seconds for the argon-to-helium transition. The helium-to-argon transition shows 78.7% of the transition is complete after 2.4 seconds.

The actual TCD output for this experiment is shown in Figure 5.30. The difference in the efficiency of gas replacement between helium and

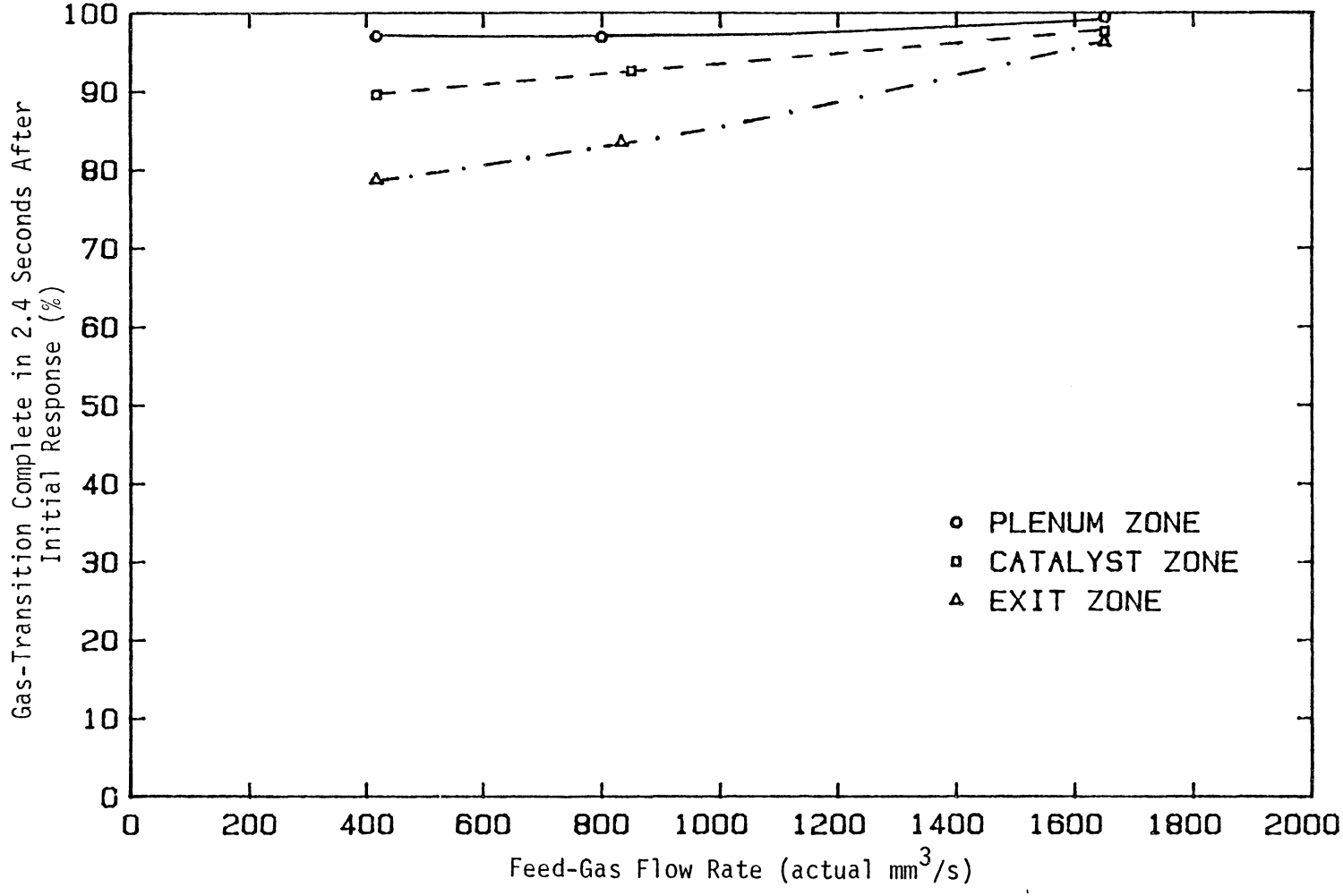

Figure 5.28. The Percent Gas-Transition Complete in 2.4 Seconds After the Initial Detector Responses for the Helium-to-Argon Transition. The Microreactor Model Was Not Vibrated.

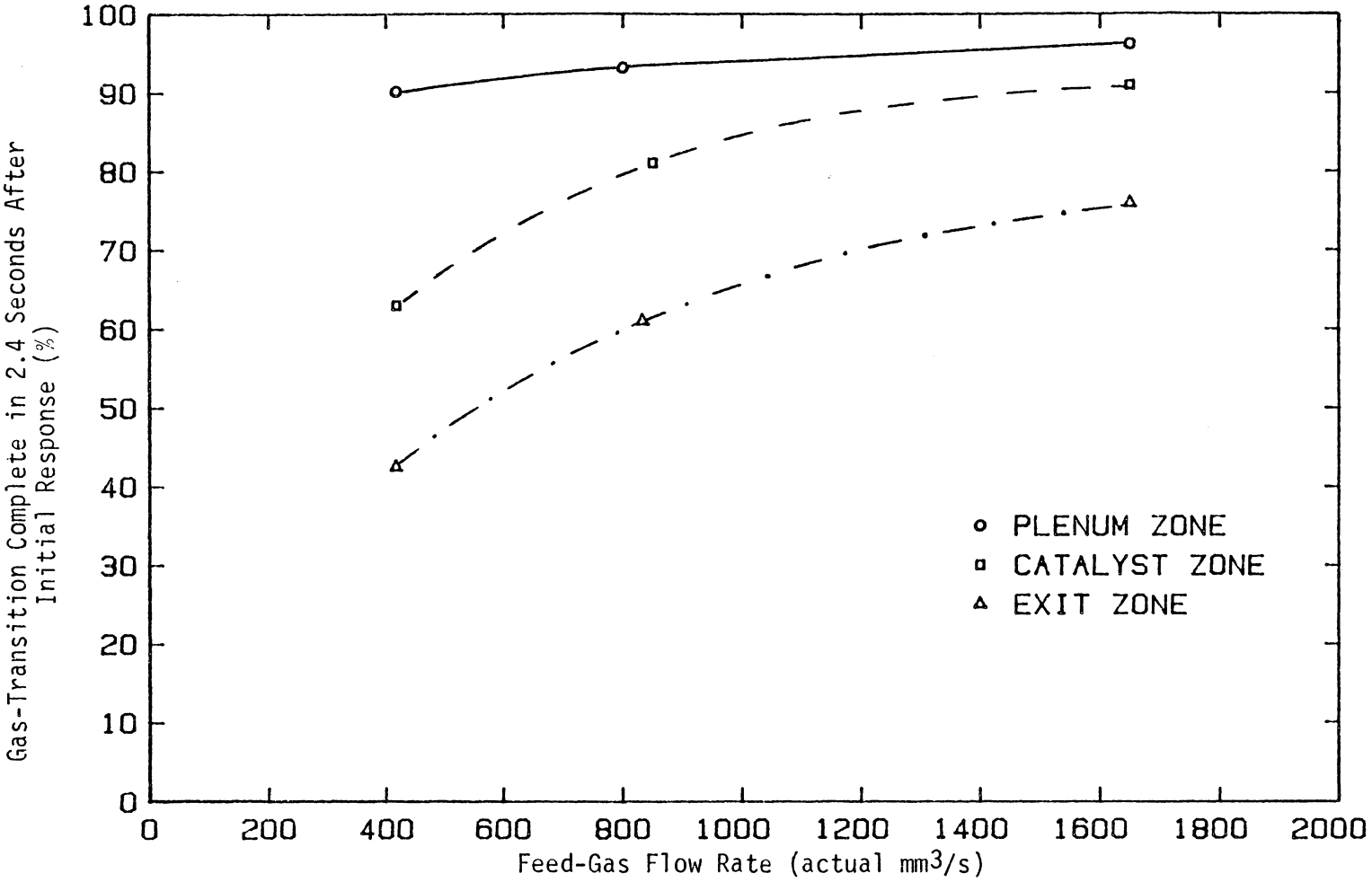

Figure 5.29. The Percent Gas-Transition Complete in 2.4 Seconds After the Initial Dectector Responses for the Argon-to-Helium Transition. The Microreactor Model Was Not Vibrated.

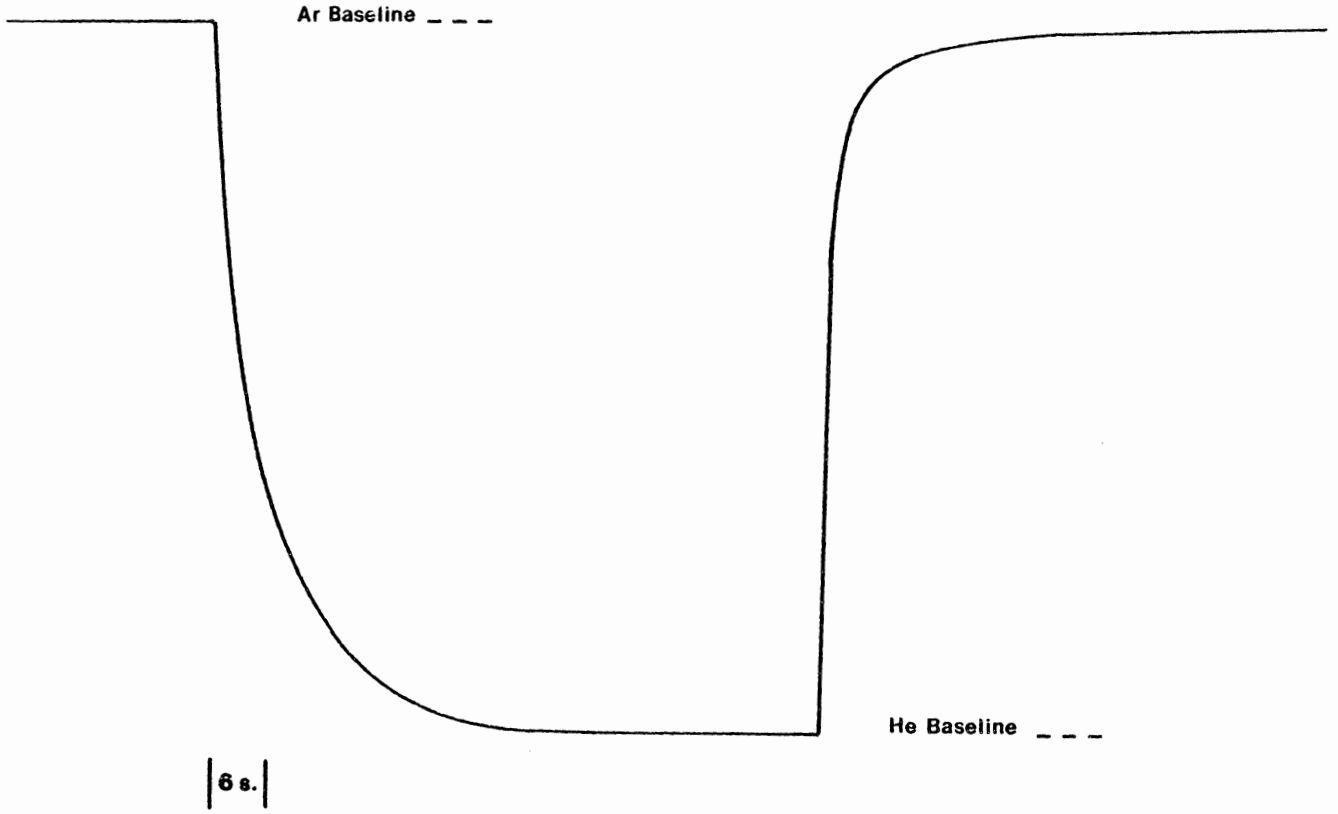

Figure 5.30. The TCD Response for Switching Between Helium and Argon Feeds at 417 Actual mm^3/s with Sampling in the Cold-Flow Microreactor Model Exit Zone. (Experiment 4-1 in Table 5.1).

argon is due largely to the difference in their densities. At 25°C and 35 kPa, the density of helium is 0.0727 g/m^3; while argon has a density of 0.726 g/m^3. Therefore, helium is more susceptible to channeling and is not as well-distributed as argon by the distributor plate.

Increasing the flow rate of the feed gases has a significant effect on the degree of gas mixing. The microreactor-induced gas mixing has been greatly reduced. For a feed-gas flow rate of 1650 actual mm^3/s with gas sampling in the plenum zone, the transition is 99.4% complete for the helium-to-argon transition and 96.2% complete for the argon-to-helium transition after 2.4 seconds. The TCD trace under these conditions is shown in Figure 5.31. The transitions produce nearly a square waveform. The helium-to-argon transition is 100% complete within 4 to 5 seconds; while the argon-to-helium transition takes several seconds longer. This suggests that the layer of catalyst directly above the distributor plate is exposed to discrete transitions of feed gas. Again referring to Figures 5.28 and 5.29, similar trends of decreases in gas mixing occur in both the catalyst zone and the gas-exit zone. In the center of the catalyst zone, the transition percent after 2.4 seconds has been increased to 97.0% and 91.0% for the helium-to-argon and argon-to-helium switches, respectively at a feed gas flow rate of 1650 actual mm^3/s .

5.2.3.2 Gas Mixing Induced by Catalyst Vibrofluidization

As stated in Section 2.4, one characteristic long attributed to vibrofluidized beds is the lack of gas backmixing under certain conditions. The effect of vibrofluidizing 1 gram of -150+300 μ fused-

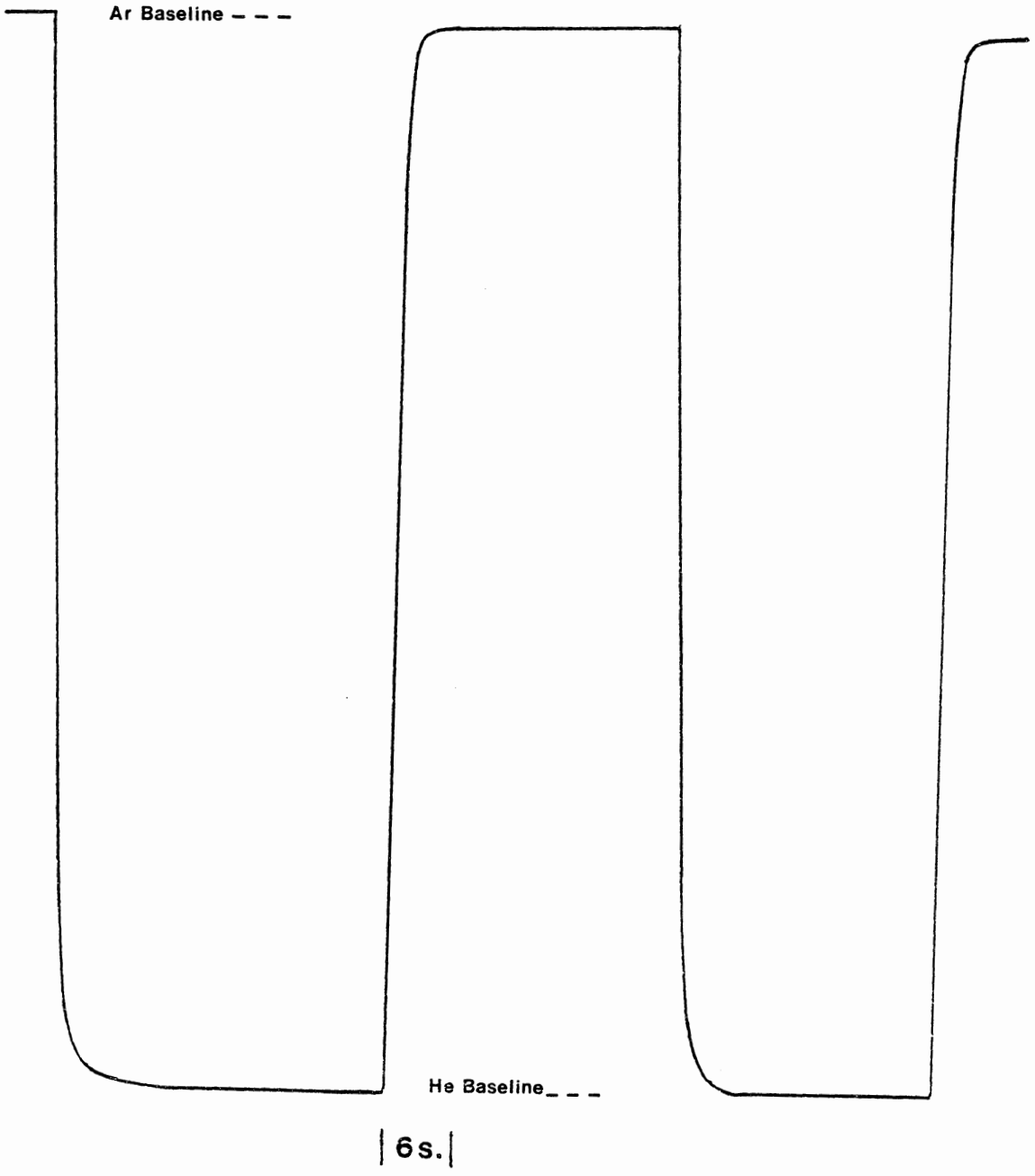

Figure 5.31. The TCD Response for Switching Between Helium and Argon Feeds at 1650 Actual mm^3/s with Sampling in the Cold-Flow Microreactor-Model Plenum Zone. (Experiment 2-12 in Table 5.1).

iron catalyst in the catalyst zone of the cold-flow microreactor model was studied. It was found that vibrofluidization in the catalyst zone did not affect the gas mixing in the plenum zone. There was, however, a change in the degree of gas mixing as measured in the center of the catalyst zone and in the gas-exit zone.

Figure 5.32 illustrates the influence of feed-gas flow rate on the helium-to-argon transition during vibrofluidization. When comparing Figure 5.32 to Figure 5.28 (with no vibrofluidization), several differences are apparent. The degree of gas mixing in the catalyst zone has increased, shifting that curve down an average of 5% from Figure 5.28 to 5.32. At the lower gas flow rates, the degree of mixing measured at the sampling point in the gas-exit zone did not change significantly with the introduction of vibration. However, at a flow rate of 1650 actual mm^3/s, the transition percentage dropped 5 points. This indicates that the replacement of helium by argon, to a noticeable degree, is influenced by the virbofluidized catalyst in the catalyst zone. At low flow rates, most of the increase in mixing is induced below the center of the catalyst section, where the sampling point is located. However, at a flow of 1650 actual mm^3/s, a significant extent of the mixing induced by vibrofluidization occurs above the center of the catalyat zone.

The effect of vibrofluidization on the argon-to-helium transition at several flow rates is illustrated in Figure 5.33. Comparing this plot to Figure 5.29 where no vibrofluidization was induced brings out several difference. The introduction of vibrofluidization has again

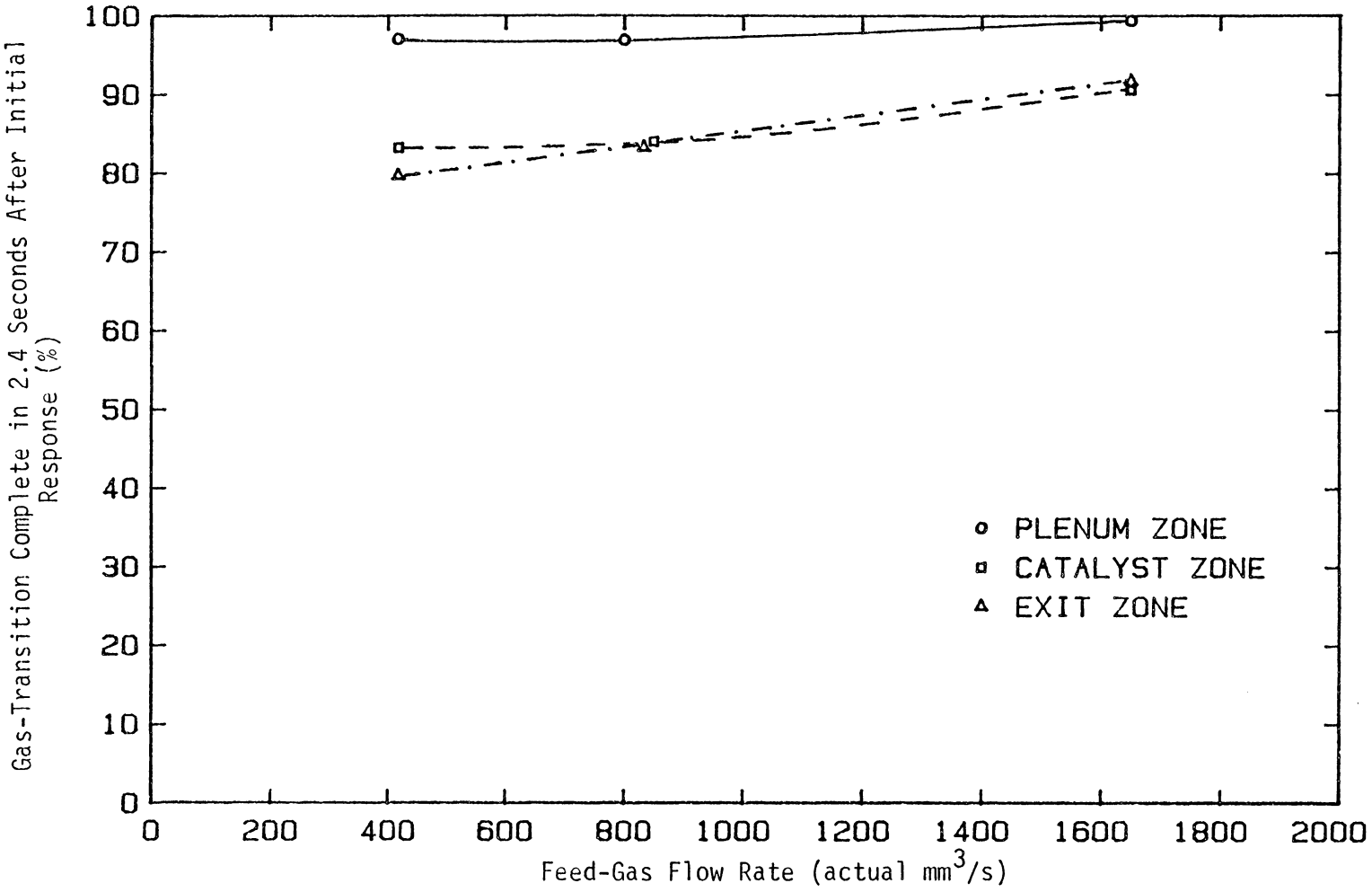

Figure 5.32. The Percent Gas-Transition Complete in 2.4 Seconds After the Initial Dectector Responses for the Helium-to-Argon Transition. The Microreactor Model Was Vibrated.

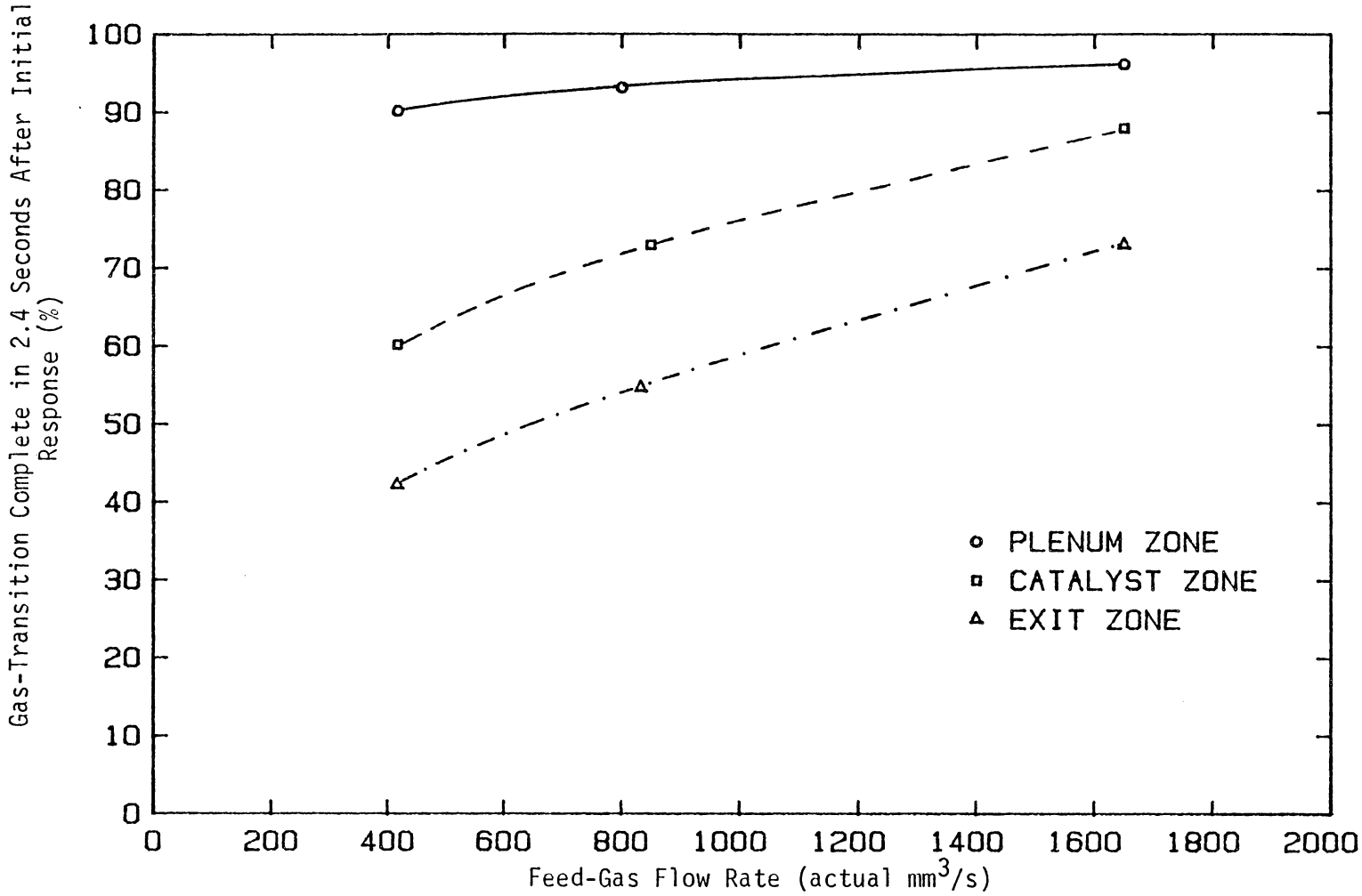

Figure 5.33. The Percent Gas-Transition Complete in 2.4 Seconds After the Initial Dectector Responses for the Argon-to-Helium Transition. The Microreactor Model Was Vibrated.

reduced the percentage of the argon-to-helium transition in the catalyst zone and gas-exit zone. The effect is minimal at 417 and 1650 actual mm^3/s and more pronounced at 833 actual mm^3/s. At a flow rate of 833 actual mm^3/s, the percent transition has dropped from 81.1 to 73.0% at the center of the catalyst zone. Similarly, it dropped from 61.0 to 54.7% at the sampling point in the gas-exit zone.

5.2.3.3 Effect of Staggering on Gas Mixing

Figures 5.34 and 5.35 illustrate the effect of 5-second staggering on the helium-to-argon and argon-to-helium transitions as a function of feed-gas flow rate. The catalyst bed is not being vibrated in the results shown here. Five-second staggering produces an initial burst of gas through the catalyst zone, immediately after the plug has traversed the plenum. For a feed-gas flow rate of 417 actual mm^3/s, the volume of gas going through the catalyst zone during this burst is approximately 2,085 mm^3. Since the volume of the catalyst zone is 1,152 mm^3, the gas in the zone is replaced 1.8 times by this initial burst. For a 5-second staggering with a flow rate of 833 actual mm^3/s, the gas in the catalyst zone is replaced 3.6 times by the initial burst.

At a flow rate of 1,650 actual mm^3/s, the 5-second staggering turns the gas in the catalyst zone over approximately 7.2 times immediately after plug movement. The result of this rapid burst of gas is illustrated in Figure 5.34 for the helium-to-argon transition. The percent transition after 2.4 seconds is greater than 90% in all cases.

Figure 5.35 shows the staggering results for the more difficult argon-to-helium transition. Note that the argon-to-helium transition

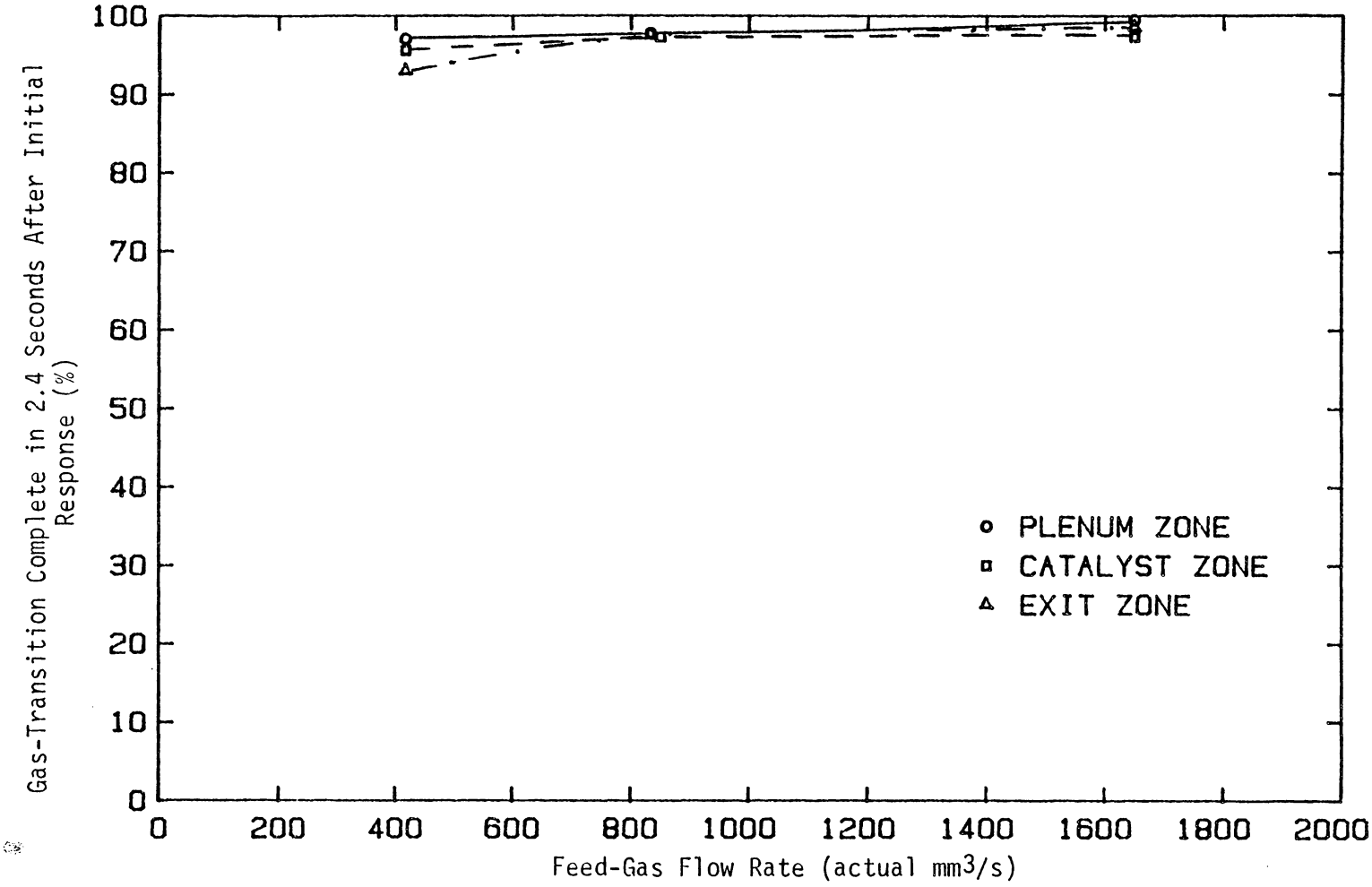

Figure 5.34. The Percent Gas-Transition Complete in 2.4 Seconds After the Initial Dectector Responses for the Helium-to-Argon Transition. Five-Second Feed-Gas Staggering Was Used.

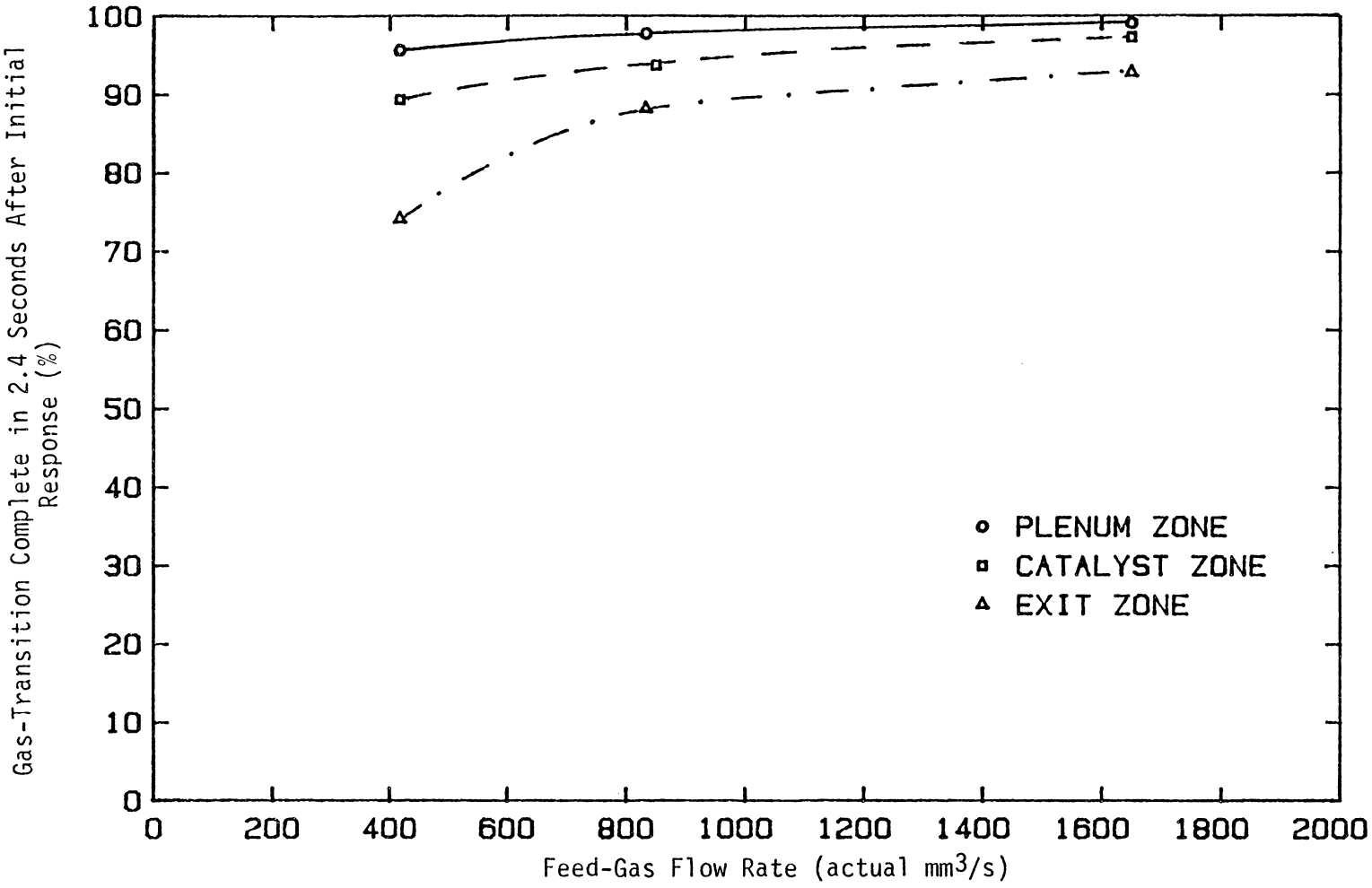

Figure 5.35. The Percent Gas-Transition Complete in 2.4 Seconds After the Initial Dectector Responses for the Argon-to-Helium Transition. Five-Second Feed-Gas Staggering Was Used.

is difficult because helium is much less dense than argon. Again, in the plenum and catalyst zones, the transitions are greater than 90% complete after 2.4 seconds for all flow rates. In addition, the gas mixing observed at the gas-exit sampling point has been decreased when compared to the case with no staggering (Figure 5.29). With no staggering at 417 actual mm^3/s, the transition was only 42.5 percent complete in this period. At the same flow rate the transition had improved to 74.1 percent using 5-second staggering.

Figures 5.36 and 5.37 display the results of introducing 5-second feed-gas staggering, while the catalyst bed is vibrofluidized. The results for the helium-to-argon transition with (Figure 5.36) and without (Figure 5.34) vibrofluidization are nearly identical. The only significant difference is for feed-gas flow rates of 417 actual mm^3/s, where the resulting transition with vibrofluidization is 2 to 3% slower in the catalyst and gas-exit zones. For the argon-to-helium transition, the extent of gas mixing with 5-second staggering is significantly greater when the catalyst bed is vibrofluidized.

An examination of Figure 5.37 in comparison with Figure 5.35 shows that the introduction of the vibrofluidized catalyst bed causes a 12% decrease in gas-transition completion at 417 actual mm^3/s in the catalyst zone. Overall at this flow rate, the sample taken from the gas-exit zone shows a new 7-percent decrease in gas-transition completion. As flow rate is increased, the backmixing effect of vibrofluidization on the feed gases decreases, finally resulting in nearly identical, rapid transitions at 1,650 actual mm^3/s.

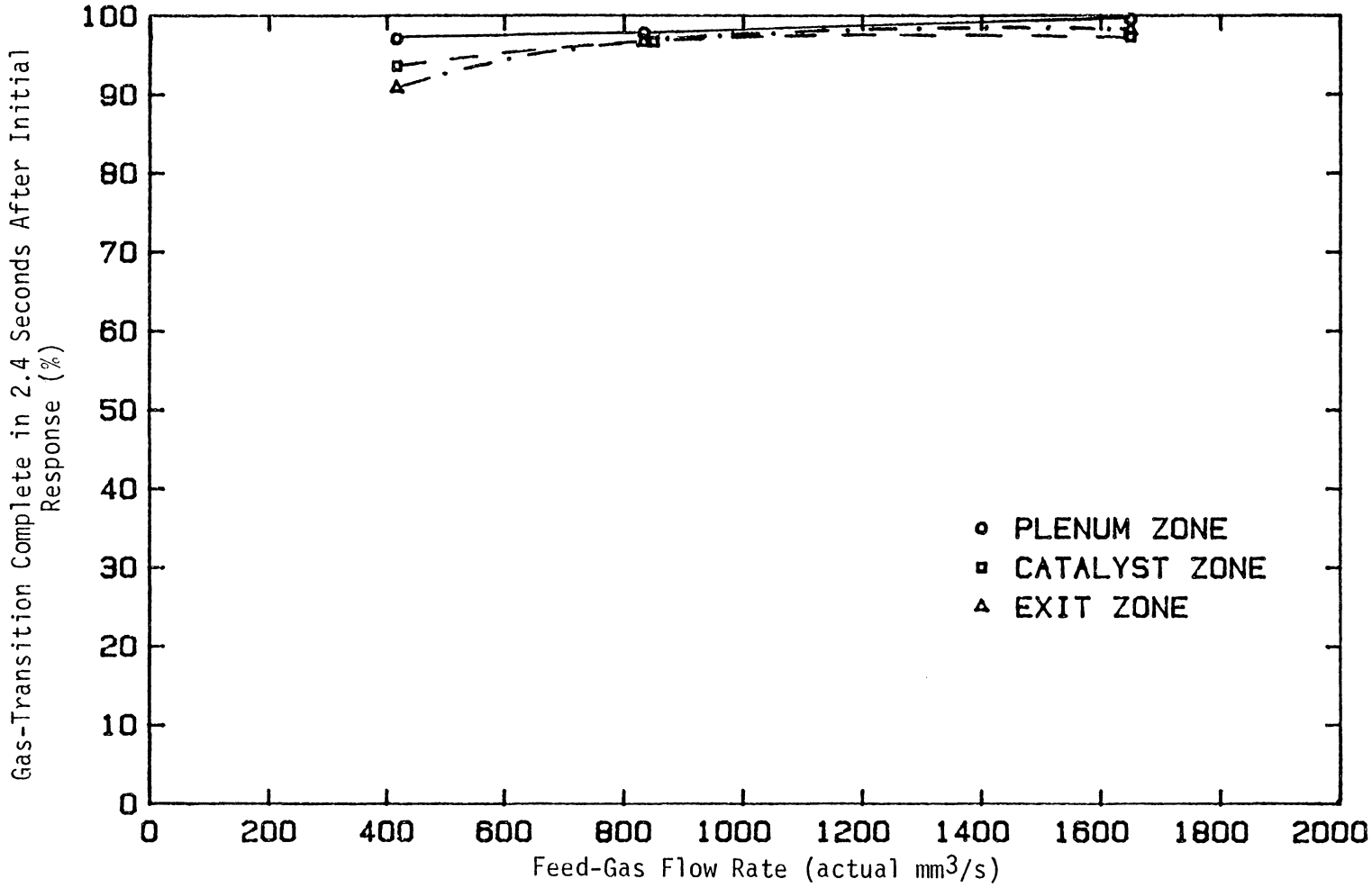

Figure 5.36. The Percent Gas-Transition Complete in 2.4 Seconds After the Initial Dectector Responses for the Helium-to-Argon Transition. Five-Second Feed-Gas Staggering and Vibrofluidization Were Used.

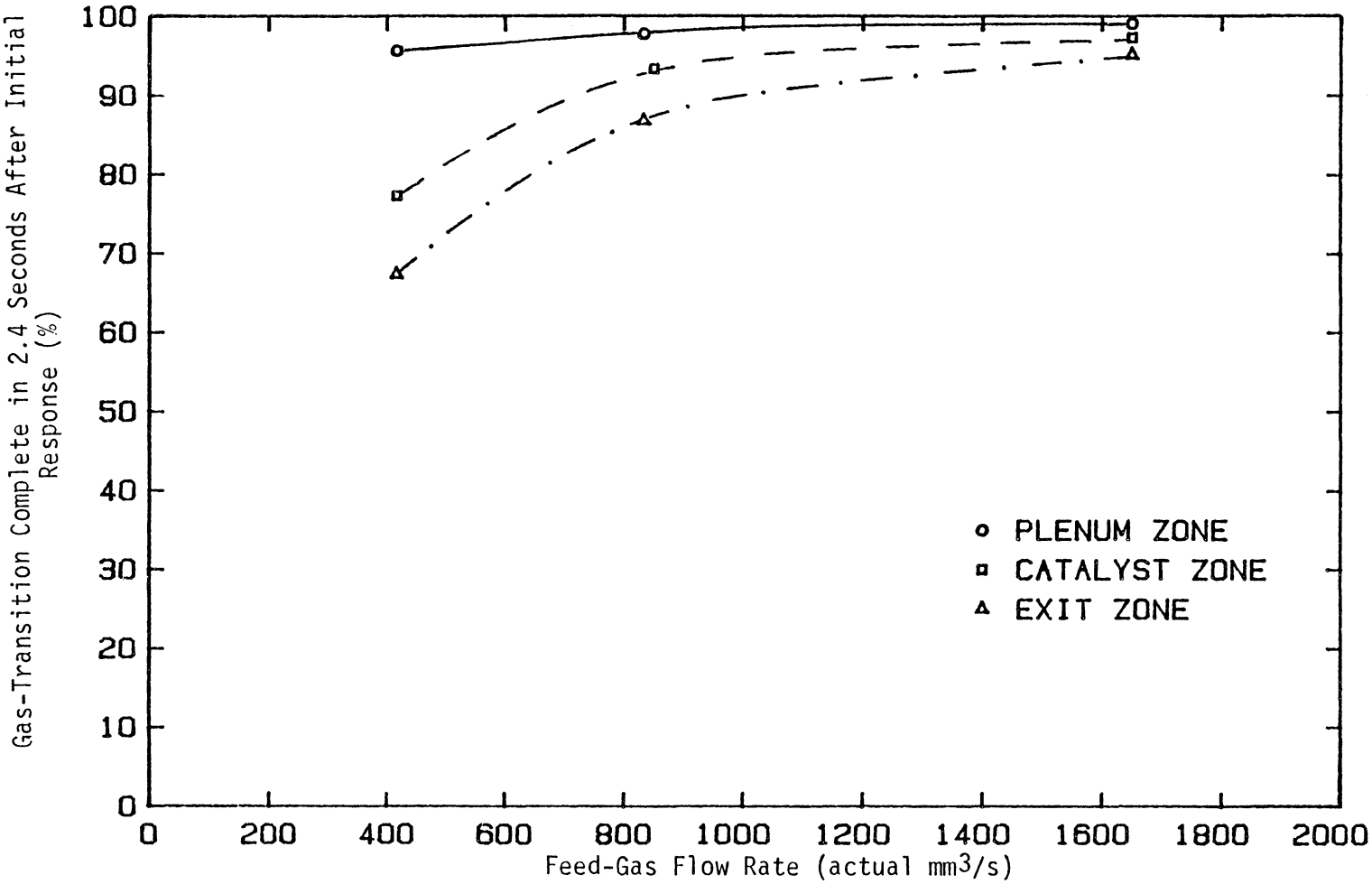

Figure 5.37. The Percent Gas-Transition Complete in 2.4 Seconds After the Initial Dectector Responses for the Argon-to-Helium Transition. Five-Second Feed-Gas Staggering and Vibrofluidization Were Used.

5.2.3.4 Trends in Gas Mixing

Figures 5.38-5.43 summarize the trends in gas mixing in the cold-flow microreactor model. Each bar graph presents the percent of gas-transition completion as a function of the sampling point in the microreactor, 2.4 seconds after the initial detector response. The sampling points were placed in the plenum zone, the catalyst zone and the gas-exit zone. Two bars are presented for the plenum zone representing results from experiments with and without feed-gas staggering. Note that vibrofluidation in the catalyst zone has not been found to affect gas mixing in the plenum zone. Four bars are presented for both the catalyst zone and the gas-exit zone.

The bars in Figures 5.39-5.43 represent the following:

bar 1: percent transition during catalyst vibrofluidization

bar 2: percent transition without catalyst vibrofluidization

bar 3: percent transition with 5-second staggering but without vibrofluidization

bar 4: percent transition with both 5-second staggering, and vibrofluidization

A separate figure is presented for the helium-to-argon and argon-to-helium transitions at each of the three feed-gas flow rates studied.

As can be seen from these graphs, the introduction of catalyst vibrofluidization causes an increase in gas mixing, resulting in the decrease in percent gas-transition completion represented. Most of the backmixing caused by vibrofluidization of the catalyst is experienced in the lower half of the catalyst zone, below the sampling point.

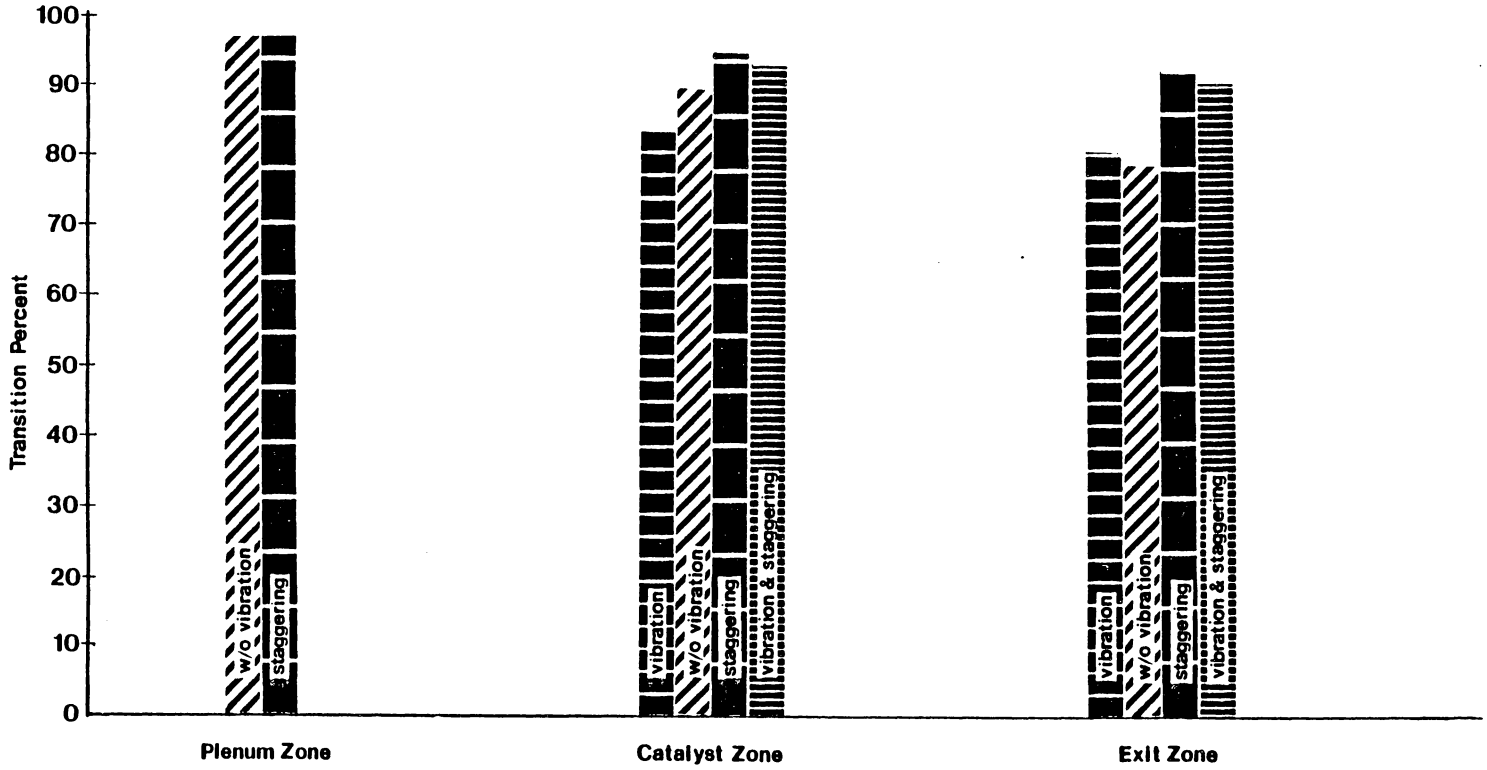

Figure 5.38. A Summary of Percent Gas-Transition Completion in the Cold-Flow Microreactor 2.4 Seconds After the Initial Detector Response. Shown Is the Helium-to-Argon Feed Transition at 417 Actual mm^3/s.

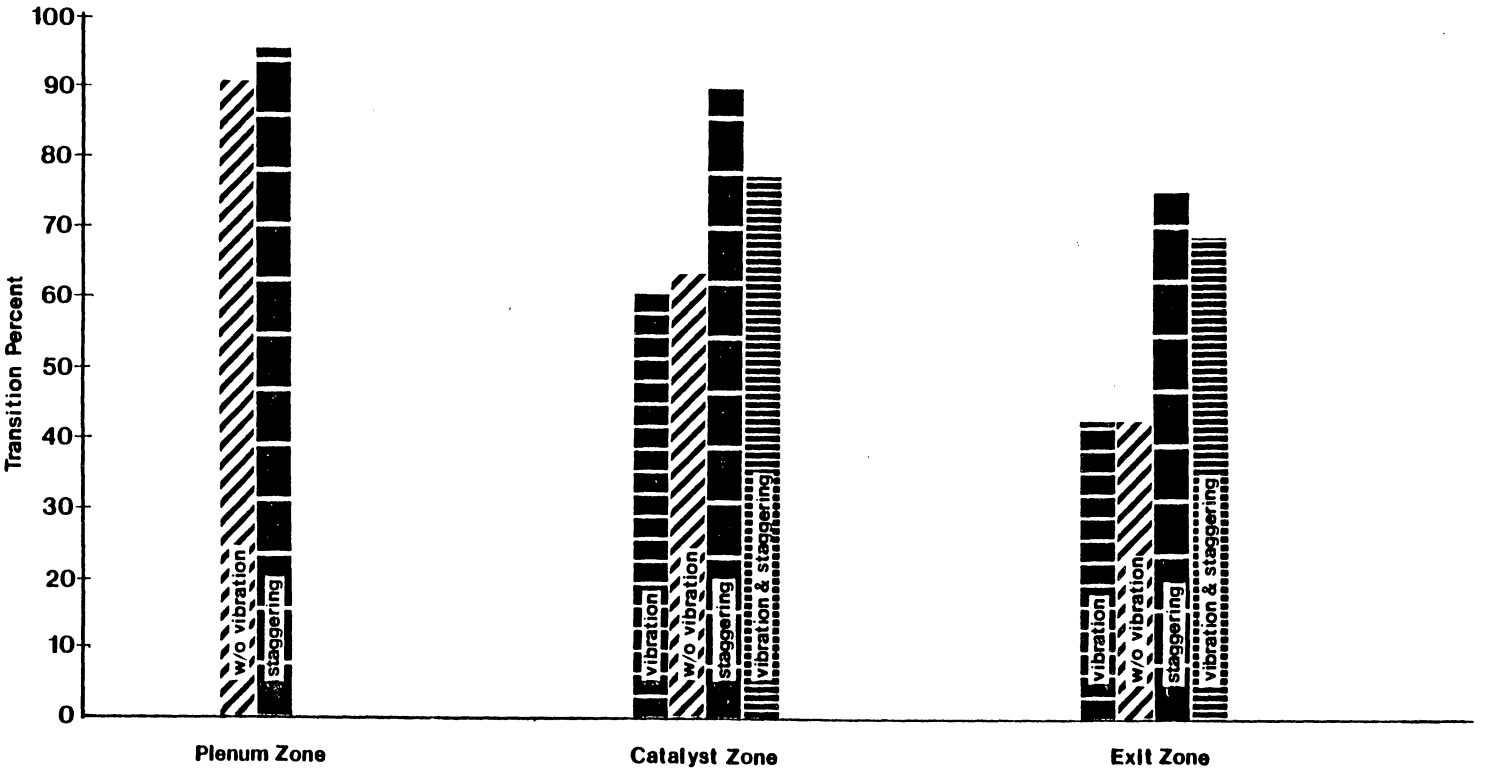

Figure 5.39. A Summary of Percent Gas-Transition Completion in the Cold-Flow Microreactor 2.4 Seconds After the Initial Detector Response. Shown Is the Argon-to-Helium Feed Transition at 417 Actual mm^3/s.

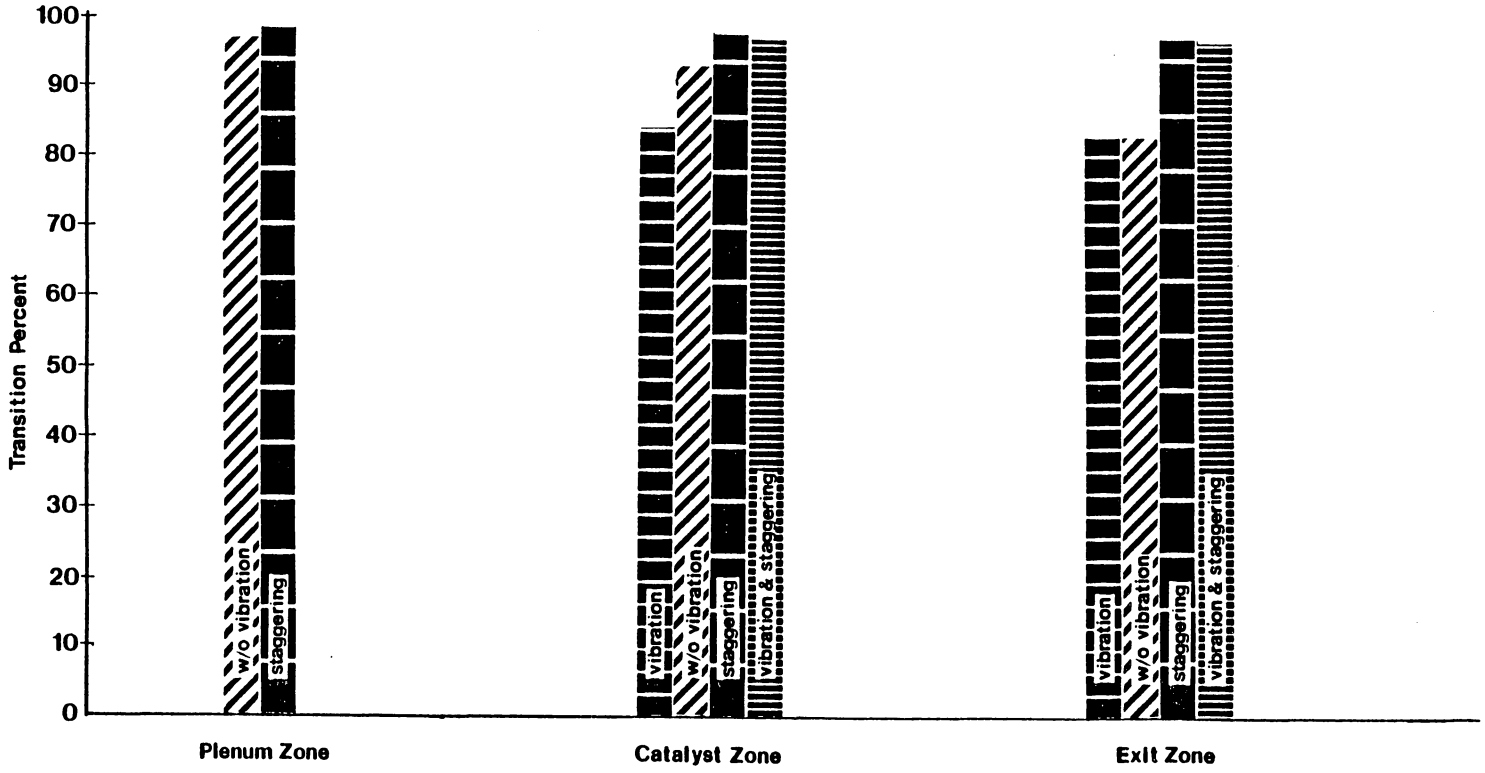

Figure 5.40. A Summary of Percent Gas-Transition Completion in the Cold-Flow Microreactor 2.4 Seconds After the Initial Detector Response. Shown Is the Helium-to-Argon Feed Transition at 833 Actual mm^3/s.

Figure 5.41. A Summary of Percent Gas-Transition Completion in the Cold-Flow Microreactor 2.4 Seconds After the Initial Detector Response. Shown Is the Argon-to-Helium Feed Transition at 833 Actual mm^3/s.

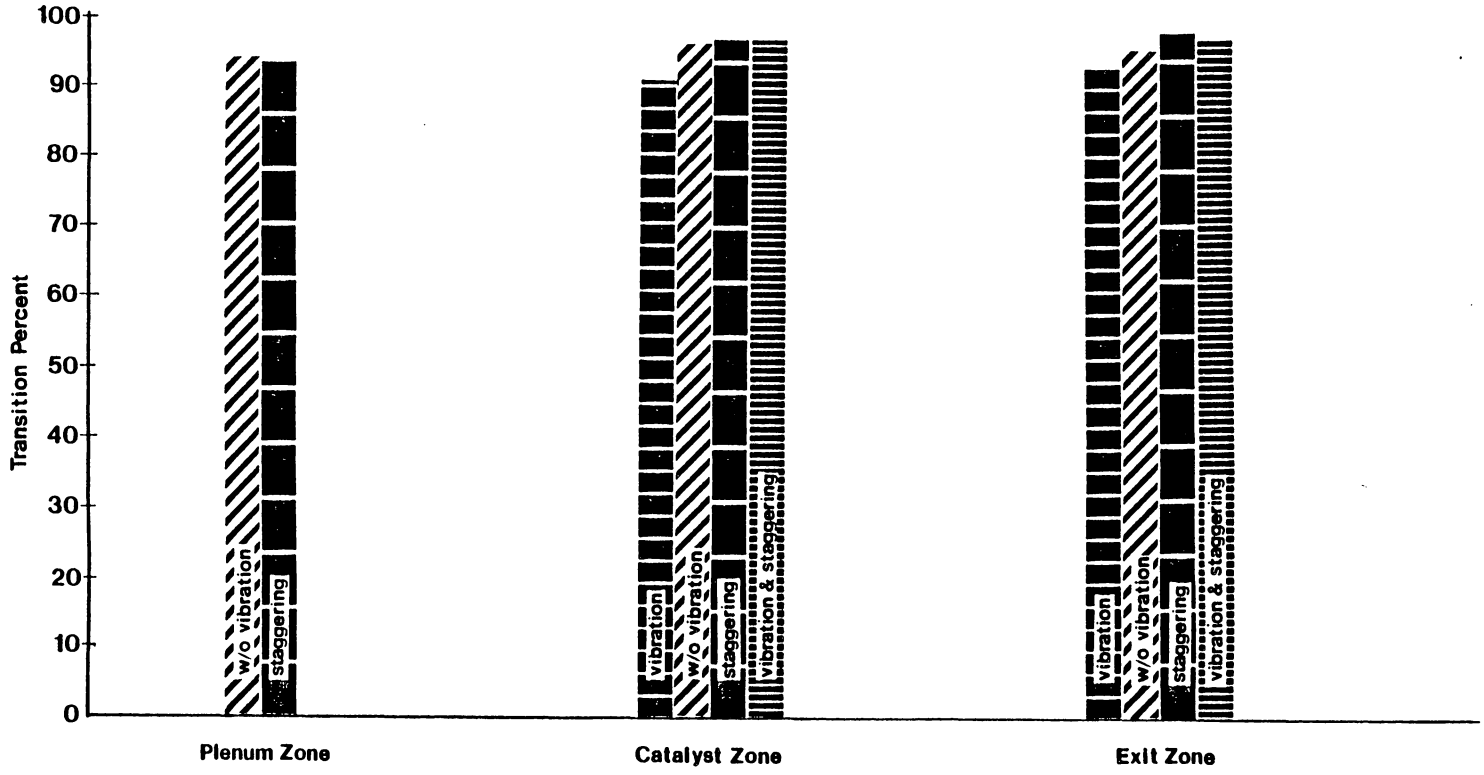

Figure 5.42. A Summary of Percent Gas-Transition Completion in the Cold-Flow Microreactor 2.4 Seconds After the Initial Detector Response. Shown Is the Helium-to-Argon Feed Transition at 1650 Actual mm^3/s.

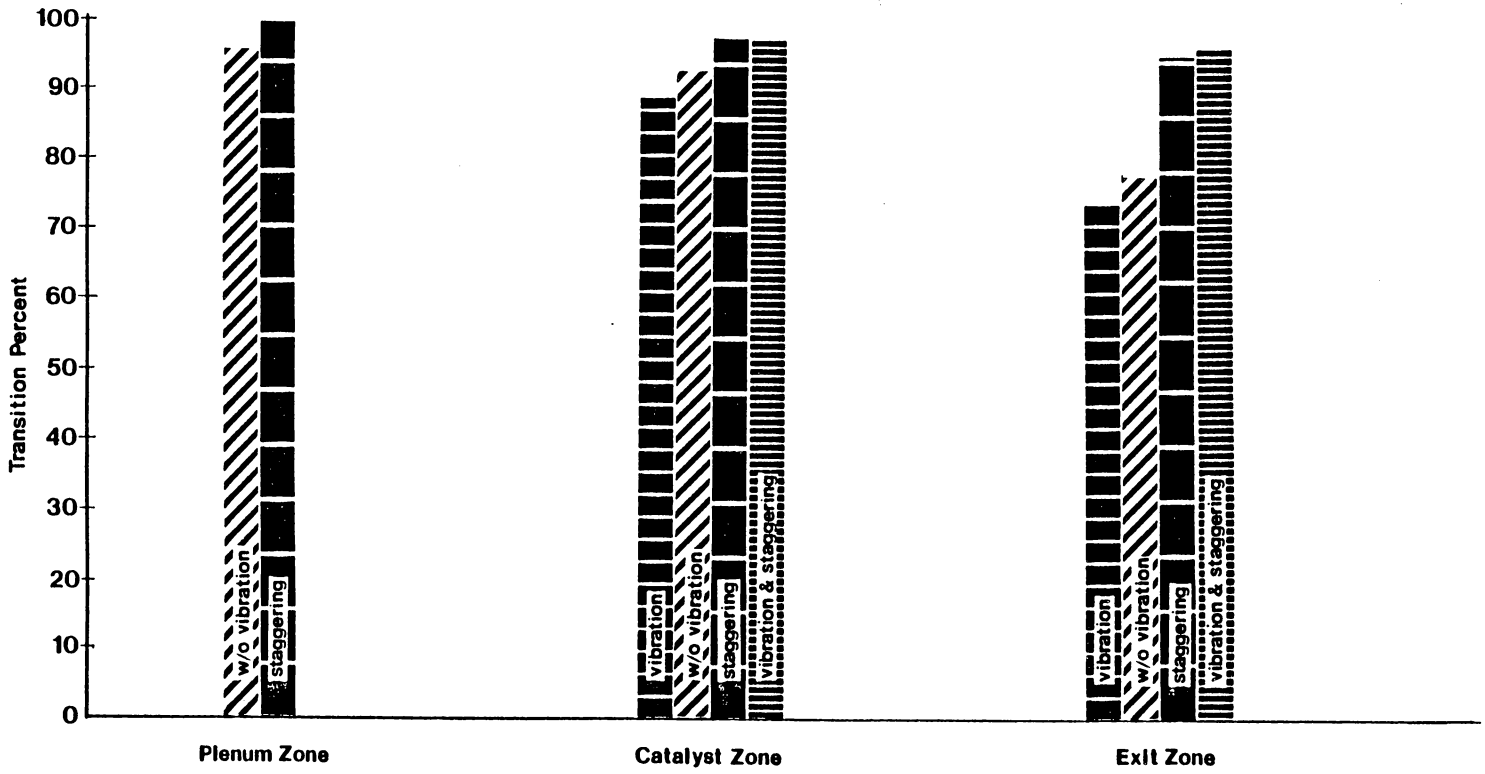

Figure 5.43. A Summary of Percent Gas-Transition Completion in the Cold-Flow Microreactor 2.4 Seconds After the Initial Detector Response. Shown Is the Argon-to-Helium Feed Transition at 1650 Actual mm^3/s.

Staggering of the feed gas results in a significant reduction in gas mixing as expressed in the increase in percent gas-transition completion. This is the case when the catalyst is vibrofluidized and when it is not. Staggering produces a greater percentage improvement for the argon-to-helium transition than for the helium-to-argon transition. Also, the improvement is greater at the lower feed-gas flow rate. In general, the helium-to-argon transition is much more rapid than the argon-to-helium transition, presumably due to the density difference of the gases. When compared to argon, helium is more likely to channel through the distributor plate, the catalyst bed and the catalyst retention plate. Argon, however, is more apt to push out the less dense helium and is not as prone to bypassing.

The main objectives of this cold-flow model study were to identify conditions which produce discrete pulses of helium and argon below the catalyst bed, and to determine the gas-mixing properties of the vibrofluidized bed. Notable reductions in gas-mixing have been achieved, as expected, through the use of higher gas flow rates and feed-gas staggering.

The limitation of using high gas flow rates is that under F-T synthesis conditions, an increase in flow rate at constant pressure will cause a parallel increase in space velocity. An effective means to avoid using high gas flow rates would be to decrease the system pressure. The space velocity, and therefore the conversion, could be maintained constant and the transition to a new gas upon sliding-plug movement would be more discrete.

Feed-gas staggering causes a sudden burst of gas through the reaction zone of the microreactor followed by a much lower, constant gas flow rate. The space velocity through the reactor would consequently follow the same pattern. If equal gas flow rates are used, a uniform space velocity through the catalyst bed results.

5.2.4 Characteristics of the Vibrofluidized Bed of Catalyst

This study is the first to use a shallow vibrofluidized bed of catalyst to simulate the solids mixing characteristics of a gas-fluidized bed. As stated earlier, one gram of -150+300 μ fused-iron catalyst is used in the reaction zone (3.18-mm wide, 25.4-mm long and 14.29-mm deep) of the microreactor. In reference to the cold-flow model, this zone has been called the catalyst zone. The catalyst is vibrofluidized by imparting a vertical motion to the microreactor using a vibrator and an associated support structure. The microreactor is vibrated at the resonance frequency of the leaf-spring support system, typically 18 to 25 Hz. The peak-to-peak amplitude of vibration, as measured at the microreactor, is approximately 4 mm. The static bed height of the catalyst in the reaction zone is approximately 4.3 mm, thus occupying nearly one-third of the volume.

Figure 5.44 is a photograph of the catalyst zone of the cold-flow microreactor model, showing the static bed height. The sliding plug has been captured in mid-motion as it traverses the plenum zone.

Figure 5.45 shows two photographs of the catalyst bed as it is being vibrofluidized at a frequency of 24 Hz and a peak-to-peak amplitude of 4 mm. These photographs are typical of the bed behavior

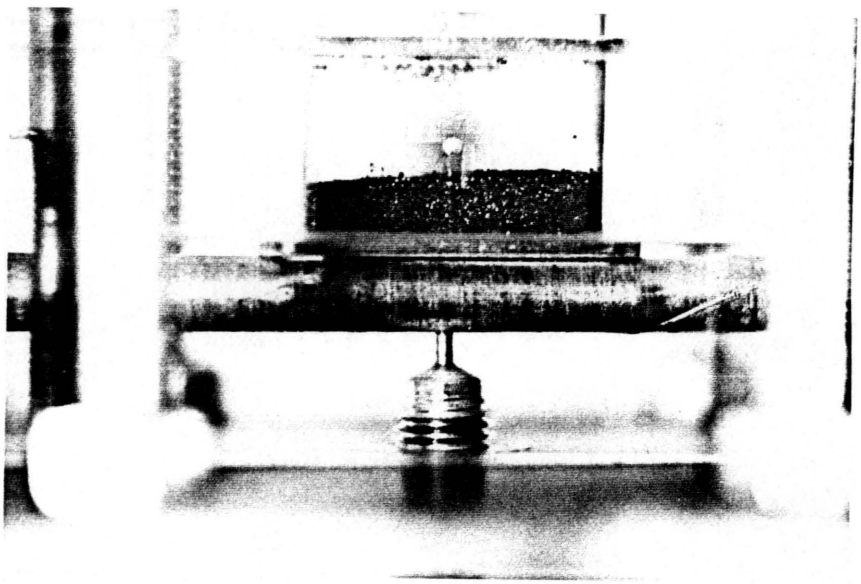

Figure 5.44. A Photograph of the Static Bed-Height of the Cold-Flow Microreactor Model.

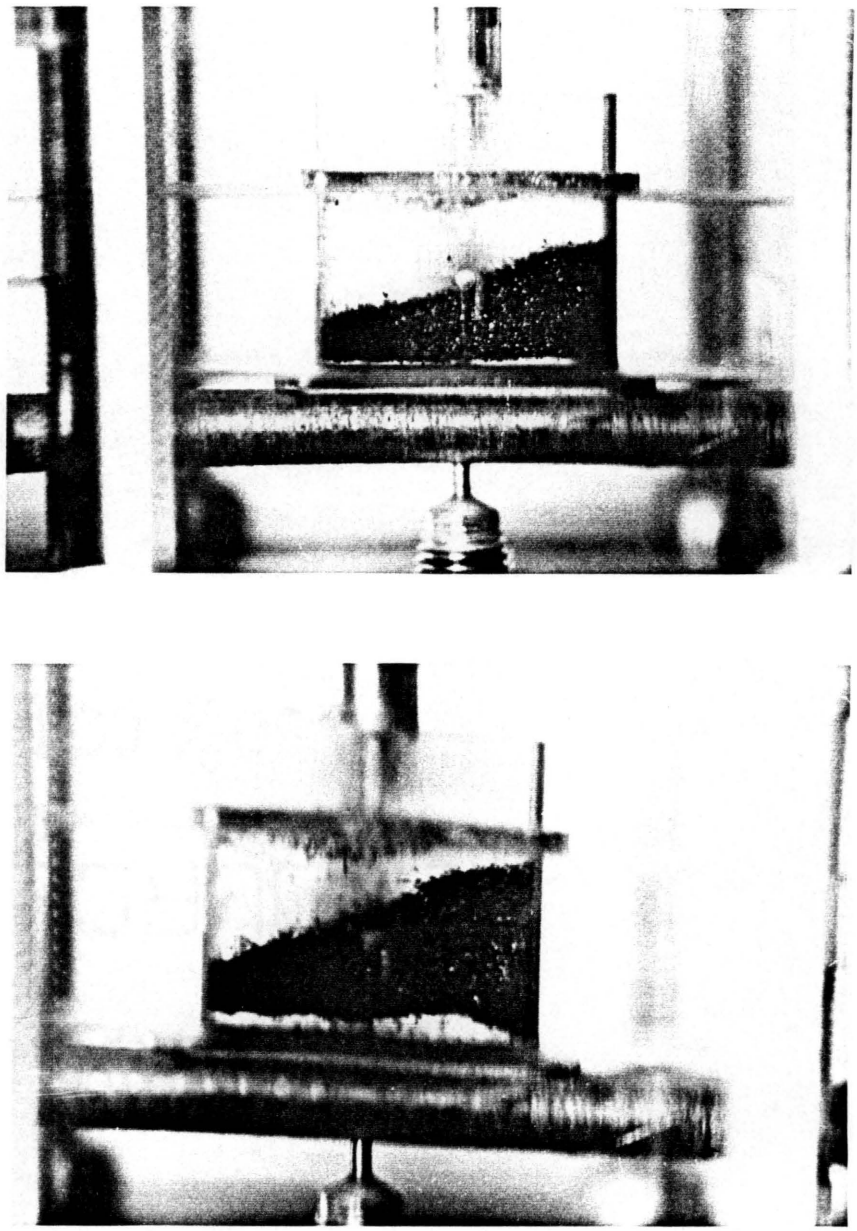

Figure 5.45. A Vibrofluidized-Bed of Fused-Iron Catalyst at a Gas Velocity Well Below the Minimum Gas-Fluidization Velocity.

when the velocity of the feed gas passing through the catalyst zone is well below the minimum gas-fluidization velocity. This is the case for the three flow rates (417, 833, and 1650 actual mm^3/sec) used for gas mixing studies in the cold-flow model experiments as well as the flow rate used in the steady-state F-T synthesis experiments (411 actual mm^3/sec).

Table 5.2 summarizes calculated minimum fluidization velocities for gases of interest at conditions of interest. The values obtained for helium and argon correspond to observed values of minimum fluidization velocity in the cold-flow model.

The photographs in Figure 5.45 show that the catalyst bed actually lifts off from the distributor plate as the microreactor vibrates. In addition, catalyst particles can be seen airborne at the top surface of the catalyst mass. There is an intense circulation of catalyst particles in the reaction zone at this point. Also note that the bed slants toward one end of the reaction zone. At low gas velocities, this tends to happen, unless the microreactor was perfectly level and the tension on all three flexible metal hoses as well as on the leaf-springs are equal.

As the linear gas velocity through the catalyst bed is increased, the bed height begins to level out and then oscillate. Oscillation usually occurs at gas velocities greater than one-half of the minimum gas-fluidization velocity. Figure 5.46 shows the vibrofluidized bed as it oscillates. In this picture, the left-hand side of the bed is falling as the right-hand side is rising. In turn, the left-hand side will strike the distributor plate and start to rise as the right-hand

TABLE 5.2

Calculated Miminum Gas-Fluidization Velocities for Gases Used in the Cold-Flow Microreactor Model and Fischer-Tropsch Synthesis Microreactors (Refer to Appendix A for Method of Calculation).

Gas	Conditions		Minimum Gas-Fluidization Velocity, v_ε (m/s)	Flow Rate Corresponding to v_ε (actual mm^3/s)
	Temperature (°C)	Pressure (kPa)		
Helium	20	101	0.22	17,700
Argon	20	101	0.24	19,200
Hydrogen	400	2,230	0.29	23,300
Carbon Monoxide	400	2,230	0.08	6,390

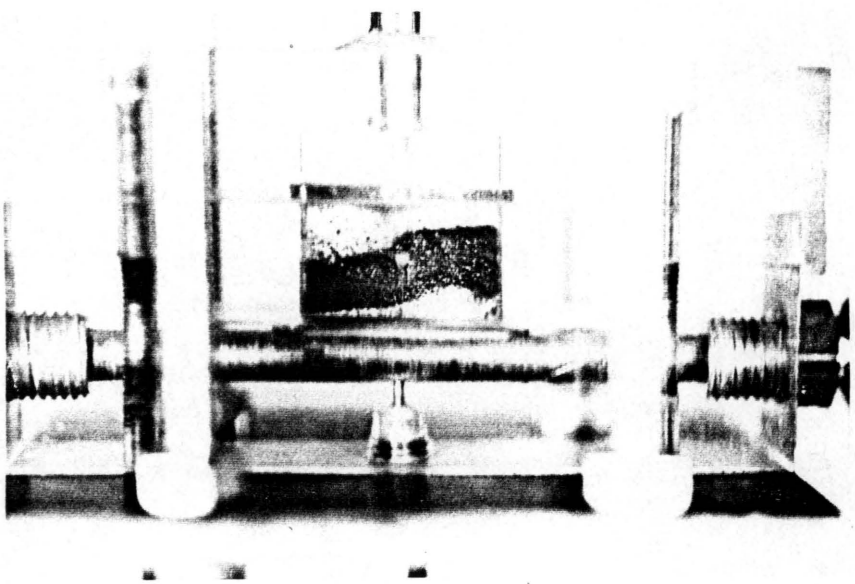

Figure 5.46. The Oscillation of a Vibrofluidized-Bed of Fused-Iron Catalyst.

side peaks out and begins to fall. One full bed-oscillation cycle involves two cycles of the distributor plate. This suggests that the bed oscillates at approximately 12 cycles per second. In real time, the alternate rising and falling of the two sides of the catalyst bed produce the illusion of a half-cycle cosine wave. Indeed, at slightly higher velocities, a full-cycle sine wave has been observed.

As the gas velocity through the catalyst bed surpasses the minimum gas-fluidization velocity, the bed technically is classified as a vibrated fluid-bed rather than a vibrofluidized bed. Figure 5.47 shows a series of pictures taken of the vibrated fluid-bed. The catalyst bed has become more dilute and bubbles can sometimes be identified. The bed continues to strike the distributor plate and then lifts off from it. As can be seen in these photographs, the bed has expanded to the point of nearly filling the entire reaction zone. Velocities above the minimum gas-fluidization velocity are much too high to be considered for use in the F-T synthesis studies presented here. Vibrofluidized beds, such as those shown in Figures 5.45 and 5.46, allow for the use of low feed-gas velocities, while the intense particle mixing of a gas fluidized-bed is still obtainable.

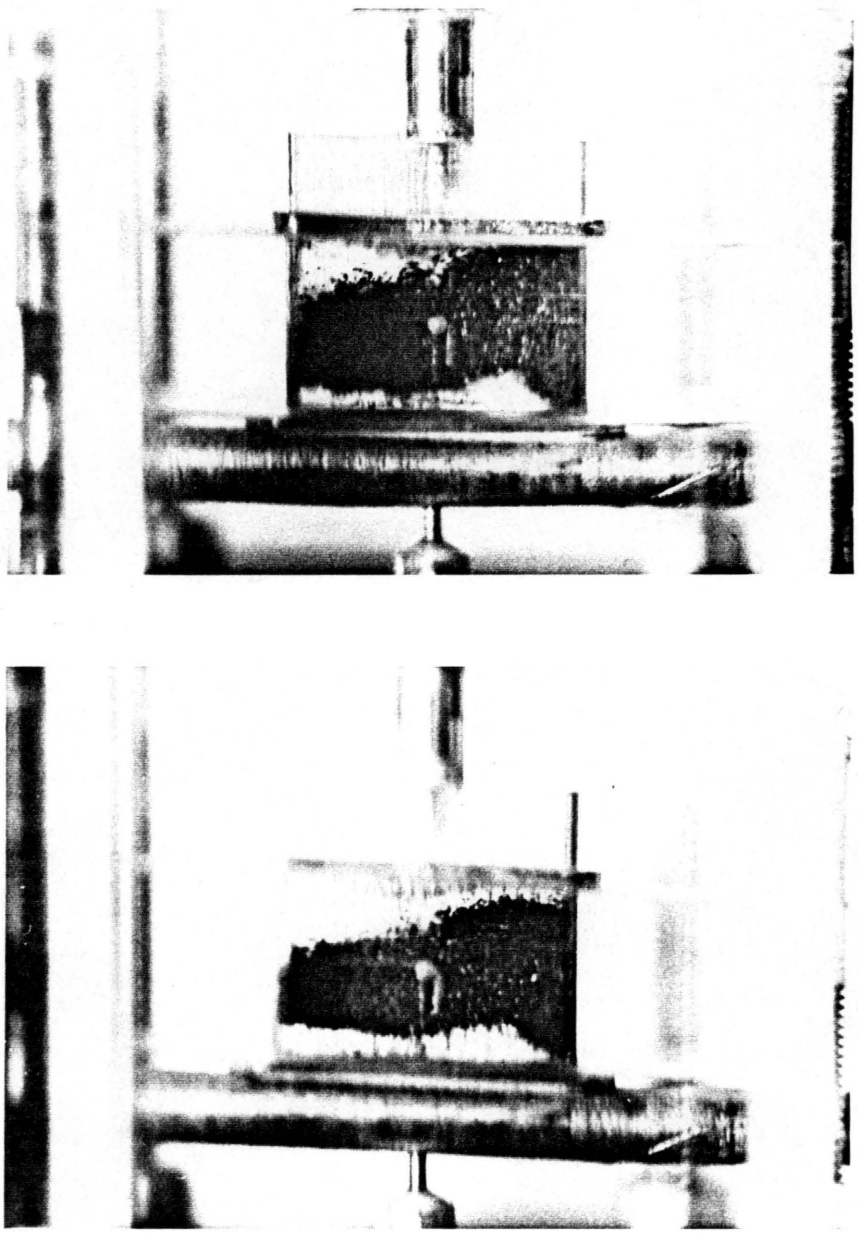

Figure 5.47. A Vibrated Fluid-Bed of Fused-Iron Catalyst. The Gas Velocity Is Above the Minimum Gas-Fluidization Velocity.

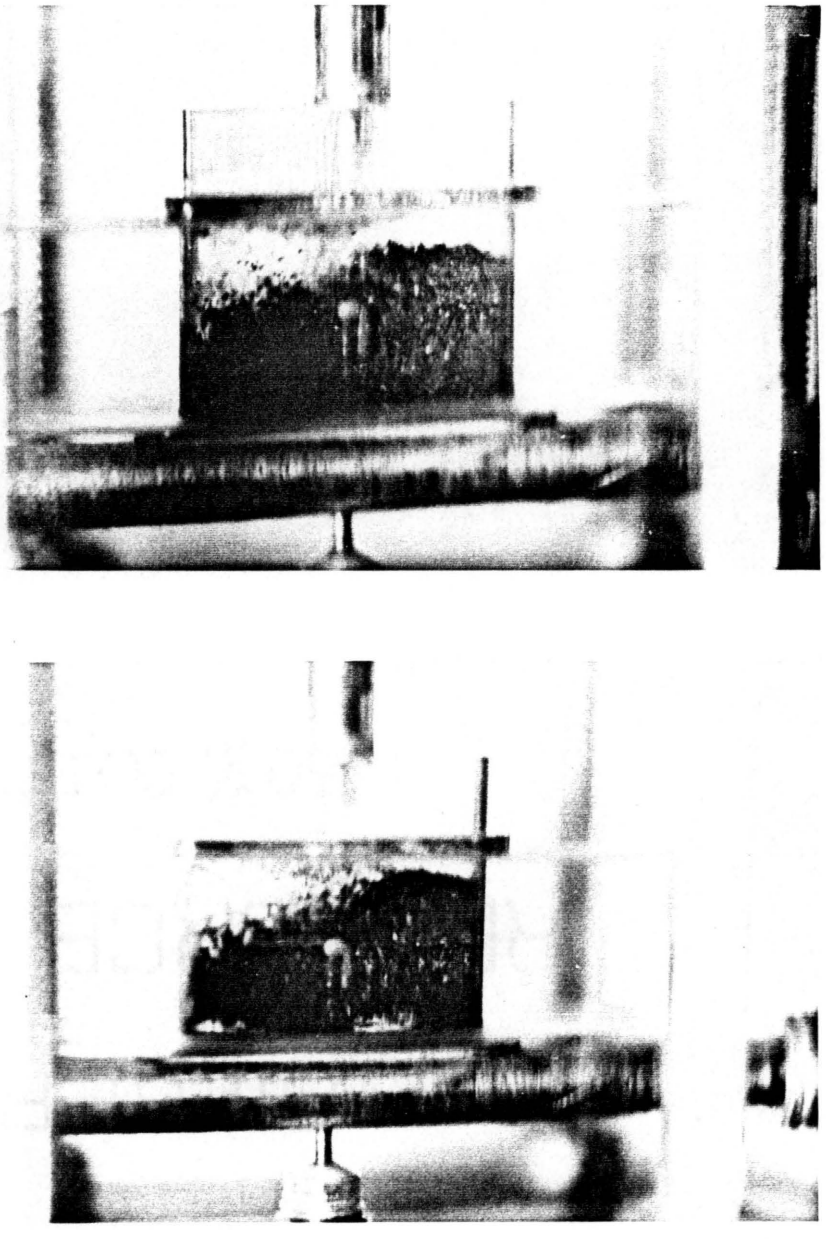

Figure 5.47. (Continued)

CHAPTER 6

DESIGN AND CONSTRUCTION OF A VIBROFLUIDIZED-BED MICROREACTOR SYSTEM FOR UNSTEADY-STATE FISCHER-TROPSCH SYNTHESIS

6.1 Experimental Apparatus and Procedure

6.1.1 Experimental Apparatus

A vibrofluidized-bed microreactor system was designed and constructed for the study of unsteady-state Fischer-Tropsch synthesis. The goal was to provide for rapid feed-gas switching on the order of seconds at temperatures approaching 400°C and pressures of 2,220 kPa (323 psia). In order to do this, a microreactor system similar in concept to the cold-flow sliding-plug vibrofluidized-bed model was constructed.

The purpose of the study was to rapidly switch between a feed gas of a high H_2/CO ratio (F-gas) and another feed gas of a low H_2/CO ratio (S-gas) so as to simulate the residence time of the iron catalyst in the supernatant and fluidizing zones of a "heat-tray" reactor (see Figure 1.1). The effect of catalyst exposure to the rapidly changing partial pressures of hydrogen and carbon monoxide will be studied with emphasis on reduction of the rate of carbon deposition.

Figure 6.1 shows two photographs of the system. Figure 6.2 is a schematic diagram of microreactor system.

Hydrogen and a premixed synthesis gas containing hydrogen, carbon monoxide and argon enter the system through high-pressure regulators (Airco model 49). The feed gases, "F-gas" and "S-gas", then pass through an activated-carbon filter used to remove impurities. The carbon filters

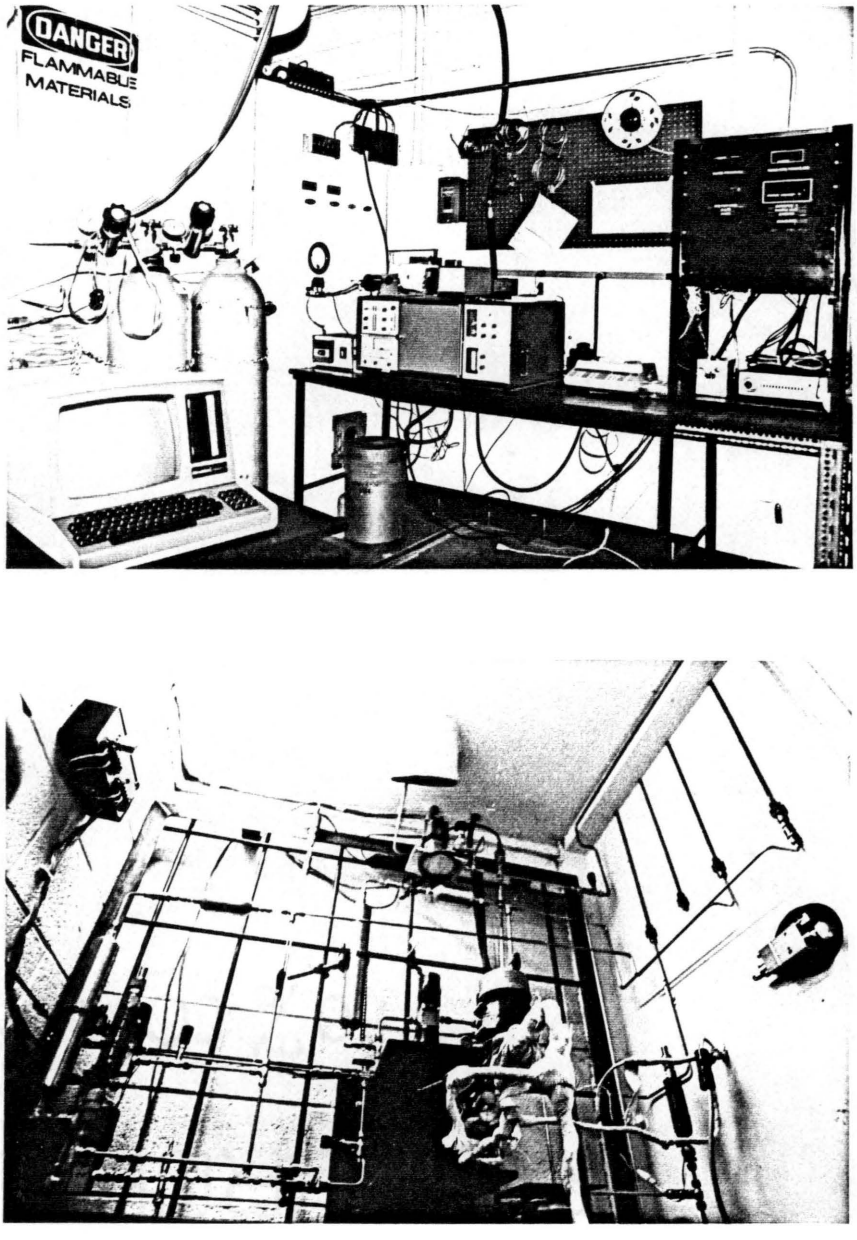

Figure 6.1. Photographs of a Sliding-Plug Vibrofluidized-Bed Microreactor System for Unsteady-State Fischer-Tropsch Synthesis.

Top: Control and Analysis Systems.
Bottom: Microreactor System.

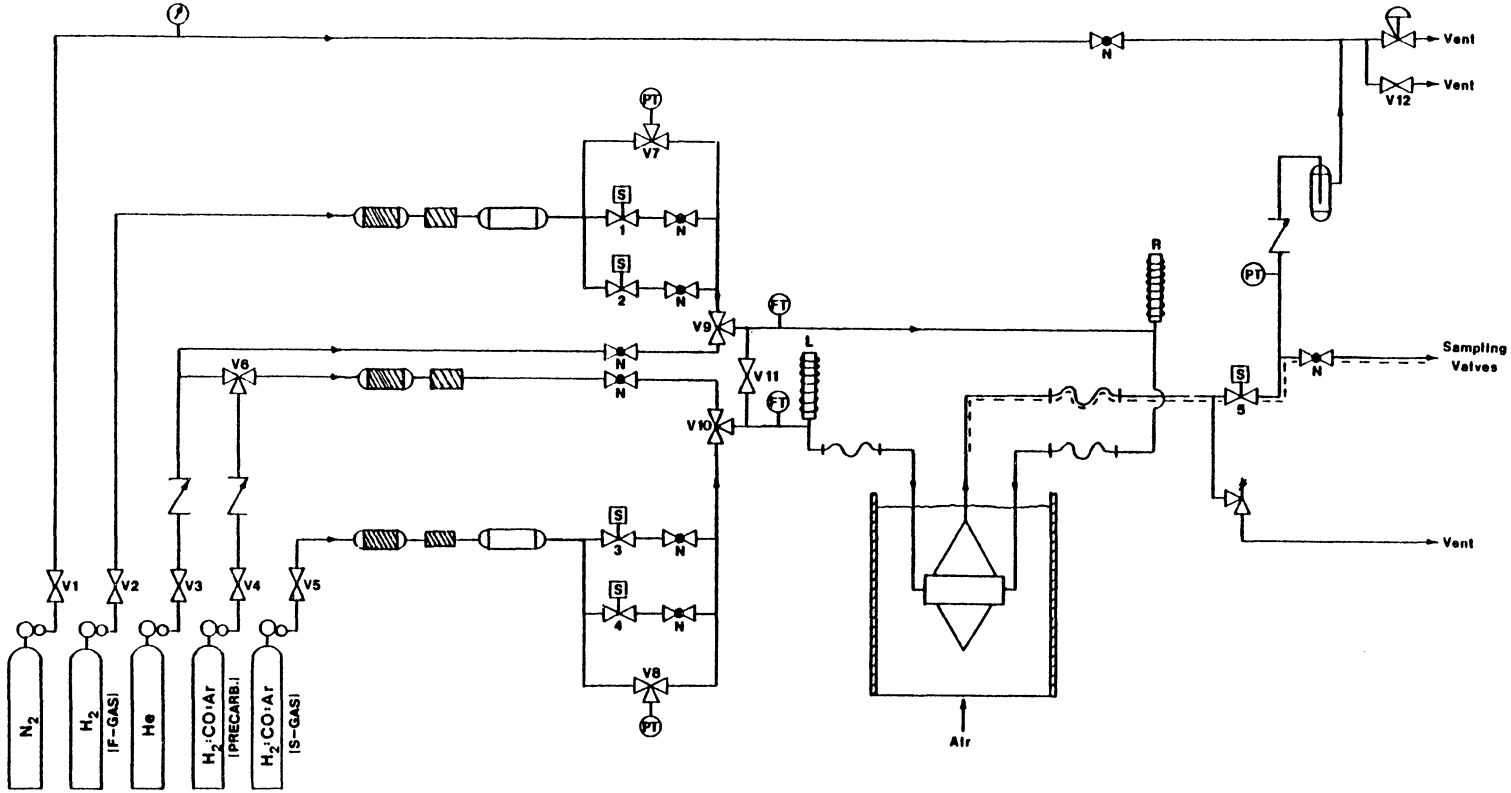

Figure 6.2. A Sliding-Plug Vibrofluidized-Bed Microreactor System for Unsteady-State Fischer-Tropsch Synthesis. (See Figure 4.1b for Equipment Symbols).

are followed by a 15-micron sintered stainless-steel element filter which protects the downstream equipment, such as needle and solenoid valves. Two 1000-ml sample cylinders (304- stainless-steel) act as reservoirs, storing the gas upstream of solenoid valves 1-4.

Two-way, normally-closed, high-pressure, stainless-steel solenoid valves manufactured by Circle Seal Controls (model SV10) control the flow of feed gases to the microreactor. The needle valves associated with these solenoid valves are low-flow stainless-steel types made by Nupro. Series SG needle valves are used in conjunction with solenoid valves 1 and 3, and are typically only used for gas purging before an experiment. Series SGD double-needle valves associated with solenoid valves 2 and 4 are used to set feed-gas flow rates in conjunction with a thermal mass flow meter (Brooks model 5810). The range of this flow meter is 0-2000 standard cm^3/min. A critical pressure drop is again maintained across the needle valves so that feed-gas flow rates are independent of downstream pressures.

Three-way valve V9 allows helium to be directed to the sliding-plug microreactor for gas purging before and after an experiment. Similarly, three-way valve V10, in association with three-way valve V6, can be used to direct helium for purging, or a feed gas of high H_2/CO ratio for precarburization of the catalyst to the microreactor. A manual shut-off valve V11, connects the two feed streams that lead to the microreactor. This valve is opened only before and after, but never during an experiment. Its purpose is to produce a balanced pressure across the sliding-plug during the purging procedure.

Three-way valves V7 and V8 allow selection of either the pressure upstream or downstream of the needle valves. Pressures are monitored at these points using absolute-pressure transducers of the strain-gage type (Schaevitz Model P721) with a range of 0-6,893 kPa. The sliding-plug microreactor is suspended into a constant-temperature bath (Techne SBL-2D) as described in Section 4.1.1.

Flexible stainless-steel hoses connect the vibrating sliding-plug microreactor to the stationary feed-gas lines and solenoids. A 0.356-mm stainless-steel wire connects the plunger inside each solenoid, labeled by L and R in Figure 6.2, to the sliding plug in the plenum zone of the microreactor. Feed gases enter this section of the system at a "tee"-union directly below the solenoids.

The product-gas exit section of the microreactor is identical to that for the steady-state system described in Section 4.1.1. Product gases exit the reactor via a stainless-steel line heated to 200°C. Solenoid valve 5 is a high-temperature, high-pressure, normally-closed stainess-steel valve manufactured by Atkomatic Solenoid Valves. This solenoid valve is held open continuously during catalyst reduction and synthesis.

An over-pressure relief valve (Nupro model 4CA) set for 4,135 kPa has been placed upstream of solenoid valve 5 as a safety precaution. A small amount of product gas is drawn off continuously via a double-needle valve (Nupro SGD) and a 1/16-inch O.D. stainless-steel tube. This line is heated to 200°C and reduces the gas to nearly atmospheric pressure before it flows through the sampling valves associated with the gas chromatograph. After

passing the sampling point, the product gas goes through a check valve and into a liquid trap.

The system pressure is maintained at 2,220 kPa through the use of a back-pressure regulator manufactured by Circle Seal Controls (model BPR-8A). Nitrogen is used as a ballast gas in order to maintain a constant system pressure as described in Section 4.1.1. Valve V12 is a manual shut-off valve used to bleed down the system pressure at the end of an experiment.

All equipment and tubing in contact with hydrogen or synthesis gas are constructed of either 304- or 316- stainless steel. The solenoid plungers and stops are made of 416- stainless steel which is magnetizable. Regulators and tubing coming in contact with only helium or nitrogen are made of brass.

In general, all tubing is 316- stainless steel, 1/4-inch O.D. with a 0.035-inch wall thickness. The maximum safe working pressure of this system at 21°C is approximately 7,000 kPa.

6.1.1.2 A Sliding-Plug Vibrofluidized-Bed Microreactor

The design and construction of the sliding-plug vibrofluidized-bed microreactor for F-T synthesis is based in part on the design of the steady-state microreactor (Section 4.1.1.2) and in part on the design of the cold-flow model (Section 5.1.1.2). Figure 6.3 shows photographs of the microreactor. Figures 6.4 and 6.5 are schematic cross-sectional front and side views of the sliding-plug microreactor.

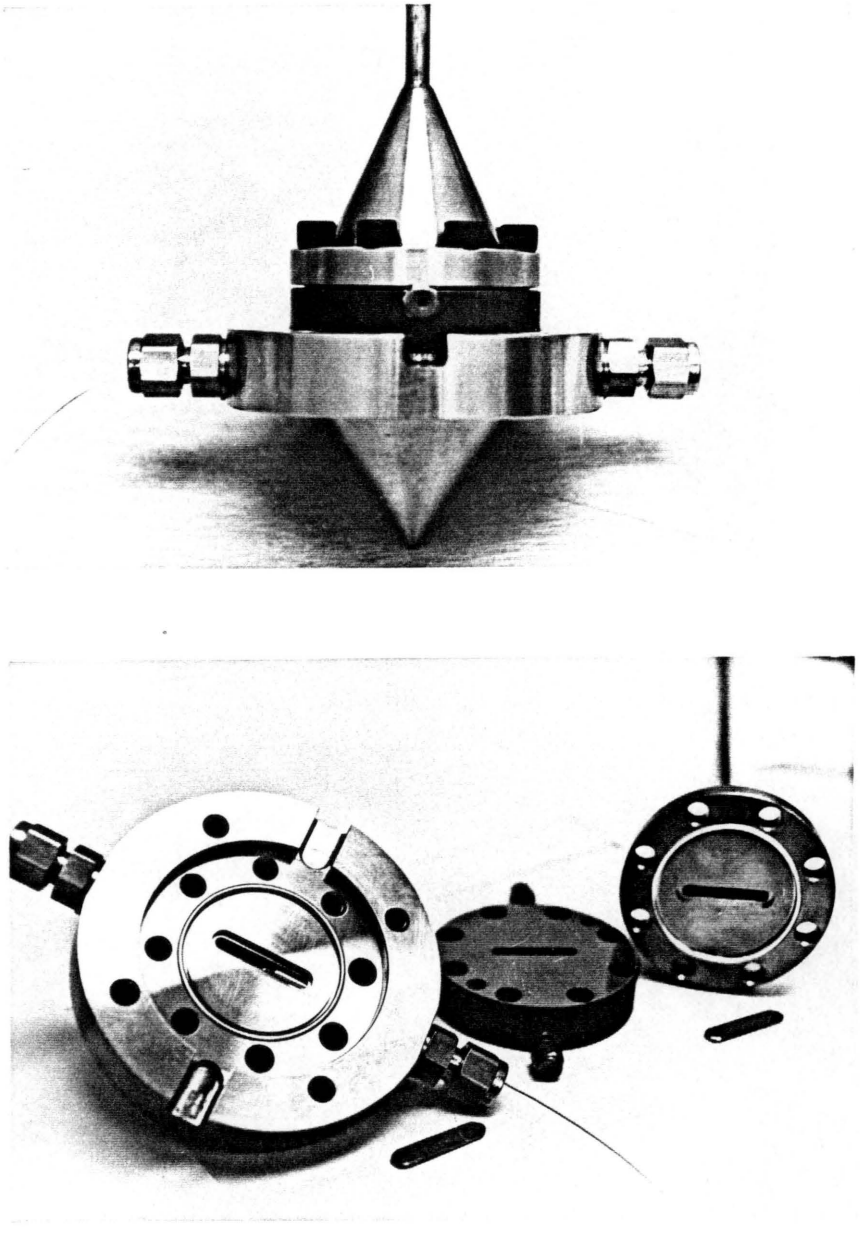

Figure 6.3. Photographs of the Sliding-Plug Vibrofluidized-Bed Microreactor for Unsteady-State F-T Synthesis: (a) The Assembled Microreactor Less Feed-Line Tubing; (b) The Microreactor Base Section, Reaction Section and Gas-Exit Section.

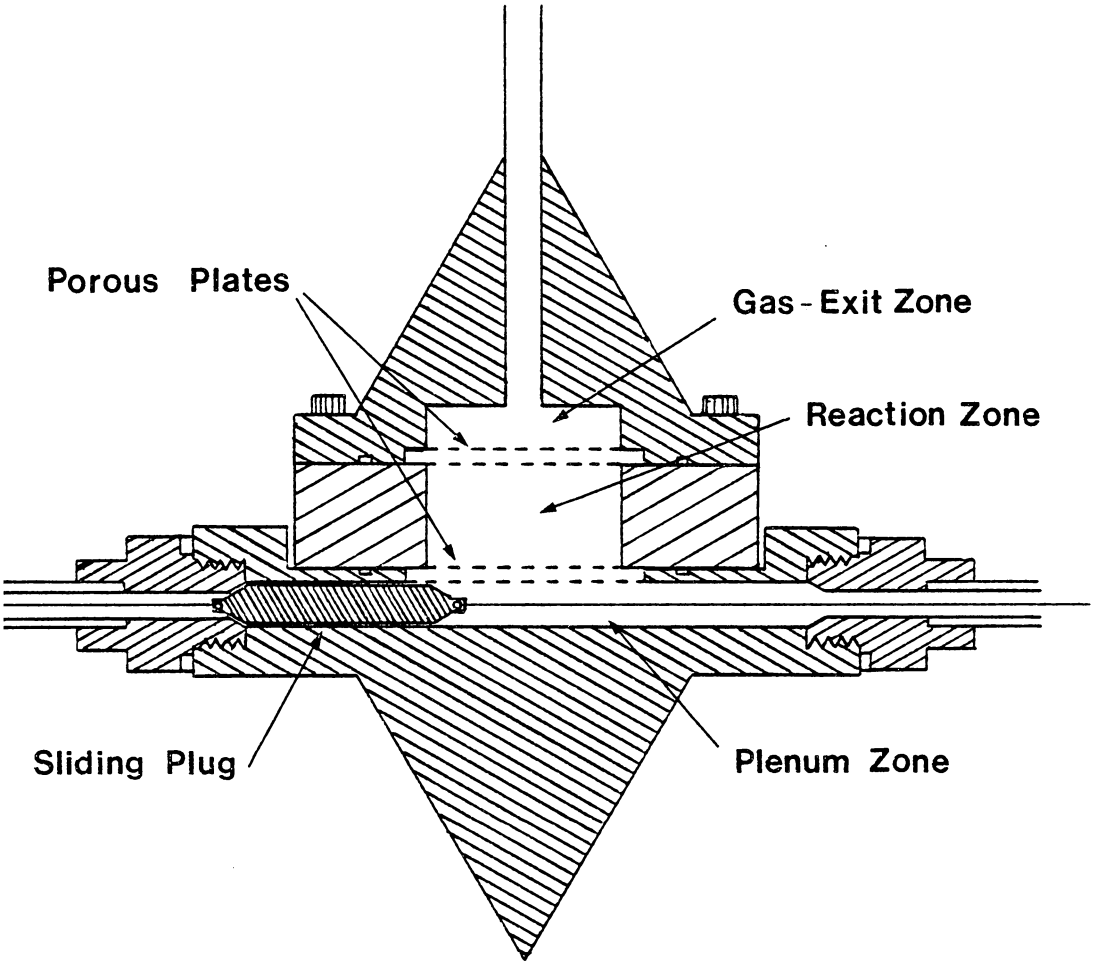

Figure 6.4. A Schematic Cross-Sectional Diagram of the Sliding-Plug Microreactor. (Front View).

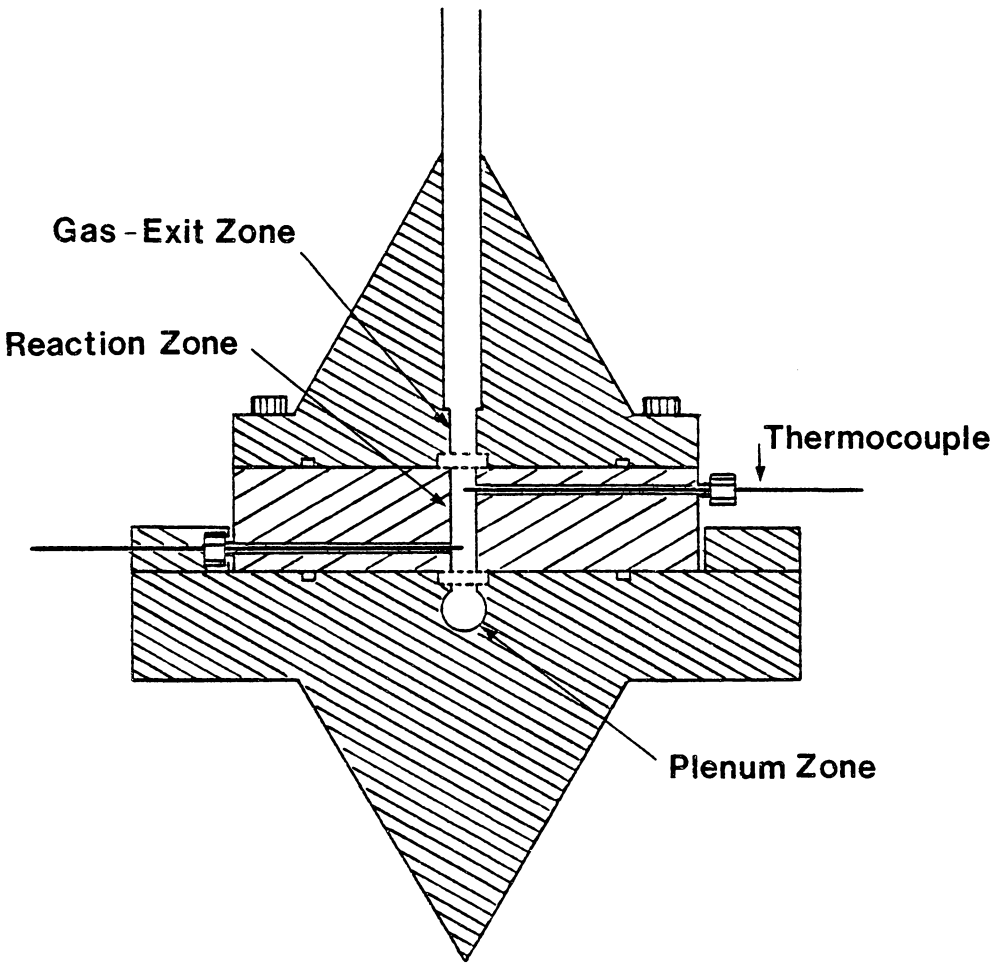

Figure 6.5. A Schematic Cross-Sectional Diagram of the Sliding-Plug Microreactor. (Side View).

As before, the microreactor consists of three sections: (1) the base (plenum) section, (2) the reaction section; and (3) the product-gas exit section.

The base section consists of a 6.35-mm hole drilled horizontally through the conically shaped piece of 316- stainless steel. The center line of the hole lies 4.76 mm below the top surface of the base section. A 3.175-mm wide slot, 24.5-mm long, has been milled down into the drill hole from the top. A wider slot, 6.35-mm wide and 31.75 mm in length, has been milled 1.59-mm deep along the same line as the 3.175-mm wide slot. This creates a lip 3.175-mm wide around the smaller slot. This lip supports a 2-micron sintered stainless-steel distributor plate. Both slots have rounded ends as shown in Figure 6.3.

The horizontal drill-hole in the base section is, as before, the plenum zone. The plenum zone is 76.20 mm in total length. The material surrounding each end of the plenum has been tapped with straight threads. A straight-thread male connecter (Swagelok 7/16-20) is screwed into each end. These connectors serve as plug stops for the sliding plug in the plenum zone. The inner surfaces of the connectors have been tapered to approximately a 30-degree angle to mate with the sloping plug.

A gas-tight seal is maintained between the connector and the base section through the use of a copper washer. The washer thickness has been selected so that when the connector is tight, the inner end will just be touching the end of the plenum.

The sliding-plug itself is made of 316- stainless steel 6.22 mm in diameter and 34.93 mm in total length. A small hole has been drilled in each end of the plug to allow for connections to the solenoid plungers via a 0.356-mm stainless-steel wire.

The reaction section of the microreactor is made from a piece of 316- stainless steel, 63.50 mm in diameter and 14.29-mm thick. A 3.175-mm wide slot, 25.4-mm long, has been milled in the reaction section, creating the "reaction zone." As seen in Figure 6.5, two thermocouples monitor the temperature in the reaction zone. Two holes, 1.59 mm in diameter, have been drilled perpendicular to the length of the reaction-zone slot. 1/16-inch Swagelok stainless-steel male connectors have been modified and welded to reaction section.

A type "J" thermocouple with a 1/16-inch O.D. stainless-steel sheath has been inserted through each connector into each hole. In this way, a gas-tight seal is maintained. The thermocouples are 635.0 mm in total length and are attached to connectors outside of the constant-temperature bath. One thermocouple enters the reaction zone 3 mm above the distributor plate and the other 3 mm below the catalyst retention plate. Therefore they are approximately 8.29 mm apart.

The gas-exit section of the microreactor is conical in shape. A slot, 3.175-mm wide and 25.4-mm long, has been milled to a depth of 7.94 mm in this section. As is similar to the base section, a recessed area has been machined to accept a sintered stainless-steel catalyst retention plate (1.59-mm thick and 20-micron type). The recessed area is 6.35-mm wide and 31.75-mm long, with rounded ends creating a

small lip for the plate to rest on. A 1/4-inch O.D. stainless-steel tube with a 0.035-inch wall thickness has been inserted down from the top, and it breaks through the slot in the gas-exit section. This tube has been welded at the peak of the cone to insure a leak-proof seal.

The reactor maintains a gas-tight seal even against hydrogen through the use of two silver-plated stainless-steel O-rings. The O-rings are part number MS9373-047 as supplied by American Seal and Engineering Co. An O-ring groove has been machined into the base and gas-exit sections of the microreactor. Each groove is 44.69 mm ±0.06 mm O.D., 39.70 mm I.D. and 1.13 ±0.06 mm deep. Eight 1/4-28 cap screws provide enough clamping force to smash the O-ring in their grooves. The base section has been tapped to accept these screws. The gas-tight seal is created by the gas pressure, forcing the O-ring against the outer surface of the groove and against the mating surface. The silver plating tends to fill any defects and prevents hydrogen from leaking.

The vibrating system is identical to the one described in Section 4.1.1, with the exception of the way in which the threaded rods are attached to the microreactor. In the sliding-plug microreactor, 1/4-inch threaded rods are screwed directly down into tapped holes in the base section. Figure 6.3 shows these four holes.

6.1.1.3 Solenoids

The solenoids controlling the movement of the sliding plug are an integral part of the microreactor system. Figure 6.6 shows a schematic cross-sectional view of a solenoid.

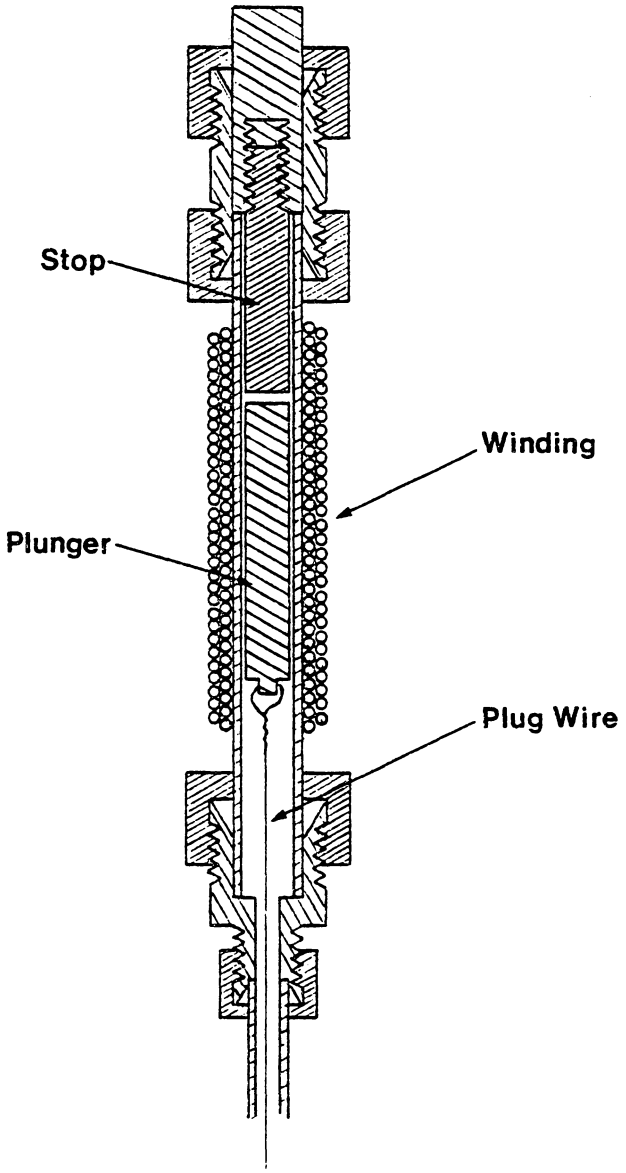

Figure 6.6. A Schematic Cross-Sectional Diagram of a Solenoid Used to Actuate the Sliding Plug.

The solenoid consists of a 187.3-mm long piece of 1/2-inch O.D. 316- stainless-steel (non-magnetizable) tubing with a 0.049-inch wall thickness. The winding is 111 mm in length and it starts 44 mm from the bottom end of the tube. It contains 2,880 turns of 23 AWG cooper-solenoid-winding wire, producing a force of 1.33 N at the start of the plunger stroke. The solenoid is connected at the base to a 1/2-inch to 1/4-inch Swagelok reducing union. This union serves as the resting point of the plunger when the solenoid is de-energized. When the plunger is in this position, approximately the top 22 mm is in the winding area.

At the top of the solenoid, an adjustable plunger stop extends down into the solenoid winding. The stop consists of a 10.0-mm diameter piece of 416- stainless steel (non-magnetizable) threaded into a 6.35-mm O.D. piece of 316- stainless steel. The stop serves to redirect the flux lines of the magnetic field so that the magnetic force at the end of the plunger stroke is greatly increased. This serves, in turn, to pull the sliding plug in the microreactor firmly against its seat. The plunger stop is fixed to the solenoid by a 1/2-inch stainless-steel Swagelok union. In this way, the solenoid can be used at high pressure with no gas leakage and the stop can still be adjusted.

The plunger itself is a piece of 416- stainless-steel rod, 76.2-mm long and 10.0 mm in diameter. Two grooves, 3.18-mm wide and 1.27-mm deep, run the length of the plunger. These grooves keep gas from building up in front of the plunger as it moves. The lower end of the plunger has a nipple to allow for attachment of the wire from the

sliding plug. The wire connecting the plungers to the sliding plug runs down from the plunger, around a 90-degree bend and through the flexible stainless-steel hose. After passing through the flexible hose, the wire goes through two more 90-degree bends and finally attaches to the plug. The feed gas enters the tubing just below the solenoid at a tee union. Therefore, the wire does not go around any sharp corners, but only 90-degree tubing bends. "Flexing" of the flexible hose during vibration causes no ill effects and the plug remains seated.

As in the cold-flow model, the solenoids are powered by a 24-VDC supply and are conencted to a relay. The latter acts to alternately energize the solenoids. Therefore, one solenoid is energized while the other is de-energized. The relay is controlled via the computer interface and the H-89 microcomputer.

6.1.1.4 Associated Systems

The product-gas sampling system and the gas-chromatographic system, used in conjunction with the sliding-plug vibrofluidized-bed microreactor system are identical to the systems described in Sections 4.1.1.3 and 4.1.1.4.

6.1.2 Materials

The sliding-plug vibrofluidized-bed microreactor system for unsteady-state F-T synthesis was designed with the use of -150+300 μ fused-iron ammonia-synthesis catalyst as described in Section 4.1.2.1. However, this system does not preclude the use of other size fractions or new types of catalysts.

Gases being used with this microreactor system are similarly described in Section 4.1.2.2.

6.1.3 Experimental Procedures

6.1.3.1 Microreactor Cleaning and Catalyst Loading

The procedure to be followed when cleaning and loading the sliding-plug vibrofluidized-bed microreactor is very similar to the procedure used for the steady-state vibrofluidized-bed microreactor.

First, however, the sliding plug had to be removed from the plenum zone. This was accomplished by removing the two Swagelok male connectors that screw into the base section of the microreactor and serve as plug seats. The mating surface of the three microreactor sections were then polished with number 500 emory cloth on a surfacing table. The entire interior surface of the microreactor was flushed with acetone and wiped with Kimwipes.

After the microreactor was thoroughly cleaned, the base section was placed in the wooden support apparatus and clamped in the vise. Appoximately 1 meter of the 0.356-mm diameter stainless-steel wire was then attached to each end of the sliding plug. The plug was slid into the plenum zone; and the wire was threaded through the washers and the Swagelok male connectors. A small amount of "Silver Goop" thread lubricant was applied to the threads of the connectors to prevent seizing and to facilitate later removal. The male conenctors were then tightened, compressing the copper washer.

The wire was threaded through the 1/4-inch O.D. stainless-steel tubing that is used to connect the microreactor to the flexible stainless-steel hose. Each piece of tubing has two 90-degree bends and is attached to the Swagelok fitting-end of the male connector in the base of the microreactor. Thread lubricant is also applied to the fitting threads which are exposed to the high temperature in the constant temperature bath.

Following the installation of the sliding plug, a new 2-micron sintered stainless-steel plate was made and positioned into the distributor plate recess in the base section. A thin, oval-shaped, Grafoil gasket was then placed on top of the distributor plate. This gasket prevents any gas from bypassing the distributor plate by sealing between the edges of the plate and the microrector base-section.

A silver-plated stainless-steel O-ring was then inserted into the O-ring groove and the reaction section of the microreactor was installed. One gram of -150+300 micron fused-iron catalyst was weighted and carefully poured into the reaction zone. The thermocouples were typically left in place in the reaction section between experiments.

A 20-micron, sintered stainless-steel catalyst retention plate was fitted to the gas-exit section as was a silver plated O-ring. The gas-exit section was placed on top of the reaction section. Thread lubricant was used on the bolts that clamp the three sections (i.e., base section, reaction section, and gas-exit section) together and these bolts were torqued in sequence to 27 N-m.

6.1.3.2 Mounting the Microreactor

Once the microreactor was cleaned and loaded with fresh catalyst, it was ready for attachment to the rest of the system. Four threaded rods were screwed into the tapped holes in the base section.

The microreactor was lowered into the cool fluidized-bed constant-temperature bath. These rods were, in turn, bolted to the leaf-spring supports. The two stainless-steel plug wires, eminating from the microreactor feed tubes, were then carefully threaded up through the flexible metal hose and tubing to the solenoid mounting position. In order to do this, guide wires had to be used. The compression fittings between the flexible metal hose and the microreactor feed and gas-exit lines were then tightened. The thermocouples from the microreactor were then connected to the panel meter.

At this point, the vibrator itself was mounted to the underside of the I-beam support and connected to the microreactor support system. The frequency generator was then adjusted to the point where the microreactor was vibrating at the maximum amplitude. This usually corresponded to a resonance frequency of 18-24 Hz with a peak-to-peak amplitude of 4 mm. The solenoid plungers were next attached to the plug wires. The plug was first drawn up tight against the left-hand plug stop by pulling on the plug wire.

The plunger was next attached to the plug wire 57.2 mm up from the point where the reducing union expands from 1/4- to 1/2-inch. Note that the reducing union serves as the resting point of the plunger when the solenoid is de-energized. In addition, the stroke of the plug in the

plenum is 50.8 mm. Consequently, when the solenoid is de-energized, there should be approximately 6.4 mm of slack in the plug wire. This provides enough slack so that the plunger in the de-energized solenoid does not keep the plug from resting on the opposite plug-seat.

After attaching the left plunger, the left solenoid was slipped down over that plunger and attached to the reducing union. The right-hand plunger and solenoid were then installed in a similar fashion and the solenoid cooling fans were turned on.

The final step in the installation involved optimizing the pulling force at the ends of the plug stroke. This was done by adjusting the length of the plunger stops in the solenoids. These stops were constructed so that they could be adjusted to make up for any difference in plug-wire length between experiments.

6.1.3.3 System Startup and Catalyst Reduction

Before an experiment, the mass-flow meters as well as the pressure transducers were calibrated. The system was then pressure-tested at 3,446 kPa for possible leaks. The portion of the system located downstream of needle valves 1-4 (Figure 6.2) was thoroughly flushed with helium. This was done by directing three-way valves V6, V9 and V10, so that helium could flow through them. Shut-off valve V11 was opened so as to keep the pressure on either side of the sliding plugs equilized. Valves V3 and V12, and solenoid valve 5 were opened, allowing helium to flow. The solenoids were then alternately switched moving the plug

back and forth. Valve V12, parallel to the back-pressure regulator, was closed and the system pressure downstream of solenoid valves 1-4 was brought up to 2,220 kPa using helium.

The F-gas feed line located upstream of solenoid valves 1 and 2 was pressurized to 4,807 kPa, as was the S-gas feed-line located upstream of solenoid valves 3 and 4. During an experiment, three-way valves V7 and V8 were always turned so that the downstream pressure was monitored. If these valves are turned from their upstream position to the downstream position during an experiment, a burst of gas will be transmitted through the microreacor.

At this point, the nitrogen ballast-gas flow was started by opening valve V1 and adjusting the associated needle valve. The back-pressure regulator was adjusted so that a downstream system-pressure of 2,220 kPa was maintained. The helium flow was stopped by shutting valve V3 and solenoid valve 5.

The next major step involved setting the F-gas, S-gas, percarburizing and reducing gas flow rates through the microreactor. The S-gas flow rate was set first. Three-way valves V9 and V10 were directed toward the F-gas and S-gas feed-lines and shut-off valve V11 remained open. The right solenoid, R, was activated, causing the plug to rest against the right-hand stop. Solenoid valves 3, 4, and 5 were then simultaneoulsy opened, purging the reactor with S-gas at 6.67×10^4 standard mm^3/s for one minute. Solenoid valve 3 was closed and the system pressure was allowed to stabilize for several minutes with a low

flow of S-gas. Valve V11 was then shut, isolating the F-gas and S-gas feed lines.

The needle valve associated with solenoid valve 4 was adjusted so that the mass-flow meter was reading the desired value for the S-gas flow rate. Solenoid valve 4 was closed and three-way valves V6 and V10 were turned so that the H_2:CO:Ar precarburizing-gas mixture was flowing through the microreactor. Valve V11 was temporarliy opened to assure pressure equilization across the sliding plug and then closed.

The flow rate of precarburizing gas was then set using the appropriate needle valve and the mass-flow meter. The pressure upstream of the precarburizarion needle valve was kept at 4,807 kPa in order to maintain a critical pressure drop. The precarburization flow was stopped by directing three-way valve V10 toward the S-gas feed line.

The reducing-gas flow rate was set in a similar fashion to the S-gas flow rate. Hydrogen was used as both F-gas and the reducing gas. Different flow rates of hydrogen were used during reduction and unsteady-state synthesis. Consequently, the needle valve associated with solenoid valve 2 had to be adjusted accordingly after the catalyst reduction period.

After the downstream system was purged with hydrogen and the reduction flow was set to 3,670 standard mm^3/s, the fluidized constant-temperature bath was heated to 450°C and the heating tapes were turned on. The bath-heating period took approximately two and one-half hours. The actual reduction period consisted of six hours of isothermal reduction of the catalyst at 450°C. At the end of the reduction period,

the hydrogen flow rate had to be adjusted. Hydrogen was used as F-gas in the later stages of the unsteady-state experiment. Its flow rate, however, must be set during a period when it is flowing steadily. As the final step in the reduction period, the temperature of the fluidized constant-temperature bath was lowered to that desired for the precarburization and unsteady-state synthesis experiments.

6.1.3.4 Precarburization and Unsteady-State Synthesis

Precarburization of the reduced fused-iron catalyst was used as a means of creating a bulk carbide structure before unsteady-state synthesis began. In this way, different unsteady-state experiments could be performed from a common starting composition of catalyst, and the rate of carbon deposition could be more easily determination. After the fused-iron catalyst had been reduced, precarburization was initiated simply by closing solenoid valve 2 and then simultaneously activating the right solenoid and turning three-way valve V10 toward the precarburization stream.

The precarburization gas typically used was a synthesis gas of a 4:1 H_2/CO ratio with a small percentage of argon. Argon was used as an internal standard for gas-chromatographic analysis.

At the start of precarburization, the microcomputer program, which contains the sampling-valve timing loops, was started. After the first twenty minutes of precarburization, a light gas sample was automatically flushed into the gas chromatograph. Seventeen minutes later, all light gas compounds of interest had eluted and the microcomputer switched the sampling valve, backflushing the packed column. This process was

repeated every 37 minutes throughout the precarburization and unsteady-state synthesis portions of the experiment.

After two hours of catalyst precarburization with the 4:1 H_2/CO synthesis gas, the unsteady-state synthesis was started. The flow rates of F-gas and S-gas had been previously set to their desired valves for unsteady-state synthesis. Hence, the only steps required to start unsteady-state synthesis were to switch three-way valve V10 toward the S-gas feed-line and to run the solenoid-switching microcomputer program. The program, used to slide the plug and switch between solenoid valves 2 and 4, is presented in Appendix C.

When solenoid valve 2 was opened, the plug was simultaneously pulled to the left. When solenoid valve 4 was opened, the sliding plug was pulled to the right. The program allowed control of the sliding plug and solenoid valves to within hundredths of a second. The response times of the solenoid valves, however, were only on the order of one-tenth of a second. As stated earlier, light gas samples were taken every 37 minutes during the unsteady-state gas pulsing. The volume of the tubing between the reaction zone and the sampling point is approximately 30 times the volume of the reaction zone itself. Therefore, the exit-gases should be well mixed by the time they reach the sampling valves. As in the steady-state experiments, gas samples to be separated using the capillary column were taken only at the end of an experiment. The gas chromatograph oven was cooled to -20°C and a sample was then flushed onto the capillary column. The column was held at -20°C for 2 minutes and then temperature programed to 150°C at 4°C/min.

6.1.3.5 System Shut-Down

At the completion of the unsteady-state reaction period, it was desirable to rapidly stop the reaction by flushing the sliding-plug microreactor and feed-gas lines with helium. This was done by first stopping the computer program and making certain that solenoid valves 2 and 4 were closed and 5 was open. Valve V11 was then rapidly opened and three-way valves V6, V9 and V10 were switched so that helium was flowing through the microreactor.

As helium flowed through the microreactor, the nitrogen ballast-gas was shut off. Valve V12, parallel to the back-pressure regulator, was slowly opened over the course of several minutes. During this period, the plug was slid back and forth several times to insure purging of both feed lines by helium.

Once the system had reached atmospheric pressure, the constant-temperature bath was shut off and the microreactor was allowed to cool. The catalyst was still vibrofluidized as the microreactor cooled. Cooling took place over five to six hours under a maximum helium flow rate of 2,200 standard mm^3/s. The heating tapes were maintained at 200°C during the cool-down period to keep any residual F-T products from condensing in the heated portion of the equipment, including the sampling valves.

6.1.3.6 Catalyst Collection and Analysis

Once the sliding-plug microreactor had been cooled to ambient temperatures, it could be removed from the constant-temperature bath. In order to so this, the solenoids were disconnected from the reducing

unions, and the plug wires were cut, releasing the solenoid plungers. The compression fittings between the flexible hose and the microreactor were disconnected, and the plug wires were removed from these hoses.

The vibrational support apparatus for the microreactor was then unbolted and the microreactor was clamped in the vise. All eight bolts holding the three sections of the microreactor together were removed. The gas-exit section was lifted off with care and the spent catalyst and any bugdust present were removed using the suction-filter apparatus. This procedure was previously described in Section 4.1.3.6.

After the spent catalyst had been meticulously removed and weighed, the sliding plug was removed from the plenum zone. Spent catalyst was stored in vials under nitrogen until being sent for total carbon and iron analyses along with Mössbauer spectroscopic determination of iron-containing phases.

CHAPTER 7

CONCLUSIONS, SIGNIFICANCE AND RECOMMENDATIONS

7.1 Conclusions

Following a review of relevant literature on F-T synthesis, vibrofluidized-beds, and unsteady-state methods for kinetic studies, an experimental investigation into the development of a microreactor system for unsteady-state F-T synthesis was carried out. Steady-state F-T synthesis experiments using a commercial fused-iron catalyst produced information on catalyst defluidization, hydrocarbon product distribution and baseline carbon deposition. Investigations in a cold-flow vibrofluidized-bed microreactor model revealed information on gas mixing in the unsteady-state system. In addition, the cold-flow model allowed observation of characteristics of the vibrofluidized catalyst in the microreactor. In the final stages of the studies, a vibrofluidized-bed microreactor system for unsteady-state F-T synthesis at commercially important reaction conditions was designed and constructed.

The following conclusions can be drawn based on the experimental studies.

1. In a vibrofluidized microreactor system for F-T synthesis under steady-state conditions using a commercial promoted fused-iron catalyst:

   a. Catalyst defluidization occurs within several hours at temperatures below 395°C when using a feed-gas H_2/CO ratio of 2:1 or less.

   b. Catalyst defluidization can be detected through observation of thermocouple temperature fluctuations in the reaction zone.

c. A shift in the probability of chain growth of hydrocarbon products to lower values occurs, as the reaction temperature is increased and as the feed-gas H_2/CO ratio is increased.

d. Bugdust is a fine, black powder produced due to excessive carbon formation which in turn causes physical degradation of the catalyst. Its structure is highly porous and bugdust contains 18-30 weight percent carbon and 50-64 weight percent iron.

e. Discrete fractions of free-flowing catalyst and bugdust (powdery, low-density carbon-rich particles) can be easily collected under conditions where liquid products and waxes do not condense in the reaction zone.

f. The rate of free carbon formation (mainly in the form of bugdust) is much greater when a feed-gas H_2/CO ratio of 1:1 was used than when a higher ratio of 2:1 is used.

2. In a cold-flow vibrofluidized-bed microreactor model for unsteady-state gas feeding:

a. Experiments with a manual 3-way ball valve substituting for the sliding-plug microreactor show quantitative gas replacement after 2.4 seconds at all flow rates investigated.

b. A 20-micron distributor plate induces feed-gas mixing by allowing gas to backflow from the reaction zone to the plenum zone during the sliding-plug movement.

c. The use of a 2-micron distributor plate eliminates the backflow of gas from the reaction zone to the plenum zone during the sliding-plug movement.

d. The geometry of the microreactor induces some mixing of the feed gases, particularly when the gases pass from the reaction zone to the gas-exit zone.

e. More gas-mixing occurs during the transition from argon to helium feeding than during the transition from helium to argon feeding. This is thought to be due to the density differences between the two gases.

f. Vibrofluidization of the catalyst in the reaction zone induces only a small amount of gas backmixing at low feed-gas velocities.

g. The use of high gas flow rates and feed-gas staggering significantly reduces undesirable gas mixing in the microreactor.

3. Experimental characterizations of a vibrofluidized-bed of fused-iron catalyst in a cold-flow microreactor model show that:

   a. The solid mixing is intense, even at very low gas velocities.

   b. At feed-gas velocities somewhat below those for normal gas-fluidization (below the minimum gas-fluidization velocity, U_{mf}) the surface of the vibrofluidized catalyst-bed levels out and begins to oscillate.

4. A vibrofluidized-bed microreactor system for unsteady-state F-T synthesis:

   a. Has been designed and constructed, and it can be operated at commercially important reaction conditions.

   b. Allows for rapid switching of feed gases on the order of several seconds.

5. In order to simulate the catalyst behavior in the freeboard region and the shallow-bed region of a "heat-tray" reactor (Figure 1.1) using the unsteady-state vibrofluidized-bed microractor system:

   a. A flow rate of approximately 1,650 actual mm^3/s should be used. This will permit rapid switching of feed gases over the catalyst in the reaction zone of the microreactor.

   b. A reaction temperature of 395°C is necessary to prevent defluidization of the fused-iron catalyst. This temperature is higher than that desired for operation of a "heat-tray" reactor. Therefore, a means should be developed for reducing the operating temperature in the microreactor, while maintaining a fluidized catalyst.

7.2 Significance of the Results

The development of a vibrofluidized-bed microreactor for both steady-state and unsteady-state catalytic gas-solid reactions has far-reaching significance. Before this development, there was no easy way of accurately determining integral fluid-bed kinetics in a laboratory reactor.

Fixed-bed reactors rely on changes in gas composition over static catalyst particles. Laboratory gas-fluidized-bed reactors require large flow rates of feed gas and therefore deep catalyst beds (requiring large quantities of catalyst) in order to obtain integral conversions.

The unique ability of the new microreactor system to rapidly switch feed-gas flows over an intensely mixed solid makes this development an even more significant contribution to the areas of chemical kinetics and reaction engineering.

7.3 Recommendations for Further Studies

Based on the results of this work, the following recommendations are forwarded for future studies:

1. Repeat the steady-state carbon-deposition experiments utilizing a bifunctional catalyst, such as synthetic zeolite Fe-HZSM-5, in order to eliminate catalyst defluidization caused by accumulation of high molecular-weight products. This will allow for use of lower operating temperatures.

2. Determine the vibrofluidization characteristics of new catalysts in the cold-flow microreactor model.

3. Further explore effective means of improving feed-gas transitions in the unsteady-state cold-flow vibrofluidized-bed microreactor model.

4. Undertake model-reaction studies in the vibrofluidized-bed microreactor system. By examining some simple reactions with well-characterized kinetics, quantitative mixing tests can be performed. Some candidates for such model-reaction studies include hydrogenation of

ethylene (Wynkoop and Wilhelm, 1950) and ethanol dehydration (Bock et al., 1984). These reaction studies could be used to determine heat- and mass-transfer effects in the reaction zone of the microreactor.

5. Experimentally determine the mass-transfer coefficient in the vibrofluidized-bed microreactor. This could be done by studying the sublimation of napthalene in nitrogen as a function of flow rate and particle size.

6. Perform feed-gas-cycling F-T synthesis experiments in the unsteady-state vibrofluidized-bed microreactor system in order to determine carbon deposition rates on: (a) a fused-iron catalyst; and (b) different formulations of Fe-HZSM-5.

REFERENCES

Abdul-Kareem, H. K., P. L. Silveston, and P. R. Hudgins, "Forced Cycling of the Catalytic Oxidation of CO over V_2O_5 Catalyst - I, Concentration Cycling," Chem. Eng. Sci., 35, 2007-84 (1980).

Afanas'ev, A. D., R. A. Buyanov, and V. V. Chesnokov, "Effect of Water Vapor on Coking of Iron Oxides," Kinet. Katal., 23, 5, 1226-30 (1982).

Agrawal, P. K., W. D. Fitzharris, and J. R. Katzer, "Sulfur Poisioning and Carbon Deactivation of Alumina-Supported Ni, Co, Fe and Ru Catalysts in CO Hydrogenation," in Catalyst Deactivation (B. Delmon and G. F. Fromont, Ed.) Elsevier Scientific Publishing Company, Amsterdam, 179-200 (1980).

Alekseeva, I. N., L. Kartashov, and Y. Treger, "Study of Hydrogen Chloride Oxidation in a Vibrating Contact Bed Reactor," Khim. Prom-st., Ser.: Khlornaya Prom-st., 5, 21-22 (1980).

Amelse, J. A., L. H. Schwartz, and J. B. Butt, "Iron Alloy Fischer-Tropsch Catalysts. III," Catalysis, 72, 95-119 (1981).

Anderson, R. B. , Catalysis, Vol. IV (P. H. Emmett, Ed.), Reinhold, New York, 1956.

Anderson, R. B., "Schulz-Flory Equation," J. Catal., 55, 114-115 (1978).

Anderson, R. B., "Reply to Rebuttal by G. Henrici-Olivé and S. Olivé," J. Catal., 60, 484 (1979).

Anderson, R. B., "Nitrided Iron Catalysts for the Fischer-Tropsch Synthesis in the Eighties," Cat. Rev.-Sci. Eng., 21(1), 53-71, (1980).

Anderson, R. B., The Fischer-Tropsch Synthesis, Academic Press, Inc., Orlando, 1984.

Anderson, R. B., and Y. Chan, "Chain Growth in the Fischer-Tropsch Synthesis--A Computer Simulation of a Catalytic Process," Symposium on Advances in F-T Chemistry, Division of Petroleum Chemistry, Preprints, American Chemical Society, 578-586 (1978).

Anderson, R. B., R. A. Friedel, and H. H. Storch, "Fischer-Tropsch Reaction Mechanism Involving Stepwise Growth of Carbon Chain," J. Chem. Phys., 19(3), 313-319 (1951).

Anderson, R. B., L. J. E. Hofer, E. M. Cohn, and B. Seligman, "Studies of the Fischer-Tropsch Synthesis. IX. Phase Changes of Iron Catalysts in the Synthesis," J. Am. Chem. Soc., 73, 944-946 (1951).

Anderson, R. B., F. S. Karn, and J. F. Schultz, "Factors in Sulfur Poisoning of Iron Catalysts in Fischer-Tropsch Synthesis," J. Catal., 4, 56-63 (1965).

Anderson, R. B. , C. B. Lee, and J. C. Machiels, "The Thermodynamics of the Hydrogenation of Oxides of Carbon," Can. J. Chem. Eng., 54, 590-594 (1976).

Anderson, R. B., B. Seligman, J. F. Shultz, R. Kelly, and M. A. Elliott, "Fischer-Tropsch Synthesis," Ind. Eng. Chem., 44(2), 391-397 (1952).

Anderson, R. B., J. F. Shulz, B. Seligman, W. K. Hall, and H .H. Storch, "Studies of the Fischer-Tropsch Synthesis. VII. Nitrides of Iron as Catalysts," J. Am. Chem Soc., 72, 3502-3508 (1950).

Araki, M., and V. Ponec, ""Methanation of Carbon Monoxide on Nickel and Nickel-Copper Alloys," J. Catal., 44, 439-448 (1976).

Arnold, J. H., and P. C. Keith, "Synthesis of Liquid Fuels from Natural Gas," Amer. Chem. Soc. Adv. Chem. Ser., 5, 120 (1951).

Atwood, H. E., "Kinetics for the Fischer-Tropsch Reaction," Report No. EPRI-AF-689, Electric Power Research Institute, Palo Alto, CA (1977).

Atwood, H. E., and C. O. Bennett, "Kinetics of the Fischer-Tropsch Reaction over Iron," Ind. Eng. Chem. Process Des. Dev., 18(1), 163-170 (1979).

Bachmann, D., Verfahenstechnik Z.V.D.I Beiheft, 2, 43 (1940).

Baiker, A., and W. Richarz, "Instationäre Betriebsart in der heterogenen Katalyse," Chimia, 30(11), 502 (1976).

Bailey. J. E., and F. J. M. Horn, "Improvement of the Performance of a Fixed-Bed Catalytic Reactor by Relaxed Steady-State Operation," AIChE J., 17(3), 550 (1971a).

Bailey, J. E., F. J. M. Horn, and R. C. Lin, "Cyclic Operation of Reaction Systems" Effect of Heat and Mass Transfer Resistence," AIChE J., 17(4), 818 (1971b).

Bailey, J. N., "Periodic Operation of Chemical Reactors: A Review," Chem. Eng. Commun., 1, 111-224 (1973).

Baird, M. H. I., "Vibrations and Pulsation: Bane or Blessingπ", Br. Chem. Eng., 11(1), 20-25 (1966).

Baird, M. J., R. R. Schehl, and W. P. Haynes, "Fischer-Tropsch Processes Investigated at the Pittsburgh Energy Technology Center Since 1944," Ind. Eng. Chem Prod. Res. Dev., 19(2), 175-191 (1980).

Baker, R. T. K., J. R. Alonzo, J. A. Dumesic, and D. J. C. Yates, "Effect of the Surface State of Iron on Filamentous Carbon Formation," J. Catal., 77, 74-84 (1982).

Ballard, D. G. H., "Mechanism of Fischer-Tropsch Synthesis: CH_2 Polymerization versus CO Insertion," J. Mol. Catal., 19, 393-398 (1983).

Barrault, J., and C. Forquy, "Hydrogenation of Carbon Monoxide to Light Olefins on Iron-Alumina Catalysts," J. Mol. Catal., 17, 195-203 (1982).

Bartholomew, C. H., "Carbon Deposition in Steam Reforming and Methanation," Catal. Rev.-Sci. Eng., 24(1), 67-112 (1982).

Baver, W., and J. Werther, "Modeling Complex Reaction Systems in Fluidized-Bed Reactors," Chemical Reaction Engineering-Boston, ACS Advances in Chemistry Series, 121-131 (1982).

Bell, A. T., "Catalytic Synthesis of Hydrocarbons Over Group VIII Metals. A Discussion of the Reaction Mechanism," Catal. Rev.-Sci. Eng., 23(1,2), 203-232 (1981).

Bell, A. T., and L. L. Hegedus, editors, Catalysis Under Transient Conditions, ACS Symp. Series No. 178, American Chemical Society, Washington, D.C. (1982).

Bennett, C. O., "The Transient Method and Elementary Steps in Heterogeneous Catalysis," Catal. Rev.-Sci. Eng., 13, 121-148 (1976).

Bennett, C. O., "Understanding Heterogeneous Catalysis Through the Transient Method," Catalysis Under Transient Conditions, ACS Symposium Series, No. 178, American Chemical Society, Washington, D.C. (1982).

Bennett, C. O., M. B. Cutlip, and C. C. Yang, "Gradientless Reactors and Transient Methods in Heterogeneous Catalysis," Chem. Eng. Sci., 27, 2255-2264 (1972).

Beno, M. A., J. M. Williams, M. Tachikawa, and E L. Muetterties, "Fischer-Tropsch Chemistry: Structure of a Seminal η^2-CH Cluster Drivative, $HFe_4(\eta^2\text{-}CH)(CO)_{12}$," J. Am. Chem. Soc., 102(13), 4542-4544 (1980).

Benziger, J. B., and R. J. Madix,. Reactions and Reaction Intermediates on Iron Surfaces II," J. Catal., 65, 49-58 (1980).

Berty, J. M., S. Lee, K. Sivagnanam, and F. Szeifert, "Diffusional Kinetics of Catalytic Vapor-Phase Reversible Reactions with Decreasing Total Number of Moles," Preprints from the Eighth Int. Symposium on Chemical Reaction Engineering, p. 455 (1984).

Bianchi, D., and C. O. Bennett, "Influence of the Presence of H_2 During the CO Dissociation Reaction on Iron Catalyst," J. Catal. 86, 433-436 (1984).

Bianchi, D., S. Borcar, F. Teule-Gay, and C. O. Bennett, "Evolution of Surface and Bulk Compositions of an Iron Catalyst in Relation to Catalytic Activity for the Fischer-Tropsch Reaction," J. Catal., 82, 442-456 (1983).

Bilimoria, M. R., and J. E. Bailey, "Dynamic Studies of Acetylene Hydrogenation on Nickel Catalysts," Proc. 5th Intern. Sympos. Chem. React. Eng., Houston, p. 526 (1977).

Biloen, P., "Transient Kinetic Methods," J. Mol. Catal., 21, 17-24 (1983).

Biloen, P., J. N. Helle, and W. M. H. Sachtler, "Incorporation of Surface Carbon into Hydrocarbons during Fischer-Tropsch Synthesis: Mechanistic Implications," J. Catal., 58, 95-107 (1979).

Biloen, P., "On the Mechanism of the Fischer-Tropsch Synthesis," Recueil, 32-38 (1979).

Biskis, E., and J. W. Smith, "Pulsation in a Fixed-Bed Reactor," AIChE J., 9(5), 677 (1963).

Björkman, A., "Shaking of High Pressure Vessels According to the Resonance Principle," Ind. Eng. Chem., 44(10), 2459-2463 (1952).

Blanchard, F., J. P. Reymond, B. Pommier, and S. J. Teichner, "On the Mechanism of the Fischer-Tropsch Synthesis Involving Unreduced Iron Catalyst," J. Mol. Catal., 17, 171-181 (1982).

Blyholder, G., and P. H. Emmett, "Fischer-Tropsch Synthesis Mechanism Studies. II. The Addition of Radioactive Ketene to the Synthesis Gas," J. Phys. Chem., 64, 470 (1960).

Blyholder, G., and A. J. Goodsel, "Infrared Spectra of C_2H_4 Adsorption and CO Insertion Reactions on an Fe Surface," J. Catal., 23, 374-378 (1971).

Blyholder, G., D. Shihabi, W. V. Wyatt, and R. Bartlett, "Adsorption and Interaction of C_2H_4, H_2, CO, and Organic Acids on Fe, Co, and Ni," J. Catal., 43, 122-130 (1976).

Bock, W., W. Sitzman, G. Emig, and J. Werther, "How to Find Suitable Kinetics for Modelling and Scale-up of Fluidized Bed Reactors in the Case of Complex Reaction Systems," Preprints from Eighth Int. Symp. on Chemical Reaction Engineering, p. 479 (1984).

Boehm, H. P., "Carbon from Carbon Monoxide Disproportionation on Nickel and Iron Catalysts: Morphological Studies and Possible Growth Mechanisms," Carbon, 11, 585-590 (1973).

Bond, G. C., and B. D. Turnham, "The Kinetics and Mechanism of Carbon Monoxide Hydrogenation over Silica-Supported Ruthenium-Copper Catalysts," J. Catal., 45, 128-136 (1976).

Bonzel, H. P., and G. Brodén, "On the Adsorption and Dissociation of CO on Potassium Promoted Iron," Preprints, Symposium on New Tools in Catalysis, Division of Petroleum Chemistry, American Chemical Society, p. 1260 (1978).

Bonzel, H. P., and H. J. Krebs, "Evidence for Adsorbed Hydrocarbon Intermediates During the Initial Stages of CO Hydrogenation on Iron," Preprints, Division of Fuel Chemistry, American Chemical Society, 25(2), 19-27 (1980).

Bonzel, H. P., and H. J. Krebs, "Enhanced Rate of Carbon Decomposition During Fischer-Tropsch Synthesis on K Promoted Fe," Surf. Sci., 109, L527-L531 (1981).

Boreskov, G. K., Yu. Sh. Matros, V. S. Lakhomostov, V .I. Puzhilova, and V. I. Lugovski, USSR Patent 882,056 (1981a).

Boreskov, G. K., Yu. Sh. Matros, V. S. Lakhomostov, V .I. Puzhilova, and V. I. Lugovski, USSR Patent 865,796 (1981b).

Boreskov, G. K., Yu. Sh. Matros, and V. M. Lugovski, USSR Patent 849,594 (1982a).

Boreskov, G. K., Yu Sh Matros, V. Yu. Volkov, and A. A. Ivanov, USSR Patent 2,183,501 (1982b).

Boreskov, G. K., and Y. S. Matros, "Unsteady-State Performance of Heterogeneous Catalytic Reactions, Catal. Rev.-Sci. Eng., 25(4), 511-590 (1983).

Boreskov, G. K., V. S. Lakhomostov, and Yu. Sh. Matros, USSR Patent, 2,495,342 (1982a).

Boreskov, G. K., V. S. Lakhomostov, and Yu. Sh. Matros, USSR Patent, 811,511 (1982b).

Borghard, W. G., and C. O. Bennett, "Evaluation of Commercial Catalysts for the Fischer-Tropsch Reaction," Ind. Eng. Chem. Prod. Res. Dev., 18(1), 18-26 (1979).

Bossi, A., G. Carnisio, F. Garbassi, G. Guinchi, and G. Petrini, "Isotopic Equilibration of Carbon Monoxide Catalyzed by Supported Ruthenium," J. Catal., 65, 16-24 (1980).

Boudart, M., and M. A. McDonald, "Structure Sensitivity of Hydrocarbon Synthesis from CO and H_2," J. Phys. Chem., 88, 2185-2195 (1984).

Brady, R. C. III, and R. Pettit, "Reactions of Diazomethane on Transition Metal Surfaces and Their Relationship to the Mechanism of the Fischer-Tropsch Reaction," J. Am. Chem. Soc., 102, 6182-6184 (1980).

Brady, R. C. III, and R. Pettit, "On the Mechanism of the Fischer-Tropsch Reaction. The Chain Propagation Step," J. Am. Chem. Soc., 103(5), 1287-1289 (1981).

Bratu, E. A., and G. I. Jimescu, "The Structure of the Vibrofluidized Bed," Chim. Ind.-Genie Chim., 104(13), 1657-1662 (1971).

Bretsnajder, S., M. Jasyczak, and M. Pasiuk, "Increasing the Rate of Certain Industrial Chemical Processes by the Use of Vibration," Int. Chem. Eng., 3(4), 496 (1963).

Bridge, M. E., C. M. Comrie, and R. M. Lambert, "Hydrogen Chemisorption and the Carbon Monoxide-Hydrogen Interaction on Cobalt (0001)," J. Catal., 58, 28-33 (1979).

Briggs, J. P., R. R. Hudgins, and P. L. Silveston, 5th Canadian Symp. on Catalysis, Calgary, Preprints, Edmonton, p. 118 (1977).

Brodén, G., G. Gafner, and H. P. H.Bonzel, "CO Adsorption on Potassium Promoted Fe(110)," Surf. Sci., 84, 295-314 (1979).

Browning, L. C., T. W. DeWitt, and P. H. Emmett, "Equilibria in the Systems Fe_2C-Fe-CH_4-H_2 and Fe_3C-Fe-CH_4-H_2," J. Am. Chem. Soc., 72, 4211-4217 (1950).

Brunier, E., A. Zoulalian, G. Antonini, and A. Rodriques, "Residence Time Distributions in Laminar Flow Through Reservoirs From Momentum and Mass Transport Equations," Preprints from the Eighth Int. Symp. on Chemical Reaction Engineering, p. 439 (1984).

Bub, G., and M. Baerns, "Prediction of the Performance of Catalytic Fixed Bed Reactors for Fischer-Tropsch Synthesis," Chem Eng. Sci., 35, 348-355 (1980).

Büssemeier, B., C. D. Frohning, and B. Cornils, "Lower Olefins via Fischer-Tropsch," Hydrocarbon Process., 105-112, Nov. (1976).

Butt, J. B., L. H. Schwartz, M. Baerns, and R. Malessa, "Comparison of Activity and Selectivity Maintenance for Supported Fe and FeCo Fischer-Tropsch Catalysts," Ind. Eng. Chem. Prod. Res. Dev., 23, 51-56 (1984).

Caesar, P. D., J. A. Brennan, W. E. Garwood, and J. Ciric, "Advances in Fischer-Tropsch Chemistry," J. Catal., 56, 274-278 (1979).

Caldwell, L., "An Oxidation-Reduction Model for Reaction Rate Oscillations in Fischer-Tropsch Synthesis Over Iron Catalysts," Preprint from Eighth International Symposium on Chemical Reaction Engineering, p. 151 (1984).

Cant, N. W., and A. T. Bell, "Studies of Carbon Monoxide Hydrogenation over Ruthenium Using Transient Response Techniques," J. Catal., 73, 257-271 (1982).

Chang, C. D., J. C. W. Kuo, W. H. Lang, S. M. Jacob, J.J. Wise, and A. J. Silvestri, Ind. Eng. Chem. Process Res. Dev., 17, 255 (1978).

Chang, C. D., W. H. Lang, and A. J. Silvestri, "Synthesis Gas Conversion to Aromatic Hydrocarbons," J. Catal., 56, 268 (1979).

Chen, Y. W., H. T. Wang, and J. G. Goodwin, Jr., "Effect of Preparation Methods on the Catalytic Properties of Zeolite-Supported Ruthenium in the Fischer-Tropsch Synthesis," J. Catal., 83, 415-427 (1983).

Chlenov, V. A., and N.V. Miklailov, "A New Principle in the Production of a Fluidized Bed," Dokl. Akad. Nauk SSSR, 154(3), 703-706 (1964).

Chlenov, V. A., and N. V. Miklailov, "Vibro-fluidized Bed," Russ. J. Phys. Chem., 39(2), 250-251 (1965).

Christoffel, E. G., "Laboratory Reactors and Heterogeneous Catalysis Processes," Catal. Rev.-Sci. Eng., 24(2), 159-232 (1982).

Christoffel, E. G., I. Surjo, and M. Baerns, Chemiker-Z., 102, 19 (1978).

Claybaugh, B. E., J. R. Griffin, and A. T. Watson, U.S. Patent 3,472,829 (1969).

Cohen, R. L., Applications of Mössbauer Spectroscopy, Volume 1, Academic Press, N.Y. (1976).

Collis, F. P., and J. A. Schwarz, "Selectivity Effects and Hydrocarbon-Chain Growth During Fischer-Tropsch Synthesis," J. Comp. Chem., 3(2), 135-139 (1982).

Cooper, B. J., and D. L. Trimm, "Carbon Deposition from Propylene on Polycrystalline and Single Crystal Iron," J. Catal., 62, 35-43 (1980).

Craxford, S. R., and E. K. Rideal, "The Mechanism of the Synthesis of Hydrocarbons from Water Gas," J. Chem. Soc., 1, 604 (1939).

Crone, G., and A. Renker, "Der Einflub periodischer ProzeBführung auf radikalische Polymerisationreaktionen," Chem. Ing. Tech., 51(1), 42 (1979).

Cutlip, M. B., "Concentration Forcing of Catalytic Surface Rate Processes: Part 1. Isothermal Carbon Monoxide Oxidation Over Supported Platinum," AIChE J., 25, 502-508 (1979).

Cutlip, M. B., C. N. Kenney, W. Morton, D. Mukesh, and S. C. Capsaskis, "Transient and Oscillatory Phenomena in Catalytic Reactors," Preprints from Eighth Int. Symp. on Chemical Reaction Engineering, p. 135 (1984).

Dadyburjor, D. B., "Use of Adsorption Entropy to Choose between Kinetic Mechanisms and Rate Equations for Fischer-Tropsch Synthesis," J. Catal., 82, 489-492 (1983).

Dalla Betta, R. A., and M. Shelef, "Heterogeneous Methanation: In Situ Infrared Spectroscopic Study of Ru/Al_2O_3 during the Hydrogenation of CO," J. Catal., 48, 111-119 (1977a).

Dalla Betta, R. A., and M. Shelef, "Heterogeneous Methanation: Absence of H_2-D_2 Kinetic Isotope Effect of Ni, Ru, and Pt," J. Catal., 49, 383-385 (1977b).

Dalla Betta, R. A., A. G. Piken, and M. Shelef, "Heterogeneous Methanation: Initial Rate of CO Hydrogenation on Supported Ruthenium and Nickel," J. Catal., 35, 54-60 (1974).

Darby, P. W., and C. Kemball, "Observations on the Fischer-Tropsch Synthesis over a Cobalt Catalyst at Low Pressure Using Gas Chromatography," Trans. Faraday Soc., 833-841 (1958).

Dautzenberg, F. M., J. N. Helle, R. A. van Santen, and H. Verbeek, "Pulse-Technique Analysis of the Kinetics of the Fischer-Tropsch Reaction," J. Catal., 50, 8-14 (1977).

Deans, D. R., M. T. Huckle, and R. M. Peterson, "New Column System for Isothermal Gas Chromatographic Analysis of Light Gases (H_2, O_2, N_2, CO, C_2H_4, and C_2H_2) Employing a Column Switching Technique," Chromatographia, 4, 279-285 (1971).

Deckwer, W. D., "FT Process Alternatives Hold Promise," Oil α Gas J., 198-213, Nov. 10 (1980).

Delgass, W. N., G. L. Haller, R. Kellerman, and J. H. Lunsford, Spectroscopy in Heterogeneous Catalysis, Academic Press, N.Y. (1979).

Deluzarche, A., J. P. Hindermann, R. Kieffer, A. Muth, M. Papadopoulos, and C. Tanielian, "Synthese de Fischer-Tropsch II," Tetrahedron Lett., No. 9, 797-800 (1977).

Deluzarche, A, J. P. Hindermann, and R. Kieffer, "Carbon-Monoxide-Hydrogen Reactions; Possible Reaction Mechanisms in Heterogeneous Catalysis," J. Chem. Research, 934-948 (1981).

Demitras, G. C., and E. L. Muetterties, "Metal Clusters in Catalysis-10. A New Fischer-Tropsch Synthesis," J. Am. Chem. Soc., 99(8), 2796-2797 (1977).

Denis, G. H., and R. L. Kabel, "The Effect of Temperature Changes on a Tubular Heterogeneous Catalytic Reactor," Chem. Eng. Sci., 25(6), 1057 (1970a).

Denis, G. H., and R. L. Kabel, "The Effect of Conversion of Flow Rate Variation in a Heterogeneous Catalytic Reactor," AIChE J., 16(6), 972 (1970b).

Dictor, R. A., and A. T. Bell, "An Explanation for Deviations of Fischer-Tropsch Products from a Schulz-Flory Distribution," Ind. Eng. Chem. Process Des. Dev., 22(4), 678-681 (1983).

Dictor, R. A., and A. R. Bell, "On-Line Analysis of Fischer-Tropsch Synthesis Products," Ind. Eng. Chem. Fundan., 23, 252-256 (1984).

Dietz, W. A., "Response Factors for Gas Chromatographic Analyses," J. Gas Chromatogr., 67-71, Feb. (1967).

Diffenbach, R. A., T. H. Johnson, and R. R. Schehl, "A Study of the Fischer-Tropsch Reaction Using On-Line Gas-Chromatographic Analysis," Report No. DOE/PETC/TR-82/10, U.S. Department of Energy, Washington, D. C., July (1982).

Ding, J. S. I., S. Sharma, and D. Luss, "Steady-State Multiplicity and Control of the Chlorination of Liquid n-Decane in an Adiabatic Continuous Stirred Tank Reactor," Ind. Eng. Chem. Fund., 13(1), 76 (1974).

DiSanzo, F. P., "Characterization of High Boiling Fischer-Tropsch Liquids by Liquid and Gas Chromatography," Anal. Chem., 53, 1911-1914 (1981a).

DiSanzo, F. P., "Characterization of High Boiling Fischer-Tropsch Liquids," ACS Div. of Fuel Chemistry, 26(2), 13-27 (1981b).

Dixit, R. S., and L. L. Tavlarides, "Integral Method of Analysis of Fischer-Tropsch Synthesis Reactions in a Catalyst Pellet," Chem. Eng. Sci., 37(4), 539-544 (1982).

Doriswamy, L. K., and D. G. Tajbl, "Laboratory Catalytic Reactors," Cat. Rev.-Sci. Eng., 10, 177-219 (1975).

Douglas, J. M., Process Dynamics and Control, Prentice Hall, Englewood Cliffs, N.J. (1972).

Douglas, J. M., "Periodic Reactor Operation," Ind. Eng. Chem. Process Des. Dev., 6, 43 (1967).

Douglas, J. M., and D. H. T. Rippon, "Unsteady-State Process Operation," Chem. Eng. Sci., 21, 305 (1966).

Dry, M. E., "Advances in Fischer-Tropsch Chemistry," Ind. Eng. Chem. Prod. Res. Dev., 15(4), 282-286 (1976).

Dry, M. E., "Predict Carbonation Rate on Iron Catalyst," Hydrocarbon Process., 92-94, February (1980).

Dry, M.E., "The Fischer-Tropsch Synthesis," in Catalysis (M. Boundart and J. Anderson, ed.), Vol. 1, Chapter 4, Springer-Verlag, N.Y. (1981).

Dry, M. E., "Catalytic Aspects of Industrial Fischer-Tropsch Synthesis," J. Mol. Catal., 17, 133-144 (1982a).

Dry, M. E., "Sasol's Fischer-Tropsch Experience," Hydrocarbon Process., 121-124, August (1982b).

Dry, M. E., J. A. K. DuPlessis, G. M. Leuteritz, "The Influence of Structural Promoters on the Surface Properties of Reduced Magnetite Catalysts," J. Catal., 6, 194-199 (1966).

Dry, M. E., and L. C. Ferreira, "The Distribution of Promoters in Magnetite Catalysts," J. Catal., 7, 352-358 (1967).

Dry. M. E., and G. J. Oostuizen, "The Correlation between Catalyst Surface Basicity and Hydrocarbon Selectivity in the Fischer-Tropsch Synthesis," J. Catal., 11, 18-24 (1968).

Dry, M. E., T. Shingles, and L. J. Boshoff, "Rate of the Fischer-Tropsch Reaction Over Iron Catalysts," J. Catal., 25, 99-104 (1972).

Dry, M. E., T. Shingles, L. J. Boshoff, and G. J. Oosthuizen, "Heats of Chemisorption on Promoted Iron Surfaces and the Roles of Alkali in Fischer-Tropsch Synthesis," J. Catal., 15, 190-199 (1969).

Dry, M. E., T. Shingles, L. J. Boshoff, and S. C. van H. Botha, "Factors Influencing the Formation of Carbon on Iron Fischer-Tropsch Catalysts, I," J. Catal., 17, 341-346 (1970).

Dry, M. E., T. Shingles, L. J. Boshoff, and S. C. van H. Botha, "Factors Influencing the Formation of Carbon on Iron Fischer-Tropsch Catalysts, II," J. Catal., 17, 347-354 (1970).

Dutartre, R., P. Bussière, J. A. Dalmon, and G. A. Martin, "Activation of Hydrogen on Fe/MgO Catalysts Studied by Magnetic Methods and Mössbauer Spectroscopy," J. Catal., 59, 382-394 (1979).

Dutta, S., S. C. Arnold, G. D. Suciu, and L. Verde, "Scale-up of a Catalytic Fluid-Bed Reactor Involving Complex Kinetics," Preprints from Eighth Int. Symp. on Chemical Reaction Engineering, p. 517 (1984).

Dwyer, D. J., and G. A. Somorjai, "The Role of Readsorption in Determining the Product Distribution during CO Hydrogenation over Fe Single Crystals," J. Catal., 56, 249-257 (1979).

Dwyer, D., K. Yoshida, and G. A. Somorjai, "Hydrogenation of CO and CO_2 on Clean Rhodium and Iron Foils--Correlations of Reactivities and Surface Compositions," Preprints, Symposium on Advances in Fischer-Tropsch Chemistry, Div. of Petroleum Chemistry, Amer. Chem. Soc., 521-537 (1978).

Egiazarov, Y. S., N. P. Krut'ro and A. I. Trokhimeto, " Kinetic Principles of Ethane Pyrolysis in the Presence of an Indium Oxide Catalyst," Vestsi Akad. Navuk BSSR, Ser. Khim. Navuk, 1, 44-47 (1982).

Egiebor, N. O., K. R. Ungar, and B. W. Wojciechowski, "A Classification of Fischer-Tropsch Synthesis Product Distributions,' Can. J. Chem. Eng., 62, 425-430 (1984).

Eidus, Y. T., "The Mechanism of the Fischer-Tropsch Reaction and the Initiated Hydropolymerisation of Alkenes, from Radiochemical and Kinetic Data," Russ. Chem. Rev., 36(15), 228-350 (1967).

Eisenlohr, K. H., and H. Gaensslen, "Motor Fuels from Coal--Technology and Economics," Fuel Process. Tech., 4 43-61 (1981).

Ekerdt, J. G., and A. T. Bell, "Synthesis of Hydrocarbons from CO and H_2 over Silica-Supported Ru: Reaction Rate Measurements and Infrared Spectra of Adsorbed Species," J. Catal., 58, 170-187 (1979).

Ekerdt, J. G., and A. T. Bell, "Evidence for Intermediates Involved in Fischer-Tropsch Synthesis over Ru," J. Catal., 62, 19-25 (1980).

Evans, U. R., "Oxidation of Iron in the Range 100-400°C," Nature (London), 164, 909 (1949).

Everson, R. C., E. T. Woodburn, and A. R. M. Kirk, "Fischer-Tropsch Reaction Studies with Supported Ruthenium Catalysts, J. Catal., 53, 186-197 (1978).

Feimer, J. L., "A Study of Forced-Feed Composition Cycling in the Fischer-Tropsch Synthesis," Ph.D. Thesis, University of Waterloo (1982).

Feimer, J. L., P. L. Silveston, and R. R. Hudgins, "Steady-State Study of the Fischer-Tropsch Reaction, Ind. Eng. Chem, Prod. Res. Dev., 20, 609-615 (1981).

Feimer, J. L., A. K. Jain, R. R. Hudgins, and P. L. Silveston, "Modelling Forced Periodic Operation of Catalytic Reactors," Chem. Eng. Sci. 37(2), 1797-1805 (1982a).

Feimer, J. L., P. L. Silveston, and R. R. Hudgins, "Influence of Forced Cycling on the Fischer-Tropsch Synthesis," Preprints, 8th Canadian Sympos. on Catalysis, Ontario, p. 104 (1982b).

Feimer, J. L., P. L. Silveston, and R. R. Hudgins, "Influence of Forced Cycling on the Fischer-Tropsch Syhtnesis, Part I. Response to Feed Concentration Step-Changes," Can. J. Chem. Eng., 62, 241-248 (1984).

Feldhousen, R. W., Jr., "A Cold-Flow Experimental Simulation of Gas-Mixing Characteristics in a Vibrofluidized Microreactor System for Fischer-Tropsch Synthesis from a Low H_2:CO Gas," Masters Thesis, Virginia Polytechnic Institute and State University (1984).

Field, J. H., H. E. Benson, and R. B. Anderson, "Synthetic Liquid Fuels by Fischer-Tropsch Process," Chem. Eng. Prog., 56(4), 44-48 (1960).

Field, J. H., J. J. Demeter, A. J. Forney, and D. Bienstock, "Development of Catalysts and Reactor Systems for Methanation," Ind. Eng. Chem. Prod. Res. and Dev., 3(2), 150-153 (1964).

Fischer, J. and H. Tropsch, Brennst.-Chem., 4, 276 (1923).

Fischer, J. and H. Tropsch, Brennst.-Chem., 7, 97 (1926).

Fischer, J. and H. Koch, Brennst.-Chem., 13, 428 (1932).

Fischer, J. and H. Pichler, Brennst.-Chem., 17, 24 (1936).

Fischer, R. H. and R. E. Hildebrand, "Transportation Fuels from Synthetic Gas," Proceedings of the Symposium on Advances in Coal Utilization Technology, Institute of Gas Technology, pp. 331-344 (1979).

Flory, P. J., "Molecular Size Distribution in Linear Condensation Polymers," J. Am. Chem. Soc., 58, 1877 (1936).

Forsey, R. R., "A Dual-Column Gas Chromatographic Method for the Analysis of Light Gases," J. Gas Chromatogr., 6, 555 (1968).

Fraenkel, D., and B. C. Gates, "Shape-Selective Fischer-Tropsch Synthesis Catalyzed by Zeolite-Entrapped Cobalt Clusters," J. Am. Chem. Soc. 102(7), 2478-2480 (1980).

Friedel, R. A., and R. B. Anderson, "Composition of Synthetic Liquid Fuels. I. Product Distribution and Analysis of C_5-C_8 Paraffin Isomers from Cobalt Catalyst, J. Am. Chem Soc., 72, 1215-2307 (1950).

Frohning, C. D., and B. Cornils, "Chemical Feedstocks from Coal," Hydrocarbon Process., 1453-146, November (1974).

Frohning, C. D., H. Kölbel, M. Ralek, H. Rottig, F. Schnur, and H. Schulz, in Chemical Feedstocks From Coal, (J. Falbe, Ed.), Wiley, New York (1982).

Garrett, L. W., Jr., "Gasoline from Coal via the Synthol Process," Chem. Eng. Prog., 56(4), 39-43 (1960).

Gierlich, H. H., and M. Fremery, "Deactivation Phenomena of a Ni-based Catalyst for High Temperature Methanation," in Catalyst Deactivation (B. Delmon and G. F. Froment, Ed.), Elesvier Scientific Publishing Company, Amsterdam, Netherlands, 459-469 (1980).

Glasser, D., and R. Jackson, "A Generalized Residence Time Distribution Model for a Chemical Reactor," Reprints from the Eighth Int. Symposium on Chemical Reaction Engineering, p. 535 (1984).

Gonzalez, R. D., and H. Miura, "Methanation and Fischer-Tropsch Studies on Potassium-Promoted Silica-Supported Ru Catalysts," J. Catal., 77, 338-347 (1982).

Goodman, D. W., R. D. Kelley, T. E. Madey, and J. M. White, "Measurement of Carbide Buildup and Removal Kinetics on Ni(100)," J. Catal., 64, 479-481 (1980).

Gray, D. W., M. Lytton, M. B. Neuworth, and G. C. Tomlinson, "The Impact of Developing Technology on Indirect Liquefaction," Proceedings of Symposium on Advances in Coal Utilization Technology, Institute of Gas Technology, pp. 93-109 (1981).

Greyson, M., in Catalysis, Vol. IV (P. H. Emmett, Ed.), Reinhold, New York (1956).

Grekel. H., K. L. Hujsak, and R. Mungen, "Contracting Efficiency in Hydrocarbon Synthesis," Chem. Eng. Prog., 60(1), 56-60 (1964).

Grenoble, D. C., and M. M. Estadt, "The Chemistry and Catalysis of the Water Gas Shift Reaction," J. Catal., 67, 90-102 (1981).

Gupta, R., and A. S. Mujumdar, "Aerodynamic and Thermal Characteristics of Vibrated Fluid Beds - A Review," in Drying '80, Vol. 1 (A. S. Mujumdar,Ed.), Hemisphere, Washington, 141-150 (1980).

Gupta, R., B. Viswanathan, and M. V. C. Sastri, "Interaction of Hydrogen and Carbon Monoxide on Cobalt Catalysts. Part I," J. Catal., 26, 212-217 (1972).

Hackenbruch, J., W. Keim, M. Rober, and H. Strutz, "Mechanistic Considerations for the Formation of Oxygenated Species in the Fischer-Tropsch Synthesis," J. Mol. Catal. 26, 129-134 (1984).

Haggin, J., "C_1 Chemistry Development Intensities," Chem. Eng. News, 39-47 February 23 (1981).

Haggin, J., "Fischer-Tropsch: New Life for Old Technology," Chem. Eng. News, 22-32, October 26 (1981).

Haggin, J., "Progress in C_1 Chemistry Aired," Chem. Eng. News, 31-34, June 18 (1982).

Hall, W. K., W. H. Tarn, and R. B. Anderson, "Studies of the Fischer-Tropsch Synthesis. VIII. Surface Area and Pore Volume Studies of Iron Catalysts," J. Am. Chem. Soc., 72, 5436-5443 (1950).

Hall, W. K., W. H. Tarn, and R. B. Anderson, "Studies of the Fischer-Tropsch Synthesis. XIII. Structural Changes of a Reduced Iron Catalyst on Reoxidation and on Formation of Interstitial Phases," J. Am. Chem. Soc., 56, 688 (1950).

Happel, J., I. Suzuki, P. Kokayeff, and V. Fthenakis. "Multiple Isotope Tracing of Methanation over Nickel Catalyst," J. Catal., 65, 59-77 (1980).

Harney, B. M., and G. A. Mills, "Coal to Gasoline via Syngas," Hydrocarbon Process., 67-71, February (1980).

Harney, B. M., G. A. Mills, and L. M. Joseph, "High Quality Transportation Fuels from CO-H_2: A Competitive Option," Preprints, Symposium on Advances in Fischer-Tropsch Chemistry, Div. of Petroleum Chem., Amer. Chem. Soc., 573-577, March (1978).

Haynes, W. P., M. J. Baird, R. R. Schehl, and M. F. Zarochak, "Fischer-Tropsch Studies in a Bench-Scale Tube Wall Reactor Using Magnetite, Raney Iron, and Taconite Catalysts," Preprints, Symposium on Advances in Fischer-Tropsch Chemistry, Div. of Petroleum Chem, Amer. Chem. Soc., 599-572, (March, 1978).

Helrich, H., A. Renken, and K. Schügest, "Beeinflussung der effektiven Geschwindingkeit heterogen-katalytischer Reaktionendurch aufgezwungene Konzentrationsschwankungen," Chem. Ing. Tech., 46(15), 647 (1974).

Henrici-Olivé, G., and S. Olivé, "Mechanism of the Fischer-Tropsch Synthesis: Origin of Oxygenates," J. Mol. Catal., 24, 7-13 (1984).

Henrici-Olivé, G., and S. Olivé, "The Fischer-Tropsch Synthesis: Molecular Weight Distribution of Primary Products and Reaction Mechanism," Angew. Chem. Ind. Ed. Engl., 15(3), 136-141 (1976).

Henrici-Olivé, G., and S. Olivé, "The 'Carbide Theory' of the Fischer-Tropsch Synthesis in the Light of Homogeneous Coordination Chemistry," J. Mol. Catal., 18, 367-373 (1983).

Henrici-Olivé, G., and S. Olivé, "Letters to the Editors in Re: Fischer-Tropsch. Comments to Notes by R. B. Anderson (1) and R. J. Madon (2)," J. Catal., 60, 481-483 (1979).

Henry, J. P., "Economics and Siting of Fischer-Tropsch Coal Liquefaction," Report No. DOE/ET/2625-9, U. S. Department of Energy, Washington, D.C., July (1979).

Herrington, E. F. S., "The Fischer-Tropsch Synthesis Considered as a Polymerization Reaction," Chemistry and Industry, 346-347, Sept. 21 (1946).

Herrmann, W. A., "Organometallic Aspects of the Fischer-Tropsch Synthesis," Angew. Chem., Int. Ed., Engl., 21, 117-130 (1982).

Hirt, D. E., "Heat Transfer Between a Supernatant Gas and a Flowing Vibrofluidized Bed of Soilds," M.S. Thesis, Chemical Engineering, Virginia Polytechnic Institute and State University (July, 1984).

Hofer, L. J. E., and E. M. Cohn, "Thermomagnetic Determination of Hägg Carbide in Used Iron Fischer-Tropsch Catalysts," Anal. Chem., 22, 907-910 (1950).

Hofer, L. J. E., E. M. Cohn, and W. C. Peebles, "The Modifications of the Carbide, Fe_2C; Their Properties and Identificaation," J. Am. Chem. Soc., 71 (1949).

Hojlund-Nielsen, P. E., and J. Bogild-Hansen, "Conversion Limitations in Hydrocarbon Synthesis," J. Mol. Catal., 17, 183-193 (1982).

Hollis, O. L., and W. V. Hayes, "Water Analysis by G. C. Using Porous Polymor Columns," J. Gas Chromatogr., 235 (1966).

Hoogendoorn, J. C., "Clean Fuels from Coal," Symposium Papers, IGT, 353-365 (1973).

Hoogendoorn, J. C., "New Applications of the Fischer-Tropsch Process," Proceedings of the Symposium on Clean Fuels from Coal II, Institute of Gas Technology, Chicago, 343-358 (1975).

Horn, F. J. M., and R. C. Lin, "Periodic Processes: A Variational Approach," Ind. Eng. Chem. Process Des. Dev., 6, 21 (1967).

Hu, Y. C., "Unconventional Olefin Processes," Hydrocarbon Process., 88-96, May (1983).

Huff, G. A., Jr., "Fischer-Tropsch Synthesis in a Slurry Reactor," Doctoral Dissertation, Massachusetts Institute of Technology (1982).

Huff, G. A., Jr., and C. N. Satterfield, "Evidence for Two-Chain Growth Probabilities on Iron Catalists in the Fischer-Tropsch Synthesis," J. Catal., 85, 370-379 (1984a)

Huff, G. A., Jr., and C. N. Satterfield, "Intrinsic Kinetics of the Fischer-Tropsch Synthesis on a Reduced Fused-Magnetite Catalyst," Ind. Eng. Chem., Process Des. Dev., 23, 696-705 (1984b).

Huff, G. A., Jr., and C. N. Satterfield, "Some Kinetic Design Considerations in the Fischer-Tropsch Synthesis on a Reduced Fused-Magnetite Catalyst," Ind. Eng. Chem., Process Des. Dev., 23, 851-854 (1984c).

Hugues, F., B. Besson, P. Bussière, J. A. Dalmon, J. M. Basset, and D. Olivier, "Catalysis by Supported Iron Clusters: Unusual Selectivities in Fischer-Tropsch Synthesis and in Olefin Homologation. Considerations on the Mechanism of Fischer-Tropsch Synthesis," Nouv. J. Chim., 5(4), 207-210 (1981).

Hurst, N. W., S. J. Gentry, and A. Jones, "Temperature Programmed Reduction," Catal. Rev. - Sci. Eng., 24(2), 233-309 (1982).

Ichikawa, M., M. Sudo, M. Soma, T. Onishi, and K. Tamaru, " Catalytic Formation of Hydrocarbons (C_1-C_5) from Hydrogen and Carbon Monoxide over the Electron Donor-Acceptor Complex Films of Alkali Metals with Transition Metal Phthalocyanines or Graphite," J. Am. Chem. Soc., 91(6), 1538-1539 (1969).

Ino, T., H. Watanabe, and Y. Morita, "Synthesis of Gaseous Hydrocarbons from Carbon Monoxide and Hydrogen over Transition Metal Catalysts. Part 5. Carbon Accumulation of a Precipitated Iron Catalyst During the Reaction," Sekiyu Gakkaishi (J. Japan Petrol. Inst.), 24(3), 181-8 (1981).

Jacobs, P. A., and D. Van Wouwe, "Selective Synthesis of Hydrocarbons via Heterogeneous Fischer-Tropsch Chemistry," J. Mol. Catal., 17, 145-160 (1982).

Jain, A. K., R. R. Hudgins, and P. L. Silveston, "Evidence for Bulk-Phase Nitrogen Dissolution in Iron in Catalytic Ammonia Synthesis," Can. J. Chem. Eng., 60, 809-811 (1982a).

Jain, A. K., P. L. Silveston, and R. R. Hudgins, "Reaction Rate Resonance in the Concentration Cycling of the Catalytic Oxidation of Carbon Monoxide," Catalysis Under Transient Conditions (A. T. Bell, and L. L. Hegedus, Eds.), ACS Sympo. Ser. 178, 267-275 (1982b).

Jain, A. K., P. L. Silveston, and R. R. Hudgins, "Forced Composition Cycling Experiments in a Fixed-Bed Ammonia Synthesis Reactor," Proc. Seventh Intern. Sympos. Chem. Reaction. Eng., Boston, ACS Sympos. Ser. 196, 97-107 (1982c)

Jain, A. K., R. R. Hudgins, and P. L. Silveston, "Adsorption/Desorption Models: How Useful for Predicting Reaction Rates Under Cyclic Operation," Can. J. Chem. Eng., 61, 46-49 (1983a).

Jain, A. K., R. R. Hudgins, and P. L. Silveston, "Influence of Forced Feed Composition Cycling on the Rate of Ammonia Synthesis over an Industrial Iron Catalyst. Part I. Effect of Cycling Parameters and Mean Composition," Can. J. Chem. Eng., 61, 824-832 (1983b).

Jones, A., and B. D. McNicol, "Comparison of the Fischer-Tropsch Synthesis of Hydrocarbons and the Haber Synthesis of Ammonia," J. Catal., 47, 384-388 (1977).

Joyner, R. W., "Mechanism of Hydrocarbon Synthesis from Carbon Monoxide and Hydrogen," J. Catal., 50, 176-180 (1977).

Kadelka, J., H. Loevenich, and W. Keim, "The Reactions of Fischer-Type Carbene Complexes with Ethene," J. Organomet. Chem., 231, 219-223 (1982).

Karcher, W., and P. Glande, "Kinetic Aspects of the Carbon Deposition Reaction on Iron from CO/H_2 Mixtures," Bien. Conf. Carbon, Ext. Abstr. Program, 11th, 43-4 (1973), CONF-730601.

Karn, F. S., B. Seligman, J. F. Shultz, and R. B. Anderson, "Kinetics of the Fischer-Tropsch Synthesis on Iron Catalysts. I. Rate Data on Reduced and Nitrided Catalysts," J. Phys. Chem., 64(4), 446-451 (1960).

Karn, F. S., J. F. Shultz, and R. B. Anderson, "Kinetics of the Fischer-Tropsch Synthesis on Iron Catalysts. Pressure Dependence and Selectivity of Nitrided Catalysts," J. Am. Chem. Soc., 64, 446-451 (1960).

Kehrer, V. J., and H. Leidheiser, Jr., "The Catalytic Decomposition of Carbon Monoxide on Large Metallic Single Crystals," J. Phys. Chem., 58, 550-555 (1954).

Kelley, R. D., and D. W. Goodman, "Catalytic Methanation over Single Crystal Nickel and Ruthenium: Reaction Kinetics on Different Crystal Planes," Preprints, Div. Fuel Chem., Amer. Chem. Soc., 25(2), 26-41 (1980).

Kellner, C. S., and A. T. Bell, "Evidence for H_2/D_2 Isotope Effects on Fischer-Tropsch Synthesis over Supported Ruthenium Catalysts," J. Catal., 67, 175-185 (1981a).

Kellner, C. S., and A. T. Bell, "The Kinetics and Mechanism of Carbon Monoxide Hydrogenation over Alumina-Supported Ruthenium," J. Catal., 70, 418-432 (1981b).

Kibby, C. L., and T. P. Kobylinski, "Models of Product Distributions in Fischer-Tropsch Synthesis," Preprints, Symp. in Adv. in Synthetic Fuels, Div. of Pet. Chem., Amer. Chem. Soc., 1332-1335 (1978).

Kieffer, E. P., and H. S. Van Der Baan, "Transient Kinetics of the Fischer-Tropsch Synthesis," in Chemical Reaction Engineering--Boston, (J. Wei and C. Geogakis, Ed.), pp. 200-212, Amer. Chem. Soc., Washington, D.C. (1982).

Kikuchi, E., T. Ino, and Y. Morita, "Catalytic Synthesis of Hydrocarbon from Carbon Monoxide and Hydrogen on Lamellar Compound of Graphite Intercalated by Ferric Chloride," J. Catal., 57, 27-34 (1979).

King, D. L., "A Fischer-Tropsch Study of Supported Ruthenium Catalysts," J. Catal., 51, 386-397 (1978).

King, D. L., "An in-Situ Infared Study of CO Hydrogenation over Silica and Alumina-Supported Ruthenium and Silica-Supported Iron," J. Catal., 61, 77-86 (1980).

King, D. L., J. A. Cusumano, and R. L. Garten, "A Technological Perspective for Catalytic Processes Based on Synthesis Gas," Catal. Rev.-Sci. Eng., 23(1,2), 233-263 (1981).

King, D. L., and J. B. Peri, "An Infrared Study of Nitric Oxide Chemisorption on Alumina Supported Iron and Alkalized Iron Fischer-Tropsch Catalysts," J. Catal., 79, 164-175 (1983).

King, R. B., A. D. King, Jr., M. Z. Iqbal, and C. C. Frazier, "Transition Metal Chemistry under High Carbon Monoxide Pressure: An Infrared Spectroscopic Study of Catalysis in the Fischer-Tropsch Reaction," National Technical Information Service, Publication Nos. SRO-933-1, SRO-933-1, SRO-933-3 (1977, 1978, 1979).

Kölbel, H., and M. Ralek, "The Fischer-Tropsch Synthesis in the Liquid Phase," Catal. Rev.-Sci. Eng., 21(2), 225-274 (1980).

Krebs, H. J., H. P. Bonzel, and W. Schwarting, "Microreactor and Electron Spectroscopy Studies of Fischer-Tropsch Synthesis on Magnetite," J. Catal., 72, 199-209 (1981).

Kroeker, R. M., W. C. Kaska, and P. K. Hansma, "Formation of Hydrocarbons from Carbon Monoxide on Rhodium/Alumina Model Catalysts," J. Catal., 61, 87-95 (1980).

Kroll, W., Chem. Ing. Tech., 27, 33 (1955).

Kuchynka, K., J. Fusek, and O. Strouf, "Modelling of Fischer-Tropsch Catalytic Synthesis by Pattern Recognition Method. Chemisorption of Hydrogen on Metals," Collect. Czech. Chem. Commun., 46, 2328-2335 (1981).

Kummer, J. T., T. W. Dewitt, and P. H. Emmett, "Some Mechanism Studies on the Fischer-Tropsch Synthesis Using C^{14}," J. Am. Chem. Soc., 70, 3632 (1948).

La Cava, A. I., C. A. Bernado, and D. L. Trimm, "Studies of Deactivation of Metals by Carbon Deposition," Carbon, 20(3), 219-223 (1982).

Lazar, K., Z. Schay, and L Guczi, "Direct Evidence for the Correlation between Surface Carbon and CO + H_2 Selectivity on Iron and Iron-Ruthenium Catalysts Prepared from Metal Carbonyl Clusters," J. Mol. Catal., 17, 205-218 (1982).

Le Blanc, J.R., D. O. Moore, and A. E. Cover, "Coal Can Be Gasoline," Hydrocarbon Process., 133-138, June (1981).

Le Caër, G., J. M. Dubois, M. Pijolat, V. Perrichon, and P. Bussière, "Characterization by Mössbauer Spectoscopy of Iron Carbides Formed by Fischer-Tropsch Synthesis," J. Phys. Chem., 86 4799-4808 (1982).

le Roux, J. H., and L. J. Dry, "Fischer-Tropsch Waxes: VI. Distribution of Branches and Mechanism of Branch Formation," J. Appl. Chem. Biotechnol, 22, 719-726 (1972).

Leupold, E. J., and A. Renken, "Ein neuses verfahren zur Herstellung von Essigsaüthylester unter Anwendung instationärer ProzeBführung," Chem. Ing. Tech., 49(8) 667 (1977).

Liu, Y. A., Squires, A. M., and K. Konrad, "Fischer-Tropsch Synthesis from a Low H_2:CO Gas in a Dry Fluidized-Bed System," U.S. Dept. of Energy Report No. DOE/PC/50791-T1, DOE Technical Information Center, Oak Ridge, TN (1982).

Loktev, S. M., "Alcohols and Hydrocarbons from Carbon Oxides and Hydrogen on Fused Iron Catalysts: Developments of Synthesis and Mechanism," J. Mol. Catal., 17, 225-230 (1982).

Loktev, S. M., L. I. Makarenkova, E. V. Slivinskii, and S. D. Éntin, "Thermomagnetic Analysis of Fused Iron Catalysts for the Synthesis of Alcohols from Carbon Monoxide and Hydrogen," Kinet. Catal., 13(4), 861-990 (1972).

Loktev, S. M., L. I. Makarenkova, E. V. Slivinskii, and S. D. Éntin, "Thermomagnetic Analysis of Fused Iron Catalysts for the Synthesis of Alcohols from Carbon Monoxide and Hydrogen," Kinet. Catal., 13, 933 (1972).

Low, G. G., and A. T. Bell, "Studies of CO Desorption and Reaction with H_2 on Alumina-Supported Ru," J. Catal., 57, 397-405 (1979).

Madon, R. J., "Reply to Comments by G. Henrici-Olivé and S. Olivé," J. Catal., 60, 485-486 (1979).

Madon, R. J. and H. Shaw, "Effects of Sulfur on the Fischer-Tropsch Synthesis," Catal. Rev.-Sci. Eng., 15(1), 69-106 (1977).

Madon, R. J., and W. F. Taylor, Fischer-Tropsch Synthesis on a Precipitated Iron Catalyst," J. Catal., 69, 32-43 (1981).

Madon, R. J., E. R. Bucker, and W. Taylor, U.S. Dept. of Energy Report, Contract No. E(46-1) 8008, July (1977).

Maksimov, Y. V., I. P. Suzdalev, R. A. Arents, and S. M. Loktev, "Mössbauer Study of the ε-Iron Carbide Formed on a Fused Iron Catalyst in the Synthesis of Higher Alcohols from Carbon Monoxide and Hydrogen," Kinet. Catal., 15(5), 1097-1216 (1974).

Matsumoto, H., "The Catalytic Effct of Carbide Formation During Fischer-Tropsch Synthesis," Chem. Lett., 1041-1044 (1981).

Matsumoto, H. and C. O. Bennett, "The Transient Method Applied to the Methanation and Fischer-Tropsch Reactions over a Fused Iron Catalyst," J. Catal., 53, 331-344 (1978).

McCandlish, L. E., "On the Mechanism of Carbon-Carbon Bond Formation in the CO Hydrogenation Reaction," J. Catal., 83, 363-370 (1983).

McCarty, J. G., and H. Wise, "Hydrogenation of Surface Carbon on Alumina-Supported Nickel," J. Catal., 57, 406-416 (1979).

McCarty, J. G., P. Y. Hou, D. Sheridan, and H. Wise, "Reactivity of Surface Carbon on Nickel Catalyst: Temperature Programmed Surface Reaction with H_2 and H_2O," The North American Meeting of the Catalysis Society, Boston, MA', October (1981).

McClory, M. M., and R. D. Gonzalez, "The Role of Alkali Metals as Promoters in the Methanation and Fischer-Tropsch Reaction: An in-Situ Study," J. Catal., 89, 392-403 (1984).

Mills, G. A., and F. W. Steffgen, "Catalytic Methanation," Catal. Rev.-Sci. Eng., 8(2), 159 (1973).

Moore, S. E., and J. H. Lunsford, "The Role of Hydrogen in the Reaction of Water with Surface Carbon to Form Methane," J. Catal., 77, 297-300 (1982).

Muetterties, E. L., and J. Stein, "Mechanistic Features of Catalytic Carbon Monoxide Hydrogenation Reactions," Chem. Rev., 79(6), 479-490 (1979).

Niemantsverdriet, J. W., A. M. van der Kraan, W. L. wan Dijik, and H. S. van der Bann "Behavior of Metallic Iron Catalysts during Fischer-Tropsch Synthesis Studied with Mössbauer Spectroscopy, X-ray Diffraction, Carbon Content Determination, and Reaction Kinetic Measurements," J. Phys. Chem., 84, 3363-3370 (1980).

Niemantsverdriet, J. W., and A. M. van der Kraan, "On the Time-Dependent Behavior of Iron Catalysts in Fischer-Tropsch Synthesis," J. Catal., 72, 385-388 (1981).

Nijs, H. H., and P. A. Jacobs, "Metal Particle Size Distributions and Fischer-Tropsch Selectivity. An Extended Schulz-Flory Model," J. Catal., 65, 328-334 (1980).

Nijs, H. H., and P. A. Jacobs, "New Evidence for the Mechanism of the Fischer-Tropsch Synthesis of Hydrocarbons," J. Catal., 66, 401-411 (1980).

Nijs, H. H., and P. A. Jacobs, "On-Line Single Run Analysis of Effluents from a Fischer-Tropsch Reactor," J. Chromatogr. Sci., 19, 40-45 (1981).

Nijs, H. H., P. A. Jacobs, and J. B. Uytterheven, "Chain Limitations of Fischer-Tropsch Products in Zeolites," J. Chem. Soc., Chem. Commun., 4, 180 (1979a).

Nijs, H. H., P. A. Jacobs, and J. B. Uytterheven, "Selective Fischer-Tropsch Synthesis of Hydrocarbons: Particle Size Effect of Ruthenium Metal in Faujasite-type Zeolites," J. Chem. Soc., Chem. Commun., 23, 1095 (1979b).

Novak, S., and R. J. Madon, "Models of Hydrocarbon Product Distributions in Fischer-Tropsch Synthesis. 2. Model for Hydrocarbon Chain Growth and Cracking," Ind. Eng. Chem. Fundam., 23, 274-280 (1984).

Novak, S., R. J. Madon, and H. Suhl, "Models of Hydrocarbon Product Distributions in Fischer-Tropsch Synthesis. I," J. Chem. Phys., 74(11), 6083-6091 (1981).

Novak, S., R. J. Madon, and H. Suhl, "Secondary Effects in the Fischer-Tropsch Synthesis," J. Catal., 77, 141-151 (1982).

O'Hara, J. B., A. Bela, N. E. Jentz, and S. K. Khaderi, "Fischer-Tropsch Plant Design Criteria," Chem. Eng. Prog., 65-67, August (1976).

O'Hara, J. B., F. E. Cumare, and S. N. Rippee, "Synthetic Fuels from Coal by Fischer-Tropsch," CEP Technical Manual, Coal Processing Technology, Amer. Inst. Chem. Eng., 2, 83-87 (1975).

Ollis, D. F., and M. A. Vannice, "The Catalytic Synthesis of Hydrocarbons from H_2/CO Mixtures over the Group VIII Metals: Comments on Methanation Kinetics," J. Catal., 38, 514-515 (1975).

Olsson, R. G., and E. T. Turkdogan, "Catalytic Effect of Iron on Decomposition of Carbon Monoxide: II. Effect of Additions of H_2, H_2O, CO_2, SO_2 and H_2S," Metal Trans., 5, 21-26 (1974).

Ott, G. L., T. Fleisch, and W. N. Delgass, "Carbon Deposition and Activity Changes over FeRu Alloys during Fischer-Tropsch Synthesis," J. Catal., 65, 253-262 (1980).

Pakowski, Z., A. S. Mujumdar, and C. Strumillo, "Theory and Application of Vibrated Beds and Vibrated Fluid Beds for Drying Processes," in Advances in Drying, Volume 3 (A. S. Mujumdar, Ed.), Hemisphere Publishing Company, Washington, 245 306 (1984).

Palmer, R. L., and D. A. Vroom, "Mass-Spectrometric Measurements of Enhanced Methanation Activity over Cobalt and Nickel Foils," J. Catal., 50, 244-252 (1977).

Papic, M., "The Simultaneous Separation of C_1-C_4 Hydrocarbons on a Single Porapak Column," J. Gas Chromatogr., 6, 483 (1968).

Papic, M. M., "Coal Liquefaction via Sasol Fischer-Tropsch Synthesis," CIM Bull., 74, 60-64 (1980).

Parkash, S., S. K. Chakrabartty, and M. P. Rosynek, "Hydrocarbon Synthesis and Carbon Dioxide Adsorption on Iron Catalysts," Fuel Process. Technol., 3, 63-70 (1980).

Parkash, S., T. Kotanigawa, and S. K. Chakrabartty, "Changes in Pore Structure of Precipitated Iron Oxide Catalysts During Pretreatment and Hydrocarbon Synthesis Reaction," Fuel Process. Technol., 5, 203-212 (1982).

Pattipati, R. R., and C. Y. Wen, "Minimum Fluidization Velocity at High Temperatures," Ind. Eng. Chem., Process Des. Dev., 20, 705-708 (1981).

Peacock-Lopéz, E., and K. Lindenberg, "The Transient Flory Model and Its Application to Catalytic Polymerization," J. Phys. Chem., 88, 2270-2275 (1984).

Pichler, H., "Twenty-five Years of Synthesis of Gasoline by Catalytic Conversion of Carbon Monoxide and Hydrogen," Adv. Catal., 4, 271-341 (1952).

Pichler, H., and H. Merkel, "Chemical and Thermomagnetic Studies on Iron Catalysts for Synthesis of Hydrocarbons," U. S. Bureau of Mines Technical Paper 718 (1949).

Pichler, H. and H. Schulz, Chem. Ing. Tech., 42, 1162 (1970).

Podgurski, H. H., J. T. Kummer, T. W. DeWitt, and P. H. Emmett, "Preparation, Stability and Adsorptive Properties of the Carbides of Iron," J. Am. Chem. Soc., 72, 5382-5388 (1950).

Polyakov, L. M., Abrasion of Granular Zeolites Under Vibration Loading," Kinet. Katel, 15(3), 765-772 (1972).

Polyvakov, L. M., and É. I. Vinokurov, "Kinetics of the Abrasion of Zeolites Under Vibrations and Elevated Temperatures," Kinet. Katel, 20(5), 1311-1314 (1977).

Ponec, V., "Some Aspects of the Mechanism of Methanation and Fischer-Tropsch Synthesis," Catal. Rev. - Sci. Eng., 18(1), 151-171 (1978).

Ponec, V., and W. A. van Barneveld, "The Role of Chemisorption in Fischer-Tropsch Synthesis," Ind. Eng. Chem., Prod. Res. Dev., 18, 268-271 (1979).

Ponec, V., Z. Knor, and S. Cerny, "Role of Chemisorption in Simple Catalytic Reactions," Discuss. Faraday Soc., 41, 149-161 (1966).

Potter, O.E., "Modelling Fluidized-Bed Reactors," Catal. Rev. - Sci. Eng., 17(2), 155-202 (1978).

Probstein, R. F., and R. E. Hicks, Synthetic Fuels, McGraw-Hill Book, Co., New York (1982).

Rabo, J. A., A. P. Risch, and M. L. Poutsma, "Reactions of Carbon Monoxide and Hydrogen on Co, Ni, Ru, and Pd Metals," J. Catal., 53, 295-311 (1978).

Rao, V. U. S., R. J. Gormley, H. W. Pennline, L. C. Schneider, and R. Obermeyer, "Synthesis Gas Conversion to Gasoline Range Hydrocarbons over Medium Pore Zeolite Catalysts Containing 3d-Metals and Bimetallics," Preprints, Div. Fuel Chem., Amer. Chem. Soc., 25(2), 119-126 (1980).

Raupp, G. B., and W. N. Delgass, "Mössbauer Investigation of Supported Fe and FeNi Catalysts, I. Effect of Pretreatment on Particle Size," J. Catal., 58, 337-347 (1979a).

Raupp, G. B., and W. N. Delgass, "Mössbauer Investigation of Supported Fe and FeNi Catalysts, II. Carbides Formed by Fischer-Tropsch Synthesis," J. Catal., 58, 348-360 (1979b).

Raupp, G. B., and W. N. Delgass, "Mössbauer Investigation of Supported Fe Catalysts, III. In Situ Kinetics and Spectroscopy during Fischer-Tropsch Synthesis," J. Catal., 58 361-369 (1979c).

Renken, A., M. Muller, and H. Helmrich, "Untersuchungen zur Instabilität isothermer heterogener Festbettreaktoren," Chem. Ing. Tech., b47(24), 1029 (1975).

Renken, A., M. Muller, and C. Wandry, 4th Int. 16th Eur. Symp. Chem React. Eng. (Frankfurt/M.), 1, 107 (1976).

Renshaw, G. D., C. Roscoe, and P. L. Walker, Jr., "Disproportionation of CO, I. Over Iron and Silicon-Iron Single Crystals," J. Catal., 18, 164-183 (1970).

Renshaw, G. D., C. Roscoe, and P. L. Walker, Jr., "Disproportionation of CO, II. Over Cobalt and Nickel Single Crystals," J. Catal., 22, 394-410 (1971).

Reusov, A. V., A. Milknevich, and I. Taganov, "Study of Mass Transfer in a Fluidized Bed Confined by a Vibratory Grid," Teor. Osn. Khim. Tekhnol., 14(6), 866-70 (1980).

Reymond, J. P., P. Mériaudeau, B. Pommier, and C. O. Bennett, "Further Results on the Reaction of H_2/CO on Fused Iron by the Transient Method," J. Catal., 64, 163-172 (1980a).

Reymond, J. P., P. Mériaudeau, B. Pommier, and C. O. Bennett, "Further Results on the Reaction of H_2/CO on Fused Iron by the Transient Method," Preprints, Division of Fuel Chemistry, American Chemical Society, 25(2), 71-81 (1980b).

Riekena, M. L., A. G. Vickers, E. C. Haun, and R. C. Koltz, "A Comparison of Fischer-Tropsch Reactors," Chem. Eng. Prog., 86-90, April (1982).

Rofer-DePoorter, C. K., A Comprehensive Mechanism for the Fischer-Tropsch Synthesis," Chem. Rev., 81, 447-474 (1981).

Ruston, W. R., M. Warzee, J. Hennaut, and J. Waty, "The Solid Reaction Products of the Catalytic Decomposition of Carbon Monoxide on Iron at 550°C," Carbon, 7, 47-57 (1969).

Sacco, A., Jr., P. Thacker, T. N. Chang, and A. T. S. Chiang, "The Initiation and Growth of Filamentous Carbon from α-Iron in H_2, CH_4, H_2O, CO_2, and CO Gas Mixtures," J. Catal., 85, 224-236 (1984).

Sachtler, J. W. A., J. M. Kool, and V. Ponec, "The Role of Carbon in Methanation by Cobalt and Ruthenium," J. Catal., 56, 284-286 (1979).

Sancier, K. M., W. E. Isakson, and H. Wise, "Carburization Studies of Iron Fischer-Tropsch Catalysts," ACS Symposium Series, Amer. Chem. Soc., No. 33, 129-145 (1979).

Sanders, W. N., and J. B. Maynard, "Capillary Gas Chromatographic Method for Determining the C_3-C_{12} Hydrocarbons in Full-Range Motor Gasolines," Anal. Chem., 40, 527-535 (1968).

Sastri, M. V. C., R. Balaji Gupta, and B. Viswanathan, "Interaction of Hydrogen and Carbon Monoxide on Cobalt Catalysts. Part II," J. Catal., 32, 325-332 (1974).

Satterfield, C. N., Heterogeneous Catalysis in Practice, McGraw-Hill, New York (1980).

Satterfield, C. N., and G. A. Huff, Jr., "Usefulness of a Slurry-Type Fischer-Tropsch Reactor for Processing Synthesis Gas of Low Hydrogen-Carbon Monoxide Ratios," Can. J. Chem. Eng., 60, 159-162, (1982a).

Satterfield, C. N., and G. A. Huff, Jr., "Carbon Number Distribution of Fischer-Tropsch Products Formed on an Iron Catalyst in a Slurry Reactor," J. Catal., 73, 187-197 (1982b).

Satterfield, C. N. , G. A. Huff, Jr., and J. P. Longwell, "Product Distribution from Iron Catalyst in Fischer-Tropsch Slurry Reactors," Ind. Eng. Chem., Proc. Des. Dev., 21, 465-470 (1982).

Satterfield, C. N., G. A. Huff, Jr., and H. G. Stenger," "Effect of Carbon Formation on Liquid Viscosity and Preformance of Fischer-Tropsch Bubble Column Reactors," Ind. Eng. Chem., Process Des. Dev., 20, 666-670 (1981).

Satteffield, C. N., and H. G. Stenger, "Fischer-Tropsch Synthesis in a Slurry Reactor: Precipitated Iron-Copper-Potassium Catalyst," Ind. Eng., Chem., Process Des. Dev., 23, 849-851 (1984a).

Satterfield, C. N., and H. G. Stenger, " Fischer-Tropsch Synthesis on a Precipitated Mn/Fe Catalyst in a Well-Mixed Surry Reactor," Ind. Eng. Chem., Process Des. Dev., 23, 26-29 (1984b).

Scherzer, J., and D. Fort, "Zeolite-Supported Metal Catalysts for Fischer-Tropsch Reactions," J. Catal., 71, 111-118 (1981).

Schlesinger, M. D., H. E. Benson, E. M. Murphy, and H. H. Storch, "Chemicals from the Fischer-Tropsch Synthesis," Ind. Eng. Chem., 46, 1322-1331 (1954).

Schulz, G. V., Z. Phys. Chem, B, 30, 379 (1935).

Schulz, H., "Future Sources of Organic Raw Materials," CHEMRAWN, I, pp. 167-183, Peragamon Press, New York (1978).

Schulz, H., B. R. Rao, and M. Elstner, "^{14}C-Studien zum Reaktionsmechanismus der Fischer-Tropsch-Synthese," Erdöl Kohle, 23, 651 (1970).

Schulz, H., and A. Zein El Deen, "New Concepts and Results Concerning the Mechanism of Carbon Monoxide Hydrogenation. I. Organic Oxygen Compounds Produced During Medium-Pressure Synthesis with Iron Catalysts," Fuel Process. Technol., 1, 31-44 (1977).

Schulz, H., and A. Zein El Deen, "New Concepts and Results Concerning the Mechanism of Carbon Monoxide Hydrogenation. II. Evolution of Reaction Steps on the Basis of Detailed Product Composition and Other Data," Fuel Process. Technol., 1, 45-56 (1977).

Shah, Y. T., and A. J. Perrotta, "Catalysts for Fischer-Tropsch and Isosynthesis," Ind. Eng. Chem., Prod. Des. Dev., 15(2), 123-131 (1976).

Sharma, B. K., and K. A. Kini, "Adsoption of H_2 on Precipitated Fischer-Tropsch Iron Catalysts," Curr. Sci., 45(3), 98-99 (1976)

Sharma, B. K., and P. S. M. Tripathi, "Crystal Field Surface Orbital-Bond Energy Bond Order Calculation for Hydrogen Chemisorption on Fischer-Tropsch Iron Catalyst," Indian J. Chem., 20A, 1105-1107 (1981).

Shchel'tsyn, V. K., R. M. Flid, I. L. Varsman, and T. P. Shapirovskaya, "Kinetics of the Gas-Phase Vinylation of α-pyriolidone Using Basic Catalysts," Russ. J. Phy. Chem., 42(7), 869-872 (1968).

Shelef, M., and R. A. Dalla Betta, "Reply to Comments on Heterogeneous Methanation: Absence of H_2-D_2 Kinetic Isotope Effect on Ni, Ru, and Pt," J. Catal., 60, 169-170 (1979).

Shinnar, R., and J. C. W. Kuo, "Gasifier Study for Mobil Coal to Gasoline Processes," U.S. Dept. of Energy Report FE-2766-13 (1978).

Shirazi, Z. H., and C. Stojanov, "Reaction Gas-Chromatography of Fischer-Tropsch Synthesis Products Including the Oxygen Containing Compounds," Pak. J. Sc. Ind. Res., 20(1), 1-10 (1977).

Shultz, J. F., B. Seligman, J. Lecky, and R. B. Anderson, "Studies of the Fischer-Tropsch Synthesis. XII. Composition Changes of Nitrided Iron Catalysts During Synthesis," J. Am. Chem. Soc., 74, 637-40 (1952a).

Shultz, J. F., B. Seligman, L. Shaw, and R. B. Anderson, "Effect of Nitriding on Three Types of Iron Catalysts," Ind. Eng. Chem., 44, 397-401 (1952b).

Shultz, J. F., W. K. Hall, B. Seligman, and R. B. Anderson, "Studies of the Fischer-Tropsch Synthesis. XIV. Hägg Iron Carbide as Catalysts," J. Am. Chem. Soc., 77, 213-221 (1955).

Shultz, J. F., M. Abelson, L. Shaw, and R. B. Anderson, "Fischer-Tropsch Synthesis: Nitrides and Carbonitrides of Iron as Catalysts," Ind. Eng. Chem., 49(12), 2055-2060 (1957).

Silverman, D. C, and M. Boudart, "Surface Composition of Promoted Iron Catalysts, " J. Catal., 77, 208-220 (1982).

Singh, M., "Why Not Use Fischer-Tropschπ", Hydrocarbon Process., p. 138, June (1981).

Solbakken, V., A. Solbakken, and P. H. Emmett, "The Exchange of $H_2{}^{18}O$ with the Oxygen Promoters on the Surface of Iron Catalysts," J. Catal., 15, 90-98 (1969).

Squires, A. M., "Contributions Toward a History of Fluidization," Proceedings of the Joint Meeting of American Institute of Chemical Engineers and Chemical Industry and Engineering Society of China, Beijing, Vol. 1, pp. 322-353, September (1982).

Squires, A. M., "Applications of Fluidized Beds in Coal Technology," in Alternative Energy Sources (J. P. Harnett, Ed.), pp. 59-109, Academic Press, New York, N.Y. (1976).

Stein, K. C., G. P. Thompson, and R. B. Anderson, "Iron Catalysts and the Fischer-Tropsch Synthesis," Ind. Eng. Chem., 49 410 (1957).

Stein, K. C., G. P. Thompson, and R. B. Anderson, "Studies of the Fischer-Tropsch Synthesis. XVII. Changes of Iron Catalysts During Pretreatment and Synthesis," J. Am. Chem. Soc., 61, 928-932 (1957).

Stenger, H. G., H. E. Johnson, and C. N. Satterfield, "Molecular Weight Distribution of the Heavy Wax Formation from Fischer-Tropsch Synthesis," J. Catal., 86, 477-480 (1984).

Stockinger, J. H., "Quantitative Analysis of Gaseous Products Obtained in the Conversion of Methanol-to-Gasoline," J. Chromatogr. Sci., 15 198-202 (1977).

Storch, H. H., N. Golumbic, and R. B. Anderson, The Fischer-Tropsch and Related Synthesis, John Wiley α Sons, Inc., New York (1951).

Stowe, R. A., and C. B. Murchison, Upgrade Fischer-Tropsch Liquids to Olefins and Aromatics," Hydocarbon Process., 147-150, January (1982).

Strouf, O., K. Kuchynka, and J. Fusek, "Modelling of the Catalytic Fischer-Tropsch Synthesis by Pattern Recognition. Chemisorption and Dissociation of Carbon Monoxide on Metals," Collect. Czech. Chem. Commun., 46, 2336-2344 (1981).

Studier, M. H., and R. Hayatsu, "Analyses of Complex Mixtures of Hydrocarbons by Time-of-Flight Mass Spectrometry-Open Tube Chromatography," Anal. Chem., 40(6), 1011-1013 (1968).

Suib, S. L., K. C. McMahon, L. M. Tau, and C. O. Bennett, "Synthesis, Characterization, and Fischer-Tropsch Studies of Iron-Containing Zeolites," J. Catal., 89, 20-34 (1984).

Swart, J. S., G. J. Czajkowski, and R. E. Conser, "Sasol Upgrades," Oil and Gas J., 62-66 (1981).

Takeuchi, A., J. R. Katzer, G. C. A. Schuit, "Fischer-Tropsch Product Distribution for Rh/TiO_2," J. Catal., 82, 477-478 (1983).

Tamarin, A. I., and G. Kovenski, "Effect of Gas-Distributing Grate Vibrations on the Uniformity of a Fluidized Bed," Veststt Akad. Navuk B. SSR, Ser. Fiz.-Energ. Navuk, 3, 74-77 (1974).

Tauser, S. J., and R. M. Koros, "Removal of Coke Precursors with Hydrogen: Studies with Alternating Pulses of Propane and Hydrogen," J. Catal., 27, 307-310 (1972).

Taylor, P. D., and B. W. Wojciechowski, "A Quantitative Theoretical Treatment of the Fischer-Tropsch Synthesis," Can. J. Chem. Eng., 61, 98-102 (1983).

Ta-Yu, C., L. Nan-Tsuen, and C. Chun-Hao, "Report on Pilot Plant Synthesis of Liquid Fuels," Chem. Eng. Prog., 54(3), 55-58 (1958).

Thomson, W. J., J. M. Arndt, and K .L. Wright, "Applied Fischer-Tropsch Kinetics for a Flame Sprayed Iron Catalyst," Preprints, Div. Fuel Chem., Amer. Chem Soc., 25(2), 101-118 (1980).

Trimm, D. L., "The Formation and Removal of Coke from Nickel Catalyst," Catal. Rev.-Sci. Eng., 16(2), 155-189 (1977).

Trimm, D. L., "Carbon Formation on Metals other than Nickel and on Alloys," in Progress in Catalyst Deactivation (J. L. Figueiredo, Ed.), Matrinus Nijhoff Publishers, 55-70 (1982).

Tsotsis, T. T., and V. U. S. Rao, and L. M. Polinski, "Reaction Rate Oscillations During Fischer-Tropsch Synthesis on Fe-Precipitated Nu-1 Zeolite-Type Catalysts," AIChE J., 28(5), 847-860 (1982).

Turkdogan, E. T., and J. V. Vinters, "Catalytic Effect of Iron on Decomposition of Carbon Monoxide: 1. Carbon Deposition in H_2-CO Mixtures," Metal. Trans., 5, 11-19 (1974).

Underwood, R. P., and C. O. Bennett, "The CO/H_2 Reaction over Nickel-Alumina Studied by the Transient Method," J. Catal., 86, 245-253 (1984).

Unmuth, E. E., L. H. Schwartz, and J. B. Butt, "Iron Alloy Fischer-Tropsch Catalysts. I. Oxidation-Reduction Studies of the Fe-Ni System," J. Catal., 61, 242-255 (1980a).

Unmuth, E. E., L. H. Schwartz, and J. B. Butt, "Iron Alloy Fischer-Tropsch Cataylsts. II. Carburization Studies of the Fe-Ni System," J. Catal., 63, 404-414 (1980b).

Unni, M. P., R. R. Hudgins, and P. L. Silveston, "Influence of Cycling on the Rate of Oxidation of SO_2 on a Vanadia Catalyst," Can. J. Chem. Eng., 51, 623-629 (1973).

van Barneveld, W. A. A., and V. Ponec, "Influence of Alloying on the Selectivity in Fischer-Tropsch Synthesis by Nickel-Copper Alloys," J. Catal., 51, 426-430 (1978).

van Barneveld, W. A. A., and V. Ponec, "Reactions of CH_xCl_{4-x} with Hydrogen: Relation to the Fischer-Tropsch Synthesis of Hydrocarbons," J. Catal., 88, 382-387 (1984a).

van Barneveld, W. A. A., and V. Ponec, "On the Apparent Controversy Regarding the Effect of Alloying on the Selectivity of the Fischer-Tropsch Synthesis, " J. Catal., 89, 542-544 (1984b).

van Dijk, W. L., and H. S. van der Baan, "The Role of Carbon and Oxygen in the Activation of an Iron Fischer-Tropsch Catalyst at Low Pressures," J. Catal., 78, 24-33 (1982).

Vanhove, D., P. Marambo, and M. Blanchard, "Selective Analytic Synthesis of Linear Paraffins from Co and H_2 Over Cobalt Supported Catalysts," J. Chem. Soc., Chem. Commun., 14, 603 (1979).

Vogler, G. L., X. J. Jiang, J. A. Dumesic, and R. J. Madon, "The Use of Nitrous Oxide as a Surface Probe of Iron Catalysts for Fischer-Tropsch Synthesis," J. Catal., 89, 116-130 (1984).

Vannice, M. A., "The Catalytic Synthesis of Hydrocarbons from H_2/CO Mixtures over the Group VII Metals I," J. Catal., 37, 449-461 (1975a).

Vannice, M. A., "The Catalytic Synthesis of Hydrocarbons from H_2/CO Mixtures over the Group VIII Metals. II," J. Catal., 37, 462-473 (1975b).

Vannice, M. A., "The Catalytic Synthesis of Hydrocarbons from H_2/CO Mixtures over Group VIII Metals, III," J. Catal., 4, 129-134 (1975c).

Vannice, M. A., "The Catalytic Synthesis of Hydrocarbons from H_2/CO Mixtures over the Group VIII Metals, IV," J. Catal., 44 152-162 (1976a).

Vannice, M. A., "The Catalytic Synthesis of Hydrocarbons from Carbon Monoxide and Hydrogen," Catal. Rev.-Sci. Eng., 14(2), 153-191 (1976b).

Vannice, M. A., "Solid State Chemistry of Energy Conversion and Storage," Advances in Chemistry Series, Amer. Chem. Soc. No. 163, 15-32 (1977a).

Vannice, M. A., "The Catalytic Synthesis of Hydrocarbons from H_2/CO Mixtures over the Group VIII Metals, V. The Catalytic Behavior of Silica-Supported Metals," J. Catal., 50, 228-236 (1977b).

Vannice, M. A., "Catalytic Activation of Carbon Monoxide on Metal Surfaces," Catalysis (J. R. Anderson and M. Bondart, Ed.), 3, Chapter 3, Springer-Verlag, N.Y. (1982).

Vannice, M. A., and R. L. Garten, "Metal-Supported Effects on the Activity and Selectivity of Ni Catalysts in CO/H_2 Synthesis Reactions," J. Catal., 56, 236-248 (1979).

Vannice, M. A., and R. L. Garten, "The Influence of the Support on the Catalytic Behavior of Ruthenium in CO/H_2 Synthesis Reactions," J. Catal., 63, 255-260 (1980a).

Vannice, M. A., and R. L. Garten, "CO Hydrogentation Reactions over Titania-Supported Nickel," J. Catal., 66, 2452-247 (1980b).

Wandrey, V. and A. Renken, "Zur Beeinflussung der Produktverteilungdurch periodische Kozentrationsschwankungen bei der Oxidation von Kohlenwasserstoffen," Chem. Ing. Tech., 45(12), 854 (1977a).

Wandrey, V., and A. Renken, "Ignition and Extinction of Autothermal Reactors at Periodic Operation," Chem. Eng. Sci., 32(4), 448 (1977b).

Wang, C. J., and J. C. Ekerdt, "Evidence for Alkyl Intermediates during Fischer-Tropsch Synthesis and Their Relation to Hydrocarbon Products," J. Catal., 86, 239-244 (1984).

Weil, B. H., and J. C. Lane, The Technology of the Fischer-Tropsch Process, Constable α Co., Ltd., London (1949).

Wen, C. Y., and L. T. Fan, Models for Flow Systems and Chemical Reactors, Marcel Dekker, Inc., N.Y. (1975).

Wen, C. Y., and Y. H. Yu, "A Generalized Method for Predicting the Minimum Fluidization Velocity, AIChE J., 12, 610-612 (1966).

Wentrcek, P. R., B. J. Wood, and H. Wise, "The Role of Surface Carbon in Catalytic Methanation," J. Catal., 43, 363-366 (1976).

White, G. A., T. R. Roszkowski, and D. W. Stanbridge, "Predict Carbon Formation," Hydrocarbon Process., 120-136, July (1975).

Wilson, T. P., "Comments on Heterogeneous Methanation: Absence of H_2-D_2 Kinetic Isotope Effect on Ni, Ru, and Pt," J. Catal., 60, 167-168 (1979).

Wroski, S., R. Pohorecki, A. Wolny, A. Mroz, and H. Moniuk, Polish Patent 96, 257 (1976).

Wynkoop, R., and R. Wilhelm, "Kinetics in a Tubular Reactor: Hydrogenation of Ethylene over a Cooper-Magnesia Catalyst," Chem. Eng. Prog., 46, 300 (1950).

Yang, C. H., and A. G. Oblad, "Catalytic Synthesis of Light Olefinic Hydrocarbons from CO and H_2 over Some Iron Catalysts," Symposium on Advances in Fischer-Tropsch Chemistry, Div. of Pet. Chem., ACS, pp. 513-521 (1978).

Yokoyama, A., H. Komiyama, H. Inoue, T. Masumoto, and H. Kimura, "The Fischer-Tropsch Synthesis by Amorphous $Fe_{20}Ni_{60}P_{20}$ and $Fe_{90}Zr_{10}$ Catalysts," Chemical Reaction Engineering, Advances in Chemistry Series, Amer. Chem. Sco. pp. 237-248 (1982).

Zein el Deen, A., J. Jacobs, and M. Baerns, Proceedings of 5th International Sympos. Chem. Reac. Eng., Houston, pp. 26-36 (1977).

Zenz, F. A., and D. F. Othmer, Fluidization and Fluid-Particle Systems, Reinhold Publishing Corp., New York (1960).

APPENDIX A

Calculations for (1) Minimum Fluidization Velocity of the Fused-Iron Catalyst in the Microreactor, (2) Pressure Drop Across the Distributor Plates and (3) Changes in Feed-Line Volume Upon Switching the Sliding Plenum Across the Plenum Zone

A.1. Minimum Fluidization Velocity of the Fused-Iron Catalyst in the Microreactor

For the calculation, the smoothed correlation of particulate fluidization as given by Zenz and Othmer (1960) was used. The minimum fluidization velocity v_ε, under actual conditions was read from Figure A.1 after first calculating Ω and Δ. A void fraction of 0.5 was assumed.

$$\Omega = \frac{4}{3}\left[\frac{\mu_f(\rho_p-\rho_f)g}{\rho_f^2}\right]^{1/3}$$

$$\Delta = \frac{3}{4}\left[\frac{\mu_f^2}{\rho_f(\rho_p-\rho_f)g}\right]^{1/3}$$

where:

v_ε = superficial velocity $(\frac{ft}{s})$

D_p = partical diameter (ft)

μ_f = fluid viscosity (lb/ft-s)

ρ_p = apparent particle density (lb/ft^3)

ρ_f = fluid density (lb/ft^3)

g = 32.2 ft/s

An average particle diameter of 225μ was assumed as well.

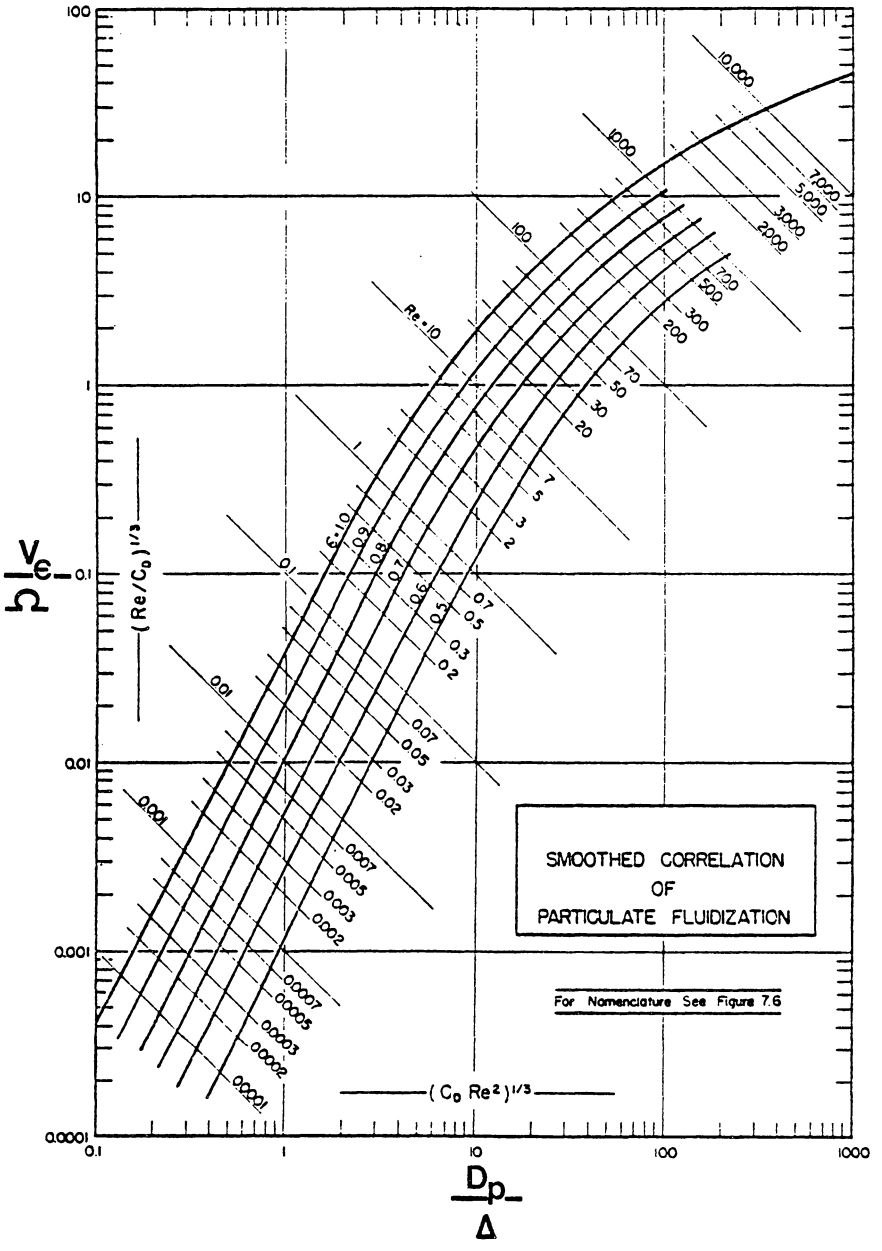

Figure A.1. The Smoothed Correlation of Particulate Fluidization Used to Calculate the Minimum Gas-Fluidization Velocity (V_ε) of a Fused-Iron Catalyst (Taken from Zenz and Othmer, 1960). D_p is the Particle Diameter, Ω and Δ are Defined in Section A.1.

A.2 Pressure Drop Across Different Micron-Grade Sintered Stainless-Steel Distributor Plates

The following equation relating the fluid flow to pressure drop across porous plates has been provided by Mott Metallurgical Corporation for their products:

$$\Delta P^2 = P^2_{\text{upstream}} - P^2_{\text{downstream}} = \delta\mu RT \frac{\rho_s}{30} t\left[1 + \frac{\beta\rho_s}{60\alpha\mu} Q\right]Q$$

P = pressure (psi)

α = viscous resistance coefficient (in^{-2})

β = inertial resistance coefficient (in^{-1})

ρ_s = density of gas at S.T.P. ($slugs/ft^3$)

R = gas constant = 1.71×10^3 ($ft.lb/slug\ ^\circ R$)

T = temperature ($^\circ R$)

t = porous wall thickness (in)

Q = flow ($SCFM/in^2$)

μ = viscosity of flow (slugs/in.sec.)

For 1/16-inch thick porous stainless steel the following coefficients are specified:

Micron Grade	α (in^{-2})	β (in^{-1})
2	8.41×10^8	1.25×10^5
20	3.55×10^7	6.02×10^3

An approximation to the volume of gas backflowing across the distributor plate can be made. This is done by measuring the magnitude and duration

of the pressure inversion with a rapid-response differential-pressure transducer. The pressure drop across the distributor plate for the same gas at a typical flow rate is then calculated. By ratioing the measured pressure inversion and the calculated pressure drop, the volume of gas backflowing can be approximated. For example:

Given a 20-μ distributor plate and argon flowing at 400 actual mm^3/s and conditions of 25°C and 101 kPa, what is the pressure drop?

$$\Delta P = 1.42 \times 10^{-2} \text{ kPa}$$

If a pressure inversion of 0.346 kPa is observed for a duration of 0.013 seconds after the feed gas is switched from argon to helium, what is the volume of gas backflowing across the distributor plate?

$$\frac{0.346 \text{ kPa}}{0.0142 \text{ kPa}} \cdot 400 \frac{mm^3}{S} \cdot 0.013S \simeq 127 \text{ } mm^3$$

A.3 Changes in Feed-Line Volume Upon Switching the Sliding Plug Across the Plenum Zone.

When the sliding plug is drawn across the plenum zone, gas is compressed into the feed line ahead of the plug. By measuring the increase in pressure in the appropriate feed line, the amount of gas entering that feed line by compression can be calculated. The remainder of the gas originally in the plenum is either compressed through the distributor plate or flows anularly around the plug.

Volume of Feed Line = 26,383 mm^3

$\Delta P_{Ar \rightarrow He}$ = ΔP upon switching from Ar to He = 3.175 kPa

$\Delta P_{He \rightarrow Ar}$ = ΔP upon switching from He to Ar = 2.864 kPa

$P_{final\ Ar \rightarrow He}$ = final feed-line pressure upon switching from Ar to He = 141.000 kPa

$P_{final\ He \rightarrow Ar}$ = final feed-line pressure upon switching from He to Ar = 140.685 kPa

Absolute System Pressure = 137.825 kPa

$\Delta V_{Feed\ Line}$ = change in volume of the feed line upon plug switching

$$\Delta V_{Feed\ Line} = \frac{\Delta P \cdot V_{Feed\ Line}}{P_{final}}$$

For the transition from argon-to-helium flow how much argon is compressed into the feed line? (Experiment 1-4)

$\Delta V_{feed\ line,\ Ar \rightarrow He}$ = 594 mm^3 or 37% of the gas in the plenum

For the transition from helium-to-argon flow how much helium is compressed into the feed line?

$$\Delta V_{\text{feed line, He}\rightarrow\text{Ar}} = 537 \text{ mm}^3 \text{ or } 33\% \text{ of the gas in the plenum.}$$

APPENDIX B

Steady-State Analysis Results Including Definitions of Input Parameters and Output Labels on Gas-Chromatographic Data Tables for (1) Light Gas Analyses and Mass Balances and (2) Hydrocarbon Product Distribution and Rate of Production from Capillary Analyses. In Addition (3) Temperature-Fluctuation Plots are Presented for Steady-State Experiments.

B.1 Light Gas Analysis--Output from the Microcomputer Data Compilation Program "MASSBAL. BAS."

1. Input

   A. Number of moles of CO fed per mole of Ar fed

      i. obtained by GC analysis of S-gas.

   B. H_2/CO ratio of feed gas

      i. As specified by AIRCO.

   C. Temperature

   D. Number of data points.

   E. Peak areas from light gas chromatogram for Co, Ar, CH_4 and CO_2.

2. Output

   A. CO CONV: Fractional molar conversion of CO fed to the microreactor.

   B. CO_2/CO CONV: The number of moles of CO_2 produced per mole of CO converted (fraction of C from CO converted that goes to CO_2).

   C. CH_4/CO CONV: The number of moles of CH_4 produced per mole of CO converted (fraction of CO converted that goes to CH_4).

   D. CO/Ar FED; The number of moles of CO fed per mole of Ar fed. An input parameter.

   E. H_2/CO RATIO: Molar ratio of feed gases. An input parameter.

   F. H_2O IMPLIED: An approximation of water production. Calculation of this value assumes the following:

      i. All oxygen produced from the reacted amount of CO and not as as CO_2 is present as H_2O.

      ii. No oxygenates are produced. Huff (1982) states that with the same catalyst in a slurry reactor, less than 1.1% of oxygen is present as oxygenates.

   G. $-CH_2-$IMPLIED: Carbon which is not produced as CO, CO_2, or CH_4 is assumed to be in the form of $-CH_2-$. This is the mole fraction of C fed converted to $-CH_2-$.

H. H_2 CONV IMPLIED: An approximation based on actual CH_4 production and the above approximations for H_2O and $-CH_2-$ production.

I. H_2 USED IMPLIED: Estimate of the number of moles of H_2 used. The maximum number of moles of H_2 that can be used is the H_2/CO ratio of the feed gas.

J. H_2/CO USAGE: An estimate of the number of moles of H_2 used divided by the number of moles of CO used, the H_2/CO usage ratio.

K. $-CH_2-/CO$ CONV: The mole fraction of converted carbon that went into making $-CH_2-$.

L. CALC KEQ: The calculated equilibrium constant for the water-gas shift reaction at the temperature of the reaction.

$$K_{eq} = 0.0102e^{4730/T}$$

M. EXPT KEQ: The estimated experimental value of the equilibrium constant for the water-gas shift reaction.

$$K_{eq} = \frac{X_{CO_2} X_{H_2}}{X_{CO} X_{H_2O}}$$

N. SUM = 1π: The sum of the moles of CO_2, CH_4 and $-CH_2-$ produced per mole of CO converted should add up to 1. This is an internal check on the calculation.

O. SAMPLE NUMBER: The light-gas sample identification listed chronologically. The first sample is taken 17 minutes after the start of the reaction. Subsequent samples are taken every 37 minutes.

Table B-1

The Light Gas Analysis and Implied Mass Balance
from Steady-State Experiment B-1.

DATE OF EXPERIMENT 8/4/84 STEADY STATE EXPERIMENT B-1

THIS EXPERIMENT USES 2.08:1 S-GAS FOR A 10 HOUR RUN.

TEMPERATURE= 633 # DATA PTS.= 16

SAMPLE NUMBER	CO CONV	CO2/CO CONV	CH4/CO CONV	CO/AR FED	H2/CO RATIO
1	.966422	.276265	.134523	4.636	2.08
2	.911641	.324402	.0908617	4.636	2.08
3	.800833	.362191	.103271	4.636	2.08
4	.891407	.346604	.092408	4.636	2.08
5	.895311	.340445	.0851629	4.636	2.08
6	.856242	.342975	.0873825	4.636	2.08
7	.803611	.348946	.0925898	4.636	2.08
8	.788492	.351884	.0946133	4.636	2.08
9	.764561	.353385	.0958475	4.636	2.08
10	.747883	.347915	.0969203	4.636	2.08
11	.736883	.350057	.0970436	4.636	2.08
12	.712298	.356382	.0974296	4.636	2.08
13	.666796	.354057	.0972869	4.636	2.08
14	.648861	.35015	.0955955	4.636	2.08
15	.612656	.353272	.0992682	4.636	2.08
16	.593922	.354004	.0994546	4.636	2.08

SAMPLE NUMBER	H2 CONV IMPLIED	-CH2- IMPLIED	H2O IMPLIED	H2 USED IMPLIED	H2/CO USAGE
1	.606675	.569428	.432445	1.26188	1.30573
2	.489857	.53307	.320165	1.0189	1.11766
3	.391446	.428074	.220725	.814207	1.0167
4	.451101	.500068	.273476	.938291	1.0526
5	.457913	.51426	.285704	.952458	1.06383
6	.43572	.487752	.263903	.906297	1.05846
7	.404027	.448787	.242777	.840376	1.04575
8	.393853	.434433	.233577	.819214	1.03896
9	.381432	.419566	.224192	.793379	1.03769
10	.378679	.415198	.227488	.787652	1.05317
11	.370876	.407422	.220981	.771422	1.04687
12	.353162	.389759	.206021	.734576	1.03128
13	.329909	.364508	.191962	.686211	1.02912
14	.326036	.359635	.194464	.678155	1.04515
15	.306167	.335405	.179788	.636827	1.03945
16	.296231	.324603	.173421	.61616	1.03744

SAMPLE NUMBER	-CH2- /CO CONV	CALC KEQ	EXPT KEQ	SUM=1?
1	.589213	17.9392	15.0427	1
2	.584737	17.9392	11.0927	1
3	.534538	17.9392	8.35168	1
4	.560988	17.9392	11.879	1
5	.574393	17.9392	11.4905	1
6	.569643	17.9392	8.9164	1
7	.558464	17.9392	7.2907	1
8	.553503	17.9392	7.08078	1
9	.548768	17.9392	6.58585	1
10	.555164	17.9392	5.84222	1
11	.552899	17.9392	5.80543	1
12	.547188	17.9392	5.74582	1
13	.546656	17.9392	5.17351	1
14	.554255	17.9392	4.66432	1
15	.54746	17.9392	4.48525	1
16	.546542	17.9392	4.37039	1

Table B-2

The Light Gas Analysis and Implied Mass Balance
from Steady-State Experiment B-2.

DATE OF EXPERIMENT 8/8/84 STEADY STATE EXPERIMENT B-2

THIS EXPERIMENT USES 2.08:1 S-GAS FOR A 2 HOUR AND 3 MIN RUN.

TEMPERATURE= 633 # DATA PTS.= 3

SAMPLE NUMBER	CO CONV	CO2/CO CONV	CH4/CO CONV	CO/AR FED	H2/CO RATIO
1	.963068	.13424	.142716	4.636	2.08
2	.892212	.329666	.0931131	4.636	2.08
3	.754651	.363142	.0994475	4.636	2.08

SAMPLE NUMBER	H2 CONV IMPLIED	-CH2- IMPLIED	H2O IMPLIED	H2 USED IMPLIED	H2/CO USAGE
1	.805642	.696341	.704504	1.67573	1.74
2	.473608	.515004	.303948	.985105	1.10412
3	.366449	.405557	.20656	.762214	1.01002

SAMPLE NUMBER	-CH2- /CO CONV	CALC KEQ	EXPT KEQ	SUM=1?
1	.723044	17.9392	2.00872	1
2	.577221	17.9392	9.82983	1
3	.537411	17.9392	7.12582	1

Table B-3

The Light Gas Analysis and Implied Mass Balance
from Steady-State Experiment B-3.

DATE OF EXPERIMENT 8/10/84 STEADY STATE EXPERIMENT B-3

THIS EXPERIMENT USES 4.0:1 S-GAS FOR A 10 HOURS AND 0 MIN RUN.

TEMPERATURE= 633 # DATA PTS.= 15

SAMPLE NUMBER	CO CONV	CO2/CO CONV	CH4/CO CONV	CO/AR FED	H2/CO RATIO
1	.973567	.0962746	.201998	4.636	4
2	.956313	.17781	.156962	4.636	4
3	.952031	.186857	.150122	4.636	4
4	.951405	.182455	.164748	4.636	4
5	.951987	.175773	.169086	4.636	4
6	.949969	.181263	.174073	4.636	4
7	.949731	.178116	.18173	4.636	4
8	.947566	.179716	.191255	4.636	4
9	.94181	.182996	.19458	4.636	4
10	.932798	.189936	.200122	4.636	4
11	.929033	.194449	.196096	4.636	4
12	.925626	.202317	.193371	4.636	4
13	.923659	.203195	.191573	4.636	4
14	.927369	.199923	.184958	4.636	4
15	.926805	.207322	.179122	4.636	4

SAMPLE NUMBER	H2 CONV IMPLIED	-CH2- IMPLIED	H2O IMPLIED	H2 USED IMPLIED	H2/CO USAGE
1	.465651	.683179	.786108	1.8626	1.91317
2	.388151	.636167	.61623	1.55261	1.62353
3	.378326	.631217	.596244	1.5133	1.58955
4	.384696	.621074	.604227	1.53878	1.61738
5	.390735	.623686	.61732	1.56294	1.64177
6	.38718	.612412	.605582	1.54872	1.63029
7	.391143	.607974	.611407	1.56457	1.64738
8	.391371	.596047	.606981	1.56548	1.65211
9	.387459	.586205	.597115	1.54983	1.64559
10	.380188	.568953	.578454	1.52075	1.63031
11	.374574	.566204	.567734	1.4983	1.61275
12	.367108	.559367	.551086	1.46843	1.58642
13	.365306	.559024	.548294	1.46122	1.58199
14	.367514	.570442	.556565	1.47006	1.58519
15	.360795	.568647	.542511	1.44318	1.55716

SAMPLE NUMBER	-CH2- /CO CONV	CALC KEQ	EXPT KEQ	SUM=1?
1	.701727	17.9392	9.64139	1
2	.665229	17.9392	15.4583	1
3	.663021	17.9392	15.4668	1
4	.652797	17.9392	14.5504	1
5	.655141	17.9392	13.7587	1
6	.644665	17.9392	13.9315	1
7	.640154	17.9392	13.4043	1
8	.629029	17.9392	13.0264	1
9	.622424	17.9392	12.1533	1
10	.609942	17.9392	11.3996	1
11	.609455	17.9392	11.2168	1
12	.604312	17.9392	11.567	1
13	.605228	17.9392	11.3836	1
14	.615119	17.9392	11.6034	1
15	.613556	17.9392	12.3721	1

Table B-4

The Light Gas Analysis and Implied Mass Balance
from Steady-State Experiment B-4.

DATE OF EXPERIMENT 8/14/84 STEADY STATE EXPERIMENT B-4

THIS EXPERIMENT USES 1.03:1 S-GAS FOR A 1 HOURS AND 2 MIN RUN.

TEMPERATURE= 633 # DATA PTS.= 2

SAMPLE NUMBER	CO CONV	CO2/CO CONV	CH4/CO CONV	CO/AR FED	H2/CO RATIO
1	.962388	.152279	.0953146	10.882	1.03
2	.388091	.428382	.0931238	10.882	1.03

SAMPLE NUMBER	H2 CONV IMPLIED	-CH2- IMPLIED	H2O IMPLIED	H2 USED IMPLIED	H2/CO USAGE
1	1.53092	.724106	.669284	1.57685	1.63848
2	.304436	.1857	.0858888	.313569	.807978

SAMPLE NUMBER	-CH2- /CO CONV	CALC KEQ	EXPT KEQ	SUM=1?
1	.752406	17.9392	-3.18361	1
2	.478494	17.9392	3.50159	1

Table B-5

The Light Gas Analysis and Implied Mass Balance
from Steady-State Experiment B-5.

DATE OF EXPERIMENT 8/16/84 STEADY STATE EXPERIMENT B-5

THIS EXPERIMENT USES 1.03:1 S-GAS FOR A 2 HOURS AND 13 MIN RUN.

TEMPERATURE= 633 # DATA PTS.= 4

SAMPLE NUMBER	CO CONV	CO2/CO CONV	CH4/CO CONV	CO/AR FED	H2/CO RATIO
1	.96013	.152638	.0943774	10.882	1.03
2	.402497	.465347	.0911527	10.882	1.03
3	.344521	.43468	.0937697	10.882	1.03
4	.328153	.449026	.10217	10.882	1.03

SAMPLE NUMBER	H2 CONV IMPLIED	-CH2- IMPLIED	H2O IMPLIED	H2 USED IMPLIED	H2/CO USAGE
1	1.52545	.722963	.667026	1.57122	1.63646
2	.271632	.178508	.0278959	.279781	.695113
3	.264155	.162459	.0450085	.272079	.789731
4	.240569	.147276	.0334546	.247786	.755093

SAMPLE NUMBER	-CH2- /CO CONV	CALC KEQ	EXPT KEQ	SUM=1?
1	.752985	17.9392	-2.98244	1
2	.443501	17.9392	8.43039	1
3	.471551	17.9392	3.8473	1
4	.448804	17.9392	5.12799	1

Table B-6

The Light Gas Analysis and Implied Mass Balance
from Steady-State Experiment B-6.

DATE OF EXPERIMENT 8/19/84 STEADY STATE EXPERIMENT B-6

THIS EXPERIMENT USES 2.08:1 S-GAS FOR A 2 HOURS AND 57 MIN RUN.

TEMPERATURE= 633 # DATA PTS.= 5

SAMPLE NUMBER	CO CONV	CO2/CO CONV	CH4/CO CONV	CO/AR FED	H2/CO RATIO
1	.968713	.108859	.125136	4.636	2.08
2	.911443	.322224	.0769925	4.636	2.08
3	.778902	.353329	.0937585	4.636	2.08
4	.603076	.370037	.0914459	4.636	2.08
5	.418807	.35195	.0998239	4.636	2.08

SAMPLE NUMBER	H2 CONV IMPLIED	-CH2- IMPLIED	H2O IMPLIED	H2 USED IMPLIED	H2/CO USAGE
1	.837639	.74204	.757808	1.74229	1.79856
2	.486536	.54758	.324065	1.01199	1.11032
3	.387118	.430664	.228484	.805206	1.03377
4	.284528	.324766	.156755	.591819	.981334
5	.210204	.229601	.124009	.437224	1.04397

SAMPLE NUMBER	-CH2- /CO CONV	CALC KEQ	EXPT KEQ	SUM=1?
1	.766006	17.9392	1.50202	1
2	.600783	17.9392	10.9297	1
3	.552912	17.9392	6.94483	1
4	.538517	17.9392	5.3376	1
5	.548226	17.9392	3.3597	1

Table B-7

The Light Gas Analysis and Implied Mass Balance
from Steady-State Experiment B-7.

DATE OF EXPERIMENT 8/21/84 STEADY STATE EXPERIMENT B-7

THIS EXPERIMENT USES 2.08:1 S-GAS FOR A 2 HOURS AND 45 MIN RUN.

TEMPERATURE= 633 # DATA PTS.= 4

SAMPLE NUMBER	CO CONV	CO2/CO CONV	CH4/CO CONV	CO/AR FED	H2/CO RATIO
1	.972577	.103765	.127887	4.636	2.08
2	.915845	.321638	.0791721	4.636	2.08
3	.72949	.367079	.0964375	4.636	2.08
4	.568199	.375146	.0904873	4.636	2.08

SAMPLE NUMBER	H2 CONV IMPLIED	-CH2- IMPLIED	H2O IMPLIED	H2 USED IMPLIED	H2/CO USAGE
1	.849411	.747277	.770737	1.76677	1.81659
2	.49062	.548766	.326705	1.02049	1.11426
3	.349034	.39136	.19393	.72599	.965202
4	.263625	.303627	.141884	.54834	.965048

SAMPLE NUMBER	-CH2- /CO CONV	CALC KEQ	EXPT KEQ	SUM=1?
1	.768348	17.9392	1.49556	1
2	.59919	17.9392	11.3516	1
3	.536484	17.9392	6.9115	1
4	.534366	17.9392	5.32904	1

Table B-8

The Light Gas Analysis and Implied Mass Balance
from Steady-State Experiment C-1.

DATE OF EXPERIMENT 8/24/84 STEADY STATE EXPERIMENT C-1

THIS EXPERIMENT USES 2.08:1 S-GAS FOR A 2 HOURS AND 4 MIN RUN.

TEMPERATURE= 673 # DATA PTS.= 3

SAMPLE NUMBER	CO CONV	CO2/CO CONV	CH4/CO CONV	CO/AR FED	H2/CO RATIO
1	.967754	.102517	.175733	4.636	2.08
2	.879722	.323356	.162606	4.636	2.08
3	.934199	.300684	.129202	4.636	2.08

SAMPLE NUMBER	H2 CONV IMPLIED	-CH2- IMPLIED	H2O IMPLIED	H2 USED IMPLIED	H2/CO USAGE
1	.869202	.698477	.769332	1.80794	1.86818
2	.504376	.452211	.310795	1.0491	1.19254
3	.551155	.532599	.372401	1.1464	1.22715

SAMPLE NUMBER	-CH2- /CO CONV	CALC KEQ	EXPT KEQ	SUM=1?
1	.721751	11.5059	1.088	1
2	.514038	11.5059	7.84478	1
3	.570114	11.5059	10.702	1

Table B-9

The Light Gas Analysis and Implied Mass Balance from Steady-State Experiment C-2.

DATE OF EXPERIMENT 8/27/84 STEADY STATE EXPERIMENT C-2

THIS EXPERIMENT USES 1.03:1 S-GAS FOR A 1 HOUR AND 0 MIN RUN.

TEMPERATURE= 673 # DATA PTS.= 2

SAMPLE NUMBER	CO CONV	CO2/CO CONV	CH4/CO CONV	CO/AR FED	H2/CO RATIO
1	.95979	.15042	.132879	10.882	1.03
2	.947319	.396854	.0796436	10.882	1.03

SAMPLE NUMBER	H2 CONV IMPLIED	-CH2- IMPLIED	H2O IMPLIED	H2 USED IMPLIED	H2/CO USAGE
1	1.56699	.687883	.671048	1.614	1.63162
2	.817712	.495923	.195424	.842243	.889081

SAMPLE NUMBER	-CH2- /CO CONV	CALC KEQ	EXPT KEQ	SUM=1?
1	.716702	11.5059	-3.12471	1
2	.523502	11.5059	6.85627	1

Table B-10.

The Light Gas Analysis and Implied Mass Balance from Steady-State Experiment D-1.

DATE OF EXPERIMENT 8/29/84 STEADY STATE EXPERIMENT D-1

THIS EXPERIMENT USES 1.03:1 S-GAS FOR A 1 HOUR AND 15 MIN RUN.

TEMPERATURE= 653 # DATA PTS.= 2

SAMPLE NUMBER	CO CONV	CO2/CO CONV	CH4/CO CONV	CO/AR FED	H2/CO RATIO
1	.968372	.117161	.12634	10.882	1.03
2	.489223	.438333	.112811	10.882	1.03

SAMPLE NUMBER	H2 CONV IMPLIED	-CH2- IMPLIED	H2O IMPLIED	H2 USED IMPLIED	H2/CO USAGE
1	1.66866	.732573	.741461	1.71872	1.77486
2	.378939	.21959	.0603374	.390307	.797811

SAMPLE NUMBER	-CH2- /CO CONV	CALC KEQ	EXPT KEQ	SUM=1?
1	.756499	14.2695	-3.33199	1
2	.448855	14.2695	4.45107	1

Table B-11

The Light Gas Analysis and Implied Mass Balance from Steady-State Experiment D-2.

DATE OF EXPERIMENT 9/4/84 STEADY STATE EXPERIMENT D-2

THIS EXPERIMENT USES 2.08:1 S-GAS FOR A 2 HOUR AND 48 MIN RUN.

TEMPERATURE= 653 # DATA PTS.= 5

SAMPLE NUMBER	CO CONV	CO2/CO CONV	CH4/CO CONV	CO/AR FED	H2/CO RATIO
1	.98133	.0654104	.183736	4.636	2.08
2	.913697	.315628	.115818	4.636	2.08
3	.908702	.325845	.11064	4.636	2.08
4	.919892	.32283	.101275	4.636	2.08
5	.887258	.332828	.10012	4.636	2.08

SAMPLE NUMBER	H2 CONV IMPLIED	-CH2- IMPLIED	H2O IMPLIED	H2 USED IMPLIED	H2/CO USAGE
1	.937691	.736835	.852951	1.9504	1.98751
2	.513486	.519486	.33692	1.06805	1.16893
3	.495026	.512067	.316509	1.02965	1.1331
4	.500981	.529761	.325954	1.04204	1.13279
5	.46992	.503121	.296649	.977434	1.10164

SAMPLE NUMBER	-CH2- /CO CONV	CALC KEQ	EXPT KEQ	SUM=1?
1	.750853	14.2695	.522391	1
2	.563554	14.2695	10.0365	1
3	.563515	14.2695	10.7626	1
4	.575894	14.2695	11.8048	1
5	.567052	14.2695	9.7352	1

Table B-12

The Light Gas Analysis and Implied Mass Balance
from Steady-State Experiment E-1.

DATE OF EXPERIMENT 9/8/84 STEADY STATE EXPERIMENT E-1

THIS EXPERIMENT USES 2.08:1 S-GAS FOR A 2 HOUR AND 50 MIN RUN.

TEMPERATURE= 663 # DATA PTS.= 5

SAMPLE NUMBER	CO CONV	CO2/CO CONV	CH4/CO CONV	CO/AR FED	H2/CO RATIO
1	.959728	.153064	.146365	4.636	2.08
2	.851051	.339254	.144345	4.636	2.08
3	.931852	.314146	.116154	4.636	2.08
4	.932198	.313923	.110444	4.636	2.08
5	.94235	.300319	.110482	4.636	2.08

SAMPLE NUMBER	H2 CONV IMPLIED	-CH2- IMPLIED	H2O IMPLIED	H2 USED IMPLIED	H2/CO USAGE
1	.778475	.672358	.665929	1.61923	1.68717
2	.460951	.439483	.273606	.958779	1.12658
3	.525804	.530857	.346339	1.09367	1.17365
4	.523768	.536604	.346921	1.08944	1.16868
5	.547979	.555231	.376338	1.1398	1.20952

SAMPLE NUMBER	-CH2- /CO CONV	CALC KEQ	EXPT KEQ	SUM=1?
1	.700571	12.7926	2.52392	1
2	.516401	12.7926	7.94345	1
3	.56968	12.7926	12.2342	1
4	.575634	12.7926	12.3236	1
5	.589198	12.7926	12.2643	1

Table B-13

The Light Gas Analysis and Implied Mass Balance
from Steady-State Experiment F-1.

DATE OF EXPERIMENT 9/11/84 STEADY STATE EXPERIMENT F-1

THIS EXPERIMENT USES 4.0:1 S-GAS FOR A 3 HOUR AND 30 MIN RUN.

TEMPERATURE= 668 # DATA PTS.= 6

SAMPLE NUMBER	CO CONV	CO2/CO CONV	CH4/CO CONV	CO/AR FED	H2/CO RATIO
1	.991424	.0230512	.32396	4.636	4
2	.952072	.148586	.245386	4.636	4
3	.953104	.143642	.285975	4.636	4
4	.948115	.151278	.319167	4.636	4
5	.937733	.163681	.328821	4.636	4
6	.933078	.166705	.322957	4.636	4

SAMPLE NUMBER	H2 CONV IMPLIED	-CH2- IMPLIED	H2O IMPLIED	H2 USED IMPLIED	H2/CO USAGE
1	.558867	.647389	.245717	2.23547	2.25481
2	.429344	.576983	.669144	1.71338	1.79963
3	.442014	.543635	.679293	1.76806	1.85505
4	.442138	.502079	.661258	1.76855	1.84533
5	.430836	.475898	.630755	1.72335	1.83778
6	.425213	.476185	.62198	1.70085	1.82284

SAMPLE NUMBER	-CH2- /CO CONV	CALC KEQ	EXPT KEQ	SUM=1?
1	.652989	12.1274	4.97222	1
2	.606028	12.1274	10.0863	1
3	.570383	12.1274	9.59208	1
4	.529565	12.1274	9.32846	1
5	.507499	12.1274	8.89719	1
6	.510338	12.1274	8.59189	1

Table B-14

The Light Gas Analysis and Implied Mass Balance
from Steady-State Experiment F-2.

DATE OF EXPERIMENT 9/13/84 STEADY STATE EXPERIMENT F-2

THIS EXPERIMENT USES 4.0:1 S-GAS FOR A 2 HOUR AND 0 MIN RUN.

TEMPERATURE= 668 # DATA PTS.= 3

SAMPLE NUMBER	CO CONV	CO2/CO CONV	CH4/CO CONV	CO/AR FED	H2/CO RATIO
1	.971771	*******	.296196	4.636	4
2	.964579	.10431	.287981	4.636	4
3	.965401	.0996195	.33188	4.636	4

SAMPLE NUMBER	H2 CONV IMPLIED	-CH2- IMPLIED	H2O IMPLIED	H2 USED IMPLIED	H2/CO USAGE
1	.557842	.683934	.971764	2.23137	2.29619
2	.476273	.586184	.763348	1.90509	1.97505
3	.49067	.548831	.773055	1.96268	2.03302

SAMPLE NUMBER	-CH2- /CO CONV	CALC KEQ	EXPT KEQ	SUM=1?
1	.703801	12.1274	*******	1
2	.607709	12.1274	7.79565	1
3	.568501	12.1274	7.3254	1

****** INDICATES THAT THE CO2 PEAK WAS NOT INTEGRATED IN THIS SAMPLE

Table B-15

The Light Gas Analysis and Implied Mass Balance
from Steady-State Experiment F-3.

DATE OF EXPERIMENT 9/18/84 STEADY STATE EXPERIMENT F-3

THIS EXPERIMENT USES 2.08:1 S-GAS FOR A 1 HOUR AND 0 MIN RUN
AFTER FIRST EXPOSING IT TO 4:1 PRECARB. GAS FOR 2 HOURS.

TEMPERATURE= 668 # DATA PTS.= 5

SAMPLE NUMBER	CO CONV	CO2/CO CONV	CH4/CO CONV	CO/AR FED	H2/CO RATIO
1	.985622	.0361131	.312424	4.636	4
2	.955101	.139841	.248323	4.636	4
3	.950854	.145242	.282584	4.636	4
4	.949619	.147803	.319799	4.636	2.08
5	.912643	.312974	.160159	4.636	2.08

SAMPLE NUMBER	H2 CONV IMPLIED	-CH2- IMPLIED	H2O IMPLIED	H2 USED IMPLIED	H2/CO USAGE
1	.543099	.642096	.914434	2.17239	2.20409
2	.436672	.584365	.687976	1.74669	1.8288
3	.439023	.544054	.674646	1.75609	1.84686
4	.856661	.505575	.648906	1.78186	1.87639
5	.535843	.480841	.341376	1.11455	1.22124

SAMPLE NUMBER	-CH2- /CO CONV	CALC KEQ	EXPT KEQ	SUM=1?
1	.651463	12.1274	4.94773	1
2	.611835	12.1274	9.74309	1
3	.572175	12.1274	9.34639	1
4	.532398	12.1274	1.24172	1
5	.526866	12.1274	9.2472	1

Table B-16

The Light Gas Analysis and Implied Mass Balance
from Steady-State Experiment F-4.

DATE OF EXPERIMENT 9/20/84 STEADY STATE EXPERIMENT F-4

THIS EXPERIMENT USES 2.08:1 S-GAS FOR A 2 HOUR RUN
AFTER FIRST EXPOSING IT TO 4:1 PRECARB. GAS FOR 2 HOURS.

TEMPERATURE= 668 # DATA PTS.= 6

SAMPLE NUMBER	CO CONV	CO2/CO CONV	CH4/CO CONV	CO/AR FED	H2/CO RATIO
1	.984279	.0403726	.29192	4.636	4
2	.951694	.145227	.245333	4.636	4
3	.949076	.149819	.289544	4.636	4
4	.942934	.153585	.314931	4.636	2.08
5	.920779	.309185	.152934	4.636	2.08
6	.93619	.296109	.134311	4.636	2.08

SAMPLE NUMBER	H2 CONV IMPLIED	-CH2- IMPLIED	H2O IMPLIED	H2 USED IMPLIED	H2/CO USAGE
1	.534163	.65721	.904801	2.13667	2.1708
2	.430559	.58	.675271	1.72224	1.80965
3	.436596	.532087	.664697	1.74638	1.84009
4	.840561	.501155	.653294	1.74837	1.85418
5	.542454	.495269	.351397	1.1283	1.22588
6	.560807	.533236	.381762	1.16648	1.24599

SAMPLE NUMBER	-CH2- /CO CONV	CALC KEQ	EXPT KEQ	SUM=1?
1	.667707	12.1274	5.20561	1
2	.60944	12.1274	9.65094	1
3	.560637	12.1274	9.46677	1
4	.531484	12.1274	1.28826	1
5	.53788	12.1274	9.73277	1
6	.569581	12.1274	10.3957	1

Table B-17

The Light Gas Analysis and Implied Mass Balance
from Steady-State Experiment F-5.

DATE OF EXPERIMENT 9/25/84 STEADY STATE EXPERIMENT F-5

THIS EXPERIMENT USES 1.03:1 S-GAS FOR A 22 MINUTE RUN
AFTER FIRST EXPOSING IT TO 4:1 PRECARB. GAS FOR 2 HOURS.

TEMPERATURE= 668 # DATA PTS.= 3

SAMPLE NUMBER	CO CONV	CO2/CO CONV	CH4/CO CONV	CO/AR FED	H2/CO RATIO
1	.937643	.242925	.171306	10.882	4
2	.88993	.284862	.196517	10.882	4
3	.930952	.26168	.175897	10.882	4

SAMPLE NUMBER	H2 CONV IMPLIED	-CH2- IMPLIED	H2O IMPLIED	H2 USED IMPLIED	H2/CO USAGE
1	.338145	.549243	.48209	1.35258	1.44253
2	.298556	.461536	.382915	1.19422	1.34193
3	.323705	.523589	.443729	1.29482	1.39086

SAMPLE NUMBER	-CH2- /CO CONV	CALC KEQ	EXPT KEQ	SUM=1?
1	.585769	12.1274	20.0596	1
2	.518621	12.1274	16.8761	1
3	.562423	12.1274	21.5092	1

B.2 Major Hydrocarbon Product Analysis--Output from the Microcomputer Data Compilation Program "HEAVY. BAS."

1. Input

   A. Moles of CH_4 produced per mole of CO converted.

      i. Obtained from light-gas analysis.

   B. Flow Rate of the synthesis gas.

   C. Fraction of CO in the S-gas feed.

   D. Moles of CO converted per mole of CO fed.

      i. Obtained from the light-gas analysis.

   E. Moles of CO_2 produced per mole of CO converted.

      i. Obtained from the light-gas analysis.

   F. Peak areas for 24 hydrocarbons.

2. Output

   A. NORM AREA: Normalized peak areas of the 24 hydrocarbon. Normalized to CH_4.

   B. WT FRACT: The weight fraction of each hydrocarbon peak. Assumes FID response factors for all hydrocarbons are 1.

   C. HC/CO CONV: The moles of hydrocarbon produced per mole of CO consumed.

   D. RATE PROD: The rate of production of each hydrocarbon product in mmoles per hour.

   E. M.W.: The molecular weight of each hydrocarbon. For fused peaks (C_2 and C_3) the average molecular weight is used.

   F. MOLE CΔ: The number of moles of each carbon number hydrocarbon product produced per mole of CO converted.

   G. MOLFRC CΔ: The mole fraction of each carbon number hydrocarbon product produced.

   H. WT CΔ: The weight fraction of each carbon number of hydrocarbon product.

I. WTFRAC CΔ: The weight fraction of each carbon number hydrocarbon product.

J. RATE CΔ: The rate of production of each carbon number hydrocarbon product in mmoles per hour.

Table B-18

The Hydrocarbon Product Distribution and Rate of Production as Analyzed by Gas Chromatography for Steady-State Experiment B-1.

DATE OF EXPERIMENT 8/4/84 STEADY STATE W/O PRECARB.

EXPERIMENT B-1: THIS EXPERIMENT CONSISTS OF 10 HOURS OF 2.08:1 S-GAS FLOW AT 633K.

PEAK #	NORM AREA	WT FRACT.	HC/CO CONV	RATE PROD	M.W.
1	1	.262098	.09945	10.7847	16.043
2	.578784	.151698	.0317747	3.44574	29.062
3	.696402	.182525	.025786	2.79631	43.089
4	.429139	.112476	.0122029	1.32332	56.108
5	.066838	.0175181	1.83467E-03	.198957	58.124
6	.0162383	4.25601E-03	4.61748E-04	.0500734	56.108
7	.019747	5.17565E-03	5.61523E-04	.0608933	56.108
8	.271563	.0711759	6.17768E-03	.669926	70.135
9	.0498735	.0130717	1.10285E-03	.119597	72.151
10	.0128193	3.3599E-03	2.91621E-04	.0316242	70.135
11	.0105182	2.75678E-03	2.39274E-04	.0259476	70.135
12	.205957	.0539808	3.90436E-03	.423401	84.162
13	.0377479	9.89362E-03	6.98854E-04	.0757858	86.178
14	.0127213	3.33423E-03	2.41161E-04	.0261522	84.162
15	.12519	.0328119	2.03421E-03	.220596	98.189
16	.0261281	6.84811E-03	4.16015E-04	.0451139	100.205
17	3.37005E-03	8.83283E-04	5.47601E-05	5.93835E-03	98.189
18	8.60057E-03	2.25419E-03	1.39751E-04	.015155	98.189
19	.0930641	.0243919	1.32318E-03	.143489	112.216
20	.0255406	6.69413E-03	3.56725E-04	.0386843	114.232
21	.0638107	.0167246	8.06448E-04	.0874537	126.243
22	.0174623	4.57682E-03	2.17222E-04	.0235562	128.259
23	.0309017	8.09926E-03	3.51486E-04	.0381162	140.27
24	.012958	3.39625E-03	1.453E-04	.0157568	142.286

CARBON #	MOLES C#	MOLFRC C#	WT C#	WTFRAC C#	RATE C#
1	.09945	.521849	.262098	.262098	10.7847
2	.0317747	.166733	.151698	.151698	3.44574
3	.025786	.135308	.182525	.182525	2.79631
4	.0150609	.0790296	.139426	.139426	1.63325
5	7.81143E-03	.0409893	.0903643	.0903643	.847095
6	4.84438E-03	.0254201	.0672086	.0672086	.525339
7	2.64474E-03	.0138779	.0427975	.0427975	.286803
8	1.6799E-03	8.81503E-03	.031086	.031086	.182174
9	1.02367E-03	5.37155E-03	.0213014	.0213014	.11101
10	4.96786E-04	2.60681E-03	.0114955	.0114955	.0538729

TOTAL PEAK AREA= 467574
TOTAL MOLE CARBON PRODUCED AS OLE&PAR/MOLE CO CONV= .414857
MOLE RATIO C1/(C2-C4)= 1.16619
WEIGHT FRACTION C1/(C2-C5) .415222
RATES ARE IN UNITS OF MMOLES PER HOUR
AVG MOL WTS ARE USED FOR C2 AND C3 HYDROCBNS DUE TO FUSED PEAKS
TOT MOLE C PRODUCED AS CO2 AND OLE&PARA/MOLE CO CONV= .768858

Table B-19

The Hydrocarbon Product Distribution and Rate of Production as Analyzed by Gas Chromatography for Steady-State Experiment B-2.

DATE OF EXPERIMENT 8/8/84 STEADY STATE W/O PRECARB.

EXPERIMENT B-2: THIS EXPERIMENT CONSISTS OF 2 HOURS AND 3 MIN OF 2.08:1 S-GAS FLOW AT 633K.

PEAK #	NORM AREA	WT FRACT.	HC/CO CONV	RATE PROD	M.W.
1	1	.268172	.09945	13.4465	16.043
2	.601216	.161229	.0330062	4.46273	29.062
3	.681716	.182817	.0252422	3.41297	43.089
4	.415909	.111535	.0118247	1.59907	56.108
5	.0607859	.0163011	1.66854E-03	.225602	58.124
6	.0161563	4.33266E-03	4.59417E-04	.0621172	56.108
7	.0176762	4.74026E-03	5.02637E-04	.0679609	56.108
8	.262424	.0703748	5.96979E-03	.807168	70.135
9	.0426875	.0114476	9.43948E-04	.12763	72.151
10	.0133902	3.59271E-03	2.81861E-04	.0381101	70.135
11	.0107239	2.87586E-03	2.43955E-04	.0329849	70.135
12	.213358	.0572168	4.04468E-03	.546876	84.162
13	.034249	9.18463E-03	6.34078E-04	.0857328	86.178
14	.0144168	3.86618E-03	2.73302E-04	.0369529	84.162
15	.115633	.0310095	1.87892E-03	.254046	98.189
16	.0273474	7.33382E-03	4.35429E-04	.0588739	100.205
17	3.22E-03	8.63512E-04	5.23218E-05	7.07437E-03	98.189
18	.0101385	2.71886E-03	1.64741E-04	.0222744	98.189
19	.0720671	.0193264	1.02464E-03	.138541	112.216
20	.0175918	4.71762E-03	2.45704E-04	.0332213	114.232
21	.0497973	.0133542	6.29346E-04	.085093	126.243
22	.0142367	3.81787E-03	1.77097E-04	.023945	128.259
23	.0261709	7.0183E-03	2.97676E-04	.0402485	140.27
24	9.04076E-03	2.42448E-03	1.01376E-04	.0137069	142.286

CARBON #	MOLES C#	MOLFRC C#	WT C#	WTFRAC C#	RATE C#
1	.09945	.524651	.268172	.268172	13.4465
2	.0330062	.174125	.161229	.161229	4.46273
3	.0252422	.133166	.182817	.182817	3.41297
4	.0144573	.0762698	.136909	.136909	1.95475
5	7.43956E-03	.0392476	.0880209	.0880209	1.00589
6	4.95206E-03	.0261247	.0702676	.0702676	.669562
7	2.53141E-03	.0133545	.0419256	.0419256	.342269
8	1.27035E-03	6.70175E-03	.024044	.024044	.171762
9	8.06442E-04	4.25441E-03	.0171721	.0171721	.109038
10	3.99052E-04	2.10521E-03	9.44278E-03	9.44278E-03	.0539553

TOTAL PEAK AREA= 662411
TOTAL MOLE CARBON PRODUCED AS OLE&PAR/MOLE CO CONV= .40506
MOLE RATIO C1/(C2-C6)= 1.16866
WEIGHT FRACTION C1/(C2-C5) .419514
RATES ARE IN UNITS OF MMOLES PER HOUR
AVG MOL WTS ARE USED FOR C2 AND C3 HYDROCBNS DUE TO FUSED PEAKS
TOT MOLE C PRODUCED AS CO2 AND OLE&PARA/MOLE CO CONV= .768059

Table B-20

The Hydrocarbon Product Distribution and Rate of Production as Analyzed by Gas Chromatography for Steady-State Experiment B-3.

DATE OF EXPERIMENT 8/10/84 STEADY STATE W/O PRECARB.

EXPERIMENT B-3: THIS EXPERIMENT CONSISTS OF 10 HOURS OF 4.0:1 S-GAS FLOW AT 633K.

PEAK #	NORM AREA	WT FRACT.	HC/CO CONV	RATE PROD	M.W.
1	1	.327338	.1791	18.8321	16.043
2	.47654	.155989	.0471145	4.95401	29.062
3	.572579	.189718	.038648	4.06377	40.089
4	.347677	.113808	.0178046	1.87212	56.108
5	.0570124	.0186623	2.81835E-03	.296345	58.124
6	.013626	4.4603E-03	6.97789E-04	.0733714	56.108
7	.0147805	4.83822E-03	7.56913E-04	.0795881	58.108
8	.208017	.0680919	8.52209E-03	.896083	70.135
9	.0389259	.0127419	1.55016E-03	.162997	72.151
10	.0105226	3.44444E-03	4.31091E-04	.0453285	70.135
11	7.23268E-03	2.36753E-03	2.96309E-04	.0311564	70.135
12	.112713	.0368951	3.84802E-03	.404613	84.162
13	.0241421	7.90263E-03	8.04935E-04	.0846375	86.178
14	7.63145E-03	2.49806E-03	2.60539E-04	.0273952	84.162
15	.053626	.0175538	1.56926E-03	.165005	98.189
16	.0112655	3.68761E-03	3.23029E-04	.033966	100.205
17	1.62084E-03	5.30562E-04	4.74306E-05	4.98725E-03	98.189
18	6.00418E-03	1.96539E-03	1.757E-04	.0184746	98.189
19	.0360765	.0118092	9.33743E-04	.0971301	112.216
20	9.4967E-03	3.10863E-03	2.38873E-04	.0251171	114.232
21	.0196077	6.41832E-03	4.46272E-04	.0469247	126.243
22	5.96559E-03	1.95276E-03	1.33643E-04	.0140524	128.259
23	9.34556E-03	3.05915E-03	1.91435E-04	.0201291	140.27
24	3.54398E-03	1.16008E-03	7.15666E-05	7.525IE-03	142.286

CARBON #	MOLES C#	MOLFRC C#	WT C#	WTFRAC C#	RATE C#
1	.1791	.583817	.327338	.327338	18.8321
2	.0471145	.15358	.155989	.155989	4.95401
3	.038648	.125982	.189718	.189718	4.06377
4	.0220776	.071967	.141768	.141768	2.32143
5	.0107997	.0352039	.0866458	.0866458	1.13537
6	4.9135E-03	.0160167	.0472958	.0472958	.516646
7	2.11542E-03	6.89567E-03	.0237374	.0237374	.222432
8	1.16262E-03	3.78981E-03	.0149178	.0149178	.122247
9	5.79915E-04	1.89036E-03	8.37108E-03	8.37108E-03	.0609771
10	2.63002E-04	8.57313E-04	4.21923E-03	4.21923E-03	.0276542

TOTAL PEAK AREA= 949937
TOTAL MOLE CARBON PRODUCED AS OLE&PAR/MOLE CO CONV= .593021
MOLE RATIO C1/(C2-C6)= 1.44958
WEIGHT FRACTION C1/(C2-C5) .52676
RATES ARE IN UNITS OF MMOLES PER HOUR
AVG MOL WTS ARE USED FOR C2 AND C3 HYDROCBNS DUE TO FUSED PEAKS
TOT MOLE C PRODUCED AS CO2 AND OLE&PARA/MOLE CO CONV= .800321

Table B-21

The Hydrocarbon Product Distribution and Rate of Production as Analyzed by Gas Chromatography for Steady-State Experiment C-1.

DATE OF EXPERIMENT 8/24/84 STEADY STATE W/O PRECARB.

EXPERIMENT C-1: THIS EXPERIMENT CONSISTS OF 2 HOURS AND 4 MIN OF 2.08:1 S-GAS FLOW AT 673K.

PEAK #	NORM AREA	WT FRACT.	HC/CO CONV	RATE PROD	M.W.
1	1	.342877	.1292	21.6253	16.043
2	.458467	.157198	.0326987	5.47305	29.062
3	.54247	.186001	.026095	4.36774	43.089
4	.333099	.114212	.0123054	2.05966	56.108
5	.0434648	.0149031	1.55E-03	.259435	58.124
6	.0129689	4.44674E-03	4.791E-04	.0801909	56.108
7	.0147911	5.07153E-03	5.46417E-04	.0914582	56.108
8	.185355	.0635539	5.47794E-03	.916887	70.135
9	.0383379	9.71642E-03	8.14092E-04	.136261	72.151
10	9.11623E-03	3.12575E-03	2.69419E-04	.0450949	70.135
11	.0103033	3.53276E-03	3.04501E-04	.0509668	70.135
12	.0991332	.0339905	2.44147E-03	.408649	84.162
13	.0178055	6.10511E-03	4.2826E-04	.0716813	86.178
14	7.92919E-03	2.71874E-03	1.95282E-04	.0326859	84.162
15	.0536379	.0183912	1.32229E-03	.13955	98.189
16	.0104542	3.58452E-03	2.16248E-04	.0361952	100.205
17	2.69166E-03	9.22908E-04	5.68205E-05	9.51052E-03	98.189
18	3.31381E-03	1.13623E-03	6.99541E-05	.0117088	98.189
19	.0340752	.0116836	6.29403E-04	.105349	112.216
20	8.62163E-03	2.95616E-03	1.56441E-04	.0261848	114.232
21	.0216504	7.42343E-03	3.55473E-04	.0594985	126.243
22	4.6284E-03	1.58697E-03	7.47982E-05	.0125196	128.259
23	.0104725	3.59077E-03	1.54751E-04	.0259019	140.27
24	3.70949E-03	1.2719E-03	5.40381E-05	9.0448E-03	142.286

CARBON #	MOLES C#	MOLFRC C#	WT C#	WTFRAC C#	RATE C#
1	.1292	.598964	.342877	.342877	21.6253
2	.0326987	.151589	.157198	.157198	5.47305
3	.026095	.120975	.186001	.186001	4.36774
4	.0148809	.0689872	.138633	.138633	2.49075
5	6.86595E-03	.0318301	.0799288	.0799288	1.14901
6	3.06501E-03	.0142092	.0428143	.0428144	.513016
7	1.47531E-03	6.83946E-03	.0240349	.0240349	.246935
8	7.85849E-04	3.64315E-03	.0146398	.0146398	.131534
9	4.30271E-04	1.99471E-03	9.0104E-03	9.0104E-03	.0720181
10	2.08789E-04	9.67933E-04	4.86267E-03	4.86267E-03	.0349467

TOTAL PEAK AREA= 1.12037E+06
TOTAL MOLE CARBON PRODUCED AS OLE&PAR/MOLE CO CONV= .4077
MOLE RATIO C1/(C2-C6)= 1.54535
WEIGHT FRACTION C1/(C2-C5) .567138
RATES ARE IN UNITS OF MMOLES PER HOUR
AVG MOL WTS ARE USED FOR C2 AND C3 HYDROCBNS DUE TO FUSED PEAKS
TOT MOLE C PRODUCED AS CO2 AND OLE&PARA/MOLE CO CONV= .7084

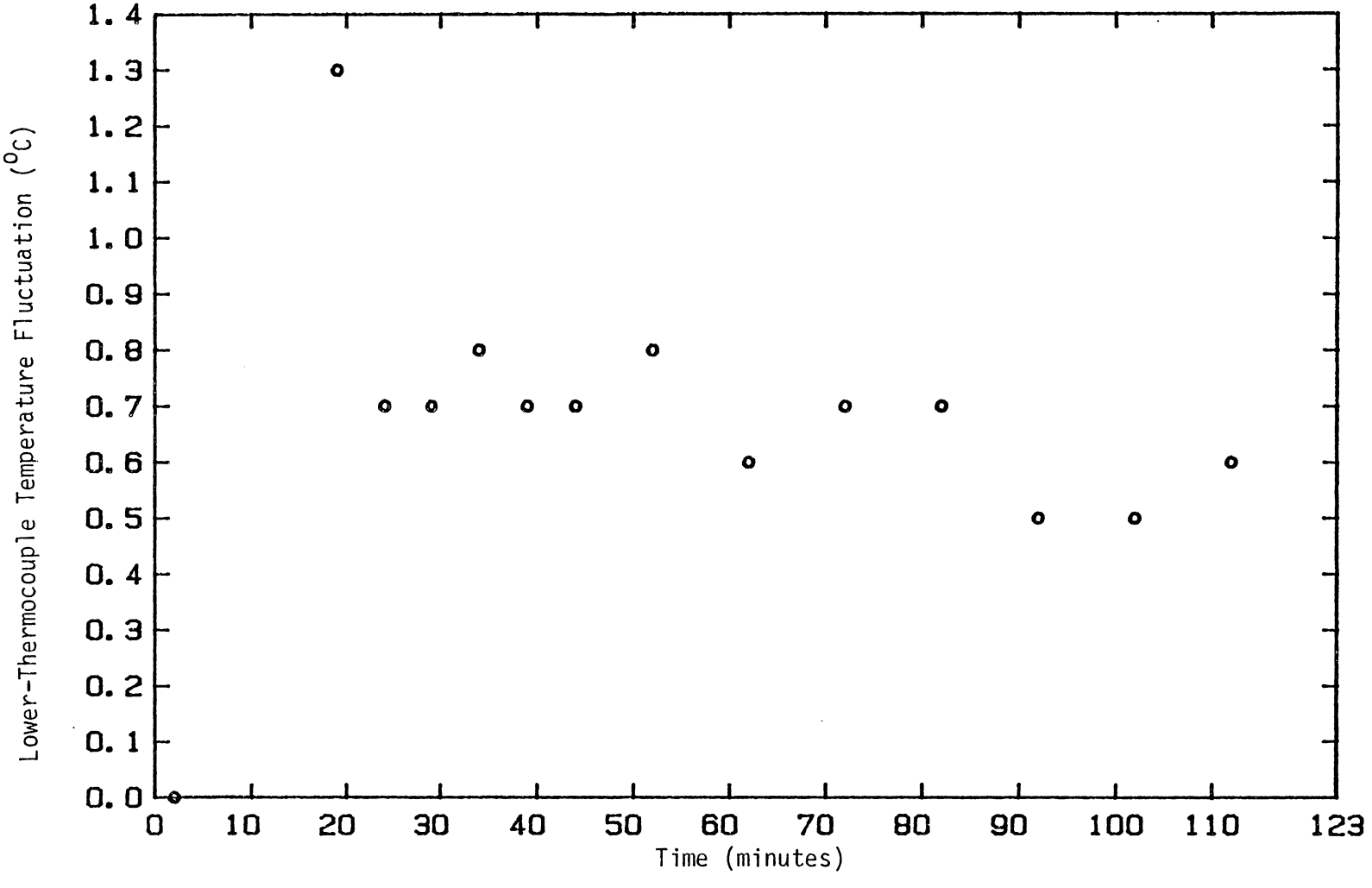

Figure B.1. Lower-Thermocouple Temperature Fluctuation as a Function of Time for Run B-2 Using a Feed Gas of 2.08:1 H_2/CO Ratio at 360°C and 2220 kPa.

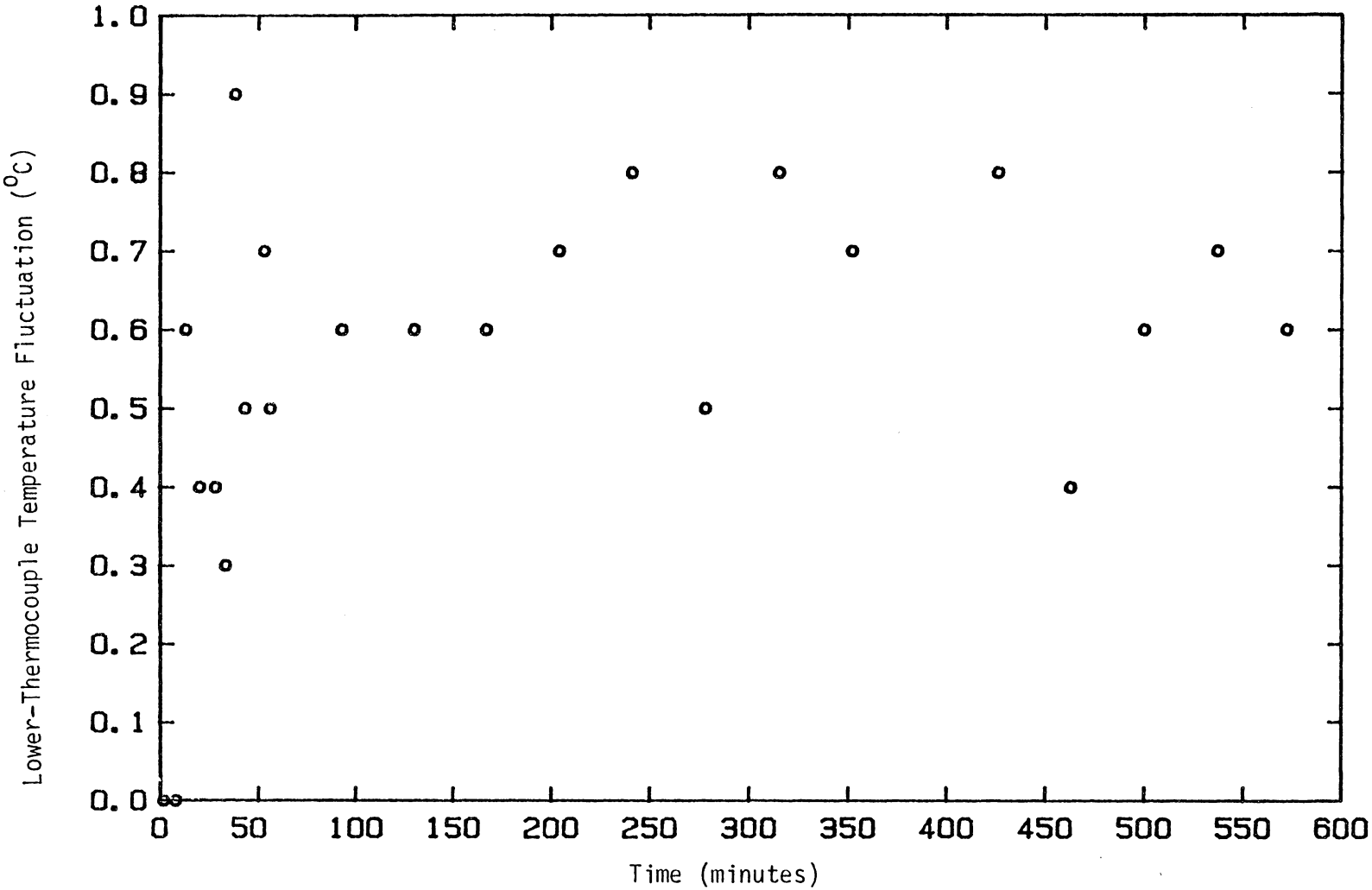

Figure B.2. Lower-Thermocouple Temperature Fluctuation as a Function of Time for Run B-3 Using a Feed Gas of 4:1 H_2/CO Ratio at 360°C and 2220 kPa.

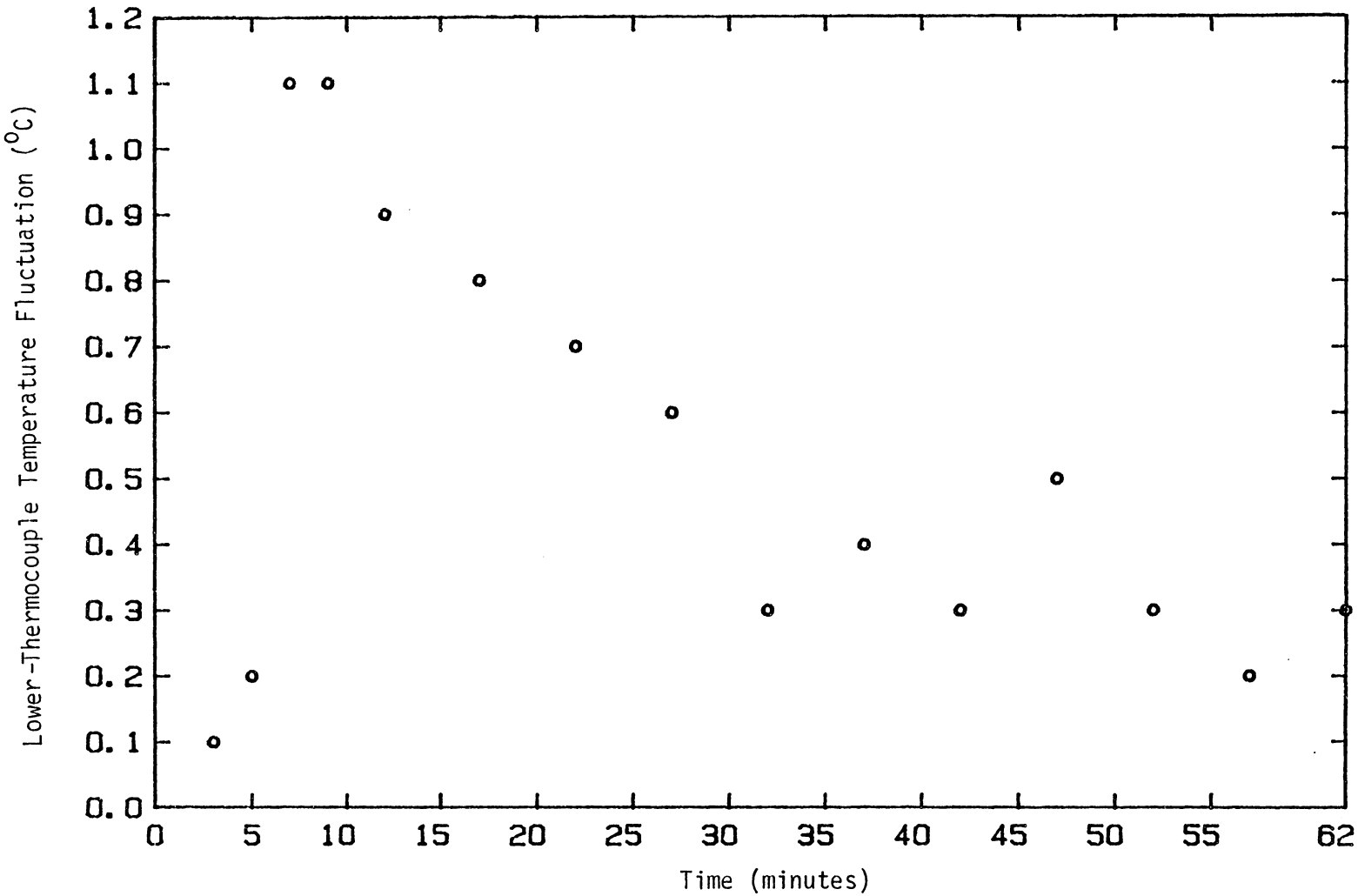

Figure B.3. Lower-Thermocouple Temperature Fluctuation as a Function of Time for Run B-4 Using a Feed Gas of 1.03:1 H_2/CO Ratio at 360°C and 2220 kPa.

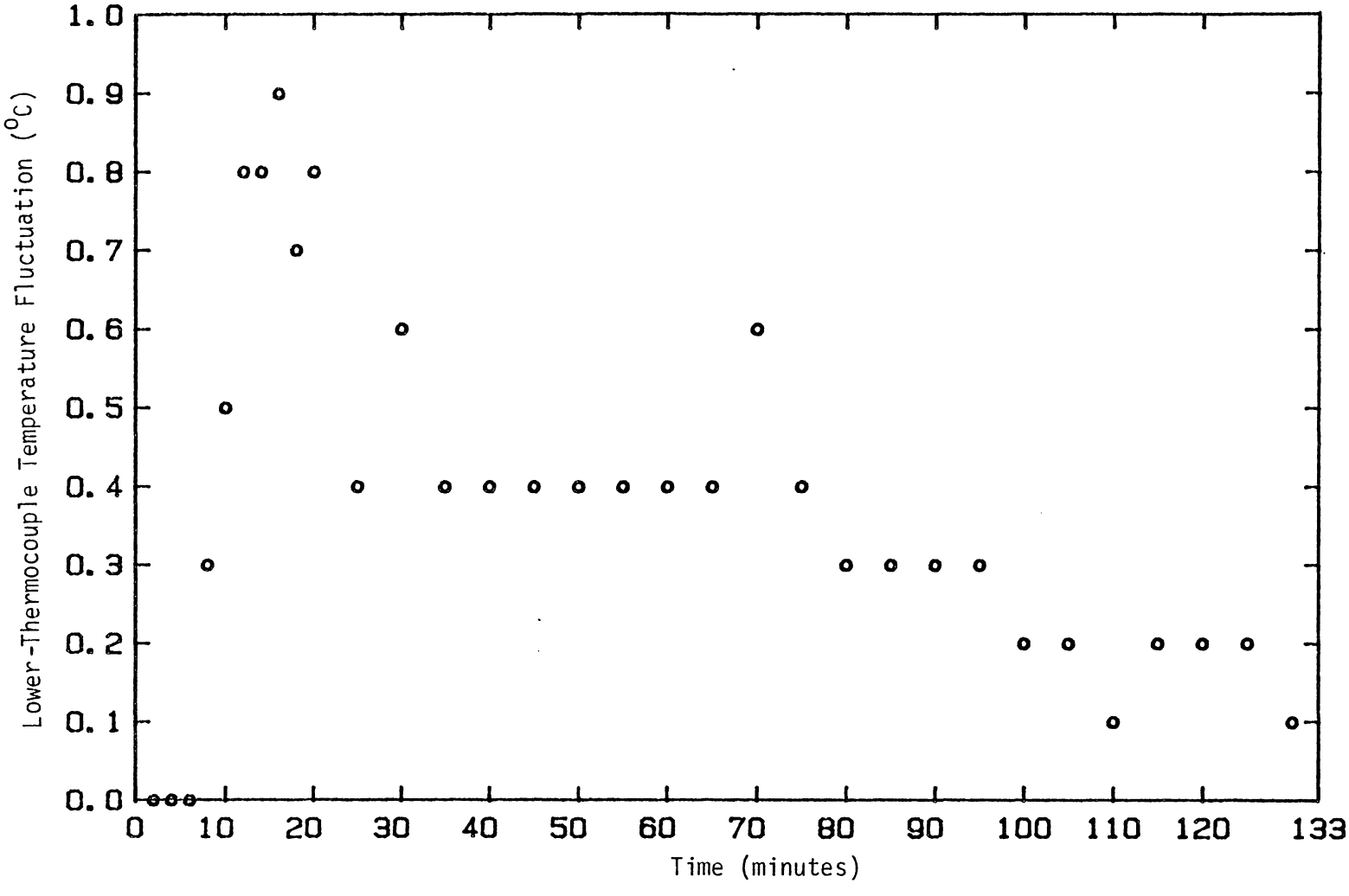

Figure B.4. Lower-Thermocouple Temperature Fluctuation as a Function of Time for Run B-5 Using a Feed Gas of 1.03:1 H_2/CO Ratio at 360°C and 2220 kPa.

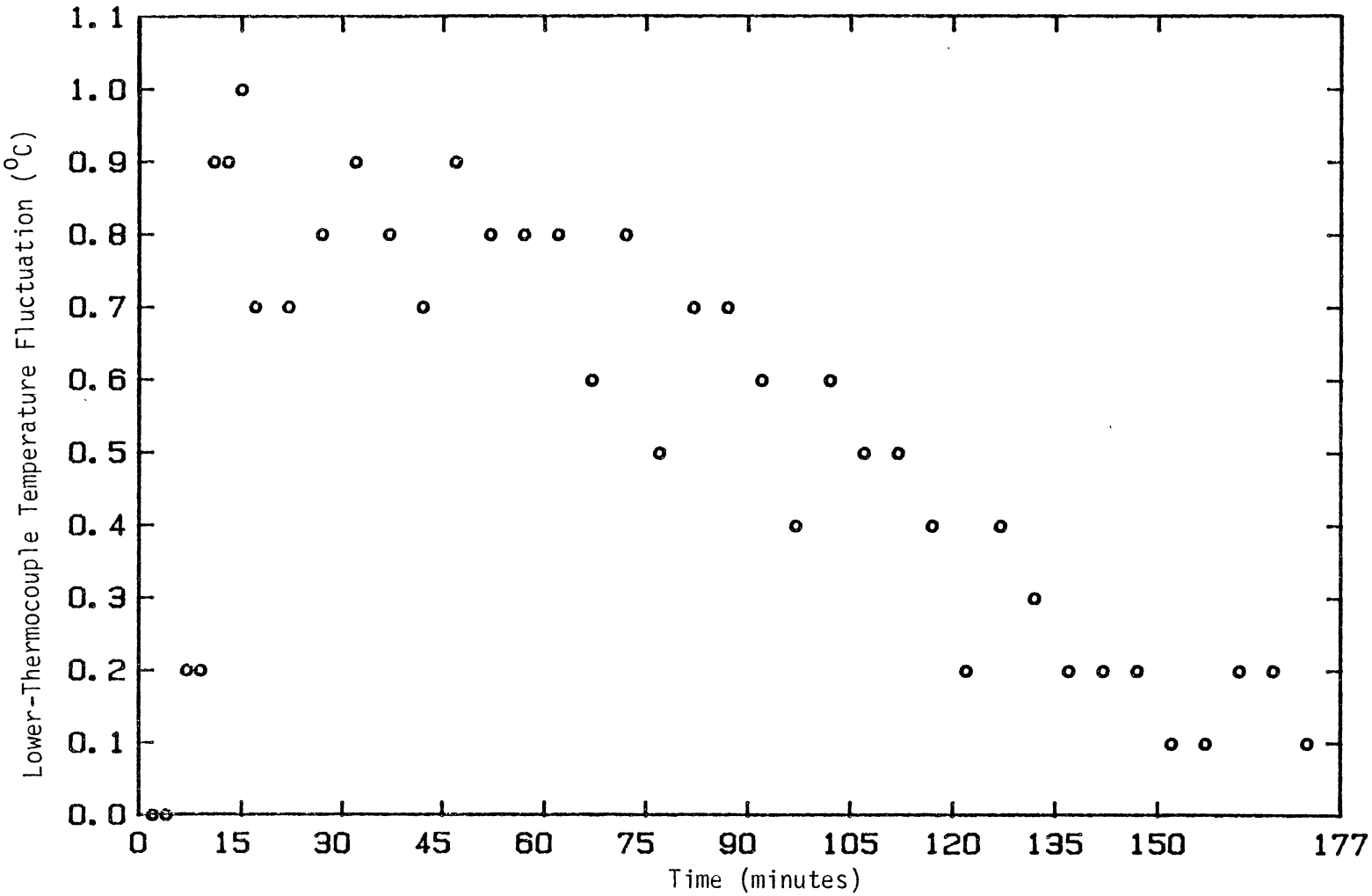

Figure B.5. Lower-Thermocouple Temperature Fluctuation as a Function of Time for Run B-6 Using a Feed Gas of 2.08:1 H_2/CO Ratio at 360°C and 2220 kPa.

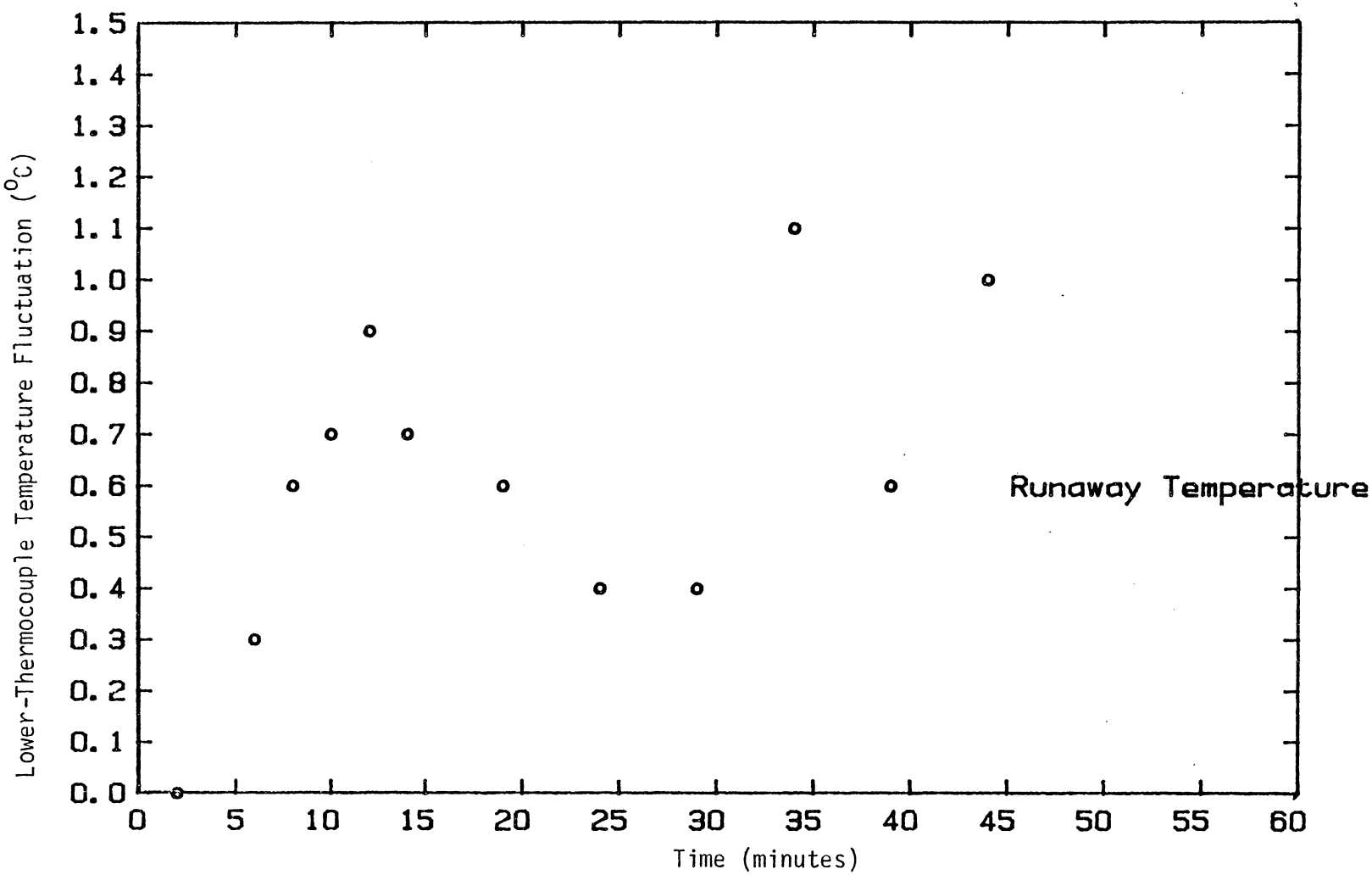

Figure B.6. Lower-Thermocouple Temperature Fluctuation as a Function of Time for Run C-2 Using a Feed Gas of 1.03:1 H_2/CO Ratio at 400°C and 2220 kPa.

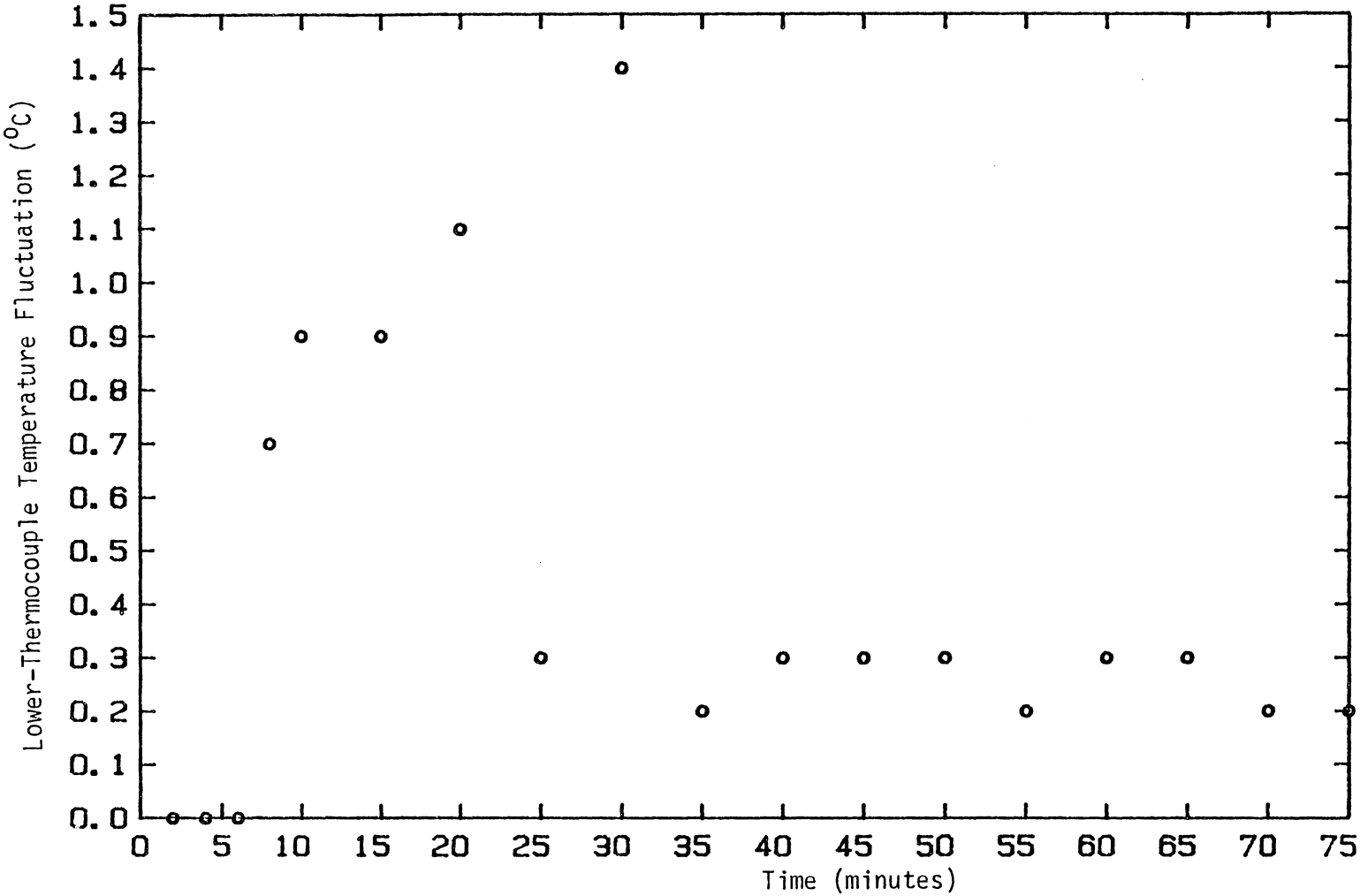

Figure B.7. Lower-Thermocouple Temperature Fluctuation as a Function of Time for Run D-1 Using a Feed Gas of 1.03:1 H_2/CO Ratio at 380°C and 2220 kPa.

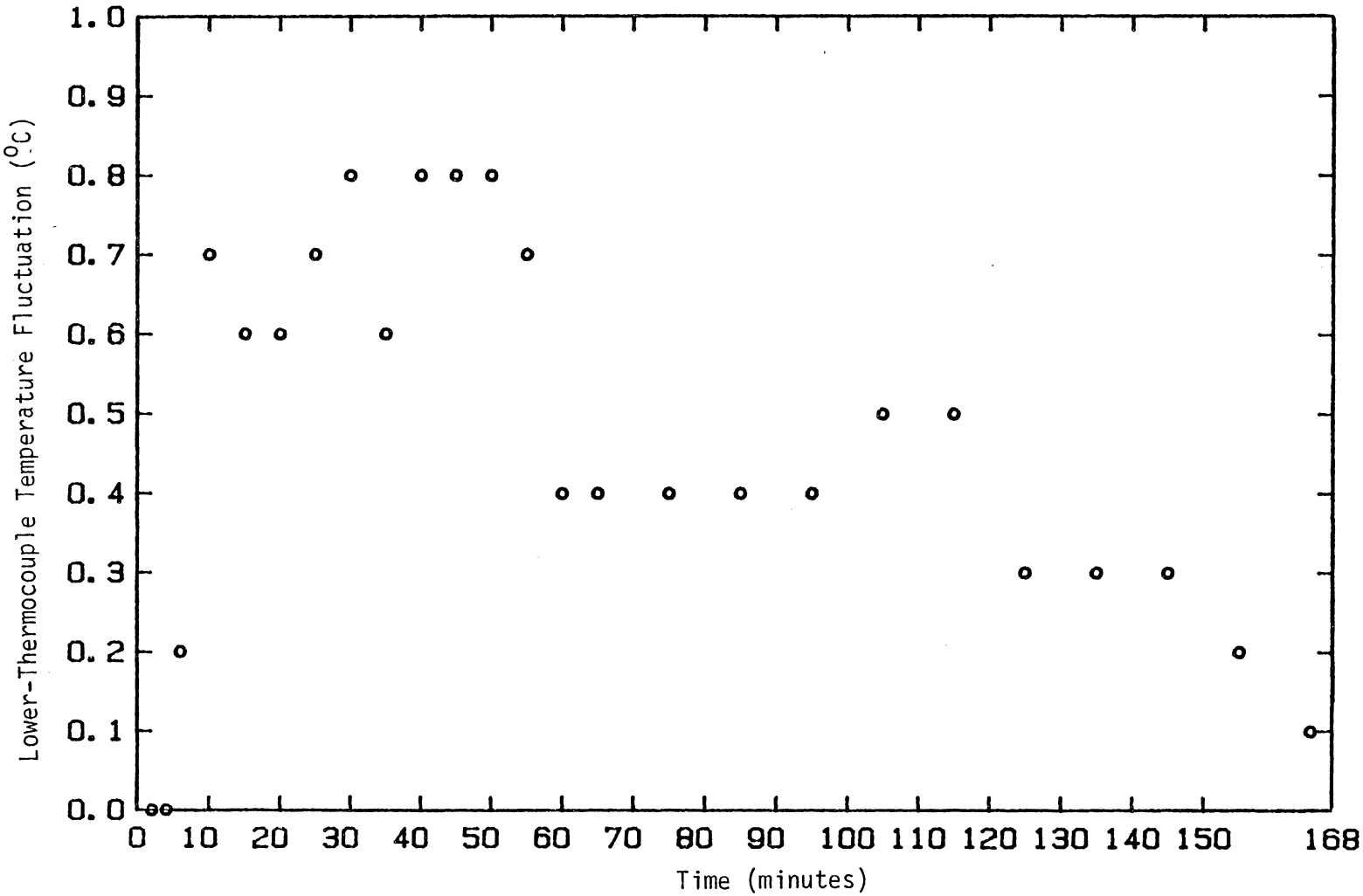

Figure B.8. Lower-Thermocouple Temperature Fluctuation as a Function of Time for Run D-2 Using a Feed Gas of 2.08:1 H_2/CO Ratio at 380°C and 2220 kPa.

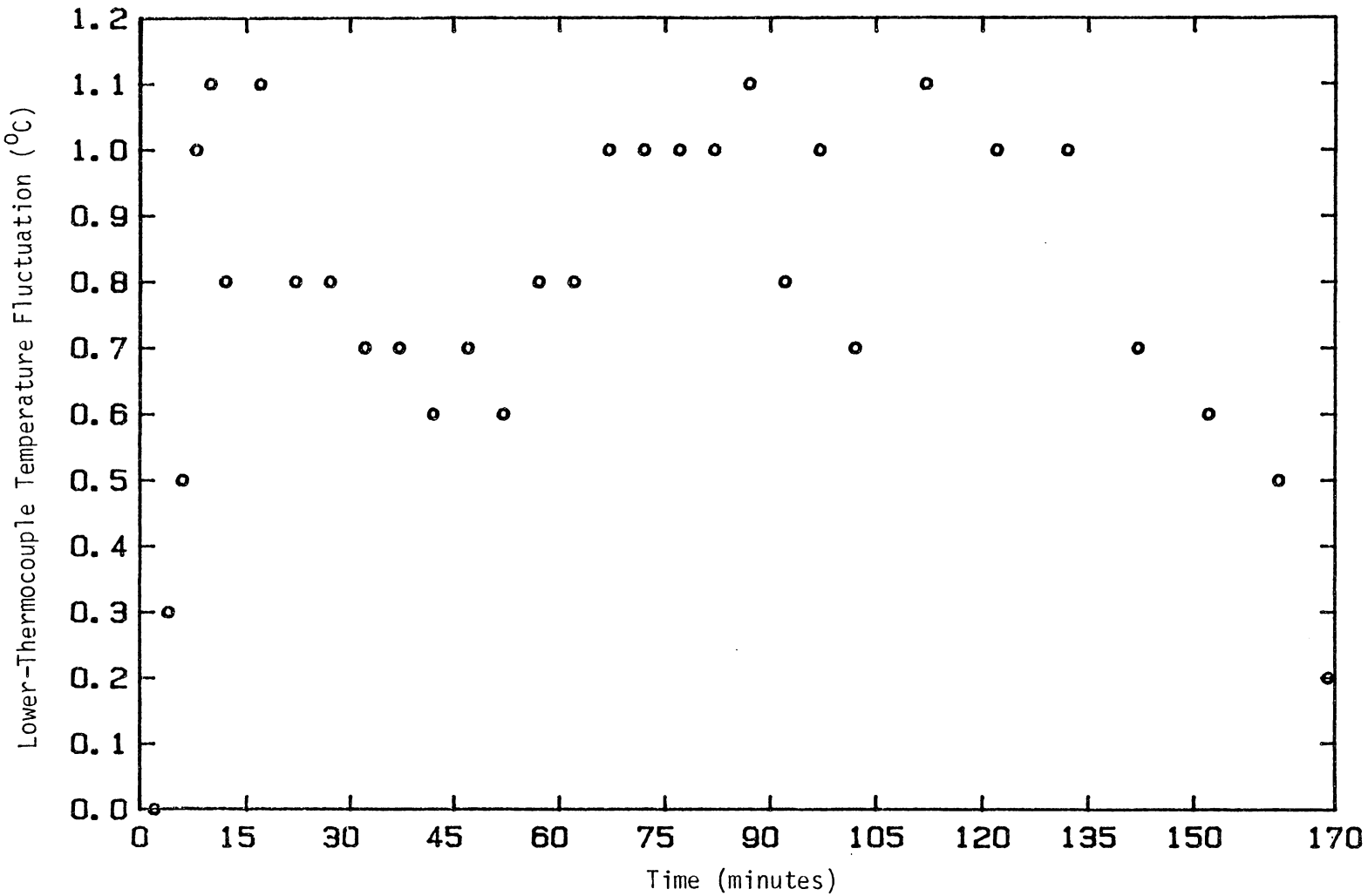

Figure B.9. Lower-Thermocouple Temperature Fluctuation as a Function of Time for Run E-1 Using a Feed Gas of 208:1 H_2/CO Ratio at 390°C and 2220 kPa.

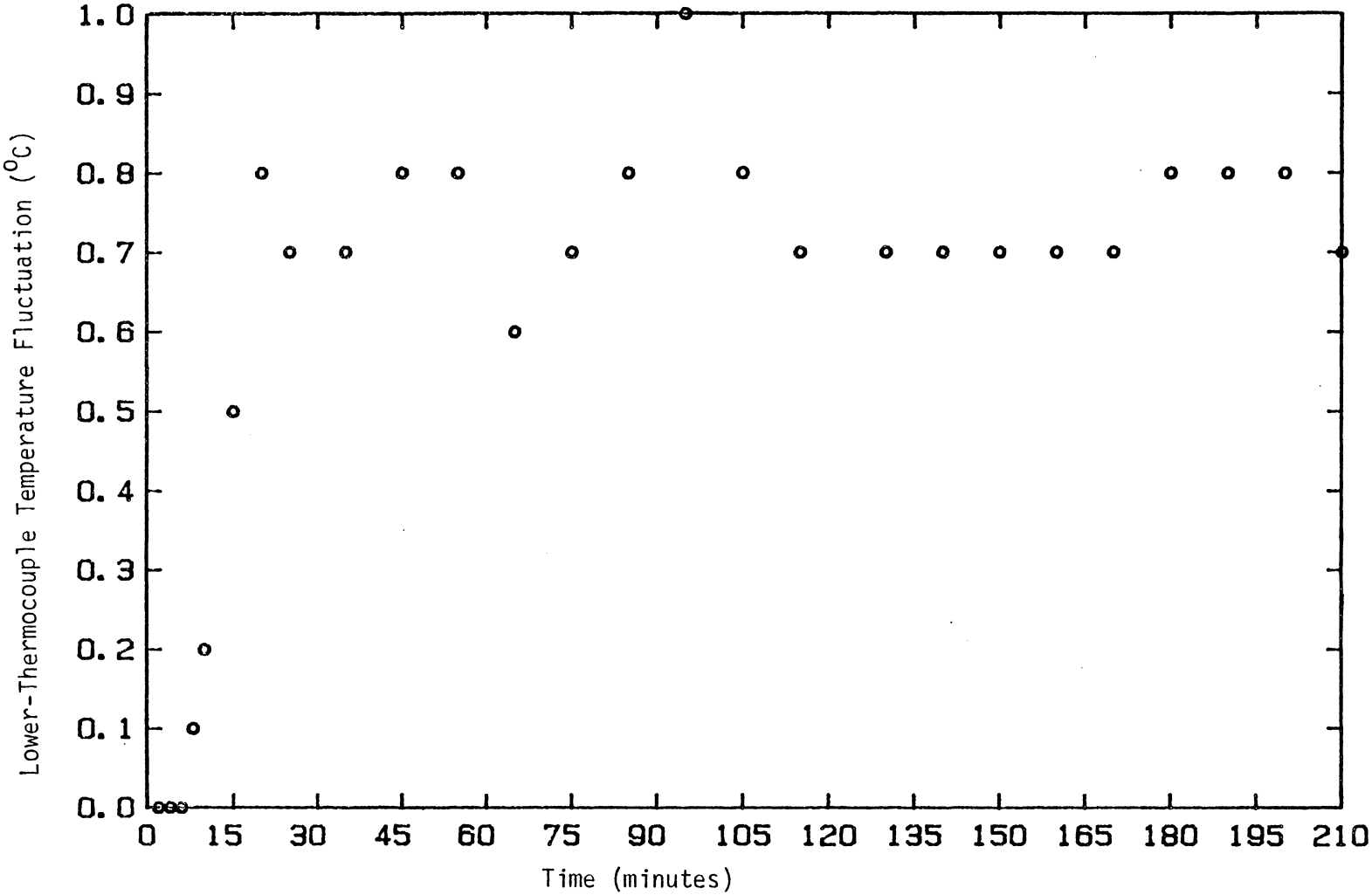

Figure B.10. Lower-Thermocouple Temperature Fluctuation as a Function of Time for Run F-1 Using a Feed Gas of 4:1 H_2/CO Ratio at 395°C and 2220 kPa.

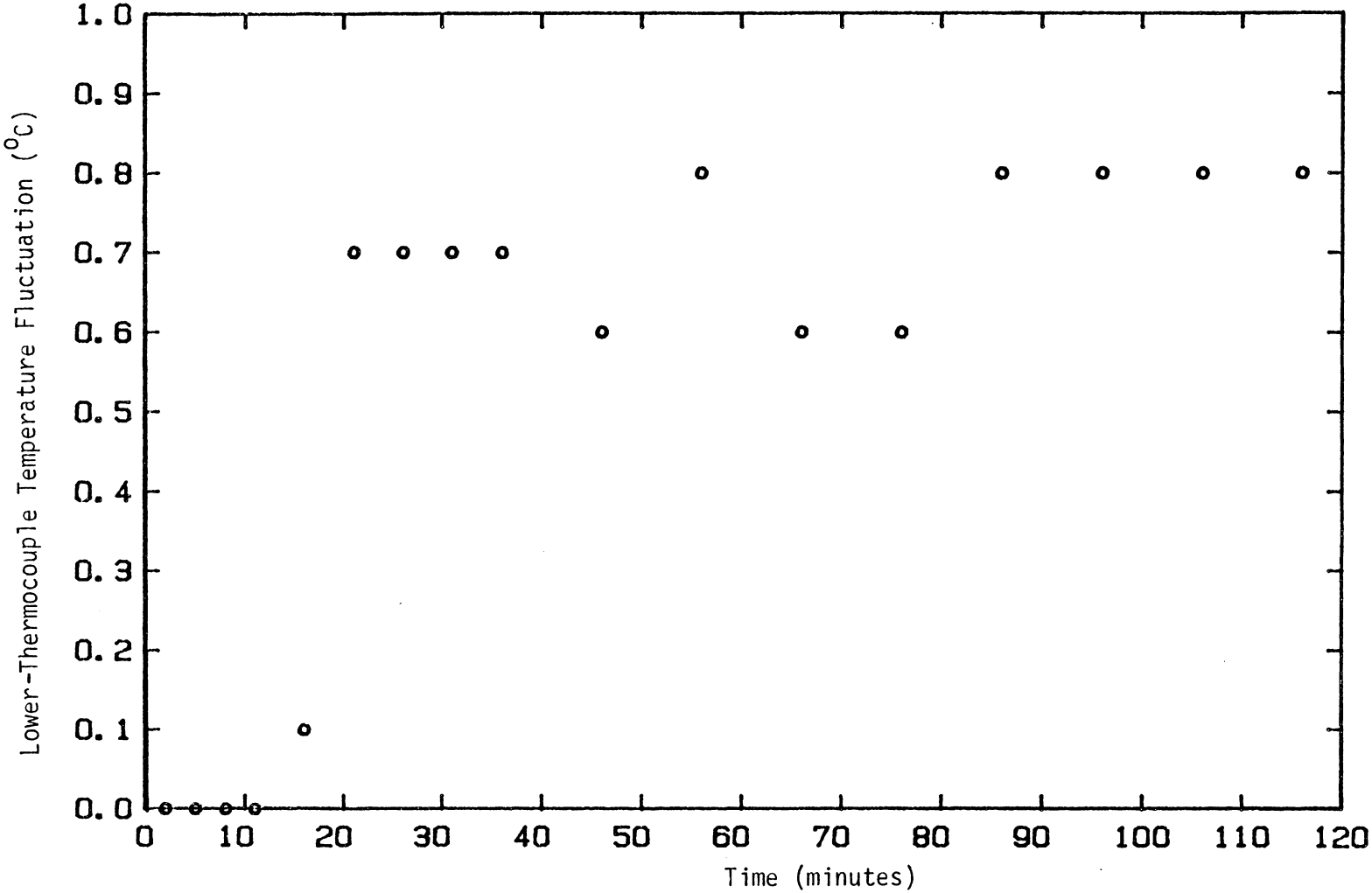

Figure B.11. Lower-Thermocouple Temperature Fluctuation as a Function of Time for Run F-2 Using a Feed Gas of 4:1 H_2/CO Ratio at 395°C and 2220 kPa.

APPENDIX C

Microcomputer Programs for: (1) Feed-Gas Cycling and Product Analysis During Unsteady-State Fischer-Tropsch Synthesis; (2) Data Compilation for Light-Gas Products (MASSBAL.BAS); and (3) Data Compilation for the Hydrocarbon Product Distribution from Capillary Analysis (HEAVY.BAS).

```
10 GOSUB 540
20 REM  THIS SECTION SWITCHES S- AND F-GAS SOLENOID VALVES
30 REM  AS WELL AS THE SLIDING PLUG.
40 CN=0
50 OUT 215,128
60 OUT 212,16
70 OUT 213,4
80 CN=CN+1
90 GOSUB 230
100 IF CN=10 THEN GOSUB 1690 ELSE
110 IF CN=20  THEN GOSUB 2020 ELSE
120 FOR I=1 TO 1500
130 NEXT I
140 OUT 215,128
150 OUT 212,8
160 OUT 213,6
170 GOSUB 380
180 FOR I=1 TO 750
190 NEXT I
200 GOTO 50
210 REM  THIS SUBROUTINE CONTROLS CHANGES IN COMPUTER GRAPHICS DURING
220 REM  CYCLING.
230 PRINT CHR$(27);CHR$(70);
240 PRINT CHR$(27);CHR$(89);CHR$(37);CHR$(37);CHR$(97);
250 PRINT CHR$(27);CHR$(89);CHR$(37);CHR$(43);CHR$(97);
260 PRINT CHR$(27);CHR$(89);CHR$(37);CHR$(71);CHR$(104);
270 PRINT CHR$(27);CHR$(89);CHR$(37);CHR$(92);CHR$(97);
280 PRINT CHR$(27);CHR$(89);CHR$(37);CHR$(98);CHR$(107);
290 PRINT CHR$(27);CHR$(89);CHR$(48);CHR$(63);CHR$(105);
300 PRINT CHR$(105);CHR$(105);CHR$(32);CHR$(32);CHR$(32);
310 PRINT CHR$(32);CHR$(32);CHR$(125);
320 PRINT CHR$(27);CHR$(71);
330 PRINT CHR$(27);CHR$(112);CHR$(27);CHR$(89);CHR$(54);CHR$(47);
340 PRINT "********* F-GAS REACTOR FEED *********";
350 PRINT "CYCLE # =";CN;"  ";
360 PRINT CHR$(27);CHR$(113);
370 RETURN
380 PRINT CHR$(27);CHR$(70);
390 PRINT CHR$(27);CHR$(89);CHR$(37);CHR$(37);CHR$(97);
400 PRINT CHR$(27);CHR$(89);CHR$(37);CHR$(43);CHR$(107);
410 PRINT CHR$(27);CHR$(89);CHR$(37);CHR$(71);CHR$(104);
420 PRINT CHR$(27);CHR$(89);CHR$(37);CHR$(92);CHR$(97);
430 PRINT CHR$(27);CHR$(89);CHR$(37);CHR$(98);CHR$(97);
440 PRINT CHR$(27);CHR$(89);CHR$(48);CHR$(63);CHR$(124);
450 PRINT CHR$(32);CHR$(32);CHR$(32);CHR$(32);CHR$(32);
460 PRINT CHR$(105);CHR$(105);CHR$(105);
470 PRINT CHR$(27);CHR$(71);
480 PRINT CHR$(27);CHR$(112);CHR$(27);CHR$(89);CHR$(54);CHR$(47);
490 PRINT "********* S-GAS REACTOR FEED *********";
500 PRINT CHR$(27);CHR$(113);
510 RETURN
520 REM THIS SUBROUTINE DRAWS A DIAGRAM OF THE REACTOR SYSTEM
530 REM AND ALLOWS VISUAL MONITORING OF THE GAS SWITCHING.
540 PRINT CHR$(27);CHR$(69);CHR$(27);CHR$(70);
550 FOR J=1 TO 6
560 PRINT CHR$(32);
570 NEXT J
580 PRINT "S-GAS";
590 FOR J=1 TO 50
600 PRINT CHR$(32);
610 NEXT J
620 PRINT "F-GAS"
630 FOR I=1 TO 4
640 FOR J=1 TO 4
650 PRINT CHR$(32);
660 NEXT J
670 PRINT CHR$(32);CHR$(96);CHR$(32);CHR$(32);CHR$(32);CHR$(32);CHR$(32);
680 PRINT CHR$(96);
690 FOR J=1 TO 47
700 PRINT CHR$(32);
710 NEXT J
720 PRINT CHR$(32);CHR$(96);CHR$(32);CHR$(32);CHR$(32);CHR$(32);CHR$(32);
```

Figure C.1 A Microcomputer Program for Control of Feed-Gas Cycling and Product Sampling During Unsteady-State Fisher-Tropsch Synthesis Experiments.

```
730 PRINT CHR$(96)
740 NEXT I
750 FOR J=1 TO 35
760 PRINT CHR$(32);
770 NEXT J
780 PRINT CHR$(102);
790 FOR J=1 TO 3
800 PRINT CHR$(97);
810 NEXT J
820 PRINT CHR$(96);
830 FOR J=1 TO 4
840 PRINT CHR$(97);
850 NEXT J
860 PRINT CHR$(32);
870 PRINT "F-T PRODUCT"
880 FOR I=1 TO 7
890 FOR J=1 TO 4
900 PRINT CHR$(32);
910 NEXT J
920 PRINT CHR$(32);CHR$(96);CHR$(32);CHR$(32);CHR$(32);CHR$(32);CHR$(32);
930 PRINT CHR$(96);
940 FOR J=1 TO 23
950 PRINT CHR$(32);
960 NEXT J
970 PRINT CHR$(96);
980 FOR J=1 TO 24
990 PRINT CHR$(32);
1000 NEXT J
1010 PRINT CHR$(96);
1020 FOR J=1 TO 5
1030 PRINT CHR$(32);
1040 NEXT J
1050 PRINT CHR$(96)
1060 NEXT I
1070 FOR I=1 TO 3
1080 FOR J=1 TO 5
1090 PRINT CHR$(32);
1100 NEXT J
1110 PRINT CHR$(96);
1120 FOR J=1 TO 5
1130 PRINT CHR$(32);
1140 NEXT J
1150 PRINT CHR$(96);
1160 FOR J=1 TO 19
1170 PRINT CHR$(32);
1180 NEXT J
1190 FOR J=1 TO 9
1200 PRINT CHR$(105);
1210 NEXT J
1220 FOR J=1 TO 20
1230 PRINT CHR$(32);
1240 NEXT J
1250 PRINT CHR$(96);
1260 FOR J=1 TO 5
1270 PRINT CHR$(32);
1280 NEXT J
1290 PRINT CHR$(96)
1300 NEXT I
1310 FOR J=1 TO 5
1320 PRINT CHR$(32);
1330 NEXT J
1340 PRINT CHR$(101);
1350 FOR J=1 TO 3
1360 PRINT CHR$(97);
1370 NEXT J
1380 PRINT CHR$(117);
1390 FOR J=1 TO 19
1400 PRINT CHR$(97);
1410 NEXT J
1420 FOR J=1 TO 3
1430 PRINT CHR$(105);
1440 NEXT J
```

Figure C.1 (Continued)

```
1450 FOR J=1 TO 5
1460 PRINT CHR$(32);
1470 NEXT J
1480 PRINT CHR$(125);
1490 FOR J=1 TO 20
1500 PRINT CHR$(97);
1510 NEXT J
1520 PRINT CHR$(117);
1530 FOR J=1 TO 5
1540 PRINT CHR$(97);
1550 NEXT J
1560 PRINT CHR$(100)
1570 FOR J=1 TO 31
1580 PRINT CHR$(32);
1590 NEXT J
1600 FOR J=1 TO 8
1610 PRINT CHR$(105);
1620 NEXT J
1630 PRINT CHR$(105)
1640 PRINT CHR$(27);CHR$(71)
1650 RETURN
1660 REM THIS SUBROUTINE CAUSES A SAMPLE TO BE FLUSHED INTO THE
1670 REM PACKED COLUMN OF THE GAS CHROMATOGRAPH BY TURNING THE
1680 REM SAMPLING VALVE.
1690 FOR I=1 TO 80
1700 PRINT CHR$(27);CHR$(60);CHR$(7);
1710 PRINT CHR$(27);CHR$(91);CHR$(63);CHR$(50);CHR$(104);
1720 NEXT I
1730 PRINT CHR$(27);CHR$(106);
1740 CR=5
1750 PRINT CHR$(27);CHR$(120);CHR$(49);
1760 PRINT CHR$(27);CHR$(60);CHR$(7);
1770 PRINT CHR$(27);CHR$(91);CHR$(63);CHR$(50);CHR$(104);
1780 PRINT CHR$(27);CHR$(89);CHR$(56);CHR$(32);
1790 IF CR=0 THEN PRINT ">>>>LIGHT GAS SAMPLING<<<<<<<<<<<<<<<<<<<<"  ELSE
1800 IF CR=0 THEN 1820 ELSE
1810 PRINT "              ";CR;"                                        ";
1820 CR=CR-1
1830 FOR J=1 TO 65
1840 NEXT J
1850 IF CR<0 THEN 1870 ELSE
1860 GOTO 1760
1870 PRINT CHR$(27);CHR$(107);
1880 OUT 215,128
1890 OUT 213,4
1900 OUT 212,16
1910 OUT 214,128
1920 FOR I=1 TO 250
1930 NEXT I
1940 OUT 215,128
1950 OUT 213,4
1960 OUT 212,16
1970 OUT 214,0
1980 I=1500
1990 RETURN
2000 REM  THIS SUBROUTINE TURNS THE SAMPLING VALVE EFFECTIVELY
2010 REM  BACKFLUSHING THE PACKED COLUMN.
2020 PRINT CHR$(27);CHR$(106);
2030 PRINT CHR$(27);CHR$(120);CHR$(49);
2040 PRINT CHR$(27);CHR$(89);CHR$(56);CHR$(32);
2050 PRINT CHR$(27);CHR$(60);CHR$(7);
2060 PRINT CHR$(27);CHR$(91);CHR$(63);CHR$(50);CHR$(104);
2070 PRINT ">>>>THE PACKED COLUMN IS BEING BACKFLUSHED<<<<"
2080 PRINT CHR$(27);CHR$(107);
2090 OUT 215,128
2100 OUT 213,4
2110 OUT 212,144
2120 OUT 214,0
2130 FOR I=1 TO 250
2140 NEXT I
2150 OUT 215,128
2160 OUT 213,4
2170 OUT 212,16
2180 OUT 214,0
2190 CN=0
2200 RETURN
```

Figure C.1 (Continued)

```
10 REM R=ARGON  O=CO  S=CH4  T=CO2  MCMA=MOLES CO/MOLE AR FED
20 REM  K=RXN TEMP,KELVINS  RA=H2/CO RATIO FED(EFFECTIVE RATIO FOR CYCLE)
25 REM PMCMA=MCMA DURING PRECARBID.  SMCMA=MCMA DURING SYNTHESIS
26 REM PRA=RA DURING PRECARB.        SRA=RA DURING SYNTHESIS
30 DIM R(50),O(50),S(50),T(50),A(50),B(50),C(50),D(50),E(50)
40 DIM F(50),G(50),H(50),Q(50),U(50),V(50),W(50),L(50)
50 DIM X(50),Y(50),Z(50)
60 REM*****PLACE THE DATE & COMMENTS ON THE NEXT 2 LINES*********
70 L$="9/25/84"
80 LM$="STEADY STATE EXPERIMENT F-5   "
82 LR$=" THIS EXPERIMENT USES 1.03:1 S-GAS FOR A 22 MINUTE RUN "
85 LS$=" AFTER FIRST EXPOSING IT TO 4:1 PRECARB. GAS FOR 2 HOURS.        "
87 LT$="                                                                 "
90 REM +++++++SPECIFY INPUT AND OUTPUT FILE NAMES AND PARAMETERS+++++++++
100 LP$="EXF5.DAT"
110 LO$="RESF5.DAT"
115 NN=3
120 N=3
122 REM                                  INPUT PARAMETERS!
125 PMCMA=10.882
128 SMCMA=10.882
130 REM SMCMA=7.745
135 PRA=4.0
140 SRA=1.03
150 K=648
151 REM  ++++++++++++++++++++++++++++++++++++++++++++++++++++++++++++++++++++
152 MCMA=PMCMA
154 RA=PRA
160 REM ***READ IN INTEGRATED PEAK AREAS**************************
170 OPEN "I",1,LP$
180 FOR I=1 TO N
190 INPUT#1,R(I),O(I),S(I),T(I)
200 NEXT I
210 CLOSE#1
220 REM ***WEIGHT THE PEAK AREAS USING TC WEIGHT FACTORS*********
230 FOR I=1 TO N
235 IF I>NN THEN MCMA=SMCMA
240 R(I)=R(I)*.95
250 O(I)=O(I)*.67
260 S(I)=S(I)*.45
270 T(I)=T(I)*.915
280 REM ***MOLES CO CONVERTED/MOLE AR*****************************
290 A(I)=MCMA-(O(I)/R(I)*1.426)
300 REM ***MOLES CH4/MOLE AR*************************************
310 B(I)=(S(I)/R(I)*2.49)
320 REM ***MOLES CO2/MOLE AR*************************************
330 C(I)=(T(I)/R(I)*.9077)
340 REM ***MOLES CH4 PRODUCED/MOLE CO CONVERTED*******************
350 D(I)=B(I)/A(I)
360 REM ***MOLES CO2 PRODUCED/MOLE CO CONVERTED*******************
370 E(I)=C(I)/A(I)
380 NEXT I
390 FOR I=1 TO N
392 MCMA=PMCMA
395 IF I>NN THEN MCMA=SMCMA
400 REM ***CO CONVERSION, CO UNCONVERTED*****************************
410 F(I)=A(I)/MCMA
420 G(I)=1!-F(I)
430 REM ***CO2 PRODUCED, CH4 PRODUCED********************************
440 H(I)=F(I)*E(I)
450 Q(I)=F(I)*D(I)
460 REM ***IMPLIED MOLES OF -CH2-  **********************************
470 U(I)=1!-(G(I)+H(I)+Q(I))
480 REM ***IMPLIED MOLES OF H2O  ************************************
490 V(I)=1!-(2*H(I)+G(I))
500 REM ***IMPLIED MOLES OF H2 USED**********************************
510 W(I)=(2*U(I)+4*Q(I)+2*V(I))/2!
520 REM *** H2/CO USAGE RATIO ***************************************
530 X(I)=W(I)/F(I)
540 REM *** CALCULATED EQUILIBRIUM CONSTANT FOR WATER-GAS SHIFT******
550 Y(I)=.0102*EXP(4730/K)
560 REM *** EXPERIMENTAL EQUILIBRIUM CONSTANT FOR WATER-GAS SHIFT****
562 RA=PRA
```

Figure C.2 A Microcomputer Program (MASSBAL.BAS) Used to Compile the Data Obtained From the Light-Gas Analysis.

```
565 IF I>NN THEN RA=SRA
570 Z(I)=(H(I)*(RA-W(I))/(G(I)*V(I)))
580 REM ***IMPLIED CONVERSION OF HYDROGEN*****************************
590 L(I)=W(I)/RA
600 NEXT I
610 OPEN "O",2,LQ$
620 PRINT#2,"DATE OF EXPERIMENT ",L$,LM$
630 PRINT "DATE OF EXPERIMENT ",L$,LM$
631 PRINT#2," "
632 PRINT#2,LR$
633 PRINT#2,LS$
634 PRINT#2,LT$
640 PRINT#2," "
650 PRINT
660 PRINT#2,"TEMPERATURE=",K,"# DATA PTS.=",N
670 PRINT   "TEMPERATURE=",K,"# DATA PTS.=",N
680 PRINT#2," "
690 PRINT
700 PRINT#2," SAMPLE "," CO CONV","CO2/CO","CH4/CO"," CO/AR"," H2/CO"
710 PRINT   " SAMPLE "," CO CONV","CO2/CO","CH4/CO"," CO/AR"," H2/CO"
720 PRINT#2," NUMBER "," ","CONV "," CONV ","  FED "," RATIO"
730 PRINT   " NUMBER "," ","CONV "," CONV ","  FED "," RATIO"
740 FOR I=1 TO N
742 RA=PRA
743 IF I>NN THEN RA=SRA
744 MCMA=PMCMA
745 IF I>NN THEN MCMA=SMCMA
750 PRINT#2,I,F(I),E(I),D(I),MCMA,RA
760 PRINT   I,F(I),E(I),D(I),MCMA,RA
770 NEXT I
780 PRINT#2," "
790 PRINT
800 PRINT#2," "
810 PRINT
820 PRINT#2," SAMPLE ","H2 CONV"," -CH2-","  H2O"," H2 USED","H2/CO"
830 PRINT   " SAMPLE ","H2 CONV"," -CH2-","  H2O"," H2 USED","H2/CO"
840 PRINT#2," NUMBER","IMPLIED","IMPLIED","IMPLIED","IMPLIED","USAGE"
850 PRINT   " NUMBER","IMPLIED","IMPLIED","IMPLIED","IMPLIED","USAGE"
860 FOR I=1 TO N
870 PRINT#2,I,L(I),U(I),V(I),W(I),X(I)
880 PRINT   I,L(I),U(I),V(I),W(I),X(I)
890 NEXT I
900 PRINT#2," "
910 PRINT
920 PRINT#2," "
930 PRINT
940 PRINT#2," SAMPLE "," -CH2- ","CALC KEQ","EXPT KEQ","SUM=1?"
950 PRINT   " SAMPLE "," -CH2- ","CALC KEQ","EXPT KEQ","SUM=1?"
960 PRINT#2," NUMBER "," /CO CONV  "
970 PRINT   " NUMBER "," /CO CONV  "
980 FOR I=1 TO N
985 UPRIME=U(I)/F(I)
986 SUM=UPRIME+E(I)+D(I)
990 PRINT#2,I,UPRIME,Y(I),Z(I),SUM
1000 PRINT   I,UPRIME,Y(I),Z(I),SUM
1010 NEXT I
1020 CLOSE#2
```

Figure C.2 (Continued)

```
10 REM  THIS PROGRAM CALCULATES THE NUMBER OF MOLES OF A SPECIFIC HYDRO-
20 REM   CARBON (OR FUSED PEAK OF HC'S) FROM THE INTEGRATED PEAK AREAS
30 REM   ON THE CHROMATOGRAM.  ASSUMPTIONS= 1) FUSED C2 AND C3 PEAKS
40 REM   USE THE AVERAGE MOL. WT. TO CALCULATE MOLES CONVERTGD.
50 DIM A(24),B(24),C(24),D(24),E(24),F(24),G(24),H(24),J(24),K(24),M(24)
51 DIM Q(24),R(24)
60 REM   X=MOLES CH4 PRODUCED PER MOLE CO CONVERTED  XX=FLOW RATE IN SCCM
65 REM   YY=FRACTION CO IN S-GAS FEED  ZZ=CO CONVERTED/CO FED
66 REM   WW=RATIO OF S-GAS FEED DURATION TO TOTAL FEED DURATION(S+F)
67 REM      [VALUE OF WW FOR STEADY-STATE REACTION IS 1.0]
68 REM   HH=MOLES OF CO2 PRODUCED/ MOLE CO CONV.
70 L$="3/10/84"
80 LM$="STEADY STATE W/O PRECARB."
90 LQ$="HPRESB3.DAT"
100 LP$="HPB3.DAT"
101 LT$="EXPERIMENT B-3: THIS EXPERIMENT CONSISTS OF 10 HOURS "
103 LS$="OF 4.0:1 S-GAS FLOW AT 633K.                         "
110 X=.1791
102 XX=220
104 YY=0.1925
106 ZZ=.9268
107 WW=1.0
108 HH=0.2073
109 GOSUB 1400
120 REM INPUT INTEGRATED PEAK AREAS FOR OLEFINS AND PARAFINS
130 OPEN "I",1,LP$
140 FOR I=1 TO 24
150 INPUT#1,A(I)
160 NEXT I
170 CLOSE#1
180 REM  NORMALIZED PEAK AREAS
190 FOR I=1 TO 24
200 D(I)=A(I)/A(1)
210 Z=Z+D(I)
220 NEXT I
230 REM  CALCULATE THE WEIGHT FRACTION OF EACH SPECIES
240 FOR I=1 TO 24
250 B(I)=D(I)/Z
260 NEXT I
270 GOSUB 590
280 REM  CALCULATE MOLES HYDROCARBON PRODUCED PER MOLE CO CONSUMED, C(I)
290 FOR I=1 TO 24
300 C(I)=D(I)*M(1)*X/M(I)
310 IF I=1 THEN E(I)=C(I) ELSE
320 IF I=2 THEN E(I)=C(I)*2 ELSE
330 IF I=3 THEN E(I)=C(I)*3 ELSE
340 IF I>3 THEN IF I<8 THEN E(I)=C(I)*4  ELSE
350 IF I>7 THEN IF I<12 THEN E(I)=C(I)*5  ELSE
360 IF I>11 THEN IF I<15 THEN E(I)=C(I)*6  ELSE
370 IF I>14 THEN IF I<19 THEN E(I)=C(I)*7  ELSE
380 IF I>18 THEN IF I<21 THEN E(I)=C(I)*8  ELSE
390 IF I>20 THEN IF I<23 THEN E(I)=C(I)*9  ELSE
400 IF I>22 THEN E(I)=C(I)*10 ELSE
410 T=T+E(I)
420 NEXT I
421 GOSUB 1500
422 GOSUB 900
430 OPEN "O",2,LQ$
440 PRINT#2,"DATE OF EXPERIMENT",L$,LM$
450 PRINT  "DATE OF EXPERIMENT",L$,LM$
451 PRINT#2," "
452 PRINT#2,LT$
455 PRINT#2,LS$
460 PRINT#2,"  "
470 PRINT "  "
480 PRINT#2,"PEAK #","NORM AREA","WT FRACT.","HC/CO CONV","RATE PROD","M.W."
490 PRINT  "PEAK #","NORM AREA","WT FRACT.","HC/CO CONV","RATE PROD","M.W."
500 FOR I=1 TO 24
510 PRINT#2,I,D(I),B(I),C(I),Q(I),M(I)
520 PRINT I,D(I),B(I),C(I),Q(I),M(I)
530 NEXT I
531 PRINT#2,"  "
532 PRINT "  "
```

Figure C.3 A Microcomputer Program (HEAVY.BAS) Used to Compile the Data Obtained From the Capillary Column Analysis.

```
533 PRINT#2,"CARBON #","MOLES C#","MOLFRC C#","WT C#","WTFRAC C#","RATE C#"
534 PRINT  "CARBON #","MOLES C#","MOLFRC C#","WT C#","WTFRAC C#","RATE C#"
535 FOR I=1 TO 10
536 PRINT#2,I,F(I),G(I),H(I),J(I),R(I)
537 PRINT I,F(I),G(I),H(I),J(I),R(I)
538 NEXT I
540 W=Z*A(1)
541 PRINT#2,"  "
542 PRINT "  "
543 PRINT#2,"  "
544 PRINT "  "
550 PRINT#2,"TOTAL PEAK AREA=",W
560 PRINT  "TOTAL PEAK AREA=",W
562 PRINT#2,"TOTAL MOLE CARBON PRODUCED AS OLE&PAR/MOLE CO CONV=",T
563 PRINT  "TOTAL MOLE CARBON PRODUCED AS OLE&PAR/MOLE CO CONV=",T
564 PRINT#2,"MOLE RATIO C1/(C2-C6)=",S1
565 PRINT  "MOLE RATIO C1/(C2-C6)=",S1
566 PRINT#2,"WEIGHT FRACTION C1/(C2-C5)",S2
567 PRINT  "WEIGHT FRACTION C1/(C2-C5)",S2
568 PRINT#2,"RATES ARE IN UNITS OF MMOLES PER HOUR"
569 PRINT#2,"AVG MOL WTS ARE USED FOR C2 AND C3 HYDROCBNS DUE TO FUSED PEAKS"
570 GG=T+HH
571 PRINT#2,"TOT MOLE C PRODUCED AS CO2 AND OLE&PARA/MOLE CO CONV=",GG
572 CLOSE#2
580 STOP
590 REM ASSIGN MOLECULAR WEIGHTS TO THE PEAKS
600 C=12.011
610 H=1.008
620 M(1)=C+4*H
630 REM MUST AVG NEXT 2 SETS OF PEAKS, OLEFIN & PARAFIN CUMBINED
640 M(2)=C*2+H*5
650 M(3)=C*3+H*7
660 M(4)=C*4+H*8
670 M(5)=C*4+H*10
680 M(6)=C*4+H*8
690 M(7)=C*4+H*8
700 M(8)=C*5+H*10
710 M(9)=C*5+H*12
720 M(10)=C*5+H*10
730 M(11)=C*5+H*10
740 M(12)=C*6+H*12
750 M(13)=C*6+H*14
760 M(14)=C*6+H*12
770 M(15)=C*7+H*14
780 M(16)=C*7+H*16
790 M(17)=C*7+H*14
800 M(18)=C*7+H*14
810 M(19)=C*8+H*16
820 M(20)=C*8+H*18
830 M(21)=C*9+H*18
840 M(22)=C*9+H*20
850 M(23)=C*10+H*20
860 M(24)=C*10+H*22
870 RETURN
900 REM CALCULATE THE MOLES OF EACH CARBON # FRACTION AND MOLE%
910 F(1)=C(1)
920 F(2)=C(2)
930 F(3)=C(3)
940 F(4)=C(4)+C(5)+C(6)+C(7)
950 F(5)=C(8)+C(9)+C(10)+C(11)
960 F(6)=C(12)+C(13)+C(14)
970 F(7)=C(15)+C(16)+C(17)+C(18)
980 F(8)=C(19)+C(20)
990 F(9)=C(21)+C(22)
1000 F(10)=C(23)+C(24)
1010 FOR I=1 TO 24
1020 MT=MT+C(I)
1030 NEXT
1040 FOR I=1 TO 10
1050 G(I)=F(I)/MT
1060 NEXT I
1100 WT=0
```

Figure C.3 (Continued)

```
1110 H(1)=B(1)
1120 H(2)=B(2)
1130 H(3)=B(3)
1140 H(4)=B(4)+B(5)+B(6)+B(7)
1150 H(5)=B(8)+B(9)+B(10)+B(11)
1160 H(6)=B(12)+B(13)+B(14)
1170 H(7)=B(15)+B(16)+B(17)+B(18)
1180 H(8)=B(19)+B(20)
1190 H(9)=B(21)+B(22)
1200 H(10)=B(23)+B(24)
1210 FOR I=1 TO 24
1220 WT=WT+B(I)
1230 NEXT
1240 FOR I=1 TO 10
1250 J(I)=H(I)/WT
1260 NEXT I
1270 FOR I=2 TO 14
1280 QT=QT+C(I)
1290 RT=RT+B(I)
1300 NEXT I
1310 S1=C(1)/(QT)
1320 S2=B(1)/(RT)
1330 RETURN
1400 REM THIS SUBROUTINE CALCULATES THE MMOLES OF CO CONVERTED PER HR
1410 REM NN=NUMBER OF MMOLES CO FED/HR  TT=MMOLES OF CO CONVERTED/HR
1412 REM    XX=FLOW RATE IN SCCM
1413 REM    YY=FRACTION CO IN S-GAS FEED  ZZ=CO CONVERTED/CO FED
1415 REM    WW=RATIO OF S-GAS FEED DURATION TO TOTAL FEED DURATION(S+F)
1420 NN=(XX/(82.04*273))*1000*60*YY*WW
1430 TT=NN*ZZ
1440 RETURN
1500 REM    THIS SUBROUTINE CALCULATES THE RATE OF PRODUCTION OF EACH
1510 REM     PRODUCT IN MMOLES PER HOUR ,Q(I). THE RATE OF PRODUCTION
1515 REM     OF EACH SPECIES IN TERMS OF CARBON NUMBER IS ALSO FOUND, R(I).
1518 FOR I=1 TO 24
1520 Q(I)=C(I)*TT
1530 NEXT I
1540 R(1)=Q(1)
1550 R(2)=Q(2)
1560 R(3)=Q(3)
1570 R(4)=Q(4)+Q(5)+Q(6)+Q(7)
1580 R(5)=Q(8)+Q(9)+Q(10)+Q(11)
1590 R(6)=Q(12)+Q(13)+Q(14)
1600 R(7)=Q(15)+Q(16)+Q(17)+Q(18)
1610 R(8)=Q(19)+Q(20)
1620 R(9)=Q(21)+Q(22)
1630 R(10)=Q(23)+Q(24)
1700 RETURN
```

Figure C.3 (Continued)

APPENDIX D

Safety Provisions for the Fischer-Tropsch Synthesis Microreactor System

Location of the Microreactor System

The vibrofluidized microreactor system described in Section 5.1 is located in the Laboratory for Coal Science and Process Chemistry ("coal lab"), Room 319A, on the third floor, northeast wing of Randolph Hall, Virginia Polytechnic Institute and State Unviersity. Above the microreactor system is the building roof, and below it is the Unit Operations Laboratory ("U.O. Lab"). Figure D.1 shows a schematic of the location of the microreactor system ("reactor lab"). The system is surrounded by cinderblock walls on three sides, and by plywood on the fourth side and on the top, forming a "reactor box" as labelled in Figure D.1. The dimensions of this reactor box are 1.45 m × 2.13 m (width × length × height), giving a total volume of 4.0768 m^3. The laboratory surrounding this box, labelled as "reactor lab" in Figure D.1, has the dimensions of 3.5 m × 7 m × 4.5 m or a total voluime of 84.53 m^3.

Ventilation of the Microreactor System

Ventilation for the entire reactor laboratory is provided by a large roof-fan which draws air from both the coal laboratory and the unit operations laboratory. This roof-fan draws air at a volumetric flow rate of approximately 9.46×10^{-3} m^3/sec (0.334 ft^3/sec or 20.04 cfm) at the grate of the reactor laboratory. Thus, the entire air content of the reactor laboratory would be replaced approximately once every two and one-half hours if there was no other air exit. However, an additional vent fan draws air from the reactor box at a faster rate of 9.91×10^{-2} m^3/sec (3.5 ft^3/sec or 2,100 cfm). This means that the air content in the reactor box can be replaced approximately once every 41 seconds. Also, the entire

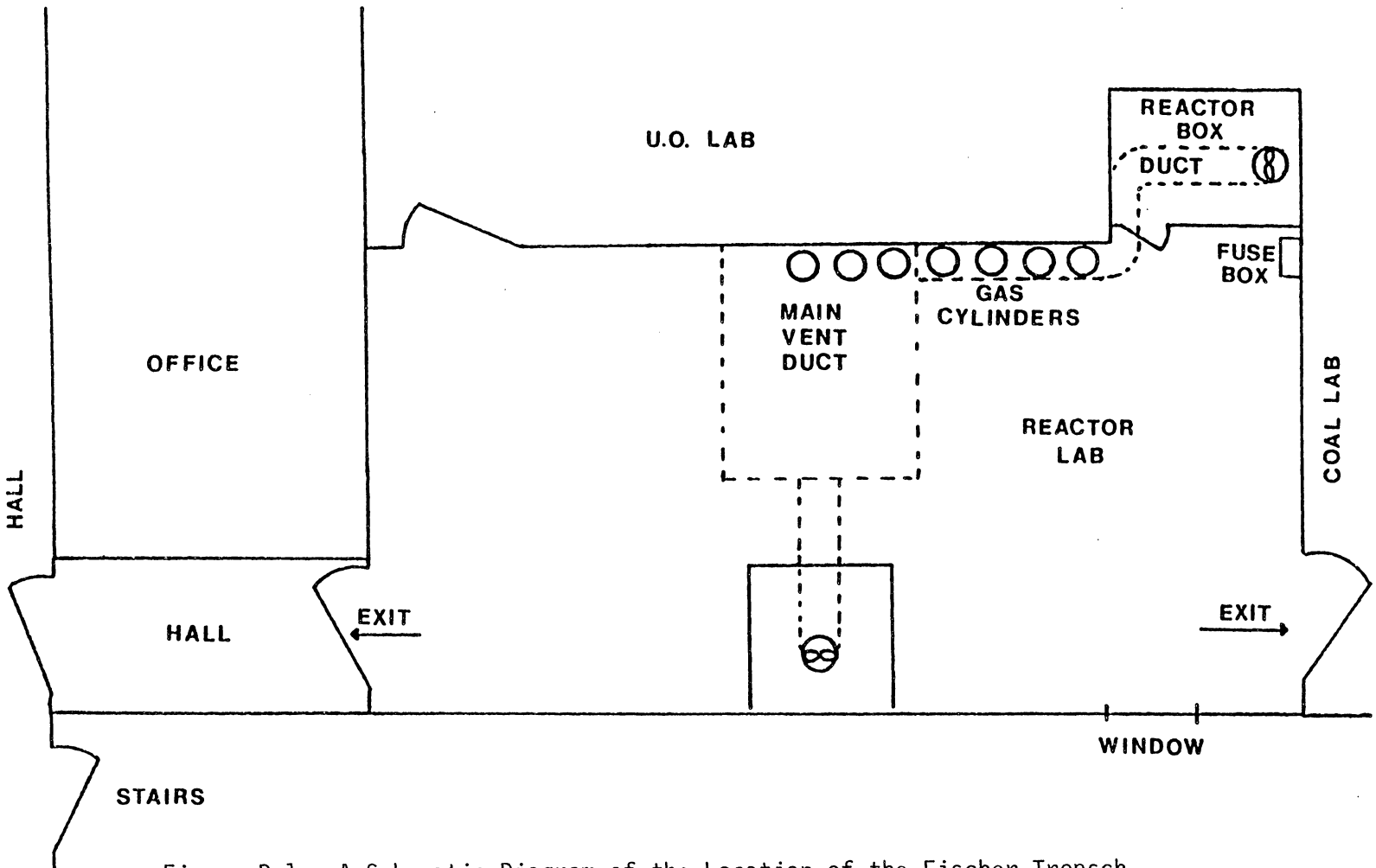

Figure D.1. A Schematic Diagram of the Location of the Fischer-Tropsch Synthesis Microreactor System.

room air in the reactor laboratory is replace about once every 7 minutes. Note that fresh air is drawn into the reactor laboratory via the unit operations laboratory and an air duct in the coal laboratory.

The reactor box has been caulked with silicone rubber at all of its joints and around the edges of the plexiglass at the roof light. The small piece of plywood covering a vent hole in the wall has also been carefully caulked. The roof light is located on top of the reactor box and shines light through the plexiglass to eliminate any possibility of spark hazard.

Table D.1 summarizes the estimated volumes of different components of the microreactor system and the estimated air renewal rates of the reactor box and the reactor laboratory. The American Conference of Governmental Industrial Hygienists has recommended a threshold limit value of 50 ppm for CO representing the concentration of CO in air to which nearly all workers may be continuously exposed without adverse effects.

The flammable limit of H_2 in air is 4 to 75% by volume, depending upon the surrounding situations.

High Temperature and Pressure Precautions

The vibrofluidized microreactor system is to be run at pressures up to 3030 kPa and parts of the system at temperatures up to 450°C. Thus, the upper limits of operating temperatures and pressures of different system components must be known. Those are summarized in Table D.2.

Electrical System

All electrical switches and plugs are external to the reactor box. The only electrical devices located in the box are the solenoid valves, pressure and flow transducers, and CO detector, and the fluidized constant-

TABLE D.1

Estimates of Microreactor System Volumes and Room Air Renewal Rates

System Description	Quantity	Volume (m^3) or Air Renewal Rate (m^3/s)
A. Microreactor System Components		
1. 1/4-inch 316 SS tubing. 0.035-inch wall thickness	12.2 m	2.86×10^{-4}
2. 1/16-inch 316 SS tubing, 0.028-inch wall thickness	3.7 m	2.21×10^{-6}
3. 500-ml reactant and inert gas reservoir	3	1.5×10^{-3}
4. 150-ml reactant and inert gas reservoir	1	1.5×10^{-4}
5. Microreactor	1	5.63×10^{-7}
6. Estimated Microreactor System Volume (components 1 to 5)		1.94×10^{-3} m^3
B. Reactor Box Volume		4.08 m^3
C. Reactor Laboratory Volume		84.53 m^3
D. Air Renewal Rates		
1. Reactor Box		9.91×10^{-2} m^3/s
2. Reactor Laboratory		9.46×10^{-3} m^3/s

TABLE D.2

Upper Limits of Operating Temperatures and Pressures for Different Components of the Vibrofluidized Microreactor System

Component	Maximum Working Pressure at 21°C (kPa)	Maximum Working Pressure (kPa) at Selected Temperature
1. High pressure air regulators	17,175	
2. Stainless-steel tubing, 1/4-inch O.D.	40,574	37,325 at 315°C
3. Whitey 1/4-inch ball values	20,610	
4. Whitey sample cylinders	12,366	
5. Nupro check values	20,610	
6. Circle seal 2-way and 3-way solenoid valves	20,610	
7. Atkomatic solenoid valve	34,350	34,350 at 260°C
8. Nupro metering valves:		
4SG	13,740	
5MG	6,870	
9. Flexible stainless steel hose	18,274	47,870 at 315°C
10. Brooks mass-flow meters: 5810	20,610	
5811	10,305	
11. Circle-seal back-pressure regulator	6,870	
12. Nupro filters	20,610	
13. Valco 6- and 10-port sampling valves		20,610 at 300°C (max)
14. Nupro in-line relief valves (350-600 psi adjustable)	20,610	

temperature sand-bath. On-off switches for these devices are located on the control panel outside the box. The fuse box is located adjacent to the reactor box so that in case of an emergency, all electricity can be shut off immediately.

The Circle-Seal solenoid valves are activated by 28 VDC via a Zenith Z-89 microcomputer. The Atkomatic solenoid valve is actuated by 24 VDC via the microcomputer. The pressure transducers are excited using 10 VDC; and both the mass-flow meters and CO detector require 120 VAC. The fluidized constant-temperature sand-bath uses 240 VAC.

Emergency Equipment

A Toxgard Model C carbon-monoxide detector (Mine Safety Appliances Company) is mounted inside the reactor box as a first line of defense against CO leaks. This detector continuously samples the air by diffusion and reports concentration in ppm. If the limit is reached, both visual and audible alarms are tripped. The sensor life of this unit is about one year. The unit is powered by the 120 VDC builidng supply.

One 5-pound CO_2 fire extinguisher is located approximately 15 m from the reactor box inside the coal laboratory. At the same location is a first-aid kit and an eyewash station.

A sling air mask, available for rescue in toxic environments, is located on the wall outside of Room 155, Randolph Hall. A telephone is located inside the coal laboratory. Emergency telephone numbers are as follows:

1.	Blacksburg Rescue Squad	9-911
2.	Blacksburg Fire Department	9-552-2222
3.	Campus Police	6411
4.	University Health Services	6444
5.	Montgomery County Hospital	9-951-1111

Emergency Shutdown Procedures

A. Fire Emergency

1. Turn off the main valve on the hydrogen cylinder.
2. Turn off the main valve on the H_2:CO:Ar cylinder.
3. Call Blacksburg Fire Department at 9-552-2222.
4. Notify a close-by person to sound the fire alarm and evacuate the building.
5. If fire is small and confined in nature, steps may be taken to extinguish it with the CO_2 fire extinguisher.

B. Gas Leaks

1. Turn off all electricity to the experiment at the control panel of the fuse box.
2. Turn off the main valve on the hydrogen cylinder.
3. Turn off the main valve on the H_2:CO:Ar cylinder.
4. Locate leak site using nitrogen and repair the leak.
5. Pessure-test the system after leak repair.

C. Loss of Building Power

1. Turn off the main valve on the H_2:CO:Ar cylinder.
2. Turn off the main valve on the hydrogen cylinder.
3. Turn off the main valve on the nitrogen cylinder.
4. Turn off all meters and solenoid valves.
5. Wait for power restoration in another room.

APPENDIX E

EARLIER EXPLORATORY WORK

The development of the present unsteady-state microreactor system for F-T synthesis has taken place over a three-year period. During this time, the design of the microreactor system as well as the microreactor itself has been revised several times.

Figures E.1 and E.2 are photographs of the original stainless-steel vibrofluidized microreactor used in preliminary experiments (Liu et al., 1982). This microreactor consisted of four primary zones: (1) the plenum zone, (2) the reaction zone, (3) the freeboard zone and (4) the product-gas exit zone. The internal dimensions of the microreactor were very similar to those of the steady-state microreactor shown in Figure 4.2. Asbestos impregnated gaskets were used between the four sections of the microreactor. This is in contrast to the silver-plated stainless-steel O-rings now being used in the present reactor. The use of gaskets coupled with the lack of compressive force exerted by the four connecting bolts, resulted in gas leakage at the high temperatures and pressures used. Leakage also occurred at silver-soldered tubing joints which tended to soften at high temperature. In the present microreactor, all tubing joints have been welded for leak-proof seals.

Figure E.3 is a schematic diagram of the original design of the vibrofluidized-bed microreactor system for unsteady-state F-T synthesis. This system consisted of two feed legs, a product-exit leg and a purge gas-exit leg. The idea was to provide discrete pulses of gas to the catalyst bed by alternately purging the plenum zone of the previous gas. Figures E.4 through E.8 illustrate the feeding and purging sequence:

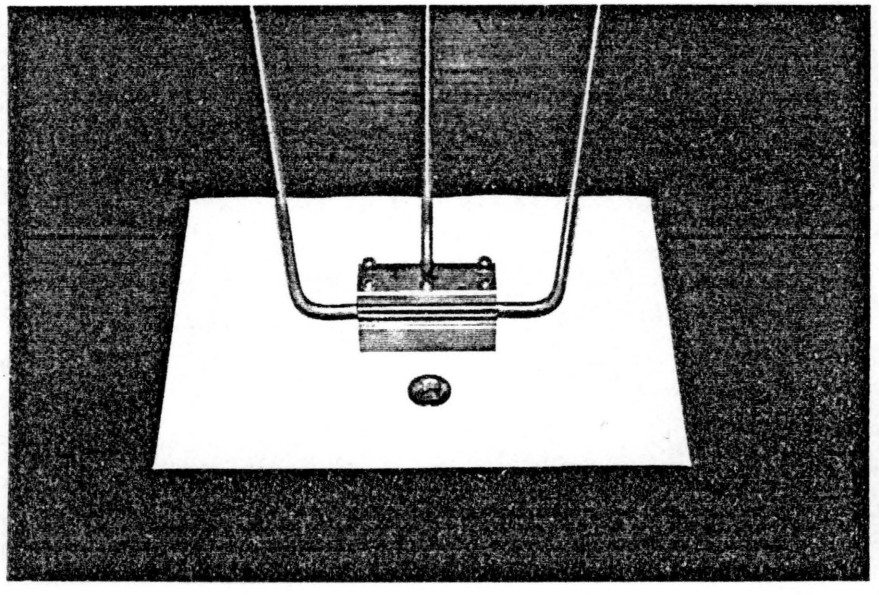

Figure E.1. The Original Vibrofluidized Microreactor for Fischer-Tropsch Synthesis Studies.

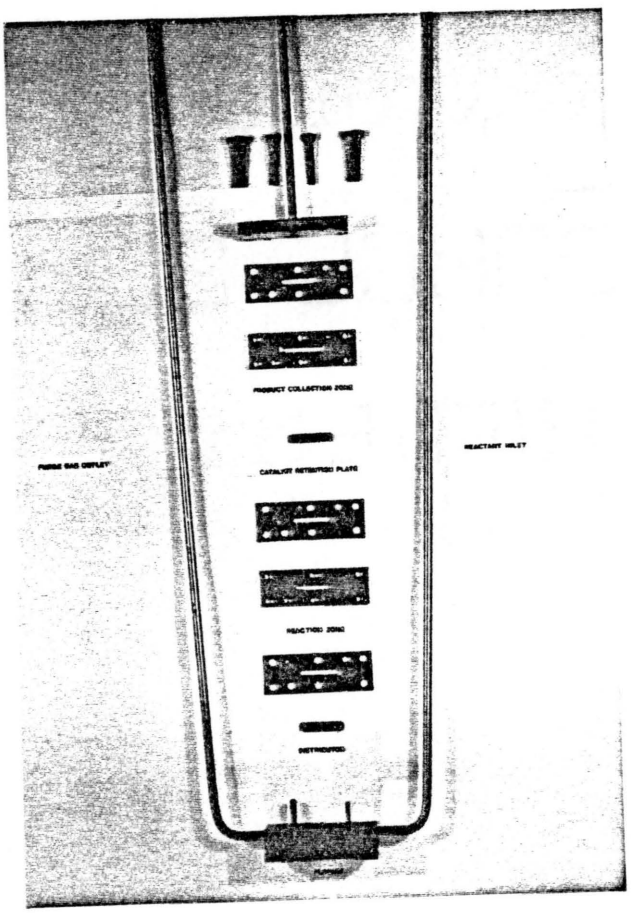

Figure E.2. Key Components of the Vibrofluidized Microreactor for Fischer-Tropsch Synthesis Studies.

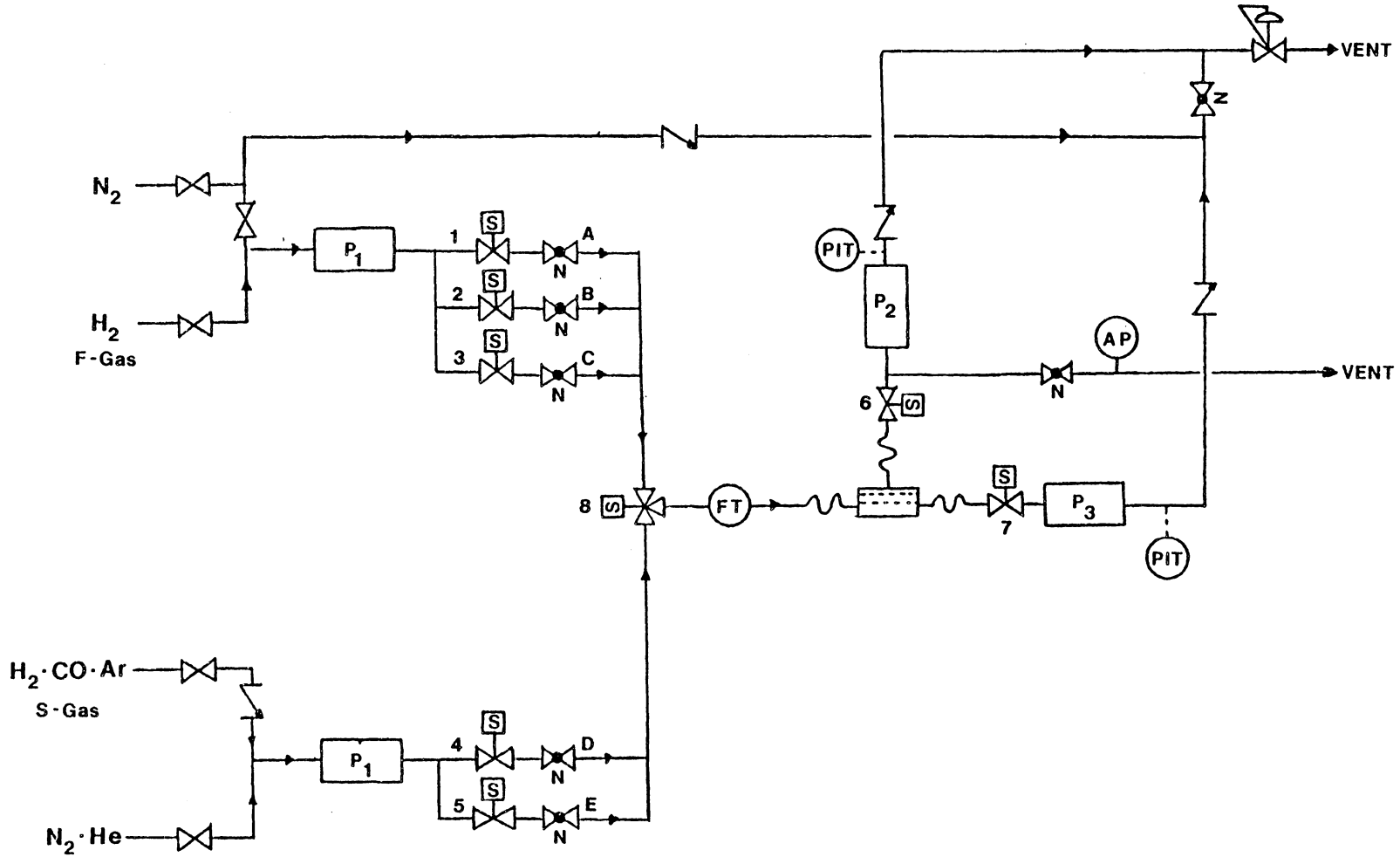

Figure E.3. A Schematic Diagram of the Original Vibrofluidized-Bed Microreactor System for Unsteady-State Fischer-Tropsch Synthesis (Refer to Figure 4.1b for Equipment Symbols).

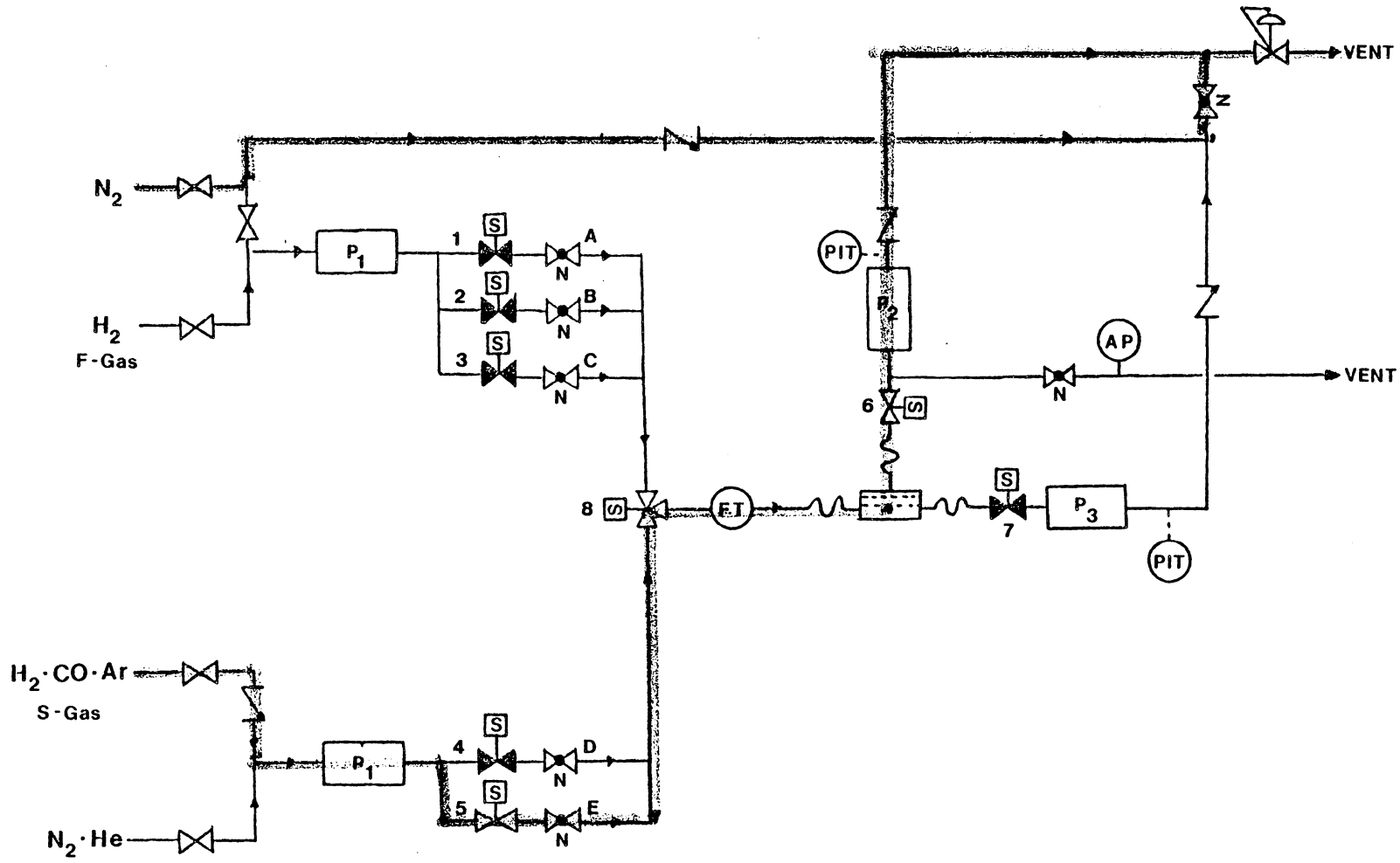

Figure E.4. High Flow Rate of S-Gas Feed through Valve E for a Short Duration.

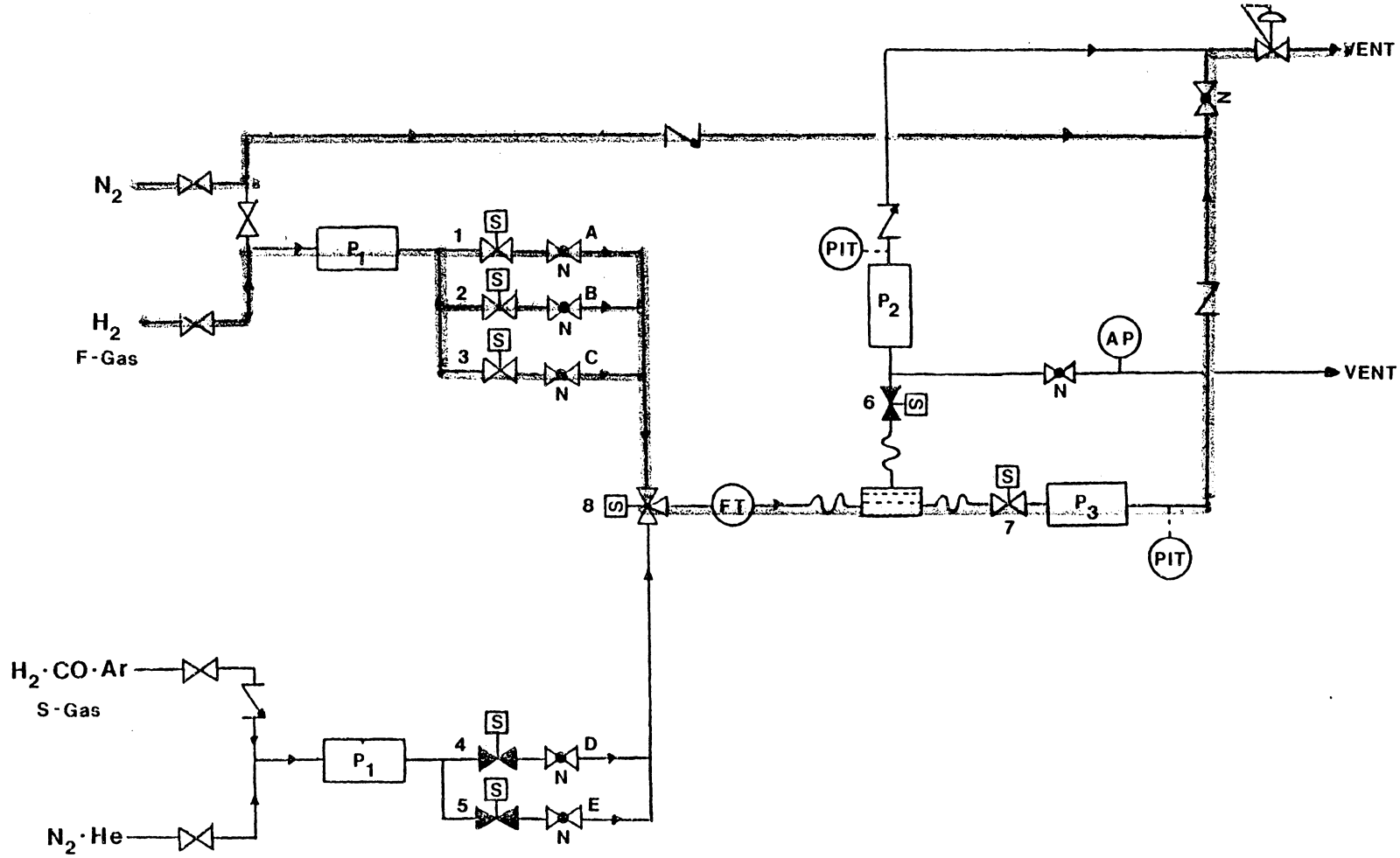

Figure E.5. Plenum Purge of S-Gas by a High Flow Rate of F-Gas for a Short Duration.

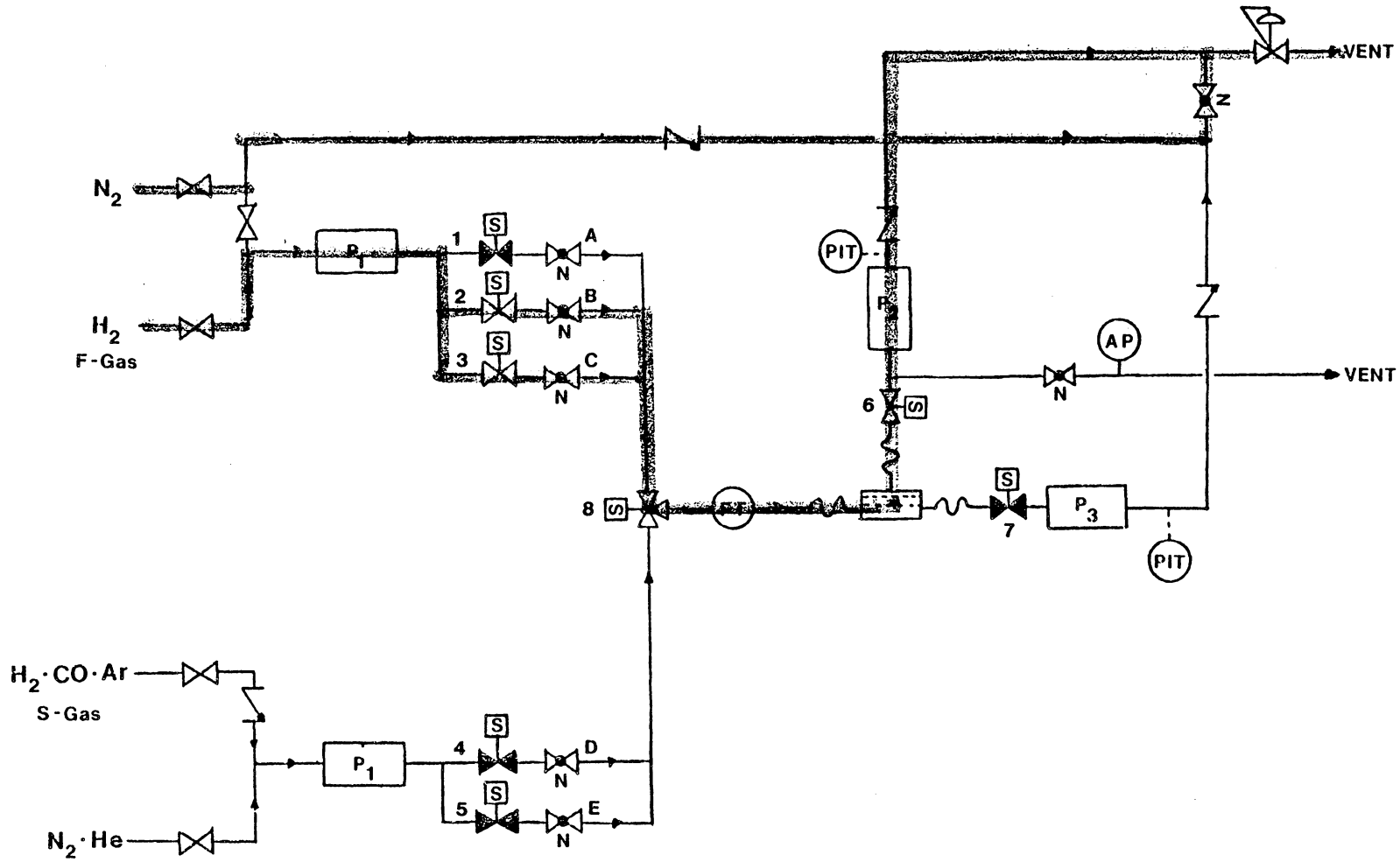

Figure E.6. Reaction Zone Purge by a Relatively High Flow Rate of F-Gas for a Short Duration.

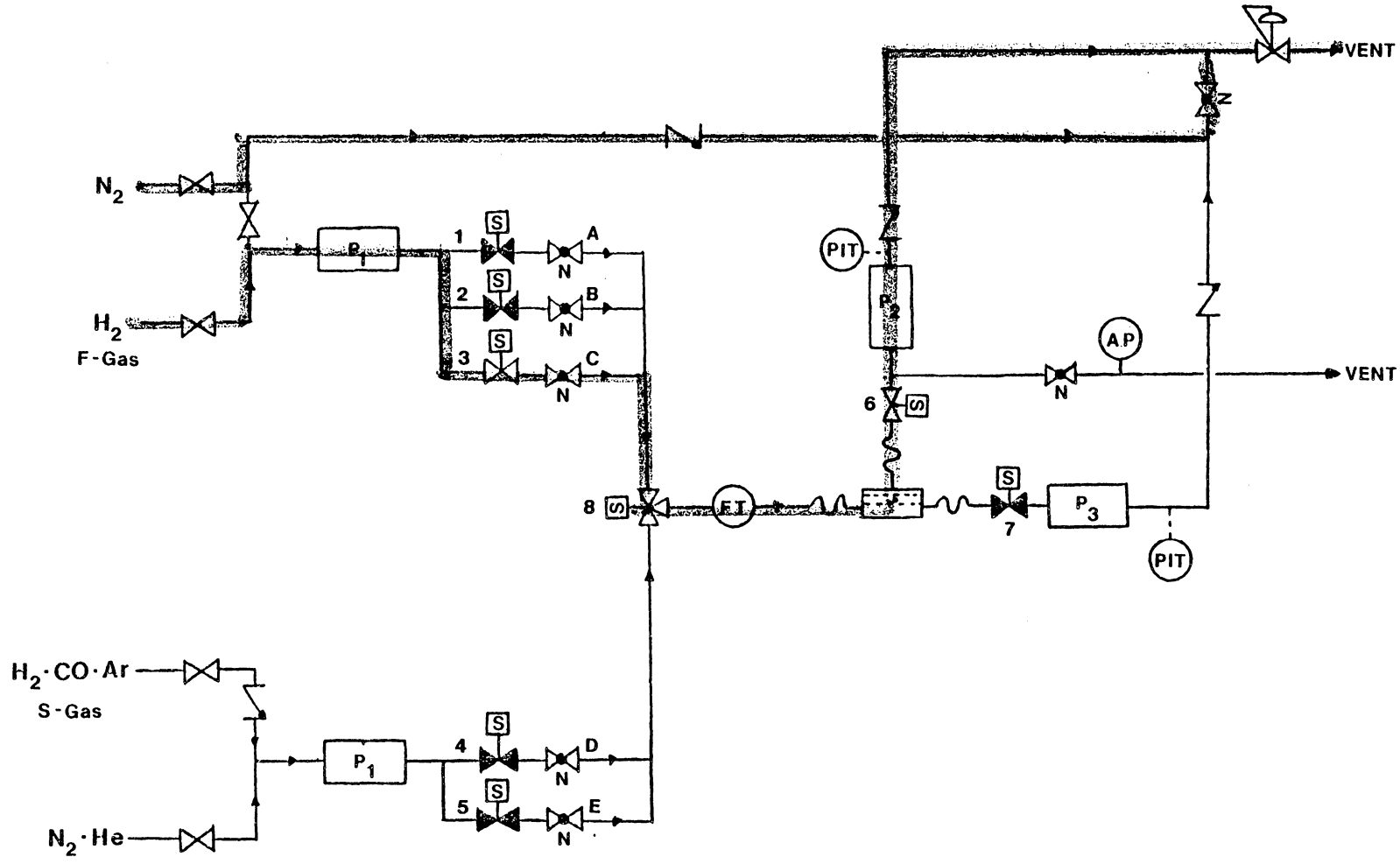

Figure E.7. A Low Flow Rate of F-Gas Feed into the Reaction Zone through Valve C for a Long Duration.

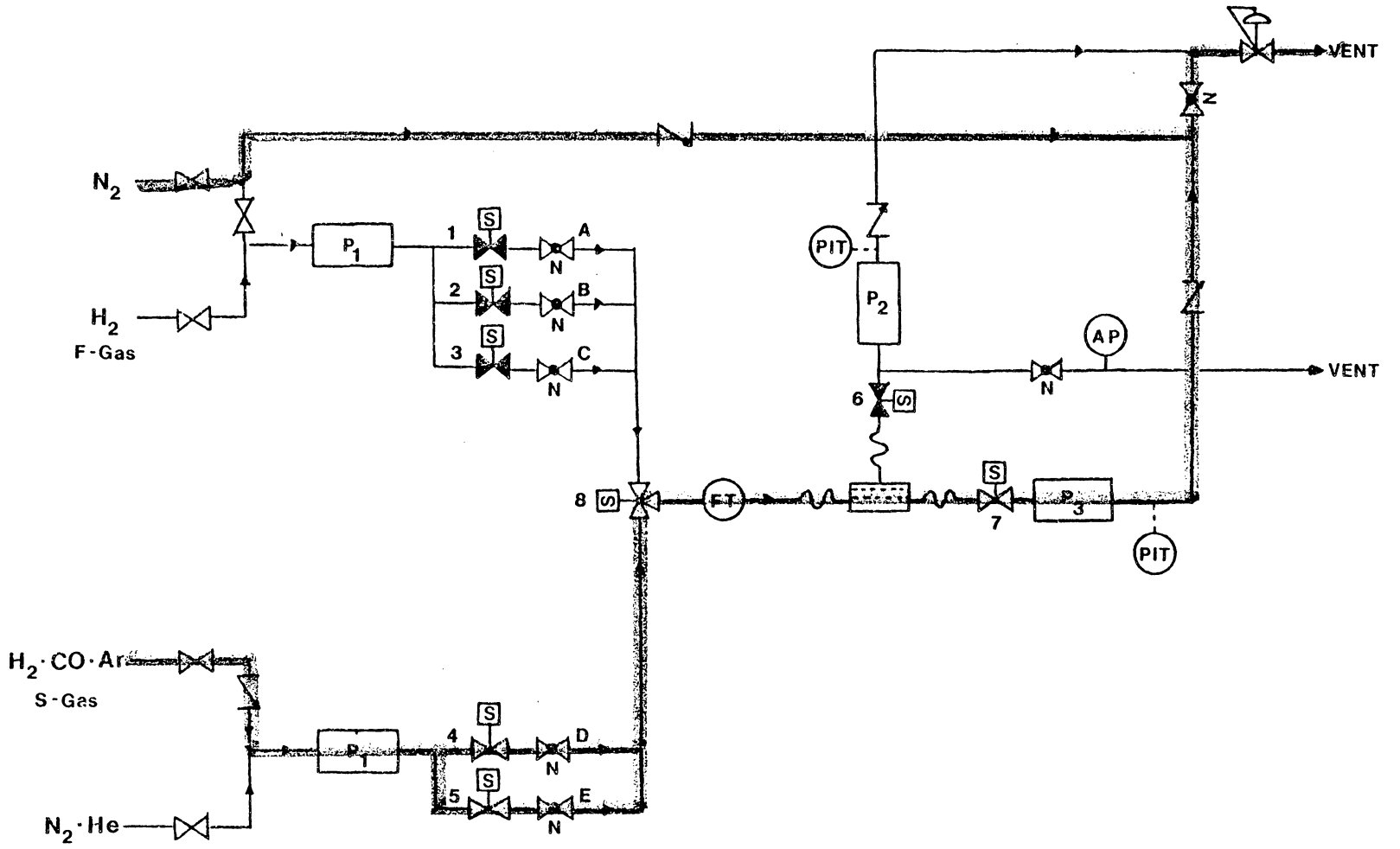

Figure E.8. Plenum Purge of F-Gas by a High Flow Rate of S-gas for a Short Duration.

(i) S-gas (H_2:CO:Ar) is being fed at the beginning of a cycle (Figure E.4). Solenoid valves 1, 2, 3, 4, and 7 are closed. Three-way solenoid valve 8 is shifted to permit a high flow rate of S-gas into the microreactor for a short duration (e.g., 2 seconds).

(ii) The plenum zone beneath the catalyst zone is being purged of S-gas by F-gas (Figure E.5). Solenoid valves 4, 5, and 6 are closed and three-way valve 8 is shifted to permit the F-gas to flow. At this time, solenoid valves 1, 2, 3, and 7 are opened simultaneously for a relatively high flow rate of F-gas through needle valves A, B, and C into the plenum zone of the microreactor for a short duration (e.g., 1 second). This flow should be able to purge the gas contained in the plenum zone completely.

(iii) The reaction zone is being purged by F-gas (Figure E.6). Solenoid valve 1 and 7 are closed and 6 is opened. This permits a relatively high flow rate of F-gas through needle valves B and C for a short duration (e.g., 1 second).

(iv) F-gas is being fed into the reaction zone (Figure E.7). Valve 2 is closed and valves 3 and 6 remain open. A low flow rate of F-gas passes through valves 3 and C into the reaction zone for a long duration.

(v) The plenum zone is being purged of F-gas by S-gas (Figure E.8). Valves 3 and 6 are closed, and valves 4, 5, and 7 remain open. Three-way value 8 is shifted to its original position which allows for the S-gas to flow into the plenum zone through valves D and E at a high flow rate for a very short duration. This flow should be able to sweep out the gas contained in the plenum zone in the microreactor.

After several preliminary experiments, a cold-flow model of the unsteady-state microreactor system was constructed. The purpose of this model was to determine the gas-mixing characteristics of the microreactor system. The results of the earlier cold-flow model studies have been given by Feldhousen (1984). It was found that undesirable mixing of F-gas and S-gas occurred in the plenum zone of the microreactor. In addition, it has been suggested that the plenum purge period provided an "aging" time for the catalyst during which no gas was flowing through the catalyst bed.

Because of these results, the sliding-plug vibrofluidized-bed microreactor system described in Sections 5 and 6 has been developed. The sliding-plug vibrofluidized-bed microreactor system drastically reduces gas mixing and allows the catalyst to be continually exposed to gas flow.

APPENDIX F

Thermal Conductivity Detector Traces of Gas Mixing in the Sliding-Plug Vibrofluidized-Bed Cold-Flow Microreactor Model

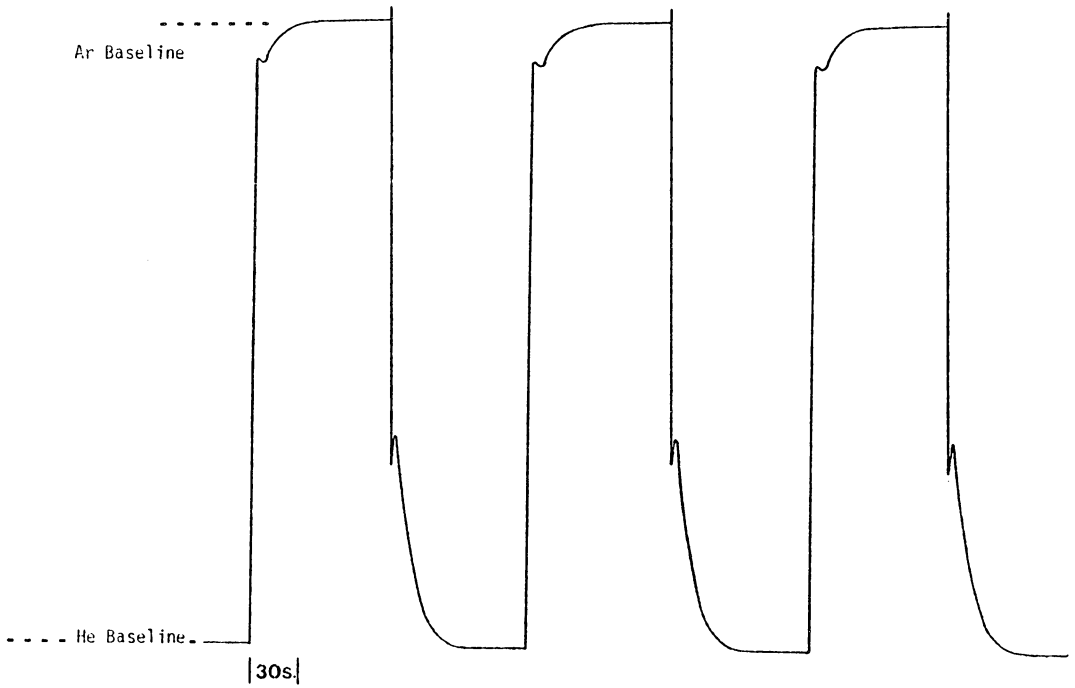

Figure F.1. The Thermal Conductivity Response for Switching Between Helium and Argon Feeds in the Cold-Flow Microreactor Model during Experiment 1-1. (Refer to Table 5.1 for the Experimental Conditions).

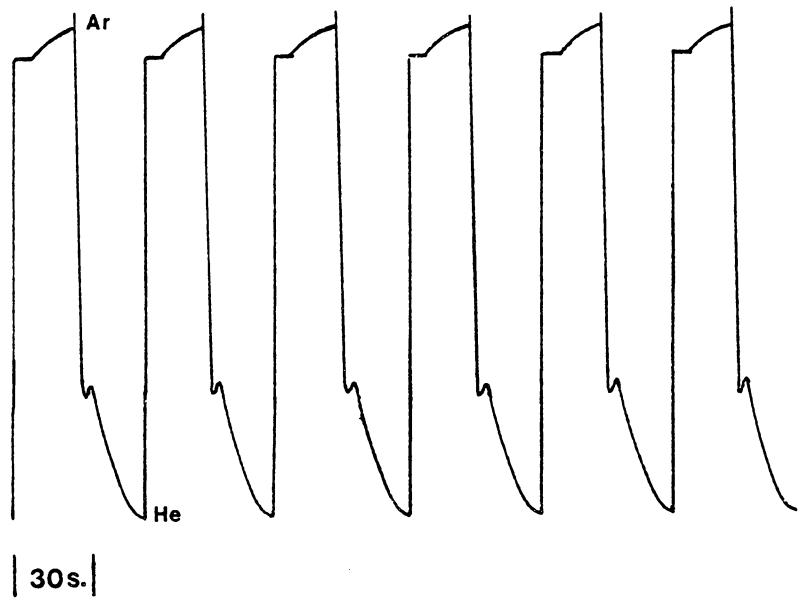

Figure F.2. The Thermal Conductivity Response for Switching Between Helium and Argon Feeds in the Cold-Flow Microreactor Model during Experiment 1-2 (Refer to Table 5.1 for the Experimental Conditions).

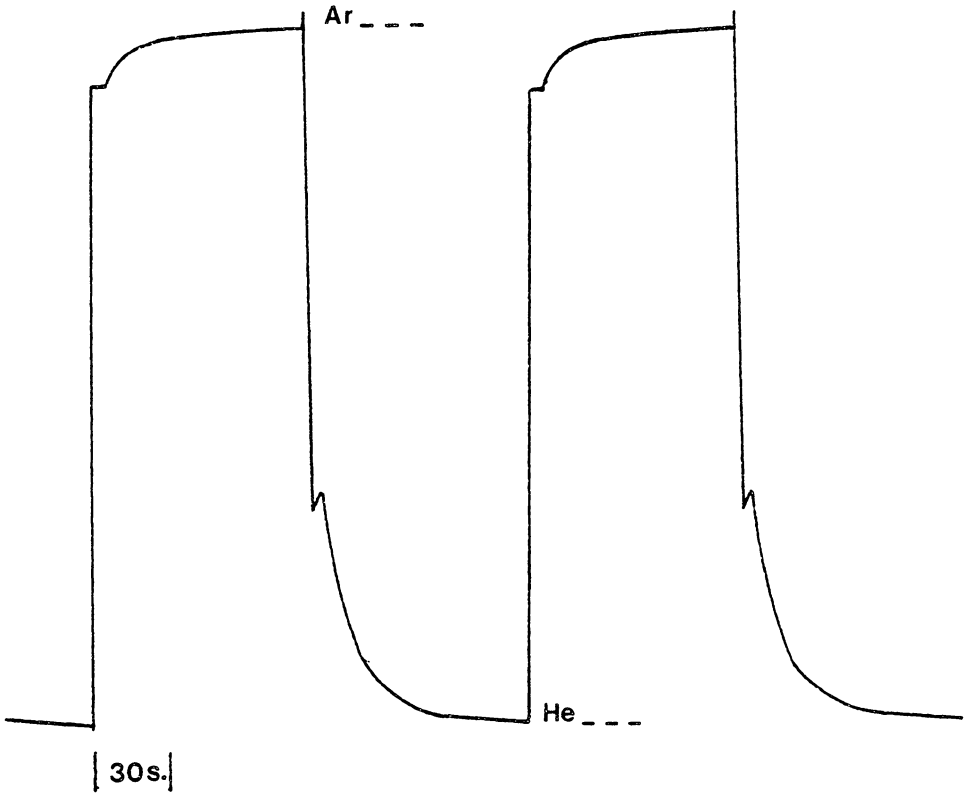

Figure F.3. The Thermal Conductivity Response for Switching Between Helium and Argon Feeds in the Cold-Flow Microreactor Model during Experiment 1-4 (Refer to Table 5.1 for the Experimental Conditions).

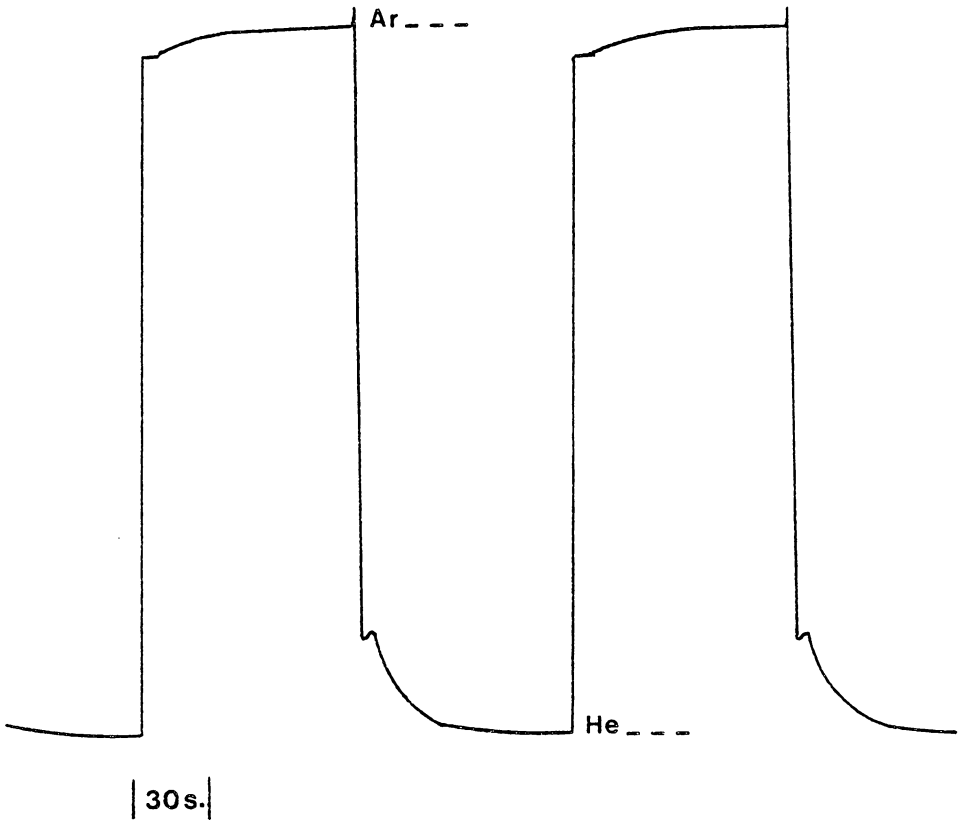

Figure F.4. The Thermal Conductivity Response for Switching Between Helium and Argon Feeds in the Cold-Flow Microreactor Model during Experiment 1-5 (Refer to Table 5.1 for the Experimental Conditions).

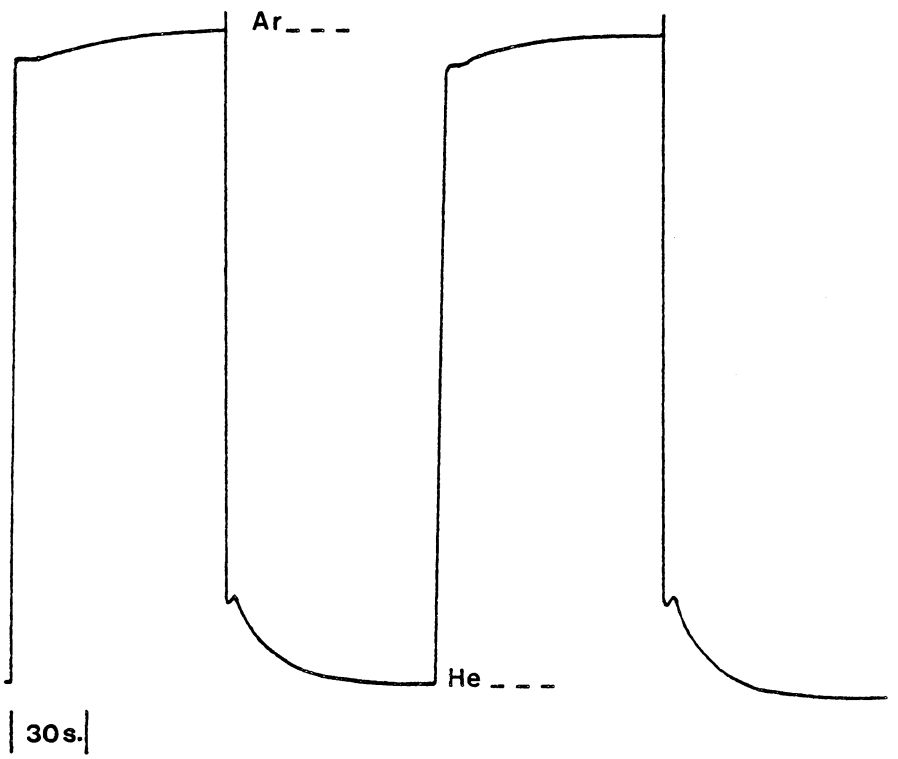

Figure F.5. The Thermal Conductivity Response for Switching Between Helium and Argon Feeds in the Cold-Flow Microreactor Model during Experiment 1-6 (Refer to Table 5.1 for the Experimental Conditions).

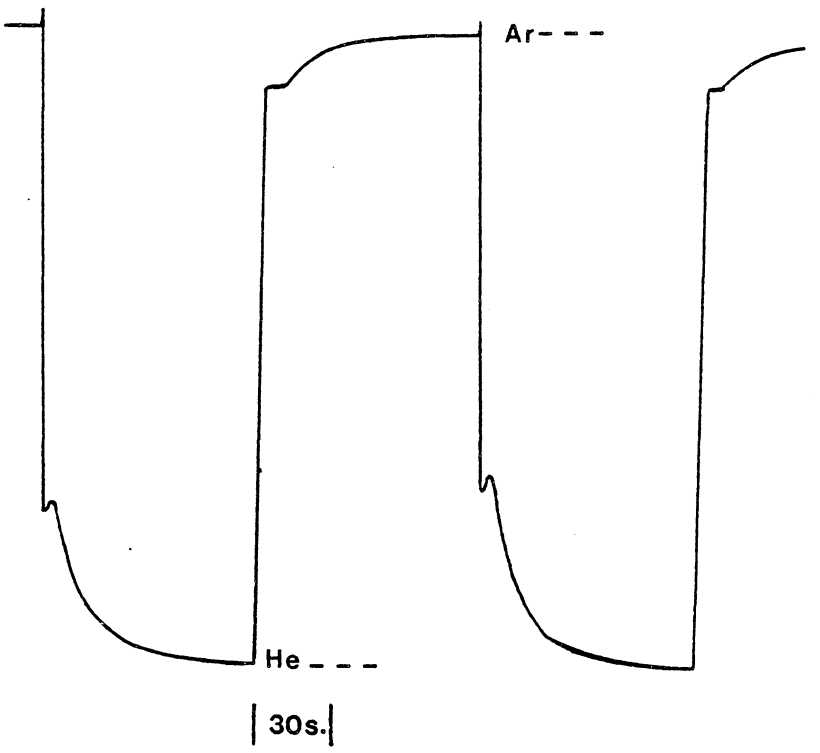

Figure F.6. The Thermal Conductivity Response for Switching Between Helium and Argon Feeds in the Cold-Flow Microreactor Model during Experiment 1-7 (Refer to Table 5.1 for the Experimental Conditions).

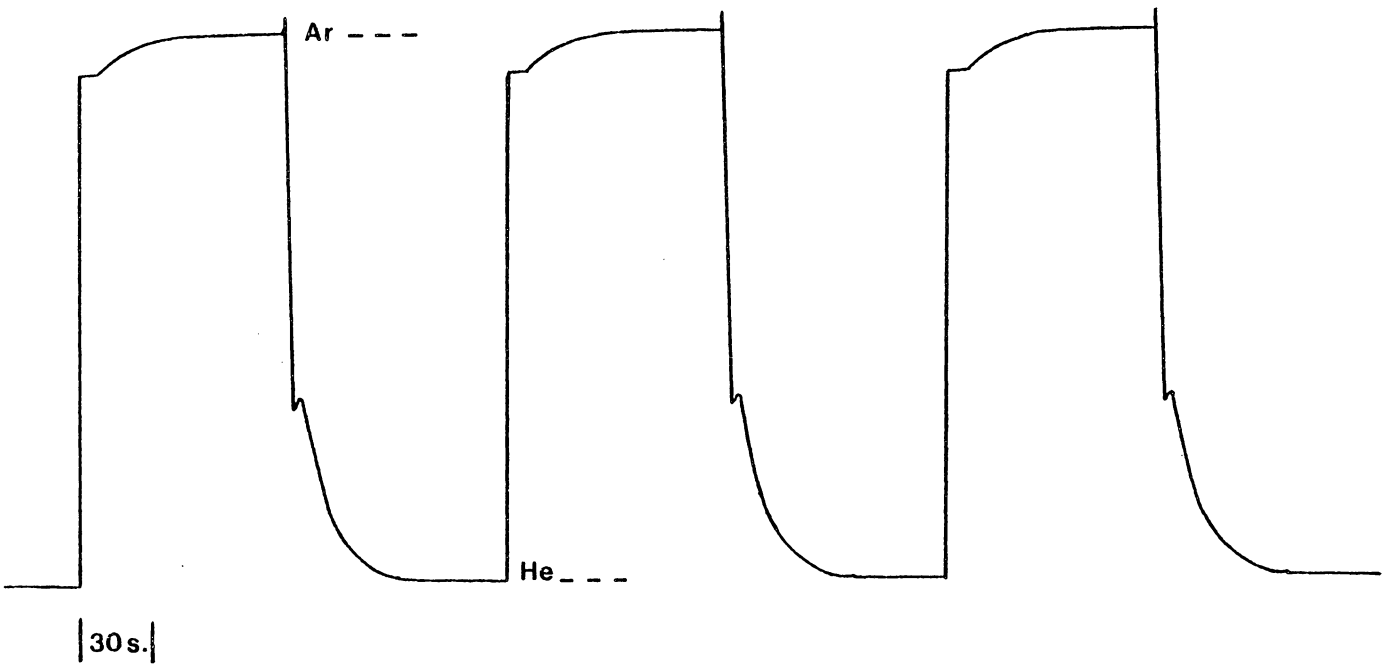

Figure F.7. The Thermal Conductivity Response for Switching Between Helium and Argon Feeds in the Cold-Flow Microreactor Model during Experiment 1-8 (Refer to Table 5.1 for the Experimental Conditions).

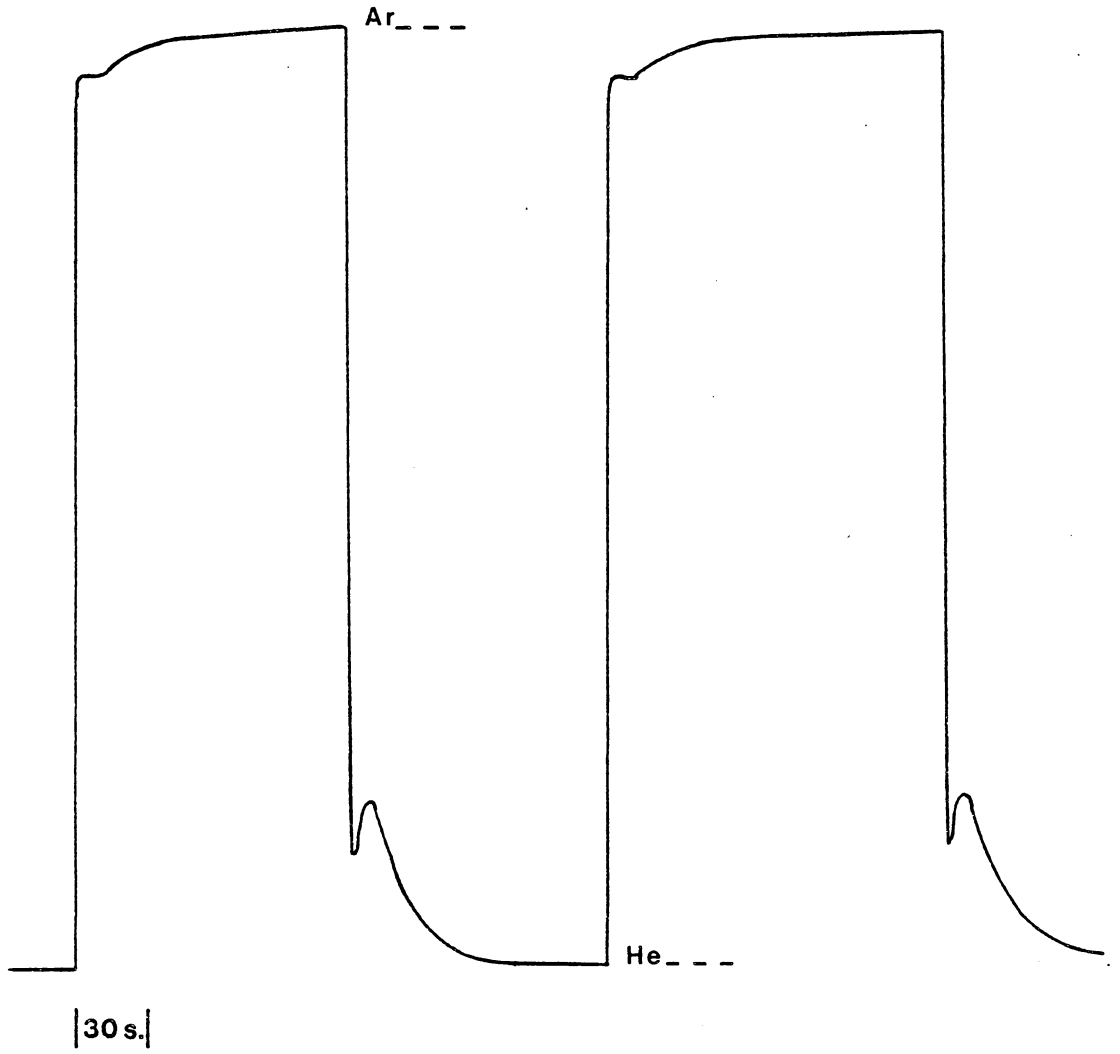

Figure F.8. The Thermal Conductivity Response for Switching Between Helium and Argon Feeds in the Cold-Flow Microreactor Model during Experiment 2-1 (Refer to Table 5.1 for the Experimental Conditions).

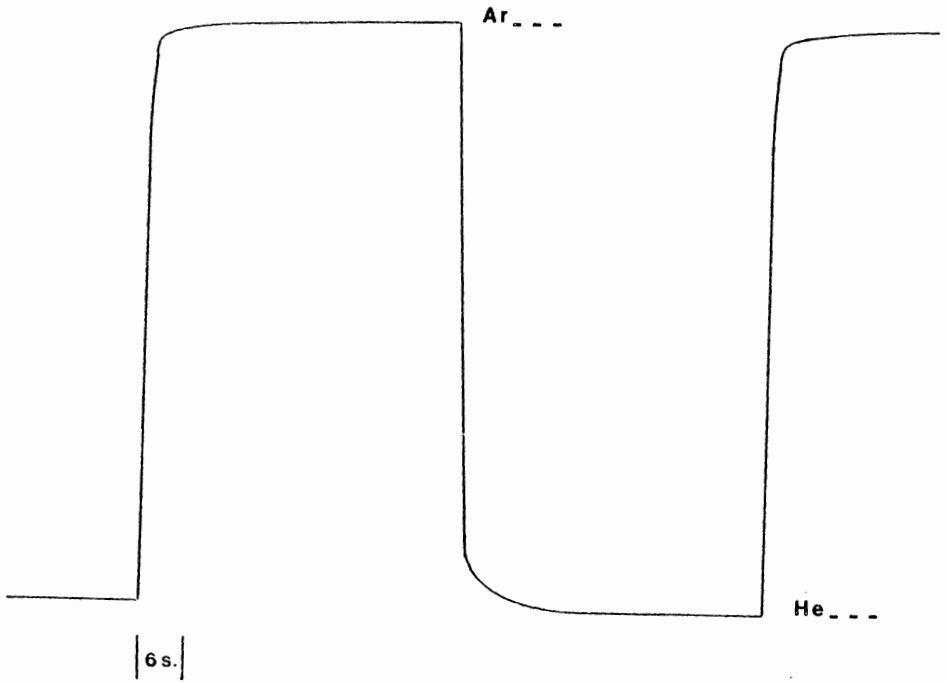

Figure F.9. The Thermal Conductivity Response for Switching Between Helium and Argon Feeds in the Cold-Flow Microreactor Model during Experiment 2-3 (Refer to Table 5.1 for the Experimental Conditions).

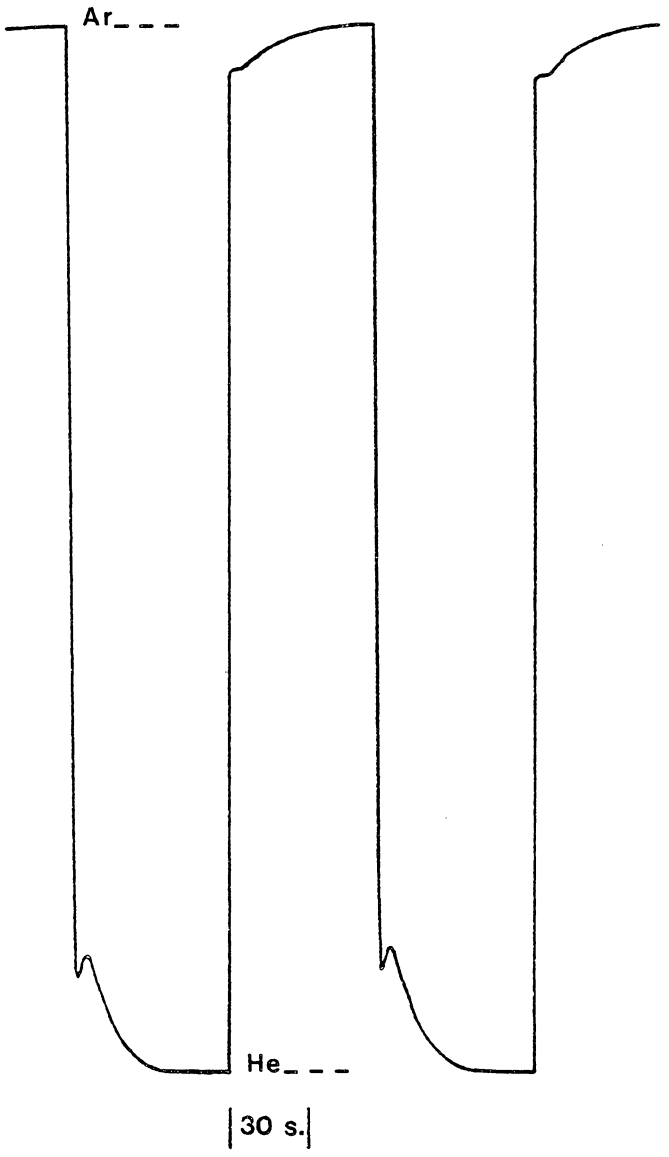

Figure F.10. The Thermal Conductivity Response for Switching Between Helium and Argon Feeds in the Cold-Flow Microreactor Model during Experiment 2-4 (Refer to Table 5.1 for the Experimental Conditions).

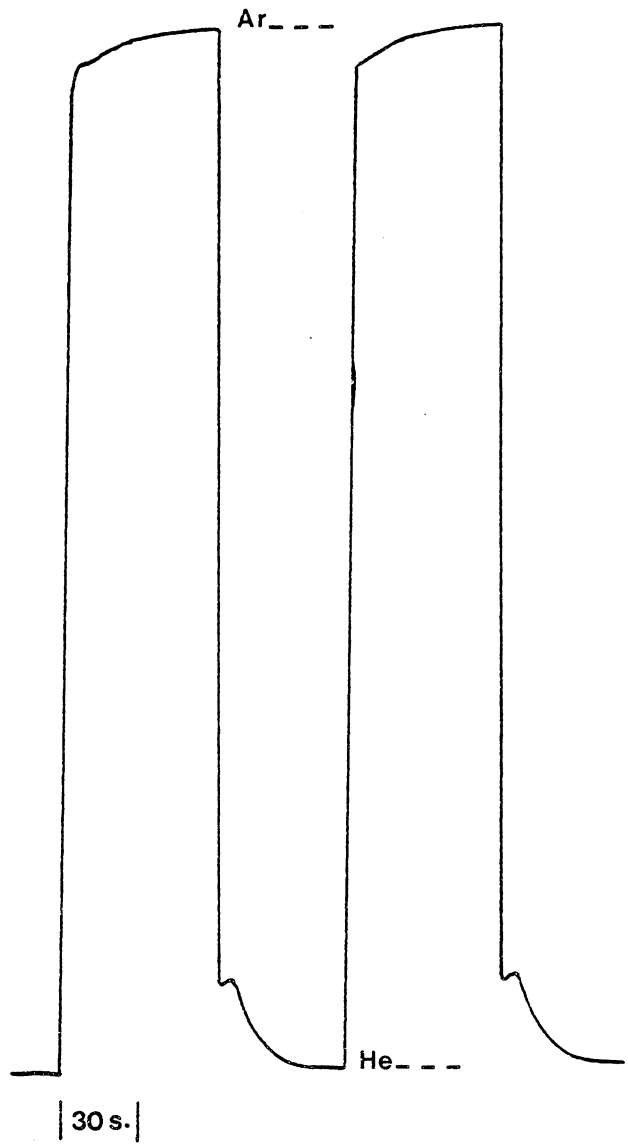

Figure F.11. The Thermal Conductivity Response for Switching Between Helium and Argon Feeds in the Cold-Flow Microreactor Model during Experiment 2-5 (Refer to Table 5.1 for the Experimental Conditions).

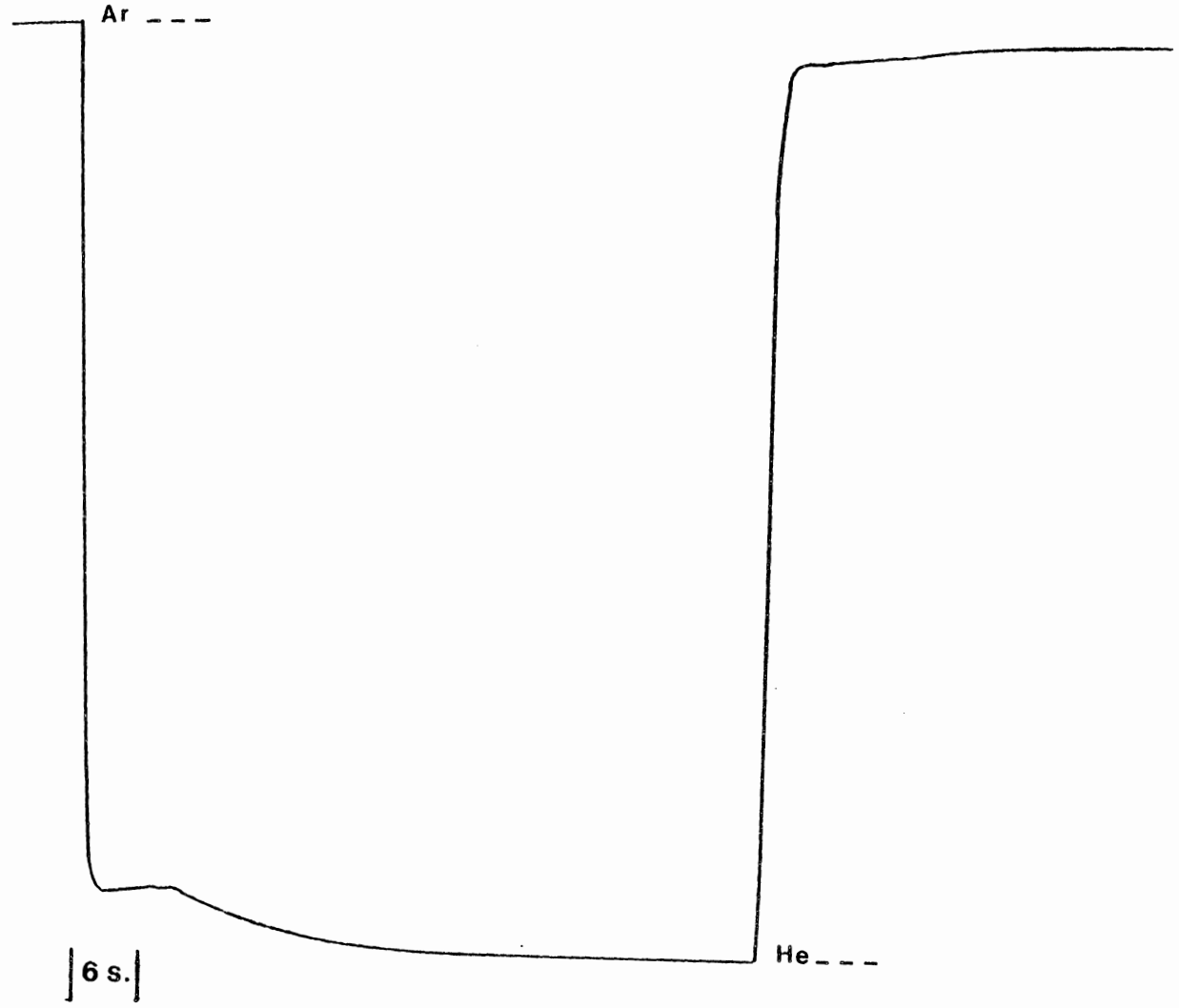

Figure F.12. The Thermal Conductivity Response for Switching Between Helium and Argon Feeds in the Cold-Flow Microreactor Model during Experiment 2-6 (Refer to Table 5.1 for the Experimental Conditions).

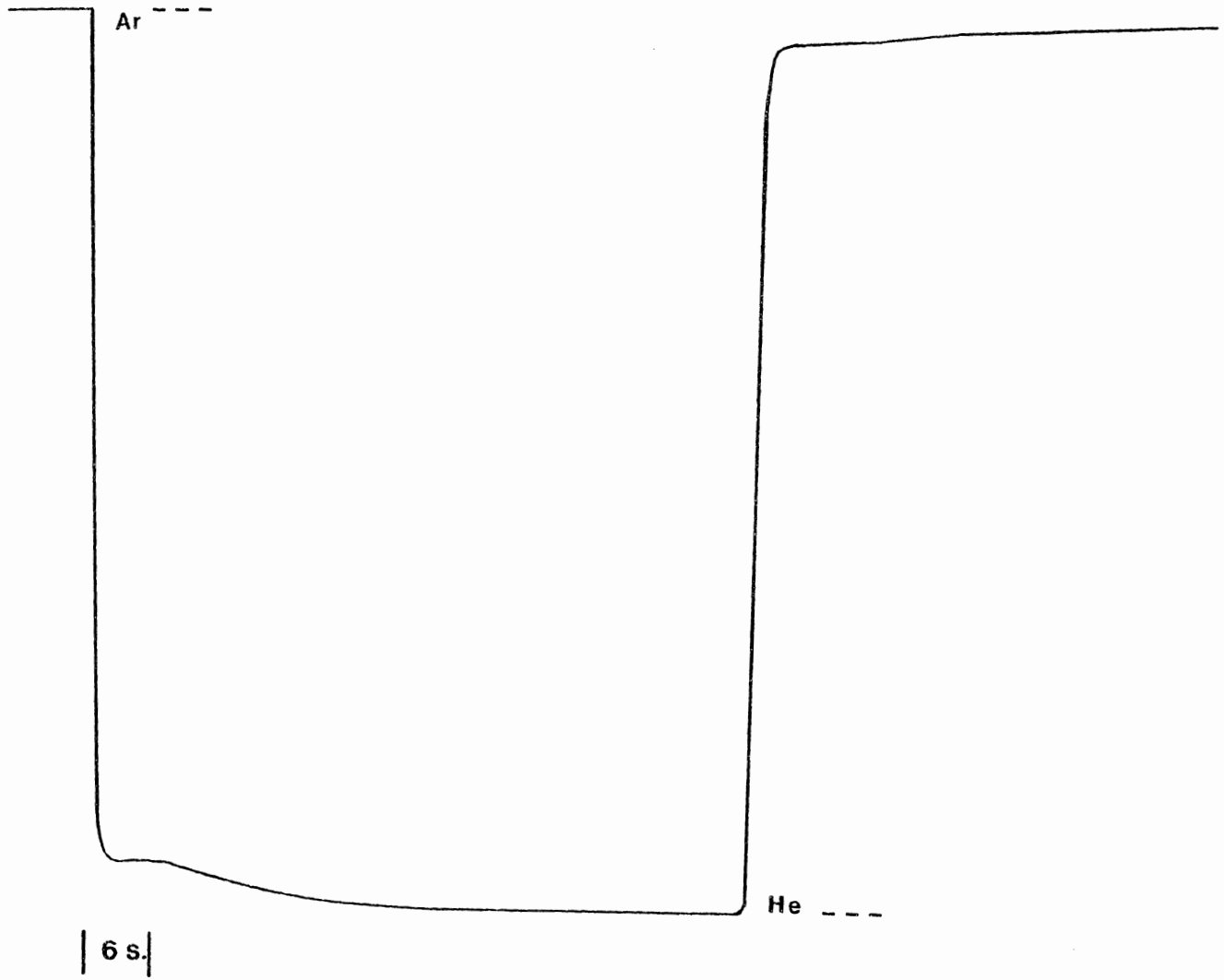

Figure F.13. The Thermal Conductivity Response for Switching Between Helium and Argon Feeds in the Cold-Flow Microreactor Model during Experiment 2-7 (Refer to Table 5.1 for the Experimental Conditions).

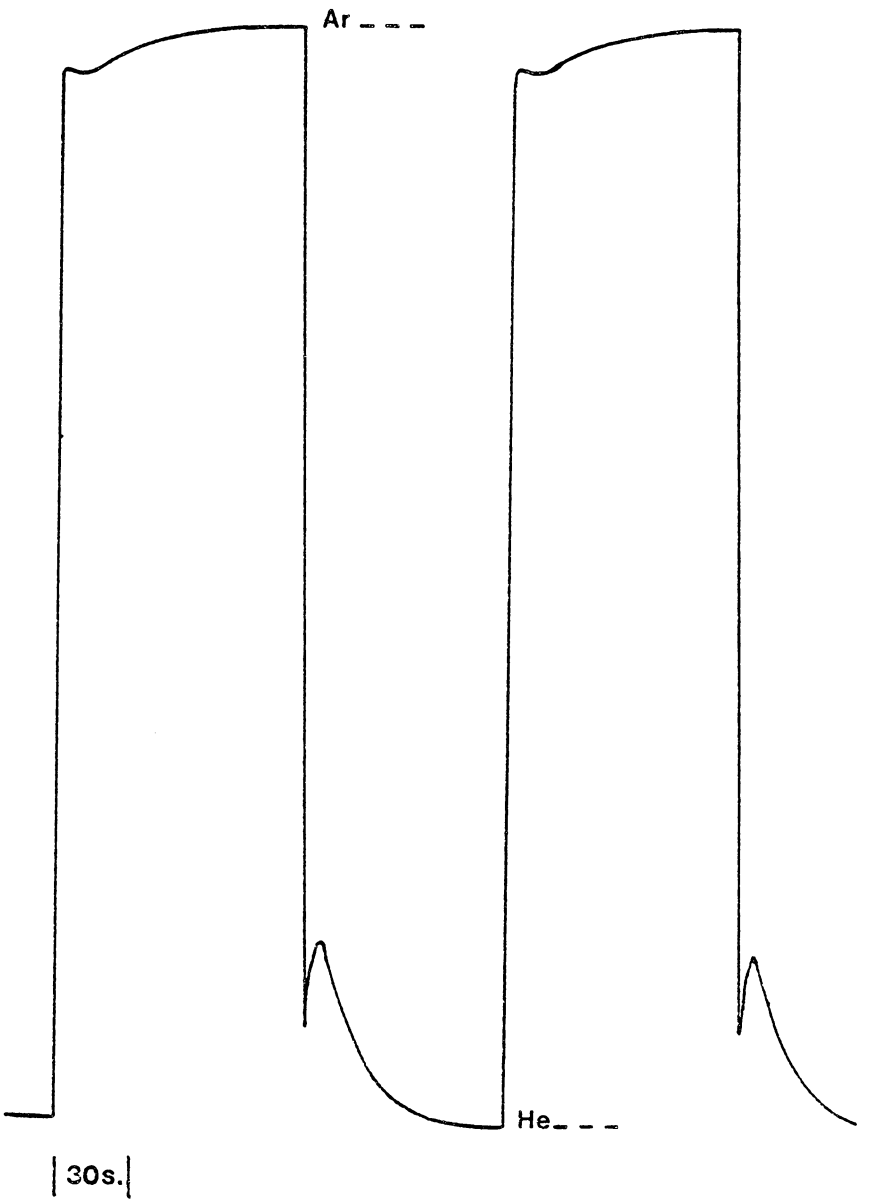

Figure F.14. The Thermal Conductivity Response for Switching Between Helium and Argon Feeds in the Cold-Flow Microreactor Model during Experiment 2-8 (Refer to Table 5.1 for the Experimental Conditions).

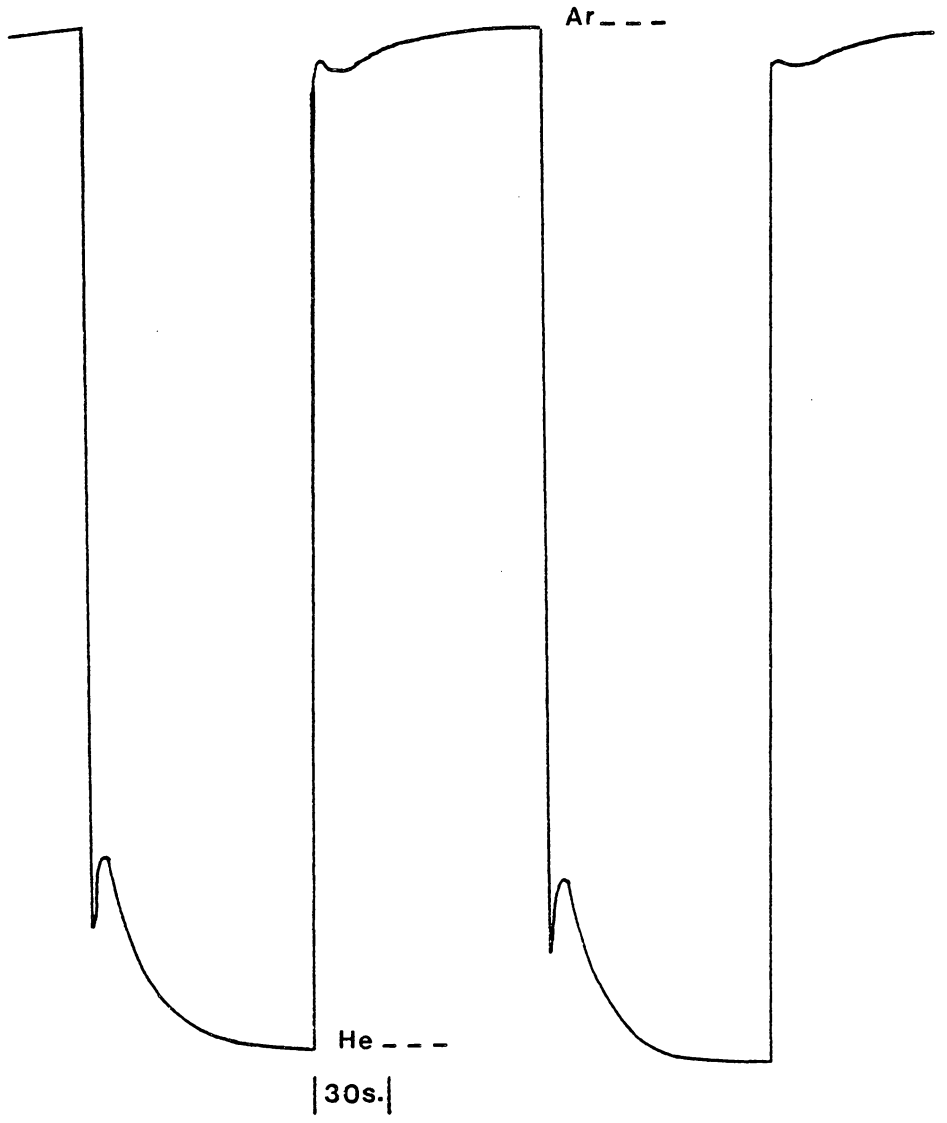

Figure F.15. The Thermal Conductivity Response for Switching Between Helium and Argon Feeds in the Cold-Flow Microreactor Model during Experiment 2-9 (Refer to Table 5.1 for the Experimental Conditions).

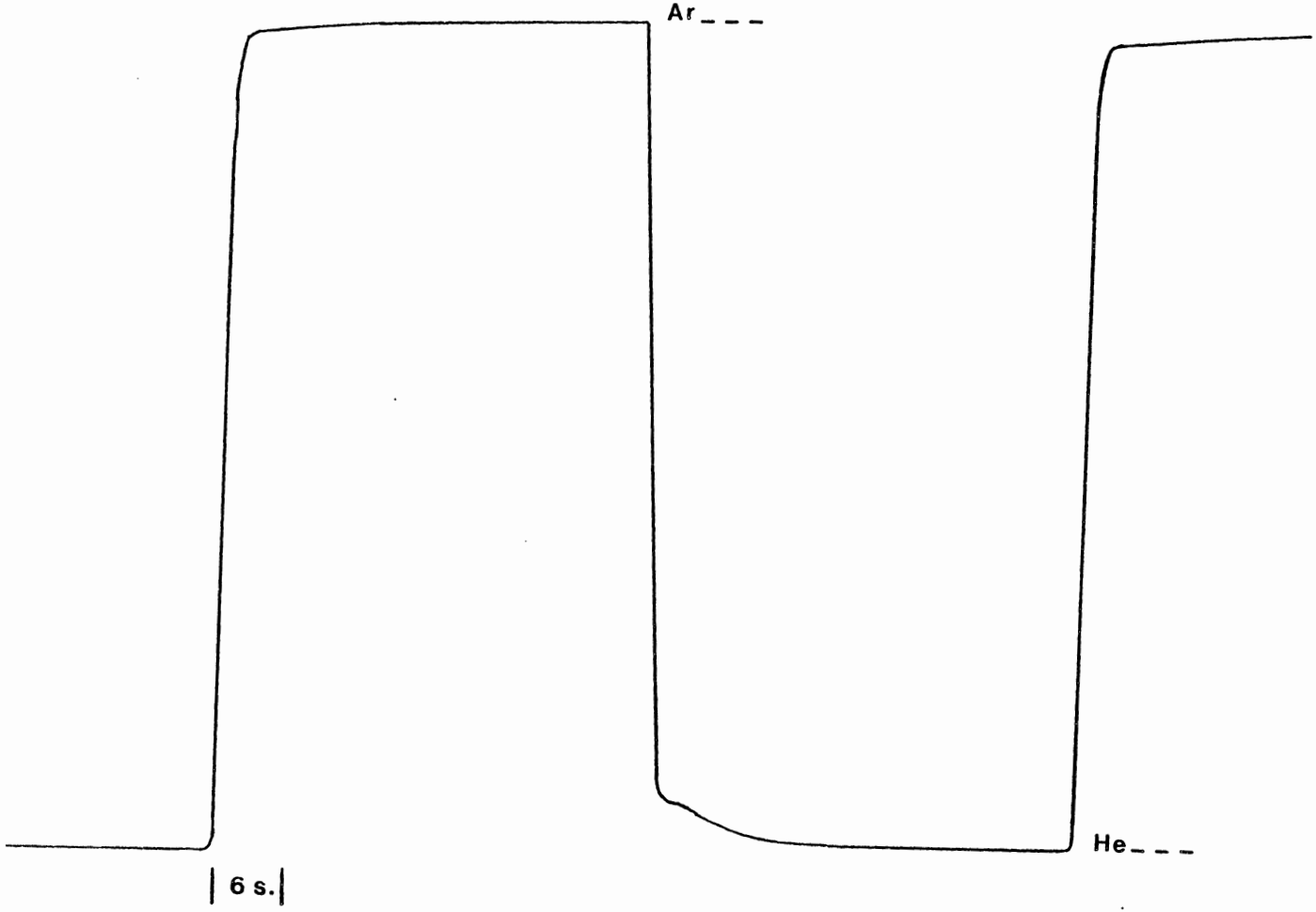

Figure F.16. The Thermal Conductivity Response for Switching Between Helium and Argon Feeds in the Cold-Flow Microreactor Model during Experiment 2-10 (Refer to Table 5.1 for the Experimental Conditions).

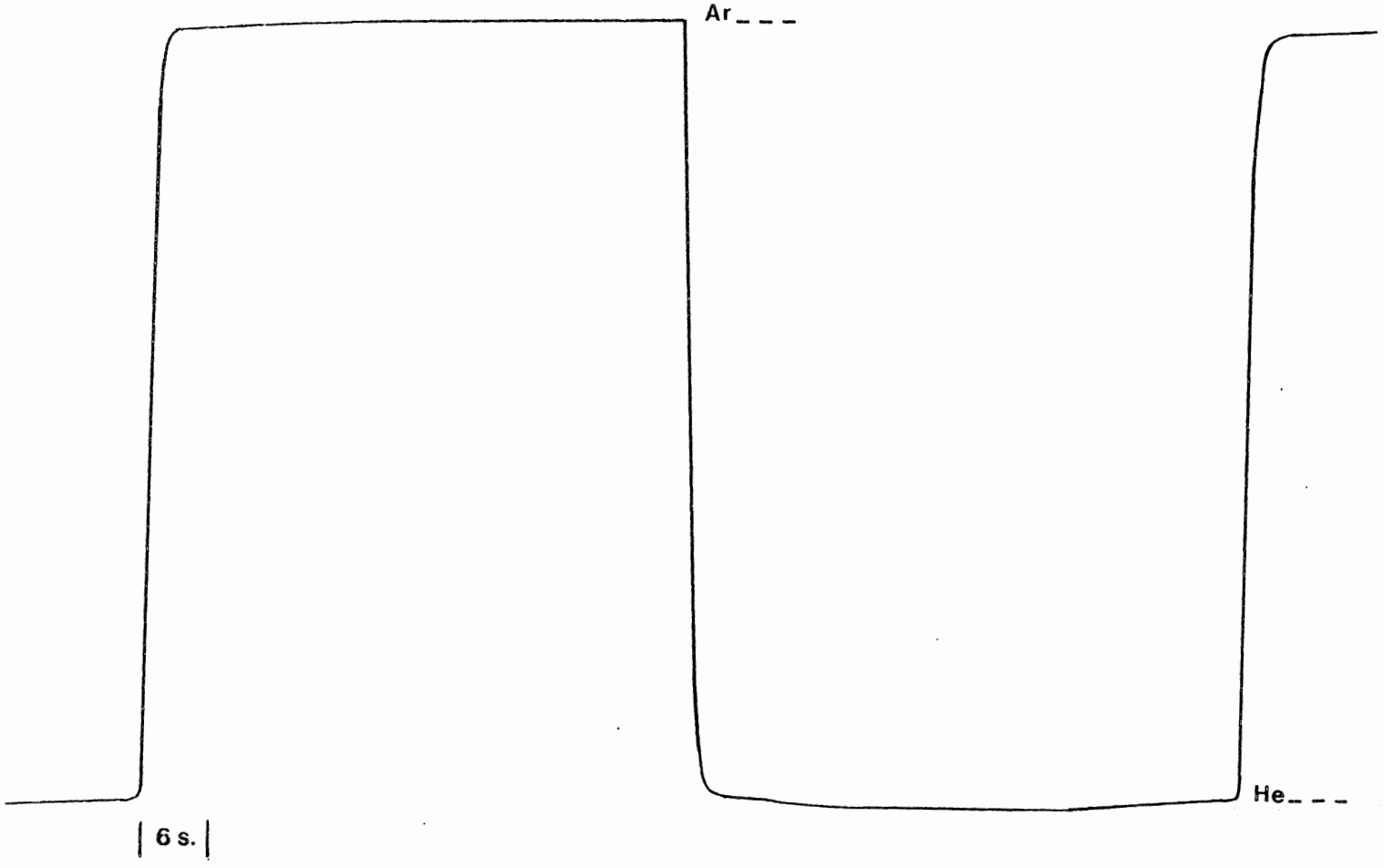

Figure F.17. The Thermal Conductivity Response for Switching Between Helium and Argon Feeds in the Cold-Flow Microreactor Model during Experiment 2-11 (Refer to Table 5.1 for the Experimental Conditions).

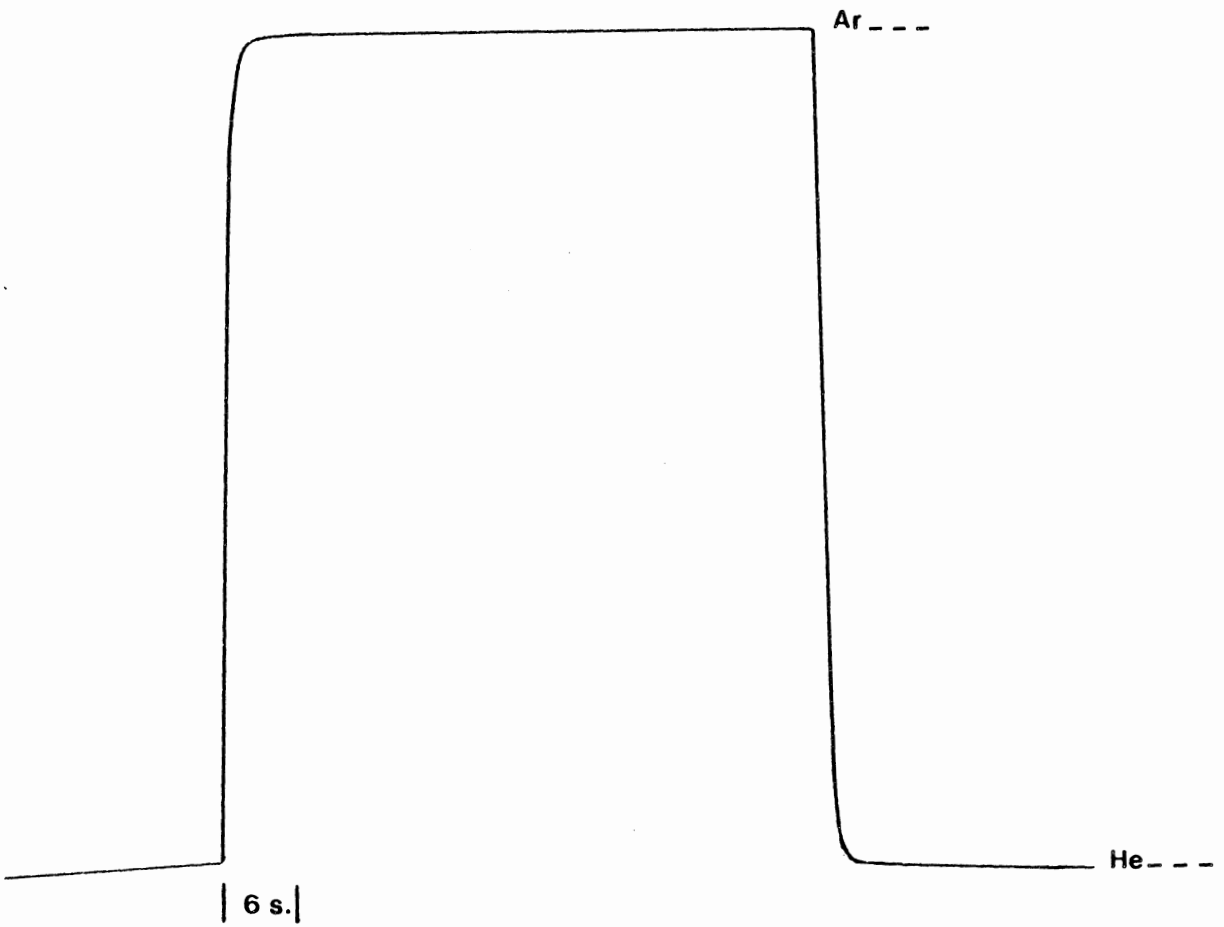

Figure F.18. The Thermal Conductivity Response for Switching Between Helium and Argon Feeds in the Cold-Flow Microreactor Model during Experiment 2-13 (Refer to Table 5.1 for the Experimental Conditions).

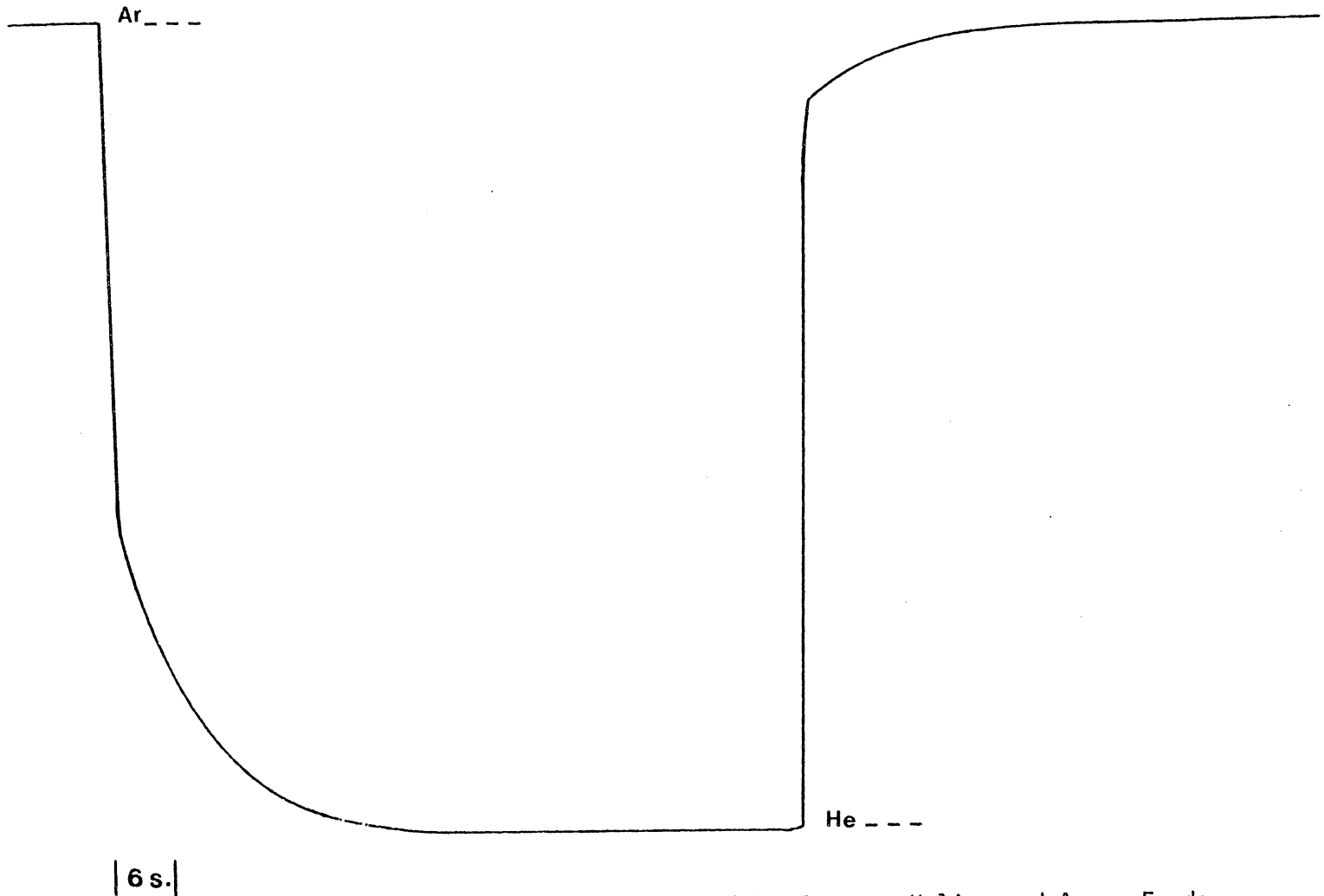

Figure F.19. The Thermal Conductivity Response for Switching Between Helium and Argon Feeds in the Cold-Flow Microreactor Model during Experiment 3-1 (Refer to Table 5.1 for the Experimental Conditions).

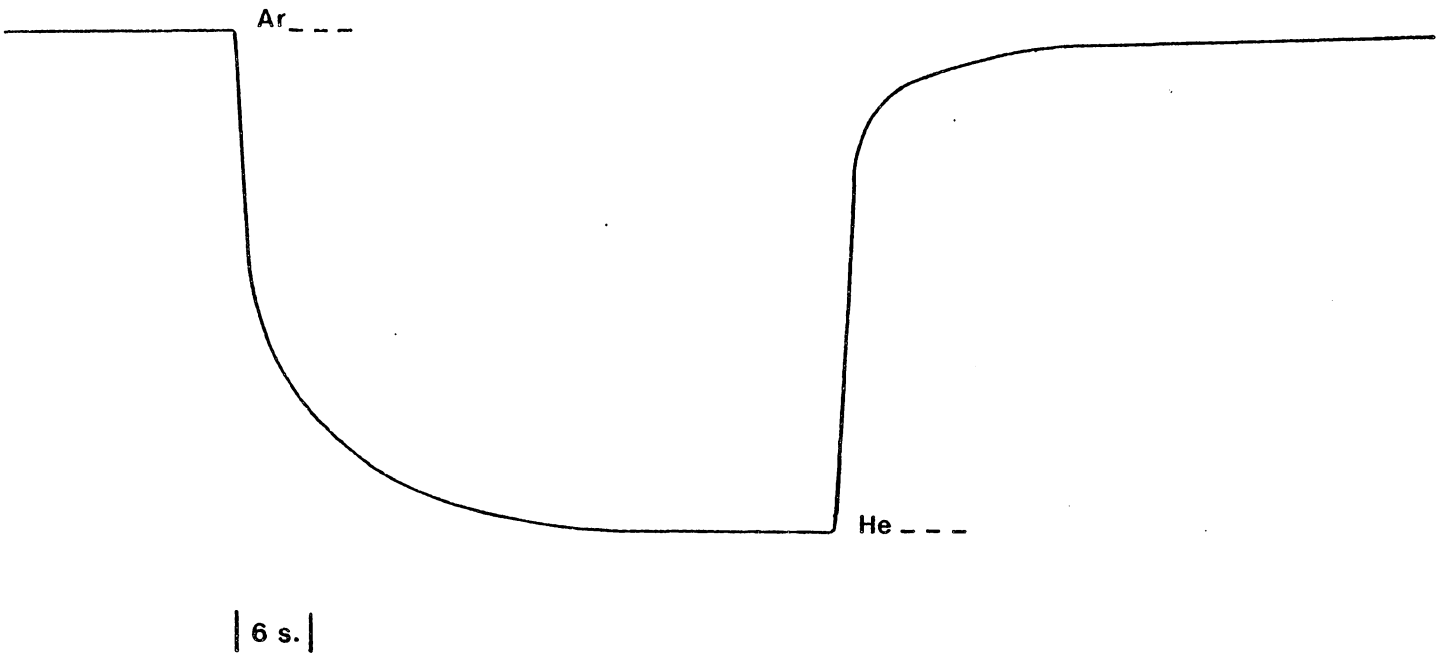

Figure F.20. The Thermal Conductivity Response for Switching Between Helium and Argon Feeds in the Cold-Flow Microreactor Model during Experiment 3-2 (Refer to Table 5.1 for the Experimental Conditions).

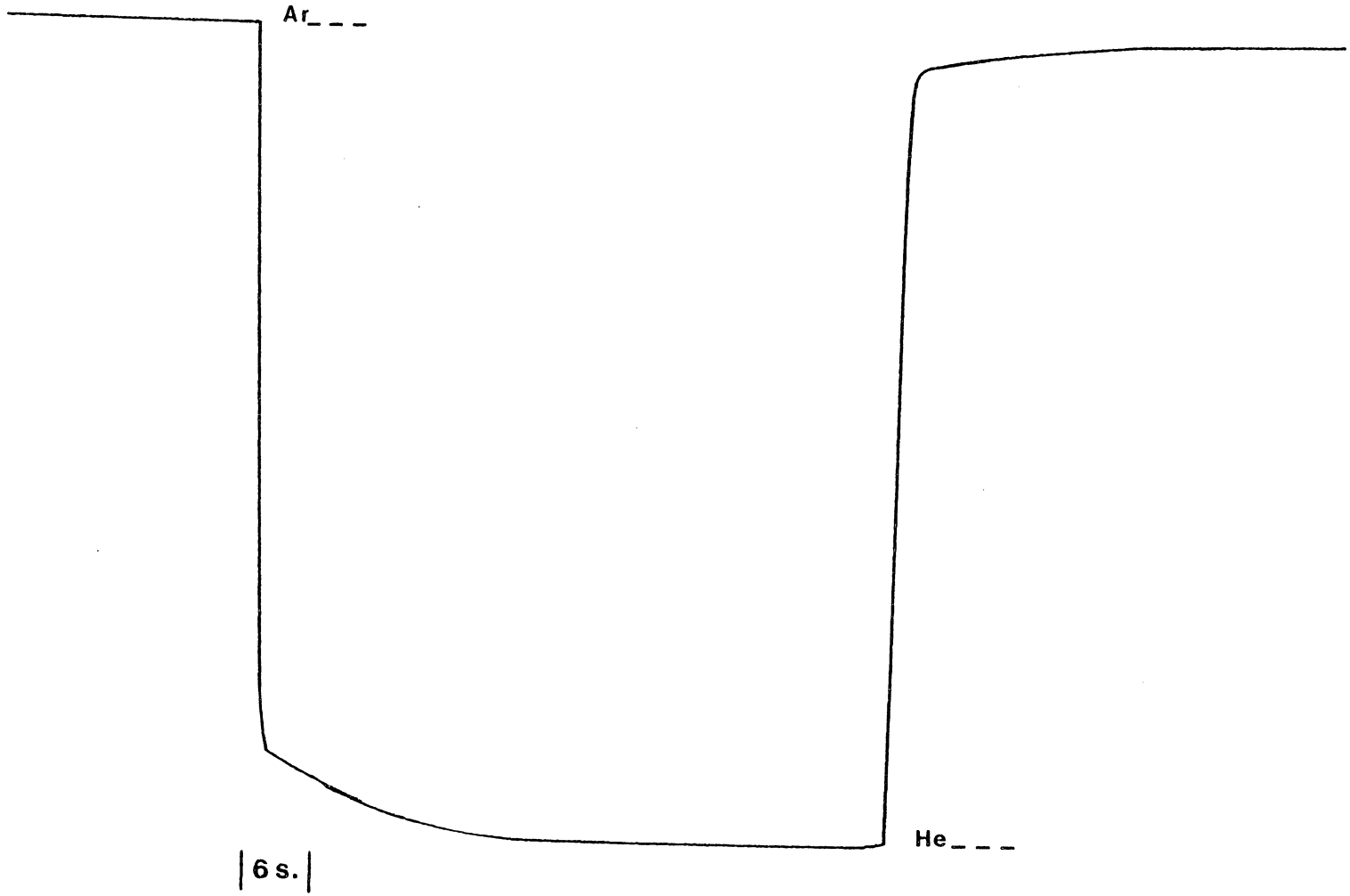

Figure F.21. The Thermal Conductivity Response for Switching Between Helium and Argon Feeds in the Cold-Flow Microreactor Model during Experiment 3-3 (Refer to Table 5.1 for the Experimental Conditions).

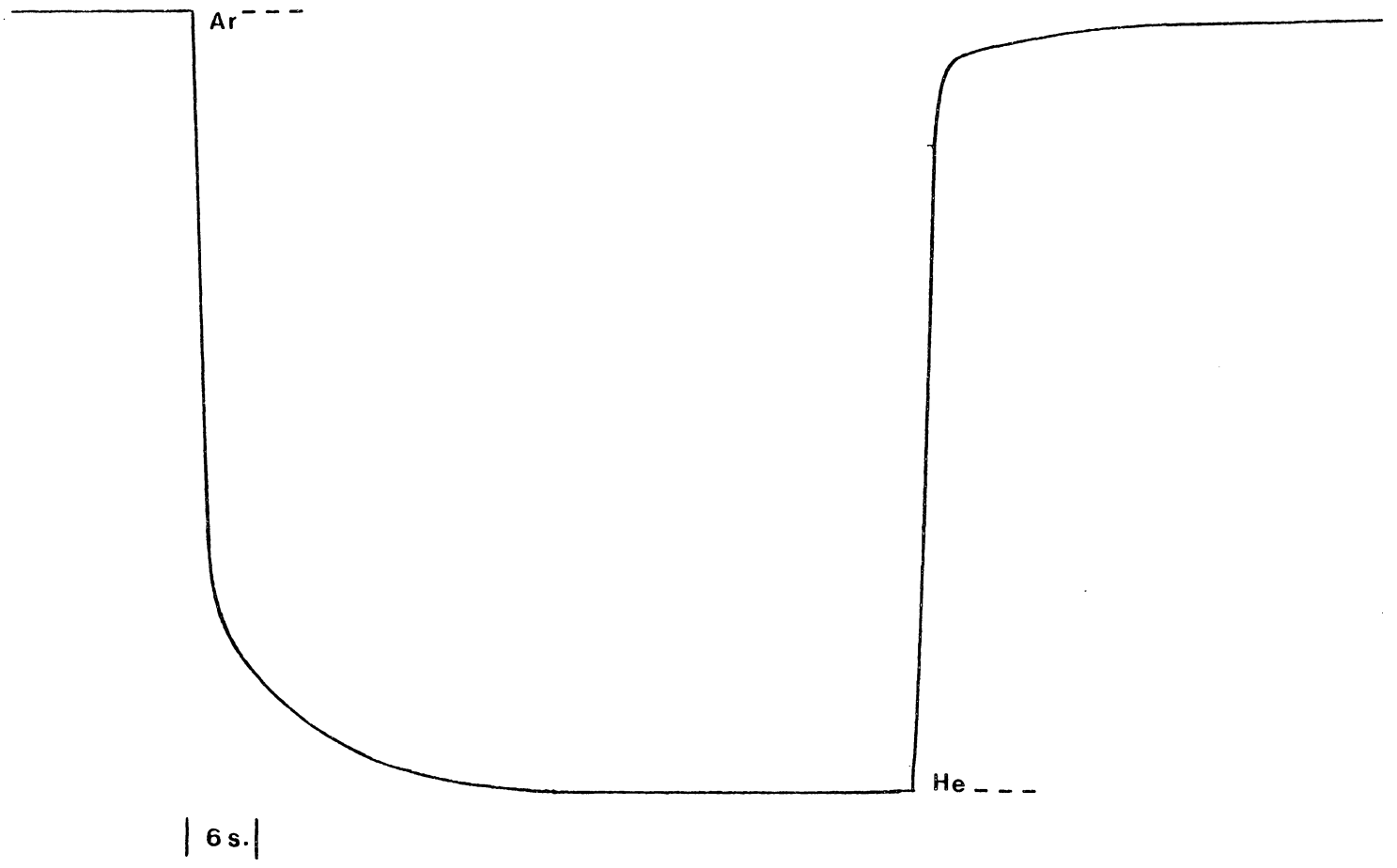

Figure F.22. The Thermal Conductivity Response for Switching Between Helium and Argon Feeds in the Cold-Flow Microreactor Model during Experiment 3-4 (Refer to Table 5.1 for the Experimental Conditions).

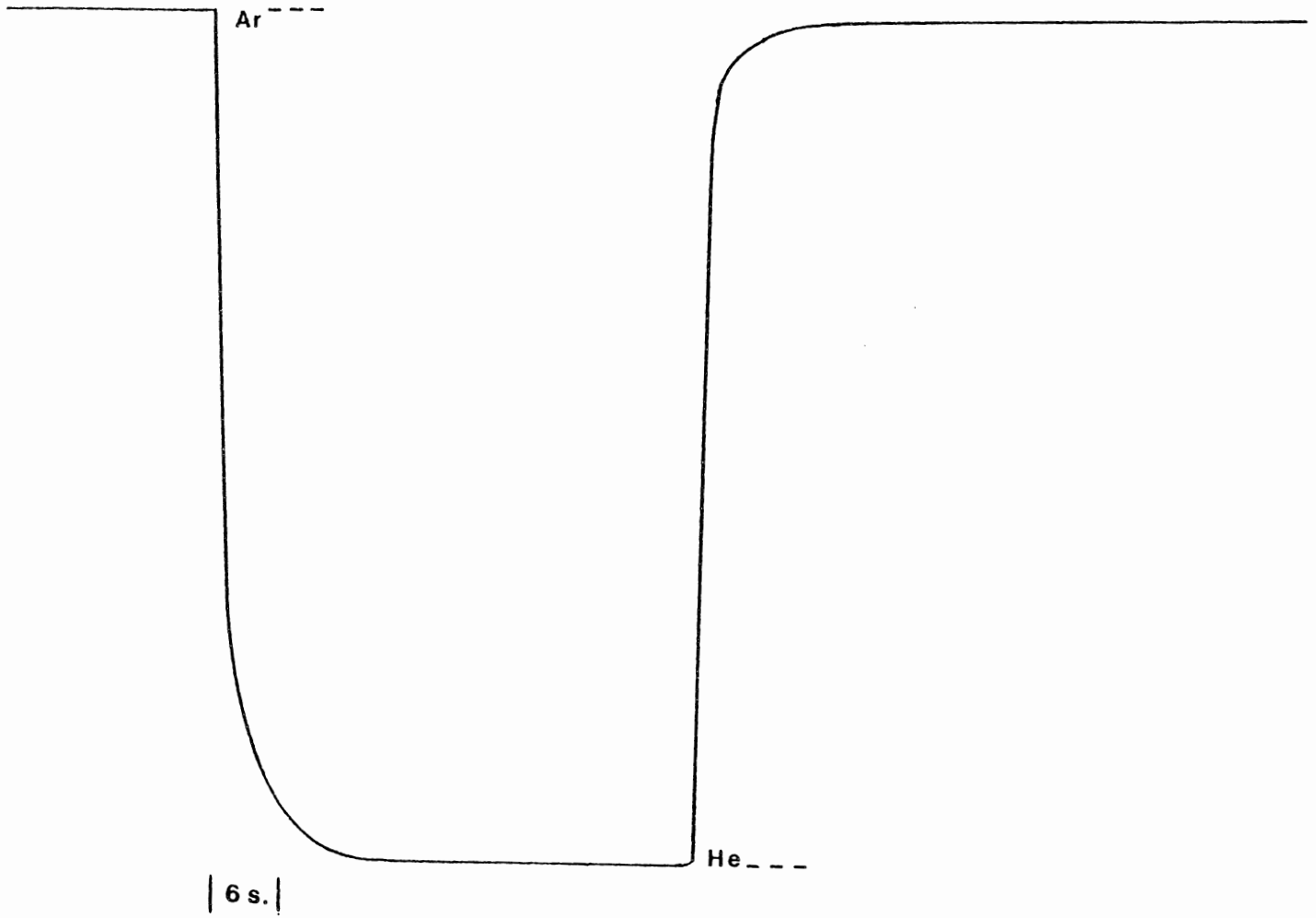

Figure F.23. The Thermal Conductivity Response for Switching Between Helium and Argon Feeds in the Cold-Flow Microreactor Model during Experiment 3-5 (Refer to Table 5.1 for the Experimental Conditions).

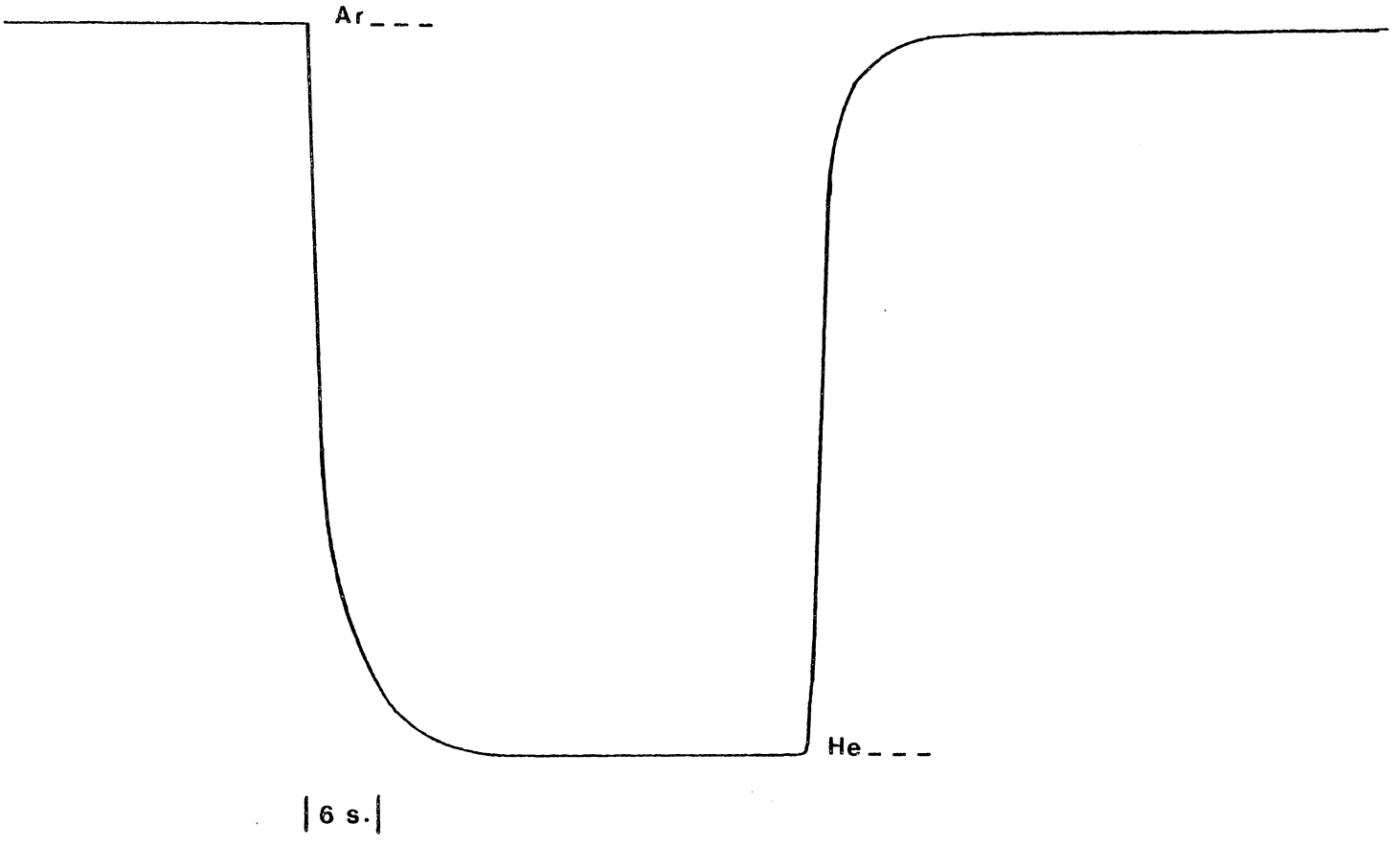

Figure F.24. The Thermal Conductivity Response for Switching Between Helium and Argon Feeds in the Cold-Flow Microreactor Model during Experiment 3-6 (Refer to Table 5.1 for the Experimental Conditions).

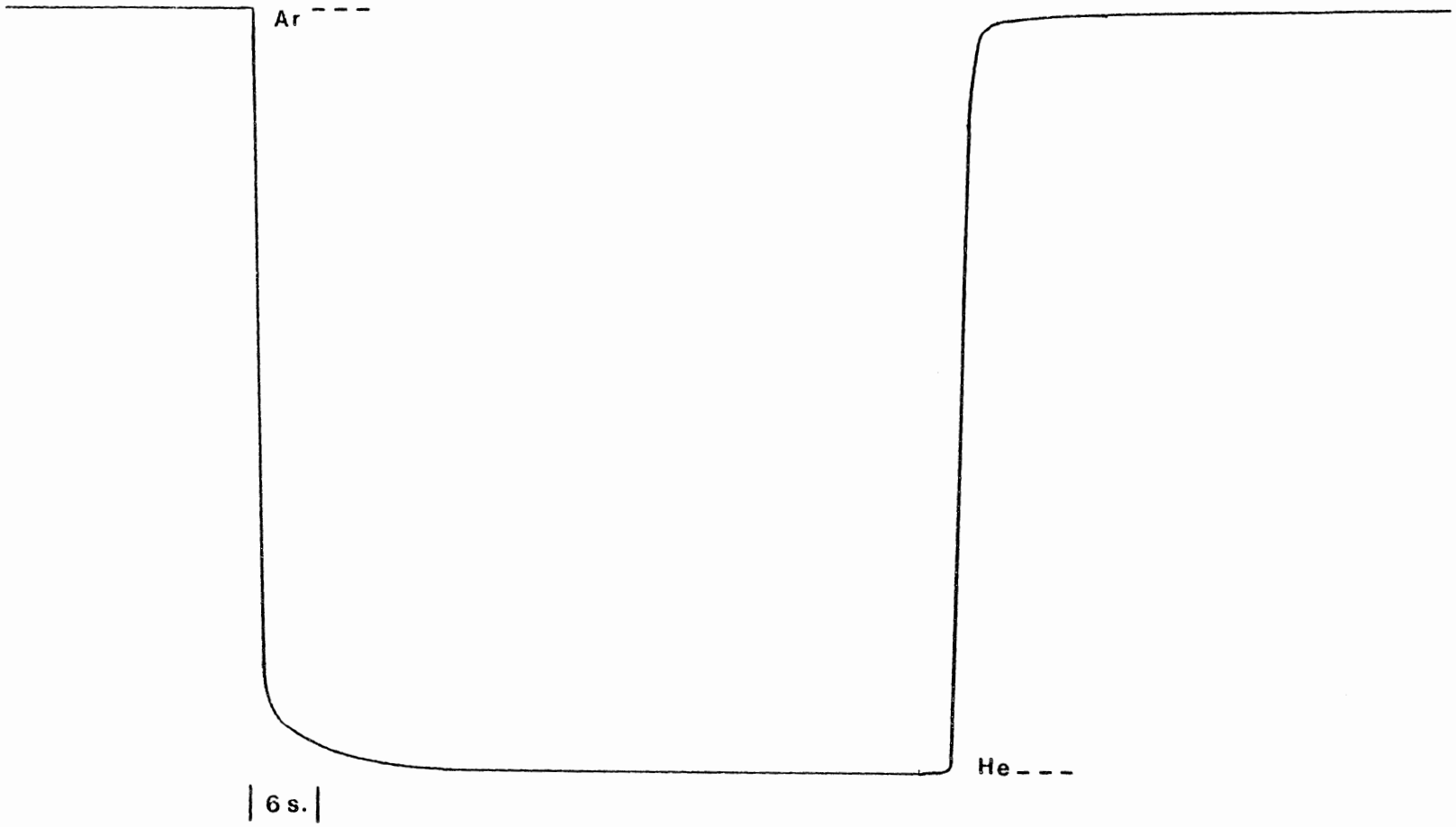

Figure F.25. The Thermal Conductivity Response for Switching Between Helium and Argon Feeds in the Cold-Flow Microreactor Model during Experiment 3-7 (Refer to Table 5.1 for the Experimental Conditions).

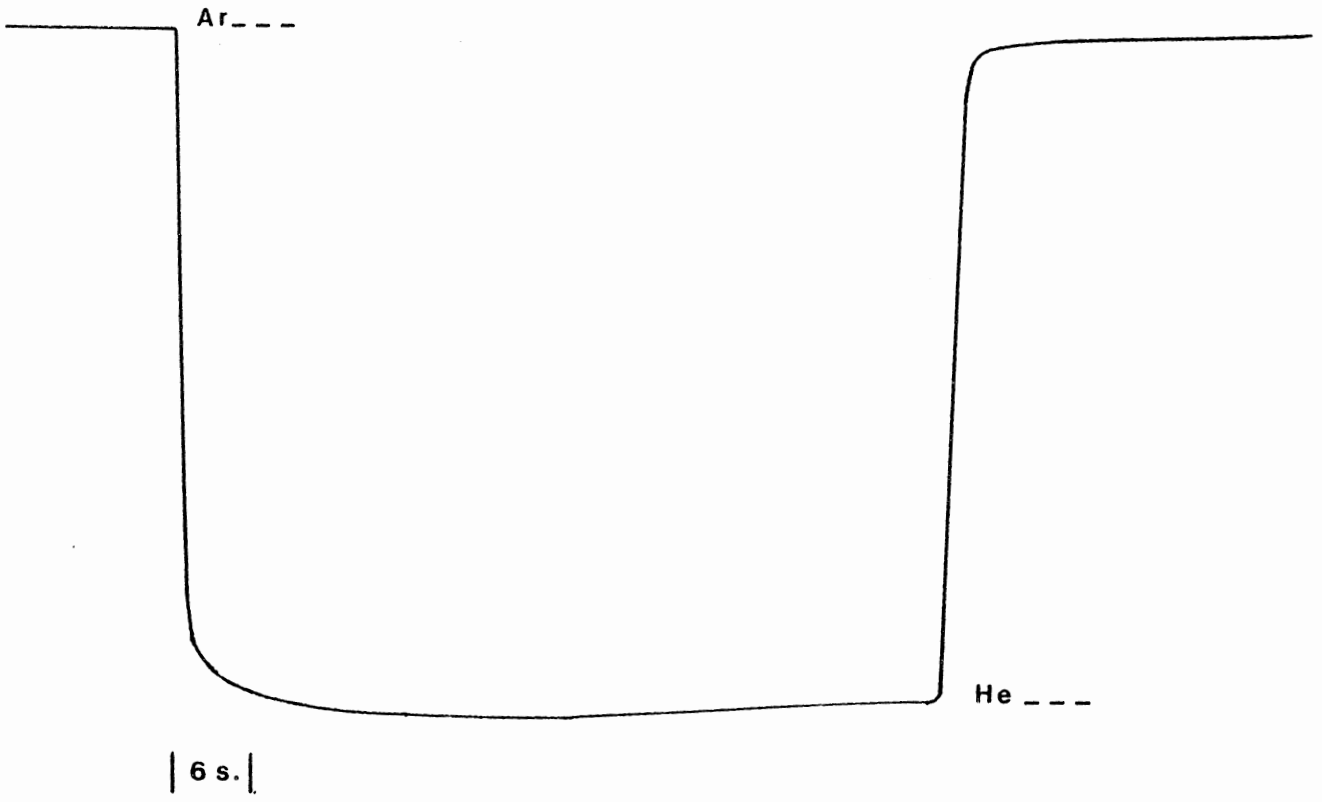

Figure F.26. The Thermal Conductivity Response for Switching Between Helium and Argon Feeds in the Cold-Flow Microreactor Model during Experiment 3-8 (Refer to Table 5.1 for the Experimental Conditions).

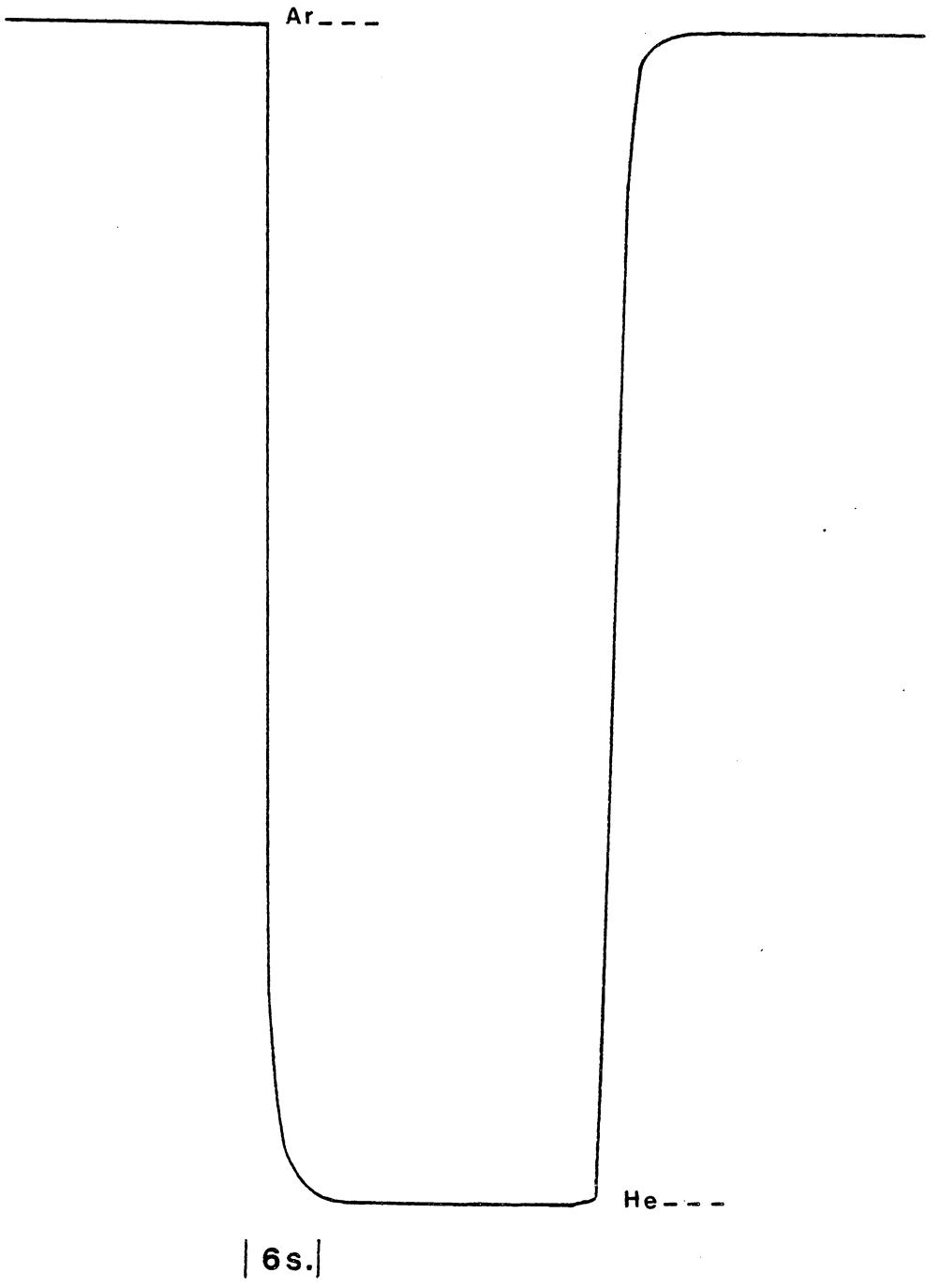

Figure F.27. The Thermal Conductivity Response for Switching Between Helium and Argon Feeds in the Cold-Flow Microreactor Model during Experiment 3-9 (Refer to Table 5.1 for the Experimental Conditions).

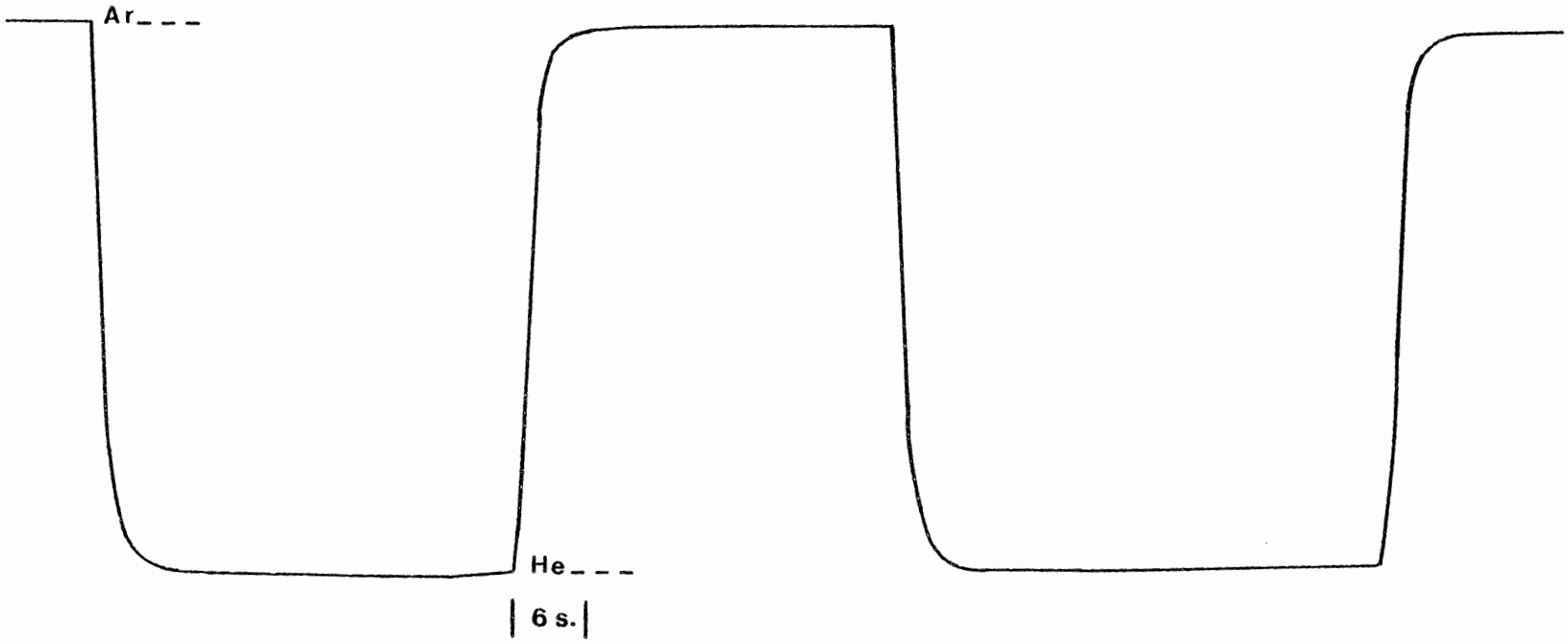

Figure F.28. The Thermal Conductivity Response for Switching Between Helium and Argon Feeds in the Cold-Flow Microreactor Model during Experiment 3-10 (Refer to Table 5.1 for the Experimental Conditions).

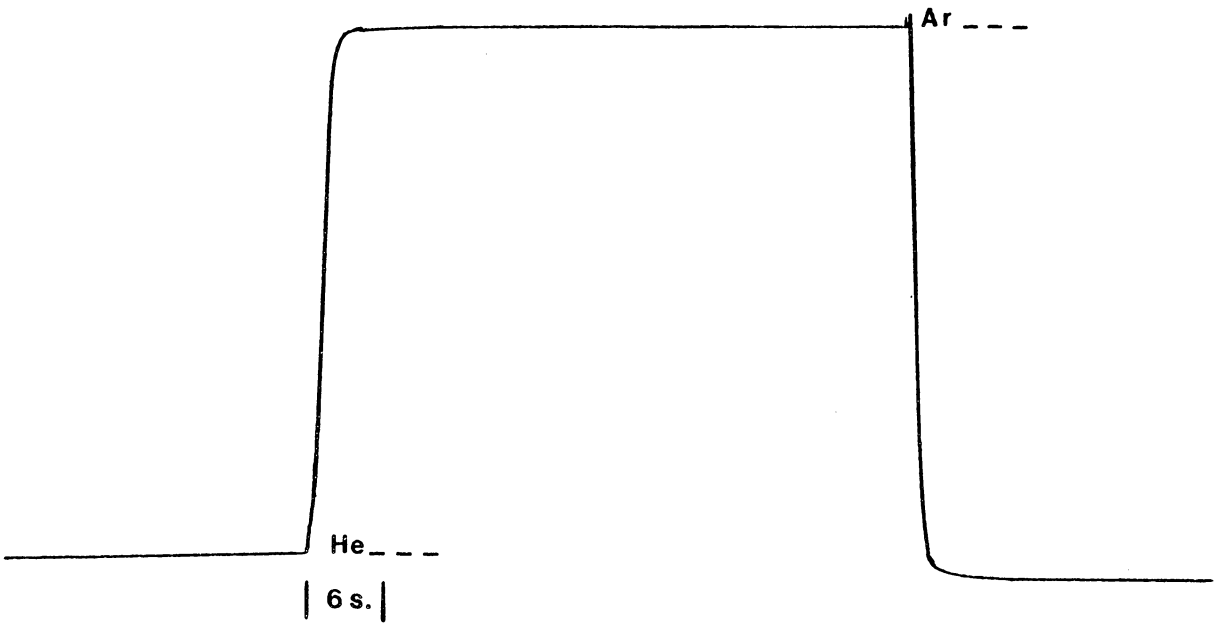

Figure F.29. The Thermal Conductivity Response for Switching Between Helium and Argon Feeds in the Cold-Flow Microreactor Model during Experiment 3-11 (Refer to Table 5.1 for the Experimental Conditions).

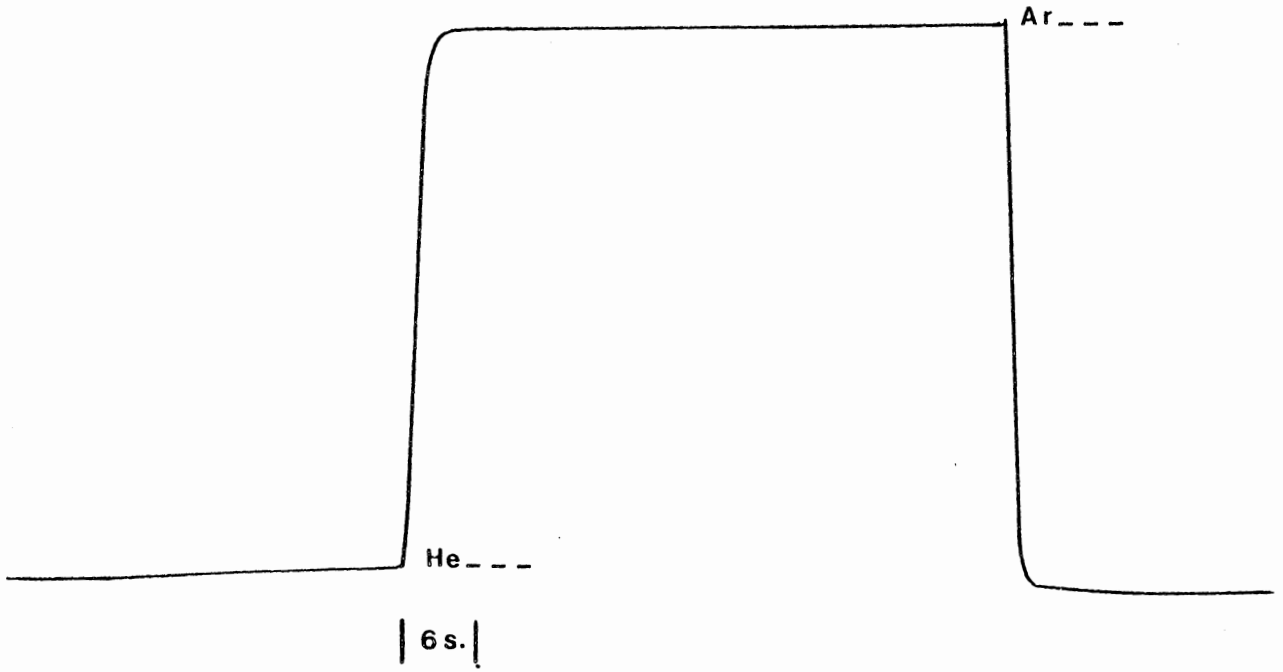

Figure F.30. The Thermal Conductivity Response for Switching Between Helium and Argon Feeds in the Cold-Flow Microreactor Model during Experiment 3-12 (Refer to Table 5.1 for the Experimental Conditions).

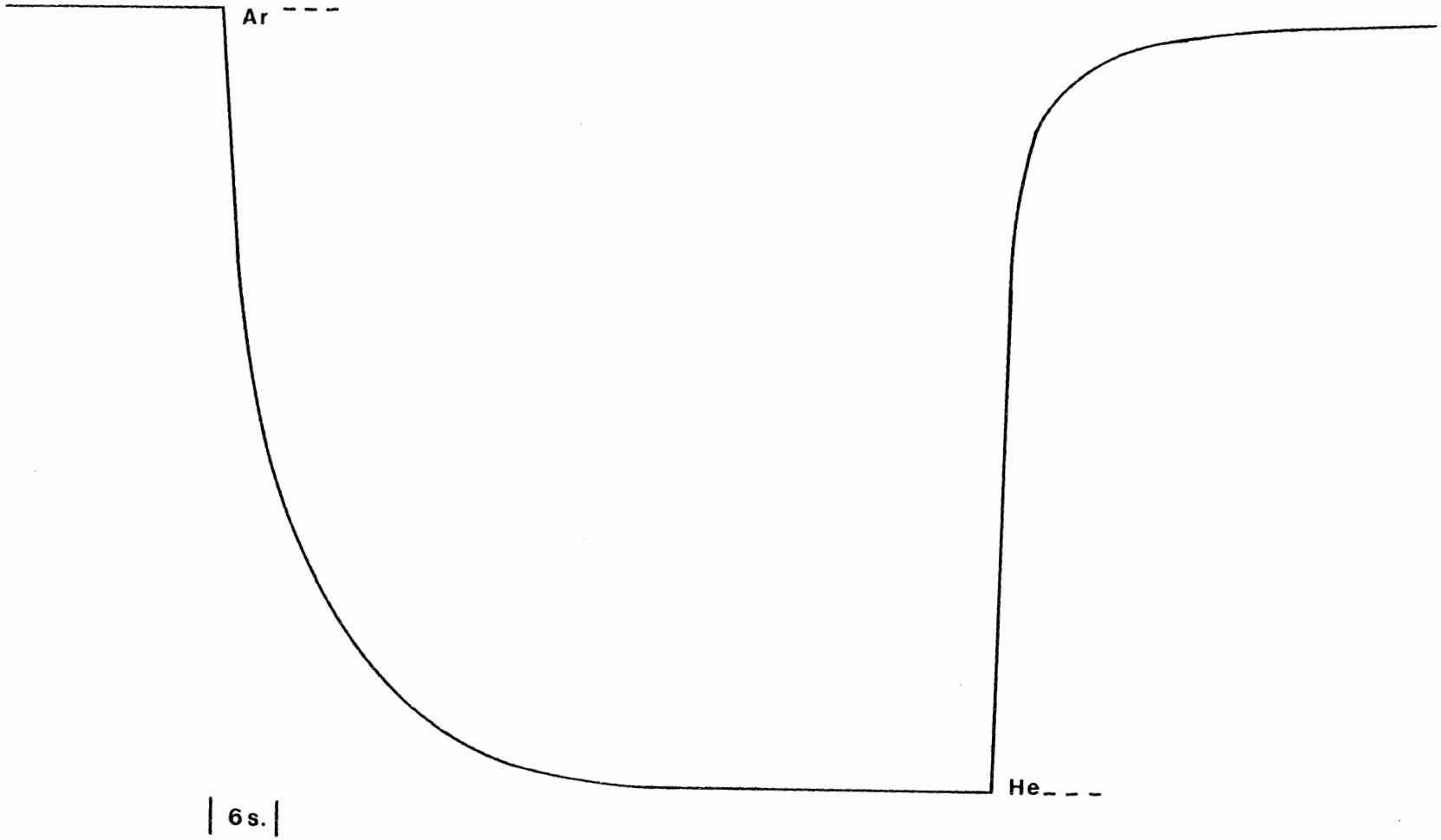

Figure F.31. The Thermal Conductivity Response for Switching Between Helium and Argon Feeds in the Cold-Flow Microreactor Model during Experiment 4-2 (Refer to Table 5.1 for the Experimental Conditions).

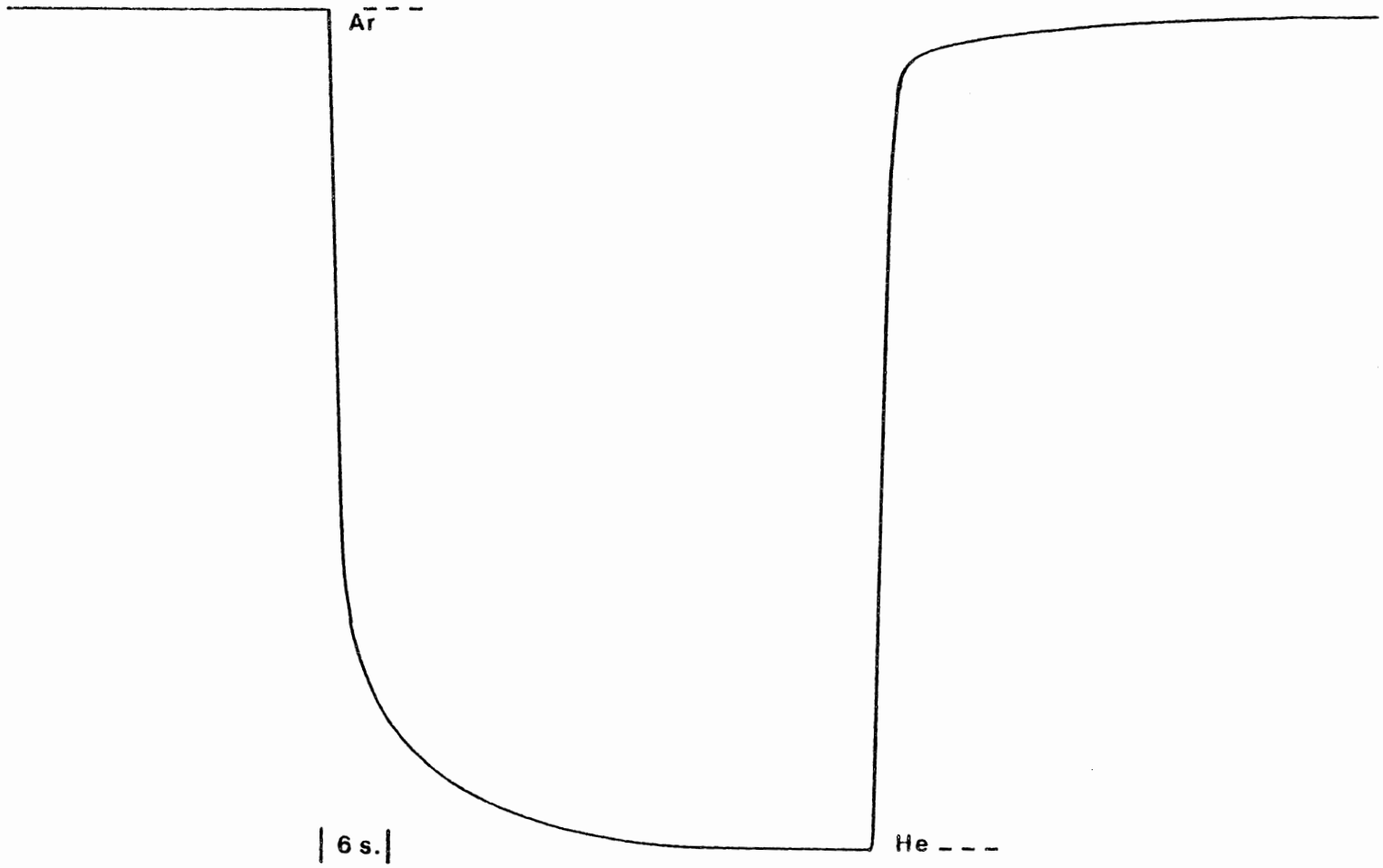

Figure F.32. The Thermal Conductivity Response for Switching Between Helium and Argon Feeds in the Cold-Flow Microreactor Model during Experiment 4-3 (Refer to Table 5.1 for the Experimental Conditions).

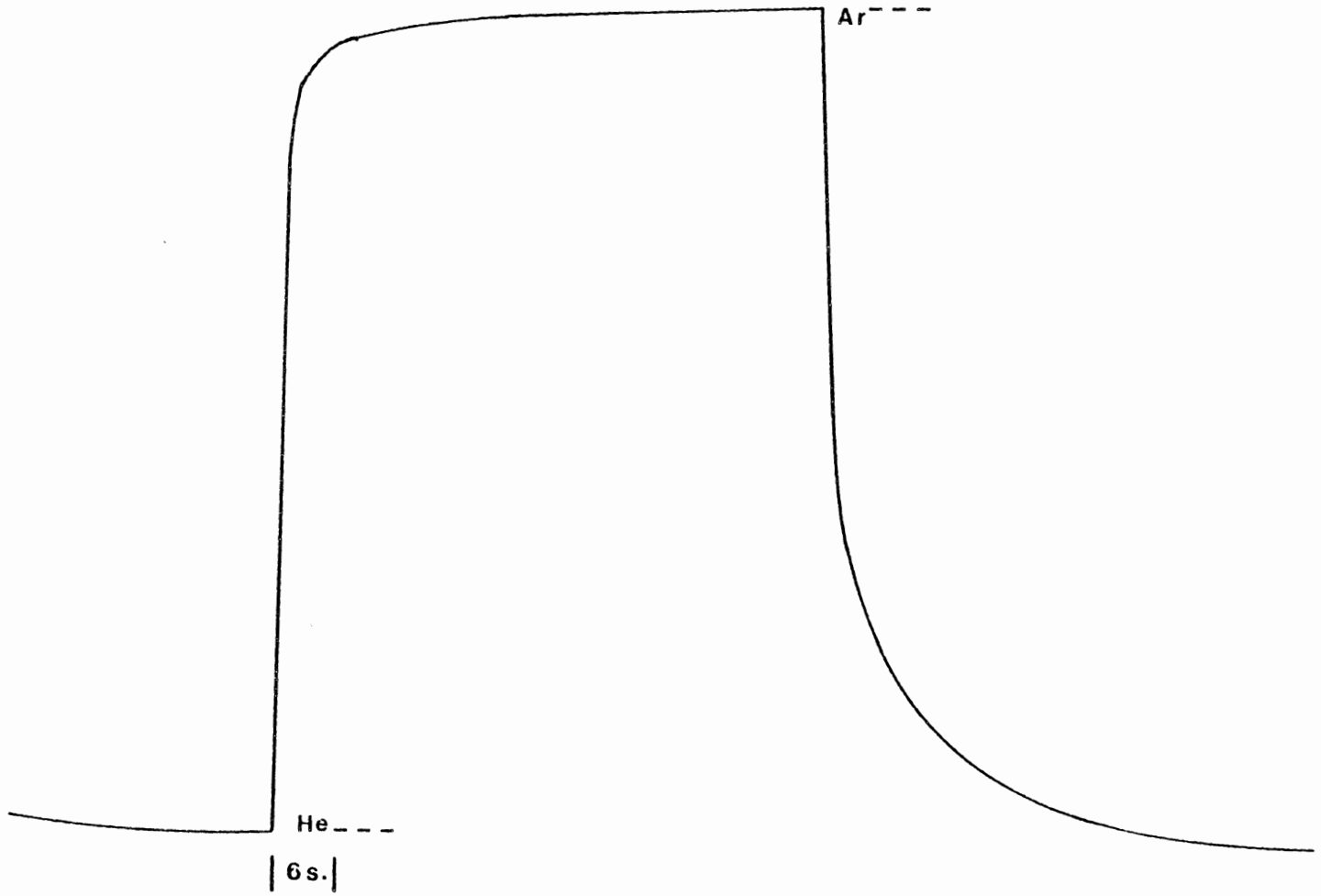

Figure F.33. The Thermal Conductivity Response for Switching Between Helium and Argon Feeds in the Cold-Flow Microreactor Model during Experiment 4-4 (Refer to Table 5.1 for the Experimental Conditions).

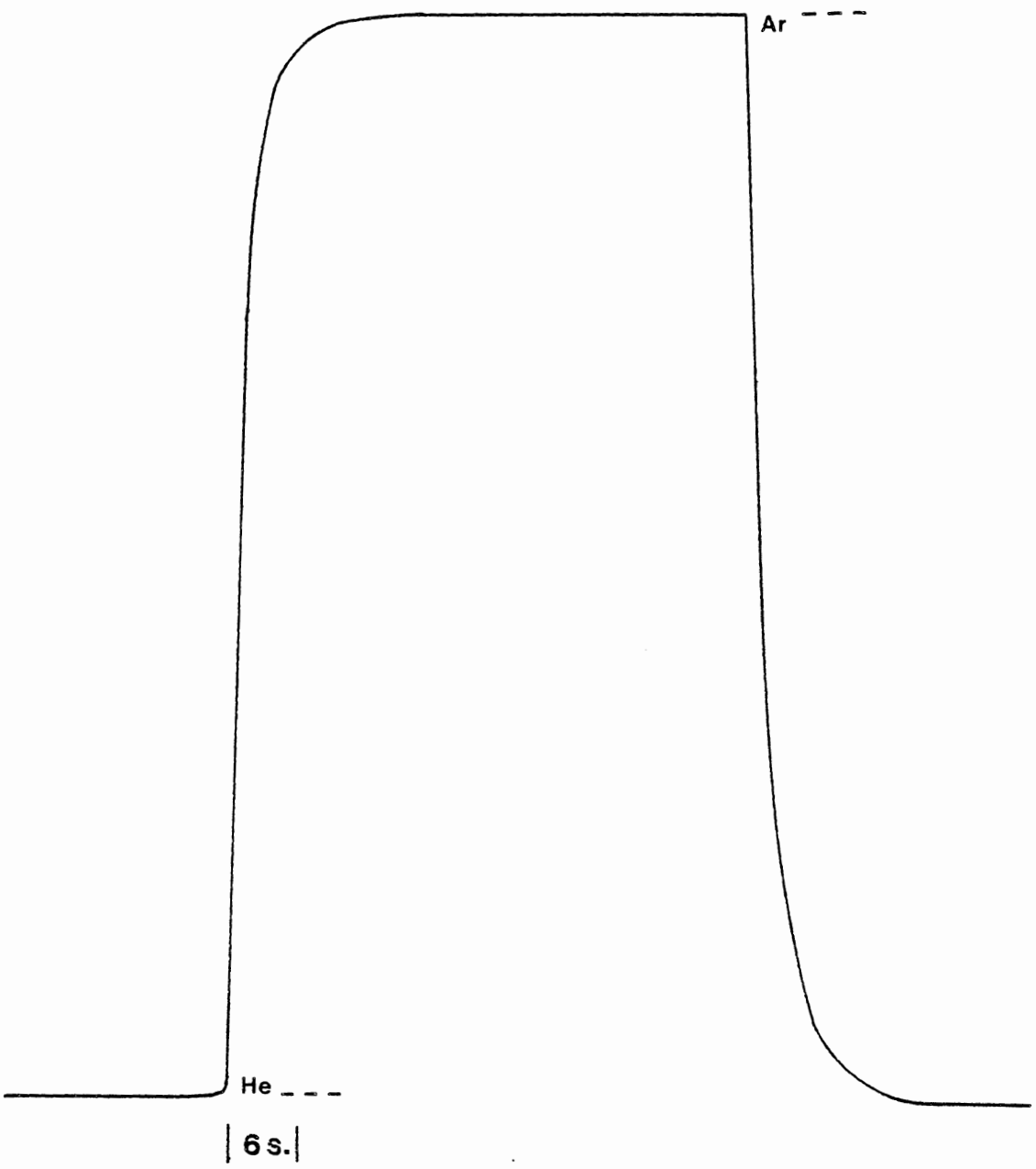

Figure F.34. The Thermal Conductivity Response for Switching Between Helium and Argon Feeds in the Cold-Flow Microreactor Model during Experiment 4-5 (Refer to Table 5.1 for the Experimental Conditions).

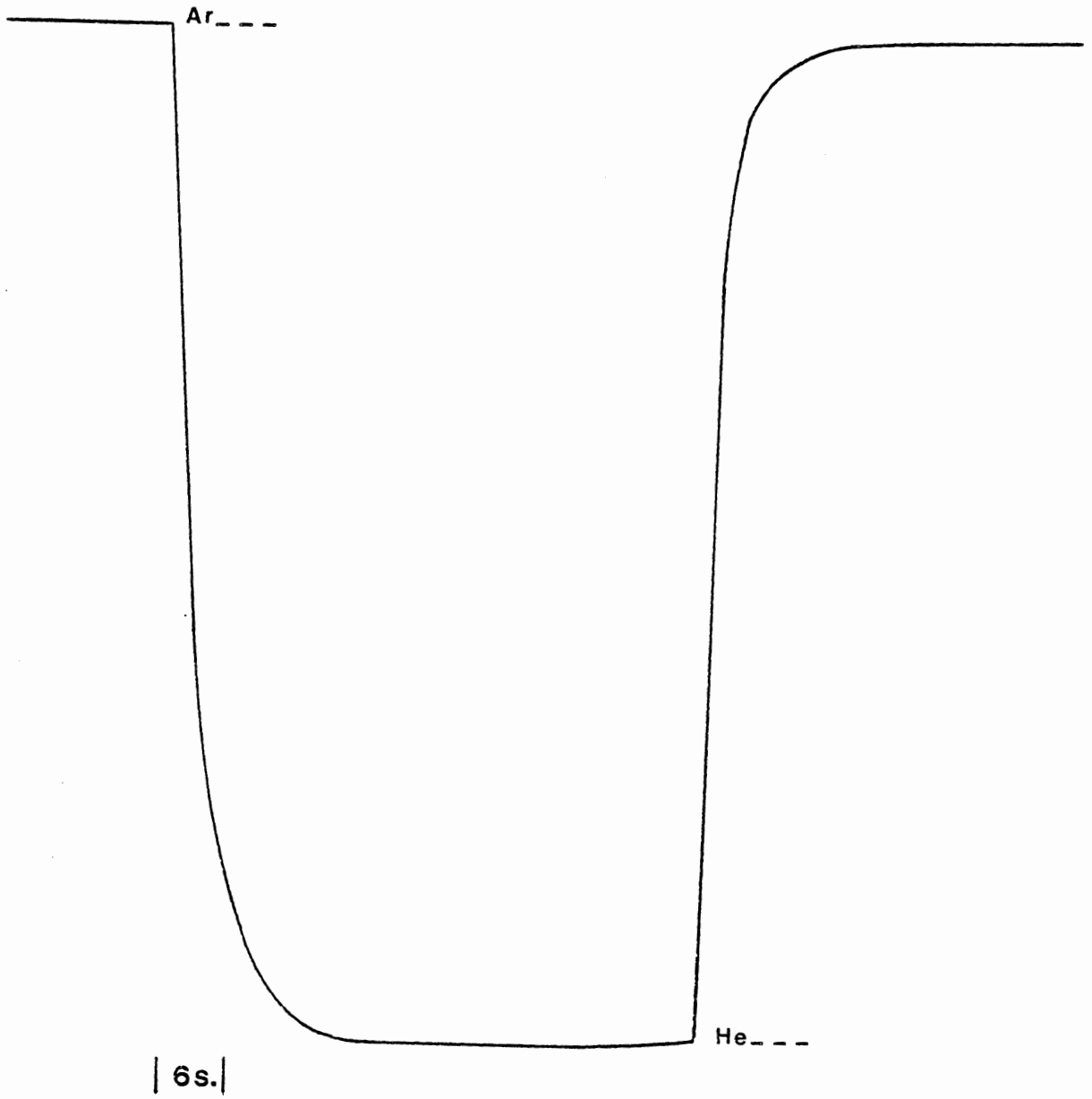

Figure F.35. The Thermal Conductivity Response for Switching Between Helium and Argon Feeds in the Cold-Flow Microreactor Model during Experiment 4-6 (Refer to Table 5.1 for the Experimental Conditions).

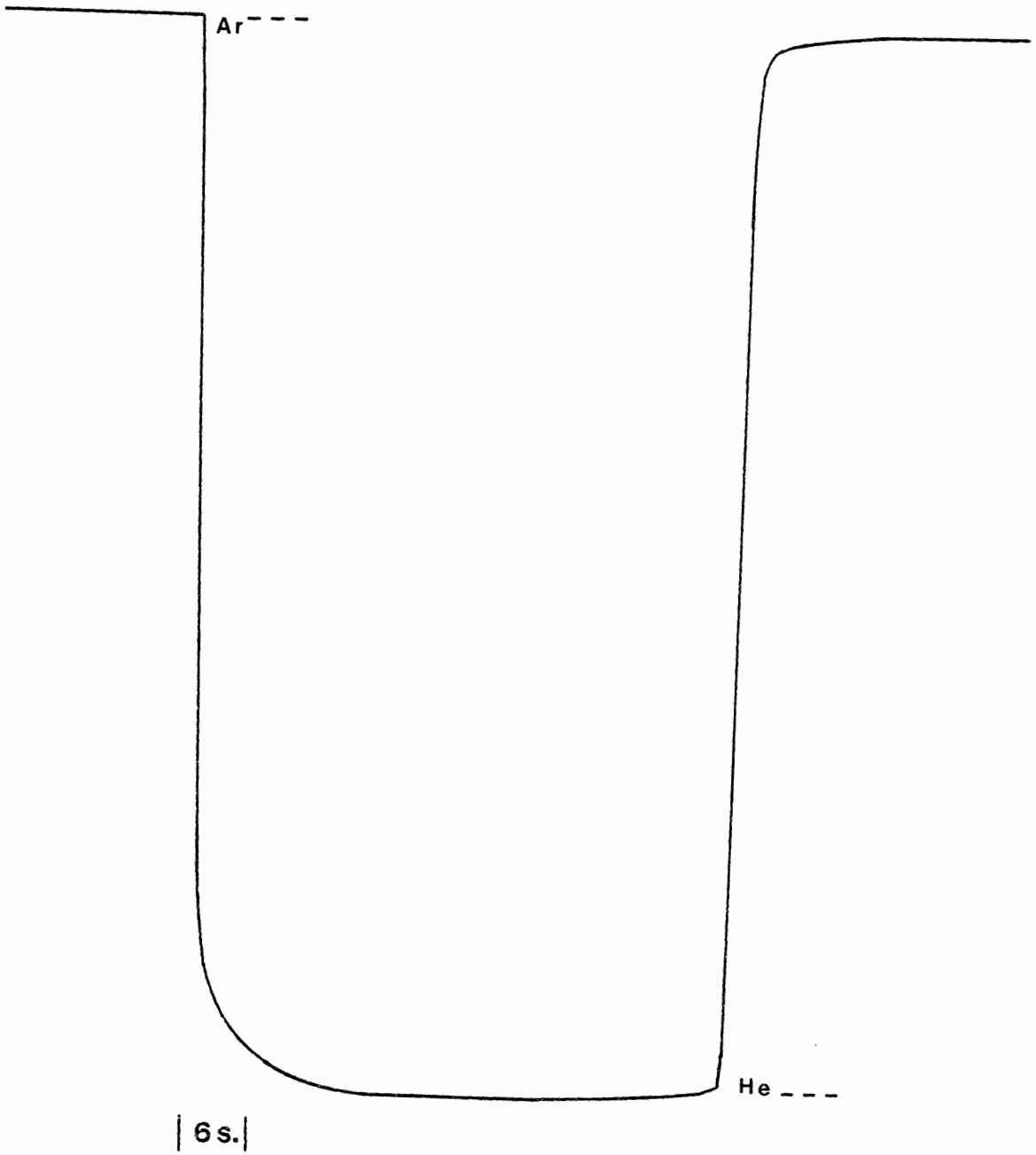

Figure F.36. The Thermal Conductivity Response for Switching Between Helium and Argon Feeds in the Cold-Flow Microreactor Model during Experiment 4-7 (Refer to Table 5.1 for the Experimental Conditions).

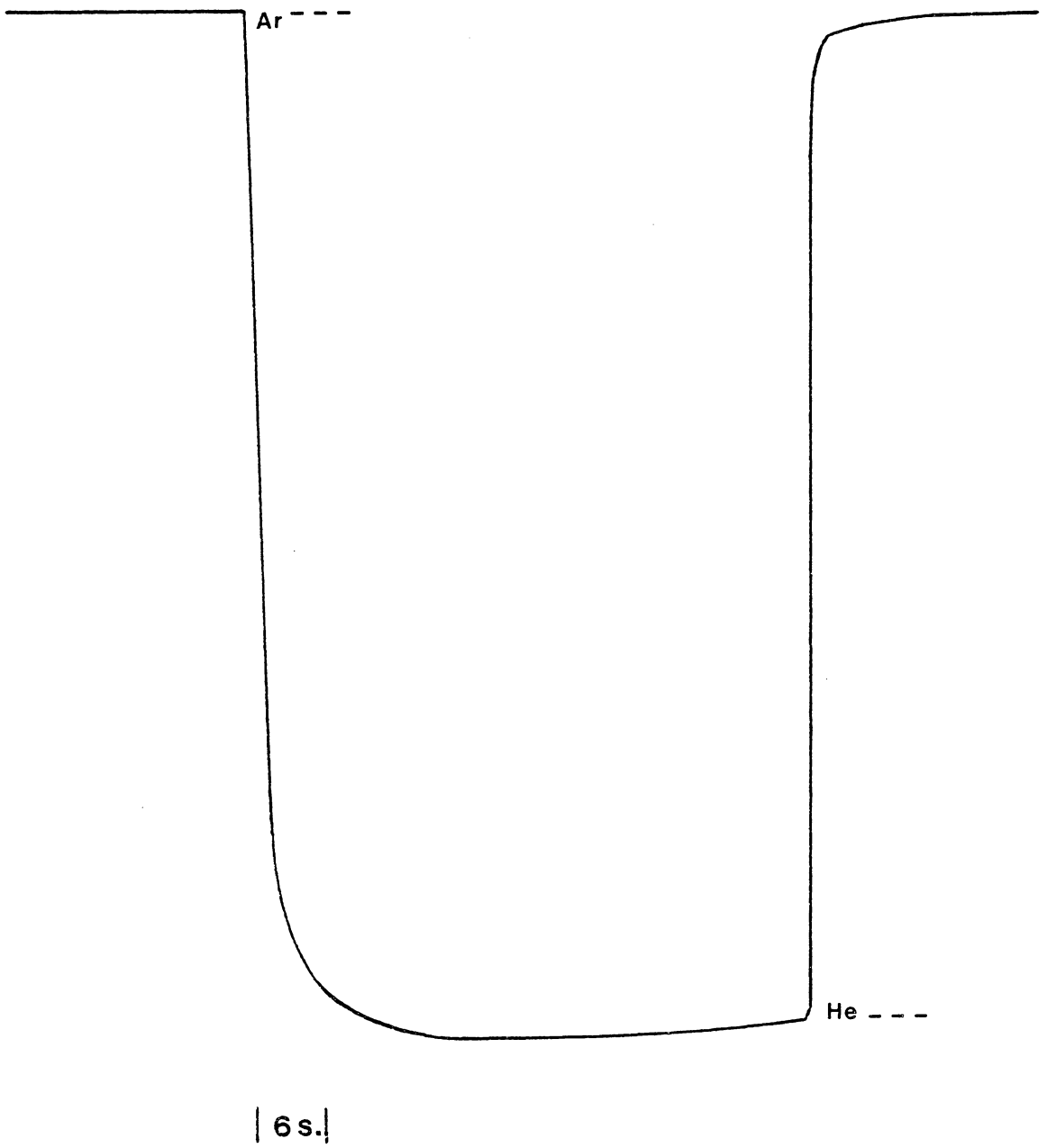

Figure F.37. The Thermal Conductivity Response for Switching Between Helium and Argon Feeds in the Cold-Flow Microreactor Model during Experiment 4-8 (Refer to Table 5.1 for the Experimental Conditions).

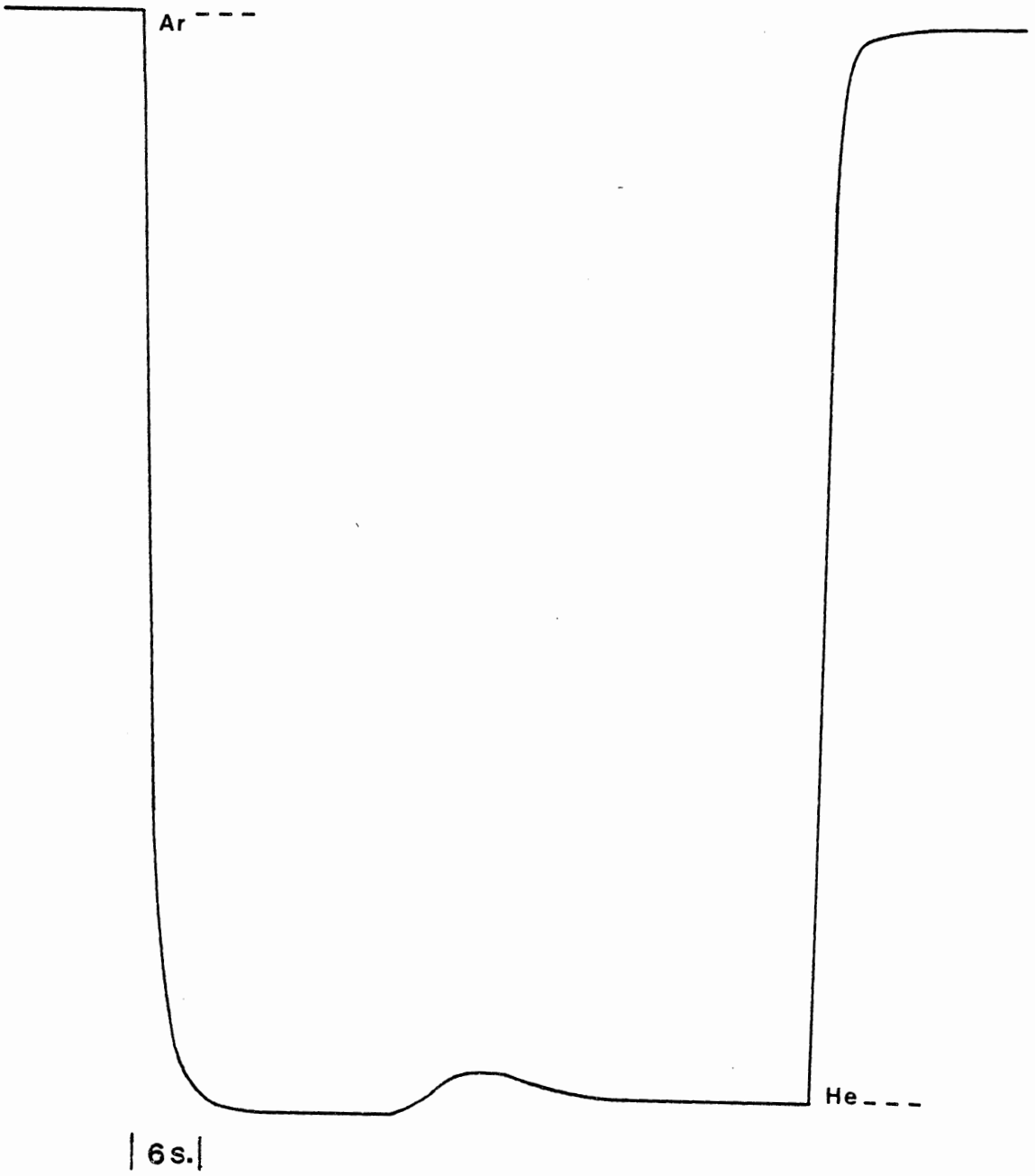

Figure F.38. The Thermal Conductivity Response for Switching Between Helium and Argon Feeds in the Cold-Flow Microreactor Model during Experiment 4-9 (Refer to Table 5.1 for the Experimental Conditions).

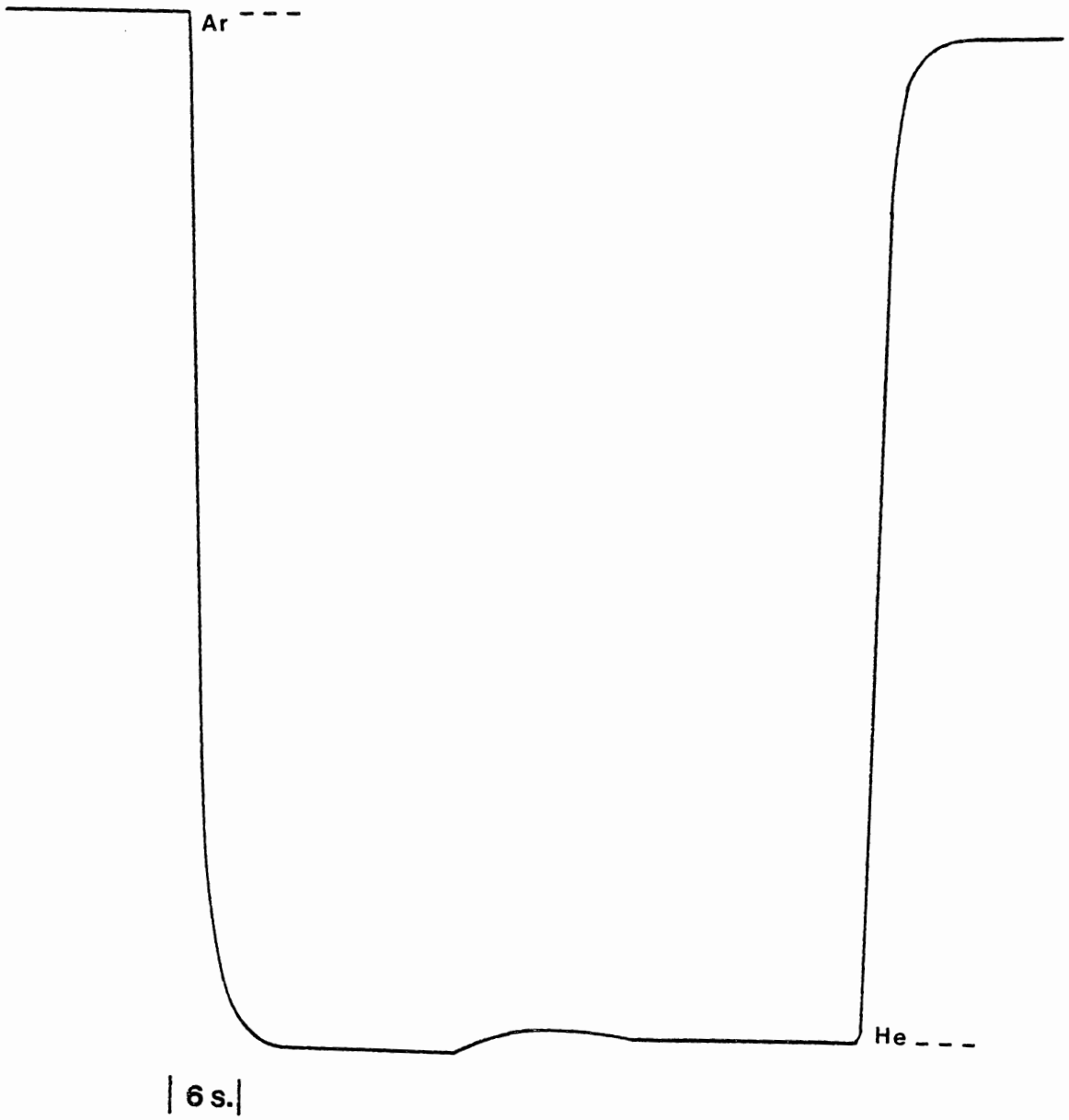

Figure F.39. The Thermal Conductivity Response for Switching Between Helium and Argon Feeds in the Cold-Flow Microreactor Model during Experiment 4-10 (Refer to Table 5.1 for the Experimental Conditions).

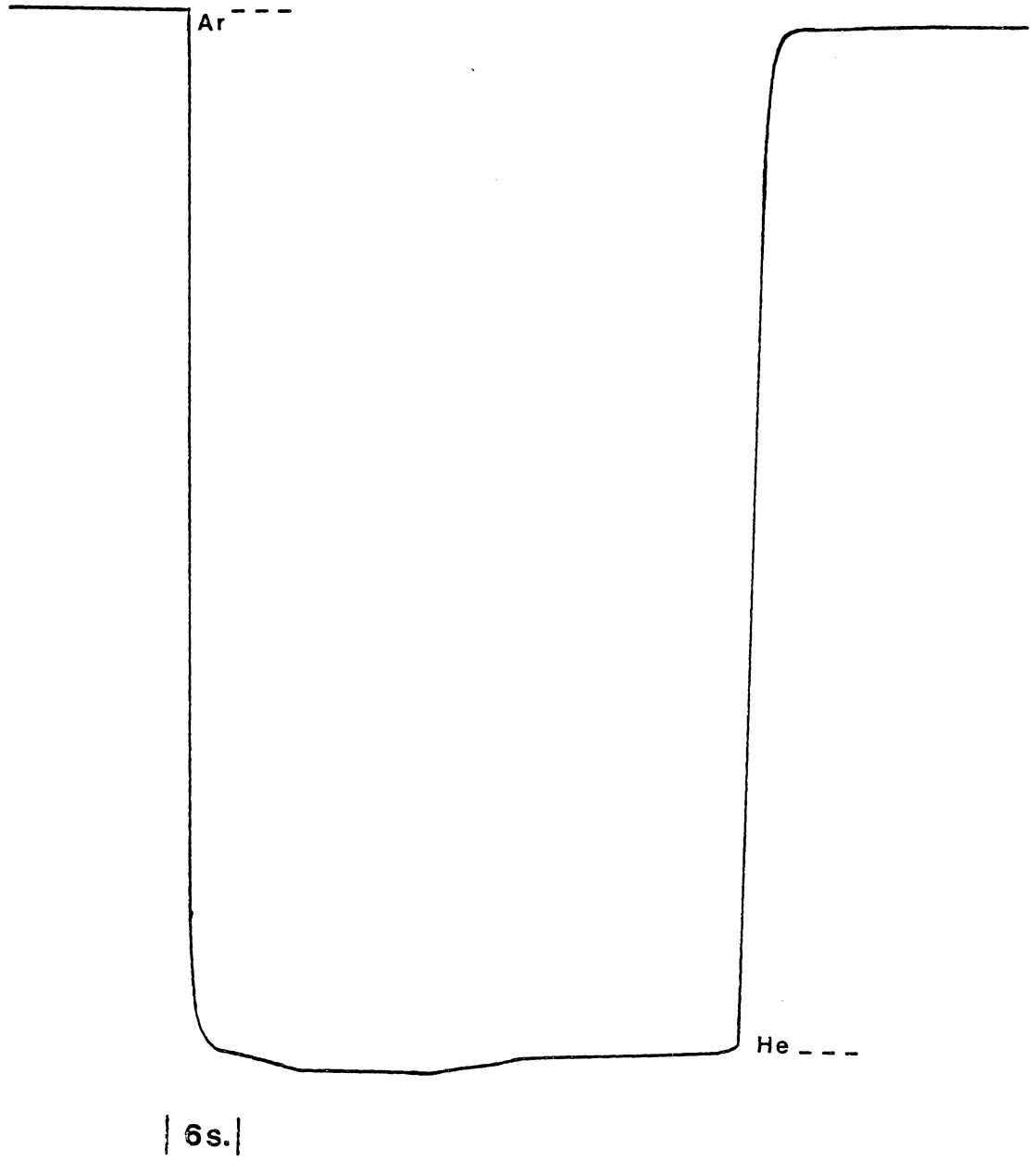

Figure F.40. The Thermal Conductivity Response for Switching Between Helium and Argon Feeds in the Cold-Flow Microreactor Model during Experiment 4-11 (Refer to Table 5.1 for the Experimental Conditions).

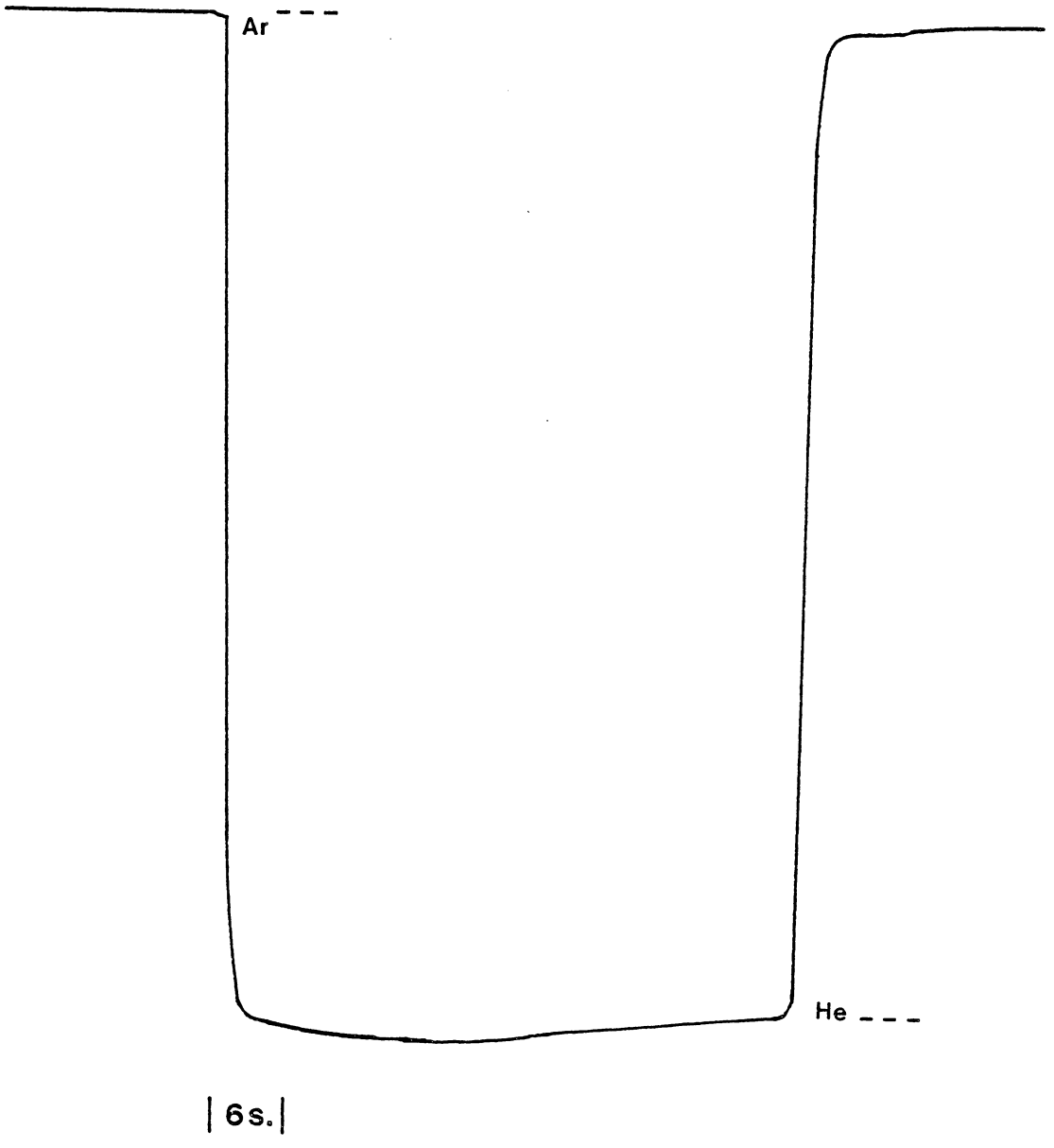

Figure F.41. The Thermal Conductivity Response for Switching Between Helium and Argon Feeds in the Cold-Flow Microreactor Model during Experiment 4-12 (Refer to Table 5.1 for the Experimental Conditions).

The vita has been removed from the scanned document